Hybrid Cardiac Imaging

Stephan G. Nekolla
Christoph Rischpler
Editors

Springer

Hybrid Cardiac Imaging

Stephan G. Nekolla • Christoph Rischpler
Editors

Hybrid Cardiac Imaging

Springer

Editors
Stephan G. Nekolla
Department of Nuclear Medicine
Technical University Munich
Munich
Germany

Christoph Rischpler
Department of Nuclear Medicine
University of Duisburg-Essen
Essen, Nordrhein-Westfalen
Germany

ISBN 978-3-030-83166-0 ISBN 978-3-030-83167-7 (eBook)
https://doi.org/10.1007/978-3-030-83167-7

This Springer imprint is published by the registered company Springer Nature Switzerland AG
The registered company address is: Gewerbestrasse 11, 6330 Cham, Switzerland

Preface

It was our great pleasure to compile this book as an up-to-date review on the various hybrid imaging modalities that may be employed for the purpose of cardiac imaging. We both spent quite some time together in front of those hybrid systems and later analyzing and integrating data—sharing frustrations but predominately enjoying the wealth of information such systems are capable of generating.

After discussion of generic aspects of hybrid imaging, SPECT/CT, PET/CT, and PET/MRI are each considered in depth. In addition, information is provided on upcoming technologies, such as dedicated so-called fast cardiac cameras (CZT detector technology) and novel probes and radiotracers. We tried to address a wide variety of topics, including important technological aspects, possible applications, imaging protocols, and peculiarities of the available modalities. Last but not least, an estimation of the cost efficiency of dedicated and hybrid imaging devices in cardiology is provided and possible scenarios with respect to health care economics are described.

The editors would like to thank all the chapter authors for their competent inspiring contributions. We appreciate the support by Springer and sincerely hope that this book might support the interdisciplinary community working in this fascinating field.

Munich, Germany — Stephan G. Nekolla
Essen, Germany — Christoph Rischpler

Contents

Part I

Generic Aspects of Hybrid Imaging

Hybrid Imaging and Healthcare Economics

1

Danilo Neglia, Valentina Lorenzoni, and Giuseppe Turchetti

Owing to the rapid technological advancement in cardiovascular diagnostic imaging, many non-invasive diagnostic tests are currently available which either evaluate cardiac anatomy or function or both. Although these tests are relatively non-invasive, they still pose a burden to the individual patient, the healthcare system, and society at large, because they are associated with significant patient time, costs, radiation exposure, and the risk of adverse events. Nevertheless, physicians often request multiple tests in order to increase their confidence in the diagnosis and treatment plan of patients. In order to minimize risks and burden to patients, radiation exposure, and healthcare costs, diagnostic algorithms have been developed which define a sequence of tests, where the choice of each imaging modality is determined by patient characteristics and the results of previously performed diagnostic tests. Imaging algorithms recommended by guidelines vary widely, demonstrating variability in clinical practice and attesting to the uncertainty about which imaging algorithm is optimal in terms of both costs and outcomes, i.e. is cost-effective.

In many clinical scenarios one of the reasons for multiple imaging testing is the need to complement anatomical information, best provided by some modalities, with functional information best provided by others. In this respect the introduction of "hybrid" imaging, i.e. the combination and/or fusion of two imaging modalities, has been considered a relevant advancement [1]. The term "hybrid imaging" is generally applied for the combination of images providing additional anatomical and

D. Neglia (✉)
Fondazione Toscana Gabriele Monasterio, Pisa, Italy

Faculty PhD Course "Translational Medicine", Scuola Superiore Sant'Anna, Pisa, Italy
e-mail: dneglia@ftgm.it

V. Lorenzoni · G. Turchetti
Institute of Management, Scuola Superiore Sant'Anna, Pisa, Italy

S. G. Nekolla, C. Rischpler (eds.), *Hybrid Cardiac Imaging*,
https://doi.org/10.1007/978-3-030-83167-7_1

functional information beyond that achievable with either imaging modality alone, possibly leading to a more effective management of the patient. Different imaging datasets can be used from various modalities such as Coronary CT angiography (CTCA), single photon-emission CT (SPECT), positron emission tomography (PET), and cardiac magnetic resonance imaging (CMR). Images may be acquired on a hybrid scanner or by separate stand-alone devices with manual, software-based co-registration of both datasets for fusion. For some clinical indications and in some sites with appropriate infrastructure and tracer availability single session hybrid imaging may be a good option since it gives obvious potential benefits for the patients. For some other clinical indications and sites, however, the use of stand-alone scanners in sequence may be more efficient because it allows to keep some flexibility with regard to scanner occupation, to apply best imaging protocols for each modality and because of the difficulty in predicting a priori which patients would benefit from the dual scanning. Furthermore, most advanced scanners, such as high-end CT systems allowing imaging of the entire heart region within a single heartbeat, are currently not offered in hybrid configurations. Therefore, the practical approach for overall clinical effectiveness and the minimization of the cost and radiation dose may be sequential scanning, facilitated by software tools for automatic image registration and fusion [2].

At present, no health-economic evaluation of cardiac "hybrid" imaging is available which takes into account all these factors, i.e. its clinical effectiveness as well as direct and indirect costs, to demonstrate whether and in which patients it may be more cost-effective than a traditional imaging approach [2, 3]. However, there are increasing evidences that applying the "hybrid" imaging concept, i.e. the appropriate combination and fusion of anatomical and functional imaging modalities, may be useful in terms of costs and outcomes in some clinical scenarios.

1.1 Hybrid Imaging in Stable CAD (SCAD): CTCA and MPI

In the evaluation of patients with known or suspected stable coronary artery disease (CAD) the use of an anatomical-functional "hybrid" imaging approach is promising from both a clinical and healthcare economics perspective.

CTCA permits direct visualization of both the lumen and the walls of the coronary arteries and thus is a robust tool for identifying the presence and extent of CAD and for providing prognostic information. From the diagnostic endpoint, numerous studies have confirmed the high negative predictive value (NPV) and sensitivity of CTCA which thus can reliably "rule out" the presence of anatomical disease. On the other hand, however, the positive predictive value (PPV) and specificity of this modality are typically lower, in particular to detect functionally significant coronary lesions [4]. For this reason and for pathophysiologic considerations, i.e. the concept that an anatomic coronary lesion does not necessarily imply a "functionally significant" disease, a purely anatomical CTCA-guided diagnostic strategy is suboptimal to "rule in" patients requiring invasive coronary angiography (ICA) as potential candidates to revascularization. Functional measurements such as FFR_{CT} have been

recently developed to complement traditional CTCA imaging even if they have not yet gained widespread clinical use. In a multicentre, prospective study of stable symptomatic patients with suspected CAD, an evaluation strategy based on use of CTCA selectively augmented by FFR_{CT} was associated with a high rate (60%) of cancellation of planned invasive catheterization a significantly lower rate of ICA showing no obstructive CAD with significantly lower resource utilization and cost as compared with standard care [5]. These findings suggest that the combination of anatomic and functional imaging data may safely reduce the use of invasive catheterization and costs of care in selected patients undergoing evaluation for suspected CAD without no negative effect on clinical outcome.

Following a similar concept CTCA can be complemented with functional myocardial perfusion imaging (MPI). Traditional MPI includes SPECT, PET, and CMR. These modalities identify stress-induced wall motion abnormalities or regional myocardial perfusion defects and abnormal flow reserve. They have an established role in identifying patients with flow-limiting coronary stenoses or, in the case of angiographically normal coronary vessels, functional coronary/microvascular disease. In pooled analyses, the sensitivity and specificity of MPI to diagnose functionally significant obstructive CAD (documented by invasive FFR) is typically between 70 and 90% and 75 and 94%, respectively [4]. However, in real-world practice MPI has a lower accuracy for a number of reasons such as suboptimal quality of protocols and images and lower prevalence of obstructive disease in current populations which increase the likelihood of false negative and false positive studies decreasing sensitivity and specificity [6]. A hybrid approach combining MPI and CTCA has the advantage of fusing the anatomic CTCA derived data with functional MPI perfusion data. In doing so, this dual-modality approach is expected to improve diagnostic performance for detecting obstructive CAD by overcoming many of the drawbacks relative to stand-alone CTCA and MPI. Among MPI modalities SPECT and PET enable acquisition of three-dimensional datasets of the entire heart as for CTCA, which substantially facilitates the process of image fusion and, thus, renders these modalities ideal for fused hybrid imaging. A number of studies have demonstrated the added diagnostic accuracy of hybrid SPECT/CTCA and PET/CTCA for the diagnosis of hemodynamically significant CAD. Hybrid imaging has been shown to be particularly useful for enhancing specificity and PPV of CTCA [7], although significant improvement of diagnostic accuracy has been reported also compared with PET or SPECT alone [8–11]. The integration of anatomical information by CTCA with the functional information by SPECT or PET also allows for accurate localization of the coronary lesion responsible for downstream myocardial perfusion deficit. In almost 1 patient over 5 hybrid imaging may lead to complete reassignment of the ischemic territory to the culprit lesion of a different vessel than originally suggested [12]. This potentially translates into a better guide to patient management and downstream resources utilization. In single centre and multicentre studies in patients with suspected stable CAD, a matched finding (i.e., in fused hybrid images, a significantly obstructed coronary vessel at CTCA subtending a perfusion defect on SPECT or PET) was associated with a relatively high rate of revascularization as compared with mismatched or discordant

findings [12, 13]. When used as a gatekeeper to invasive procedures, hybrid imaging had a strong impact on downstream resources utilization as 100% of patients with a match, but only 13% of patients without match were referred for catheterization, and 91% were revascularized [14]. As a result, the positive diagnostic yield of invasive coronary angiography may be higher than 90% comparing favourably to the yield of less than 40% recently reported in large populations [15]. However, not all patients may benefit from hybrid imaging and in routine practice a logical approach would be sequential testing after an initial equivocal test [1, 2]. For example, in patients with a low-to-moderate pre-test probability (PTP) of CAD, it is rational to perform CTCA first as its excellent NPV allows for definite exclusion of obstructive disease. On the other hand, a tailored approach may allow immediate assessment by additional MPI of the functional relevance of an intermediate stenosis documented at CTCA or may assist in differentiating artifact-driven stenosis from true coronary luminal diameter narrowing.

Routine implementation of a hybrid anatomic-functional approach, either performed on hybrid scanners or on sequential stand-alone modalities, would necessitate evaluation of costs, potential harms (including radiation doses), and benefits. The addition of a second imaging exam would increase upfront costs which should be balanced against its effect on reduction of downstream testing and procedures. The potential harm associated with radiation doses (which with current technology and protocols may be reduced below 5 mSv) must be balanced against the risk of avoidable or inappropriate invasive procedures. Finally, and most importantly, it should be assessed whether diagnostic benefits may translate into improvement of long-term patient outcome. Integration of CTCA and SPECT or PET perfusion imaging allows to identify patients at higher future risk of adverse events [16, 17] but how this risk can be favourably modified by hybrid imaging-guided management has not yet been established. In stable CAD populations revascularizations have failed to confer a prognostic superiority compared to optimal medical therapy [18]. Unfortunately, a large randomized outcome based cost-effectiveness study where a tailored CTCA/MPI hybrid approach guiding invasive procedures is compared with standard care is not yet available.

1.2 Health-Economic Implications

In symptomatic patients with suspected SCAD available guidelines recommend using stress imaging and CTCA according to the PTP of disease [19] or CTCA as the first-line investigation in all patients [20]. Additional non-invasive testing is also considered in case of uncertain results of the first test [19, 20]. By their nature guidelines consider whether a test is appropriate for various clinical scenarios, but not their cost. The costs of an expensive non-invasive imaging strategy may be justified if it implies a reduction of downstream unnecessary utilization of further non-invasive or invasive procedures while maintaining or improving outcomes. Since the cost dimension is considered one of the relevant factors currently influencing clinical choices, cost-effectiveness studies of imaging-guided strategies in stable CAD have gained increasing attention [21].

Nevertheless, available health-economic studies [22–24] are controversial with no single modality consistently emerging as superior to all others and across all patient subgroups. The PROMISE study was a large pragmatic randomized controlled trial where CTCA or functional testing, including stress SPECT or ECHO, were compared as alternative diagnostic strategies to select patients for ICA [25]. The most remarkable finding, similar to the results of the EVINCI study which also included stress PET and CMR [6], was the better diagnostic performance of CTCA over functional testing. This translated into a higher positive diagnostic yield of ICA in the CTCA-guided arm than in the stress-imaging arm (71% vs 48%). However, the mean costs were similar for the two strategies at 90 days ($2494 versus $2240) and at 3 years follow-up, with more revascularizations and catheterizations performed with CTCA use. In another cost-effectiveness analysis, based on simulation models using published effectiveness and costs data, integrated anatomical-functional imaging strategies were also assessed [26]. In patients with intermediate-low PTP of CAD, CTCA followed by any cardiac stress-imaging test was cost-effective as compared with single imaging strategies. In particular in the USA and the Netherlands the optimal cost-effective strategy, i.e. that which provided the lower cost for one Quality Adjusted Life Year gain (around 20,000 $/QALY) began with CTCA, followed by cardiac stress imaging if the CTCA demonstrated at least a 50% stenosis in at least one coronary artery and ended with ICA if the stress test was positive. The cost-effectiveness of different strategies varied somewhat among different countries and according to patients' characteristics such as gender and PTP of disease. In any case it is suggested that CTCA is cost-effective as an initial gatekeeper test under varying assumptions in patients with a low-to-intermediate PTP of CAD [27] but integration with functional imaging may help to avoid that an over-reliance on coronary anatomy might result in an excessive use of ICA and revascularization procedures, as seen in the SPARC registry [28] and the PROMISE trial [29]. However, it must be taken into account that in contemporary populations referred to cardiac imaging, cardiac event rates with optimal medical therapy, even in patients with established CAD, are quite low [18, 25, 30] thus it is not known whether any imaging strategy will reduce cardiac events in a cost-effective manner when compared with appropriate risk factor modification. For patients with higher risk, direct ICA might be a cost-effective initial strategy but, due to the overestimation of disease probability by current clinical predictive models [6, 31, 32] in real-world practice an integrated CTCA and stress-imaging strategy as gatekeeper to ICA could remain cost-effective in the majority of patients.

In this respect, the health-economic analysis of the EVINCI study provided additional evidence [33]. EVINCI was a multicentre, multinational European, non-randomized controlled clinical trial comparing all available non-invasive imaging modalities for the diagnosis of obstructive CAD in patients with stable chest pain symptoms, intermediate PTP and without prior evidence of disease [6]. Cost-effectiveness analysis was performed in 350 patients (209 males, mean age 59 ± 9 years) undergoing both CTCA and stress imaging prior to ICA. According to Guidelines [19], combined strategies were built with CTCA as first test followed by one stress imaging in case of uncertain CTCA results or with one stress imaging as first test followed by CTCA in case of uncertain stress-test results. Any test was

defined uncertain by core-labs whether the image quality was judged as suboptimal or the stress protocols were inadequate (submaximal stress, therapy not withdrawn). The diagnostic endpoint was obstructive CAD defined as >50% stenosis at quantitative ICA in at least one major coronary vessel. Effectiveness was defined as the percentage of correct diagnosis and costs were calculated using country-specific reimbursements. Incremental cost-effectiveness ratios (ICERs) were obtained using per-patient data and considering "no-imaging" as reference. The prevalence of obstructive CAD was 28%. Strategies using stand-alone CTCA, a specific stress test, their combinations (CTCA first or stress test first) or direct referral to ICA were compared. Combined non-invasive strategies including CTCA-ECHO, CTCA-CMR, CTCA-PET, CTCA-SPECT and direct referral to ICA were all cost-effective and dominated stand-alone stress imaging or the other combinations. Stand-alone CTCA had lower induced costs but only a marginal improvement in effectiveness as compared with "no-imaging." Costs saving per one additional correct diagnosis over 100 patients ranged from −969 €/cd for CTCA-CMR to −1490 €/cd for CTCA-PET, −3092 €/cd for CTCA-SPECT, and

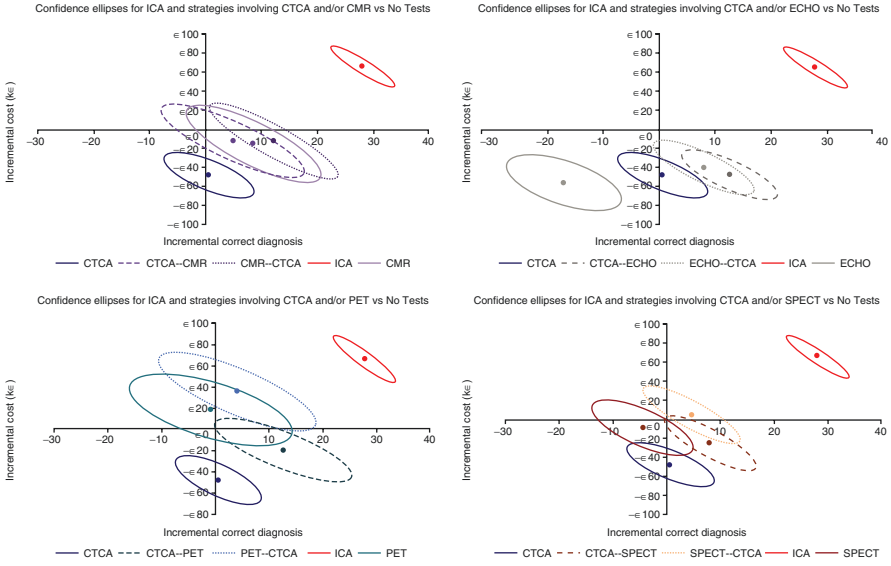

Fig. 1.1 The differences in mean cost and in mean effectiveness (with relative contour plots representing confidence intervals of the distribution generated from bootstrap analysis) are shown. The distribution plot for ICA (continuous red line) is located in the upper right quadrant thus indicating higher effectiveness at the price of higher costs. The distribution plot for stress ECHO is located in the lower left quadrant demonstrating reduction of costs but also lower diagnostic effectiveness while uncertainty exists for all other self-standing tests. For combined strategies, the distribution plots for CTCA-CMR, CTCA-ECHO, CTCA-PET, and CTCA-SPECT (dotted lines) are consistently located in the lower right quadrants indicating gain in effectiveness with reduced costs with some uncertainty. (Adapted from Lorenzoni V et al., The European Journal of Health Economics (with permission))

−3776 €/cd €/cd for CTCA-ECHO. Direct referral to ICA was cost-effective but with additional costs (+2362 €/cd) (Fig. 1.1).

When concordance of imaging results with early revascularization was also considered as an alternative measure of effectiveness, combined strategies with CTCA as gatekeeper followed by either stress CMR, ECHO, PET, or SPECT were all cost-effective as compared with "no-imaging" and dominated stand-alone or other combined strategies, despite some uncertainty. Direct referral to ICA was cost-effective requiring additional costs (+6876 €/correct prediction of revascularization). In general, whether the combination of CTCA with stress imaging would have been used as gatekeeper to catheterization, the positive yield of ICA for the diagnosis of obstructive CAD would have increased from 28 to 57% and the rate of revascularizations performed from 19% up to 40% (Fig. 1.2).

In summary, no outcome based comparative cost-effectiveness study of cardiac "hybrid" imaging in stable CAD is currently available. However, there is some evidence that a "hybrid" strategy, i.e. an appropriate sequential combination and fusion of anatomical imaging by CTCA with perfusion imaging in particular by SPECT or PET, is associated with higher diagnostic efficacy, better guide to invasive procedures and treatment and overall reduced costs as compared with self-standing single non-invasive tests. In the common practice, however, the evaluation of the health-economic impact will be difficult since it depends on multiple variables related to the patient

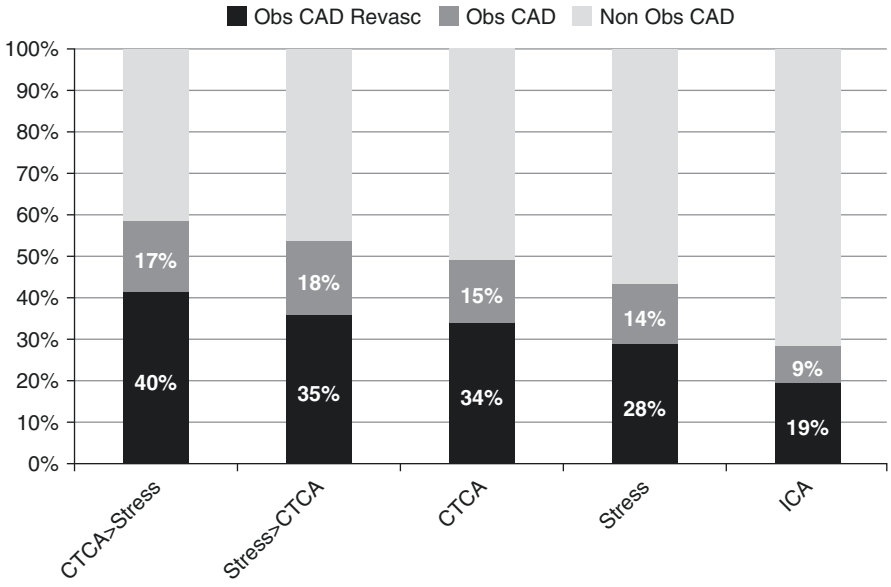

Fig. 1.2 The diagnostic and therapeutic yield of invasive angiography, if indicated on the basis of non-invasive imaging strategies (without distinction among stress modalities). For comparison, the same figures are obtained whether all patients would have been referred directly to ICA. (Adapted from Lorenzoni V et al., The European Journal of Health Economics (with permission))

population (all comers vs selected patients), the estimation of the costs (hybrid technology vs sequential self-standing modalities, differences in regional tariffs), and the estimation of the benefits (diagnosis vs outcome vs potential additional risks).

1.3 Hybrid PET-MRI and Health-Economics Implications

Integrated PET/MRI scanners are available since 2010 and many promising fields of application in cardiology have been developed including suspected coronary artery disease, acute myocardial infarction, heart failure, inflammatory heart diseases such as myocarditis and cardiac sarcoidosis, as well as cardiac tumours. However, it is recognized that large studies are still needed to demonstrate added value in comparison with current standards of care [3]. PET-MRI is an expensive modality that requires proximity to a cyclotron, specialists trained in PET and MRI for patient preparation, image acquisition, post-processing, analysis, and reporting. Simultaneous PET-MR imaging may improve patient workflow and patient experience of a single scan. However, health-economic analyses have to clarify where integrated scanners demonstrate a competitive advantage and where sequential PET and MR acquisition with post hoc image fusion with software is a good alternative. With the current evidence available, clinical PET-MR may be well suited to conditions such as cardiac masses and suspected cardiac sarcoidosis where hybrid imaging offers precise co-registration and fusion of complementary information that may provide incremental value. Once clear clinical indications and pathways are developed, these will need to be recognized as cost-effective for healthcare systems with a defined route for reimbursement [34].

References

1. Flotats A, Knuuti J, Gutberlet M, Marcassa C, Bengel FM, Kaufmann PA, et al. Hybrid cardiac imaging: SPECT/CT and PET/CT. A joint position statement by the European Association of Nuclear Medicine (EANM), the European Society of Cardiac Radiology (ESCR) and the European Council of Nuclear Cardiology (ECNC). Eur J Nucl Med Mol Imaging. 2011;38:201–12.
2. Kaufmann PA, Buechel RR. Cardiac SPECT/CTCA hybrid imaging : one answer to two questions? Herz. 2016;41(5):391–7.
3. Nensa F, Bamberg F, Rischpler C, Menezes L, Poeppel TD, la Fougère C, Beitzke D, Rasul S, Loewe C, Nikolaou K, Bucerius J, Kjaer A, Gutberlet M, Prakken NH, Vliegenthart R, Slart RHJA, Nekolla SG, Lassen ML, Pichler BJ, Schlosser T, Jacquier A, Quick HH, Schäfers M, Hacker M, European Society of Cardiovascular Radiology (ESCR), European Association of Nuclear Medicine (EANM) Cardiovascular Committee. Hybrid cardiac imaging using PET/MRI: a joint position statement by the European Society of Cardiovascular Radiology (ESCR) and the European Association of Nuclear Medicine (EANM). Eur Radiol. 2018;28:4086–101.
4. Danad I, Szymonifka J, Twisk JWR, Norgaard BL, Zarins CK, Knaapen P, Min JK. Diagnostic performance of cardiac imaging methods to diagnose ischaemia-causing coronary artery disease when directly compared with fractional flow reserve as a reference standard: a meta-analysis. Eur Heart J. 2017;38:991–8.
5. Douglas PS, De Bruyne B, Pontone G, Patel MR, Norgaard BL, Byrne RA, Curzen N, Purcell I, Gutberlet M, Rioufol G, Hink U, Schuchlenz HW, Feuchtner G, Gilard M, Andreini D,

Jensen JM, Hadamitzky M, Chiswell K, Cyr D, Wilk A, Wang F, Rogers C, Hlatky MA, PLATFORM Investigators. 1-Year outcomes of FFRCT-guided care in patients with suspected coronary disease: the PLATFORM study. J Am Coll Cardiol. 2016;68:435–45.
6. Neglia D, Rovai D, Caselli C, Pietila M, Teresinska A, Aguadé-Bruix S, Pizzi MN, Todiere G, Gimelli A, Schroeder S, Drosch T, Poddighe R, Casolo G, Anagnostopoulos C, Pugliese F, Rouzet F, Le Guludec D, Cappelli F, Valente S, Gensini GF, Zawaideh C, Capitanio S, Sambuceti G, Marsico F, Perrone Filardi P, Fernández-Golfín C, Rincón LM, Graner FP, de Graaf MA, Fiechter M, Stehli J, Gaemperli O, Reyes E, Nkomo S, Mäki M, Lorenzoni V, Turchetti G, Carpeggiani C, Marinelli M, Puzzuoli S, Mangione M, Marcheschi P, Mariani F, Giannessi D, Nekolla S, Lombardi M, Sicari R, Scholte AJ, Zamorano JL, Kaufmann PA, Underwood SR, Knuuti J, EVINCI Study Investigators. Detection of significant coronary artery disease by noninvasive anatomical and functional imaging. Circ Cardiovasc Imaging. 2015;8. pii: e002179.
7. Rizvi A, Han D, Danad I, Ó Hartaigh B, Lee JH, Gransar H, Stuijfzand WJ, Roudsari HM, Park MW, Szymonifka J, Chang HJ, Jones EC, Knaapen P, Lin FY, Min JK, Peña JM. Diagnostic performance of hybrid cardiac imaging methods for assessment of obstructive coronary artery disease compared with stand-alone coronary computed tomography angiography: a meta-analysis. JACC Cardiovasc Imaging. 2018;11(4):589–99.
8. Danad I, Raijmakers PG, Appelman YE, Harms HJ, de Haan S, van den Oever ML, et al. Hybrid imaging using quantitative H215O PET and CT-based coronary angiography for the detection of coronary artery disease. J Nucl Med. 2013;54:55–63.
9. Kajander S, Joutsiniemi E, Saraste M, Pietila M, Ukkonen H, Saraste A, et al. Cardiac positron emission tomography/computed tomography imaging accurately detects anatomically and functionally significant coronary artery disease. Circulation. 2010;122:603–13.
10. Rispler S, Keidar Z, Ghersin E, Roguin A, Soil A, Dragu R, et al. Integrated single-photon emission computed tomography and computed tomography coronary angiography for the assessment of hemodynamically significant coronary artery lesions. J Am Coll Cardiol. 2007;49:1059–67.
11. Santana CA, Garcia EV, Faber TL, Sirineni GK, et al. Diagnostic performance of fusion of myocardial perfusion imaging (MPI) and computed tomography coronary angiography. J Nucl Cardiol. 2009;16:201–11.
12. Liga R, Vontobel J, Rovai D, Marinelli M, et al. Multicentre multi-device hybrid imaging study of coronary artery disease: results from the EValuation of INtegrated Cardiac Imaging for the Detection and Characterization of Ischaemic Heart Disease (EVINCI) hybrid imaging population. Eur Heart J Cardiovasc Imaging. 2016;17:951–60.
13. Pazhenkottil AP, Nkoulou RN, Ghadri JR, Herzog BA, et al. Impact of cardiac hybrid single-photon emission computed tomography/computed tomography imaging on choice of treatment strategy in coronary artery disease. Eur Heart J. 2011;32:2824–9.
14. Fiechter M, Ghadri JR, Wolfrum M, Kuest SM, Pazhenkottil AP, Nkoulou RN, Herzog BA, Gebhard C, Fuchs TA, Gaemperli O, Kaufmann PA. Downstream resource utilization following hybrid cardiac imaging with an integrated cadmium-zinc-telluride/64-slice CT device. Eur J Nucl Med Mol Imaging. 2012;39:430–6.
15. Patel MR, Peterson ED, Dai D, Brennan JM, Redberg RF, Anderson HV, et al. Low diagnostic yield of elective coronary angiography. N Engl J Med. 2010;362:886–95.
16. Pazhenkottil AP, Nkoulou RN, Ghadri JR, Herzog BA, et al. Prognostic value of cardiac hybrid imaging integrating single-photon emission computed tomography with coronary computed tomography angiography. Eur Heart J. 2011;32:1465–71.
17. Maaniitty T, Stenström I, Bax JJ, Uusitalo V, Ukkonen H, Kajander S, Mäki M, Saraste A, Knuuti J. Prognostic value of coronary CT angiography with selective PET perfusion imaging in coronary artery disease. JACC Cardiovasc Imaging. 2017;10:1361–70.
18. Shaw LJ, Berman DS, Maron DJ, Mancini GB, Hayes SW, Hartigan PM, et al. Optimal medical therapy with or without percutaneous coronary intervention to reduce ischemic burden: results from the Clinical Outcomes Utilizing Revascularization and Aggressive Drug Evaluation (COURAGE) trial nuclear substudy. Circulation. 2008;117:1283–91.

19. Knuuti J, Wijns W, Saraste A, Capodanno D, Barbato E, Funck-Brentano C, et al. 2019 ESC Guidelines for the diagnosis and management of chronic coronary syndromes. Eur Heart J. 2020;41:407–77.
20. National Institute for Health and Clinical Excellence. Chest pain of recent onset: assessment and diagnosis of recent onset chest pain or discomfort of suspected cardiac origin (update). CG95. London: National Institute for Health and Clinical Excellence; 2016.
21. Van Waardhuizen CN, Khanji MY, Genders TSS, Ferket BS, Fleischman KE, Hunink MGM, et al. Comparative cost-effectiveness of non-invasive imaging tests in patients presenting with chronic stable chest pain with suspected coronary artery disease: a systematic review. Eur Heart J Qual Care Clin Outcomes. 2016;2:245–60.
22. Shaw LJ, Phillips LM, Nagel E, Newby DE, Narula J, Douglas PS. Comparative effectiveness trials of imaging-guided strategies in stable ischemic heart disease. JACC Cardiovasc Imaging. 2017;10:321–34.
23. Trägårdh E, Tan SS, Bucerius J, Gimelli A, Gaemperli O, Lindner O, et al. Systematic review of cost-effectiveness of myocardial perfusion scintigraphy in patients with ischaemic heart disease: a report from the cardiovascular committee of the European Association of Nuclear Medicine. Endorsed by the European Association of Cardiovascular Imaging. Eur Heart J Cardiovasc Imaging. 2017;18:825–32.
24. Turchetti G, Kroes MA, Lorenzoni V, Trieste L, Chapman AM, Sweet AC, et al. The cost-effectiveness of diagnostic cardiac imaging for stable coronary artery disease. Expert Rev Pharmacoecon Outcomes Res. 2015;15:625–33.
25. Douglas PS, Hoffmann U, Patel M, Mark D, Al-Khalidi HR, Cavanaugh B et al., for the PROMISE Investigators. Outcomes of anatomical vs functional testing for coronary artery disease. N Engl J Med. 2015;372:1291–300.
26. Genders TS, Petersen SE, Pugliese F, Dastidar AG, Fleischmann KE, Nieman K, et al. The optimal imaging strategy for patients with stable chest pain: a cost-effectiveness analysis. Ann Intern Med. 2015;162:474–84.
27. van Waardhuizen CN, Khanji MY, Genders TSS, Ferket BS, Fleischmann KE, Hunink MGM, Petersen SE. Comparative cost-effectiveness of non-invasive imaging tests in patients presenting with chronic stable chest pain with suspected coronary artery disease: a systematic review. Eur Heart J Qual Care Clin Outcomes. 2016;2:245–60.
28. Hlatky MA, Shilane D, Hachamovitch R, DiCarli MF, SPARC Investigators. Economic outcomes in the study of myocardial perfusion and coronary anatomy imaging roles in coronary artery disease registry: the SPARC study. J Am Coll Cardiol. 2014;63:1002–8.
29. Mark DB, Federspiel JJ, Cowper PA, Anstrom KJ, Hoffmann U, Patel MR, et al. Economic outcomes with anatomical versus functional diagnostic testing for coronary artery disease. Ann Intern Med. 2016;165:94–102.
30. Williams MC, Hunter A, Shah ASV, Assi V, Lewis S, Smith J, et al., SCOT-HEART Investigators. Use of coronary computed tomographic angiography to guide management of patients with coronary disease. J Am Coll Cardiol. 2016;67:1759–68.
31. Cheng VY, Berman DS, Rozanski A, Dunning AM, Achenbach S, Al-Mallah M, Budoff MJ, Cademartiri F, Callister TQ, Chang HJ, Chinnaiyan K, Chow BJ, Delago A, Gomez M, Hadamitzky M, Hausleiter J, Karlsberg RP, Kaufmann P, Lin FY, Maffei E, Raff GL, Villines TC, Shaw LJ, Min JK. Performance of the traditional age, sex, and angina typicality-based approach for estimating pretest probability of angiographically significant coronary artery disease in patients undergoing coronary computed tomographic angiography: results from the multinational coronary CT angiography evaluation for clinical outcomes: an international multicentre registry (CONFIRM). Circulation. 2011;124:2423–32, 1–8.
32. Foldyna B, Udelson JE, Karády J, Banerji D, Lu MT, Mayrhofer T, Bittner DO, Meyersohn NM, Emami H, Genders TSS, Fordyce CB, Ferencik M, Douglas PS, Hoffmann U. Pretest probability for patients with suspected obstructive coronary artery disease: re-evaluating Diamond-Forrester for the contemporary era and clinical implications: insights from the PROMISE trial. Eur Heart J Cardiovasc Imaging. 2018;20(5):574–81.

33. Lorenzoni V, Bellelli S, Caselli C, Knuuti J, Underwood SR, Turchetti G, Neglia D, For the EVINCI Investigators. Cost–effectiveness analysis of stand-alone or combined non-invasive imaging tests for the diagnosis of stable coronary artery disease: results from the EVINCI study. Eur J Health Econ. 2019;20(9):1437–49.
34. Nazir MS, Ismail TF, Reyes E, Chiribiri A, Kaufmann PA, Plein S. Hybrid positron emission tomography-magnetic resonance of the heart: current state of the art and future applications. Eur Heart J Cardiovasc Imaging. 2018;19:962–74.

Industry Perspective on Hybrid Cardiac Imaging

2

Thomas Krüwel

2.1 Introduction

Coronary artery disease is one of the major causes of morbidity and mortality in the Western civilization, although large progress was made as cardiovascular disease mortality rates declined dramatically in the last decades [1–3]. Besides changes of lifestyle and medical treatment, surgical revascularization of coronary arteries accounts for a big deal of the declining numbers. However, before surgical treatment, proof of myocardial ischemia is mandatory according to recent guidelines [4]. Thus, there is a need for safe, reliable, robust, fast and cost-effective procedures to detect and assess the extent of coronary artery disease.

Non-invasive cardiac imaging has witnessed huge advances in the last decades, especially for coronary artery disease where it is currently used for diagnosis, risk assessment and decision making for appropriate treatment strategies [3, 5]. As a result, the number of non-invasive cardiac imaging examinations increased over the last years which lead to an increased request of high-end devices for computed tomography (CT) and nuclear cardiology [5].

In nuclear cardiology, positron emission tomography (PET) imaging is referred as the gold standard as it is by nature a quantitative non-invasive method and allows the absolute assessment of myocardial blood flow. Additionally, PET perfusion tracers, such as Ammonia N13, have a relatively high extraction rate and a short physical half-life which allows absolute quantification. However, due to the short half-lives of the available perfusion tracer an onsite cyclotron is needed for cardiac PET imaging today. This requires large investments in equipment and infrastructure which limits the sites who can perform myocardial perfusion PET imaging.

T. Krüwel (✉)
GE Healthcare GmbH, Solingen, Germany
e-mail: thomas.kruewel@ge.com

S. G. Nekolla, C. Rischpler (eds.), *Hybrid Cardiac Imaging*,
https://doi.org/10.1007/978-3-030-83167-7_2

Single photon emission computed tomography (SPECT) imaging is still the workhorse in nuclear medicine due to the commercial availability of 99mTc by Mo/Tc generators. For myocardial perfusion, two 99mTc-based tracers sestamibi (CardioLite, Du Pont) and tetrofosmin (Myoview, GE Healthcare) are available.

Myocardial perfusion SPECT imaging advanced to the most frequently used nuclear medicine test with annually 6.3 million exams in the USA [2]. Conventional SPECT imaging involves prolonged procedure times which compromise cost-effectiveness and overall diagnostic quality. Therefore, the latest development aimed to decrease required imaging time and increase patient throughput at equivalent or better levels of spatial resolution and contrast [6].

2.2 Ultra-Fast Cardiac Cameras Based on CZT Technology

Most recent advances in myocardial SPECT imaging were made in the development of dedicated ultra-fast cardiac cameras based on semiconductor technology of cadmium zinc tellurium (CZT) detectors. In comparison to conventional sodium iodine (NaI) detectors, CZT detectors do not contain a scintillation crystal and the radiation is converted to electrical signals directly without intermediate conversion steps. Although being integral part of conventional NaI detectors and well established for many decades, the intermediate conversion steps are responsible for significant data degradation, especially the energy resolution, and thus clinical limitations. The use of CZT detectors with direct conversion technology, converts the radiation directly, circumvents these shortcomings and recovers lost spatial and energy resolution and eliminates much of the bulk of the systems.

In conventional NaI detectors, gamma rays are absorbed and converted to ultraviolet (UV) photons. The UV photons are directed to photomultiplier tubes (PMT) by light guides and optical coupling compounds (Fig. 2.1a). The detector facing side of the PMT is equipped with a photocathode, which absorbs the UV photons and releases electrons by the photoelectric effect. These electrons are accelerated and multiplied by high voltage stages and collected on the input of a sensitive signal amplifier. This process is defined as indirect conversion. In comparison to that, in the direct conversion process as happening in CZT detectors, incident gamma rays are absorbed which directly results in an electric charge (Fig. 2.1b). This direct process happens without any steps of UV light production, transport and conversion. The 140 keV gamma photon produces 33,000 electron–hole pairs. An applied electric field causes the charges to move and induces signals on the anodes. These signals are further amplified for further readout processing. This results in a better energy resolution, as it only depends on the amplifier noise and is no longer determined by a step with low statistics. In addition to the significantly improved energy resolution, the system resolution was improved due to pixilation of the detector with 2.46 mm by 2.46 mm pixels leading to reduced uncertainty of the intrinsic resolution to the boundaries of the pixel.

The CZT detector has a very compact structure with a crystal dimension of 4 cm by 4 cm by 5 mm or 7.25 mm, respectively. In comparison, a conventional

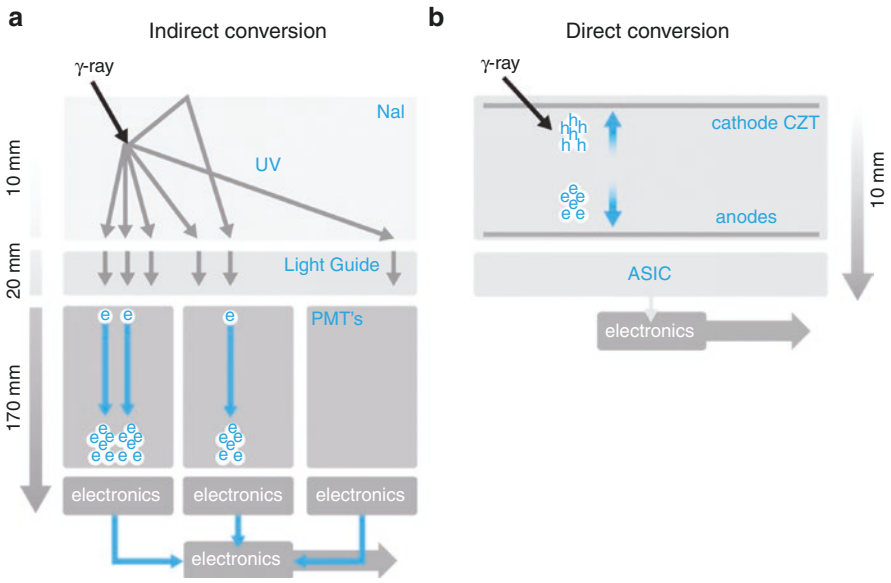

Fig. 2.1 Comparison of indirect and direct conversion in nuclear medicine event detection. (**a**) With NaI detector technology, an emitted photon is absorbed by the scintillator (i.e. NaI crystal) and a small light signal is emitted. An array of photomultiplier tubes (PMTs) collects and amplifies the light, which is then converted to 500 photo-electrons. The location of the event (location of the photon emission) is approximately calculated. (**b**) With the CZT detector technology a photon is directly converted into 30,000 photo-electrons. This eliminates the analog noise or signal noise. The location of the event is accurately identified, including the energy of the photon

detector with a PMT has a vertical dimension of 7 cm, which corresponds to a reduction of size of a factor of 10. This specific design allows the packaging of multiple detectors tightly together or to develop imaging systems with improved proximity, i.e. closer to the body. This allows many detectors to be packed together in a single system which opens a completely new possibility in cardiac imaging. Figure 2.2 shows the components of a complete CZT imaging module including CZT crystal, ASIC electronics, heat sink and digital board. The fully assembled CZT detector module including cover and connectors is depicted in Fig. 2.3.

The advantages of the CZT detector in terms of energy and spatial resolution as well its extremely compact structure makes them well suited for the use in dedicated cardiac cameras. Today, two dedicated cardiac systems based on CZT technology with fundamentally different setup are commercially available. The D-SPECT camera of Spectrum Dynamics is equipped with 6 or 9 rotating detector columns with a parallel hole collimator. Each detector column consists of 4 CZT detector modules summing up to a total of 24–36 detector modules [7].

The Discovery NM 530c of GE Healthcare is equipped with 19 stationary detectors based on pinhole collimation. Each detector consists of four CZT modules summing up to a total of 76 detector modules build in the Discovery NM 530c [6, 7].

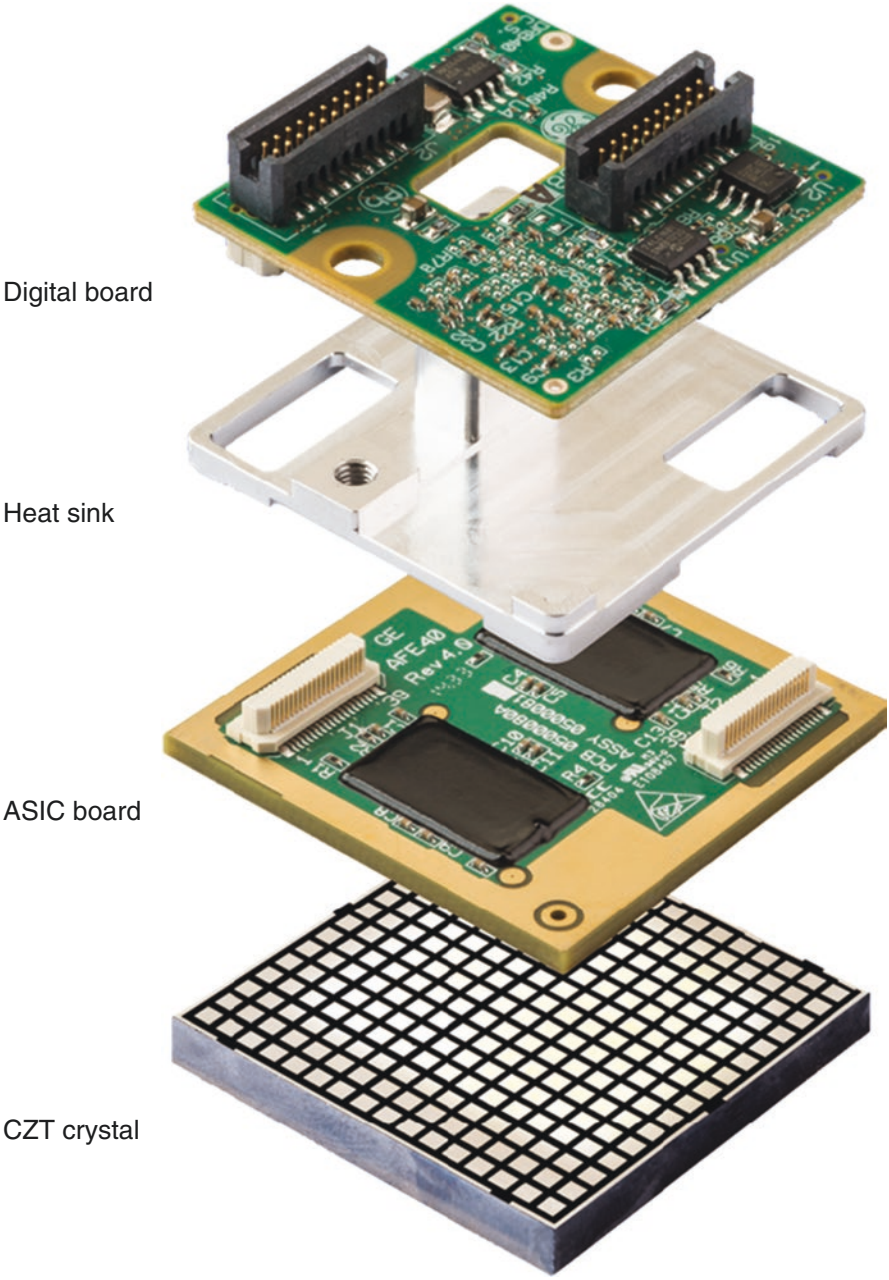

Fig. 2.2 Explosion graphic of an entire CZT module. The CZT detector module consists of the CZT crystal coupled to the ASIC board with attached heat sink and digital board

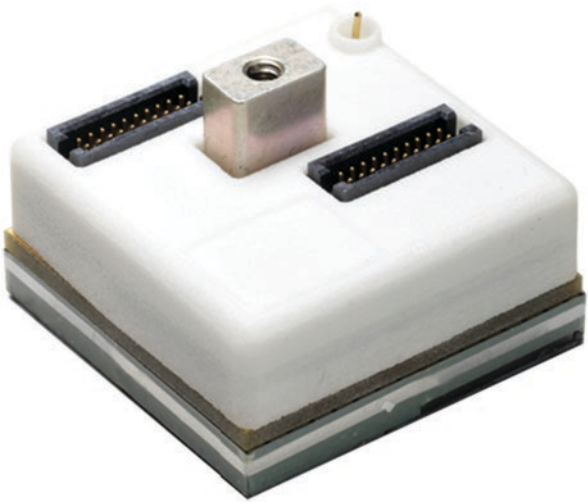

Fig. 2.3 Fully assembled CZT detector module

2.3 Pinhole Imaging

Pinhole imaging has been used historically in nuclear medicine for specialized imaging with high resolution due to the magnification of the projection of the specimen. The improvement in spatial resolution, however, comes by the cost of a reduced sensitivity [8]. In cardiac imaging, increased spatial resolution has not highest relevance due to the blurring effects of the moving heart in the cardiac cycle. However, the combination of pinhole collimation with high resolution CZT detectors provides a new means to achieve a net gain in performance without the tradeoff between spatial resolution and sensitivity. The pinhole imaging allows the high resolution of the CZT detector to be converted to high sensitivity without degrading resolution which is more valuable for cardiac imaging. The high sensitivity can then be used to optimize workflow and patient throughput, while the conserved resolution preserves the clinical character and quality of conventional images and the diagnostic protocols [6, 9, 10]. Furthermore, the multiple detectors acquire the full set of views needed for tomographic reconstruction simultaneously and without any detector motion at all (Fig. 2.4a). This capability reduces systematic error from all sources of motion blurring, including both, the detector motion and even the cardiac motion itself. Figure 2.4b shows the multi-pinhole collimator focusing the heart with each pinhole.

The principle how the combination of CZT and pinhole collimation to achieve high sensitivity and conserve resolution is depicted in Fig. 2.5. In conventional NaI imaging the pinhole resolution decreases, i.e. improves with increasing magnification factor. Thus, optimization for high resolution is achieved by moving the detectors away from the pinhole in order to increase the magnification factor. However, the small pixels with the reduced pixel size of the CZT detectors facilitate a new

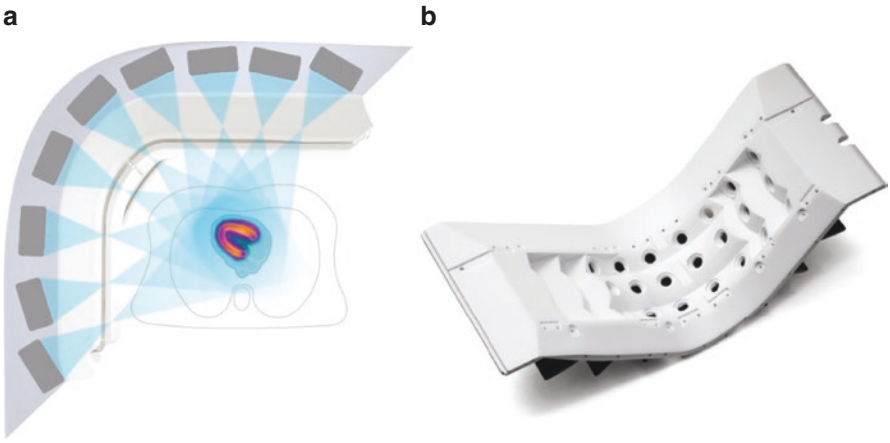

Fig. 2.4 Multi-pinhole imaging. (**a**) Scheme of the geometry of the stationary detector. No movement of the detector occurs during acquisition. (**b**) Multi-pinhole collimator of the Discovery NM 530c

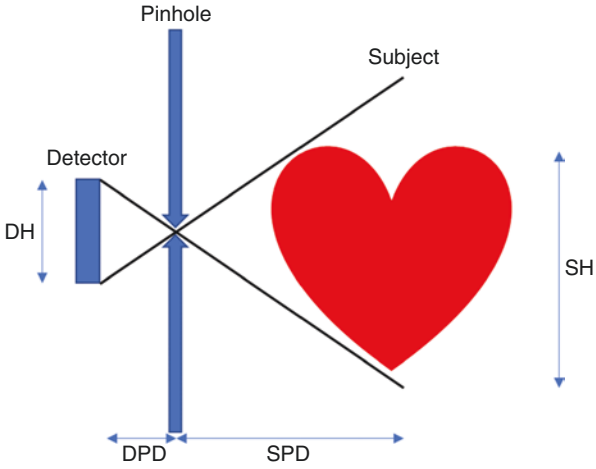

Fig. 2.5 Principle of CZT-based pinhole imaging. Due to the high resolution of the CZT detector, the detector can be closer to the pinhole than the specimen yielding a magnification factor <1. Magnification is calculated as DH/SH or DPD/SPD. *DH* detector height, *SH* source height, *DPD* detector to pinhole distance, *SPD* source to pinhole distance

counterintuitive strategy to optimize for high efficiency. In this case, the detector is moved towards the pinhole. The detector surface area needed to image the object is rapidly reduced. The number of pixels in the image is preserved by use of smaller pixels. In order to preserve the resolution, the pinhole size is reduced in accordance with the small pixel size.

In comparison to a conventional gamma camera with low energy high resolution (LEHR) collimator pinhole imaging based on CZT detectors adds up to a five times higher system efficiency.

2.4 Hybrid Imaging for Dedicated Cardiac SPECT Cameras

The new design of the CZT-based dedicated cardiac cameras was reported highly efficient in multiple studies. In comparison to conventional double-head gamma cameras the new systems yield images with higher contrast and spatial resolution, acquired in shorter time and/or with reduced radiation doses to the patient [1, 7, 11–15]. As with conventional gamma cameras, inferior wall artifacts due to soft tissue attenuation are common. The specificity can be improved by two position imaging (supine and prone), however, attenuation correction should be applied if it is available. The CT data used for attenuation correction are embedded in the reconstruction algorithm which leads to more accurate voxel values and has the potential to provide absolute radiotracer concentrations enabling a possible flow quantification with existing tracers [3]. For the dedicated cardiac camera Discovery NM 530c there is already a straightforward approach to include external CT data for attenuation correction.

Besides attenuation correction, hybrid imaging strategies for cardiac imaging are typically synergistic and provide more information than either dataset alone, leading to improved sensitivity and specificity [16–18]. This is because both, the functional consequences of coronary stenosis on myocardial perfusion and metabolism and the morphological coronary artery disease are relevant. Additionally, other entities such as microvascular or endothelial dysfunction have been recognized to contribute significantly to disease pathology [5]. To achieve this, coronary artery calcification (CAC) or coronary CT angiography (CCTA) datasets are fused SPECT or PET myocardial perfusion imaging data.

CAC can be readily compared with an attenuation correction CT because a native CT scan without contrast enhancement is required. CAC adds high clinical value as it provides an estimate of coronary atherosclerotic plaque burden and correlates strongly with the overall amount of coronary plaque. The assessment of the presence of subclinical coronary atherosclerosis with CAC, which cannot be detected by MPI, provides an opportunity to identify asymptomatic patients who are at risk for developing long-term coronary artery disease. Thus, the combination of SPECT and CAC results in a significant improvement in sensitivity and specificity for the diagnosis of angiographically significant coronary artery disease compared to SPECT alone [3, 5, 19, 20].

CCTA provides an accurate morphological assessment of coronary artery anatomy and has the ability to exclude CAD through its very high sensitivity. However, CCTA is a purely anatomical imaging modality and does not offer information on the functional relevance of the coronary lesion. Therefore, the combination and fusion of SPECT and CCTA datasets significantly improve diagnostic accuracy compared to SPECT alone or SPECT and CCTA side-by-side analysis [3, 16, 21–23].

There are many clinical evidences that hybrid imaging adds a strong clinical benefit to myocardial perfusion imaging. This can be performed in two different ways, either by using hybrid SPECT or PET/CT systems or by consecutive SPECT and CT exams on two different systems and a dedicated post-processing. Today, commercially available hybrid SPECT systems are equipped with a CT-subsystem

with a up to 2 cm detector (up to 16 rows) and PET/CT systems with a up to 4 cm detector (up to 64 rows). The in details described dedicated cardiac cameras are available as stand-alone systems only by today.

CT scans for attenuation correction and landmarking can be performed on a non-diagnostic CT scanner. CAC requires at least a diagnostic quality CT scanner and CCTA a state-of-the-art CT with at least 4 cm detector with ultra-fast tube rotation. One may ask why not every hybrid system may be equipped with a modern state-of-the-art 64 row CT, as it would enable convenient and straightforward hybrid imaging. The reason for this is of pure economic nature because every system has to be operated profitable. According to Kaufmann et al. [16], not every patient would benefit from CCTA at all and the prescription of additional CCTA has always be carefully considered, especially regarding dose exposure. If such a CT would be connected to a dedicated cardiac camera, it would be occupied with low utilization. Having a dedicated cardiac camera and a high-end CT, both systems can be operated profitable at optimal capacity utilization as patients that do not need myocardial perfusion imaging can receive their CT exam in the meantime. For those scenarios powerful post-processing was developed to easily register and fuse functional myocardial perfusion with CT data. For attenuation correction, however, an (ultra-)low dose CT combined to a cardiac camera would provide a benefit because SPECT and CT images would be inherently aligned. Although registration of SPECT and CT cardiac datasets is software assisted and a manageable region of interest, registration has to be carefully examined that no potential mismatch occurs. Here, a hybrid system could be beneficial for an improved clinical hybrid workflow.

The field of nuclear cardiac imaging underwent huge improvements by the development of CZT-based dedicated cardiac cameras. The addition of CAC or CCTA to myocardial perfusion imaging improves the diagnostic confidence of the report. Multiple post-processing tools are available to perform registration and fusion of SPECT and CT data to create meaningful SPECT/CT dataset.

References

1. Nkoulou R, Fuchs T, Pazhenkottil AP, Wolfrum M, Buechel RR, Gaemperli O, et al. High efficiency gamma camera enables ultra-low fixed dose stress/rest myocardial perfusion imaging. Eur Heart J. 2018;20(2):218–24.
2. Mensah GA, Wei GS, Sorlie PD, Fine LJ, Rosenberg Y, Kaufmann PG, et al. Decline in cardiovascular mortality: possible causes and implications. Circ Res. 2017;120(2):366–80.
3. Iskandrian AE, Dilsizian V, Garcia EV, Beanlands RS, Cerqueira M, Soman P, et al. Myocardial perfusion imaging: lessons learned and work to be done-update. J Nucl Cardiol. 2018;25(1):39–52.
4. ESCARDIO. 2019. https://www.escardio.org/Guidelines/Clinical-Practice-Guidelines/ESC-EACTS-Guidelines-in-Myocardial-Revascularisation-Guidelines-for.
5. Gaemperli O, Kaufmann PA, Alkadhi H. Cardiac hybrid imaging. Eur J Nucl Med Mol Imaging. 2014;41(Suppl 1):S91–103.
6. Bocher M, Blevis IM, Tsukerman L, Shrem Y, Kovalski G, Volokh L. A fast cardiac gamma camera with dynamic SPECT capabilities: design, system validation and future potential. Eur J Nucl Med Mol Imaging. 2010;37(10):1887–902.

7. Ben-Haim S, Kennedy J, Keidar Z. Novel cadmium zinc telluride devices for myocardial perfusion imaging-technological aspects and clinical applications. Semin Nucl Med. 2016;46(4):273–85.
8. Beekman F, van der Have F. The pinhole: gateway to ultra-high-resolution three-dimensional radionuclide imaging. Eur J Nucl Med Mol Imaging. 2007;34(2):151–61.
9. Sharir T, Pinskiy M, Pardes A, Rochman A, Prokhorov V, Kovalski G, et al. Comparison of the diagnostic accuracies of very low stress-dose with standard-dose myocardial perfusion imaging: automated quantification of one-day, stress-first SPECT using a CZT camera. J Nucl Cardiol. 2016;23(1):11–20.
10. Einstein AJ, Johnson LL, DeLuca AJ, Kontak AC, Groves DW, Stant J, et al. Radiation dose and prognosis of ultra-low-dose stress-first myocardial perfusion SPECT in patients with chest pain using a high-efficiency camera. J Nucl Med. 2015;56(4):545–51.
11. Imbert L, Poussier S, Franken PR, Songy B, Verger A, Morel O, et al. Compared performance of high-sensitivity cameras dedicated to myocardial perfusion SPECT: a comprehensive analysis of phantom and human images. J Nucl Med. 2012;53(12):1897–903.
12. Bailliez A, Lairez O, Merlin C, Piriou N, Legallois D, Blaire T, et al. Left ventricular function assessment using 2 different cadmium-zinc-telluride cameras compared with a gamma-camera with cardiofocal collimators: dynamic cardiac phantom study and clinical validation. J Nucl Med. 2016;57(9):1370–5.
13. Duvall WL, Sweeny JM, Croft LB, Ginsberg E, Guma KA, Henzlova MJ. Reduced stress dose with rapid acquisition CZT SPECT MPI in a non-obese clinical population: comparison to coronary angiography. J Nucl Cardiol. 2012;19(1):19–27.
14. Nkoulou R, Fuchs T, Pazhenkottil AP, Wolfrum M, Buechel RR, Gaemperli O, et al. High efficiency gamma camera enables ultra-low fixed dose stress/rest myocardial perfusion imaging. Eur Heart J Cardiovasc Imaging. 2019;20(2):218–24.
15. Nkoulou R, Pazhenkottil AP, Kuest SM, Ghadri JR, Wolfrum M, Husmann L, et al. Semiconductor detectors allow low-dose-low-dose 1-day SPECT myocardial perfusion imaging. J Nucl Med. 2011;52(8):1204–9.
16. Kaufmann PA, Buechel RR. Cardiac SPECT/CCTA hybrid imaging : one answer to two questions? Herz. 2016;41(5):391–7.
17. Grossmann M, Giannopoulos AA, Bechtiger FA, Messerli M, Schwyzer M, Benz DC, et al. Ultra-low-dose computed tomography for attenuation correction of cadmium-zinc-telluride single photon emission computed tomography myocardial perfusion imaging. J Nucl Cardiol. 2020;27(1):228–37.
18. Clerc OF, Fuchs TA, Possner M, Vontobel J, Mikulicic F, Stehli J, et al. Real-time respiratory triggered SPECT myocardial perfusion imaging using CZT technology: impact of respiratory phase matching between SPECT and low-dose CT for attenuation correction. Eur Heart J Cardiovasc Imaging. 2017;18(1):31–8.
19. Grani C, Buechel RR, Kaufmann PA, Kwong RY. Multimodality imaging in individuals with anomalous coronary arteries. JACC Cardiovasc Imaging. 2017;10(4):471–81.
20. Grani C, Vontobel J, Benz DC, Bacanovic S, Giannopoulos AA, Messerli M, et al. Ultra-low-dose coronary artery calcium scoring using novel scoring thresholds for low tube voltage protocols-a pilot study. Eur Heart J Cardiovasc Imaging. 2018;19(12):1362–71.
21. Pazhenkottil AP, Benz DC, Grani C, Madsen MA, Mikulicic F, von Felten E, et al. Hybrid SPECT perfusion imaging and coronary CT angiography: long-term prognostic value for cardiovascular outcomes. Radiology. 2018;288(3):694–702.
22. Pazhenkottil AP, Nkoulou RN, Ghadri JR, Herzog BA, Buechel RR, Kuest SM, et al. Prognostic value of cardiac hybrid imaging integrating single-photon emission computed tomography with coronary computed tomography angiography. Eur Heart J. 2011;32(12):1465–71.
23. Diaz-Zamudio M, Fuchs TA, Slomka P, Otaki Y, Arsanjani R, Gransar H, et al. Quantitative plaque features from coronary computed tomography angiography to identify regional ischemia by myocardial perfusion imaging. Eur Heart J Cardiovasc Imaging. 2017;18(5):499–507.

Global and Regional Peculiarities: The IAEA Perspective

3

Diana Paez, Maurizio Dondi, Joao V. Vitola, Pedro Prado, and Leslee J. Shaw

3.1 Introduction

The International Atomic Energy Agency (IAEA) is an independent, intergovernmental organization within the United Nations, with the mandate to accelerate and broaden the contribution of nuclear applications to peace, health and prosperity.

Cardiovascular disease (CVD) is a major contributor to premature morbidity and mortality worldwide. Low- and middle-income countries (LMICs) are particularly affected by cardiovascular diseases (CVDs), as more than 75% of all CVDs deaths occur in these countries [1]. Global prognostic figures are alarming, as an estimated 23.6 million people will die each year due to CVDs by 2030. For this reason, target 3.4 of the Sustainable Development Goals (SDGs) of the agenda of the United Nations (UN) aims at reducing premature mortality due to Non-Communicable Diseases (NCDs) by 30% by 2030 [2], also shared by the European Union [3]. In that context, among other applications, the promotion of nuclear medicine techniques for detection and guided treatment of CVD is a core target of the Division of Human Health inside the IAEA [4].

D. Paez (✉) · M. Dondi
Nuclear Medicine and Diagnostic Imaging Section, Division of Human Health, Department of Nuclear Sciences and Applications, International Atomic Energy Agency, Vienna, Austria
e-mail: D.Paez@iaea.org

J. V. Vitola · P. Prado
QUANTA, Curitiba, Brazil

L. J. Shaw
Icahn School of Medicine at Mount Sinai, New York, NY, USA

S. G. Nekolla, C. Rischpler (eds.), *Hybrid Cardiac Imaging*,
https://doi.org/10.1007/978-3-030-83167-7_3

Medical imaging has revolutionized health care in the past decades as it has enabled the delivery of individual, patient-tailored disease management. The diagnostic and prognostic value of myocardial perfusion imaging (MPI) in CAD is very well established [5].

Within the IAEA, numerous initiatives have been developed or are underway to promote quality imaging practices through regional and global clinical research, educational and training programs. These programs emphasize the importance of worldwide standards for instrumentation, protocols, appropriate use, and high-quality image interpretation and reporting practices [6, 7].

As we look into the future, the IAEA plays an important role in the development of clinical evidence and guidance documents to synthesize available data into optimal testing strategies of care [7–11].

Over the past two decades, the practice of nuclear medicine, including nuclear cardiology applications, has undergone dramatic evolution with the introduction of hybrid systems, which couple a CT scanner with either a PET or a SPECT scanner, that are now in routine clinical practice [5, 12–15]. In nuclear cardiology, the coupled CT scanner is commonly used for attenuation correction [16] but, if equipped with adequate software and an adequate number of slices, can be used to evaluate coronary artery calcium and/or perform coronary CT angiographic studies [17]. An advantage of these systems is that they provide, in one imaging study, comprehensive cardiac evaluation of anatomic information from the CT scan and physiologic information from the PET or SPECT scans [18].

The introduction of hybrid imaging into healthcare systems worldwide has implications about availability of adequate budget and human resources capacity. Both remain the main constraints in LMICs, IAEA Member States, where financial resources are often inadequate and human resources scant.

This chapter will try to discuss global and regional heterogeneity of hybrid imaging as applied in cardiology in IAEA Member States.

3.2 Health Expenditures

According to the World Health Organization (WHO), global public expense for health care (i.e., as a percentage of the gross national product) varies between 4.4 and 16.8%. In 2015, about 7.2 trillion US$ or on average 10% of global Gross Domestic Product (GDP) were spent on health [19]. Although projections for the future are fraught with challenges, it is conceivable that diagnostic imaging will encumber a significant proportion of that budget. Figure 3.1 represents the current heterogeneity in health care expenditures as a percentage of GDP.

The IAEA has collected data on nuclear medicine practices around the world through its Nuclear Medicine Database (NUMDAB) [20]. According to those records, the average age of equipment is more than 6 years for all types of gamma-cameras in LMICs. However, some systems have been operational for more than 30 years and in many cases planar cameras are still in use in almost all regions in the world, with Africa and Middle East running the oldest machines.

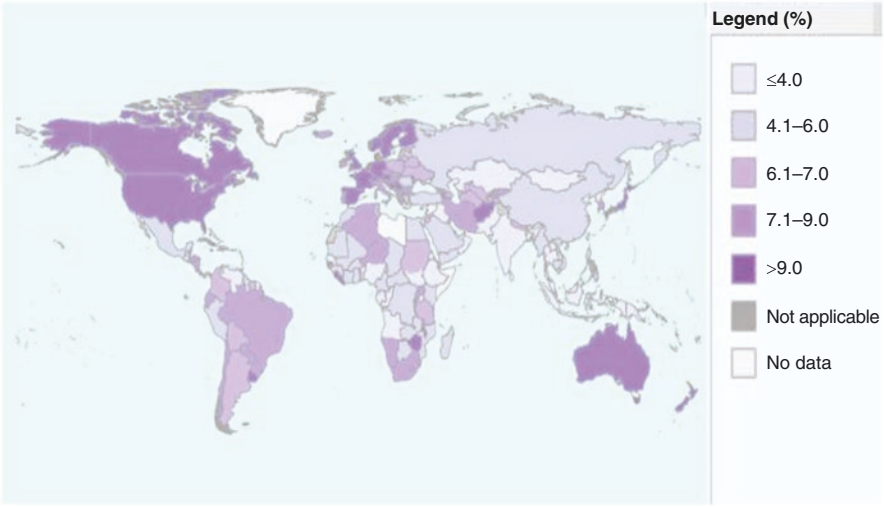

Fig. 3.1 Annual percentage of health care expenditures by country as percentage of GDP. (From: World Health Organization, Global Health Observatory data)

3.3 The Challenge of Introducing Newer Technologies

In general, we have witnessed a delay in introduction of hybrid systems, either SPECT/CT or PET/CT, in LIMCs. Among the possible factors that could explain it is the heterogeneity of investments in newer technologies, impacting nuclear medicine equipment renewal around the globe.

The introduction of newer technologies into health care practices requires a careful assessment of the impact at the medical, societal, and economical level. This is usually done with Health Technology Assessment (HTA), a branch of health care research employing specific methodologies [21] to assess the impact of any new practice in health care, e.g. a new antibiotic, a new surgical procedure, a new screening program, a new expensive technology, etc. LMICs have special needs regarding this approach as financial resources are often limited.

Indeed, economics play an important role in decision-making and a careful assessment of the diagnostic efficacy of a technology is strongly required.

3.4 Diagnostic Efficacy and Cost Effectiveness

Diagnostic imaging efficacy measures may be thought of as arranged in an hierarchical manner [22, 23] (Fig. 3.2).

At the most micro, or local, level, we are concerned with the physical imaging process itself. Efficacy evaluation at the initial level, Level 1, are more related to technical and physical characteristics of diagnostic imaging such as better

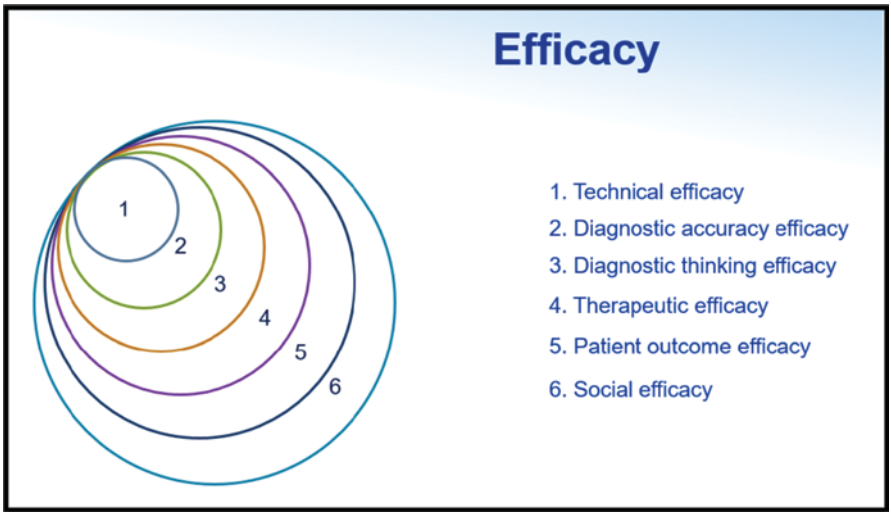

Fig. 3.2 The six levels of efficacy. (Modified, from ref. [22])

resolution or better image quality. At level 2, we are considering parameters such as sensitivity, specificity, diagnostic accuracy; negative and positive predictive values and the actual impact of the interpretation skills of readers. Most clinical research is carried out at this level.

At level 3, we deal with the effect of test results and the way imaging information may have an impact on the differential diagnosis. This usually requires a prospective randomized trial, with its ethical and practical implications [24, 25] to attribute some portion of any improved patient condition to the use of an imaging test (or not).

Level 4 concerns comparison of intended therapeutic intents before the diagnostic examination is obtained with the treatment carried out after test results and the way imaging information changed the management.

Level 5 "patient outcome efficacy" reflects whether there is any impact on patient's outcome, i.e. his/her well-being. In other words, efficacy at this level requires that a technology diverts therapeutic choices in such a way that patients' conditions improve.

Level 6 or "societal efficacy" goes beyond the question of individual risks and benefits and is the level that defines the broadest level of efficacy. Efficacy at this level is required by policy makers when they must choose allocation of resources. It means that the costs borne by society for use of a given examination are acceptable, and diagnostic imaging examination is efficacious to the extent that it is an efficient use of societal resources to provide medical benefits to society.

With regard to hybrid imaging, the key issue is that the more global, "systems" view of efficacy forces one to consider standards that go beyond quality or accuracy of hybrid studies to examine the ultimate value or benefit to society that is derived from those examinations.

This hierarchical model can be applied with equal ease to nearly all diagnostic technologies, not just diagnostic imaging, and a key feature of this model is the understanding that for an imaging procedure to be efficacious at a higher level in this hierarchy, it must be efficacious at lower levels. However, the reverse is not true.

In general, assessing the impact of diagnostic imaging studies on patient outcome remains a challenging task, as imaging usually is just one step within the overall management strategy which involves many decisions and other types of clinical information to drive decision-making.

3.5 Economic Evidence on the Use of Nuclear Cardiology

Projected annual costs associated with cardiovascular disease (CVD) continue to grow largely due to the enormous burden of the disease that impacts nearly half of all adults [26]. The resources required to care for this population at risk and living with CVD is equally hefty including costs associated with the diagnostic evaluation and treatment. For example, in the USA, CVD is associated with ~40% of total healthcare expenditures including costs associated with drug treatment [27]. For cardiac imaging, diagnostic procedural growth and utilization volume also contribute to rising costs associated with CVD [28].

Comparing the costs of a given procedure remains an important consideration for creating efficiency within the patient's evaluation and to improve selectivity and optimize the use of lower cost procedures. For nuclear cardiology procedures, the overall costs are generally higher than that of exercise electrocardiography (ECG) due to the need for more expensive equipment, isotopes, and experienced technologists; all increasing the overall cost of the test. However, around the world costs for nuclear cardiology vary when compared to the use of echocardiography, magnetic resonance imaging, or for computed tomographic imaging. So, although we will discuss the cost efficiency and effectiveness, it remains important for readers of this chapter to take the published evidence and apply it within their own healthcare system and local costs.

The total cost of a procedure should include the upfront as well as downstream or follow-up costs. This would sum across a given period of follow-up or at a minimum to include the episode of care. As well, to be comprehensive, cost analyses should also include indirect as well as direct healthcare costs. Indirect costs are those encumbered by the patient including out-of-pocket expenses, such as payments for a procedure, travel costs, or that due to missing a day of work. There is a predictable relationship between cost and patient risk whereby higher risk patients have higher rates of downstream testing. This makes sense as the patient with an abnormal SPECT-myocardial perfusion imaging will be more likely to proceed to invasive coronary angiography and potentially undergo coronary revascularization.

A brief review of the mathematical calculations required for economic modeling can help guide the reader toward a greater understanding of the literature. Cost effectiveness is defined using an incremental or comparative analysis of the differences in cost divided by the differences in outcomes. The result is the term incremental cost effectiveness ratio or ICER. ICER = (Δ cost/Δ outcome). Traditionally, the ICER calculation would include the denominator of life years saved or, in some cases, quality-adjusted life years saved. However, many other variants of this are also considered acceptable such as the cost per case detected of coronary artery disease. One challenge with the ICER is that they are often derived using decision models or simulations which rely on many assumptions and apply data inputs from varied resources. Thus, for any cost effectiveness analysis, the reader should take care to evaluate the appropriateness of the cost and outcomes as well as any assumptions made in the modeling process. All these factors may influence the results. For example, the assumption that all patients with abnormal tests proceed to invasive coronary angiography would increase overall costs and is generally not the pattern observed in clinical practice.

The calculation of an ICER can be used to compare optimal selection between two comparative diagnostic strategies and can be used to set local or national policies for a given procedural use. The use of the ICER to guide clinical application provides support for policy changes based on both clinical outcome and economic data to set appropriate standards for imaging utilization.

For nuclear cardiology, cost effectiveness analysis provides a comparison of cost and outcomes with other tests and under which circumstances a given patient indication is optimal. Moreover, the ICER allows policy and decision makers to evaluate the price of one additional outcome from switching from a given standard approach to a novel strategy. If the cost per life year saved is low enough, then the decision is considered favorable. The threshold for economic favorability in the USA has been historically set at <$50,000 per life year saved but may be set lower or higher based on a given countries economy and available resources for healthcare [29].

Several notable examples exist in the nuclear cardiology literature of cost effectiveness analysis [30–33]. One example compared 4637 patients undergoing SPECT-MPI with 4884 undergoing exercise echocardiography [31]. The results revealed that SPECT-MPI was more cost effective with an ICER of $32 thousand dollars per life year saved when compared with exercise echocardiography. The analysis revealed that prompt revascularization of patients with abnormal MPI studies improved life expectancy by nearly 3.0 years when compared with echocardiography. Overall, SPECT-MPI was more cost effective than echocardiography among higher likelihood patients including the elderly, diabetics, and those undergoing pharmacologic stress imaging. However, exercise echocardiography had a more favorable ICER (i.e., <$20,000 per life year saved) among lower risk patients, such as those with an intermediate Duke treadmill score. This analysis supports the value

of understanding patient risk to guide cost effectiveness analysis and optimal allocation of resources.

Importantly, for economic calculations, if there are no differences in outcome, then the calculation is one of cost savings or cost minimization. When differences in outcome exist between two comparative cohorts, then any identified cost savings may impact patient outcome and cause harm. Several notable examples exist in the nuclear cardiology literature when comparative outcomes were similar, yet sizeable cost savings were achieved [34–37]. In one older comparison, 3-year rates of coronary artery disease death and myocardial infarction were similar between an analysis comparing SPECT-MPI as a frontline procedure versus direct invasive coronary angiography [34]. Given the similar outcomes, differences in cost can identify a similarly safe but less expensive diagnostic strategy of care. Direct coronary angiographic costs ranged from $2900 to $4600 for low to high clinical risk subgroup as compared to $2400 to $3000 for SPECT-MPI patient risk groups ($p < 0.001$); decidedly less costly. Overall a nearly 30% cost savings for SPECT-MPI as the optimal frontline diagnostic procedure when compared with direct coronary angiography. A major driver of the lower cost is the low rate of invasive coronary angiography among patients with normal SPECT-MPI findings. These findings illustrate the importance of SPECT-MPI as a gatekeeper to invasive coronary angiography as an important means to elicit cost savings. A similar analysis was published from a multicenter registry from Europe supporting the use of SPECT-MPI as associated with sizeable cost savings in the evaluation of patients with stable chest pain [38].

A summary of these findings reveals a robust evidence base on the economic evidence of SPECT-MPI. As regards the combination of MPI with coronary calcium or CT angiographic findings done directly with hybrid imaging systems, although specific data is not available, for either SPECT/CT or PET/CT, it remains likely that the combination may improve the timeliness of diagnosis and result in prompt efficient diagnostic care pathway. It can be anticipated that such a pathway would result in more selective use of invasive coronary angiography including improved referral of patients with obstructive coronary artery disease and provocative ischemia.

3.6 The Program in Human Health of the IAEA to Support Nuclear Medicine and Hybrid Imaging

The goal of the IAEA programme in Human Health is to enhance the capabilities in Member States to address needs related to prevention, diagnosis, and treatment of diseases through the application of nuclear techniques. This mandate arises from

Article II of the IAEA's Statute: "The Agency shall seek to accelerate and enlarge the contribution of atomic energy to peace, health and prosperity throughout the world."

To accomplish its Mission, the Division of Human Health run four sub-programs: Nuclear Medicine and Diagnostic Imaging (NMDI); Radiation Oncology and Cancer Treatment; Quality Assurance and Metrology in Radiation Medicine; and Nutrition for Improved Health. The sub-program in Nuclear Medicine and Diagnostic Imaging, run by the NMDI Section, has a long-term objective on enhancing Member States' capability to address health needs by the use nuclear techniques in both imaging and therapeutic applications.

Different activities are run under this subprogram: Coordinated Research Projects (CRPs); Expert Meetings to advise the Agency on specific topics; scientific publications; guidance documents; and educational website [39] and databases [20] Many projects run under Nuclear Medicine have been oriented towards the clinical applications of standard and emerging technologies in Nuclear Medicine such as SPECT/CT, PET/CT for diseases related to two of the major causes of death: cancer and cardiovascular diseases. Focus is also given to therapeutic applications wherein the primary objective is to make available fundamental radiopharmaceuticals for routine clinical use in developing countries [40], and to develop, evaluate, and standardize new diagnostic and therapeutic radiopharmaceuticals for the effective use in diagnostic and therapeutic nuclear medicine procedures. Finally, the section manages projects related to quality improvement and implementation of quality systems in the clinical practice of nuclear medicine [41].

Besides those activities, NMDI also provides support to projects of international technical cooperation managed by the Technical Cooperation Department [42, 43] whose technical cooperation program (TCP) helps Member States to establish effective strategic partnerships with countries and development organizations. It also examines how collaborative efforts may help to meet the requirements of the United Nations' Agenda 2030 and the Sustainable Development Goals [44], of which Human Health is an integral part.

The IAEA's technical cooperation TCP supports national development priorities and needs and is the main mechanism through which the IAEA supports Member States, including support to achieve their identified SDGs. The Agency's TCP is delivered in four regions: Africa, Asia and the Pacific, Europe (and countries in Central Asia), and Latin America and the Caribbean. These needs are identified from national development plans, sectoral strategies, regional profiles, and other relevant programming strategies, such as the 2030 Agenda, including the SDGs, and United Nations Development Assistance Frameworks (UNDAFs), through the Country Programme Framework (CPF).

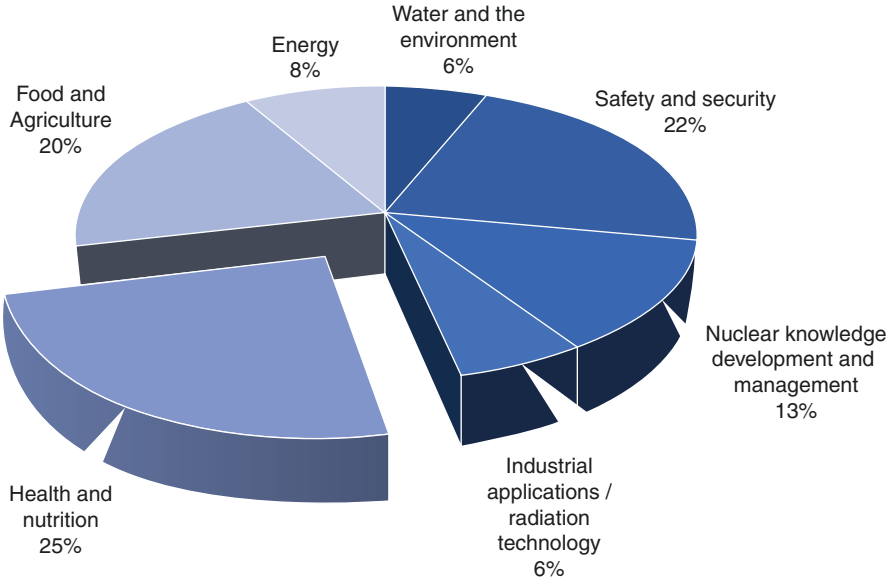

Fig. 3.3 Technical cooperation program disbursements (actuals) by technical field for 2019. (Source: Technical Cooperation report, IAEA 2019)

In 2019 the technical cooperation fund (TCF) has supported projects in 147 recipient countries and territories including 25 least develop countries, for a total budget of Euro 86 million, of which 25% pertain to the health area (Fig. 3.3).

3.7 Human Resources Capacity Building

Projects covering hybrid imaging supported by the IAEA may include procurement of machinery which in some cases could be SPECT/CT systems, while procurement of PET/CT scanners requires substantial cost-sharing from the recipient country. However, considering the magnitude of the financial investments, all projects must become self-sustainable once the Agency completes its commitments. Therefore, the IAEA puts a lot of energy into human resources capacity building and education and training remains an integral part of the assistance provided to Member States.

In the last years, supported by 134 TCP projects, more than 350 NM practitioners coming from 75 different countries were placed for fellowships (Fig. 3.4a) focused on hybrid imaging (both SPECT/CT and PET/CT) which may last from a few months, when the objective of the training is acquiring new skills or

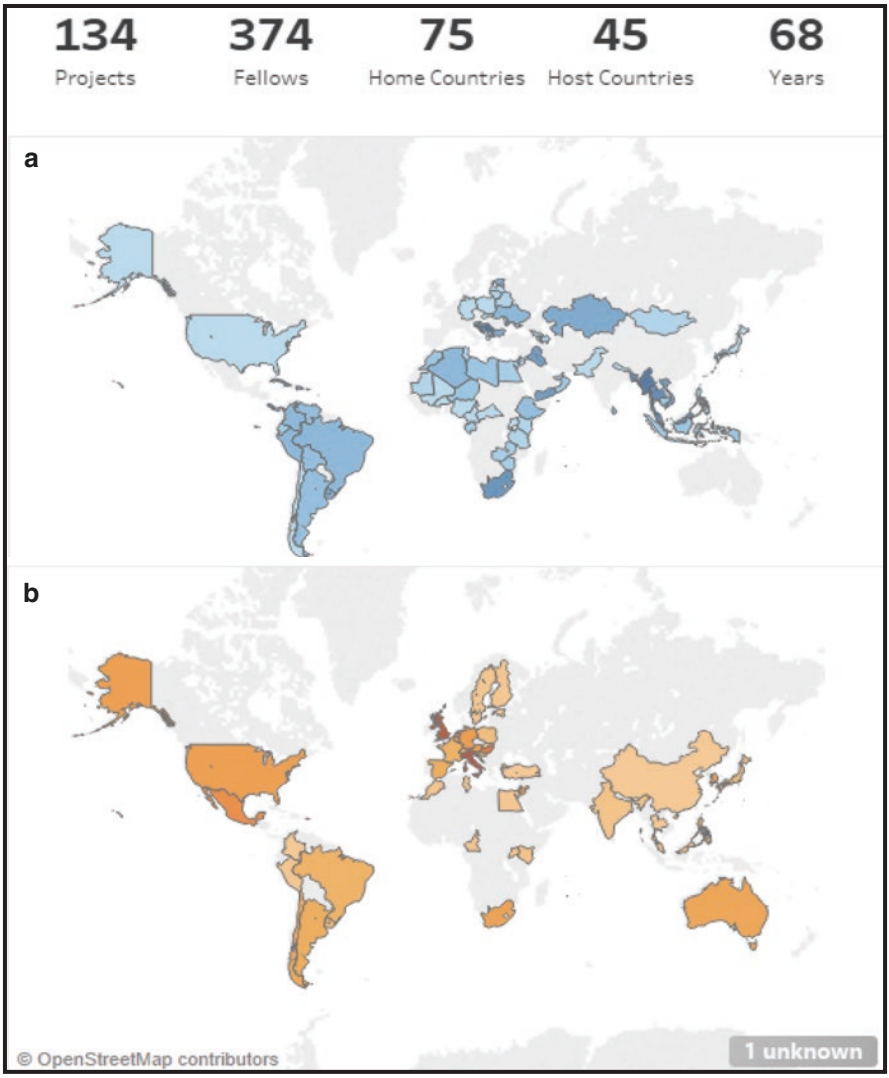

Fig. 3.4 The distribution of fellows for hybrid imaging fellowships by home country (upper half, **a**) and host country (lower half, **b**) in the last 10 years, is shown in this map. (Source: PCMF database, IAEA)

strengthening existing ones, up to 3–4 years in case of medical doctors requiring certification of specialty. The aggregate number of years of training of these fellows, hosted in 45 countries (Fig. 3.4b), has been about 68 years. A breakdown of those numbers shows that 70% of those fellowships were focused on PET/CT and only

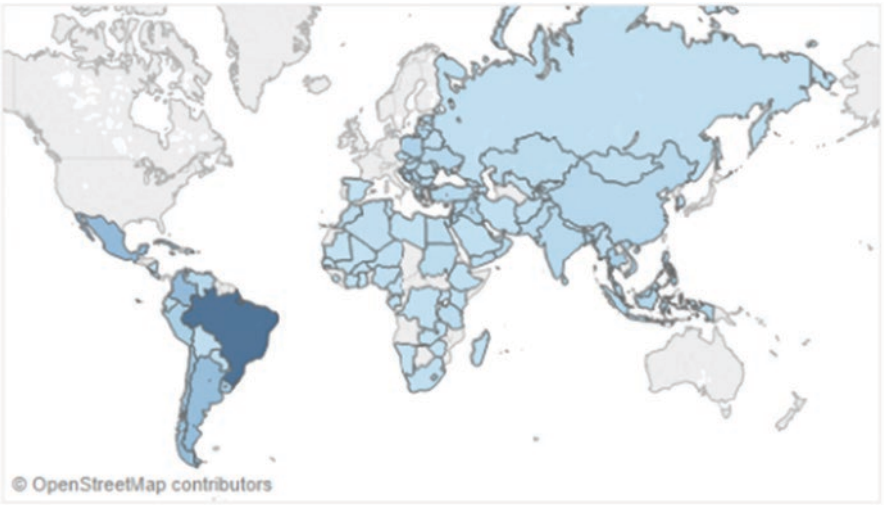

Fig. 3.5 Participants to regional training courses by place of origin. (Source: PCMF database, IAEA)

30% on SPECT/CT, probably reflecting the greater complexity of the former and the greater need in LMICs.

In addition to this, other educational activities are being supported, such as regional training courses (RTCs) on all aspects of NM clinical practice. Limiting our analysis to hybrid imaging for all its applications, we have found that, in the last 10 years, 55 RTCs have been organized and financially supported, with 1167 participants from 103 different countries of origin (Fig. 3.5). Again, a breakdown of the numbers shows that the clear majority (almost 74%) attended RTCs on PET/CT applications.

Educational activities in nuclear cardiology have always been a priority for NMDI, in consideration of the burden of CVD in the developing world, the importance of NC applications in diagnosing and managing CVDs, as well as requests from Member States. Overall, for training in nuclear cardiology at large, the IAEA has supported more than 1000 practitioners for both fellowships and RTCs. More specifically for hybrid imaging in cardiology, the IAEA has supported 55 fellows from 18 home countries who have been placed in 24 different host countries, and 5 RTCs with 104 participants.

3.8 The Growth of Hybrid Imaging in Developing World

The IAEA maintains a worldwide database [20] where information from more than 1300 centers is collected. Currently, more than 1300 centers are counted (Fig. 3.6).

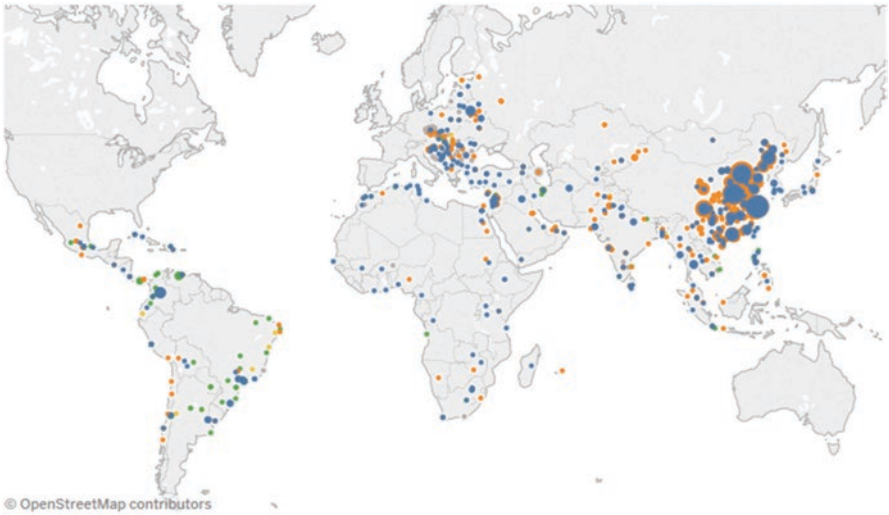

Fig. 3.6 Distribution of censored centers worldwide. (Source: NUMDAB)

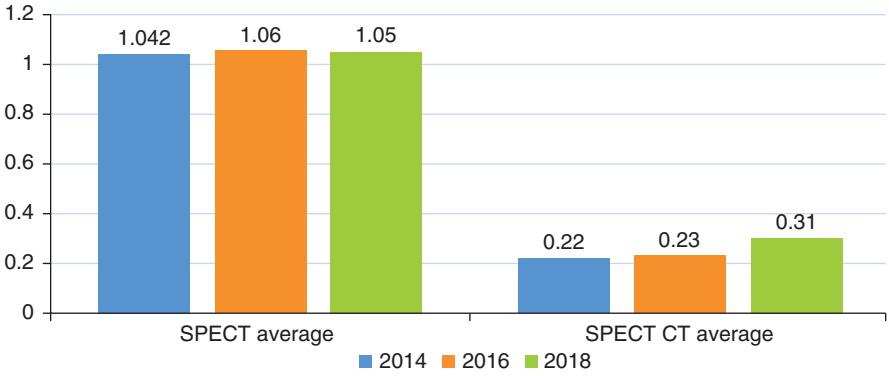

Fig. 3.7 Relative growth of SPECT and SPECT/CT scanners worldwide as counted on NUMDAB database

Through that instrument, information has been collected on the relative overall growth of SPECT/CT and PET/CT and we see that while the average number of SPECT scanners/center has not significantly increased and remained at about 1.05–1.06 scanners per center, the presence of SPECT/CT devices on average has increased from 0.22 to 0.31 per center (Fig. 3.7), a relative increase of about 50%.

Unlike stand-alone SPECT scanners which remain common, we have observed that stand-alone PET scanners are being outnumbered by hybrid PET/CT machines, similar to the developed world (Fig. 3.8).

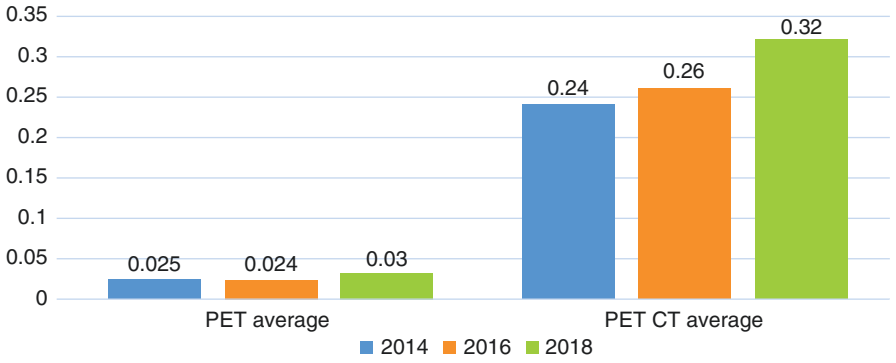

Fig. 3.8 Rate of growth of PET and PET/CT scanners in LMICs. (Source: NUMDAB)

3.9 Assessment of the Utilization of Hybrid Imaging Worldwide

A recently performed survey among physicians practicing nuclear medicine/nuclear cardiology to evaluate the current utilization of hybrid imaging (PET/CT and SPECT/CT) allowed to collect data from 80 countries in both high-income countries (HIC, $n = 16$) and low- and middle-income countries (LMIC, $n = 64$) representing all the regions of the world. This survey, together with data already available at the IAEA/NUMDAB, allowed for an assessment of the availability of hybrid imaging technology worldwide and showed that these are available at country level in all world regions (Fig. 3.9).

As seen on Fig. 3.9, both technologies are widely available in the Americas (North and Latin America), in Europe, Asia, and Oceania. The figure shows, however, a heterogeneous availability in Africa region with only five countries where both types of scanners are available. Furthermore, in this region, while 11 countries have at least one of the two, and more specifically only SPECT/CT, many others, particularly sub-Saharan countries, have none.

According to this survey, the practice of nuclear cardiology (NC), using any form of equipment, hybrid or not, is either non-existent or practiced at a very low volume in more than 50% of centers in LMIC (<50 patients/month/center). By comparison, nearly 50% of the centers in HIC perform at least 100 patients per month, a clear demonstration of the contrast between LMIC and HIC regarding NC utilization in general.

When those performing NC procedures in HIC and LMIC were queried about the use of SPECT/CT for NC procedures, it was observed that, while 37.5% of the studies are done using this technology in HIC, contrasting to only 21.7% in LMIC (Fig. 3.10). No NC studies are done using SPECT/CT in 43.3% of centers in LMIC, which could be expected due to the limited availability of the technology, but this was also reported in 30.4% of centers in HIC.

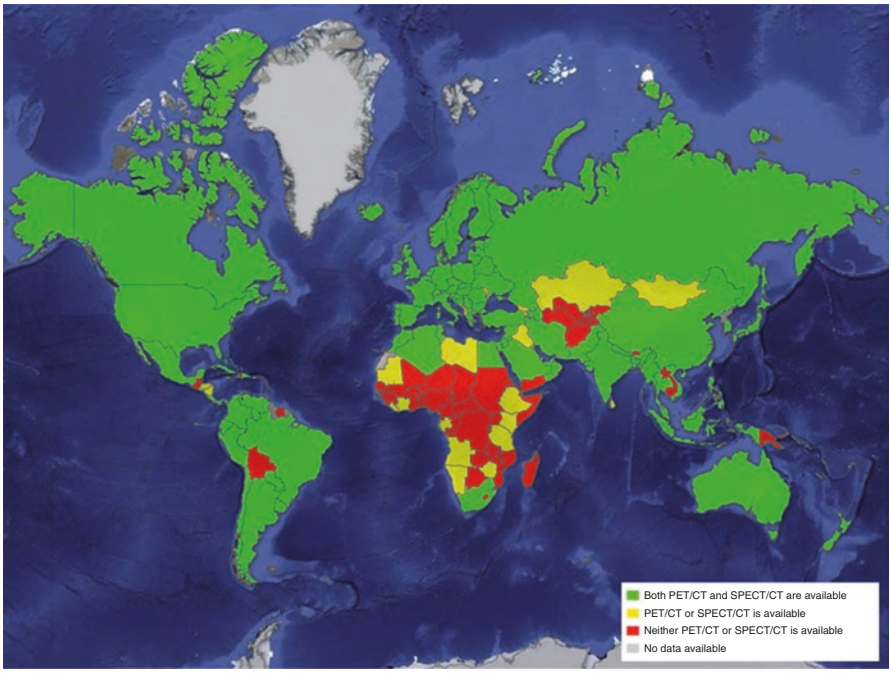

Fig. 3.9 Availability of hybrid technology (PET/CT and/or SPECT/CT) worldwide, integrating information from the survey and data from IAEA database/NUMDAB [20]

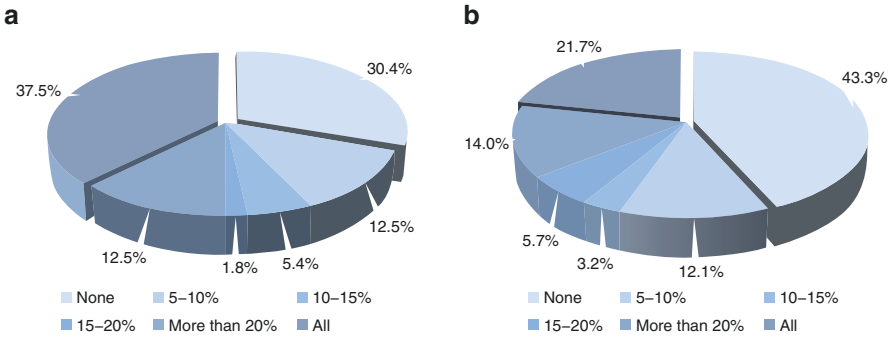

Fig. 3.10 Percentage of nuclear cardiology studies using SPECT/CT in high-income countries (**a**) and low- and middle-income countries (**b**)

As one of the explanations for the low utilization could be that, although practicing NC, some centers might not be equipped with SPECT/CT, we examined in greater detail this question from only the centers with SPECT/CT available and asked whether they use it for NC (Fig. 3.11).

Notably, when available for myocardial perfusion imaging, 67% of the participants are using their SPECT/CT for attenuation correction (AC), for assessing

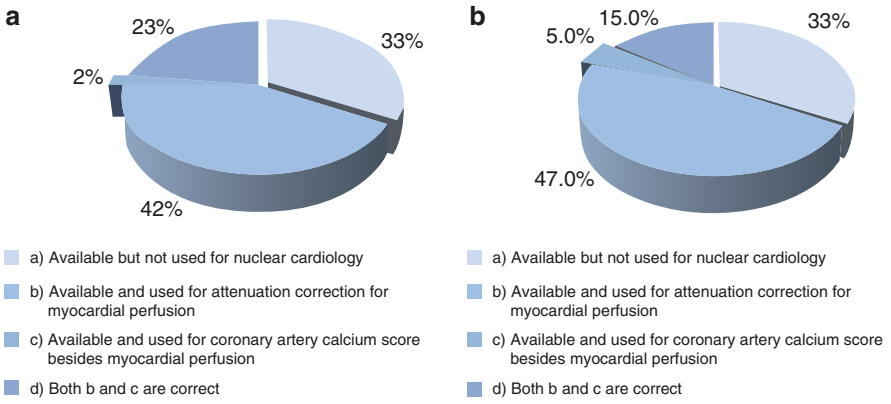

Fig. 3.11 Use of SPECT/CT for AC and/or CACS in high-income countries (**a**) and low- and middle-income countries (**b**)

coronary artery calcium score (CACS) or a combination of both. In HIC, the combination of both is more frequent compared to LMIC (23 vs 15%). These data reveal that despite SPECT/CT availability at their center, 33% of the participants to this survey are not using hybrid imaging at all for NC and this holds true for both HIC and LMIC (Fig. 3.11).

Regarding CACS evaluation, it could also be observed in Fig. 3.11 that, despite its demonstrated prognostic value [45], only 25 and 20% in HIC and LMIC of those doing NC studies using SPECT/CT are also performing CACS.

One interesting question that could be raised is why hybrid systems, even when available, are not being used fully for attenuation correction (AC) and/or CACS which could benefit patient care? Possible explanations could be related to reimbursement issues; lack of training/knowledge from either referring physicians or nuclear physicians/cardiologists; workload or time required for oncologic procedures using this equipment.

Regarding PET/CT, the survey has shown that 79.3% of participants from HIC and 63.2% from those in LMIC do have PET/CT technology available. Nevertheless, only 22.4% of those in HIC and 10.9% in LMIC PET/CT (Fig. 3.12) use it for multiple NC applications, including myocardial perfusion and others (i.e. sarcoid, viability, endocarditis).

Finally, when participants were inquired about the progress of PET/CT for NC applications at their centers, their answers showed that an increase was observed by 64.5% of participants in HIC as opposed to only 47.5% of those in LMIC (Fig. 3.13).

The same question was asked about the progress of SPECT-CT over the last 5 years and approximately 50% of the participants in both HIC and LMIC have observed no significant change in utilization (Fig. 3.14).

Indeed, a decrease was observed by 9.7% of those in HIC vs 16.4% of those in LMIC. Some reasons for this may be related to: (a) limited availability of technology within the country resulting in overload of existing scanners for oncologic indications, (b) non-availability of perfusion agents for PET/CT in LMICs, (c)

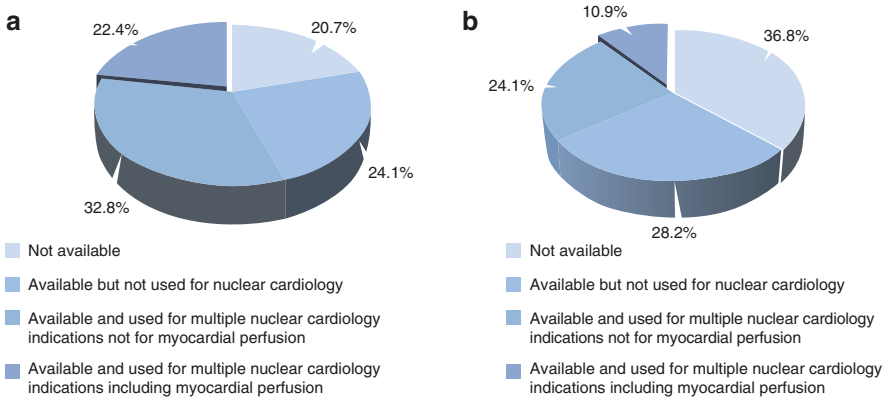

Fig. 3.12 Availability and utilization of PET/CT in high-income countries (**a**) and low- and middle-income countries (**b**)

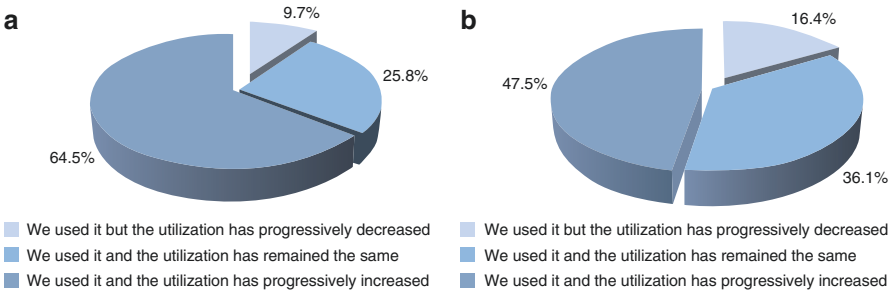

Fig. 3.13 Progress of PET/CT for NC applications in the past 5 years

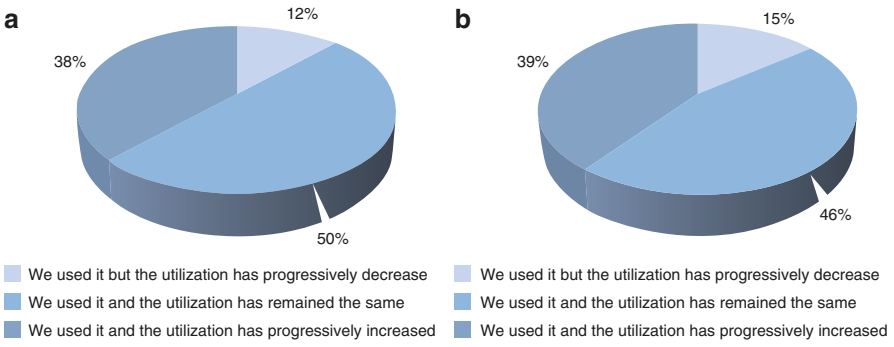

Fig. 3.14 Progress of SPECT/CT for NC applications in the past 5 years

reimbursement issues in some countries, frequently limited to oncologic applications, and/or (d) lack of knowledge/training.

In conclusion, hybrid imaging is growing worldwide and even more so for PET/CT, notably also in LMICs and the developed world. However, its application in NC is not yet so widespread and, while this finding might be related to the very limited availability of that instrumentation which is mainly employed for oncologic applications in LMICs, explanations for HICs require further analysis.

References

1. https://www.who.int/news-room/fact-sheets/detail/cardiovascular-diseases-(cvds). Accessed 8 Feb 2019.
2. https://sustainabledevelopment.un.org/post2015/transformingourworld. Accessed 16 Nov 2018.
3. https://ec.europa.eu/europeaid/policies/european-development-policy/2030-agenda-sustainable-development_en. Aaccessed 16 Nov 2018.
4. https://www.iaea.org/about/statute. Accessed 16 Nov 2018.
5. Jaarsma C, Leiner T, Bekkers SC, et al. Diagnostic performance of noninvasive myocardial perfusion imaging using single-photon emission computed tomography, cardiac magnetic resonance, and positron emission tomography imaging for the detection of obstructive coronary artery disease: a meta-analysis. J Am Coll Cardiol. 2012;59:1719–28.
6. IAEA Human Health Series No. 33. Quality management audits in nuclear medicine practices. 2nd ed. Vienna: International Atomic Energy Agency; 2015.
7. IAEA Human Health Series No. 23 (Rev. 1). Nuclear cardiology: guidance on the implementation of SPECT myocardial perfusion imaging. Vienna: International Atomic Energy Agency; 2016.
8. Einstein AJ, Pascual TN, Mercuri M, Karthikeyan G, Vitola JV, Mahmarian JJ, Better N, Bouyoucef SE, Hee-Seung Bom H, Lele V, Magboo VP, Alexánderson E, Allam AH, Al-Mallah MH, Flotats A, Jerome S, Kaufmann PA, Luxenburg O, Shaw LJ, Underwood SR, Rehani MM, Kashyap R, Paez D, Dondi M, INCAPS Investigators Group. Current worldwide nuclear cardiology practices and radiation exposure: results from the 65 country IAEA Nuclear Cardiology Protocols Cross-Sectional Study (INCAPS). Eur Heart J. 2015;36(26):1689–96. https://doi.org/10.1093/eurheartj/ehv117. Epub 2015 Apr 21.
9. Dondi M, Rodella C, Giubbini R, Camoni L, Karthikeyan G, Vitola JV, Einstein AJ, Arends BJ, Morozova O, Pascual TN, Paez D. I-MAP investigators inter-reader variability of SPECT MPI readings in low- and middle-income countries: results from the IAEA-MPI Audit Project (I-MAP). J Nucl Cardiol. 2020;27(2):465–78. https://doi.org/10.1007/s12350-018-1407-4.
10. Dondi M, Pascual T, Paez D, Einstein AJ. Nuclear cardiology: are we using the right protocols and tracers the right way? Am J Cardiovasc Drugs. 2017;17(6):441–6. https://doi.org/10.1007/s40256-017-0230-7. Review.
11. Phillips LM, Vitola JV, Shaw LJ, Giubbini R, Karthikeyan G, Alexanderson E, Dondi M, Paez D, Peix A. Value of gated-SPECT MPI for ischemia-guided PCI of non-culprit vessels in STEMI patients with multivessel disease after primary PCI. J Nucl Cardiol. 2018;25(5):1616–20. https://doi.org/10.1007/s12350-018-1368-7. Epub 2018 Aug 1.
12. Karthikeyan G, Guzic Salobir B, Jug B, Devasenapathy N, Alexanderson E, Vitola J, Kraft O, Ozkan E, Sharma S, Purohit G, Dolenc Novak M, Meave A, Trevethan S, Cerci R, Zier S, Gotthardtová L, Jonszta T, Altin T, Soydal C, Patel C, Gulati G, Paez D, Dondi M, Kashyap R. Functional compared to anatomical imaging in the initial evaluation of patients with suspected coronary artery disease: an international, multi-center, randomized controlled trial (IAEA-SPECT/CTA study). J Nucl Cardiol. 2017;24(2):507–17. https://doi.org/10.1007/s12350-016-0664-3. Epub 2016 Oct 28.

13. Mariani G, Bruselli L, Kuwert T, Kim EE, Flotats A, Israel O, Dondi M, Watanabe N. A review on the clinical uses of SPECT/CT. Eur J Nucl Med Mol Imaging. 2010;37(10):1959–85. https://doi.org/10.1007/s00259-010-1390-8. Epub 2010 Feb 25. Review.
14. Di Carli MF, Hachamovich R. New technology for noninvasive evaluation of coronary artery disease. Circulation. 2007;115:1464–80.
15. de Galiza Barbosa F, Delso G, Ter Voert EE, Huellner MW, Herrmann K, Veit-Haibach P. Multi-technique hybrid imaging in PET/CT and PET/MR: what does the future hold? Clin Radiol. 2016;71:660–72. https://doi.org/10.1016/j.crad.2016.03.013. Epub 2016 Apr 21.
16. Huang JY, Huang CK, Yen RF, Wu HY, Tu YK, Cheng MF, Lu CC, Tzen KY, Chien KL, Wu YW. Diagnostic performance of attenuation-corrected myocardial perfusion imaging for coronary artery disease: a systematic review and meta-analysis. J Nucl Med. 2016;57(12):1893–8. Epub 2016 Jul 21. Review.
17. Pazhenkottil AP, Benz DC, Gräni C, Madsen MA, Mikulicic F, von Felten E, Fuchs TA, Moch BH, Stehli J, Lüscher TF, Gaemperli O, Buechel RR, Kaufmann PA. Hybrid SPECT perfusion imaging and coronary CT angiography: long-term prognostic value for cardiovascular outcomes. Radiology. 2018;288(3):694–702. https://doi.org/10.1148/radiol.2018171303. Epub 2018 Jul 3.
18. Engbers EM, Timmer JR, Ottervanger JP, Mouden M, Knollema S, Jager PL. Prognostic value of coronary artery calcium scoring in addition to single-photon emission computed tomographic myocardial perfusion imaging in symptomatic patients. Circ Cardiovasc Imaging. 2016;9(5). pii: e003966 https://doi.org/10.1161/CIRCIMAGING.115.003966.
19. http://www.who.int/gho/health_financing/health_expenditure/en/. Accessed 19 Nov 2018.
20. https://humanhealth.iaea.org/HHW/NuclearMedicine/NUMDAB/index.html. Accessed 19 Nov (under renovation).
21. Raftery J, Hanney S, Greenhalgh T, Glover M, Blatch-Jones A. Models and applications for measuring the impact of health research: update of a systematic review for the health technology assessment programme. Health Technol Assess. 2016;20(76):1–254. Review.
22. Fryback DG, Thornbury MD. The efficacy of diagnostic imaging. Med Decis Mak. 1991;11:88–94.
23. Gazelle GS, Kessler L, Lee DW, et al. A framework for assessing the value of diagnostic imaging in the era of comparative effectiveness research. Radiology. 2011;261:692–8.
24. Freedman B. Equipoise and the ethics of clinical research. N Engl J Med. 1987;317(3):141–5.
25. Edwards SJ, Lilford RJ, Hewison J. The ethics of randomised controlled trials from the perspectives of patients, the public, and healthcare professionals. Br Med J. 1998;317(7167):1209–12.
26. Papanicolas I, Woskie LR, Jha AK. Health care spending in the United States and other high-income countries. JAMA. 2018;319(10):1024–39. https://doi.org/10.1001/jama.2018.1150. [Published Online First: 2018/03/15].
27. Shaw LJ, Goyal A, Mehta C, et al. 10-Year resource utilization and costs for cardiovascular care. J Am Coll Cardiol. 2018;71(10):1078–89. https://doi.org/10.1016/j.jacc.2017.12.064. [Published Online First: 2018/03/10].
28. Mark DB, Anderson JL, Brinker JA, et al. ACC/AHA/ASE/ASNC/HRS/IAC/Mended Hearts/NASCI/RSNA/SAIP/SCAI/SCCT/SCMR/SNMMI 2014 health policy statement on use of noninvasive cardiovascular imaging: a report of the American College of Cardiology Clinical Quality Committee. J Am Coll Cardiol. 2014;63(7):698–721. https://doi.org/10.1016/j.jacc.2013.02.002. [Published Online First: 2014/02/22].
29. Anderson JL, Heidenreich PA, Barnett PG, et al. ACC/AHA statement on cost/value methodology in clinical practice guidelines and performance measures: a report of the American College of Cardiology/American Heart Association Task Force on Performance Measures and Task Force on Practice Guidelines. J Am Coll Cardiol. 2014;63(21):2304–22. https://doi.org/10.1016/j.jacc.2014.03.016. [Published Online First: 2014/04/01].
30. Shaw LJ. Cost-effectiveness and future implications for cardiovascular imaging. Can J Cardiol. 2013;29(3):350–7. https://doi.org/10.1016/j.cjca.2012.10.017. [Published Online First: 2013/01/22].

31. Shaw LJ, Marwick TH, Berman DS, et al. Incremental cost-effectiveness of exercise echocardiography vs. SPECT imaging for the evaluation of stable chest pain. Eur Heart J. 2006;27(20):2448–58. https://doi.org/10.1093/eurheartj/ehl204. [Published Online First: 2006/09/28].
32. Underwood SR, Shaw LJ, Anagnostopoulos C, et al. Myocardial perfusion scintigraphy and cost effectiveness of diagnosis and management of coronary heart disease. Heart. 2004;90(Suppl 5):v34–6. https://doi.org/10.1136/hrt.2003.019133. [Published Online First: 2004/07/16].
33. Hachamovitch R, Berman DS, Kiat H, et al. Value of stress myocardial perfusion single photon emission computed tomography in patients with normal resting electrocardiograms: an evaluation of incremental prognostic value and cost-effectiveness. Circulation. 2002;105(7):823–9. [Published Online First: 2002/02/21].
34. Shaw LJ, Heller GV, Travin MI, et al. Cost analysis of diagnostic testing for coronary artery disease in women with stable chest pain. Economics of Noninvasive Diagnosis (END) Study Group. J Nucl Cardiol. 1999;6(6):559–69. [Published Online First: 1999/12/23].
35. Shaw LJ, Hachamovitch R, Berman DS, et al. The economic consequences of available diagnostic and prognostic strategies for the evaluation of stable angina patients: an observational assessment of the value of precatheterization ischemia. Economics of Noninvasive Diagnosis (END) Multicenter Study Group. J Am Coll Cardiol. 1999;33(3):661–9. [Published Online First: 1999/03/18].
36. Shaw LJ, Miller DD, Berman DS, et al. Clinical and economic outcomes assessment in nuclear cardiology. Q J Nucl Med. 2000;44(2):138–52. [Published Online First: 2000/09/01].
37. Des Prez RD, Shaw LJ, Gillespie RL, et al. Cost-effectiveness of myocardial perfusion imaging: a summary of the currently available literature. J Nucl Cardiol. 2005;12(6):750–9. https://doi.org/10.1016/j.nuclcard.2005.10.001. [Published Online First: 2005/12/14].
38. Underwood SR, Godman B, Salyani S, et al. Economics of myocardial perfusion imaging in Europe—the EMPIRE study. Eur Heart J. 1999;20(2):157–66. [Published Online First: 1999/04/01].
39. https://humanhealth.iaea.org/HHW/NuclearMedicine/index.html. Accessed 7 Feb 2019.
40. https://www-pub.iaea.org/MTCD/publications/PDF/Pub1342/Pub1342_web.pdf. Accessed 7 Feb 2019.
41. https://www-pub.iaea.org/books/IAEABooks/10714/Quality-Management-Audits-in-Nuclear-Medicine-Practices-Second-Edition. Accessed 7 Feb 2019.
42. https://www.iaea.org/services/technical-cooperation-programme. Accessed 26 Nov 2018.
43. https://www.iaea.org/sites/default/files/publications/reports/2019/gc64-3.pdf. Accessed 26 Nov 2018.
44. https://www.un.org/sustainabledevelopment/sustainable-development-goals/. Accessed 26 Nov 2018.
45. Budoff MJ, Mayrhofer T, Ferencik M, et al., for the PROMISE Investigators. Prognostic value of coronary artery calcium in the PROMISE study (prospective multicenter imaging study for evaluation of chest pain). Circulation. 2017;136(21):1993–2005. https://doi.org/10.1161/CIRCULATIONAHA.117.030578. Epub 2017 Aug 28.

Part II

SPECT/CT

Perfusion, Calcium Scoring, and CTA

4

Kenji Fukushima and Michinobu Nagao

4.1 Coronary Dominancy and Variations

The dominancy of coronary artery distribution is typically defined according to the origin of posterior descending artery [1]. From large number registry of The National Cardiovacular Database Cath Percutaneus Coronary Intervention Registry, Parikh et al. reported that right dominant coronary was found in 169,809 out of 207,926 patients (about 80%), while 20,974 (10%) were found to be left dominant [2]. The variation analysis using CTA (64 slice-CT) reported that 76% showed right dominant and left dominant was only 9.1% out of 700 patients [3]. These findings were similar to the results of Parikh et al's study. Individual coronary anatomy shows significantly wide variation in second branch level, while the dominancy of major coronary tree can be categorized in several patterns. It is occasionally necessary to presume individual coronary path in interpretation of nuclear cardiology. Image interpretation of myocardial perfusion SPECT usually requires nuclear cardiologist to focus on branch distribution of left ventricle which is mainly supplied by left coronary artery (LCA), while right coronary artery (RCA) is mostly dominant vessel in the whole heart. The distribution of distal branch from

K. Fukushima (✉)
Department of Nuclear Medicine, Saitama Medical University International Medical Center, Saitama, Japan

Department of Cardiology, Saitama Medical University International Medical Center, Saitama, Japan

M. Nagao
Department of Diagnostic Imaging and Nuclear Medicine, Tokyo Women's Medical University, Tokyo, Japan

S. G. Nekolla, C. Rischpler (eds.), *Hybrid Cardiac Imaging*,
https://doi.org/10.1007/978-3-030-83167-7_4

left circumferential artery (LCX) and RCA is one of the challenges for nuclear cardiologist to determine culprit vessel in regional ischemia or infarction on inferior to postero-lateral wall.

Territorial analysis in the coronary artery is challenging due to the difficulty of comprehension of dominance in its microvascular level. Several studies suggest to employ coronary CTA based myocardial segmentation (alternatively, called voronoi-based segmentation) [4]. Validation analysis was conducted both in and ex vivo [5–7]. The algorithm is based on segmentation on the area of epicardial surface, and has the limitation of incapability in endomyocardial segmentation, including the papillary muscle level. However, to date, nuclear cardiology has access to only territorial interpretation by default territory presets which can be discrepant from individual coronary dominance and path. Sample illustration of 2D bull's eye output from 3D coronary CTA with typical coronary dominancy is shown in Fig. 4.1. The assessment of coronary dominancy can be more intuitive, and the territorial difference among cases is obvious in these 2D output when compared to default coronary territory presets.

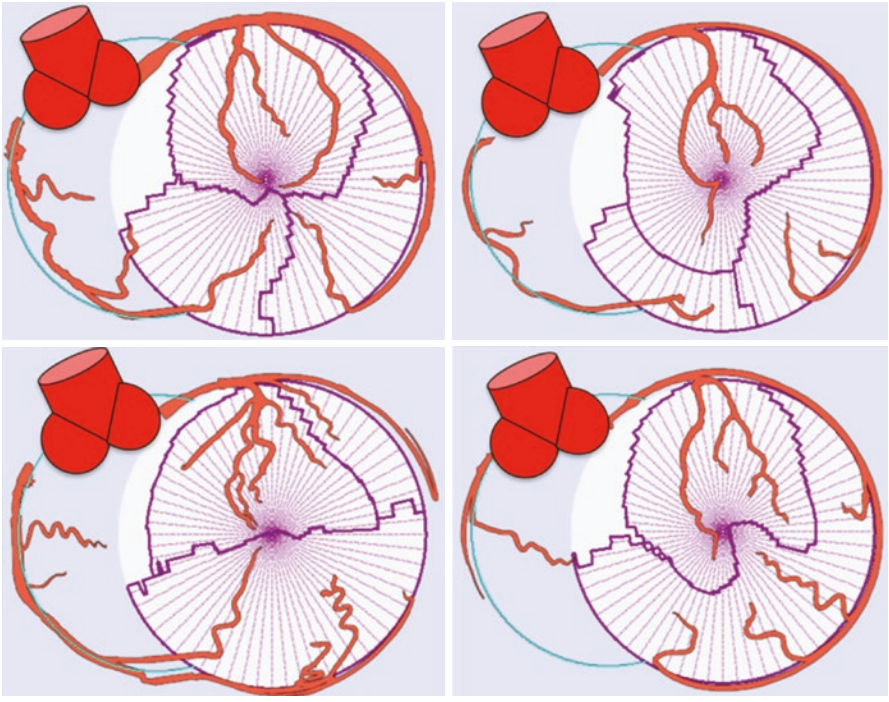

Fig. 4.1 Sample illustrations of 2D bull's eye output from 3D coronary CTA with typical coronary dominancy are shown. Left upper shows balanced distribution in left ventricle, upper right shows left descending artery dominant. Lower left shows right coronary artery dominant which covers whole inferior wall with posterior descending artery, and atrioventricular nodal branch. Lower right shows left circumflex artery dominant which distributes whole inferior wall, and RCA is hypoplastic which was not reachable posterior intraventricular groove

4.2 Calcium Scoring and Assessment of Plaque and Stenosis

Coronary calcium surrogates the pathophysiology of the various causes including atherosclerosis and inflammation. Cumulative evidence suggests that the coronary atherosclerosis is associated with adverse cardiac events and increases mortality [8]. Calculation of coronary calcification had been initially established by Agatston et al. [9]. The initial calcium scoring was done by mostly 4–16 slice-CT which had significant limitation for time resolution and radiation exposure. In the era of high-speed, 320 row-detector CT with reduced radiation exposure, it has become more common to use CT as a part of preventive medicine [10, 11]. The main process of measuring coronary calcium is to use region of interest on coronary calcification along major coronary arteries. Using thresholds (mostly 130HU), volume over CT value was calculated as total Agatston score [12]. This step of calcium scoring is similar among most venders. The illustrative images for measurement of coronary calcium are shown in Fig. 4.2. Risk management using non-contrast enhanced CT has become the established stratification for low-intermediate risk groups combined with conventional non-invasive risk analysis such as MESA database [13]. As a limitation, extensive coronary calcification can frequently hinder reliable analysis of coronary artery in contrast enhanced scan. However, severe coronary calcification is known to be closely associated with significant coronary obstruction. For its simplicity, the novel approaches for calcium scoring have been attemped in the various opportunities to use CT scan, i.e. lung screening or attenuation correction [14–16]. The weakness of this method is that is no longer available after revascularization including stenting or bypass surgery, device implantation, and chest surgery due to trauma or disease. Vessel specific calcium scoring or

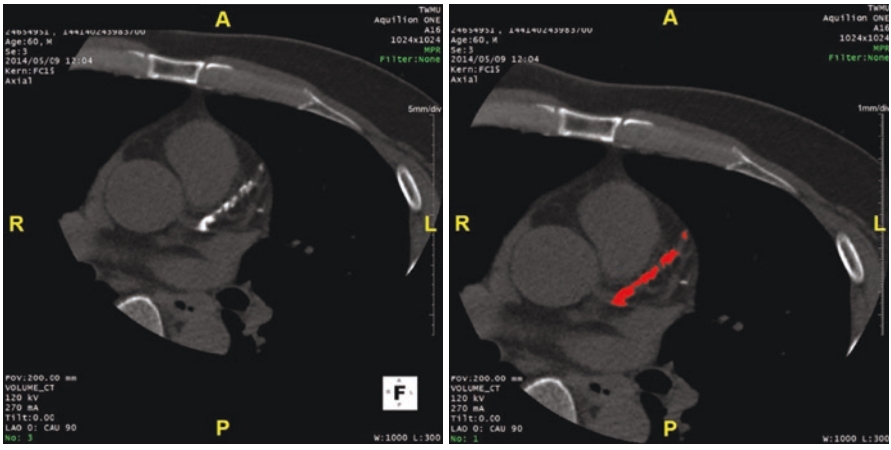

Fig. 4.2 Illustrative figure for coronary calcium scoring is shown. After manual ROI setting, CT value over 130 Hounsfield Units are automatically extracted, and total volume is generated as total Agatston score. Figure shows significant coronary calcification in left descending artery which is calculated as 360

analysis avoiding stent is available in almost all vendors, while those separated analysis remain unclear for its clinical value. Recently, a novel analysis beyond conventional CAC scoring has revealed to investigate the distribution of calcification among vessels in addition to summed value for whole coronary artery calcification [17].

Coronary atherosclerosis represents the course of the development of coronary atherosclerotic change, including soft plaque, and remodelling, and calcification. Despite the incomplete comprehension of the true mechanism due to multifaceted nature of plaque progression, the imaging modalities have successfully managed to visualise those pathological features [18]. The existence of mixed plaque is mostly observed as coexisting with calcified and soft plaque and occasionally contains a certain pattern of calcification on vessel wall with internal low-dense plaque, which is called "napkin ring sign." These findings can be visually identified in clinical routine. However, the measurement of CT value in the cross-sectional reconstruction is necessary for precise plaque evaluation [19]. Although a number of studies have demonstrated CTA analysis for prediction of plaque characteristics, wide variation of CT values for plaque composition are observed. Plaque is usually categorized as Hounsfield Units (lipid rich plaque as <30 or 50, fibrotic plaque as over 70–90) [19, 20]. The so-called 'vulnerable plaque' can be defined as high-risk plaque feature, including specific findings, i.e. spotty calcification, soft plaque, and positive remodelling [21, 22]. Figure 4.3 shows the representative case of routine coronary analysis using volume rendering, curved planar reconstruction images of mild and severe atherosclerosis, and typical high-risk plaque.

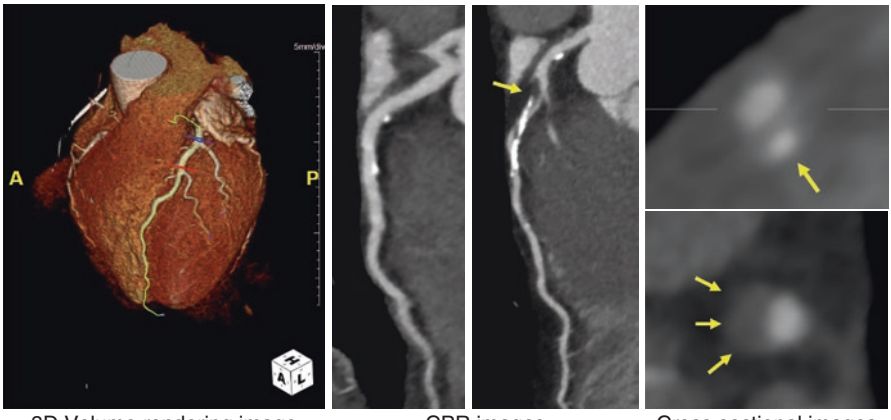

Fig. 4.3 Coronary CT analysis with volume rendering 3D, curved planar reformatted images (CPR), and cross-sectional images are shown. Left shows 3D volume rendering image for whole heart. Middle-left shows CPR for RCA with minimum coronary atherosclerosis. Middle-right shows severe atherosclerosis with obstructive proximal LAD. Right upper and lower show cross-sectional view images for high-risk plaque feature. Upper shows calcified vessel with internal low attenuation plaque (napkin ring like), and lower shows positive remodeling, lipid rich plaque (attenuation lower than 50HU), and spotty calcification

Basically, CTA has a strong feature for high negative predictive value (> 95%), while positive predictive value remains moderate [23]. Namely, the evaluation of organic stenosis is not clinically useful for prediction of flow-limiting coronary atherosclerosis. The assessment and/or decision-making in coronary revascularization has been based on the degree of luminal stenosis for decades. In 1980's, Quantitative Coronary Angiography (QCA) has been used in catheterization laboratory [24]. Various measuring methods (i.e. Caliper, Densitometry) have failed to overcome beyond the limitation of conventional visual estimation. This issue has not been resolved for decades, and FAME trial finally proved poor predictability of evaluating luminal stenosis for beneficial effect of coronary revascularization [25]. At present, functional assessment by fractional flow reserve (FFR) with the use of vasodilator stress during invasive coronary angiography has been common and required procedure for intermediate stenosis. Similar as above, the limitation of CTA has been incapability of detecting significant flow-limiting coronary artery disease, which can be frequently identified as transient regional ischemia for rest/stress myocardial perfusion SPECT or PET. Thus, functional and physiological evaluation has emerged as clinical needs for CTA, while it has provided anatomical informartion. Trans attenuation gradient (TAG) has been employed as potential method to detect flow-limiting coronary stenosis using routine CTA [26]. However, the latest studies revealed the significant diagnostic limitation of TAG for detecting functional flow-limiting coronary stenosis [27].

FFRct has emerged as powerful no-invasive FFR prediction tool, employing super computing technology with novel algorithm called computational fluid dynamics [28]. Initial studies demonstrated promising results to predict functional stenosis [29]. The large clinical trials, PROMISE trial, and ADVANCE registry have followed, and PROMISE trial demonstrated the threshold of FFRct = 0.8 significantly improved in predicting revasucularization and cardiac mortality. From ADVANCE registry, 1-year outcome revealed that FFRct higher than 0.8 showed lower rates of cardiac events, and long-term prognostic value of FFRct is expected [30]. However, it should be noted that in PROMISE trial, 67% patients was available to analysis for decision making, namely more than 30% subjects needs further analysis. This result indicated that there are frequent inappropriate candidates in clinical routine for FFRct.

4.3 Myocardial CT Perfusion by Dynamic CTA

The evolution of machine enable us to perform dynamic study during administration of contrast agent. CT perfusion has emerged as novel technique to detect stress induced hypo-attenuation as regional ischemia. Large clinical trials for stress myocardial CT perfusion such as CORE64, and CORE320 have demonstrated the promising results for predicting myocardial ischemia [31, 32].

Dynamic CT with reduced radiation exposure has been challenging. CT perfusion study needs both rest and stress scan in order to differentiate stress inducible hypo-attenuation from fixed perfusion defect which indicates myocardial infarction. Despite additional radiation exposure and time extension, the latest generation of

multi-slice CT sccaner allows us to perform with lower tube voltage and faster volume scan [33, 34]. This innovation has shown potential of significant usability for CTA as one-stop shop due to have dynamic 4D myocardial perfusion and late enhancement. Stress CT perfusion is limited for pharmacological vasodilation for detecting inducible ischemia. Pharmacological agents for CTP are mainly Dipyridamole, Adenosine, Dobutamine, and Regadenoson, and each has advantage and limitation in terms of cost-effectiveness or required procedure. Current problem is that CT perfusion scan with rest and stress usually take at least about 30 min including 15 min of contrast wash-out either rest/stress or stress/rest, and it may reduce examination throughput in the clinical routine. Moreover, extra equipment is required for automatic syringe for pharmacological stress, extra venous line for infusion, and continuous ECG monitoring.

Here, some facilities has attempted to evaluate intracoronary dynamic flow by 4D-CT as another strategy to identify flow-limiting coronary stenosis [35–37]. The basic concept is development of post-processing to multiply scanned images to animate dynamic series. Using commercially available, dedicated tool (motion coherence image processing by Physiodynamics®, ZIO station®, Ziosoft, Tokyo, Japan), scanned data are interpolated by multiplying neighboring phases up to 90–100 dynamic image datasets. Animated cine is available for visual interpretation with various reconstruction images such as volume rendering, multiplanar reconstruction, slab-maximum intensity projection images, or cross-sectional views [35, 37]. Automated volumetric tracking tool for 4D-CT enable continuous measurement of luminal CT attenuation. Figure 4.4 shows the sample dynamic image series of volume rendering and curved planar reformat combined image series of dynamic perfusion PET (Munich Heart, Munich, Germany). Wall motion kinetics is also available for analysis, and the feasibility of CT derived myocardial strain is increasingly investigated [37, 38].

4.4 Hybrid Analysis and Image Fusion (SPECT or PET and CTA)

In most clinical facilities, both coronary CTA and nuclear cardiology are available for cardiac examination. CTA and nuclear cardiology are routinely performed to detect coronary atherosclerosis or myocardial perfusion abnormality. Mostly, CTA is used as a first line non-invasive tool, and abnormal findings may drive candidates for myocardial perfusion imaging, or CTA may be performed later to rule out when SPECT shows mild abnormal which possibly be artifact. In real-world clinical decision making, the EVINCI study has demonstrated that hybrid interpretation by CTA and SPECT was recognized as a reliable approach for patient management [39]. A picture archiving and communication system (PACS) is available for most radiological image data, and side-by-sided image interpretation using PACS is available and easy in most facilities. Image fusion of CTA and

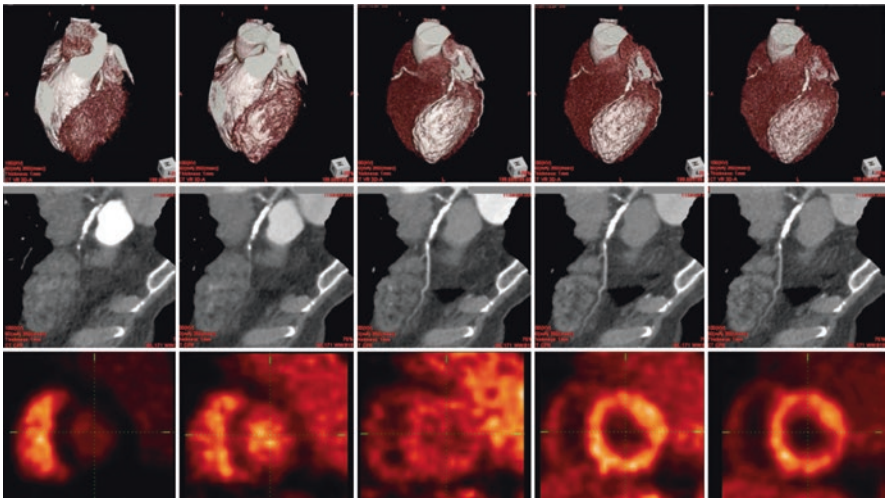

Fig. 4.4 Serial images for dynamic CTA is shown. Dynamic 4D images of whole heart and coronary flow is visualised using motion coherence image processing technique. This technique is based on image interpolation of scanned images up to four times. Dynamic images were made from 20 scans of diastole phase with low tube voltage. Volume rendering and CPR are also available for measurement of intracoronary or intramyocardium time density. Lower panel shows dynamic scan for myocardial perfusion with N-13 ammonia PET

nuclear cardiology is known as most persuasive approach to manifest the colocalization of regional myocardial ischemia and culprit vessel [40]. However, the image fusion of different modalities can be occasionally challenging due to the frequent misalignments and the discrepancy of temporal resolution among modalities. Figure 4.5 shows the schematic presentation of image fusion by CTA and PET or SPECT scan. Cardiac PET usually show high myocardial uptake with sufficient contrast. In advanced PET machine with time of flight technique, both ventricles are mostly visual and easy to merge one modality to another and confirm registration. Figure 4.6 shows the image fusion of CTA and ^{13}N ammonia PET. Image fusion can demonstrate regional flow reserve with the help of CTA based segmentation in addition to conventional fusion analysis of coronary path and regional ischemia [41]. On contrast, as shown in lower panel of figure 4.5, cardiac SPECT with conventional anger gamma camera shows lower contrast and blur myocardial contour. Consequently, it should be difficult to confirm image registration. Nevertheless, hybrid analysis by image fusion can bring convincing assessment for challenging case. Figure 4.7 shows CTA and SPECT for a patient with post-status of bypass surgery. Significant regional ischemia was identified in antero-lateral wall, while CTA revealed no stenosis or obstruction in bypass grafts. CTA-SPECT fusion showed that the ischemia was localized in distal region of narrowed native diagonal branch.

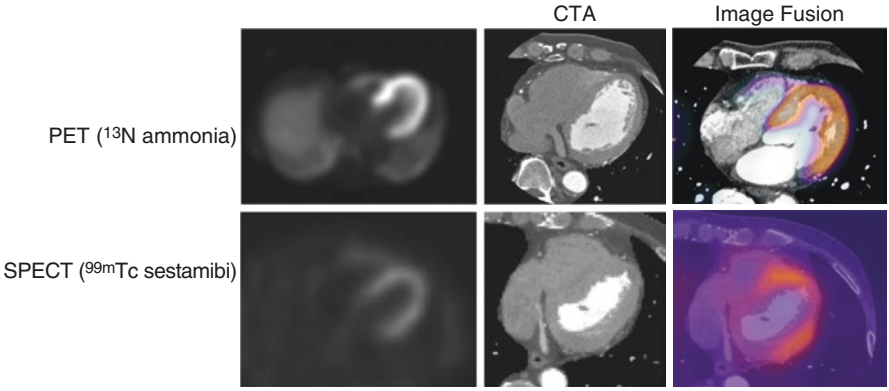

Fig. 4.5 The figure shows comparison of image fusion for CTA and PET or SPECT. Panels show transaxial view of each modality. Upper shows ^{13}N ammonia PET, CTA, and image fusion. Lower shows ^{99m}Tc sestamibi SPECT, CTA, and image fusion. Using high-resolution PET, image fusion to CTA is obviously feasible due to both RV and LV are visual, while it is occasionally challenging due to lower contrast and blur contour in SPECT images

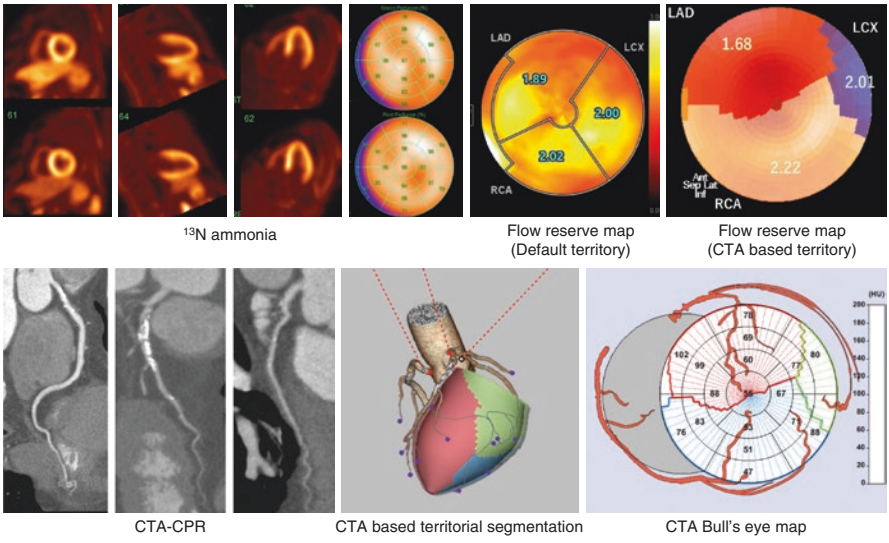

Fig. 4.6 Territorial analysis derived from 3D image fusion of CTA and PET is shown. CPR images show significant atherosclerosis in proximal LAD and suspect of obstructive. PET flow reserve map shows impaired flow response in anterior wall, while relative perfusion is normal from rest/stress static images. In default territorial map shows relatively impaired flow reserve in LAD territory (1.89). However, it shows 1.68 from patient based territorial flow analysis

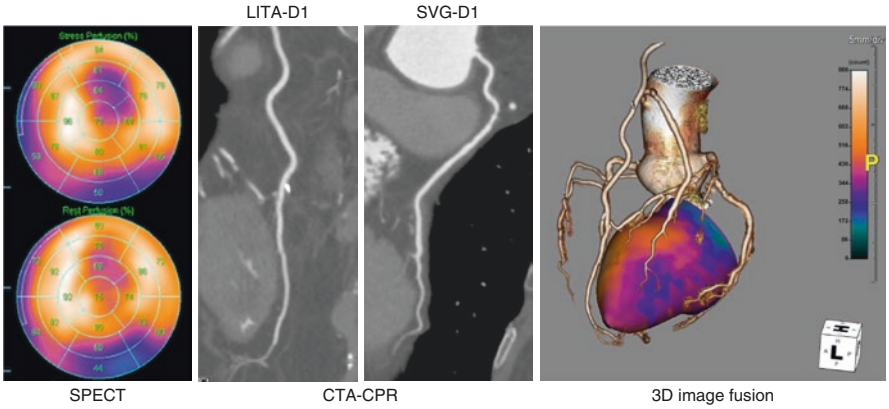

Fig. 4.7 3D fusion image of CTA and SPECT in a patient post status of bypass surgery is shown. SPECT shows regional ischemia in mid-anterolateral wall, while CTA shows no significant stenosis or obstruction in bypass grafts. Image fusion demonstrates the ischemia is corresponding for distal site of native diagonal branches

4.5 Future Direction and Visions

In view of the current trend, FFRct has a potential as a standard decision-making tool in clinical routine. Recent investigation has demonstrated the usability of CTA, FFRct, and CT perfusion in single cardiac CT session, optimizing CTA for the standard imaging technique of detecting organic, functional stenosis, and perfusion abnormality [42]. This promising development will enable us to perform anatomical and functional assessments within a single modality.

However, myocardial perfusion imaging provides different clinical information and the established evidence. Moreover, myocardial perfusion study with nuclear cardiology has substantial advantage in obtaining valuable information, including ischaemic burden, size of infarction, viability, stress induced functional impairment, wall motion abnormality, and transient stunning. Of note, the COURAGE nuclear substudy demonstrated that the reduction in ischaemic burden by coronary intervention was directly linked to better prognosis [43]. These clinical evidences are quite valuable information and CTA has not provided yet.

Non-invasive imaging technique including simple test such as calcium scan, or advanced hybrid assessment of coronary atherosclerosis and endothelial dysfunction will remain as primal strategy and provide significant incremental value in clinical decision-making.

References

1. Engel HJ, Torres C, Page HL Jr. Major variations in anatomical origin of the coronary arteries: angiographic observations in 4,250 patients without associated congenital heart disease. Catheter Cardiovasc Diagn. 1975;1(2):157–69.
2. Parikh NI, et al. Left and codominant coronary artery circulations are associated with higher in-hospital mortality among patients undergoing percutaneous coronary intervention for acute coronary syndromes: report from the National Cardiovascular Database Cath Percutaneous Coronary Intervention (CathPCI) Registry. Circ Cardiovasc Qual Outcomes. 2012;5(6):775–82.
3. Kosar P, et al. Anatomic variations and anomalies of the coronary arteries: 64-slice CT angiographic appearance. Diagn Interv Radiol. 2009;15(4):275–83.
4. Kurata A, et al. Quantification of the myocardial area at risk using coronary CT angiography and Voronoi algorithm-based myocardial segmentation. Eur Radiol. 2015;25(1):49–57.
5. Kang SJ, et al. Impact of subtended myocardial mass assessed by coronary computed tomographic angiography-based myocardial segmentation. Am J Cardiol. 2019;123(5):757–63.
6. Ide S, et al. Cardiac computed tomography-derived myocardial mass at risk using the Voronoi-based segmentation algorithm: a histological validation study. J Cardiovasc Comput Tomogr. 2017;11(3):179–82.
7. Sumitsuji S, et al. Reproducibility and clinical potential of myocardial mass at risk calculated by a novel software utilizing cardiac computed tomography information. Cardiovasc Interv Ther. 2016;31(3):218–25.
8. Budoff MJ, et al. Long-term prognosis associated with coronary calcification: observations from a registry of 25,253 patients. J Am Coll Cardiol. 2007;49(18):1860–70.
9. Agatston AS, et al. Quantification of coronary artery calcium using ultrafast computed tomography. J Am Coll Cardiol. 1990;15(4):827–32.
10. Greenland P, et al. Coronary calcium score and cardiovascular risk. J Am Coll Cardiol. 2018;72(4):434–47.
11. Hecht H, et al. Clinical indications for coronary artery calcium scoring in asymptomatic patients: expert consensus statement from the Society of Cardiovascular Computed Tomography. J Cardiovasc Comput Tomogr. 2017;11(2):157–68.
12. Bos D, Leening MJG. Leveraging the coronary calcium scan beyond the coronary calcium score. Eur Radiol. 2018;28(7):3082–7.
13. Naoum C, et al. Predictive value of age- and sex-specific nomograms of global plaque burden on coronary computed tomography angiography for major cardiac events. Circ Cardiovasc Imaging. 2017;10(3):e004896.
14. Patchett ND, Pawar S, Miller EJ. Visual identification of coronary calcifications on attenuation correction CT improves diagnostic accuracy of SPECT/CT myocardial perfusion imaging. J Nucl Cardiol. 2017;24(2):711–20.
15. Engbers EM, et al. Visual estimation of coronary calcium on computed tomography for attenuation correction. J Cardiovasc Comput Tomogr. 2016;10(4):327–9.
16. Berman DS, Arnson Y, Rozanski A. Assessment of coronary calcium density on noncontrast computed tomography. JACC Cardiovasc Imaging. 2017;10(8):855–7.
17. Blaha MJ, et al. Improving the CAC score by addition of regional measures of calcium distribution: multi-ethnic study of atherosclerosis. JACC Cardiovasc Imaging. 2016;9(12):1407–16.
18. Arbab-Zadeh A, Fuster V. The myth of the "vulnerable plaque": transitioning from a focus on individual lesions to atherosclerotic disease burden for coronary artery disease risk assessment. J Am Coll Cardiol. 2015;65(8):846–55.
19. Achenbach S, Raggi P. Imaging of coronary atherosclerosis by computed tomography. Eur Heart J. 2010;31(12):1442–8.
20. Willemink MJ, Leiner T, Maurovich-Horvat P. Cardiac CT imaging of plaque vulnerability: hype or hope? Curr Cardiol Rep. 2016;18(4):37.
21. Motoyama S, et al. Plaque characterization by coronary computed tomography angiography and the likelihood of acute coronary events in mid-term follow-up. J Am Coll Cardiol. 2015;66(4):337–46.

22. Kolossvary M, et al. Plaque imaging with CT-a comprehensive review on coronary CT angiography based risk assessment. Cardiovasc Diagn Ther. 2017;7(5):489–506.
23. Villines TC, et al. Prevalence and severity of coronary artery disease and adverse events among symptomatic patients with coronary artery calcification scores of zero undergoing coronary computed tomography angiography: results from the CONFIRM (Coronary CT Angiography Evaluation for Clinical Outcomes: An International Multicenter) registry. J Am Coll Cardiol. 2011;58(24):2533–40.
24. Foley DP, et al. Quantitative coronary angiography (QCA) in interventional cardiology: clinical application of QCA measurements. Prog Cardiovasc Dis. 1994;36(5):363–84.
25. Boden WE, et al. Optimal medical therapy with or without PCI for stable coronary disease. N Engl J Med. 2007;356(15):1503–16.
26. Wong DT, et al. Transluminal attenuation gradient in coronary computed tomography angiography is a novel noninvasive approach to the identification of functionally significant coronary artery stenosis: a comparison with fractional flow reserve. J Am Coll Cardiol. 2013;61(12):1271–9.
27. Gould KL, Johnson NP, Kirkeeide R. TAG, you're out. JACC Cardiovasc Imaging. 2019;12(2):334–7.
28. Fairbairn TA, et al. Real-world clinical utility and impact on clinical decision-making of coronary computed tomography angiography-derived fractional flow reserve: lessons from the ADVANCE registry. Eur Heart J. 2018;39(41):3701–11.
29. Nakazato R, et al. Noninvasive fractional flow reserve derived from computed tomography angiography for coronary lesions of intermediate stenosis severity: results from the DeFACTO study. Circ Cardiovasc Imaging. 2013;6(6):881–9.
30. Patel MR, et al. 1-Year impact on medical practice and clinical outcomes of FFRCT: the ADVANCE registry. JACC Cardiovasc Imaging. 2020;13(1 Pt 1):97–105.
31. Miller JM, et al. Diagnostic performance of coronary angiography by 64-row CT. N Engl J Med. 2008;359(22):2324–36.
32. Rochitte CE, et al. Computed tomography angiography and perfusion to assess coronary artery stenosis causing perfusion defects by single photon emission computed tomography: the CORE320 study. Eur Heart J. 2014;35(17):1120–30.
33. Chen MY, Shanbhag SM, Arai AE. Submillisievert median radiation dose for coronary angiography with a second-generation 320-detector row CT scanner in 107 consecutive patients. Radiology. 2013;267(1):76–85.
34. Einstein AJ, et al. Radiation dose from single-heartbeat coronary CT angiography performed with a 320-detector row volume scanner. Radiology. 2010;254(3):698–706.
35. Nagao M, et al. Quantification of coronary flow using dynamic angiography with 320-detector row CT and motion coherence image processing: detection of ischemia for intermediate coronary stenosis. Eur J Radiol. 2016;85(5):996–1003.
36. Hayashida E, et al. Additive value of 320-section low-dose dynamic volume CT in relation to 3-T MRI for the preoperative evaluation of brain tumors. Jpn J Radiol. 2016;34(10):691–9.
37. Marwan M, et al. CT-derived left ventricular global strain in aortic valve stenosis patients: a comparative analysis pre and post transcatheter aortic valve implantation. J Cardiovasc Comput Tomogr. 2018;12(3):240–4.
38. Buss SJ, et al. Quantitative analysis of left ventricular strain using cardiac computed tomography. Eur J Radiol. 2014;83(3):e123–30.
39. Liga R, et al. Multicentre multi-device hybrid imaging study of coronary artery disease: results from the EValuation of INtegrated Cardiac Imaging for the Detection and Characterization of Ischaemic Heart Disease (EVINCI) hybrid imaging population. Eur Heart J Cardiovasc Imaging. 2016;17(9):951–60.
40. Flotats A, et al. Hybrid cardiac imaging: SPECT/CT and PET/CT. A joint position statement by the European Association of Nuclear Medicine (EANM), the European Society of Cardiac Radiology (ESCR) and the European Council of Nuclear Cardiology (ECNC). Eur J Nucl Med Mol Imaging. 2011;38(1):201–12.

41. Fukushima K, Matsuo Y, Momose M, Nagao M, et al. Patient based territorial coronary flow analysis by Voronoi algorithm with 13N ammonia PET CTA fusion. J Am Coll Cardiol. 2017;69(11 Suppl):1609.
42. Pontone G, et al. Dynamic stress computed tomography perfusion with a whole-heart coverage scanner in addition to coronary computed tomography angiography and fractional flow reserve computed tomography derived. JACC Cardiovasc Imaging. 2019;12(12):2460–71.
43. Shaw LJ, et al. Optimal medical therapy with or without percutaneous coronary intervention to reduce ischemic burden: results from the Clinical Outcomes Utilizing Revascularization and Aggressive Drug Evaluation (COURAGE) trial nuclear substudy. Circulation. 2008;117(10):1283–91.

Hybrid Imaging of the Autonomic Cardiac Nervous System

5

Walter Noordzij, Lars Stegger, and Riemer H. J. A. Slart

5.1 Introduction

Cardiac autonomic innervation is an integrative part of the physiology of the heart. Myocardial innervation plays an important role in adapting the cardiac function in daily life. Autonomic cardiac innervation is linked to the pathophysiology of several cardiovascular diseases. Arrhythmias are connected to regional as well to global alterations of the electrophysiological function, influenced by autonomic innervations. The cardiac sympathetic innervation system seems to be more sensible to ischemia as compared with myocytes, and may represent an important cause for the development of arrhythmias. Derangements in autonomic function have also been detected in heart failure [1], and appear to have a significant prognostic value [2, 3]. Also, the ability to predict potential lethal ventricular arrhythmias will be important for accurate selection of patient that really need an implantable cardioverter defibrillator (ICD). Non-invasive imaging methods are needed to evaluate the cardiac autonomic function. A number of imaging techniques, including radiopharmaceuticals are available now, applicable on SPEC T and PET cameras.

W. Noordzij
Medical Imaging Center, Department of Nuclear Medicine and Molecular Imaging, University Medical Center Groningen, University of Groningen, Groningen, The Netherlands

L. Stegger
Department of Nuclear Medicine, University Hospital Münster, Münster, Germany

Riemer H. J. A. Slart (✉)
Medical Imaging Center, Department of Nuclear Medicine and Molecular Imaging, University Medical Center Groningen, University of Groningen, Groningen, The Netherlands

Department of Biomedical Photonic Imaging, University of Twente, Enschede, The Netherlands
e-mail: r.h.j.a.slart@umcg.nl

S. G. Nekolla, C. Rischpler (eds.), *Hybrid Cardiac Imaging*,
https://doi.org/10.1007/978-3-030-83167-7_5

To improve quality, better delineation of the heart, accurate matching of molecular properties and morphology, SPECT and PET are equipped these days with a CT component. This chapter focuses on SPECT/CT and PET/CT application for visualizing and measurement of the cardiac innervation in vivo, using specific SPECT and PET radiopharmaceuticals.

5.2 Cardiac Sympathetic Nervous System Imaging

The autonomous nervous system, consisting of the sympathetic and parasympathetic branches, plays a very important role in cardiac functioning. Sympathetic activation leads to an adjustment of cardiac output (e.g., increased heart rate, conduction, and contractility), vessel tone with improved perfusion in brain and muscle, decreased perfusion in the gastrointestinal system, and cardiac metabolism in order to adapt to requirements of mental and physical activity ("fight or flight") [4]. Sympathetic innervation pertains both to pacemaker cells and normal cardiomyocytes. Both, adrenergic nerves and receptors can be found in abundance in the whole heart. The parasympathetic branch of the autonomous nervous system has an antagonistic effect and adjusts the cardiovascular system to resting conditions with a decrease in heart rate, myocardial contractility, and a redistribution of blood to the gastrointestinal system, e.g. after a meal. While a high density of receptors for the neurotransmitter acetylcholine can be found in the heart, nerve fibers of the parasympathetic function supply the sinus and atrioventricular nodes but also the cardiomyocytes [5]. For both branches, the presynaptic and postsynaptic sides of innervation can be imaged. For the sympathetic branch, radiotracers that mimic the physiological neurotransmitter noradrenalin have been developed for both conventional planar and tomographic (SPECT) scintigraphy and PET [6]. Also, ligands for the relevant receptors are available (see below). The same can be said about the parasympathetic system. Especially with PET, biokinetic modelling can be used together with dynamic data acquisition (and blood sampling) for quantification of physiological properties such as the distribution volume of a neurotransmitter or the density of receptors. Depending on the model and the sophistication of the employed technique biokinetic modelling can require dual or multiple injections of cold and hot substances. In addition, analysis of metabolites may be required. Biokinetic modelling provides meaningful quantitative and not only qualitative/regional information. This is especially relevant in diseases that lead to global and not regional changes of innervation.

5.3 SPECT and PET Tracers

5.3.1 Presynaptic

Several tracers for cardiac sympathetic innervation imaging have been introduced, with iodine-123 labelled metaiodobenzylguanidine (^{123}I-MIBG) being widely used in conventional nuclear medicine, and carbon-11 labelled meta-hydroxy-ephedrine

Table 5.1 SPECT and PET radiopharmaceuticals for the autonomic cardiac nervous system

Name	Target	Category	Advantage	Disadvantage
^{123}I-MIBG	Presynaptic NE transport	Transporter substrate	– Availability – Experience	– SPECT – Semi-quantitative
^{11}C-mHED	Presynaptic NE transport	Transporter substrate	– Quantification – Most PET experience	Cyclotron dependent
^{11}C-epinephrine	Presynaptic NE transport	Transporter substrate	– Quantification – True neurotransmitter	– Cyclotron dependent – Peripheral metabolism
^{11}C-phenylephrine	Presynaptic NE transport	Transporter substrate	Quantification	– Synthetic catecholamine – Rapid myocardial washout
^{18}F-LMI1195	Presynaptic NE transport	Transporter substrate	– Transportable – Quantification – High quality	– Not commercial available – Higher radiation dose
^{11}C-CGP12177	Post-synaptic beta-adrenoceptor	Receptor antagonist	Quantification	– Cyclotron dependent – Production complicated
^{11}C-CGP12388	Post-synaptic beta-adrenoceptor	Receptor antagonist	Quantification	Cyclotron dependent
^{11}C-MQNB	Post-synaptic muscarinic receptor	Receptor antagonist	– Quantification – Highly specific	– Cyclotron dependent – Multiple injection protocols

(^{11}C-mHED) within positron emission tomography (PET) (Table 5.1). In addition to ^{11}C-mHED, amongst others also ^{11}C-ephedrine, ^{11}C-epinephrine, ^{11}C-phenylephrine and—more recently—fluorine-18 labelled *N*-[3-bromo-4-(3-fluoropropoxy)-benzyl]-guandine (^{18}F-LMI1195) have been studied. All tracers visualize presynaptic sympathetic innervation.

^{123}I-MIBG is actually an analogue of norepinephrine, as it results from chemical modification of the false neurotransmitter analogue guanethidine. Therefore, its uptake mechanism is similarly to that of norepinephrine (Fig. 5.1). The uptake occurs mainly by a specific uptake system ("uptake-1") and to a much lesser extent, by a non-specific uptake system (passive diffusion, "uptake-2"). Like norepinephrine, ^{123}I–MIBG is stored in presynaptic nerve terminals granules. Unlike norepinephrine, ^{123}I–MIBG is not bound to receptors on the myocyte membrane, in the case of sympathetic de-innervation, and will not undergo catabolization by monoamine oxidase (MOA). In healthy subjects ^{123}I –MIBG is retained in these granules and will not undergo washout into the synaptic cleft [7, 8].

Carbon-11 labelled meta-hydroxy-ephedrine (^{11}C-mHED) is the main PET tracer in cardiac sympathetic innervation imaging. ^{11}C-mHED is derived from the

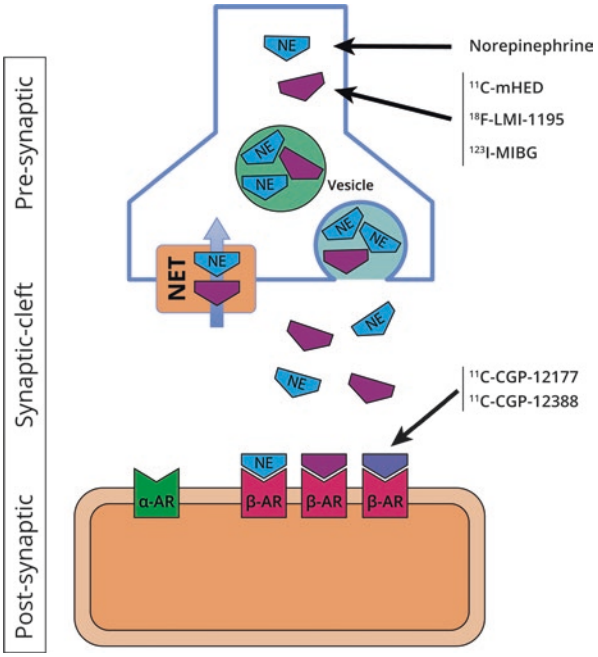

Fig. 5.1 Schema of myocardial adrenergic neuronal terminals. It shows the schematic representation of myocardial adrenergic neuronal terminals and demonstrates the chemical structure of the tree main tracers ^{11}C-HED, ^{123}I-MIBG, and ^{18}F-LMI-1195. Abbreviations: *NET* neuroendocrine transporter, via the uptake-1 mechanism, *AR* adrenergic receptor, *NE* norepinephrine. (*Acknowledgement: David Vallez Garcia for preparing this illustration*)

false norepinephrine analogue *metaraminol*, which is taken up by the presynaptic nerve terminals similarly to norepinephrine (through the "uptake-1" mechanism) [9, 10]. Like ^{123}I-MIBG, ^{11}C-mHED is not metabolized by catechol-*O*-methyl transferase or oxidatively deaminated by MOA. However, ^{11}C-mHED rapidly leaks out of the presynaptic vesicles and diffuses into the interstitial space and will dynamically recycle into the neurons again [11]. In the case of sympathetic denervation, there is an increase in spillover of ^{11}C-mHED from the nerve terminal, leading to a decreased reuptake [12]. ^{11}C-epinephrine has high affinity for uptake-1 as well [13], and shows higher vesicular packaging and breakdown by MAO. The higher vesicular packaging can be considered as an advantage, since it results in a lower washout rate of the tracer [14]. Especially this breakdown results in radioactive metabolites, with the necessity for correction in quantification of tracer uptake. Unlike norepinephrine, these tracers have no postsynaptic effect when released into the synaptic cleft.

The two most important advantages of PET over conventional nuclear medicine techniques are the better spatial resolution, and the possibility of absolute quantification of tracer uptake. The uptake of ^{11}C-mHED is expressed by the retention index, which is defined as the myocardial activity divided by the integral of the

time-activity curve in plasma [15]. Since myocardial perfusion determines the retention of ^{11}C-mHED, a nitrogen-13 labelled ammonia (^{13}N-ammonia) PET has to be acquired just before ^{11}C-mHED acquisition. Myocardial ^{11}C-mHED uptake in control subjects is homogeneous, characterized by intense accumulation in all myocardial segments [16]. Therefore, the PET tracer ^{11}C-mHED is an attractive non-invasive method for quantification of cardiac sympathetic innervation. The major disadvantage of these ^{11}C-labelled PET tracers is the necessity of an on-site cyclotron. This may be become less of a problem with the introduction of ^{18}F-LMI1195, which is actually an analogue to ^{123}I–MIBG [17] (Fig. 5.1).

Head-to-head comparisons of ^{123}I-MIBG and ^{11}C-mHED have not been extensively studied, so far. One study in patients with left ventricular dysfunction showed that defect size (defined as <60% of maximum) determined by ^{123}I-MIBG and ^{11}C-mHED is closely correlated: $r = 0.88$ [18]. ^{123}I-MIBG scintigraphy underestimates tracer uptake in inferior to inferoapical (or even inferolateral) wall segments. This is probably not a consequence from heart failure, since the same distribution is found in healthy controls [19]. At present, the explanation for this defect has not been fully elucidated, but may be caused by the so-called liver-heart artifact and filtered back projection algorithm. In short, it is likely that ^{11}C-mHED outperforms ^{123}I–MIBG. Despite the advantage of ^{11}C-mHED over ^{123}I–MIBG in tracer uptake quantification, ^{11}C-mHED does not provide in washout kinetics, in contrast to ^{123}I–MIBG. At present, direct comparison between ^{123}I–MIBG and ^{18}F-LMI1195 have not been performed in clinical setting.

5.3.2 Post-synaptic

Several postsynaptic receptor ligands have been labeled and proposed as PET tracers for cardiac quantification and imaging (Table 5.1). However, the clinical use of receptor-targeted tracers is limited to a relative low number of studies. High specific binding, high affinity, and hydrophilicity, which avoids binding to internalized inactive receptors, lack of pharmacologic effects and, finally, a simple and reliable tracer synthesis are requirements that must be met for a widespread application of receptor ligands for myocardial PET. ^{11}C-CGP12177, a hydrophilic non-selective β-adrenoreceptor antagonist, is still the most widely used tracer for adrenergic receptor imaging [20–23]. ^{11}C-CGP12388 is a non-subtype-selective β-adrenergic receptor antagonist and an isopropyl analog of CGP 12177. CGP12388 can be labeled easier than CGP12177 via a one-step procedure using 2-[^{11}C]acetone [24]. It is equally hydrophilic compared to ^{11}C-CGP12177 and the biodistribution and retention of CGP12388 is reported to be similar to 11C-CGP12177 [25]. β-adrenoceptor density with ^{11}C-CGP12177 PET in patients showed a decreased β-adrenoceptor density in vivo in a group of patients with heart failure due to idiopathic dilated cardiomyopathy [26].

Caldwell and colleagues evaluated in 13 patients with ischemic congestive heart failure and 25 aged-matched healthy volunteers the presynaptic function with ^{11}C-mHED and the post-synaptic function with ^{11}C-CGP12177 [20]. They

demonstrated a mismatch between pre- and postsynaptic left ventricular sympathetic function is present in patients with severe CHF and may be more marked in those with adverse outcomes. A more recent ^{11}C-CGP12177 PET study found out that in the remote non-infarcted region in patients, β-adrenoceptor downregulation was observed, which was related to deterioration of local myocardial systolic function [27]. In patients with syndrome X [28] and asthma [29], i.e. patients with normal left ventricular function, myocardial β-adrenoceptor density was found to be equal to that in normal volunteers, which is in agreement with the general hypothesis that β-adrenoceptor downregulation is only associated with heart failure. Interestingly, myocardial β-adrenoceptor downregulation was also observed in patients with arrhythmogenic right ventricular cardiomyopathy [30]. Although these patients have no heart failure, some evidence suggests that their local synaptic catecholamine levels are increased, which apparently causes downregulation of β-adrenoceptor similar to that in patients with heart failure [31]. So far, production methods of beta-receptor PET-ligands were very complex, hampering their widespread use. Because of the potential clinical importance of cardiac β-adrenergic receptor imaging with PET, radiopharmaceuticals should be developed for PET sites without proper production facilities. To this end new radiopharmaceuticals need to be developed which are labelled with [^{18}F] instead of [^{11}C], as [^{18}F] has a longer half-life (110 min) and can be transported to sites within a range of 4 h transport time, which is routinely done on a commercial basis for ^{18}F-FDG. Future perspectives may include the development of ^{18}F-labeled subtype-selective β-adrenoceptor ligands to obtain more information about the pathophysiological role of the different subpopulations in vivo. Subtype-selective ligands are being developed for the β_1-adrenoceptor as well as the β_2-adrenoceptor but thus far no suitable ligands have been produced and evaluated in clinical studies. Furthermore, noradrenaline uptake-1 mechanism and β-adrenoceptor density are reduced in the myocardium of patients with chronic LV dysfunction and evidence of hibernating myocardium [32].

5.4 Principles in Analysis, Quantification, and Software

The quantification of ^{123}I-MIBG uptake is a longstanding and a relatively straightforward method: uptake signals from two regions drawn in planar images result in the so-called heart-to-mediastinum ratio (H/M). Usually two measurements are performed, one after 1.5 and one after 4 h, which also yields the diagnostic information of tracer washout [33]. However, although planar imaging is logistically and technically easy to perform, PET offers, through better spatial resolution and sensitivity, access to the regional tracer distribution. PET imaging, however, needs kinetic analysis and is now used basically in all modern medical imaging modalities. From a conceptual point of view, 2–3 general approaches are used: the use of compartmental models, their simplifications, and non-compartmental parameters [34]. It requires a good understanding of the different compartments where the tracer is

distributed such as blood, extracellular, and intracellular compartments, where the tracer is bound. Regarding innervations tracers, the cellular compartments would be the axoplasm and the vesicles. For ^{11}C-mHED, a simplified parameter is available and is the so-called retention (also called retention fraction, retention index or fractional uptake rate). This parameter is calculated by the activity found at a defined time point (e.g. 30–40 min p.i.) and divided by the integral of the arterial input function which is usually derived from the dynamic images. As the tracer uptake of ^{11}C-mHED in the myocardium is very stable in the first hour p.i. this parameter is in a practical setting highly reliable. Generic software packages and well as commercially available software packages are available to quantify the autonomic heart function with PET [34].

5.5 Clinical Applications

5.5.1 ANS and Myocardial Ischemia and Infarction and Heart Failure (CMP)/Heart Transplantation

Autonomic nerve system innervation and function is altered following an acute myocardial infarction (AMI). Excessive cardiac SNS activation is a hallmark of progressive heart failure [35–37]. A compensatory increase in adrenergic drive causes desensitization/downregulation of the uptake-1 mechanism due to excess NE in the synaptic cleft. The downregulation of uptake-1 exposes the heart and postsynaptic adrenergic receptors to greater concentrations of NE, which in turn causes desensitization/downregulation of β-adrenergic receptors, cardiac remodeling, and worsening of HF and prognosis.

Cardiac transplantation leads to sympathetic nerve system denervation (SNS) due to surgical transection of innervating postganglionic nerves at the base of the heart. Indeed, denervation leads to altered SNS cardiac responsiveness, contributing to exercise intolerance and altered coronary blood flow regulation to stress [38, 39]. Based on imaging studies, it is now well known that sympathetic reinnervation may occur later after transplantation; that presence and extent of reinnervation are determined not only by time after transplantation but also by other factors related to age, surgery, and rejection.

PET imaging with ^{11}C-HED has been extensively used to non-invasively characterize cardiac denervation and reinnervation process, and the cardiac physiological responses to reinnervation [38–40].

Longitudinal studies using ^{11}C-HED confirmed these findings and reported a reinnervation pattern that initially occurs in the anteroseptal wall in a basal to distal fashion, followed by lateral wall reinnervation, and lastly inferior wall and apical reinnervation [40]. However, the heart does not become fully reinnervated over time and some patients remain denervated late after surgery (15 years).

Studies evaluating postsynaptic SNS and PNS receptor density in transplant patients with PET are lacking.

5.5.2 Long QT, Brugada, ARVD Detection

The often genetically determined myocardial diseases LongQT-syndrome, Brugada-syndrome and arrhythmogenic right-ventricular cardiomyopathy/dysplasia (ARVC/D) may cause life-threatening arrhythmias that become apparent by syncopes and cardiac arrest and are a leading cause of sudden cardiac death in young persons.

Long QT-Syndrome (LQTS). As the name implies, this disease is characterized by an abnormal repolarization phase after cardiac excitation with a characteristic elongation of the QT interval. This change in repolarization makes cardiomyocytes prone to arrhythmias. Long QT is caused by aberrant functioning of different ion channels so that there are different subforms of the disease, most of them inherited, although this syndrome can also be acquired, e.g. if drugs interact with these channels or in cases of low potassium due to malnutrition. The most common variants of inherited Long QT syndrome are caused by mutations in the genes KCNQ1 (LQT1, most common, affecting the slow delayed potassium rectifier channel), KCNH2 (LQT2, second most common, affecting the rapid delayed potassium channel), and SCN5A (LQT3, affecting the sodium channel). It is known that sympathetic innervation can influence ion channels and cardiac arrhythmias typically occur in times of elevated stress, e.g. during physical exercise or other forms of stress such as sudden noise, for LQT1 and 2 but during rest in LQT3 subforms [41]. The fact that beta-blockers are effective treatment points to a relevant contribution of sympathetic innervation. ^{123}I-MIBG SPECT showed reduced regional tracer uptake in those patients with high QT times, with a previous episode of torsade de pointes tachycardia, ventricular fibrillation or syncope [42], corroborated by Chevalier et al. [43]. No correlation of ^{123}I-MIBG defects were found with LQT genetic subtype by Kies et al. [44]. With ^{11}C-mHED PET also regional uptake deficits were shown by Mazzadi et al. [45]. Zumhagen et al. using the same tracer showed a higher washout rate in LQTS patients, especially in patients with long QT intervals and patients with symptoms [46], but not a higher tracer retention. This is compatible with an earlier study by Calkins et al. [47] that has also not shown a different tracer retention. All in all, there is evidence that sympathetic innervation imbalance is playing a role in this disease.

Brugada syndrome (BrS). BrS is also caused by aberrant ion channels in the heart and can occur in patients without apparent structural abnormalities [48]. The most common involved gene is SCN5A that is also affected in the LQT3 subform of the Long QT syndrome, coding for a sodium channel. Other subforms may affect other ion channels. It may become apparent by a typical aberration visible in ECG (ST-segment elevation in V1-V3 leads with coved morphology, called type I form), however, the change may be hidden in normal ECG. The antiarrhythmic agent Ajmalin can be used to reveal the typical ECG changes. Arrhythmias may arise from the right ventricular outflow tract [49]. Clinical symptoms are syncopes, cardiac arrest that may result in sudden cardiac death. It is noteworthy that unlike in Long QT syndrome cardiac arrhythmias are triggered during resting conditions and not typically during exercise, conditions in which not the sympathetic but the parasympathetic branch of the autonomous nervous system is active. Regional uptake

deficits in the LV myocardium were revealed by Agostini et al. and corroborated by Wichter et al. using ^{123}I-MIBG SPECT [50, 51], albeit not correlated to clinical characteristics of the disease. Kawaguchi and coworkers were able to show a correlation of more significant uptake deficits with type I ECG patients, considered patients with a higher risk [52]. A dual-tracer PET study addressing the presynaptic and postsynaptic sides of the sympathetic innervation (radiotracers ^{11}C-mHED and ^{11}C-CGP-12177) showed increased presynaptic catecholamine recycling without reduction in beta-receptor densities [53].

ARVC/D. Mutations in genes, in most cases coding for desmosomes that link cells together [54], lead to a cardiomyopathy located mainly in the right ventricular wall, although the left ventricular myocardium may be also affected, so that it may be better to talk of arrhythmogenic cardiomyopathy (ACM) in general [55]. Functional imaging with echocardiography or MRI can find hypokinesia and fatty or fibrofatty replacement of cardiomyocytes and formation of aneurysms and in later stages global impairment of ventricular function [56]. In addition, arrhythmias can arise from these abnormally structured parts of the heart wall with remaining conducting myocardium within scar formations similar to the situation in the post-infarct myocardium. Arrhythmias typically occur during times of elevated sympathetic drive during exercise. Beta-blockers are one of the established treatments pointing also to an involvement of the sympathetic nervous system in this disease. Imaging of the sympathetic function in the LV myocardium has been performed with ^{123}I-MIBG SPECT by Wichter et al., showing the presynaptic side [57]. A large proportion of patients showed regional uptake deficits correlating with the presumed origin of tachycardia. This regional reduction in uptake has prognostic implications with a higher rate of tachyarrhythmias [58]. The density of receptors (postsynaptic side) were also shown to be reduced by the same group using PET and ^{11}C-CGP-12177 as the radiotracer [31].

All these inherited diseases may overlap, e.g. genetic alterations are affecting gene locations underlying more than one disease, e.g. patients may have electrical changes of Brugada syndrome and structural changes of ARVC. Also, cardiac arrhythmias may be associated with other genetic aberrations such as deafness.

As seen from the above examples, there is not (yet) relevant published data on hybrid imaging of autonomous cardiac innervation in LQTS, BrS and ARVC/D investigating both molecular and anatomic and functional data at the same time. The role of hybrid imaging with SPECT-CT, PET-CT, and PET-MRI for the investigation of the autonomic nervous system in these diseases can be found in a molecular assessment by the SPECT and PET components as shown above and by a structural and functional analysis of the heart by the CT and MRI components. MRI has become the modality of choice for most evaluations of cardiac anatomy and function [59] including the assessment of the right ventricular outflow tract [60] relevant in the above diseases. In addition, spatially and temporally (PET-MRI) aligned data sets of molecular and function-anatomic images may help in PET and SPECT uptake quantification in left ventricular and, with potential worth, right ventricular myocardium by means of motion and partial volume corrections.

The value of imaging of anatomic and functional changes is especially obvious for ARVC/D since this cardiomyopathy is frequently associated with typical

anatomical and functional changes to the (in most cases right ventricular) myocardium. MRI is the most relevant modality to assess both anatomical changes/function loss and fibrosis at the same time and newer MRI techniques such as strain analysis with additional potential [54, 56]. However, also in the "channelopathies" LQTS and BrS with primarily electrical changes, anatomical and functional changes can occur. As an example Papavassiliu et al. have found a dilatation of the right ventricular outflow tract in patients with BrS and obvious, non-hidden ECG changes [61]. Gray and colleagues have also found equivalent changes with MRI [62]. Bastiaenen et al. have identified myocardial fibrosis with MRI in patients with BrS [63]. Structural and functional abnormalities measured with MRI are correlated with the SCN5A mutation status [64, 65]. The aberrant QT intervals in LQTS lead to regionally different changes in diastolic function as shown with MRI by Brado et al. [66].

Limited resolution of SPECT and PET and cardiac motion caused by cardiac contraction and respiration lead to image blurring and impaired uptake quantification. Complementary CT and MRI data with a much higher spatial resolution than SPECT and PET can delineate cardiac anatomy more exactly. This information may be used to correct for partial volume effects [67]. Hybrid PET-MRI systems are especially suited to depict motion since MRI imaging over a longer time does not increase radiation burden and can be acquired concurrently with PET [68].

5.5.3 Predicting Ventricular Arrhythmias and Sudden Cardiac Death with ANS Imaging

Selective denervation of myocardial tissue is a key feature in the development of ventricular arrhythmia, in patients with ischemic as well as patients with non-ischemic cardiomyopathies. In addition, even patients without structural or functional heart disease or genetic susceptibility may develop ventricular arrhythmia: idiopathic ventricular fibrillation. Several studies have been performed in these different patient groups [2, 69, 70]. The common features from the results of both PET and MIBG studies are: (1) decreasing cardiac tracer accumulation is linearly correlated with patient survival, (2) the presence of disturbed innervation increases the risk on ventricular arrhythmia, and (3) the risk on ventricular arrhythmia is also determined by the defect size (defined as <60% uptake from maximum). Despite the established higher risk of ventricular arrhythmia with decreasing myocardial tracer uptake, low late HMR could not be identified as an independent prognostic factor from a meta-analysis of 600+ heart failure patients [71]. However, defect size was identified was identified as the only independent prognostic factor for the development of ventricular arrhythmia in ischemic cardiomyopathy patients, based on a prospective multicenter center [72]. This finding could not be confirmed in (non-) ischemic cardiomyopathy patients treated with prophylactic ICD implantation, despite that univariate analysis revealed large late ^{123}I-MIBG sized defect as an independent prognostic predictor of appropriate ICD discharge and sudden cardiac death [73]. Comparable results were shown in the PAREPET study: defect size was identified as the only independent predictive factor for sudden cardiac death [74]. At present, little is known about the role of cardiac sympathetic innervation imaging in

determining cost-effectiveness of ICD implantation in patients with ischemic cardiomyopathy. Not all patients will develop ventricular arrhythmia. In fact, approximately 30% of all patients will benefit from prophylactic ICD implantation. At present, low late HMR has not been able to identify those patients with improved survival after ICD treatment [75].

5.5.4 ANS and Cardiac Resynchronization

Cardiac resynchronization therapy (CRT) can improve cardiac performance in patients with advanced heart failure and LV dyssynchrony. The immediate effect is an improvement in hemodynamics by restoring in-sync contraction of all portions of the ventricular wall. Secondary effects such as an improvement in nerval function also play an important role. However, a significant proportion of patients (30–40%) does not benefit from this therapy and the contributing pathomechanisms in success and non-success are not clear [76]. Identification of the regional distribution of viable myocardium and scar tissue can explain part of the failed therapy and can be measured by SPECT, PET, and MRI. Also, the amount of dyssynchrony, conveniently assessed from the same images [77, 78], can predict the potential for improvement. Alterations of the autonomous nervous system present in heart failure and restoration of sympathetic function by CRT may also contribute to a successful treatment (Fig. 5.2). It is known that ^{123}I-MIBG scintigraphy can predict hard adverse events such as life-threatening arrhythmias and cardiac death in patients

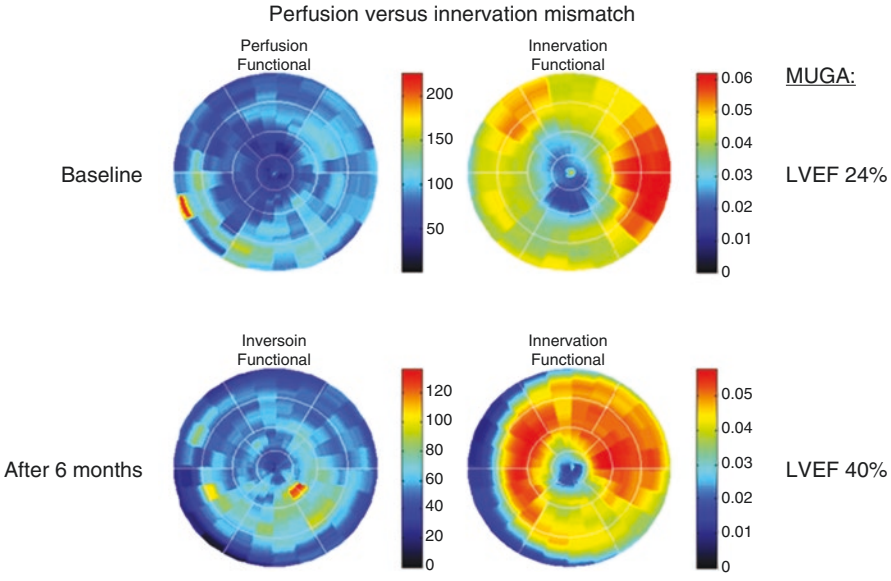

Fig. 5.2 Left polar maps indicate myocardial perfusion (^{13}N-ammonia), right polar maps indicate sympathetic innervation, using ^{11}C-mHED. Patient who showed response to the CRT scanned after 6 months. Mean ^{11}C-mHED increased from 0.035 to 0.041 mL/min/mL after CRT application, combined with improvement of LVEF. (From book Springer Verlag: Alexanderson et al. [79])

with heart failure (lower myocardial tracer uptake means higher risk) [2]. Martignani et al. have investigated the presynaptic sympathetic function with PET and ^{11}C-mHED. Responders to CRT have shown a higher tracer uptake before and after CRT and also an improvement in homogeneity of tracer uptake [80]. Therefore, patients with a structurally preserved sympathetic nervous system benefit better from CRT. Capitanio et al. used the same technique to evaluate whether improved hemodynamics after CRT is accompanied by improved sympathetic innervation [81]. PET images were acquired before, 1 week after and 3 months after initiation of CRT. Results showed that overall uptake did not change significantly but that homogeneity and therefore regional neuronal dysfunction improved over time (measured 3 months after therapy initiation) and not immediately after CRT. Also, radiotracer retention in arterial blood decreased over time, possibly owing to a global improvement of sympathetic function also in other organs. Both factors can be measured separately but are mixed in planar MIBG imaging using the heart-to-mediastinum (blood pool) ratio, showing that planar MIBG imaging is inferior to PET. It remains difficult to predict success from the baseline images alone [82].

5.5.5 ANS and Cardiac Amyloidosis

Patients with amyloidosis have an increased risk of developing cardiac sympathetic innervation abnormalities, in the absence of myocardial perfusion disturbances [83]. Especially patients with transthyretin-related amyloidosis (ATTR type) and patients with immunoglobulin light chain-derived amyloidosis (AL type) may suffer from amyloid infiltration into the conductive system [84]. Specifically, patients with the hereditary form of ATTR (hATTR) frequently develop polyneuropathy and cardiac sympathetic innervation abnormalities. On the other hand, the typical restrictive cardiomyopathy occurs more often in wild-type ATTR amyloidosis (wtATTR) patients.

Despite limitation of nuclear medicine modalities for the visualization of actual amyloid infiltrations, semi-quantitative HMR analysis is assumed to represent amyloid deposits in the sympathetic nerve system [85]. However, ^{123}I-MIBG scintigraphy is not able to discriminate ATTR from AL type amyloidosis [85].

Low late HMR has important implications for amyloidosis patients, since low late HMR is associated with decreased survival. Late HMR is an independent prognostic factor for all-cause mortality. Reported mortality rate was 42% in amyloidosis patients with late HMR <1.60, whereas 7% in patients with late HMR ≥1.60 (hazard ratio (HR) 7.2, $p < 0.001$) [86]. Liver transplantation, which is the only curative option in ATTR patients, may even improve survival in patients with late HMR <1.60. Furthermore, late HMR after liver transplantation may seem to be of prognostic importance. Although low late HMR has a larger area under the receiver-operating curve (AUC) than clinical parameters and heart rate variability (AUC: 0.79 versus 0.66 and 0.52, respectively) in, this did not results to be of value in multivariate analysis (AUC 0.80 versus 0.79 for reference model, respectively) [87].

Little is known about the contribution of low late HMR to cardiovascular outcome measurements. Although decrease in late HMR stops after liver transplantation, these patients have a higher risk of developing ventricular arrhythmia [88]. At present it is unclear whether continuous amyloid infiltration despite liver transplantation may play an additional role in the prognosis of these patients.

5.5.6 ANS and DM

The long-term complications of DM include microvascular damage of the eyes, kidneys, and nerves, and macrovascular complications including ischemic heart disease, stroke, and peripheral vascular disease. Coronary artery disease (CAD) is the leading cause of morbidity and death in individuals with DM type 2 [89]. The 10-year mortality rate in patients with known CAD and diabetes exceeds 70%.

Another important complication of DM is diabetic neuropathy. Diabetic neuropathies are a heterogeneous group of diabetic complications that affect different parts of peripheral nervous system. Its pathophysiology is likely to be multifactorial, involving alterations in metabolism, micro- and macrovascular dysfunction, deficiency of neurohormonal growth factor, and autoimmune nerve damage [90]. Cardiac autonomic neuropathy (CAN) is one of the most important neuropathies for patients with DM, because it is related with poor cardiac outcome. The prevalence of CAN in type 2 diabetic patients is estimated to be around 20–30% of patients. CAN is particularly associated with an increased risk of silent myocardial infarction and associated with poor outcome related to ventricular arrhythmias and sudden cardiac death [91, 92]. This is contributing to significant cardiovascular morbidity and mortality [93]. CAN results from damage to the autonomic nerve fibers innervating the heart and blood vessels, which causes abnormalities in heart rate control and impairs vascular dynamics. It was estimated that the 5-year mortality rate is five times higher in diabetic patients with CAN than without CAN [90, 94]. Early diagnosis and recognition of CAN are crucial as it may impact on the clinical decision-making of these patients. However, all these tests are indirect assessments of the autonomic nervous system and are less sensitive than direct assessments by cardiac sympathetic adrenergic imaging with SPECT or PET [95–97]. At present, several studies using ^{123}I-MIBG imaging have demonstrated the presence of global and regional abnormalities in sympathetic innervation in diabetic patients [98–102]. Nagamachi and colleagues subsequently evaluated the prognostic value of cardiac ^{123}I-MIBG imaging by retrospectively evaluating 144 type 2 diabetic patients for the occurrence of cardiac events (arrhythmia, heart failure, or acute myocardial infarction), and all-cause mortality [99]. After a mean follow-up period of 7.2 ± 3.2 years, 17 (11.8%) patients experienced a cardiac event, of which 7 died. Previous data have suggested that ^{123}I-MIBG scintigraphy may be more sensitive than HRV for detection of CAN in diabetic subjects [97, 103]. Langer and colleagues investigated CAN according to HRV and ^{123}I-MIBG scintigraphy in 23 normal subjects and 65 asymptomatic patients with diabetes type 2 and silent myocardial ischemia [104]. The authors showed that ^{123}I-MIBG

uptake was largely reduced in diabetic patients, especially in those with clinically detectable CAN; in particular diffuse abnormalities in ^{123}I-MIBG uptake were observed in patients with silent myocardial ischemia. While HRV and other traditional parameters provide an impression of global innervation abnormalities, ^{123}I-MIBG scintigraphy with SPECT provides information on regional innervation. The findings in the study from Scholte indicated that regional abnormalities occur often in patients with asymptomatic diabetes [105].

Regional abnormalities in cardiac sympathetic innervation with ^{11}C-mHED PET imaging in 29 diabetic patients compared with 10 healthy subjects have been studied by Stevens and coworkers [96]. The diabetic patients were categorized into the presence of mild or severe diabetic autonomic neuropathy. Using the absolute difference in myocardial tracer uptake, the extent of regional sympathetic denervation was expressed as the percentage of the left ventricle (LV) in all subjects with diabetes. The study showed that the extent of regional sympathetic denervation was significantly larger in patients with severe autonomic neuropathy compared with patients with mild autonomic neuropathy (48 ± 19% vs 6 ± 5%, $p < 0.01$). The role of ^{123}I-MIBG scintigraphy in predicting heart failure (HF) progression in patients with and without DM has been worked out in a substudy of the ADMIRE-HF study [2, 106]. In this international multicenter study, the prognostic value of ^{123}I-MIBG cardiac imaging in 961 subjects with NYHA class II-II heart failure and left ventricular ejection fraction (LVEF) <35% have been evaluated. Progression of HF, defined as an increase in NYHA class (from II to III/IV or from III to IV) was observed in 22% of patients with DM compared to 14% in those without DM ($p = 0.005$). In patients with DM the late H/M ratio was lower than in those without DM, and only 21% of patients with DM in the study had a late H/M ratio ≥1.6. This is consistent with cardiac autonomic neuropathy in patients with HF in general, regardless of the presence of DM. Moreover, in heart failure patients with H/M ratio <1.6, DM was associated with an three times increased risk of HF progression over 2 years compared to those with DM with normal ^{123}I-MIBG uptake (RR, 2.99; $p < 0.001$).

5.6 Conclusion and Future Perspectives

5.6.1 Potential Novel Tracers

The PAREPET trial identified a prognostic value of regional heterogenous ^{11}C-mHED uptake (denervation) and ^{11}C-mHED/^{13}N-ammonia mismatch (perfused and denervated) for subsequent ventricular arrhythmia manifesting as sudden cardiac death or Implantable Cardioverter Defibrillator (ICD) discharge [74]. The regional abnormalities reported in this study suggest a benefit for PET imaging, in which spatial resolution permits more thorough evaluation of segment innervation. Small-scale trials suggest that postsynaptic β-adrenoceptor imaging may be used to identify patients who will most benefit from targeted β-blocker therapy with carvedilol [23]. These trials demonstrate the potential for sympathetic neuronal

imaging in advanced management of cardiac patients, identify at-risk patients, and guide therapeutic interventions in a sophisticated manner.

There remain challenges with the routine application of currently available radiotracers of the sympathetic nervous system. The complex kinetics of neuronal agents, including some combination of reuptake, vesicular storage, metabolism, active release, and passive diffusion limits the true quantification of sympathetic neuronal integrity. While retention indices, heart to background ratios, or washout rates provide rudimentary data, the accuracy, repeatability, and reproducibility of these measurements can be questionable. Development of novel neuronal tracers with more favorable kinetics, such as the phenethylguanidine series, may overcome some of these challenges and provide more concrete measurements for clinical practice. Second, the majority of PET tracers currently available are labeled with carbon-11, necessitating on-site production for clinical application. Continued development of [^{18}F]-labeled alternatives, particularly ^{18}F-LMI1195 (Fig. 5.3), would overcome these rollout issues to generate a wider clinical relevance. Third,

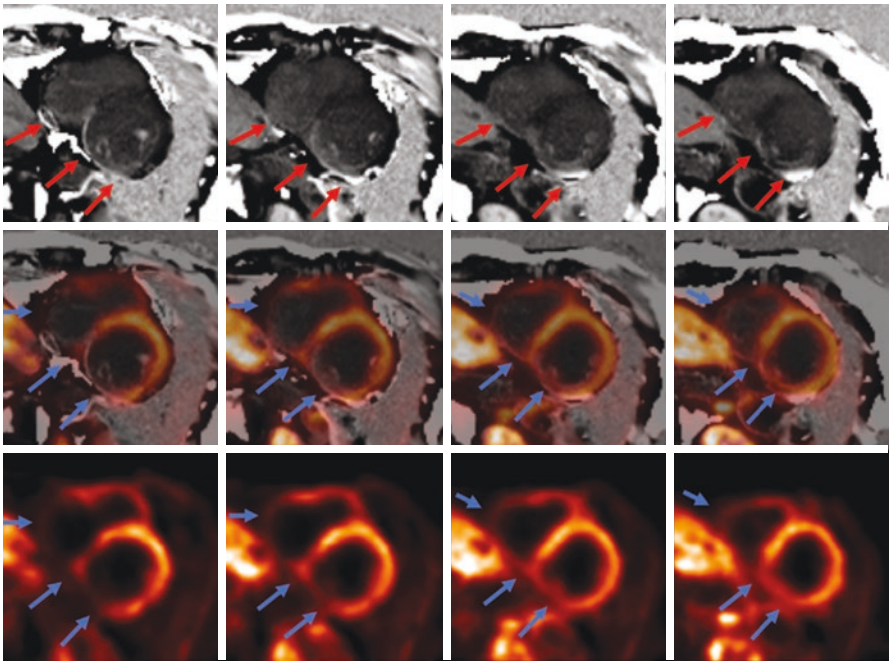

Fig. 5.3 Case example of a patient with a history myocardial infarction of the inferior wall who underwent F-18 flubrobenguane (^{18}F-LMI1195) PET/MRI. Red arrows depict late gadolinium enhancement in MRI as a sign of scarring (upper row), while blue arrows point at decreased tracer uptake in PET indicating denervated areas (bottom row). Overlay of PET and MRI is demonstrated in the middle row. Note that scarring and denervation can also be seen in the inferior part of the right ventricle. (Reprinted with permission from Rischpler C et al. "Cardiac PET/MRI: Current Clinical Status and Future Perspectives.", Semin Nucl Med. 2020 May;50(3):260–269)

imaging of β-adrenoceptors is complicated by application in a patient population that is frequently treated with chronic β-adrenoceptor blockade. This complication underscores the value of developing novel tracers targeting intracellular second messengers and response elements of the signal cascade. Continued research and development with radiotracers targeting adenylate cyclase, cAMP, PKA, regulatory proteins, other specific downstream targets not only overcome the complication of β-blockade, but also may provide invaluable information on compensatory cardiac function under medical therapy. Alternatively, future tracer development may be targeted upstream of adrenergic signaling, aiming at systems and receptors that modulate sympathetic activity in the heart, such as the renin-angiotensin system or the parasympathetic nervous system. Further development of tracers targeting angiotensin receptors, muscarinic and nicotinic acetylcholine receptors, and other targets could contribute to a more complete picture of autonomic regulation of myocardial contractility.

Taken together, while great strides have been made with sympathetic neuronal tracers, many opportunities for molecular imaging remain to be confronted.

5.6.2 Role of PET/MR

The newest hybrid system on the market is the PET-MRT device that combines a PET and an MRI component in one enclosure. One advantage for imaging of the autonomous nervous system of the heart with PET-MRI compared to PET-CT is the superior information gained from MRI. MRI has become the de-facto standard for anatomic and functional assessment of the heart, except for non-invasive coronary angiography that is still in the realm of CT. MRI can also depict tissue properties of the myocardium such as edema and fibrosis, making it a very versatile multimodality imaging technique. Since MRI does not operate with ionizing radiation, PET-MRI causes significantly less radiation exposure than PET-CT, especially when PET-CT is conducted with contrast-enhanced full-dose diagnostic CT. Therefore, longitudinal studies with PET-MRI are easier to justify. The unique feature if this combined system is its ability to image the same field of view with PET and MRI at the same time, allowing for perfect spatial and temporal alignment. This can be an advantage when a physiological intervention, e.g. pharmacological or physical stress, is applied during data acquisition. Only with concurrent imaging the same physiological state is imaged with both MRI and PET. Concurrent PET-MRI acquisition also opens a door to MR-based PET image improvement via partial volume and motion correction. Last but not least, total imaging time is significantly less when both time-consuming MRI and (dynamic) PET can be acquired at the same time. Also, biokinetic modelling of PET data may be improved with MRI, either by using MRI vessel data for partial volume correction of the arterial input function or by using an MRI-derived parameter (e.g., first pass tracer distribution, quantitative perfusion) within the mathematical framework of PET quantification.

5.6.3 New Clinical Trial

Large trials are necessary for future implementation of cardiac sympathetic imaging into different guidelines. Recently, the PAREPET II trial (ClinicalTrial.gov Identifier: NCT03493516) started recruiting patients. This prospective study will use ^{18}F-LMI1195 for the quantification of denervated area of the left ventricle. The aim of the study is to better identify those patients with coronary artery disease who will benefit from ICD implantation for primary prevention of ventricular arrhythmia and sudden cardiac death. Furthermore, this study aims to identify those patients in whom ICD implantation can be safely withheld. A total of 302 patients are expected to be enrolled before January 2023. First results are expected in 2024.

5.6.4 Clinical Implementation

Before cardiac sympathetic imaging will be incorporated within clinical guidelines, not only large clinical trials will be pivotal, but also consensus in standardization of both image acquisition and analysis is warranted [107]. In general, the use of medium energy collimators is preferred over low energy collimators. In recent years, conversion algorithms showed to adequately overcome the difference in acquired HMR [108, 109]. In addition, meta-analyses of the results from previous studies by means of these conversion factors have been recently published. Recalculation of standardized HMR from previously published ^{123}I-MIBG HMR values in patients with chronic heart failure resulted in a 2-year mortality risk model [110]. Despite good correlation with actual cardiac mortality, the model underestimated mortality in patients with highest risk of cardiac death.

Finally, dedicated software applications for analysis of both PET and ^{123}I-MIBG based data for quantification of cardiac sympathetic function are still lacking. Introduction of these software packages would fast-forward the clinical implementation of this imaging modality.

5.7 Conclusion

Imaging cardiac sympathetic innervation has a large potential in clinical decision-making. This potential lies mainly in identifying those patients that would benefit from prophylactic ICD implantation, in predicting of response to CRT, and novel drug-driven indications. Incorporation of sympathetic innervation imaging into clinical guidelines relies on standardization of both imaging acquisition and data analysis.

References

1. Thackeray JT, Bengel FM. Assessment of cardiac autonomic neuronal function using PET imaging. J Nucl Cardiol. 2013;20:150–65.
2. Jacobson AF, Senior R, Cerqueira MD, Wong ND, Thomas GS, Lopez VA, et al. Myocardial iodine-123 meta-iodobenzylguanidine imaging and cardiac events in heart failure. Results of the prospective ADMIRE-HF (AdreView Myocardial Imaging for Risk Evaluation in Heart Failure) study. J Am Coll Cardiol. 2010;55:2212–21.
3. Pietilä M, Malminiemi K, Ukkonen H, Saraste M, Någren K, Lehikoinen P, Voipio-Pulkki LM. Reduced myocardial carbon-11 hydroxyephedrine retention is associated with poor prognosis in chronic heart failure. Eur J Nucl Med. 2001;28:373–6.
4. Esler M. The sympathetic regulation of the heart. Eur Heart J. 2016;37:2808–9.
5. Coote JH. Myths and realities of the cardiac vagus. J Physiol. 2013;591:4073–85.
6. Werner RA, Chen X, Hirano M, Rowe SP, Lapa C, Javadi MS, et al. SPECT vs. PET in cardiac innervation imaging: clash of the titans. Clin Transl Imaging. 2018;6:293–303.
7. Kline RC, Swanson DP, Wieland DM, Thrall JH, Gross MD, Pitt B, et al. Myocardial imaging in man with I-123 meta-iodobenzylguanidine. J Nucl Med. 1981;22:129–32.
8. Wieland DM, Brown LE, Rogers WL, Worthington KC, Wu JL, Clinthorne NH, et al. Myocardial imaging with a radioiodinated norepinephrine storage analog. J Nucl Med. 1981;22:22–31.
9. Crout JR, Alpers HS, Tatum EL, Shore PA. Release of metaraminol (Aramine) from the heart by sympathetic nerve stimulation. Science. 1964;145:828–9.
10. Rosenspire KC, Haka MS, Van Dort ME, Jewett DM, Gildersleeve DL, Schwaiger M, et al. Synthesis and preliminary evaluation of carbon-11-meta-hydroxyephedrine: a false transmitter agent for heart neuronal imaging. J Nucl Med. 1990;31:1328–34.
11. Hartmann F, Ziegler S, Nekolla S, Hadamitzky M, Seyfarth M, Richardt G, et al. Regional patterns of myocardial sympathetic denervation in dilated cardiomyopathy: an analysis using carbon-11 hydroxyephedrine and positron emission tomography. Heart. 1999; 81:262–70.
12. Vesalainen RK, Pietilä M, Tahvanainen KU, Jartti T, Teräs M, Någren K, et al. Cardiac positron emission tomography imaging with [11C]hydroxyephedrine, a specific tracer for sympathetic nerve endings, and its functional correlates in congestive heart failure. Am J Cardiol. 1999;84:568–74.
13. Raffel DM, Chen W. Binding of [3H]mazindol to cardiac norepinephrine transporters: kinetic and equilibrium studies. Naunyn Schmiedeberg's Arch Pharmacol. 2004;370:9–16.
14. Raffel DM, Wieland DM. Assessment of cardiac sympathetic nerve integrity with positron emission tomography. Nucl Med Biol. 2001;28:541–59.
15. Allman KC, Wieland DM, Muzik O, Degrado TR, Wolfe ER Jr, Schwaiger M. Carbon-11 hydroxyephedrine with positron emission tomography for serial assessment of cardiac adrenergic neuronal function after acute myocardial infarction in humans. J Am Coll Cardiol. 1993;22:368–75.
16. Schwaiger M, Kalff V, Rosenspire K, Haka MS, Molina E, Hutchins GD, et al. Noninvasive evaluation of sympathetic nervous system in human heart by positron emission tomography. Circulation. 1990;82:457–64.
17. Yu M, Bozek J, Lamoy M, Guaraldi M, Silva P, Kagan M, et al. Evaluation of LMI1195, a novel 18F-labeled cardiac neuronal PET imaging agent, in cells and animal models. Circ Cardiovasc Imaging. 2011;4:435–43.
18. Matsunari I, Aoki H, Nomura Y, Takeda N, Chen WP, Taki J, et al. Iodine-123 metaiodobenzylguanidine imaging and carbon-11 hydroxyephedrine positron emission tomography compared in patients with left ventricular dysfunction. Circ Cardiovasc Imaging. 2010;3:595–603.
19. Morozumi T, Kusuoka H, Fukuchi K, Tani A, Uehara T, Matsuda S, et al. Myocardial iodine-123-metaiodobenzylguanidine images and autonomic nerve activity in normal subjects. J Nucl Med. 1997;38:49–52.

20. Caldwell JH, Link JM, Levy WC, Poole JE, Stratton JR. Evidence for pre- to postsynaptic mismatch of the cardiac sympathetic nervous system in ischemic congestive heart failure. J Nucl Med. 2008;49:234–41.
21. Elsinga PH, van Waarde A, Visser TJ, Vaalburg W. Visualization of beta-adrenoceptors using PET. Clin Positron Imaging. 1998;1:81–94.
22. Link JM, Stratton JR, Levy W, Poole JE, Shoner SC, Stuetzle W, Caldwell JH. PET measures of pre- and post-synaptic cardiac beta adrenergic function. Nucl Med Biol. 2003;30:795–803.
23. Naya M, Tsukamoto T, Morita K, Katoh C, Nishijima K, Komatsu H, Yamada S, Kuge Y, Tamaki N, Tsutsui H. Myocardial beta-adrenergic receptor density assessed by 11C-CGP12177 PET predicts improvement of cardiac function after carvedilol treatment in patients with idiopathic dilated cardiomyopathy. J Nucl Med. 2009;50:220–5.
24. Elsinga PH, Van Waarde A, Visser GM, Vaalburg W. Synthesis and preliminary evaluation of (R,S)-1-[2-((carbamoyl-4-hydroxy)phenoxy)-ethylamino]-3-[4-(1-[11C]-met hyl-4-trifluoromethyl-2-imidazolyl)phenoxy]-2-propanol ([11C]CGP 20712A) as a selective beta 1-adrenoceptor ligand for PET. Nucl Med Biol. 1994;21:211–7.
25. Doze P, Elsinga PH, Maas B, Van Waarde A, Wegman T, Vaalburg W. Synthesis and evaluation of radiolabeled antagonists for imaging of beta-adrenoceptors in the brain with PET. Neurochem Int. 2002;40:145–55.
26. de Jong RM, Willemsen AT, Slart RH, Blanksma PK, van Waarde A, Cornel JH, Vaalburg W, van Veldhuisen DJ, Elsinga PH. Myocardial beta-adrenoceptor downregulation in idiopathic dilated cardiomyopathy measured in vivo with PET using the new radioligand (S)-[11C]CGP12388. Eur J Nucl Med Mol Imaging. 2005;32(4):443–7.
27. Ohte N, Narita H, Iida A, Fukuta H, Iizuka N, Hayano J, Kuge Y, Tamaki N, Kimura G. Cardiac β-adrenergic receptor density and myocardial systolic function in the remote non-infarcted region after prior myocardial infarction with left ventricular remodelling. Eur J Nucl Med Mol Imaging. 2012;39:1246–53.
28. Rosen SD, Boyd H, Rhodes CG, Kaski JC, Camici PG. Myocardial beta-adrenoceptor density and plasma catecholamines in syndrome X. Am J Cardiol. 1996;78:37–42.
29. Qing F, Rahman SU, Rhodes CG, Hayes MJ, Sriskandan S, Ind PW, Jones T, Hughes JM. Pulmonary and cardiac beta-adrenoceptor density in vivo in asthmatic subjects. Am J Respir Crit Care Med. 1997;155:1130–4.
30. Schäfers M, Lerch H, Wichter T, Rhodes CG, Lammertsma AA, Borggrefe M, Hermansen F, Schober O, Breithardt G, Camici PG. Cardiac sympathetic innervation in patients with idiopathic right ventricular outflow tract tachycardia. J Am Coll Cardiol. 1998;32:181–6.
31. Wichter T, Schäfers M, Rhodes CG, Borggrefe M, Lerch H, Lammertsma AA, et al. Abnormalities of cardiac sympathetic innervation in arrhythmogenic right ventricular cardiomyopathy: quantitative assessment of presynaptic norepinephrine reuptake and postsynaptic beta-adrenergic receptor density with positron emission tomography. Circulation. 2000;101:1552–8.
32. John AS, Mongillo M, Depre C, Khan MT, Rimoldi OE, Pepper JR, Dreyfus GD, Pennell DJ, Camici PG. Pre- and post-synaptic sympathetic function in human hibernating myocardium. Eur J Nucl Med Mol Imaging. 2007;34:1973–80.
33. Verberne HJ, Scholte AJ. General principles of [123I]-MIBG scintigraphy for the assessment of the cardiac sympathetic activity: from planar to SPECT. In: Slart RH, Tio RA, Elsinga PH, Schwaiger M, editors. Autonomic innervation of the heart: role of molecular imaging. Heidelberg: Springer; 2015. p. 187–99.
34. Nekolla SG, Rischpler C. Principles of PET/CT and autonomic innervation of the heart including kinetics and software. In: Slart RH, Tio RA, Elsinga PH, Schwaiger M, editors. Autonomic innervation of the heart: role of molecular imaging. Heidelberg: Springer; 2015. p. 161–85.
35. Cohn JN, Levine TB, Olivari MT, Garberg V, Lura D, Francis GS, et al. Plasma norepinephrine as a guide to prognosis in patients with chronic congestive heart failure. N Engl J Med. 1984;311:819–23.

36. Haider N, Baliga RR, Chandrashekhar Y, Narula J. Adrenergic excess, hNET1 down-regulation, and compromised mIBG uptake in heart failure poverty in the presence of plenty. J Am Coll Cardiol Img. 2010;3:71–5.
37. Kaye DM, Lambert GW, Lefkovits J, Morris M, Jennings G, Esler MD. Neurochemical evidence of cardiac sympathetic activation and increased central nervous system norepinephrine turnover in severe congestive heart failure. J Am Coll Cardiol. 1994;23:570–8.
38. Bengel FM, Ueberfuhr P, Schiepel N, Nekolla SG, Reichart B, Schwaiger M. Effect of sympathetic reinnervation on cardiac performance after heart transplantation. N Engl J Med. 2001;345:731–8.
39. Di Carli MF, Tobes MC, Mangner T, Levine AB, Muzik O, Chakroborty P, et al. Effects of cardiac sympathetic innervation on coronary blood flow. N Engl J Med. 1997;336:1208–15.
40. Bengel FM, Ueberfuhr P, Ziegler SI, Nekolla S, Reichart B, Schwaiger M. Serial assessment of sympathetic reinnervation after orthotopic heart transplantation. A longitudinal study using PET and C-11 hydroxyephedrine. Circulation. 1999;99:1866–71.
41. Roden DM. Keep the QT interval: it is a reliable predictor of ventricular arrhythmias. Heart Rhythm. 2008;5(8):1213–5. https://doi.org/10.1016/j.hrthm.2008.05.008. Epub 2008 May 15. PMID: 18675237; PMCID: PMC3212752.
42. Göhl K, Feistel H, Weikl A, Bachmann K, Wolf F. Congenital myocardial sympathetic dysinnervation (CMSD)–a structural defect of idiopathic long QT syndrome. Pacing Clin Electrophysiol. 1991;14:1544–53.
43. Chevalier P, Rodriguez C, Bontemps L, Miquel M, Kirkorian G, Rousson R, et al. Non-invasive testing of acquired long QT syndrome: evidence for multiple arrhythmogenic substrates. Cardiovasc Res. 2001;50:386–98.
44. Kies P, Paul M, Gerss J, Stegger L, Mönnig G, Schober O, et al. Impaired cardiac sympathetic innervation in symptomatic patients with long QT syndrome. Eur J Nucl Med Mol Imaging. 2001;38:1899–907.
45. Mazzadi AN, André-Fouët X, Duisit J, Gebuhrer V, Costes N, Chevalier P, et al. Cardiac retention of [11C]HED in genotyped long QT patients: a potential amplifier role for severity of the disease. Am J Physiol Heart Circ Physiol. 2003;285:1286–93.
46. Zumhagen S, Vrachimis A, Stegger L, Kies P, Wenning C, Ernsting M, et al. Impact of presynaptic sympathetic imbalance in long-QT syndrome by positron emission tomography. Heart. 2018;104:332–9.
47. Calkins H, Lehmann MH, Allman K, Wieland D, Schwaiger M. Scintigraphic patternof regional cardiac sympathetic innervation in patients with familial long QT syndrome using positron emission tomography. Circulation. 1993;87:1616–21.
48. Brugada P, Brugada J. Right bundle branch block, persistent ST segment elevation and sudden cardiac death: a distinct clinical and electrocardiographic syndrome: A multicenter report. J Am Coll Cardiol. 1992;20:1391–6.
49. Antzelevitch C, Brugada P, Brugada J, Brugada R. The Brugada syndrome: from cell to bedside. Curr Probl Cardiol. 2005;30:9–54.
50. Agostini D, Scanu P, Loiselet P, Babatasi G, Darlas Y, Grollier G, et al. Iodine-123-metaiodobenzylguanidine SPECT of regional cardiac adrenergic denervation in Brugada syndrome. J Nucl Med. 1998;39:1129–32.
51. Wichter T, Matheja P, Eckardt L, Kies P, Schäfers K, Schulze-Bahr E, et al. Cardiac autonomic dysfunction in Brugada syndrome. Circulation. 2002;105:702–6.
52. Kawaguchi T, Nomura M, Tujikawa T, Nakaya Y, Ito S. 123I-metaiodo-benzylguanidine myocardial scintigraphy in the Brugada-type ECG. J Med Investig. 2006;53:95–102.
53. Kies P, Wichter T, Schäfers M, Paul M, Schäfers KP, Eckardt L, et al. Abnormal myocardial presynaptic norepinephrine recycling in patients with Brugada syndrome. Circulation. 2004;110:3017–22.
54. Gandjbakhch E, Redheuil A, Pousset F, Charron P, Frank R. Clinical diagnosis imaging, and genetics of arrhythmogenic right ventricular cardiomyopathy/dysplasia: JACC state-of-the-art review. J Am Coll Cardiol. 2018;72:784–804.

55. Bennett RG, Haqqani HM, Berruezo A, Della Bella P, Marchlinski FE, Hsu CJ, et al. Arrhythmogenic cardiomyopathy in 2018-2019: ARVC/ALVC or both? Heart Lung Circ. 2019;28:164–77.
56. Dalal D, Tandri H, Judge DP, Amat N, Macedo R, Jain R, et al. Morphologic variants of familial arrhythmogenic right ventricular dysplasia/cardiomyopathy a genetics-magnetic resonance imaging correlation study. J Am Coll Cardiol. 2009;53:1289–99.
57. Wichter T, Hindricks G, Lerch H, Bartenstein P, Borggrefe M, Schober O, et al. Regional myocardial sympathetic dysinnervation in arrhythmogenic right ventricular cardiomyopathy. Ananalysis using 123I-meta-iodobenzylguanidine scintigraphy. Circulation. 1994;89:667–83.
58. Paul M, Wichter T, Kies P, Gerss J, Wollmann C, Rahbar K, et al. Cardiac sympathetic dysfunction in genotyped patients with arrhythmogenic right ventricular cardiomyopathy and risk of recurrent ventricular tachyarrhythmias. J Nucl Med. 2011;52:1559–65.
59. Report of the Task Force of the European Society of Cardiology. The clinical role of magnetic resonance imaging in cardiovascular disease. Eur Heart J. 1998;19:19–39.
60. Carlson MD, White RD, Trohman RG, Adler LP, Biblo LA, Merkatz KA, et al. Right ventricular outflow tract ventricular tachycardia: detection of previously unrecognized anatomic abnormalities using cine magnetic resonance imaging. J Am Coll Cardiol. 1994;24:720–7.
61. Papavassiliu T, Veltmann C, Doesch C, Haghi D, Germans T, Schoenberg SO, et al. Spontaneous type 1 electrocardiographic pattern is associated with cardiovascular magnetic resonance imaging changes in Brugada syndrome. Heart Rhythm. 2010;7:1790–6.
62. Gray B, Gnanappa GK, Bagnall RD, Femia G, Yeates L, Ingles J, et al. Relations between right ventricular morphology and clinical, electrical and genetic parameters in Brugada syndrome. PLoS One. 2018;13:e0195594.
63. Bastiaenen R, Cox AT, Castelletti S, Wijeyeratne YD, Colbeck N, Pakroo N, et al. Late gadolinium enhancement in Brugada syndrome: a marker for subtle underlying cardiomyopathy? Heart Rhythm. 2017;14:583–9.
64. Rudic B, Schimpf R, Veltmann C, Doesch C, Tülümen E, Schoenberg SO, et al. Brugada syndrome: clinical presentation and genotype-correlation with magnetic resonance imaging parameters. Europace. 2016;18:1411–9.
65. van Hoorn F, Campian ME, Spijkerboer A, Blom MT, Planken RN, van Rossum AC, et al. SCN5A mutations in Brugada syndrome are associated with increased cardiac dimensions and reduced contractility. PLoS One. 2012;7:e42037.
66. Brado J, Dechant MJ, Menza M, Komancsek A, Lang CN, Bugger H, et al. Phase-contrast magnet resonance imaging reveals regional, transmural, and base-to-apex dispersion of mechanical dysfunction in patients with long QT syndrome. Heart Rhythm. 2017;14:1388–97.
67. Turco A, Nuyts J, Gheysens O, Duchenne J, Voigt JU, Claus P, et al. Lesion quantification and detection in myocardial (18)F-FDG PET using edge-preserving priors and anatomical information from CT and MRI: a simulation study. EJNMMI Phys. 2016;3:9.
68. Würslin C, Schmidt H, Martirosian P, Brendle C, Boss A, Schwenzer NF, et al. Respiratory motion correction in oncologic PET using T1-weighted MR imaging on a simultaneous whole-body PET/MR system. J Nucl Med. 2013;54:464–71.
69. Gill JS, Hunter GJ, Gane J, Ward DE, Camm AJ. Asymmetry of cardiac [123I] meta-iodobenzyl-guanidine scans in patients with ventricular tachycardia and a “clinically normal” heart. Br Heart J. 1993;69:6–13.
70. Schäfers M, Wichter T, Lerch H, Matheja P, Kuwert T, Schäfers K, et al. Cardiac 123I-MIBG uptake in idiopathic ventricular tachycardia and fibrillation. J Nucl Med. 1999;40:1–5.
71. Verschure DO, Veltman CE, Manrique A, Somsen GA, Koutelou M, Katsikis A, et al. For what endpoint does myocardial 123I-MIBG scintigraphy have the greatest prognostic value in patients with chronic heart failure? Results of a pooled individual patient data meta-analysis. Eur H J Cardiovasc Imaging. 2014;15:996–1003.
72. Bax JJ, Kraft O, Buxton AE, Fjeld JG, Parizek P, Agostini D, et al. 123 I-mIBG scintigraphy to predict inducibility of ventricular arrhythmias on cardiac electrophysiology testing: a prospective multicenter pilot study. Circ Cardiovasc Imaging. 2008;1:131–40.

73. Boogers MJ, Borleffs CJ, Henneman MM, van Bommel RJ, van Ramshorst J, Boersma E, et al. Cardiac sympathetic denervation assessed with 123-iodine metaiodobenzylguanidine imaging predicts ventricular arrhythmias in implantable cardioverter-defibrillator patients. J Am Coll Cardiol. 2010;55:2769–77.
74. Fallavollita JA, Heavey BM, Luisi AJ Jr, Michalek SM, Baldwa S, Mashtare TL Jr, et al. Regional myocardial sympathetic denervation predicts the risk of sudden cardiac arrest in ischemic cardiomyopathy. J Am Coll Cardiol. 2014;63:141–9.
75. Hachamovitch R, Nutter B, Menon V, Cerqueira MD. Predicting risk versus predicting potential survival benefit using 123I-mIBG imaging in patients with systolic dysfunction eligible for implantable cardiac defibrillator implantation: analysis of data from the prospective ADMIRE-HF study. Circ Cardiovasc Imaging. 2015;8(12):e003110.
76. Young JB, Abraham WT, Smith AL, Leon AR, Lieberman R, Wilkoff B, et al. Multicenter InSync ICD Randomized Clinical Evaluation (MIRACLE ICD) Trial Investigators. Combined cardiac resynchronization and implantable cardioversion defibrillation in advanced chronic heart failure: the MIRACLE ICD trial. JAMA. 2003;289:2685–94.
77. Chen J, Garcia EV, Folks RD, Cooke CD, Faber TL, Tauxe EL, et al. Onset of left ventricular mechanical contraction as determined by phase analysis of ECG-gated myocardial perfusion SPECT imaging: development of a diagnostic tool for assessment of cardiac mechanical dyssynchrony. J Nucl Cardiol. 2005;12:687–95.
78. Lardo AC, Abraham TP, Kass DA. Magnetic resonance imaging assessment of ventricular dyssynchrony: current and emerging concepts. J Am Coll Cardiol. 2005;46:2223–8.
79. Alexanderson E, Flotats A, Juarèz-Orozco LE. Imaging sympathetic innervations of gthe heart: therapeutic strategies SPECT/CT and PET/CT. In: Slart RH, Tio RA, Elsinga PH, Schwaiger M, editors. Autonomic innervation of the heart: role of molecular imaging. Heidelberg: Springer; 2015. p. 367–86.
80. Martignani C, Diemberger I, Nanni C, Biffi M, Ziacchi M, Boschi S, et al. Cardiac resynchronization therapy and cardiac sympathetic function. Eur J Clin Investig. 2015;45:792–9.
81. Capitanio S, Nanni C, Marini C, Bonfiglioli R, Martignani C, Dib B, et al. Heterogeneous response of cardiac sympathetic function to cardiac resynchronization therapy in heart failure documented by 11[C]-hydroxy-ephedrine and PET/CT. Nucl Med Biol. 2015;42:858–63.
82. Boogers MM, Chen J, Bax JJ. Role of nuclear imaging in cardiac resynchronization therapy. Expert Rev Cardiovasc Ther. 2009;7:65–72.
83. Slart RHJA, Glaudemans AWJM, Hazenberg BPC, Noordzij W. Imaging cardiac innervation in amyloidosis. J Nucl Cardiol. 2019;26(1):174–87.
84. Falk RH, Comenzo RL, Skinner M. The systemic amyloidoses. N Engl J Med. 1997;337:898–909.
85. Noordzij W, Glaudemans AW, van Rheenen RW, Hazenberg BP, Tio RA, Dierckx RA, et al. (123)I-Labelled metaiodobenzylguanidine for the evaluation of cardiac sympathetic denervation in early stage amyloidosis. Eur J Nucl Med Mol Imaging. 2012;39:1609–17.
86. Coutinho MC, Cortez-Dias N, Cantinho G, Conceição I, Oliveira A, Bordalo e Sá A, et al. Reduced myocardial 123-iodine metaiodobenzylguanidine uptake: a prognostic marker in familial amyloid polyneuropathy. Circ Cardiovasc Imaging. 2013;6:627–36.
87. Simoes MV, Barthel P, Matsunari I, Nekolla SG, Schömig A, Schwaiger M, et al. Presence of sympathetically denervated but viable myocardium and its electrophysiologic correlates after early revascularised, acute myocardial infarction. Eur Heart J. 2004;25:551–7.
88. Delahaye N, Rouzet F, Sarda L, Tamas C, Dinanian S, Plante-Bordeneuve V, et al. Impact of liver transplantation on cardiac autonomic denervation in familial amyloid polyneuropathy. Medicine (Baltimore). 2006;85:229–38.
89. American Diabetes Association. Consensus development conference on the diagnosis of coronary heart disease in people with diabetes: 10-11 February 1998, Miami, Florida. Diabetes Care. 1998;21(9):1551–9.
90. Vinik AI, Ziegler D. Diabetic cardiovascular autonomic neuropathy. Circulation. 2007;115:387–97.

91. Gerritsen J, Dekker JM, TenVoorde BJ, Kostense PJ, Heine RJ, Bouter LM, et al. Impaired autonomic function is associated with increased mortality, especially in subjects with diabetes, hypertension, or a history of cardiovascular disease: the Hoorn study. Diabetes Care. 2001;24:1793–8.
92. Zipes DP, Wellens HJ. Sudden cardiac death. Circulation. 1998;98:2334–51.
93. Boulton AJ, Vinik AI, Arezzo JC, Bril V, Feldman EL, Freeman R, et al. Diabetic neuropathies: a statement by the American Diabetes Association. Diabetes Care. 2005; 28:956–62.
94. Vinik AI, Maser RE, Mitchell BD, Freeman R. Diabetic autonomic neuropathy. Diabetes Care. 2003;26:1553–79.
95. Scholte AJ, Verberne HJ. Imaging the cardiac autonomic nervous system in diabetes mellitus. In: Slart RH, Tio RA, Elsinga PH, Schwaiger M, editors. Autonomic innervation of the heart: role of molecular imaging. Heidelberg: Springer; 2015. p. 161–85.
96. Stevens MJ, Dayanikli F, Raffel DM, Allman KC, Sandford T, Feldman EL, et al. Scintigraphic assessment of regionalized defects in myocardial sympathetic innervation and blood flow regulation in diabetic patients with autonomic neuropathy. J Am Coll Cardiol. 1998;31:1575–84.
97. Ziegler D, Weise F, Langen KJ, Piolot R, Boy C, Hübinger A, et al. Effect of glycaemic control on myocardial sympathetic innervation assessed by [123I]metaiodobenzylguanidine scintigraphy: a 4-year prospective study in IDDM patients. Diabetologia. 1998;41: 443–51.
98. Kreiner G, Wolzt M, Fasching P, Leitha T, Edlmayer A, Korn A, et al. Myocardial m-[123I]iodobenzylguanidine scintigraphy for the assessment of adrenergic cardiac innervation in patients with IDDM. Comparison with cardiovascular reflex tests and relationship to left ventricular function. Diabetes. 1995;44:543–9.
99. Nagamachi S, Fujita S, Nishii R, Futami S, Tamura S, Mizuta M, et al. Prognostic value of cardiac I-123 metaiodobenzylguanidine imaging in patients with non-insulin-dependent diabetes mellitus. J Nucl Cardiol. 2006;13:34–42.
100. Nagamachi S, Jinnouchi S, Kurose T, Nishii R, Kawai K, Futami S, et al. Serial change in 123I-MIBG myocardial scintigraphy in non-insulin-dependent diabetes mellitus. Ann Nucl Med. 2002;16:33–8.
101. Scognamiglio R, Avogaro A, Casara D, Crepaldi C, Marin M, Palisi M, et al. Myocardial dysfunction and adrenergic cardiac innervation in patients with insulin-dependent diabetes mellitus. J Am Coll Cardiol. 1998;31:404–12.
102. Turpeinen AK, Vanninen E, Kuikka JT, Uusitupa MI. Demonstration of regional sympathetic denervation of the heart in diabetes. Comparison between patients with NIDDM and IDDM. Diabetes Care. 1996;19:1083–90.
103. Schnell O, Hammer K, Muhr-Becker D, Ziegler A, Weiss M, Tatsch K, et al. Cardiac sympathetic dysinnervation in type 2 diabetes mellitus with and without ECG-based cardiac autonomic neuropathy. J Diabetes Complicat. 2002;16:220–7.
104. Langer A, Freeman MR, Josse RG, Armstrong PW. Metaiodobenzylguanidine imaging in diabetes mellitus: assessment of cardiac sympathetic denervation and its relation to autonomic dysfunction and silent myocardial ischemia. J Am Coll Cardiol. 1995;25:610–8.
105. Scholte AJ, Schuijf JD, Delgado V, Kok JA, Bus MT, Maan AC, et al. Cardiac autonomic neuropathy in patients with diabetes and no symptoms of coronary artery disease: comparison of 123I-metaiodobenzylguanidine myocardial scintigraphy and heart rate variability. Eur J Nucl Med Mol Imaging. 2010;37:1698–705.
106. Gerson MC, Caldwell JH, Ananthasubramaniam K, Clements IP, Henzlova MJ, Amanullah A, et al. Influence of diabetes mellitus on prognostic utility of imaging of myocardial sympathetic innervation in heart failure patients. Circ Cardiovasc Imaging. 2011;4:87–93.
107. Noordzij W, Glaudemans AWJM, Juarez-Orozco LE, Slart RHJA. Towards consensus in acquisition and image analysis of PET and SPECT in the assessment of cardiac sympathetic innervation: a mini-review. Clin Transl Imaging. 2019;7:33–8.

108. Nakajima K, Okuda K, Yoshimura M, Matsuo S, Wakabayashi H, Imanishi Y, et al. Multicenter cross-calibration of I-123 metaiodobenzylguanidine heart-to-mediastinum ratios to overcome camera-collimator variations. J Nucl Cardiol. 2014;21:970–8.
109. Travin MI, Matsunari I, Thomas GS, Nakajima K, Yoshinaga K. How do we establish cardiac sympathetic nervous system imaging with ^{123}I-mIBG in clinical practice? Perspectives and lessons from Japan and the US. J Nucl Cardiol. 2019;26(4):1434–51. https://doi.org/10.1007/s12350-018-1394-5.
110. Nakajima K, Nakata T, Doi T, Kadokami T, Matsuo S, Konno T, et al. Validation of 2-year ^{123}I-meta-iodobenzylguanidine-based cardiac mortality risk model in chronic heart failure. Eur Heart J Cardiovasc Imaging. 2018;19:749–56.

Dyssynchrony

6

Saurabh Malhotra, Saara Sillanmaki, and Prem Soman

Dyssynchrony is the term applied to disorganized ventricular contraction and is typified by regional variation in the timing of contraction of left ventricular (LV) segments. While minor variations in the timing of regional segmental contraction exist in normal hearts, pathologic dyssynchrony is defined by limits not encountered in normal subjects. Thus, dyssynchrony is best considered along a continuum of severity, rather than as a binary phenomenon. The term dyssynchrony has been applied to both electrical and mechanical aberrations. Electrical dyssynchrony is most commonly recognized by a wide QRS duration [1, 2], which is a strong predictor of clinical improvement after cardiac resynchronization therapy (CRT) [1–4]. In contrast, mechanical dyssynchrony can present itself as (a) atrioventricular dyssynchrony: between the atrium and the ventricle, as seen in heart blocks, (b) interventricular dyssynchrony: between left and right ventricle, and (c) intraventricular dyssynchrony: within various segments of the LV or left ventricular mechanical dyssynchrony (LVMD). Additionally, LVD can be both systolic and diastolic, with growing evidence of prognostic value of the latter [5]. Studies have shown that LVD is more significantly correlated with cardiac hemodynamic than interventricular dyssynchrony [6], and is a strong predictor of heart failure (HF) progression [7–9]. Clearly, electrical and mechanical dyssynchrony can co-exist,

S. Malhotra
Division of Cardiology, Cook County Health, Chicago, IL, USA

Division of Cardiology, Rush Medical College, Chicago, IL, USA

S. Sillanmaki
Department of Nuclear Medicine and Clinical Physiology, Kuopio University Hospital, Kuopio, Finland

P. Soman (✉)
Division of Cardiology and The Heart and Vascular Institute, University of Pittsburgh Medical Center, Pittsburgh, PA, USA
e-mail: somanp@upmc.edu

S. G. Nekolla, C. Rischpler (eds.), *Hybrid Cardiac Imaging*,
https://doi.org/10.1007/978-3-030-83167-7_6

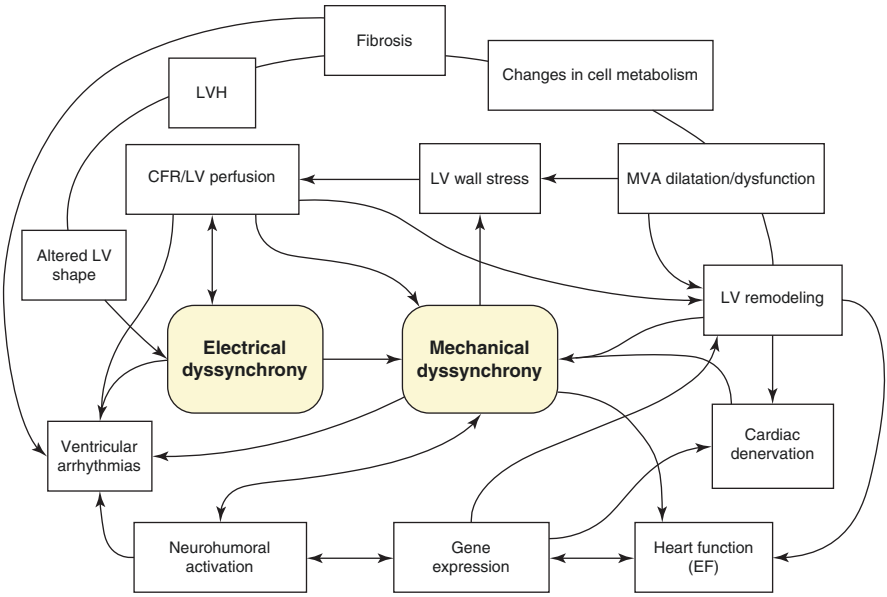

Fig. 6.1 The complex pathophysiology of electrical and mechanical dyssynchrony. *CRF* coronary flow reserve, *LV* left ventricle, *MVA* mitral valve annulus, *EF* ejection fraction. (Modified from publications of the University of Eastern Finland 2019; with permission)

for example, in left bundle branch block (LBBB) where the electrical aberration is thought to result in delayed activation of the lateral wall compared to the septum.

Though poorly understood, the genesis of LVMD can be the result of a multitude of factors such as left ventricular remodeling, regional scar and conduction abnormalities (e.g. wide QRS). A schematic representation of potential pathophysiologic determinants of LVMD is shown in Fig. 6.1. LVMD is prevalent in HF, particularly with reduced ejection fraction [7]. There is a modest correlation between QRS duration and parameters of mechanical dyssynchrony ($r = 0.69$, $p < 0.001$) [4]. Though LBBB is considered as a marker of dyssynchrony, a proportion of patients with LBBB do not have evidence of mechanical dyssynchrony, particularly if the ejection fraction is normal [4]. LVMD is more prevalent among those with a wide QRS (>150 ms) when compared to those with a narrow QRS duration (<120 ms) [8, 9]. Patients with LBBB and mechanical dyssynchrony tend to have a wider QRS duration, along with greater LV remodeling [4, 10]. Additionally, LVMD seems to be associated with sympathetic denervation, with a greater burden of denervation-perfusion mismatch predicting LVMD [11].

6.1 Assessment of Left Ventricular Dyssynchrony by SPECT

The basis of LVD assessment by gated myocardial perfusion SPECT is the assessment of the timing (phase) of regional myocardial contractility by phase analysis. Due to its relatively poor spatial resolution, SPECT imaging is prone to partial volume effects, which result in a relatively linear relationship between myocardial

thickening and myocardial count density during a cardiac cycle [12]. This can be appreciated as a "brighter" myocardium (secondary to higher count density) during systole in gated SPECT. In phase analysis the myocardial count data from a cardiac cycle is subjected to Fourier first harmonic transformation to obtain a count activity curve, which represents the timing of myocardial thickening on gated SPECT. For gated SPECT, with a typical 8 or 16 frame gating, Fourier first harmonic transformation improves the temporal resolution, allowing for comparison of timing of contraction between various myocardial voxels. The time during a cardiac cycle when the count density of a voxel increases above the mean count density of that voxel is used to delineate the onset of mechanical contraction (OMC). Thus OMC represents the phase (time in degree) when a myocardial voxel begins contracting (Fig. 6.2a) [13, 14]. The OMC data is acquired for numerous voxels (>600) and displayed as a histogram, wherein the *x*-axis represents the phase (time in degrees; 0–360°) and *y*-axis represents the frequency of OMC at that phase (Fig. 6.2b). In addition to degrees, phase analysis results can also be presented as milliseconds and percentage of cardiac cycle (%R-R). Similar principles can also be applied to derive the peak of contraction of a myocardial voxel, and software approaches variably utilize the onset or peak of regional contraction to derive dyssynchrony parameters. The most

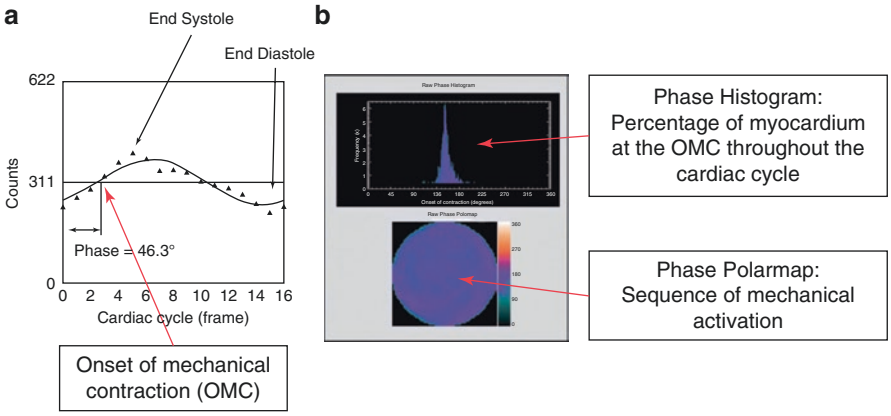

Fig. 6.2 Phase analysis by gated myocardial perfusion SPECT. (**a**) Example of a time-activity curve for a single myocardial sample volume generated by 16-bin gating. The data points (filled triangle) are then fitted to a continuous curve, using a Fourier transform. Based on the partial volume effect, this time-activity curve represents the thickening curve of this particular myocardial sample during a cardiac cycle. The point at which the continuous thickening curve intersects with the average count density of this voxel (horizontal line) is considered the onset of mechanical contraction (OMC) for this region. The software computes the OMC for all LV myocardial samples collected (>600) and then displays the composite result as a phase histogram and phase polar map (**b**). The phase histogram shows the percentage of myocardium contracting (*y*-axis) at each point in the cardiac cycle (*x*-axis). The phase polar map is a bull's-eye representation of the left ventricle, showing the sequence of mechanical activation, using a color-coded scheme. This is an example of synchronous LV contraction with a narrow and highly peaked histogram and a uniform color on the phase polar map. (Adapted from Friehling M, Chen J, Saba S, et al. A prospective pilot study to evaluate the relationship between acute change in left ventricular synchrony after cardiac resynchronization therapy and patient outcome using a single-injection gated SPECT protocol. Circ Cardiovasc Imaging 2011;4 (5):533; with permission) [56]

commonly utilized and validated indices of LVD from gated SPECT are the phase histogram bandwidth (HBW), the range of degree of the cardiac cycle that encompasses 95% of the phase distribution, and the PSD, which is the standard deviation of the phase distribution. Entropy% reflects the similarity in the contraction onset times in the LV and is calculated by $[f_i*\log(f_i)]/\mathrm{Log}(n)]$, where f is the frequency in the ith bin and n is the number of bins [15]. These values of global LVD from gated SPECT have been validated against 2D [16, 17] and 3D echocardiography [18, 19], as well speckle tracking echocardiography [20]. Several commercial software packages have been developed to make the LV perfusion interpretations more standardized including QPS-QGS from Cedars Sinai Medical Centre (California, USA) [21], Corridor4DM SPECT from Invia Medical Solutions (Eclipse Systems, Branford, USA) [22], and Emory Toolbox from Emory University (Georgia, USA) [23]. Recent studies have shown a considerable variability among measures of LVD by different software [15, 24]. Thus, software specific values should be used to interpret presence or absence of LVD. Phase histograms from patients with and without LVD are shown in Fig. 6.3. Averaging of the phase value of each voxel within a specific standard myocardial segment [25] allows for assessment of

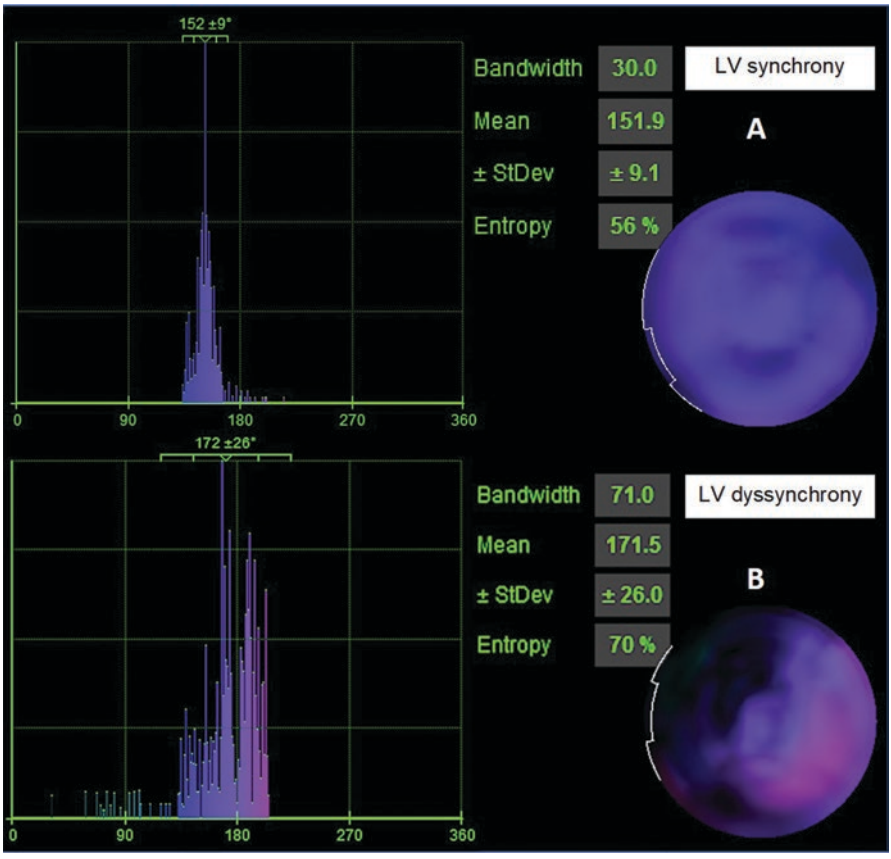

Fig. 6.3 Representative phase histograms and polar maps from two patients (**a**) without and (**b**) with left ventricular dyssynchrony

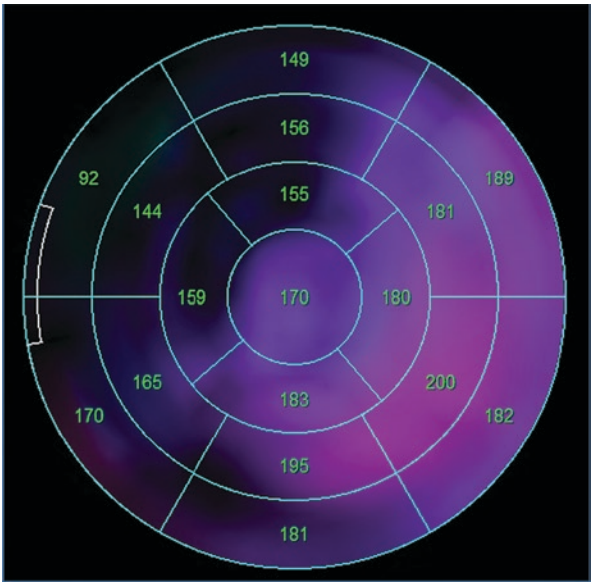

Fig. 6.4 Phase polar map depicting segmental phase values in a patient with left bundle branch block. Mean segmental phase (in degrees) is calculated for each of the standard 17 left ventricular segments by averaging the peak phases of all the voxels that form a segment. The onset of mechanical contraction is earlier (92–170°) in septal segments than in lateral segments (180–200°)

segmental phase [25] (Fig. 6.4). These phase analysis values expressed with a 17-segment model allow for comparison of regional differences in myocardial contraction. An alternative approach to detect wall motion and LVD uses an estimation of endo- and epicardial borders localized in gradient operators and information on the LV shape, location, and continuity of the LV wall. A midline between endo- and epicardium is set, and perpendicular normal vectors are placed between the corresponding sectors in end-diastolic and end-systolic borders. Regional LV motion is detected as a change in vector length in each corresponding sector. The time to peak motion is calculated throughout the cardiac cycle for each segment and a phase histogram is then produced based on that information [26].

6.2 Dyssynchrony as a Guide for Cardiac Resynchronization Therapy

In patients with HF, dyssynchrony promotes ventricular remodeling which worsens systolic function, HF symptoms and, increases morbidity and mortality [27–29]. Cardiac Resynchroniztation Therapy (CRT) via implantation of a biventricular pacemaker has been shown to promote synchronous ventricular contraction [30–32] and reversal of LV remodeling [33, 34]. Though, population based studies have shown that among patients with drug refractory HF, resynchronization therapy confers a mortality benefit, especially in the presence of dyssynchrony [35–38], symptomatic improvement from CRT is noted only in 50% of the patients receiving this invasive therapy [39]. Although patients with electrical dyssynchrony (LBBB or a wide QRS) have been shown to derive the greatest benefit from CRT in clinical trials [40], some studies have reported either modest no correlation between electrical dyssynchrony and response to CRT [41, 42]. While the presence of mechanical

dyssynchrony seems to be essential for clinical improvement following CRT [43], CRT response is a complex phenomenon and is influenced by several other parameters, such as myocardial scar burden, regional (segmental) differences in myocardial contractility, and the location of the LV lead in relation to latest contracting segments and myocardial scar. Furthermore, anatomical abnormalities attributable to congenital heart diseases or previous surgical intervention can cause technical challenges in the CRT lead placement [44]. Routine Gated SPECT allows for identification of all of these important determinants of CRT response and can thus theoretically aid in improving the efficacy of CRT.

The influence of myocardial scar on clinical response to CRT is well established. Among patients with ischemic cardiomyopathy, CRT non-responders had a significantly greater scar burden when compared to CRT responders (50% vs 28% of left ventricular myocardium) [45]. Additionally, non-responders had a greater number of severely infarcted segments and a greater density of scar near the LV lead. Similarly, among patients with ischemic cardiomyopathy, LV lead location in regions of transmural scar on SPECT was associated with the lack of clinical improvement after CRT [46], and placement of LV lead at or near myocardial scar, and ischemic myocardium was associated with greater mortality and HF hospitalization [47]. This impact of myocardial scar on CRT response was further evaluated in a larger population of 620 patients, with HF, severely reduced left ventricular EF and QRS duration >120 ms [48]. In this study, patients with a summed rest score (SRS) >27 (corresponding to approximately 40% of the left ventricular myocardium) on rest-redistribution thallium 201 chloride (Tl-201) myocardial perfusion SPECT, experienced a lack of functional improvement and poorer survival after CRT [48]. These studies suggest that a high global myocardial scar burden (~40% of the left ventricle) and regional scar at the site of the LV lead preclude a favorable response to CRT and should be accounted for when evaluating candidacy for CRT and response.

Assessment of regional or segmental phase by gated SPECT allows for the identification of the site of latest activation (SOLA), and this can be used to guide implantation of LV lead of a biventricular pacemaker [25, 49, 50]. SOLA guided LV lead placement has been shown to result in a greater response from CRT, along with reverse LV remodeling [51]. Contemporary CRT with biventricular pacing from the right ventricle and coronary sinus limits the implanter's options of positioning the left ventricular lead, which is often empirically positioned in the lateral LV wall [52]. It is thus likely that the septal and lateral positioning of the CRT leads specifically ameliorates the inherent septal to lateral wall delay seen in LBBB, thus resulting in the greatest benefit from CRT among those with HF and LBBB. A study applying phase analysis of gated SPECT among patients with non-ischemic cardiomyopathy has shown that benefit from CRT is greater among patients with a wide QRS duration (>150 ms) when compared to those with QRS duration between 120 and 150 ms [25]. This association was not observed in

patients with ischemic cardiomyopathy when the site of latest activation was at the scar, irrespective of QRS duration. In a retrospective study of HF patients undergoing gated SPECT, it was noted that among patients with non-LBBB QRS morphology, approximately 50% had a myocardial activation pattern mimicking those with LBBB (septal to lateral wall delay) [53]. This observation may explain the variable CRT response observed in patients with non-LBBB types of QRS morphology and argues for a formal assessment of dyssynchrony patterns in these patients before prescribing CRT. A small, randomized controlled trial has shown better CRT response among patients in whom the placement of left ventricular lead was guided by SOLA on speckle tracking echocardiography [54]. SOLA guided lead implantation resulted in resynchronization in 72% of the patients as opposed to only 48% in whom biventricular pacemaker was implanted without imaging guidance. These findings support the identification of SOLA in a viable segment of myocardium to guide optimal left ventricular lead placement for CRT response. An approach of identifying SOLA, myocardial scar burden and an ideal site of LV lead placement from a single gated SPECT has been recently reported [55]. This approach allows for fusion of gated SPECT images with coronary sinus venogram, allowing the operator to guide the LV lead towards an optimal location on the left ventricle, i.e. viable or non-scarred myocardium with SOLA. The combined value of identifying LVD, myocardial scar burden, and LV lead concordance with SOLA has been systematically studied in patients undergoing CRT. In a prospective study of 44 CRT candidates, SPECT was performed before and immediately after activation of the left ventricular lead, using a novel "single-injection" ^{99m}Tc-protocol [56]. An algorithm incorporating the presence of LVD at baseline, scar burden of <40%, and concordance of left ventricular lead with SOLA was shown to predict acute improvement or no change in LV synchrony with 72% sensitivity, 93% specificity, 96% positive predictive value (PPV), and 96% negative predictive value (NPV) for acute deterioration in synchrony (Fig. 6.5). Patients who had acute improvement or no change in LV synchrony following CRT had lower composite outcome of death, heart failure hospitalization, and ventricular arrhythmia compared to those who had acute deterioration [56].

These recent findings from observational and prospective studies may explain the lack of symptomatic or functional improvement in a substantial proportion of patients selected for CRT using clinical criteria. Our contemporary knowledge base suggests that CRT response is a complex phenomenon and that attempts to predict CRT response using just a few dyssynchrony parameters may be overly simplistic. The available literature strongly supports an in-depth assessment of several parameters (presence and pattern of dyssynchrony, location and extent of scar, site of latest activation) to identify myocardial substrate that is amenable to improvement after CRT. The "U-shaped" LV conduction pattern detected with MPI SPECT, MRI or echocardiography has been shown to be predictive for reverse remodeling and good CRT response [57–59].

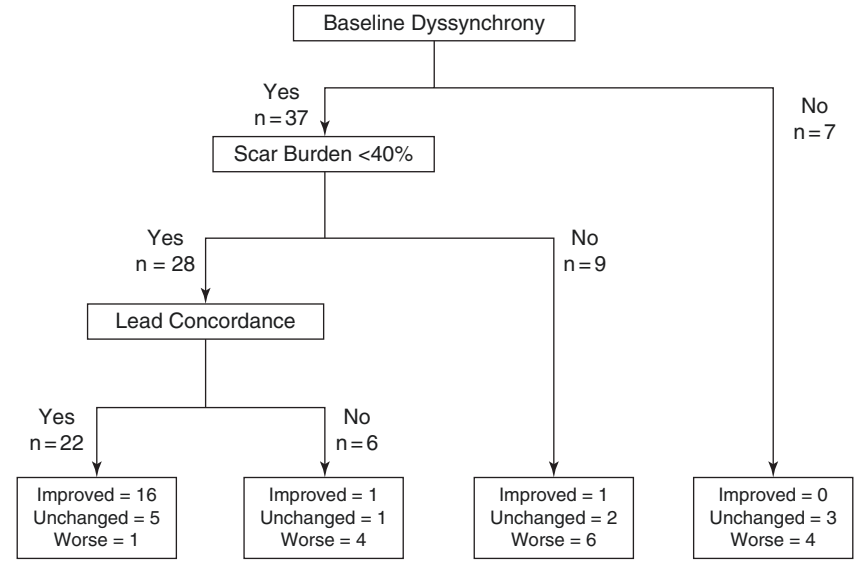

Prediction	Acute Change in Synchrony	
	Improved or Unchanged	Worse
Will Improve = 22	21	1
Will Not Improve = 22	8	14

Sensitivity	**72%**
Specificity	**93%**
PPV	**96%**
NPV	**64%**

Fig. 6.5 Algorithm for predicting acute change in synchrony from gated SPECT. (Adapted from Friehling M, Chen J, Saba S, et al. A prospective pilot study to evaluate the relationship between acute change in left ventricular synchrony after cardiac resynchronization therapy and patient outcome using a single-injection gated SPECT protocol. Circ CardiovascImaging 2011;4 (5):536; with permission) [56]

6.3 Dyssynchrony as a Guide for Implantable Cardioverter Defibrillator

Implantable cardioverter defibrillators (ICDs) are an established preventive therapy in symptomatic HF patients with low LV ejection fraction (<35%), particularly with ischemic cardiomyopathy, and confers a mortality benefit [60, 61]. Recent data suggests that the incidence of ICD shock in a real-world scenario to be only 4% and that of an appropriate ICD therapy (shock or antitachycardia pacing) to be about 14% [62, 63], indicating that only a fraction of patients with an ICD receive appropriate therapy. ICD implantation is expensive, with a relatively high cost per life-year saved [64]. Additionally, inappropriate ICD shocks are associated with a poor outcome [65]. These observations underscore the need for more selective criteria than LV ejection fraction for ICD implantation. Among patients with ischemic and

nonischemic cardiomyopathy and a primary prevention ICD, a greater severity of dyssynchrony by phase analysis of gated SPECT was associated with a greater occurrence of death and ICD shocks [66]. Similarly, among patients with biventricular pacemakers, a combination of lower LV ejection fraction, greater burden of myocardial scar, and a greater severity of dyssynchrony were associated with ventricular tachyarrhythmia [67]. These observational studies suggest that the genesis of ventricular tachyarrhythmia in HF is a complex process with an interplay of numerous factors, and that LV ejection fraction is a poor surrogate of arrhythmogenic myocardial substrate.

The interaction between dyssynchrony and myocardial substrate in predicting ventricular tachyarrhythmia has been recently reported in a population with primary prevention ICD. In 183 patients with ischemic and nonischemic cardiomyopathy, dyssynchrony was determined from by gated SPECT performed prior to ICD implantation [3], and was noted to be present in majority of the patients, with LV scar burden being the only independent predictor of dyssynchrony. Over an average follow-up of 12 months, ventricular tachyarrhythmia occurred in 48 patients (26%). Ninety-eight percent of patients who experienced VT had dyssynchrony prior to ICD implantation. Only one patient without dyssynchrony experienced VT (negative predictive value of 98%). The presence of LV dyssynchrony and a scar burden of >6% of the LV myocardium predicted ventricular tachyarrhythmia in 83% of the patients, and thus identified patients at the highest risk of ventricular tachyarrhythmia. On the contrary, lack of dyssynchrony was associated with an excellent prognosis, free of ventricular tachyarrhythmia, and thus identified HF patients with reduced ejection fraction at the lowest risk of an arrhythmic event. A diagrammatic representation of the interplay between dyssynchrony and arrhythmogenic myocardial substrate is shown in Fig. 6.6. Among patients with biventricular pacemakers (n = 43), in whom gated SPECT was performed both before and immediately after activation of biventricular pacing [3, 56], complete amelioration of dyssynchrony with CRT was associated with the absence of any ventricular arrhythmia on follow-up (Fig. 6.7). Persistent or new LVD after CRT are associated with similar rates of ventricular tachyarrhythmia after CRT (Fig. 6.7). It is likely that CRT exerts its antiarrhythmic effects by reducing dyssynchrony, which is supported by similar observations from clinical trials [68]. Contrary to this benefit, CRT may also induce dyssynchrony in previously "synchronous" ventricles and make them prone to ventricular tachyarrhythmia. The potential adverse effect of CRT has also been reported in patients undergoing an upgrade from an ICD to a biventricular pacemaker/ICD [69]. A greater frequency of sustained ventricular tachyarrhythmia (16% vs. 7%), non-sustained ventricular tachyarrhythmia VT (59% vs. 2.3%), and ventricular fibrillation (25% vs. 5%) were reported following CRT despite an improvement in left ventricular EF, though presence or resolution of LVD was not studied. These findings collectively suggest a critical role of dyssynchrony in arrhythmogenesis, and its utility in guiding ICD therapy. Furthermore, these observational studies provide consistent evidence that presence of dyssynchrony is probably essential for benefit from CRT and, that CRT can also result in worsening outcomes, possibly via induction of LVD.

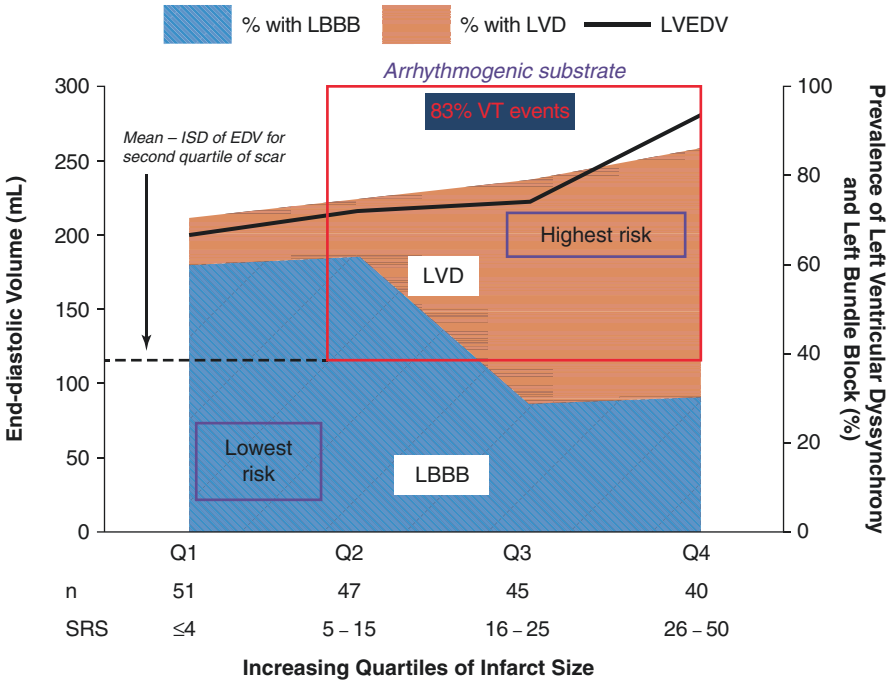

Fig. 6.6 A schematic representation of the interplay of myocardial dyssynchrony, scar and left ventricular remodeling in the generation of ventricular tachyarrhythmia. (Reproduced from Malhotra S, Pasupula DK, Sharma RK et al. Relationship between Left Ventricular Dyssynchrony and Scar burden in the Genesis of Ventricular Tachyarrhythmia. Journal of Nuclear Cardiology. 2017; with permission) [3]

6.4 Value of Dyssynchrony in Ischemic Heart Disease

Reports have suggested diagnostic and prognostic value of LVD in coronary artery disease (CAD). A retrospective study of patients with CAD reported that electrical and mechanical LVD (by phase analysis) by gated SPECT provides incremental prognostic value for all-cause mortality and cardiac death which was additive to assessment by LV ejection fraction alone [70]. In another study of 1310 patients with CAD (at least one vessel stenosis ≥50%), both systolic and diastolic LVD was measured by phase analysis of gated SPECT, and both were noted to be present in approximately 18% of the population [71]. Both systolic and diastolic LVD were associated with increased cardiovascular mortality, and diastolic LVD was noted to provide incremental predictive value to clinical history, electrical dyssynchrony, and left ventricular function. In a Tl-201 based dipyridamole-stress and 4-h rest/redistribution study, LVD was reported to be significantly greater with stress imaging among patients with ischemia [72]. There was a significant improvement in synchrony on the post-stress image (synchrony reserve) in patients with a normal perfusion and those with infarcted myocardium without significant ischemia despite

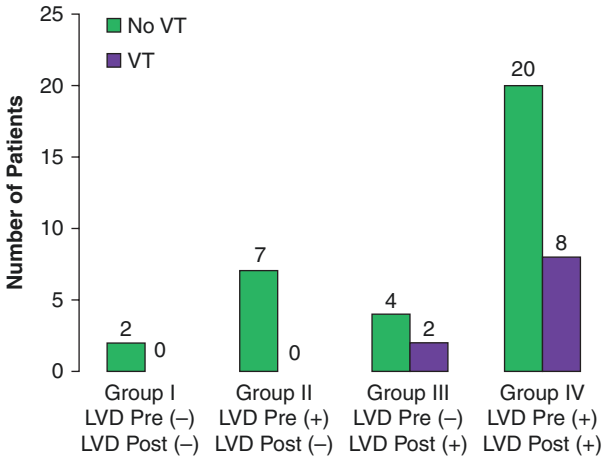

Fig. 6.7 Relationship between ventricular tachyarrhythmia and acute change in dyssynchrony after biventricular pacing. *VT* ventricular tachyarrhythmia, *LVD* left ventricular dyssynchrony, *Pre* before activation of cardiac resynchronization device, *Post* after activation of cardiac resynchronization device. (Reproduced from Malhotra S, Pasupula DK, Sharma RK et al. Relationship between Left Ventricular Dyssynchrony and Scar burden in the Genesis of Ventricular Tachyarrhythmia. Journal of Nuclear Cardiology. 2017; with permission) [3]

a much greater degree of resting LVD. Early post-stress LVD has also been noted to correctly identify patients with multi-vessel coronary artery disease [73]. In a retrospective study of 144 patients who underwent stress/rest Tl-2101 SPECT, patients with multi-vessel CAD on angiography had significantly more global dyssynchrony than the patients with <70% coronary stenosis. Additionally, patients with multi-vessel CAD showed significantly more global and territorial dyssynchrony on stress images than on rest. A combination of visual assessment and dyssynchrony allowed for more patients with 3-vessel CAD to be correctly classified as having multi-vessel disease. In a PET based study of patients with ischemic cardiomyopathy and low EF, changes in LVD between rest and vasodilator stress were identified using Rubidium-82 PET [74]. Among normally perfused ventricles, LVD decreased following stress (improvement in synchrony), while development of ischemia with stress resulted in an increase in LVD and was associated with all-cause mortality. Change in LVD with vasodilator stress was further studied in a population of 195 patients with largely preserved EF, undergoing Rubidium-82 PET for assessment of coronary artery disease [75]. Rest and stress myocardial blood flow (MBF) was calculated, along with MBF heterogeneity, which was determined as the ratio of the standard deviation of segmental MBF values to the average MBF value from 14 of the standard LV segments. A large proportion of patients with LVD at rest continued to remain dyssynchrony with stress. However, there was a reduction in LVD after stress in a small proportion of patients who had significantly higher coronary flow reserve, stress MBF and a lower coronary vascular resistance when compared to those who continued to have LVD after stress (Fig. 6.8). This study also reported a

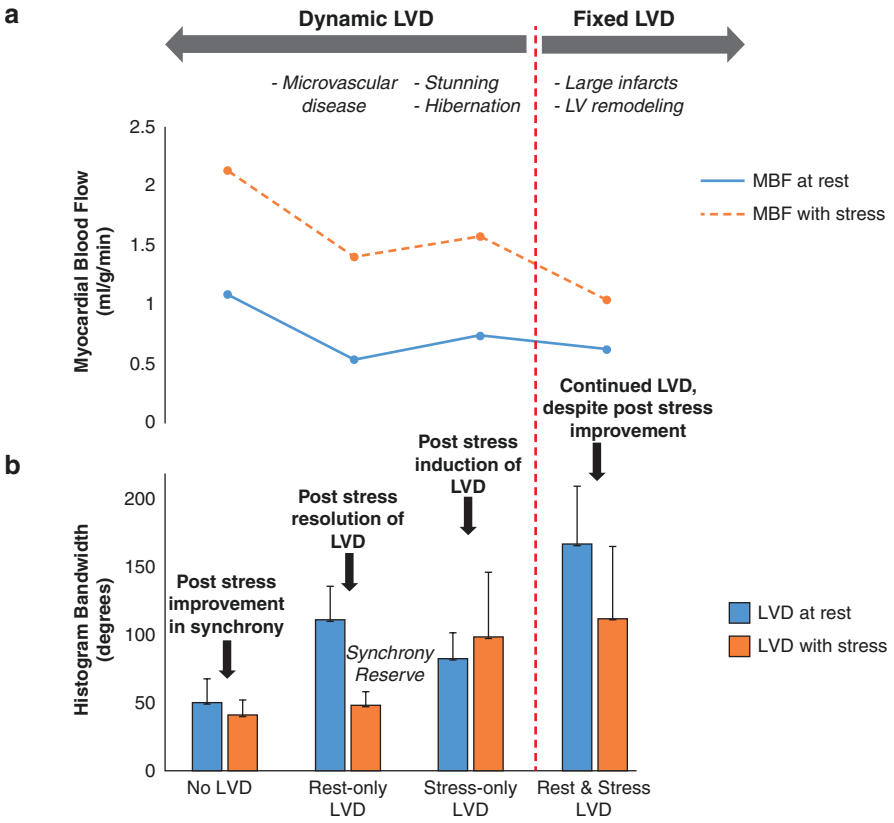

Fig. 6.8 Relationship between left ventricular dyssynchrony (LVD) and myocardial blood flow (MBF). Representation of the continuum of LVD and its relation to MBF in a population with coronary artery disease. Values of histogram bandwidth (HBW) and MBF are taken from Van Tosh et al. [88]. The population is stratified by the presence of LVD at rest or with stress. MBF (**a**) and histogram bandwidth (HBW) (**b**) data are graphed across LVD. "Synchrony reserve" applies to reduction in LVD after stress among patients with baseline LVD, that could result in complete resolution of LVD in a subset of the population. Abnormally high HBW characterizes patients with fixed LVD, despite improvement in HBW after stress. (Reproduced from Malhotra S and Canty JM, Jr. Vasodilator stress and left ventricular asynchrony. J Nucl Cardiol 2017;24:53–6; with permission) [76]

strong relationship between a stress-induced reduction in MBF heterogeneity with improvement in LVD (receiver operating characteristic area under the curve = 84%). This reduction in LVD with stress raises the possibility of a "synchrony reserve," [76] that could explain the improvement in ejection fraction (EF reserve) with vasodilator stress [77]. The association between LVD and ischemia is further substantiated by studies reporting improvement in LVD indices with anti-ischemia therapy. In a retrospective study of 230 patients who underwent serial rest/stress myocardial

perfusion SPECT before and after coronary revascularization, there was a significant reduction in LVD indices after revascularization [78] (Fig. 6.9). In addition, there was a trend toward greater improvement in synchrony among those with greater ischemic burden (≥10% vs. <10% ischemic myocardium). Improvement in LVD with medical antianginal therapy was reported in a prospective study of 32 patients with reversible perfusion defects on myocardial perfusion SPECT [79]. Serial phase analysis from gated SPECT before and 4-weeks after ranolazine therapy showed a significant reduction in all LVD indices, suggesting improvement in ventricular synchrony with medical therapy for myocardial ischemia. It is worth investigating whether the improvement in synchrony that occurs as a result of ischemia resolution also results in improved outcomes.

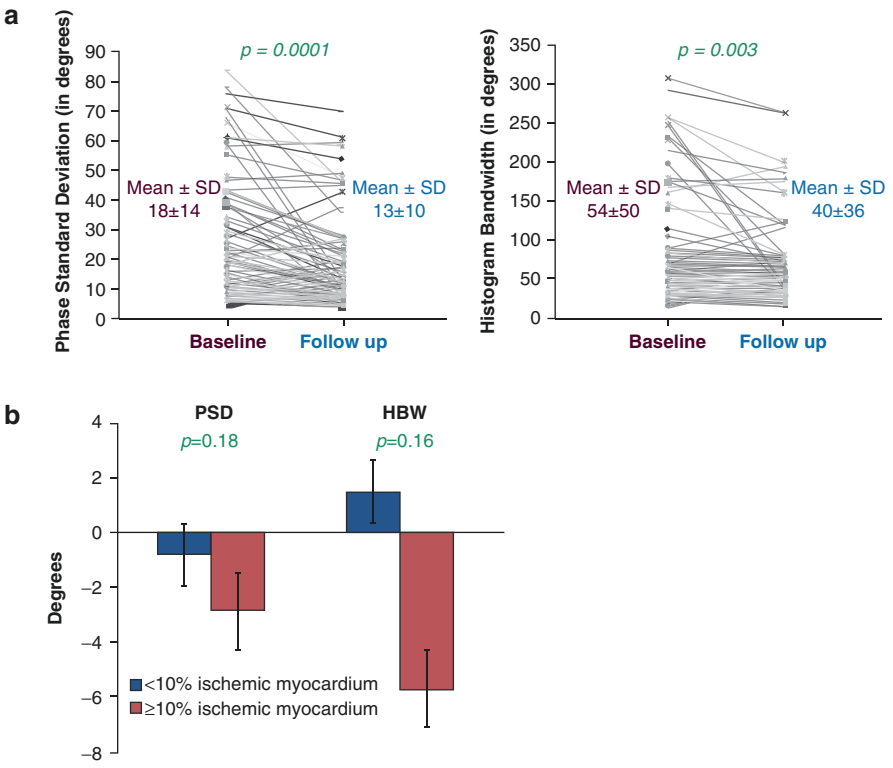

Fig. 6.9 Relationship between left ventricular dyssynchrony and myocardial ischemia. (**a**) Change in left ventricular dyssynchrony indices after revascularization in patients undergoing serial gated SPECT. (**b**) Magnitude of reduction in left ventricular dyssynchrony indices after revascularization in patients undergoing serial gated SPECT, stratified by burden of myocardial ischemia. *PSD* phase standard deviation, *HBW* histogram bandwidth. (Reproduced from Malhotra S, Pasupula D, Sharma R et al. Relationship between myocardial ischemia and left ventricular dyssynchrony on serial SPECT. American Society of Nuclear Cardiology, 18th Annual Scientific Session Chicago, IL.; 2013. p. 657–97; with permission) [78]

6.5 Technical Considerations in the Assessment of Dyssynchrony by SPECT

In single center settings, phase analysis of gated SPECT is a reproducible technique for assessment of dyssynchrony [80]. However the reproducibility of SPECT-derived dyssynchrony measurements have not been tested in a multi-center setting. Echocardiography-based measures of dyssynchrony have been found to be poorly reproducible in a muti-center trial [81]. One has to be mindful of certain technical and software considerations that may result in erroneous measures of dyssynchrony and adversely affect clinical decision making. Determination of dyssynchrony by phase analysis relies on assessment of the timing of contraction or relaxation of the myocardium. Gating artifacts have been shown to affect the assessment of myocardial thickening [82, 83]. Since phase analysis uses count density as a surrogate of myocardial thickening, gating errors can confound the measurement of dyssynchrony. Atrial arrhythmia or frequent premature ventricular beats offset the gating of tomographic images that use the R-wave on the ECG to determine the beginning of a cardiac cycle. This results in a count drop off in the "diastolic" frames of the cardiac cycle and has been shown to spuriously reduce the severity of dyssynchrony [84], which is more pronounced with a greater severity of gating artifact (Fig. 6.10). This is clinically relevant since patients in whom assessment of dyssynchrony is desired (HF and low EF) often suffer from arrhythmia. In such patients with a high likelihood of dyssynchronous LV contraction, phase analysis may label inherently dyssynchronous ventricles as being non-dyssynchronous. While the use of a narrow beat-acceptance window could minimize gating artifact, there will be a significant increase in the imaging time that could impact laboratory throughput. List-mode image acquisition can allow for gating correction and potentially reduce gating artifacts. Furthermore, there is significant discordance in indices of dyssynchrony determined by different SPECT processing software. These differences were recently studied by Nakajima et al. among 69 (36 male and 33 female) normal subjects, without any perfusion defects or regional wall motion abnormalities [15, 24]. SPECT perfusion images were processed using Emory Cardiac Toolbox, Quantitative Gated SPECT, Heart Function View (HFV) and cardioREPO (cREPO) software, using standard software settings, and measures of volume, function, and dyssynchrony were determined from each of the software. Statistically significant differences were noted for the phase analysis parameters, with ECTb and cREPO software reporting the highest PSD and HBW (Fig. 6.11). Statistically significant, though weak, correlations were observed between the phase analysis values from different software – PSD only significantly correlated between cREPO and HFV ($r = 0.36$, $p = 0.003$) and, HBW correlated between ECTb-cREPO ($r = 0.38$, $p = 0.001$) and cREPO-HFV ($r = 0.33$, $p = 0.006$). PSD values positively correlated with EDV (coefficient range for PSD: 0.12–0.37), and both PSD (correlation coefficient range: −0.24 to −0.53) and HBW (−0.46 to −0.55, only for QGS and HFV, respectively) negatively correlated with LVEF. These differences likely stem from the software specific techniques for delineating LV boundaries, that vary among different software, and can be considered similar to the differences noted in the measures of left ventricular volumes and function [85]. There are additional differences in how software programs perform phase parameters. Quantitative Gated SPECT (Cedars Sinai, Los Angeles, CA)

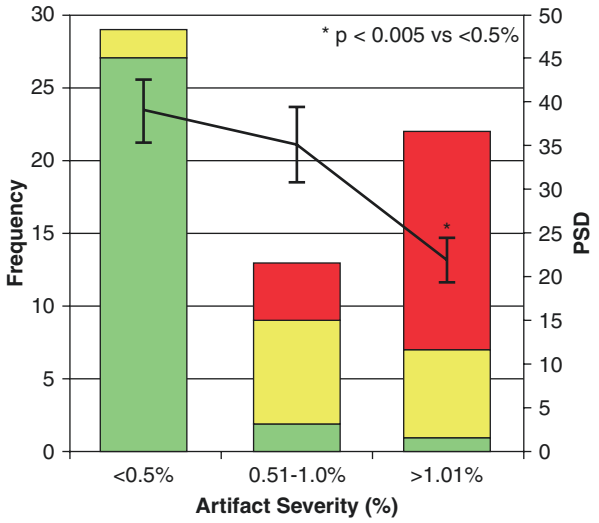

Fig. 6.10 Prevalence and influence of gating error on phase standard deviation (PSD). Bars represent frequency of gating error at each level of severity. Each bar is stratified by Emory Cardiac Toolbox's report of gating error (green, none or minor; yellow, moderate; and red, severe). Overlain is PSD for each group (mean ± SE). (Reproduced from Ludwig DR, Friehling M, Schwartzman D, et al. On the Importance of Image Gating for the Assay of Left Ventricular Mechanical Dyssynchrony Using SPECT. J Nucl Med 2012;53:1892–6; with permission) [84]

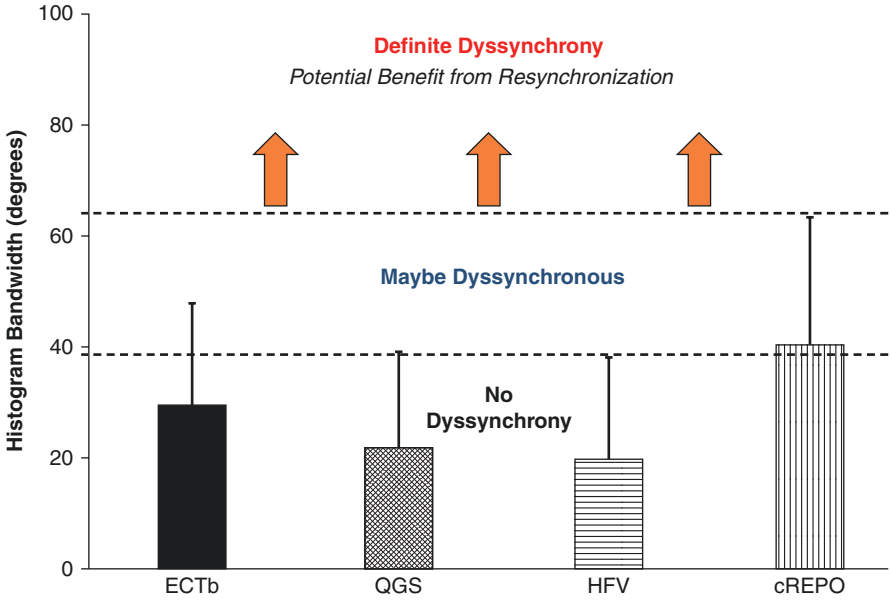

Fig. 6.11 Histogram bandwidth values from gated myocardial perfusion SPECT obtained from four different software. *ECTb* Emory Cardiac Toolbox, *QGS* Quantitative Gated SPECT, *HFV* Heart Function View, *cREPO* cardioREPO. (Adapted from Malhotra S and Soman P. Software-dependent processing variability in SPECT functional parameters: Clinical implications. J Nucl Cardiol 2017 Apr;24 (2):622–624; with permission) [89]

excludes myocardial regions with the lowest 5% of phase amplitude in the derivation of the phase bandwidth [4], and therefore can be expected to produce values of phase bandwidth that are different from Emory Cardiac Toolbox [86, 87]. Due to these software specific differences in assessment of dyssynchrony, software specific cut-offs should be utilized when identifying the presence or absence of dyssynchrony, and the same software be used when performing serial evaluations.

References

1. Leclercq C, Faris O, Tunin R, et al. Systolic improvement and mechanical resynchronization does not require electrical synchrony in the dilated failing heart with left bundle-branch block. Circulation. 2002;106:1760–3.
2. Nelson GS, Curry CW, Wyman BT, et al. Predictors of systolic augmentation from left ventricular preexcitation in patients with dilated cardiomyopathy and intraventricular conduction delay. Circulation. 2000;101:2703–9.
3. Malhotra S, Pasupula D, Sharma R, Saba S, Soman P. Relationship between left ventricular dyssynchrony and scar burden in the genesis of ventricular tachyarrhythmia. J Nucl Cardiol. 2018;25(2):555–69.
4. Sillanmaki S, Lipponen JA, Tarvainen MP, et al. Relationships between electrical and mechanical dyssynchrony in patients with left bundle branch block and healthy controls. J Nucl Cardiol. 2019;26:1228–39.
5. Wang C, Tang H, Zhu F, et al. Prognostic value of left-ventricular systolic and diastolic dyssynchrony measured from gated SPECT MPI in patients with dilated cardiomyopathy. J Nucl Cardiol. 2020;27(5):1582–91.
6. Fauchier L, Marie O, Casset-Senon D, Babuty D, Cosnay P, Fauchier JP. Interventricular and intraventricular dyssynchrony in idiopathic dilated cardiomyopathy: a prognostic study with Fourier phase analysis of radionuclide angioscintigraphy. J Am Coll Cardiol. 2002;40:2022–30.
7. Uebleis C, Hellweger S, Laubender RP, et al. Left ventricular dyssynchrony assessed by gated SPECT phase analysis is an independent predictor of death in patients with advanced coronary artery disease and reduced left ventricular function not undergoing cardiac resynchronization therapy. Eur J Nucl Med Mol Imaging. 2012;39:1561–9.
8. Hawkins NM, Petrie MC, MacDonald MR, Hogg KJ, McMurray JJ. Selecting patients for cardiac resynchronization therapy: electrical or mechanical dyssynchrony? Eur Heart J. 2006;27:1270–81.
9. Nagueh SF. Mechanical dyssynchrony in congestive heart failure: diagnostic and therapeutic implications. J Am Coll Cardiol. 2008;51:18–22.
10. van der Land V, Germans T, van Dijk J, et al. The effect of left bundle branch block on left ventricular remodeling, dyssynchrony and deformation of the mitral valve apparatus: an observational cardiovascular magnetic resonance imaging study. Int J Cardiovasc Imaging. 2007;23:529–36.
11. Gimelli A, Liga R, Menichetti F, Soldati E, Bongiorni MG, Marzullo P. Interactions between myocardial sympathetic denervation and left ventricular mechanical dyssynchrony: a CZT analysis. J Nucl Cardiol. 2019;26(2):509–18.
12. Galt JR, Garcia EV, Robbins WL. Effects of myocardial wall thickness on SPECT quantification. IEEE Trans Med Imaging. 1990;9:144–50.
13. Soman P, Chen J. Left ventricular dyssynchrony assessment using myocardial single-photon emission CT. Semin Nucl Med. 2014;44:314–9.
14. Chen J, Boogers MJ, Bax JJ, Soman P, Garcia EV. The use of nuclear imaging for cardiac resynchronization therapy. Curr Cardiol Rep. 2010;12:185–91.

15. Nakajima K, Okuda K, Matsuo S, Kiso K, Kinuya S, Garcia EV. Comparison of phase dyssynchrony analysis using gated myocardial perfusion imaging with four software programs: based on the Japanese Society of Nuclear Medicine working group normal database. J Nucl Cardiol. 2017;24:611–21.
16. Henneman MM, Chen J, Ypenburg C, et al. Phase analysis of gated myocardial perfusion single-photon emission computed tomography compared with tissue Doppler imaging for the assessment of left ventricular dyssynchrony. J Am Coll Cardiol. 2007;49:1708–14.
17. Boogers MM, Van Kriekinge SD, Henneman MM, et al. Quantitative gated SPECT-derived phase analysis on gated myocardial perfusion SPECT detects left ventricular dyssynchrony and predicts response to cardiac resynchronization therapy. J Nucl Med. 2009;50:718–25.
18. Marsan NA, Henneman MM, Chen J, et al. Real-time three-dimensional echocardiography as a novel approach to quantify left ventricular dyssynchrony: a comparison study with phase analysis of gated myocardial perfusion single photon emission computed tomography. J Am Soc Echocardiogr. 2008;21:801–7.
19. Marsan NA, Henneman MM, Chen J, et al. Left ventricular dyssynchrony assessed by two three-dimensional imaging modalities: phase analysis of gated myocardial perfusion SPECT and tri-plane tissue Doppler imaging. Eur J Nucl Med Mol Imaging. 2008;35:166–73.
20. Hsu TH, Huang WS, Chen CC, et al. Left ventricular systolic and diastolic dyssynchrony assessed by phase analysis of gated SPECT myocardial perfusion imaging: a comparison with speckle tracking echocardiography. Ann Nucl Med. 2013;27:764–71.
21. Germano G, Kavanagh PB, Slomka PJ, Van Kriekinge SD, Pollard G, Berman DS. Quantitation in gated perfusion SPECT imaging: the Cedars-Sinai approach. J Nucl Cardiol. 2007;14:433–54.
22. Ficaro EP, Lee BC, Kritzman JN, Corbett JR. Corridor4DM: the Michigan method for quantitative nuclear cardiology. J Nucl Cardiol. 2007;14:455–65.
23. Garcia EV, Faber TL, Cooke CD, Folks RD, Chen J, Santana C. The increasing role of quantification in clinical nuclear cardiology: the Emory approach. J Nucl Cardiol. 2007;14:420–32.
24. Okuda K, Nakajima K, Matsuo S, et al. Comparison of diagnostic performance of four software packages for phase dyssynchrony analysis in gated myocardial perfusion SPECT. EJNMMI Res. 2017;7:27.
25. Lin X, Xu H, Zhao X, Chen J. Sites of latest mechanical activation as assessed by SPECT myocardial perfusion imaging in ischemic and dilated cardiomyopathy patients with LBBB. Eur J Nucl Med Mol Imaging. 2014;41:1232–9.
26. van der Veen BJ, Al Younis I, Ajmone-Marsan N, et al. Ventricular dyssynchrony assessed by gated myocardial perfusion SPECT using a geometrical approach: a feasibility study. Eur J Nucl Med Mol Imaging. 2012;39:421–9.
27. Bader H, Garrigue S, Lafitte S, et al. Intra-left ventricular electromechanical asynchrony. A new independent predictor of severe cardiac events in heart failure patients. J Am Coll Cardiol. 2004;43:248–56.
28. Cho GY, Song JK, Park WJ, et al. Mechanical dyssynchrony assessed by tissue Doppler imaging is a powerful predictor of mortality in congestive heart failure with normal QRS duration. J Am Coll Cardiol. 2005;46:2237–43.
29. Fauchier L, Marie O, Casset-Senon D, Babuty D, Cosnay P, Fauchier JP. Ventricular dyssynchrony and risk markers of ventricular arrhythmias in nonischemic dilated cardiomyopathy: a study with phase analysis of angioscintigraphy. Pacing Clin Electrophysiol. 2003;26:352–6.
30. Nelson GS, Berger RD, Fetics BJ, et al. Left ventricular or biventricular pacing improves cardiac function at diminished energy cost in patients with dilated cardiomyopathy and left bundle-branch block. Circulation. 2000;102:3053–9.
31. Ukkonen H, Beanlands RS, Burwash IG, et al. Effect of cardiac resynchronization on myocardial efficiency and regional oxidative metabolism. Circulation. 2003;107:28–31.
32. Kyriacou A, Whinnett ZI, Sen S, et al. Improvement in coronary blood flow velocity with acute biventricular pacing is predominantly due to an increase in a diastolic backward-travelling decompression (suction) wave. Circulation. 2012;126:1334–44.
33. van Bommel RJ, Marsan NA, Delgado V, et al. Cardiac resynchronization therapy as a therapeutic option in patients with moderate-severe functional mitral regurgitation and high operative risk. Circulation. 2011;124:912–9.

34. Sutton MG, Plappert T, Hilpisch KE, Abraham WT, Hayes DL, Chinchoy E. Sustained reverse left ventricular structural remodeling with cardiac resynchronization at one year is a function of etiology: quantitative Doppler echocardiographic evidence from the Multicenter InSync Randomized Clinical Evaluation (MIRACLE). Circulation. 2006;113:266–72.
35. Bristow MR, Saxon LA, Boehmer J, et al. Cardiac-resynchronization therapy with or without an implantable defibrillator in advanced chronic heart failure. N Engl J Med. 2004; 350:2140–50.
36. Cleland JGF, Daubert JC, Erdmann E, et al. For the Cardiac Resynchronization-Heart Failure (Care-HF) Study Investigators. The effect of cardiac resynchronization on morbidity and mortality in heart failure. N Engl J Med. 2005;352:1539–49.
37. Gorcsan J 3rd, Oyenuga O, Habib PJ, et al. Relationship of echocardiographic dyssynchrony to long-term survival after cardiac resynchronization therapy. Circulation. 2010;122: 1910–8.
38. Chalil S, Stegemann B, Muhyaldeen S, et al. Intraventricular dyssynchrony predicts mortality and morbidity after cardiac resynchronization therapy: a study using cardiovascular magnetic resonance tissue synchronization imaging. J Am Coll Cardiol. 2007;50:243–52.
39. Abraham WT, Fisher WG, Smith AL, et al. Cardiac resynchronization in chronic heart failure. N Engl J Med. 2002;346:1845–53.
40. Zareba W, Klein H, Cygankiewicz I, et al. Effectiveness of cardiac resynchronization therapy by QRS morphology in the Multicenter Automatic Defibrillator Implantation Trial-Cardiac Resynchronization Therapy (MADIT-CRT). Circulation. 2011;123:1061–72.
41. Yu CM, Bleeker GB, Fung JW, et al. Left ventricular reverse remodeling but not clinical improvement predicts long-term survival after cardiac resynchronization therapy. Circulation. 2005;112:1580–6.
42. Mollema SA, Bleeker GB, van der Wall EE, Schalij MJ, Bax JJ. Usefulness of QRS duration to predict response to cardiac resynchronization therapy in patients with end-stage heart failure. Am J Cardiol. 2007;100:1665–70.
43. Bax JJ, Bleeker GB, Marwick TH, et al. Left ventricular dyssynchrony predicts response and prognosis after cardiac resynchronization therapy. J Am Coll Cardiol. 2004;44:1834–40.
44. Manchanda M, McLeod CJ, Killu A, Asirvatham SJ. Cardiac resynchronization therapy for patients with congenital heart disease: technical challenges. J Interv Card Electrophysiol. 2013;36:71–9.
45. Adelstein EC, Saba S. Scar burden by myocardial perfusion imaging predicts echocardiographic response to cardiac resynchronization therapy in ischemic cardiomyopathy. Am Heart J. 2007;153:105–12.
46. Ypenburg C, Schalij MJ, Bleeker GB, et al. Impact of viability and scar tissue on response to cardiac resynchronization therapy in ischaemic heart failure patients. Eur Heart J. 2007;28:33–41.
47. Bose A, Kandala J, Upadhyay GA, et al. Impact of myocardial viability and left ventricular lead location on clinical outcome in cardiac resynchronization therapy recipients with ischemic cardiomyopathy. J Cardiovasc Electrophysiol. 2014;25:507–13.
48. Adelstein EC, Tanaka H, Soman P, et al. Impact of scar burden by single-photon emission computed tomography myocardial perfusion imaging on patient outcomes following cardiac resynchronization therapy. Eur Heart J. 2011;32:93–103.
49. Boogers MJ, Chen J, van Bommel RJ, et al. Optimal left ventricular lead position assessed with phase analysis on gated myocardial perfusion SPECT. Eur J Nucl Med Mol Imaging. 2011;38:230–8.
50. Hung GU, Huang JL, Lin WY, et al. Impact of right-ventricular apical pacing on the optimal left-ventricular lead positions measured by phase analysis of SPECT myocardial perfusion imaging. Eur J Nucl Med Mol Imaging. 2014;41:1224–31.
51. Azizian N, Rastgou F, Ghaedian T, et al. LV dyssynchrony assessed with phase analysis on gated myocardial perfusion SPECT can predict response to CRT in patients with end-stage heart failure. Res Cardiovasc Med. 2014;3:e20720.
52. Tracy CM, Epstein AE, Darbar D, et al. 2012 ACCF/AHA/HRS focused update of the 2008 guidelines for device-based therapy of cardiac rhythm abnormalities: a report of the American College of Cardiology Foundation/American Heart Association Task Force on Practice Guidelines. J Am Coll Cardiol. 2012;60:1297–313.

53. Malhotra S, Pasupula D, Khanna M, Soman P. Is left bundle branch block related to the mechanism of left ventricular dyssynchrony? Washington, DC: American College of Cardiology Annual Scientific Sessions; 2014.
54. Adelstein E, Alam MB, Schwartzman D, et al. Effect of echocardiography-guided left ventricular lead placement for cardiac resynchronization therapy on mortality and risk of defibrillator therapy for ventricular arrhythmias in heart failure patients (from the Speckle Tracking Assisted Resynchronization Therapy for Electrode Region [STARTER] trial). Am J Cardiol. 2014;113:1518–22.
55. Zhou W, Hou X, Piccinelli M, et al. 3D fusion of LV venous anatomy on fluoroscopy venograms with epicardial surface on SPECT myocardial perfusion images for guiding CRT LV lead placement. JACC Cardiovasc Imaging. 2014;7:1239–48.
56. Friehling M, Chen J, Saba S, et al. A prospective pilot study to evaluate the relationship between acute change in left ventricular synchrony after cardiac resynchronization therapy and patient outcome using a single-injection gated SPECT protocol. Circ Cardiovasc Imaging. 2011;4:532–9.
57. Seo Y, Ishizu T, Kawamura R, et al. Three-dimensional propagation imaging of left ventricular activation by speckle-tracking echocardiography to predict responses to cardiac resynchronization therapy. J Am Soc Echocardiogr. 2015;28:606–14.
58. Tao N, Qiu Y, Tang H, et al. Assessment of left ventricular contraction patterns using gated SPECT MPI to predict cardiac resynchronization therapy response. J Nucl Cardiol. 2018;25:2029–38.
59. Jackson T, Sohal M, Chen Z, et al. A U-shaped type II contraction pattern in patients with strict left bundle branch block predicts super-response to cardiac resynchronization therapy. Heart Rhythm. 2014;11:1790–7.
60. Moss AJ, Zareba W, Hall WJ, et al. Prophylactic implantation of a defibrillator in patients with myocardial infarction and reduced ejection fraction. N Engl J Med. 2002;346:877–83.
61. Bardy GH, Lee KL, Mark DB, et al. Amiodarone or an implantable cardioverter-defibrillator for congestive heart failure. N Engl J Med. 2005;352:225–37.
62. Weeke P, Johansen JB, Jorgensen OD, et al. Mortality and appropriate and inappropriate therapy in patients with ischaemic heart disease and implanted cardioverter-defibrillators for primary prevention: data from the Danish ICD Register. Europace. 2013;15(8):1150–7.
63. MacFadden DR, Crystal E, Krahn AD, et al. Sex differences in implantable cardioverter-defibrillator outcomes: findings from a prospective defibrillator database. Ann Intern Med. 2012;156:195–203.
64. Zwanziger J, Hall WJ, Dick AW, et al. The cost effectiveness of implantable cardioverter-defibrillators: results from the Multicenter Automatic Defibrillator Implantation Trial (MADIT)-II. J Am Coll Cardiol. 2006;47:2310–8.
65. Daubert JP, Zareba W, Cannom DS, et al. Inappropriate implantable cardioverter-defibrillator shocks in MADIT II: frequency, mechanisms, predictors, and survival impact. J Am Coll Cardiol. 2008;51:1357–65.
66. Aljaroudi WA, Hage FG, Hermann D, et al. Relation of left-ventricular dyssynchrony by phase analysis of gated SPECT images and cardiovascular events in patients with implantable cardiac defibrillators. J Nucl Cardiol. 2010;17:398–404.
67. Hou PN, Tsai SC, Lin WY, et al. Relationship of quantitative parameters of myocardial perfusion SPECT and ventricular arrhythmia in patients receiving cardiac resynchronization therapy. Ann Nucl Med. 2015;29:772–8.
68. Kutyifa V, Pouleur AC, Knappe D, et al. Dyssynchrony and the risk of ventricular arrhythmias. JACC Cardiovasc Imaging. 2013;6:432–44.
69. Lin G, Rea RF, Hammill SC, Hayes DL, Brady PA. Effect of cardiac resynchronisation therapy on occurrence of ventricular arrhythmia in patients with implantable cardioverter defibrillators undergoing upgrade to cardiac resynchronisation therapy devices. Heart. 2008;94:186–90.
70. Hess PL, Shaw LK, Fudim M, Iskandrian AE, Borges-Neto S. The prognostic value of mechanical left ventricular dyssynchrony defined by phase analysis from gated single-photon emission computed tomography myocardial perfusion imaging among patients with coronary heart disease. J Nucl Cardiol. 2017;24:482–90.

71. Fudim M, Fathallah M, Shaw LK, et al. The prognostic value of diastolic and systolic mechanical left ventricular dyssynchrony among patients with coronary heart disease. JACC Cardiovasc Imaging. 2019;12:1215–26.
72. Chen CC, Shen TY, Chang MC, et al. Stress-induced myocardial ischemia is associated with early post-stress left ventricular mechanical dyssynchrony as assessed by phase analysis of 201Tl gated SPECT myocardial perfusion imaging. Eur J Nucl Med Mol Imaging. 2012;39:1904–9.
73. Huang WS, Huang CH, Lee CL, Chen CP, Hung GU, Chen J. Relation of early post-stress left ventricular dyssynchrony and the extent of angiographic coronary artery disease. J Nucl Cardiol. 2014;21:1048–56.
74. AlJaroudi W, Alraies MC, Menon V, Brunken RC, Cerqueira MD, Jaber WA. Predictors and incremental prognostic value of left ventricular mechanical dyssynchrony response during stress-gated positron emission tomography in patients with ischemic cardiomyopathy. J Nucl Cardiol. 2012;19:958–69.
75. Van Tosh A, Votaw JR, Cooke CD, Reichek N, Palestro CJ, Nichols KJ. Relationships between left ventricular asynchrony and myocardial blood flow. J Nucl Cardiol. 2017;24:43–52.
76. Malhotra S, Canty JM Jr. Vasodilator stress and left ventricular asynchrony. J Nucl Cardiol. 2017;24:53–6.
77. Dorbala S, Hachamovitch R, Curillova Z, et al. Incremental prognostic value of gated Rb-82 positron emission tomography myocardial perfusion imaging over clinical variables and rest LVEF. JACC Cardiovasc Imaging. 2009;2:846–54.
78. Malhotra S, Pasupula D, Sharma R, Khanna M, Soman P. Relationship between myocardial ischemia and left ventricular dyssynchrony on serial SPECT. American Society of Nuclear Cardiology, 18th Annual Scientific Session 2013, Chicago, IL. p. 657–97.
79. Venkataraman R, Chen J, Garcia EV, et al. Effect of ranolazine on left ventricular dyssynchrony in patients with coronary artery disease. Am J Cardiol. 2012;110:1440–5.
80. Trimble MA, Velazquez EJ, Adams GL, et al. Repeatability and reproducibility of phase analysis of gated single-photon emission computed tomography myocardial perfusion imaging used to quantify cardiac dyssynchrony. Nucl Med Commun. 2008;29:374–81.
81. Chung ES, Leon AR, Tavazzi L, et al. Results of the predictors of response to CRT (PROSPECT) trial. Circulation. 2008;117:2608–16.
82. Nichols K, Dorbala S, DePuey EG, Yao SS, Sharma A, Rozanski A. Influence of arrhythmias on gated SPECT myocardial perfusion and function quantification. J Nucl Med. 1999;40:924–34.
83. Nichols K, Yao SS, Kamran M, Faber TL, Cooke CD, DePuey EG. Clinical impact of arrhythmias on gated SPECT cardiac myocardial perfusion and function assessment. J Nucl Cardiol. 2001;8:19–30.
84. Ludwig DR, Friehling M, Schwartzman D, Saba S, Follansbee WP, Soman P. On the importance of image gating for the assay of left ventricular mechanical dyssynchrony using SPECT. J Nucl Med. 2012;53:1892–6.
85. Hambye AS, Vervaet A, Dobbeleir A. Variability of left ventricular ejection fraction and volumes with quantitative gated SPECT: influence of algorithm, pixel size and reconstruction parameters in small and normal-sized hearts. Eur J Nucl Med Mol Imaging. 2004;31:1606–13.
86. Chen J, Garcia EV, Folks RD, et al. Onset of left ventricular mechanical contraction as determined by phase analysis of ECG-gated myocardial perfusion SPECT imaging: development of a diagnostic tool for assessment of cardiac mechanical dyssynchrony. J Nucl Cardiol. 2005;12:687–95.
87. Van Kriekinge SD, Nishina H, Ohba M, Berman DS, Germano G. Automatic global and regional phase analysis from gated myocardial perfusion SPECT imaging: application to the characterization of ventricular contraction in patients with left bundle branch block. J Nucl Med. 2008;49:1790–7.
88. Van Tosh A, Votaw JR, Cooke CD, Reichek N, Palestro CJ, Nichols KJ. Relationships between left ventricular asynchrony and myocardial blood flow. J Nucl Cardiol. 2015;24(1):43–52.
89. Malhotra S, Soman P. Software-dependent processing variability in SPECT functional parameters: clinical implications. J Nucl Cardiol. 2017;24:622–4.

Novel Techniques: Solid-State Detectors, Dose Reduction (SPECT/CT)

7

Piotr J. Slomka, Robert J. H. Miller, Lien-Hsin Hu, and Daniel S. Berman

7.1 Introduction

Myocardial perfusion imaging (MPI) with single photon emission tomography (SPECT) is widely used for the diagnosis and management of patients with known or suspected coronary artery disease (CAD), providing crucial information regarding both myocardial perfusion and function. Since being introduced in the 1970s SPECT camera system designs have undergone several incremental improvements. More recently, however, there has been an evolutionary leap with dedicated cardiac SPECT camera systems which utilize solid-state crystals and novel collimator designs, such as multi-pinhole and locally focusing collimators configured specifically for cardiac imaging [1]. These innovations have facilitated dramatic reductions in both imaging time and radiation dose, while maintaining high diagnostic accuracy. These features are related to simultaneous improvement in sensitivity (five to eight times higher) [2, 3], (due to the collimator and imaging geometry) and

P. J. Slomka (✉) · D. S. Berman
Department of Imaging, Medicine, and Biomedical Sciences, Cedars-Sinai Medical Center, Los Angeles, CA, USA
e-mail: slomkap@cshs.org, Piotr.Slomka@cshs.org

R. J. H. Miller
Department of Imaging, Medicine, and Biomedical Sciences, Cedars-Sinai Medical Center, Los Angeles, CA, USA

Department of Cardiac Sciences, University of Calgary, Calgary, AB, Canada

L.-H. Hu
Department of Imaging, Medicine, and Biomedical Sciences, Cedars-Sinai Medical Center, Los Angeles, CA, USA

Department of Nuclear Medicine, Taipei Veterans General Hospital, Taipei, Taiwan

S. G. Nekolla, C. Rischpler (eds.), *Hybrid Cardiac Imaging*,
https://doi.org/10.1007/978-3-030-83167-7_7

image resolution (up to two times higher) [3], (due to the improved energy resolution of the new crystals). Additionally, the physical space requirements for solid-state camera systems have been significantly reduced because photomultiplier tubes are no longer required. New scanners can also be coupled with diagnostic quality CT systems-suitable for calcium scanning or coronary CT angiography. With the growing clinical experience using solid-state SPECT camera systems there is also emerging evidence demonstrating comparable or superior, diagnostic and prognostic utility.

This review summarizes the current solid-state SPECT and SPECT/CT technology and clinical applications, including emerging techniques for myocardial blood flow quantitation. We will also discuss imaging protocols, potential imaging pitfalls and review the validation efforts for this new technology regarding diagnosis and prognosis.

7.2 Technology

Several technologic advancements are responsible for the improved imaging characteristics of solid-state SPECT camera systems. No single change can be attributed to the significant improvements in both photon sensitivity and spatial resolution realized with these systems. This section will review these advances within the context of the overall camera system.

7.2.1 Solid-State Detectors

The radiation detectors are made of Cadmium-Zinc-Telluride (CZT) crystals which are more expensive than NaI(Tl) crystal detectors but have important imaging advantages. CZT detectors have improved energy response which reduces the scatter component of measured data by 30% [4], and superior intrinsic spatial resolution compared to conventional Anger cameras. Removing the need for photomultiplier tubes has resulted in more compact detector size which has facilitated more efficient camera designs with innovative imaging geometries and high-sensitivity collimation. Solid-state detectors can also be combined with scintillation crystals to indirectly detect photons. In these detectors, thallium-doped cesium iodide CsI(Tl) scintillation crystals are coupled with photodiodes (instead of photomultipliers) [5]. CsI(Tl) has superior spectral light response characteristics compared to NaI(Tl) when used with silicon photodiodes.

Solid-state detectors are integrated with innovative collimator designs which increase photon sensitivity in the myocardial region. The high-sensitivity characteristics of solid-state SPECT cameras are often mistakenly attributed to the CZT crystal. Although the density of CZT is higher than NaI(Tl) (5.8 vs. 3.7 g/cm^3), due to cost considerations CZT detectors are thinner (~5 mm) than typical NaI(Tl) crystals (9.5 mm), such that the intrinsic detection efficiency of these systems is comparable to conventional Anger detectors.

7.3 Dedicated Cardiac Systems

7.3.1 Detectors

CZT SPECT camera systems specifically designed for cardiac use are commercially available from two vendors. One system (Spectrum Dynamics, D-SPECT) uses pixelated CZT detector arrays. Nine vertical columns are arranged in a 90° gantry geometry. Each column consists of 1024 CZT elements (2.46 × 2.46 × 5 mm thick), arranged in a 16 × 64 element array with an overall size of 40 × 160 mm. Since CZT crystals are expensive, the vendor offers a system with six detector columns, creating a trade-off between cost and image quality. The other camera design (GE Healthcare, Discovery NM 530c) features a curved array of 19 CZT pixelated detector arrays coupled to pinhole collimators with geometry optimized for cardiac imaging. Each detector array consists of four detectors, each with 246 CZT detector elements (2.46 × 2.46 × 5 mm thick) arranged in 16 × 16 elements.

The indirect solid-state detector has been utilized in traditional 2- or 3-detector configurations (Digirad), allowing for a more compact design than conventional Anger cameras. Each detector head contains an array of 768 (6.1 × 6.1 × 6 mm thick) CsI(Tl) crystals coupled to individual silicon photodiodes that convert the crystal scintillations to electrical pulses, which are then processed digitally.

7.3.2 Dedicated Cardiac Collimators and Geometries

The improved sensitivity of solid-state SPECT cameras is achieved by novel collimator designs and dedicated cardiac imaging configurations. Increasing photon sensitivity is important since a conventional Anger cameras detect <0.01% of incoming photons [6]. Diagrams of these novel collimator technologies, for cardiac solid-state cameras and a general-purpose solid-state camera are shown in Fig. 7.1.

The D-SPECT features one small high-sensitivity tungsten collimator for each detector column (as described above). These collimators can be positioned close to the patient's body which increases the number of photons detected and improves spatial resolution. The collimators are square, parallel holes with dimensions of 2.26 × 2.26 mm and wall thickness of 0.2 mm matched to the dimensions of a single detector element. The hole dimensions are larger than conventional high-resolution collimators, resulting in higher sensitivity at the expense of image resolution. However, the loss in spatial resolution resulting from this design is more than compensated for by the use of pixelated CZT detectors and software-based resolution recovery [2]. During acquisition, each of the nine detectors is focused on the heart and rotates over 45°, with a rotation time of 3 s. Patients are positioned on a chair rather than on a bed, increasing patient comfort. Patients are typically imaged in both semi-supine and upright positions.

The Discovery NM 530/570c camera systems utilize pinhole collimation. The design includes 19 pinhole collimators with multiple focal depths and one hole (4.75 mm in diameter) in each collimator. The CZT detectors and

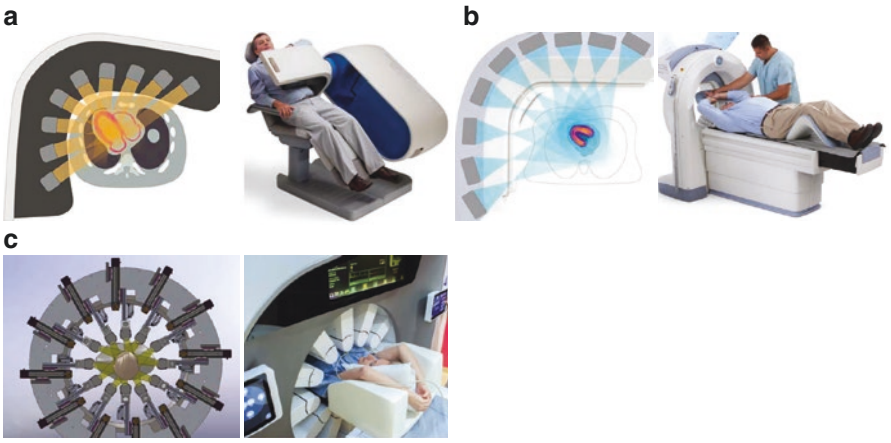

Fig. 7.1 Diagrams of three novel collimator designs used in solid-state camera systems. Panel (**a**) shows an example of high-sensitivity parallel collimators, as used in the D-SPECT camera system. The collimators are square with parallel holes, each coupled to a single detector. Panel (**b**) shows a multi-pinhole collimator design, as used in the Discovery NM 530c camera system. Panel (**c**) shows the collimator design of the new general-purpose Veriton for 3D body contouring. Images courtesy of Spectrum Dynamics and GE Healthcare

collimators do not move and photons are acquired simultaneously through all the pinholes. Simultaneously acquired pinhole views allow consistent tomographic sampling, reducing motion artifacts. Patients are typically imaged in both supine and prone positions, with their arms placed above their head. Higher sensitivity is achieved by the wider acceptance angle of photons with multi-pinhole collimation and the cardio-centric acquisition which limits photon detection to the myocardial region.

7.4 SPECT/CT

MPI can benefit from CT-based attenuation correction (CTAC) using either dedicated hybrid SPECT/CT systems or separate scanners, with many new systems offered in hybrid SPECT/CT configurations. Some systems offer basic CT capabilities with relatively slow rotating gantry CT systems—suitable only for AC of SPECT. However, an increasing number of scanners are equipped with more advanced CT components, capable of diagnostic quality cardiac imaging. In addition, it has been shown that separately acquired coronary artery calcium (CAC) scans can be used for AC of SPECT MPI studies [7]. The use of separately obtained CT for AC is supported by vendors for routine clinical use [8, 9]. CTAC using either separate systems [9] or hybrid SPECT/CT systems [10] can improve diagnostic accuracy of SPECT MPI compared to single-position non-corrected imaging.

SPECT/CT scanners provide new opportunity to enhance MPI data with additional CT information. Non-contrast CT can be used to quantify CAC, a specific

marker of coronary atherosclerosis. The CAC scan is simple to perform, low-cost, acquired without intravenous contrast, and associated with low radiation exposure [11–13]. To date, evidence has consistently shown that CAC predicts cardiovascular events beyond standard risk factors [14–26]. With complementary information regarding both ischemia (MPI) and atherosclerosis (CT), hybrid SPECT/CT imaging can outperform SPECT MPI alone. We have demonstrated the complementary role of CAC with PET and proposed a logistic-regression based score for PET + CAC, which increased the diagnostic performance [27, 28]. Additionally, several studies have shown that MPI and CAC provide an independent and complementary prediction of cardiac risk [29, 30, 31]. This widely available combination of MPI and CT provides a new opportunity to enhance MPI with additional diagnostic and prognostic information.

The scans performed for CTAC maps are acquired with a lower radiation dose than standard CAC scans and are obtained without ECG-gating. Nevertheless, it is possible to extract useful CAC information from these maps. We reported high agreement between visual estimation of calcium from CTAC and CAC scores from standard CAC scans in a multicenter study [32]. Protocols have also been proposed for modified CTAC acquisitions, optimized for quantification of CAC without increasing radiation dose [33]. Investigators at Yale University have demonstrated that visual identification of CAC on CTAC scans improves the diagnostic accuracy of SPECT/CT [34]. Although these reports are encouraging, logistically such additional assessments increase the overall complexity of SPECT MPI reporting and require additional expertise, which may not always be available. Software tools will be required which will automatically extract and integrate CTAC scan information, including CAC, with SPECT MPI results.

While CAC is a dominant parameter available from the non-contrast CT, there are additional markers of patient-specific cardiovascular conditions which have prognostic value [35, 36], and can potentially be assessed from CTAC scans. Epicardial fat tissue on non-contrast CT which can be measured in a fully automated fashion, as established, is one such additional CT marker [37]. Other potentially important cardiovascular markers include calcification of the thoracic aorta and heart valves [38], liver density [39], pulmonary artery dilatation and heart anatomy [40]. This information is currently not routinely utilized during cardiac SPECT/CT but could be part of a comprehensive assessment, enhancing the utility of SPECT/CT.

While functional testing with myocardial perfusion SPECT is well established, cardiac computed tomography angiography (CCTA) has emerged as a promising diagnostic and prognostic technique [41]. Hybrid SPECT/CT systems with 64-slice CT scanner systems are capable of obtaining both scans. CCTA-guided contour and vascular territory adjustment of SPECT MPI can improve quantitative diagnostic accuracy for left circumflex and right coronary artery lesions [42]. Similarly the diagnostic accuracy of visual analysis of SPECT MPI can improve by integrating CCTA data [43]. In addition, CCTA may help exclude hemodynamically significant CAD in patients with intermediate to high pretest likelihood of CAD or abnormal SPECT MPI [44]. Accurate registration of the data from SPECT and CCTA, even if

obtained on the same system, is complicated by the potential mismatch in cardiac image phase. However, image registration can be refined using an automated registration scheme, with correction for the cardiac phase disparities [45].

7.5 Solid-State SPECT/CT Systems

Hybrid SPECT/CT solid-state systems are not yet in widespread clinical use. Initially only multi-pinhole solid-state camera systems (GE 570c) were offered with a hybrid diagnostic CT configuration; however, there are only a few such systems operating worldwide. In the last 2 years, general-purpose solid-state SPECT cameras coupled with diagnostic quality CT scanners—capable of coronary calcium scoring—have been introduced by two vendors. While these systems are designed for general imaging use, they can also be used effectively for MPI. Spectrum Dynamics introduced the Veriton-CT system with 8 CZT modules within each of 12 detector blocks, each with individual detector arms with swivel motion, which allow precise and close 3D contouring around the patient during imaging. The field-of-view length is 320 mm and can be focused for single organ acquisitions or used for whole torso scanning. The optimized collimator design results in higher volumetric sensitivity (0.0192%) compared to dual-head camera systems with conventional collimators (<0.01%). Additionally, with image resolution recovery this system achieves high spatial resolution (4.3 mm). Initial clinical studies of the prototype design with detector design similar to Veriton demonstrate potential improvements in image quality compared to a conventional camera [46]. The Veriton-CT system is configured with up to 128-slice CT camera, allowing both calcium scoring and CT angiography studies. GE introduced a general-purpose solid-state camera, the Discovery NM/CT 870 CZT, equipped with conventional collimators. This camera system offers similar photon sensitivity to the conventional Anger system (as the collimation system is the same) but allows better energy resolution and image resolution due to the CZT detectors and has demonstrated improved image quality in early clinical implementation [46, 47].

7.6 Reconstruction Including Resolution Recovery and Anatomical Constraints

In parallel with improvements in technical aspects of SPECT scanner hardware, enhanced image reconstruction techniques have been implemented. New reconstruction algorithms include modeling of the collimators and detectors, as well as resolution recovery. Most systems compensate for spatial resolution losses by using iterative reconstruction. The aggressive resolution recovery is needed to compensate for the effects of high-sensitivity collimation, which reduces spatial resolution by accepting photons from a wider angle. Therefore, software modeling the collimator response during reconstruction is a critical component needed to achieve the simultaneous increase in spatial resolution and count sensitivity with the solid-state SPECT camera systems.

Further improvements in spatial resolution can be achieved by using iterative reconstruction with myocardial anatomical priors, which constrain the shape and thickness of myocardial walls to fit within an expected range. This approach can further improve image quality, especially for noisy images. However, if the actual patient anatomy differs significantly from the expected pattern, the convergence of the algorithm may be falsely biased by the assumed constraints. CT scan data can further enhance image reconstruction approaches. With the hybrid SPECT/CT camera systems, the CT can be used during the reconstruction not only for AC, but also as a prior to improve the anatomic constraints.

7.6.1 Performance

The clinical solid-state SPECT systems offer improved sensitivity and spatial resolution compared to conventional Anger cameras. The actual technical performance of solid-state SPECT cameras were compared with conventional dual-head scanners by Imbert at al [3]. Additionally, similar results are available from one other vendor. Comparison of count sensitivity (expressed in %) compared to positron emission tomography (PET) are shown in Fig. 7.2. The solid-state SPECT cameras

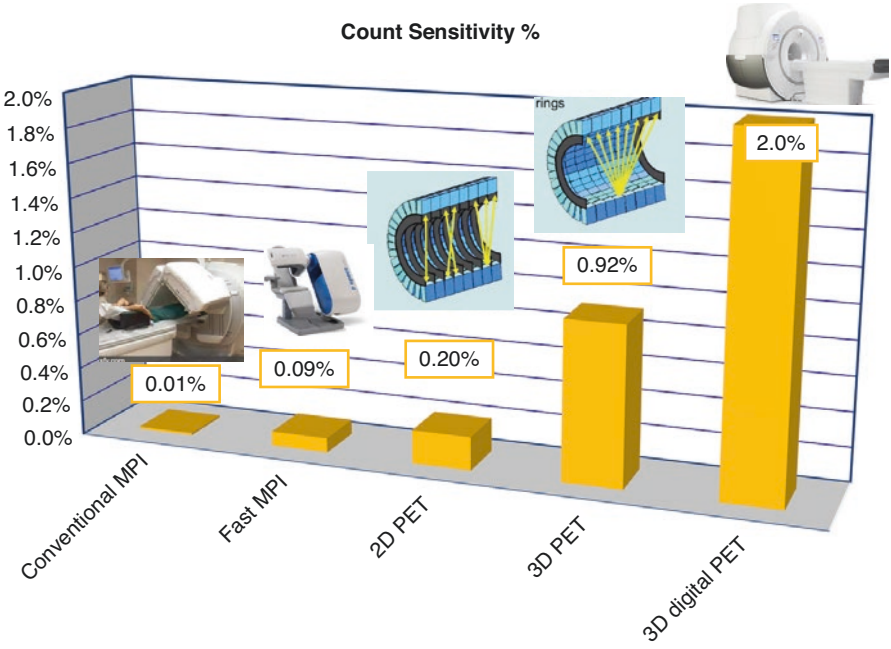

Fig. 7.2 Count sensitivity expressed as % of incoming photons for several nuclear imaging systems. Solid-state SPECT cameras (fast-MPI) have almost eight times higher count sensitivity compared to conventional Anger cameras. Therefore, the count sensitivity is more similar to 2D PET than a conventional SPECT camera

offer up to eight times higher count sensitivity and more than double the effective image resolution compared to the conventional Anger cameras. Imaging times with conventional doses of radioactivity are in the range of 2–3 min for systems with dedicated solid-state detectors [48, 49], compared to 15 min on systems with a standard collimator. The count sensitivities for dedicated cardiac CZT systems can approach those of 2D PET systems, which to date have been employed in most of the PET-MPI literature.

7.7 Impact on the Field

7.7.1 Current Clinical Use

It is estimated that over 800 solid-state dedicated cardiac CZT SPECT camera systems are currently in clinical use [50]. The improved technical performance of solid-state SPECT camera systems was initially used to dramatically reduce imaging time, improving patient comfort and minimizing motion artifacts. However, clinical protocols with these systems can also employ very low-dose radiopharmaceutical injections (150–220) MBq of the Tc-99m perfusion agents) [51–53] with standard imaging times. When employing stress-only scans with 10–12 min acquisitions, effective radiation doses under 1 mSv are achieved [54, 55]. By comparison, the average annual background radiation exposure in the US is ~3.1 mSv [56].

7.8 Clinical Protocols

7.8.1 Two-Position Imaging: Upright/Supine or Supine/Prone

The vast majority of solid-state SPECT cameras in clinical use are not in hybrid SPECT/CT configurations, and therefore do not offer CT-based AC. At the same time, very low-dose protocols with reduced image counts challenge the accuracy of visual interpretation, especially in the presence of attenuation artifacts. To address this issue, most clinical protocols employ two sequential scans performed in different patient positions (supine/upright or supine/prone). Since soft tissue shifts in different patient positions, comparing results from two positions can allow differentiation of true perfusion defects from artifacts [57–59]. Two-position protocols add only modestly to the total time of single view protocols with high-sensitivity scanners, with no added radiation exposure.

7.8.2 Low-Dose Protocols

The technical advancements of solid-state SPECT cameras can be used to dramatically reduce radiation exposure during a patient's scan. The list-mode capabilities of SPECT equipment can be used to evaluate retrospectively the efficacy of low-dose

imaging protocols. One such study simulated reduced radiation protocols in 79 patients, who were imaged with a solid-state scanner for 14 min with 802 ± 200 MBq of ^{99m}Tc injected at stress [55]. There was no significant difference in quantitative perfusion or functional measurements even with simulated activity corresponding to an effective radiation dose of <1 mSv, as outlined in Fig. 7.3. The clinical implementation of low-dose protocols was studied in patients who underwent repeat rest scans with split radiation doses. The image quality for very low-dose rest scans (mean effective dose 1.15 mSv) was superior to conventional SPECT imaging (mean effective dose 2.39 mSv) [60]. Einstein et al. reported stress-only imaging in 69 patients with a mean effective radiation dose of 0.99 mSv [61]. In a study of 284 patients undergoing SPECT MPI, Sharir et al. demonstrated similar diagnostic accuracy with low-dose imaging compared to standard dose imaging, but with 50% radiation reduction [62]. This was confirmed by another group who used 160 MBq injected doses for rest and stress acquisitions of 15 min [63]. Palyo et al. showed that regional perfusion defect size and functional parameters were similar in spite of 50% radiation reductions using a hybrid SPECT/CT system with CTAC [64]. With more aggressive radiation reduction (75%), there was a tendency to overestimate perfusion defect size in patients with abnormal results [64]. Importantly, to preserve

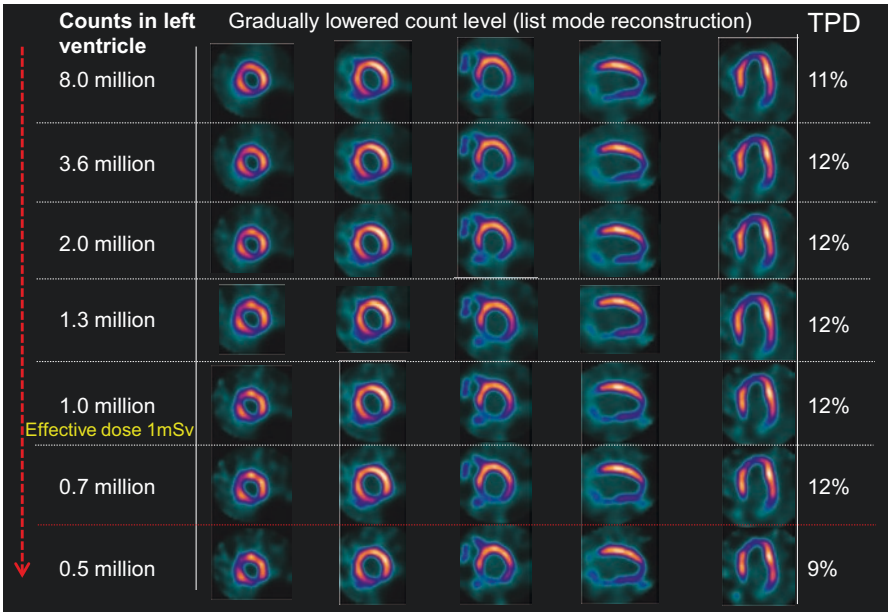

Fig. 7.3 Example of a patient with abnormal perfusion in the low-dose simulation study performed by Nakazato et al. [55]. Total perfusion deficit (TPD), which is a quantitative measure of ischemia, was not significantly different except in simulations representing an effective radiation dose <0.5 mSv. (This research was originally published in *JNM*. Nakazato R, Berman DS, Hayes SW, et al. Myocardial Perfusion Imaging with a Solid-State Camera: Simulation of a Very Low Dose Imaging Protocol. J Nucl Med. 2013;54:373–379. © SNMMI)

reproducibility between high-count and low-count data the quantification of low-dose protocols requires normal limits specifically calibrated with low-dose images due to higher variability of low-count data [65].

As noted above, the lowest total radiation exposure with current SPECT MPI (~1 mSv) can be accomplished clinically by performing stress-only imaging with a solid-state camera system. Stress-only MPI can reduce radiation exposure by up to 60% [66], and also provides a significant reduction in radiation exposure to staff performing the scan [67]. Additionally, stress-only protocols dramatically shorten total study times to as low as 30–45 min, including the stress test, improving the patient experience and laboratory efficiency. Since most SPECT MPI scans are normal [68], an ultralow-dose (1 mSv) stress-only scan, could potentially be performed in the majority of patients undergoing SPECT MPI with a solid-state camera system. Further research is needed to demonstrate the diagnostic accuracy and prognostic value of this ultralow-dose, stress-only approach.

7.9 Simultaneous Dual-Isotope MPI

Solid-state cameras with CZT detectors have superior energy resolution which allows better separation of photons from different isotopes and improved cross-talk correction [69]. In addition, stationary detector systems eliminate projection inconsistencies which confound dual-isotope imaging. One possible clinical application is a combined rest/stress protocol with simultaneous imaging of ^{99m}Tc and ^{201}Tl as proposed for conventional cameras [70], which was not implemented clinically on standard cameras due to technical difficulties and to concerns regarding higher radiation with ^{201}Tl.

To date, a few studies have demonstrated the feasibility of simultaneous imaging of ^{201}Tl (stress) and ^{99m}Tc (rest) SPECT MPI with solid-state cameras. One study proposed a single stress/rest 20-min acquisition for the two isotopes [71]. A separate study demonstrated the feasibility of simultaneous dual-isotope imaging in 24 patients with 80 MBq of ^{201}Tl injected at rest and 250 MBq of ^{99m}Tc sestamibi injected during adenosine infusion [72]. For this application, dedicated scatter correction methods are required because triple energy window corrections overestimate scatter and cross-talk in CZT-based systems [73]. These dedicated corrections have been shown to improve defect contrast and myocardium to blood pool ratios compared to triple energy window corrections [73]. Diagnostic performance and image quality of simultaneous dual-isotope MPI with solid-state systems have been demonstrated to be comparable to conventional SPECT with separate stress/rest acquisitions [69].

While the use of dual-isotope MPI with ^{99m}Tc and ^{201}Tl is now discouraged, simultaneous dual-isotope SPECT may become increasingly utilized for other imaging protocols. As an example, simultaneous dual-isotope for cardiac amyloidosis with ^{99m}Tc-pyrophosphate (PYP) and ^{201}Tl has recently been described, with ^{201}Tl allowing precise definition of myocardial boundaries [74]. This dual-isotope approach has importance for dedicated cardiac systems in which the tight gantry

and imaging focused on the heart makes it is harder to correctly position the ^{99m}Tc-PYP acquisitions.

Simultaneous dual-isotope imaging can also be used in combined SPECT perfusion/metabolism protocols. Many novel metabolism agents, either in clinical or research use, only show abnormal portions of the myocardium which are better understood within the context of perfusion imaging. As an example, ^{123}I-BMIPP has diagnostic and prognostic potential following acute myocardial infarction or in patients with Takotsubo cardiomyopathy [75]. Solid-state cameras have been shown to simultaneously acquire ^{99m}Tc perfusion agent and ^{123}I-BMIPP images with image quality similar to that achieved with separate acquisitions [76]. Simultaneous MIBG and ^{99m}Tc [77] or 123I-MIBG and ^{201}Tl imaging can also be acquired [78]. In phantom studies, ^{123}I and ^{99m}Tc images can be acquired simultaneously with similar image quality as separate acquisitions with two commercially available solid-state cameras [79]. Simultaneous dual-isotope acquisitions, which are facilitated by the high energy resolution of CZT crystals, reduce imaging time, ensure precise image co-registration, and reduce artifacts related to patient or camera motion between acquisitions.

7.10 Normal Perfusion Limits for Solid-State Cameras

Solid-state SPECT scanners have significantly different regional count distributions compared to standard Anger cameras—primarily due to different types of collimation and detector geometry. Early studies of CZT camera systems demonstrated these differences, and dedicated normal limits were subsequently recommended [49], with dedicated normal databases created for the Discovery NM 530c (GE Healthcare) [59, 80] and D-SPECT (Spectrum Dynamics) [49, 57] camera systems. Importantly—for optimal quantification—separate databases may be required for prone and supine acquisitions.

7.10.1 Combined Quantification from Two Positions

Physicians utilize multiple imaging positions to visually differentiate attenuation artifact from perfusion deficits, however, this approach has only more recently been applied to quantitative analysis. Combined quantitative analysis of upright and supine acquisitions on the solid-state D-SPECT (Spectrum Dynamics) scanner has been evaluated [57]. Quantification performed jointly from co-registered images obtained in two positions offered better identification of attenuation artifacts and reduced of false-positive defects (shown in Fig. 7.4). Compared to a reference of invasive coronary angiography, combined quantitative analysis showed higher diagnostic accuracy than separate upright or supine acquisitions. Similar results have been shown with two-position imaging in obese patients using the D-SPECT system [58] and for the Discovery NM530c scanner with supine and prone acquisitions [59]. Two-position imaging may also detect position-related truncation artifacts,

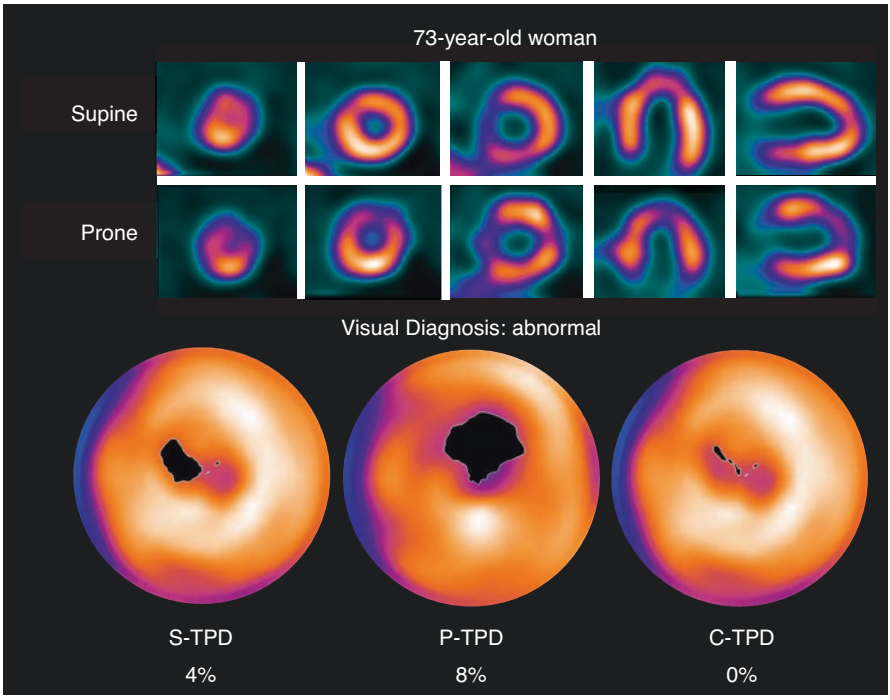

Fig. 7.4 Case example of two-position imaging. In this case, combining supine and prone imaging offers superior visual interpretation but was still interpreted as abnormal. Quantitative perfusion analysis is also improved by integrating supine total perfusion deficit (S-TPD), and prone TPD (P-TPD) into a single, combined measure (C-TPD) which shows no perfusion deficit. The patient had no significant coronary disease on invasive coronary angiography. (Case from REFINE SPECT registry)

which can occur due to the limited field of view on solid-state SPECT cameras [81]. New approaches applying deep learning with combined two-position imaging on solid-state cameras have demonstrated further improvements [82].

7.11 Motion Correction on Solid-State Cameras

Respiratory and patient motion can degrade SPECT image quality, with several recent studies investigating techniques to mitigate these effects. Due to improvements in spatial resolution, heart motion has become the dominant motion-related degrading factor in solid-state SPECT imaging. The feasibility of using list-mode data, with registration of consecutive short-time image frames, to detect and correct for respiratory motion has been demonstrated on these new systems [83]. Respiratory gating can impact functional cardiac parameters, resulting in reduced volume estimates and differences in regional LV wall motion [84]. End-expiratory gating can be used to improve contrast differences between the myocardium and blood pool

[85]. Respiratory phase matched CT attenuation maps may further improve image quality, and has been shown to significantly improve inter-observer agreement compared to uncorrected images [86]. Patient motion can also be corrected using a similar approach to reduce the rate of false-positive perfusion defects [87]. Dual respiratory/cardiac gated MPI has been demonstrated in phantoms and patients showing progressive improvement of the myocardium to blood pool contrast with the application of respiratory and then dual gating [85].

7.12 Potential Pitfalls

Although the novel designs of dedicated cardiac solid-state SPECT camera systems offer important clinical benefits, there are potential imaging pitfalls which need to be considered. The camera geometry is optimized for cardiac acquisitions, so there is non-uniform count sensitivity in the field of view [88]. Therefore, patient positioning is critical and patients with significantly abnormal cardiac anatomy may not be well imaged. Importantly, the typical attenuation defect with supine imaging is more lateral with solid-state camera designs compared to conventional cameras [89]. For example, due to increased space between the chest wall and cardiac border, obese patients may require re-positioning or multiple position imaging to ensure diagnostic quality [81]. In patients with hypertrophic cardiomyopathy, iterative reconstruction algorithms utilizing a cardiac shape model significantly underestimate wall thickness compared to ordered-subsets expectation maximization which does not use a shape constraint [90]. Two-position protocols may allow for detection of position-related artifacts and potentially address some of these concerns [58].

7.13 Emerging Clinical Techniques

7.13.1 SPECT Myocardial Blood Flow

Absolute myocardial blood flow (MBF) and myocardial flow reserve (MFR) provide clinically meaningful data beyond that obtained by assessment of relative perfusion deficit alone. Absolute measurements can identify patients with multivessel CAD and predict the extent of disease more accurately than relative perfusion quantification or visual interpretation [91]. MFR is also a useful prognostic marker, significantly improving risk stratification beyond relative perfusion defects [92, 93]. While myocardial flow measurements were initially developed and validated in PET imaging, SPECT cameras may be capable of obtaining similar measurements. The improved count sensitivity related to collimator and camera geometry advances with solid-state SPECT cameras may make them particularly well suited for flow measurements.

Human dynamic SPECT flow studies have been demonstrated on high-efficiency dedicated SPECT with factor analysis and a 2-compartment model used for

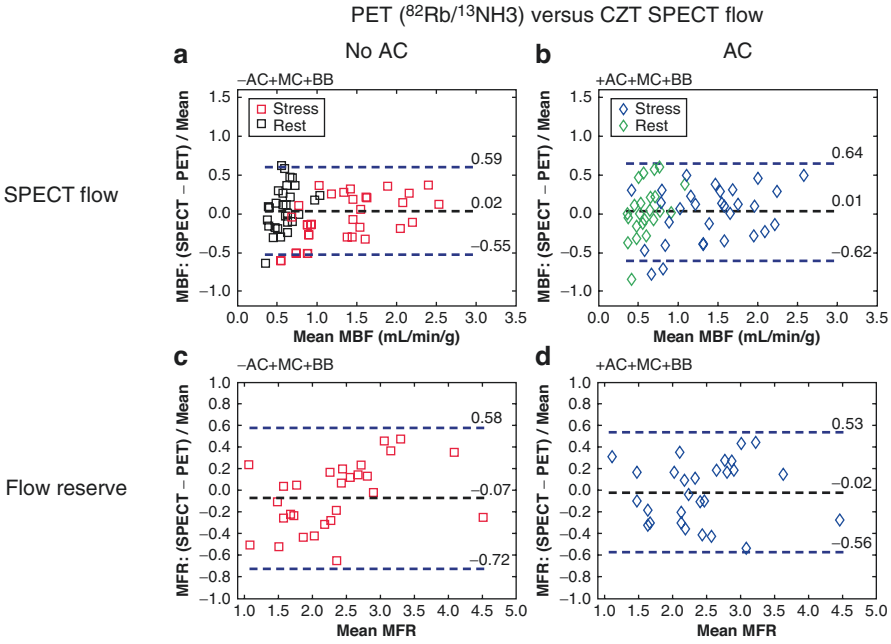

Fig. 7.5 Comparison between SPECT myocardial blood flow (MBF, panel A and B) and myocardial flow reserve (MFR, panel C and D) assessments with (panel B and D) and and without (panel A and C) attenuation correction (AC) compared to PET. SPECT MBF measurements at rest or with stress were not significantly different compared to PET values, with or without AC. Similar results were obtained with MFR measurements [96]. (This research was originally published in *JNM*. Wells RG, Marvin B, Poirier M, Renaud J, deKemp RA, Ruddy TD. Optimization of SPECT Measurement of Myocardial Blood Flow with Corrections for Attenuation, Motion, and Blood Binding Compared with PET. J Nucl Med. 2017;58:2013–2019. © SNMMI)

quantification. The clinical feasibility was demonstrated in 95 patients, in whom the data was reconstructed to 3-s frames resulting in 60–70 frames for each stress and rest study [94]. The authors demonstrated that MFR derived from such studies was higher in patients with normal scans (as established by standard relative quantification) and that lower MFR (both regional and global) was associated with stress perfusion defect on static imaging, age, and smoking. The MFR also showed step-wise reduction related to the severity of the obstructive disease in a subset of 20 patients, in which invasive coronary angiography was performed. To date, at least seven studies have been performed in humans demonstrating the SPECT MBF measurements with ^{99m}Tc and solid-state cameras [94–101]. Importantly, Wells et al. has demonstrated close agreement between SPECT MBF and MFR measurements, with or without attenuation correction, compared to PET measurements, [96] (Fig. 7.5). This finding has important implications, since the majority of the solid-state scanners are currently operating without AC capabilities. The clinical protocol for SPECT flow has gained significant attention recently, as the FDA approved dedicated clinical software with both solid-state scanners, with several sites commencing clinical SPECT flow imaging. Example of MPS flow results are shown in Fig. 7.6.

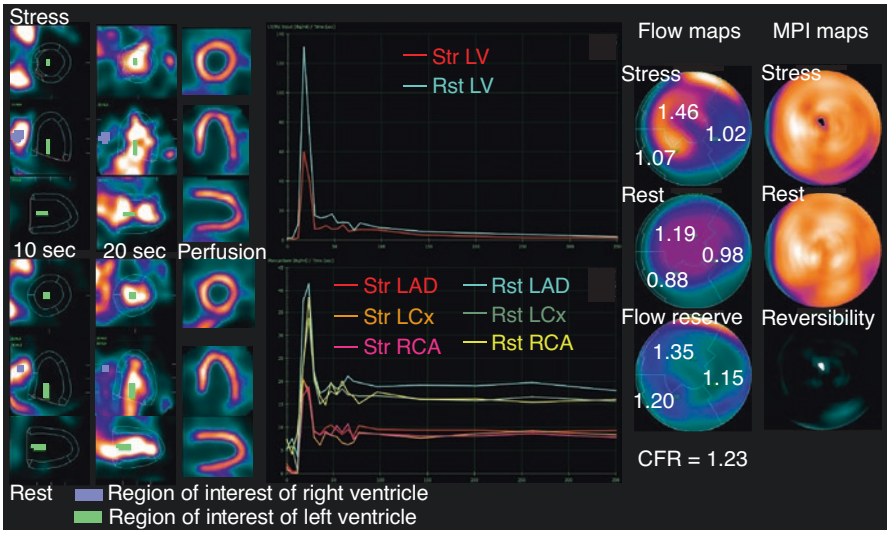

Fig. 7.6 Example of SPECT myocardial blood flow (MBF) information. One-day Tc-99m sestamibi stress-rest protocol (259 MBq for stress and 777 MBq for rest) was used. Stress (Str) and Rest (Rst) flows are computed from early dynamic imaging for each vascular territory, by deriving regional time activity curves for the myocardium and for input blood in the left atrium or left ventricle and applying compartmental models. These values can be used to calculate myocardial flow reserve (MFR) as the ratio between stress and rest MBF. Reduced MFR (<2.0) may be useful to identify the presence of multivessel-disease leading to balanced ischemia. This patient had normal regional myocardial perfusion, but decreased MFR and was ultimately found to have obstructive triple-vessel disease on coronary angiography. (Case provided courtesy of Dr. Alejandro Meretta, Instituto Cardiovascular de Buenos Aires)

Notwithstanding this early enthusiasm about SPECT MPI flow, there are well-known limitations of this use with ^{99m}Tc sestamibi or tetrofosmin. Notably, the myocardial extraction of these radiotracers from the blood is substantially reduced at high flows rates, which requires mathematical compensation. However, even after compensation, this "roll-off" phenomenon increases result variability. Despite these concerns, good agreement between PET and SPECT flows has been shown in head-to-head studies [95, 99]. In a study of 28 consecutive patients undergoing SPECT with attenuation correction and ^{13}N-ammonia PET, MFR was computed without using any extraction fraction correction for ^{99m}Tc-tetrofosmin [99]. The authors found that the hyperemic SPECT MBF values were lower than expected and consequently MFR was lower compared to PET values [99]. Agostini et al. compared ^{99m}Tc-sestamibi SPECT derived MBF and MFR, using a solid-state camera and a correction for ^{99m}Tc extraction fraction, with values obtained with ^{15}O-water PET in 30 patients [95]. SPECT MBF measurements were lower compared to PET values on stress and rest acquisitions. However. SPECT derived MFR was similar to PET values and had high diagnostic accuracy for PET defined ischemia (>93%) or ischemia defined by invasive fractional flow reserve (>81%) [95]. Therefore, while

SPECT flow measurements may not be as robust as PET, it is emerging as an important ancillary measure. Notably, no additional tracer injection is needed, thus minimizing additional costs and adding no radiation. Clinical validation studies for myocardial blood flow measurement with solid-state MPI are summarized in Table 7.1.

7.13.2 Early EF

SPECT measurements of MBF and MFR require an acquisition at the time of radiotracer injection. This facilitates measurement of stress left ventricular ejection fraction (LVEF) and LVEF reserve (defined as stress LVEF – rest LVEF)—which are important ancillary PET measurements. While post-stress LVEF changes are useful with SPECT, they are obtained at least 15 min following stress and are less sensitive than measurements during stress. High LVEF reserve has been shown to significantly reduce the probability of severe CAD during dipyridamole stress ^{82}Rb PET [102]. The feasibility of LVEF reserve measurements using early post-stress acquisitions with a dedicated cardiac solid-state SPECT scanner has been demonstrated in a study of 50 patients [103]. Significantly lower LVEF reserve was obtained in

Table 7.1 Human validation studies of myocardial blood flow quantification with solid-state SPECT cameras

Authors	Number of cases	Camera system	SPECT isotope	Validated with	model employed
Ben-Haim et al. 2013 [94]	95	D-SPECT	Sestamibi	Perfusion angiography	Factor analysis
Ben Bouallegue et al. 2015 [100]	23	Discovery 530c	Tetrofosmin	iFFR	1TC
Nkoulou et al. 2016 [99]	28	Discovery 570c	Tetrofosmin	N-13 ammonia	1TC
Miyagawa et al. 2017 [111]	69	Discovery 530c	Tetrofosmin Sestamibi	iFFR	1TC
Wells et al. 2017 [96]	31	Discovery 530c	Tetrofosmin	Rubidium-82 or N-13 ammonia	1TC
Agostini et al. 2018 [95]	30	D-SPECT	Sestamibi	O-15 water iFFR	Net retention model
Han et al. 2018 [97]	34	Discovery 530c	Thallium/ Tetrofosmin	iFFR	1TC
Ma et al. 2020 [98]	40	Discovery 530c	Sestamibi	RRG vs. solid-state	1TC
Zavadovsky et al. 2019 [112]	23	Discovery 570c	Sestamibi	iFFR	Net retention model

1TC one-tissue-compartment model, *iFFR* invasive fractional flow reserve, *RRG* rapid rotating gantry

the fifth and the ninth minute after regadenoson bolus in patients with significant ischemia compared to patients without ischemia. In the future, it may be feasible to measure LVEF reserve and MBF from the same early SPECT acquisitions, providing critical ancillary diagnostic and prognostic markers.

7.13.3 Large-Scale Clinical Validation

The increasing clinical use of solid-state SPECT camera systems has led to a large body of evidence validating their prognostic and diagnostic utility. Major studies of the diagnostic or prognostic utility of solid-state SPECT cameras are outlined in Table 7.2. One of the largest such efforts is a large, multicenter, international registry—the *RE*gistry of *F*ast Myocardial Perfusion *I*maging with *NE*xt generation *SPECT* (**REFINE SPECT**) registry [104]. The novel collaborative design of this registry features the contribution of clinical data and image datasets from nine (to date) investigative centers around the world into a comprehensive clinical-imaging database established at the central core laboratory at Cedars-Sinai Medical Center with centralized automatic quantitative analysis [104]. To date (2019), 20,418 solid-state MPI scans with collected prognostic data have been included in the registry. Initial results

Table 7.2 Major diagnostic ($N > 100$) and prognostic ($N > 1000$) validation studies for solid-state SPECT MPI

Authors	Number of cases	System	Comparator	Tracer	Dose	Time stress/rest (min)
Diagnostic validation						
Nakazato et al. 2010 [57]	56 ICA 86 LLk	D-SPECT	ICA	Sestamibi or Dual-isotope	SD	2/4
Gimelli et al. 2012 [52]	137	Discovery 530c	ICA	Tetrofosmin	LD	7/6
Duvall et al. 2013 [59]	160	Discovery 530c	ICA	Sestamibi	LD SD	3–5/3–5
Mouden et al. 2014 [113]	100	Discovery 570c	iFFR	Tetrofosmin	SD	5/4
Nakazato et al. 2015 [58]	67 ICA 51 LLk	D-SPECT	ICA	Sestamibi or Dual-isotope	SD	2–6/6–12
Chikamori et al. 2016 [114]	102	Discovery 530c	ICA/iFFR	Tetrofosmin or Sestamibi	LD	10/6
Sharir et al. 2016 [62]	208 ICA 76 LLk	Discovery 530c	ICA	Sestamibi	LD vs. SD	LD: 5–7/5–7 SD: 5/3

(continued)

Table 7.2 (continued)

Authors	Number of cases	System	Comparator	Tracer	Dose	Time stress/rest (min)
Betancur et al. 2019 [82]	1160	D-SPECT	ICA	Sestamibi	LD SD	4–6/6–10
Betancur et al. 2018 [106]	1638	D-SPECT Discovery 530c or 570c	ICA	Sestamibi/ Tetrofosmin/ dual-isotope	LD SD	4–6/6–10
Gimelli et al. 2019 [115]	1161	Discovery 530c	ICA	Tetrofosmin	LD	7/6
Prognostic validation						
Nakazato et al. 2012 [116]	1613	D-SPECT	All-cause mortality	Sestamibi Dual-isotope	SD	Sestamibi: 2/4 Dual: 6/4
Chowdhury et al. 2014 [117]	1109 (165 with ICA)	Discovery 530c	MACE ICA	Tetrofosmin	SD	3–6/3–6
De Lorenzo et al. 2016 [118]	1396	Discovery 530c	All-cause mortality	Sestamibi	SD	4/8
Yokota et al. 2016 [119]	1288 solid-state 362 conventional	Discovery 570c	MACE	Tetrofosmin	LD	5/–
Engbers et al. 2017 [120]	4057	Discovery 570c	MACE	Tetrofosmin	SD	5/4
Lima et al. 2017 [121]	3554	Discovery 530c	MACE	Sestamibi	LD	3/6
Lima et al. 2017 [122]	2930	Discovery 530c	MACE	Sestamibi	SD LD	3/6
Betancur et al. 2018 [123]	2619	D-SPECT	MACE	Sestamibi	SD	4–6/6–10
van Dijk et al. 2018 [124]	1255	Discovery 570c	MACE	Tetrofosmin	SD vs. LD	SD: 5/4 LD: 8/6
Otaki et al. 2020 [105]	19,495	D-SPECT & Discovery 530c	MACE	Tetrofosmin/ Sestamibi/ dual-isotope	LD SD	4–6/6–10

ICA invasive coronary angiography, *LD* low-dose, *SD* standard dose, *LLk* low likelihood of coronary artery disease, *iFFR* invasive fractional flow reserve, *MACE* major advanced cardiac events. The overall effective dose of the test is LD if the dose is between <6 mSv; SD if above 6 mSv
Acquisition time: if more than one position is taken, the time specified here is for the default view

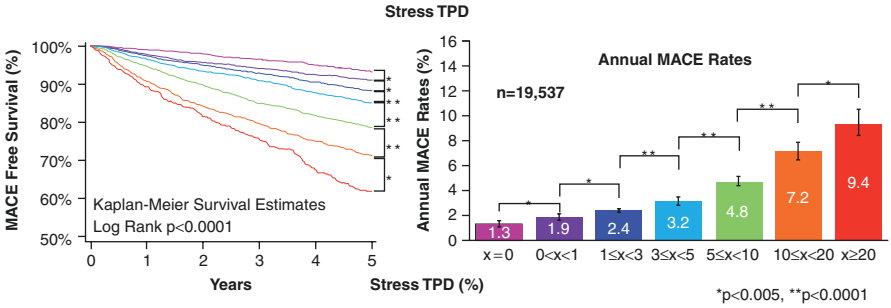

Fig. 7.7 Prognostic value of quantitative perfusion analysis from the REFINE SPECT registry with solid-state MPI. Quantitative perfusion assessments, with total perfusion deficit (TPD) provide fine gradation of cardiovascular risk. Each increase in TPD extent, including <1% ischemia compared to no ischemia, was associated with significant increase in the combined outcome of death, non-fatal myocardial infarction, unstable angina, or late revascularization [105]. (With permission from Otaki Y, Betancur J, Sharir T, et al., 5-year Prognostic Value of Quantitative vs Visual Myocardial Perfusion Imaging in Subtle Perfusion Defects: Results From REFINE SPECT, *JACC Cardiovasc Imaging,* Elsevier, 2020;13(3):774–785)

from the registry have shown that quantitative perfusion analysis, measured as total perfusion deficit (TPD), provides fine gradation of risk [105]. Increasing TPD, even at very low levels, is associated with increasing risk of death, non-fatal myocardial infarction, unstable angina, or late revascularization [105]. Notably, patients with >0 but <1% TPD had a 40% higher risk of events compared to patients with TPD 0, demonstrating the importance of even small deficits which may be missed without the higher spatial resolution of new solid-state SPECT cameras [105] (Fig. 7.7).

The registry has also allowed researchers to perform various collaborative projects, including the development of novel machine-learning methods tailored for the analysis of solid-state SPECT MPI and subsequent integration of quantitative image data variables with "pre-scan" clinical information. A machine-learning score derived with deep-convolutional neural networks has been shown to have superior diagnostic accuracy for obstructive CAD compared to quantitative ischemia assessments [82, 106]. A separate machine-learning algorithm had superior prognostic accuracy compared to either quantitative ischemia assessment or physician assessments [82]. Other validation studies have been performed for solid-state MPI, these include validation of diagnostic accuracy including two-position imaging and attenuation correction [58], determination of the transient ischemic dilation limits [107], and prognostic performance [105]. Given the rich data collected, further validation studies are expected from this large multicenter cohort in the future.

7.14 Future Hardware Designs

While these recent SPECT hardware improvements have proven to be clinically important, further advancements are still possible. One possible area for improvement is additional gains in photon sensitivity. While more sensitive than

conventional Anger cameras, even dedicated cardiac SPECT scanners detect still only <0.1% of emitted photons. Pre-clinical studies have demonstrated that higher efficiency may be possible. In a simulation, Zeng et al. [108] demonstrated that multi-divergent beam collimators could double the photon sensitivity of current SPECT camera systems without sacrificing spatial resolution. Simulations of multi-pinhole designs with paired curved paraboloid or hemi-ellipsoid detectors could improve photon sensitivity by up to 300% [109, 110]. In phantom studies these designs have improved photon sensitivity and spatial resolution compared to published characteristics or commercially available solid-state camera systems [110]. Nevertheless, these published reports are still pre-clinical, and it remains to be seen if these designs will be cost-effective and adequate for clinical implementation.

7.15 Summary

Solid-state cardiac SPECT offer substantial improvements in photon sensitivity and spatial resolution compared to conventional Anger cameras. These advances are due to novel collimator and geometric designs as well as incorporation of CZT crystals. Solid-state camera systems have facilitated dramatic reductions in both imaging time and radiation dose, while maintaining high diagnostic accuracy. Growing clinical experience has validated the excellent diagnostic and prognostic utility attained with these camera systems. With the CZT systems, simultaneous dual-isotope SPECT is feasible and has been shown to be useful in selected applications. The improved technical performance has also facilitated measurement of ancillary high-risk markers including MBF and LVEF reserve. Additionally, SPECT/CT systems are becoming more commonly used allowing hybrid imaging incorporating either coronary calcium scoring or even CT angiography. While these advances have already provided a substantial improvement over the use of standard NaI crystal-based systems, the full clinical potential of solid-state cardiac SPECT camera systems has not yet been realized.

Acknowledgements This chapter contains material from the article Slomka et al. J Nucl Med. 2019 Sep;60 (9):1194–1204 Solid-State Detector SPECT Myocardial Perfusion Imaging. Reproduced with permission.

References

1. Slomka PJ, Patton JA, Berman DS, Germano G. Advances in technical aspects of myocardial perfusion SPECT imaging. J Nucl Cardiol. 2009;16:255–76.
2. Sharir T, Ben-Haim S, Merzon K, Prochorov V, Dickman D, Ben-Haim S, et al. High-speed myocardial perfusion imaging: initial clinical comparison with conventional dual detector anger camera imaging. JACC Cardiovasc Imaging. 2008;1:156–63.
3. Imbert L, Poussier S, Franken PR, Songy B, Verger A, Morel O, et al. Compared performance of high-sensitivity cameras dedicated to myocardial perfusion SPECT: a comprehensive analysis of phantom and human images. J Nucl Med. 2012;53:1897–903.

4. Volokh L, Hugg J, Blevis I, Asma E, Jansen F, Manjeshwar R. Effect of detector energy response on image quality of myocardial perfusion SPECT. In: Nuclear science symposium conference record, 2008 NSS'08 IEEE 2008. p. 4043–6.
5. Siman W, Kappadath SC. Performance characteristics of a new pixelated portable gamma camera. Med Phys. 2012;39:3435–44.
6. Gunter DL. Gamma camera collimator characteristics and design. In: Henkin RE, editor. Nuclear medicine. Philadelphia, PA: Elsevier; 2006. p. 107–26.
7. Schepis T, Gaemperli O, Koepfli P, Ruegg C, Burger C, Leschka S, et al. Use of coronary calcium score scans from stand-alone multislice computed tomography for attenuation correction of myocardial perfusion SPECT. Eur J Nucl Med Molec Imaging. 2007;34:11–9.
8. Grossmann M, Giannopoulos AA, Bechtiger FA, Messerli M, Schwyzer M, Benz DC, et al. Ultra-low-dose computed tomography for attenuation correction of cadmium-zinc-telluride single photon emission computed tomography myocardial perfusion imaging. J Nucl Cardiol. 2018;27(1):228–37.
9. Caobelli F, Akin M, Thackeray JT, Brunkhorst T, Widder J, Berding G, et al. Diagnostic accuracy of cadmium-zinc-telluride-based myocardial perfusion SPECT: impact of attenuation correction using a co-registered external computed tomography. Eur Heart J Cardiovasc Imaging. 2016;17:1036–43.
10. Kennedy JA, Brodov Y, Weinstein AL, Israel O, Frenkel A. The effect of CT-based attenuation correction on the automatic perfusion score of myocardial perfusion imaging using a dedicated cardiac solid-state CZT SPECT/CT. J Nucl Cardiol. 2019;26:236–45.
11. Agatston AS, Janowitz WR, Hildner FJ, Zusmer NR, Viamonte M Jr, Detrano R. Quantification of coronary artery calcium using ultrafast computed tomography. J Am Coll Cardiol. 1990;15:827–32.
12. Callister T, Cooil B, Raya S, Lippolis N, Russo D, Raggi P. Coronary artery disease: improved reproducibility of calcium scoring with an electron-beam CT volumetric method. Radiology. 1998;208:807–14.
13. McCollough CH, Ulzheimer S, Halliburton SS, Shanneik K, White RD, Kalender WA. Coronary artery calcium: a multi-institutional, multimanufacturer international standard for quantification at cardiac CT. Radiology. 2007;243:527–38.
14. Arad Y, Goodman KJ, Roth M, Newstein D, Guerci AD. Coronary calcification, coronary disease risk factors, C-reactive protein, and atherosclerotic cardiovascular disease events: the St. Francis Heart Study. J Am Coll Cardiol. 2005;46:158–65.
15. Shaw L, Raggi P, Schisterman E, Berman D, Callister T. Prognostic value of cardiac risk factors and coronary artery calcium screening for all-cause mortality. Radiology. 2003;228:826–33.
16. Raggi P, Callister TQ, Cooil B, He ZX, Lippolis NJ, Russo DJ, et al. Identification of patients at increased risk of first unheralded acute myocardial infarction by electron-beam computed tomography. Circulation. 2000;101:850–5.
17. Park R, Detrano R, Xiang M, Fu P, Ibrahim Y, LaBree L, et al. Combined use of computed tomography coronary calcium scores and C-reactive protein levels in predicting cardiovascular events in nondiabetic individuals. Circulation. 2002;106:2073–7.
18. Shemesh J, Morag-Koren N, Goldbourt U, Grossman E, Tenenbaum A, Fisman EZ, et al. Coronary calcium by spiral computed tomography predicts cardiovascular events in high-risk hypertensive patients. J Hypertens. 2004;22:605–10.
19. Wong ND, Hsu JC, Detrano RC, Diamond G, Eisenberg H, Gardin JM. Coronary artery calcium evaluation by electron beam computed tomography and its relation to new cardiovascular events. Am J Cardiol. 2000;86:495–8.
20. Kondos GT, Hoff JA, Sevrukov A, Daviglus ML, Garside DB, Devries SS, et al. Electron-beam tomography coronary artery calcium and cardiac events: a 37-month follow-up of 5635 initially asymptomatic low- to intermediate-risk adults. Circulation. 2003;107:2571–6.
21. Greenland P, LaBree L, Azen SP, Doherty TM, Detrano RC. Coronary artery calcium score combined with Framingham score for risk prediction in asymptomatic individuals. JAMA. 2004;291:210–5.

22. LaMonte MJ, FitzGerald SJ, Church TS, Barlow CE, Radford NB, Levine BD, et al. Coronary artery calcium score and coronary heart disease events in a large cohort of asymptomatic men and women. Am J Epidemiol. 2005;162:421–9.
23. Taylor AJ, Bindeman J, Feuerstein I, Cao F, Brazaitis M, O'Malley PG. Coronary calcium independently predicts incident premature coronary heart disease over measured cardiovascular risk factors: mean three-year outcomes in the Prospective Army Coronary Calcium (PACC) project. J Am Coll Cardiol. 2005;46:807–14.
24. Vliegenthart R, Oudkerk M, Hofman A, Oei HH, van Dijck W, van Rooij FJ, et al. Coronary calcification improves cardiovascular risk prediction in the elderly. Circulation. 2005;112:572–7.
25. Becker A, Knez A, Becker C, Leber A, Anthopounou L, Boekstegers P, et al. [Prediction of serious cardiovascular events by determining coronary artery calcification measured by multi-slice computed tomography]. Dtsch Med Wochenschr. 2005;130:2433–8.
26. Detrano R, Guerci AD, Carr JJ, Bild DE, Burke G, Folsom AR, et al. Coronary calcium as a predictor of coronary events in four racial or ethnic groups. N Engl J Med. 2008;358:1336–45.
27. Brodov Y, Gransar H, Dey D, Shalev A, Germano G, Friedman JD, et al. Combined quantitative assessment of myocardial perfusion and coronary artery calcium score by hybrid 82Rb PET/CT improves detection of coronary artery disease. J Nucl Med. 2015;56:1345–50.
28. Zampella E, Acampa W, Assante R, Nappi C, Gaudieri V, Mainolfi CG, et al. Combined evaluation of regional coronary artery calcium and myocardial perfusion by (82)Rb PET/CT in the identification of obstructive coronary artery disease. Eur J Nucl Med Molec Imaging. 2018;45:521–9.
29. Chang SM, Nabi F, Xu J, Peterson LE, Achari A, Pratt CM, et al. The coronary artery calcium score and stress myocardial perfusion imaging provide independent and complementary prediction of cardiac risk. J Am Coll Cardiol. 2009;54:1872–82.
30. Engbers EM, Timmer JR, Ottervanger JP, Mouden M, Knollema S, Jager PL. Prognostic value of coronary artery calcium scoring in addition to single-photon emission computed tomographic myocardial perfusion imaging in symptomatic patients. Circ Cardiovasc Imaging. 2016;9(5):e003966.
31. Trpkov C, Savtchenko A, Liang Z et al. Visually estimated coronary artery calcium score improves SPECT-MPI risk stratification. Int J Cardiol Heart Vasc. 2021;35:100827.
32. Einstein AJ, Johnson LL, Bokhari S, Son J, Thompson RC, Bateman TM, et al. Agreement of visual estimation of coronary artery calcium from low-dose CT attenuation correction scans in hybrid PET/CT and SPECT/CT with standard Agatston score. J Am Coll Cardiol. 2010;56:1914–21.
33. Kaster TS, Dwivedi G, Susser L, Renaud JM, Beanlands RS, Chow BJ, et al. Single low-dose CT scan optimized for rest-stress PET attenuation correction and quantification of coronary artery calcium. J Nucl Cardiol. 2015;22:419–28.
34. Patchett ND, Pawar S, Miller EJ. Visual identification of coronary calcifications on attenuation correction CT improves diagnostic accuracy of SPECT/CT myocardial perfusion imaging. J Nucl Cardiol. 2017;24:711–20.
35. Mahabadi AA, Lehmann N, Mohlenkamp S, Pundt N, Dykun I, Roggenbuck U, et al. Noncoronary measures enhance the predictive value of cardiac CT above traditional risk factors and CAC score in the general population. JACC Cardiovasc Imaging. 2016;9:1177–85.
36. Bos D, Leening MJG. Leveraging the coronary calcium scan beyond the coronary calcium score. Eur Radiol. 2018;28:3082–7.
37. Commandeur F, Goeller M, Betancur J, Cadet S, Doris M, Chen X, et al. Deep learning for quantification of epicardial and thoracic adipose tissue from non-contrast CT. IEEE Trans Med Imaging. 2018;37:1835–46.
38. Clavel MA, Pibarot P, Messika-Zeitoun D, Capoulade R, Malouf J, Aggarval S, et al. Impact of aortic valve calcification, as measured by MDCT, on survival in patients with aortic stenosis: results of an international registry study. J Am Coll Cardiol. 2014;64:1202–13.

39. Wolff L, Bos D, Murad SD, Franco OH, Krestin GP, Hofman A, et al. Liver fat is related to cardiovascular risk factors and subclinical vascular disease: the Rotterdam study. Eur Heart J Cardiovasc Imaging. 2016;17:1361–7.
40. Marcus C, Santhanam P, Kruse MJ, Javadi MS, Solnes LB, Rowe SP. Adding value to myocardial perfusion SPECT/CT studies that include coronary calcium CT: detection of incidental pulmonary arterial dilatation. Medicine. 2018;97:e11359.
41. SCOT-HEART Investigators. Coronary CT angiography and 5-year risk of myocardial infarction. N Engl J Med. 2018;379:924–33.
42. Slomka PJ, Cheng VY, Dey D, Woo J, Ramesh A, Van Kriekinge S, et al. Quantitative analysis of myocardial perfusion SPECT anatomically guided by coregistered 64-slice coronary CT angiography. J Nucl Med. 2009;50:1621–30.
43. Santana CA, Garcia EV, Faber TL, Sirineni GK, Esteves FP, Sanyal R, et al. Diagnostic performance of fusion of myocardial perfusion imaging (MPI) and computed tomography coronary angiography. J Nucl Cardiol. 2009;16:201–11.
44. Gaemperli O, Schepis T, Valenta I, Koepfli P, Husmann L, Scheffel H, et al. Functionally relevant coronary artery disease: comparison of 64-section CT angiography with myocardial perfusion SPECT. Radiology. 2008;248:414–23.
45. Woo J, Slomka PJ, Dey D, Cheng VY, Hong BW, Ramesh A, et al. Geometric feature-based multimodal image registration of contrast-enhanced cardiac CT with gated myocardial perfusion SPECT. Med Phys. 2009;36:5467–79.
46. Goshen E, Beilin L, Stern E, Kenig T, Goldkorn R, Ben-Haim S. Feasibility study of a novel general purpose CZT-based digital SPECT camera: initial clinical results. EJNMMI Phys. 2018;5:6.
47. Keidar Z, Raysberg I, Lugassi R, Frenkel A, Israel O. Novel cadmium zinc telluride based detector general purpose gamma camera: initial evaluation and comparison with a standard camera. J Nucl Med. 2016;57:259.
48. Buechel RR, Herzog BA, Husmann L, Burger IA, Pazhenkottil AP, Treyer V, et al. Ultrafast nuclear myocardial perfusion imaging on a new gamma camera with semiconductor detector technique: first clinical validation. Eur J Nucl Med Mol Imaging. 2010;37:773–8.
49. Sharir T, Slomka PJ, Hayes SW, DiCarli MF, Ziffer JA, Martin WH, et al. Multicenter trial of high-speed versus conventional single-photon emission computed tomography imaging: quantitative results of myocardial perfusion and left ventricular function. J Am Coll Cardiol. 2010;55:1965–74.
50. Peretz A, Roth N. CZT scanners installed base (ASNC 2013 Personal communications). Chicago, IL;2012.
51. Henzlova M, Duvall W. The future of SPECT MPI: time and dose reduction. J Nucl Cardiol. 2011;18:580–7.
52. Gimelli A, Bottai M, Genovesi D, Giorgetti A, Di Martino F, Marzullo P. High diagnostic accuracy of low-dose gated-SPECT with solid-state ultrafast detectors: preliminary clinical results. Eur J Nucl Med Mol Imaging. 2012;39:83–90.
53. Nkoulou R, Pazhenkottil AP, Kuest SM, Ghadri JR, Wolfrum M, Husmann L, et al. Semiconductor detectors allow low-dose-low-dose 1-day SPECT myocardial perfusion imaging. J Nucl Med. 2011;52:1204–9.
54. Bateman T, McGhie A, Courter S, Burgett E, Cullom S, Case J. Prospective study of ultra-low dose stress-only solid-state SPECT: comparison of efficiency, dosimetry and outcomes versus traditional-dose attenuation-corrected stress-only anger SPECT. J Am Coll Cardiol. 2012;59:E1316 (abstract).
55. Nakazato R, Berman DS, Hayes SW, Fish M, Padgett R, Xu Y, et al. Myocardial perfusion imaging with a solid-state camera: simulation of a very low dose imaging protocol. J Nucl Med. 2013;54:373–9.
56. Schauer DA, Linton OW. NCRP Report No. 160. Ionizing radiation exposure of the population of the United States, medical exposure-are we doing less with more, and is there a role for health physicists? Health Phys. 2009;97:1–5.

57. Nakazato R, Tamarappoo BK, Kang X, Wolak A, Kite F, Hayes SW, et al. Quantitative upright-supine high-speed SPECT myocardial perfusion imaging for detection of coronary artery disease: correlation with invasive coronary angiography. J Nucl Med. 2010;51:1724–31.
58. Nakazato R, Slomka PJ, Fish M, Schwartz RG, Hayes SW, Thomson LE, et al. Quantitative high-efficiency cadmium-zinc-telluride SPECT with dedicated parallel-hole collimation system in obese patients: results of a multi-center study. J Nucl Cardiol. 2015;22:266–75.
59. Duvall WL, Slomka PJ, Gerlach JR, Sweeny JM, Baber U, Croft LB, et al. High-efficiency SPECT MPI: comparison of automated quantification, visual interpretation, and coronary angiography. J Nucl Cardiol. 2013;20:763–73.
60. Einstein AJ, Blankstein R, Andrews H, Fish M, Padgett R, Hayes SW, et al. Comparison of image quality, myocardial perfusion, and left ventricular function between standard imaging and single-injection ultra-low-dose imaging using a high-efficiency SPECT camera: the MILLISIEVERT study. J Nucl Med. 2014;55:1430–7.
61. Einstein AJ, Johnson LL, DeLuca AJ, Kontak AC, Groves DW, Stant J, et al. Radiation dose and prognosis of ultra-low-dose stress-first myocardial perfusion SPECT in patients with chest pain using a high-efficiency camera. J Nucl Med. 2015;56:545–51.
62. Sharir T, Pinskiy M, Pardes A, Rochman A, Prokhorov V, Kovalski G, et al. Comparison of the diagnostic accuracies of very low stress-dose with standard-dose myocardial perfusion imaging: automated quantification of one-day, stress-first SPECT using a CZT camera. J Nucl Cardiol. 2016;23:11–20.
63. Nkoulou R, Pazhenkottil AP, Wolfrum M, Gaemperli O, Kaufmann PA, Buechel RR, et al. High efficiency gamma camera enables ultra-low fixed dose stress/rest myocardial perfusion imaging. Eur Heart J Cardiovasc Imaging. 2018;20:218–24.
64. Palyo RJ, Sinusas AJ, Liu YH. High-sensitivity and high-resolution SPECT/CT systems provide substantial dose reduction without compromising quantitative precision for assessment of myocardial perfusion and function. J Nucl Med. 2016;57:893–9.
65. Slomka PJ, Rubeaux M, Germano G. Quantification with normal limits: new cameras and low-dose imaging. J Nucl Cardiol. 2017;24:1637–40.
66. Chang SM, Nabi F, Xu J, Raza U, Mahmarian JJ. Normal stress-only versus standard stress/rest myocardial perfusion imaging: similar patient mortality with reduced radiation exposure. J Am Coll Cardiol. 2010;55:221–30.
67. Duvall WL, Guma KA, Kamen J, Croft LB, Parides M, George T, et al. Reduction in occupational and patient radiation exposure from myocardial perfusion imaging: impact of stress-only imaging and high-efficiency SPECT camera technology. J Nucl Med. 2013;54:1251–7.
68. Rozanski A, Gransar H, Hayes SW, Min J, Friedman JD, Thomson LEJ, et al. Temporal trends in the frequency of inducible myocardial ischemia during cardiac stress testing: 1991 to 2009. J Am Coll Cardiol. 2013;61:1054–65.
69. Kacperski K, Erlandsson K, Ben-Haim S, Van Gramberg D, Hutton BF. Iterative deconvolution of simultaneous dual radionuclide projections for CdZnTe based cardiac SPECT. IEEE Nuclear Science Symposium Conference Record, 2008 NSS'08; 2008. p. 5260–3.
70. Kiat H, Germano G, Friedman J, Van Train K, Silagan G, Wang FP, et al. Comparative feasibility of separate or simultaneous rest thallium-201/stress technetium-99m-sestamibi dual-isotope myocardial perfusion SPECT. J Nucl Med. 1994;35:542.
71. Steele PP, Kirch DL, Koss JE. Comparison of simultaneous dual-isotope multipinhole SPECT with rotational SPECT in a group of patients with coronary artery disease. J Nucl Med. 2008;49:1080.
72. Ben-Haim S, Kacperski K, Hain S, Van Gramberg D, Hutton BF, Erlandsson K, et al. Simultaneous dual-radionuclide myocardial perfusion imaging with a solid-state dedicated cardiac camera. Eur J Nucl Med Mol Imaging. 2010;37:1710–21.
73. Fan P, Hutton BF, Holstensson M, Ljungberg M, Pretorius PH, Prasad R, et al. Scatter and crosstalk corrections for (99m)Tc/(123)I dual-radionuclide imaging using a CZT SPECT system with pinhole collimators. Med Phys. 2015;42:6895–911.

74. Tamarappoo BK, Otaki Y, Manabe O, Huynh M, Arnson Y, Gransar H, et al. Simultaneous Tc-99m PYP/Tl-201 dual-isotope SPECT myocardial imaging in patients with suspected cardiac amyloidosis. J Nucl Cardiol. 2020;27(1):28–37.
75. Matsuo S, Nakajima K, Kinuya S, Yamagishi M. Diagnostic utility of 123I-BMIPP imaging in patients with Takotsubo cardiomyopathy. J Nucl Cardiol. 2014;64:49–56.
76. Yamada Y, Nakano S, Gatate Y, Okano N, Muramatsu T, Nishimura S, et al. Feasibility of simultaneous (99m)Tc-tetrofosmin and (123)I-BMIPP dual-tracer imaging with cadmium-zinc-telluride detectors in patients undergoing primary coronary intervention for acute myocardial infarction. J Nucl Cardiol. 2021;28:187–95.
77. Blaire T, Bailliez A, Ben Bouallegue F, Bellevre D, Agostini D, Manrique A. Determination of the heart-to-mediastinum ratio of 123I-MIBG uptake using dual-isotope (123I-MIBG/99mTc-tetrofosmin) multipinhole cadmium-zinc-telluride SPECT in patients with heart failure. J Nucl Med. 2018;59:251–8.
78. D'Estanque E, Hedon C, Lattuca B, Bourdon A, Benkiran M, Verd A, et al. Optimization of a simultaneous dual-isotope (201)Tl/(123)I-MIBG myocardial SPECT imaging protocol with a CZT camera for trigger zone assessment after myocardial infarction for routine clinical settings: are delayed acquisition and scatter correction necessary? J Nucl Cardiol. 2017;24:1361–9.
79. Blaire T, Bailliez A, Ben Bouallegue F, Bellevre D, Agostini D, Manrique A. First assessment of simultaneous dual isotope ((123)I/(99m)Tc) cardiac SPECT on two different CZT cameras: a phantom study. J Nucl Cardiol. 2018;25:1692–704.
80. Nishiyama Y, Miyagawa M, Kawaguchi N, Nakamura M, Kido T, Kurata A, et al. Combined supine and prone myocardial perfusion single-photon emission computed tomography with a cadmium zinc telluride camera for detection of coronary artery disease. Circ J. 2014;78:1169–75.
81. Fiechter M, Gebhard C, Fuchs TA, Ghadri JR, Stehli J, Kazakauskaite E, et al. Cadmium-zinc-telluride myocardial perfusion imaging in obese patients. J Nucl Med. 2012;53:1401–6.
82. Betancur JA, Hu LH, Commandeur F, Sharir T, Einstein AJ, Fish MB, et al. Deep learning analysis of upright-supine high-efficiency SPECT myocardial perfusion imaging for prediction of obstructive coronary artery disease: a multicenter study. J Nucl Med. 2019;60:664–70.
83. Daou D, Sabbah R, Coaguila C, Boulahdour H. Feasibility of data-driven cardiac respiratory motion correction of myocardial perfusion CZT SPECT: a pilot study. J Nucl Cardiol. 2017;24:1598–607.
84. Buechel RR, Husmann L, Pazhenkottil AP, Nkoulou R, Herzog BA, Burger IA, et al. Myocardial perfusion imaging with real-time respiratory triggering: impact of inspiration breath-hold on left ventricular functional parameters. J Nucl Cardiol. 2010;17:848–52.
85. Chan C, Harris M, Le M, Biondi J, Grobshtein Y, Liu YH, et al. End-expiration respiratory gating for a high-resolution stationary cardiac SPECT system. Phys Med Biol. 2014;59:6267–87.
86. Clerc OF, Fuchs TA, Possner M, Vontobel J, Mikulicic F, Stehli J, et al. Real-time respiratory triggered SPECT myocardial perfusion imaging using CZT technology: impact of respiratory phase matching between SPECT and low-dose CT for attenuation correction. Eur Heart J Cardiovasc Imaging. 2017;18:31–8.
87. Kennedy JA, William Strauss H. Motion detection and amelioration in a dedicated cardiac solid-state CZT SPECT device. Med Biol Eng Comput. 2017;55:663–71.
88. Kennedy JA, Israel O, Frenkel A. 3D iteratively reconstructed spatial resolution map and sensitivity characterization of a dedicated cardiac SPECT camera. J Nucl Cardiol. 2014;21:443–52.
89. Oddstig J, Martinsson E, Jögi J, Engblom H, Hindorf C. Differences in attenuation pattern in myocardial SPECT between CZT and conventional gamma cameras. J Nucl Cardiol. 2019;26(6):1984–91.
90. Tsuboi K, Nagaki A, Shibutani T, Onoguchi M. Optimal choice of OSEM and SD reconstruction algorithms in CZT SPECT for hypertrophic cardiomyopathy patients. J Nucl Cardiol. 2021;28(1):236–44.

91. Fiechter M, Ghadri JR, Gebhard C, Fuchs TA, Pazhenkottil AP, Nkoulou RN, et al. Diagnostic value of 13N-ammonia myocardial perfusion PET: added value of myocardial flow reserve. J Nucl Med. 2012;53:1230–4.
92. Ziadi MC, Dekemp RA, Williams KA, Guo A, Chow BJ, Renaud JM, et al. Impaired myocardial flow reserve on rubidium-82 positron emission tomography imaging predicts adverse outcomes in patients assessed for myocardial ischemia. J Am Coll Cardiol. 2011;58:740–8.
93. Murthy VL, Naya M, Foster CR, Hainer J, Gaber M, Di Carli G, et al. Improved cardiac risk assessment with noninvasive measures of coronary flow reserve. Circulation. 2011;124:2215–24.
94. Ben-Haim S, Murthy VL, Breault C, Allie R, Sitek A, Roth N, et al. Quantification of myocardial perfusion reserve using dynamic SPECT imaging in humans: a feasibility study. J Nucl Med. 2013;54:873–9.
95. Agostini D, Roule V, Nganoa C, Roth N, Baavour R, Parienti JJ, et al. First validation of myocardial flow reserve assessed by dynamic (99m)Tc-sestamibi CZT-SPECT camera: head to head comparison with (15)O-water PET and fractional flow reserve in patients with suspected coronary artery disease. The WATERDAY study. Eur J Nucl Med Mol Imaging. 2018;45:1079–90.
96. Wells RG, Marvin B, Poirier M, Renaud J, deKemp RA, Ruddy TD. Optimization of SPECT measurement of myocardial blood flow with corrections for attenuation, motion, and blood binding compared with PET. J Nucl Med. 2017;58:2013–9.
97. Han S, Kim YH, Ahn JM, Kang SJ, Oh JS, Shin E, et al. Feasibility of dynamic stress (201)Tl/rest (99m)Tc-tetrofosmin single photon emission computed tomography for quantification of myocardial perfusion reserve in patients with stable coronary artery disease. Eur J Nucl Med Mol Imaging. 2018;45:2173–80.
98. Ma R, Wang L, Wu D, Wang M, Sun X, Hsu B, et al. Myocardial blood flow quantitation in patients with congestive heart failure: head-to-head comparison between rapid-rotating gantry SPECT and CZT SPECT. J Nucl Cardiol. 2020;27(6):2287–302.
99. Nkoulou R, Fuchs TA, Pazhenkottil AP, Kuest SM, Ghadri JR, Stehli J, et al. Absolute myocardial blood flow and flow reserve assessed by gated SPECT with cadmium-zinc-telluride detectors using 99mTc-tetrofosmin: head-to-head comparison with 13N-ammonia PET. J Nucl Med. 2016;57:1887–92.
100. Ben Bouallegue F, Roubille F, Lattuca B, Cung TT, Macia JC, Gervasoni R, et al. SPECT myocardial perfusion reserve in patients with multivessel coronary disease: correlation with angiographic findings and invasive fractional flow reserve measurements. J Nucl Med. 2015;56:1712–7.
101. Otaki Y, Manabe O, Miller RJH, Manrique A, Nganoa C, Roth N, et al. Quantification of myocardial blood flow by CZT-SPECT with motion correction and comparison with (15) O-water PET. J Nucl Cardiol. 2019.
102. Dorbala S, Vangala D, Sampson U, Limaye A, Kwong R, Di Carli MF. Value of vasodilator left ventricular ejection fraction reserve in evaluating the magnitude of myocardium at risk and the extent of angiographic coronary artery disease: a 82Rb PET/CT study. J Nucl Med. 2007;48:349–58.
103. Brodov Y, Fish M, Rubeaux M, Otaki Y, Gransar H, Lemley M, et al. Quantitation of left ventricular ejection fraction reserve from early gated regadenoson stress Tc-99m high-efficiency SPECT. J Nucl Cardiol. 2016;23:1251–61.
104. Slomka PJ, Betancur J, Liang JX, Otaki Y, Hu LH, Sharir T, et al. Rationale and design of the REgistry of Fast Myocardial Perfusion Imaging with NExt generation SPECT (REFINE SPECT). J Nucl Cardiol. 2018;27(3):1010–21.
105. Otaki Y, Betancur J, Sharir T, Hu L-H, Gransar H, Liang JX, et al. 5-Year prognostic value of quantitative vs visual myocardial perfusion imaging in subtle perfusion defects: results from the REFINE SPECT registry. JACC Cardiovasc Imaging. 2020;13(3):774–85.
106. Betancur J, Commandeur F, Motlagh M, Sharir T, Einstein AJ, Bokhari S, et al. Deep learning for prediction of obstructive disease from fast myocardial perfusion SPECT: a multicenter study. JACC Cardiovasc Imaging. 2018;11:1654–63.

107. Hu LH, Sharir T, Miller RJH et al. Upper reference limits of transient ischemic dilation ratio for different protocols on new-generation cadmium zinc telluride cameras: A report from REFINE SPECT registry. J Nucl Cardiol 2020;27:1180–1189.
108. Zeng GL, Stevens AM. Multidivergent-beam stationary cardiac SPECT. Med Phys. 2009;36:2860–9.
109. Dey J. Improvement of performance of cardiac SPECT camera using curved detectors with pinholes. IEEE Trans Nucl Sci. 2012;59:334–47.
110. Bhusal N, Dey J, Xu J, Kalluri K, Konik A, Mukherjee JM, et al. Performance analysis of a high-sensitivity multi-pinhole cardiac SPECT system with hemi-ellipsoid detectors. Med Phys. 2019;46:116–26.
111. Miyagawa M, Nishiyama Y, Uetani T, Ogimoto A, Ikeda S, Ishimura H, et al. Estimation of myocardial flow reserve utilizing an ultrafast cardiac SPECT: comparison with coronary angiography, fractional flow reserve, and the SYNTAX score. Int J Cardiol. 2017;244: 347–53.
112. Zavadovsky KV, Mochula AV, Boshchenko AA, Vrublevsky AV, Baev AE, Krylov AL, et al. Absolute myocardial blood flows derived by dynamic CZT scan vs invasive fractional flow reserve: correlation and accuracy. J Nucl Cardiol. 2019;28(1):249–59.
113. Mouden M, Ottervanger JP, Knollema S, Timmer JR, Reiffers S, Oostdijk AH, et al. Myocardial perfusion imaging with a cadmium zinc telluride-based gamma camera versus invasive fractional flow reserve. Eur J Nucl Med Mol Imaging. 2014;41:956–62.
114. Chikamori T, Hida S, Tanaka N, Igarashi Y, Yamashita J, Shiba C, et al. Diagnostic performance of a cadmium-zinc-telluride single-photon emission computed tomography system with low-dose technetium-99m as assessed by fractional flow reserve. Circ J. 2016;80:1217–24.
115. Gimelli A, Pugliese NR, Kusch A, Giorgetti A, Marzullo P. Accuracy of cadmium-zinc-telluride imaging in detecting single and multivessel coronary artery disease: is there any gender difference? Int J Cardiol. 2019;274:388–93.
116. Nakazato R, Berman DS, Gransar H, Hyun M, Miranda-Peats R, Kite FC, et al. Prognostic value of quantitative high-speed myocardial perfusion imaging. J Nucl Cardiol. 2012;19:1113–23.
117. Chowdhury FU, Vaidyanathan S, Bould M, Marsh J, Trickett C, Dodds K, et al. Rapid-acquisition myocardial perfusion scintigraphy (MPS) on a novel gamma camera using multipinhole collimation and miniaturized cadmium-zinc-telluride (CZT) detectors: prognostic value and diagnostic accuracy in a 'real-world' nuclear cardiology service. Eur Heart J Cardiovasc Imaging. 2014;15:275–83.
118. De Lorenzo A, Peclat T, Amaral AC, Lima RSL. Prognostic evaluation in obese patients using a dedicated multipinhole cadmium-zinc telluride SPECT camera. Int J Cardiovasc Imaging. 2016;32:355–61.
119. Yokota S, Mouden M, Ottervanger JP, Engbers E, Knollema S, Timmer JR, et al. Prognostic value of normal stress-only myocardial perfusion imaging: a comparison between conventional and CZT-based SPECT. Eur J Nucl Med Mol Imaging. 2016;43:296–301.
120. Engbers EM, Timmer JR, Mouden M, Knollema S, Jager PL, Ottervanger JP. Prognostic value of myocardial perfusion imaging with a cadmium-zinc-telluride SPECT camera in patients suspected of having coronary artery disease. J Nucl Med. 2017;58:1459–63.
121. Lima R, Peclat T, Soares T, Ferreira C, Souza AC, Camargo G. Comparison of the prognostic value of myocardial perfusion imaging using a CZT-SPECT camera with a conventional anger camera. J Nucl Cardiol. 2017;24:245–51.
122. Lima RSL, Peclat TR, Souza A, Nakamoto AMK, Neves FM, Souza VF, et al. Prognostic value of a faster, low-radiation myocardial perfusion SPECT protocol in a CZT camera. Int J Cardiovasc Imaging. 2017;33:2049–56.
123. Betancur J, Otaki Y, Motwani M, Fish MB, Lemley M, Dey D, et al. Prognostic value of combined clinical and myocardial perfusion imaging data using machine learning. JACC Cardiovasc Imaging. 2018;11:1000–9.
124. van Dijk JD, Borren NM, Mouden M, van Dalen JA, Ottervanger JP, Jager PL. Effect of a patient-specific minimum activity in stress myocardial perfusion imaging using CZT-SPECT: prognostic value, radiation dose, and scan outcome. J Nucl Cardiol. 2018;25:26–35.

Part III

PET/CT

Myocardial Blood Flow Quantification with PET/CT: Applications

8

Chaitanya S. Rojulpote and Paco E. Bravo

8.1 Introduction

Coronary artery disease (CAD) is the leading cause of death in the USA and worldwide. Nuclear imaging studies, including PET, have traditionally played a key role in the diagnosis, and management of individuals with suspected or known CAD. Experimental data using PET imaging techniques have been fundamental for enhancing the understanding of CAD, and also for the development and implementation of new myocardial perfusion tracers in clinical practice.

Current SPECT methodology is mostly limited to a qualitative assessment of the regional distribution or activity concentration of perfusion tracers in the myocardium. In contrast, PET allows additional in vivo quantitative measurement of radiotracer distribution in the heart; thereby it is possible to evaluate absolute myocardial blood flow (MBF) at baseline and during stressing conditions.

8.2 Coronary Circulation

A review of the coronary circulation physiology is critical for a better understanding of the non-invasive quantification of MBF using PET or any other modality. The heart is highly metabolically active and owns one of the highest oxygen consumptions per tissue mass of all human organs. The average resting coronary blood flow ranges between 0.5 and 1.0 mL blood per minute per gram myocardium (mL/

C. S. Rojulpote · P. E. Bravo (✉)
Divisions of Nuclear Medicine and Cardiology, Departments of Radiology and Medicine, University of Pennsylvania, Philadelphia, PA, USA
e-mail: Paco.Bravo@uphs.upenn.edu

S. G. Nekolla, C. Rischpler (eds.), *Hybrid Cardiac Imaging*,
https://doi.org/10.1007/978-3-030-83167-7_8

min/g), representing approximately 5% of the total cardiac output. Myocardial oxygen extraction is very high at baseline, averaging 60–80% of all arterially delivered oxygen (compared with 25% for the rest of the body) [1]. Consequently, further increments in oxygen consumption, for example, during exercise, are mostly met by proportional increments in coronary blood flow. Myocardial ischemia results whenever oxygen demand exceeds supply.

Anatomically, the coronary circulation can be divided into two well-defined vascular compartments: (1) the large conduit, low-resistance, epicardial coronary arteries and (2) the small, high-resistance, coronary microvasculature composed of the pre-arteriolar (100–300 μm) and arteriolar (<100 μm) vessels [2]. Blood flow across the myocardium is dependent on the coronary perfusion gradient generated between the diastolic aortic pressure and left ventricular end-diastolic pressure. Under normal hemodynamic conditions, coronary perfusion pressure does not diminish significantly along the large epicardial conduit vessels and much of the pressure drop occurs at the coronary microvascular network, where the driving pressure declines proportionally to the cross-sectional diameter of the small coronary vessels. Flow is also characterized by marked phasic variation during the cardiac cycle with coronary perfusion occurring mostly during diastole and reducing significantly during systole.

The coronary circulation is tightly auto-regulated by several factors influencing the vasomotor and metabolic tone of the coronary microcirculation, remaining constant over a wide range of perfusion pressures at baseline and potentially augmenting three- to fivefold during exercise or vasodilator stress to meet the high metabolic demands of the heart. This change in flow from baseline is known as coronary flow reserve (CFR) and has become an extremely important marker for both diagnosis and prognosis in patients being investigated for ischemic and non-ischemic heart disease. CFR is tightly related to oxygen consumption and the metabolic demand of the myocardium and will be affected by any conditions that adversely rise the resting coronary blood flow and/or impair flow during stress situations.

For example, changes in myocardial work and afterload, such as tachycardia, hypertension, and heart failure, and/or reductions in arterial oxygen supply, including anemia and hypoxia, typically lead to proportional changes in resting flow to meet the higher metabolic demands of the myocardium at baseline, and thus may reduce CFR, which is defined as the maximum hyperemic increase in coronary blood flow during exercise or pharmacologic stress above the resting or baseline coronary flow. On the other hand, the presence of flow-limiting epicardial coronary stenosis will result in downstream reduction of the coronary perfusion pressure. In this setting, autoregulation of the coronary microcirculation can maintain baseline flow even if mean coronary pressures are as low as 40 mmHg [3]. However, at this point, the myocardium subtended by the stenotic vessel will fail to further augment the coronary flow during periods of stress or higher metabolic demand, translating into impaired CFR and eventually symptomatic ischemia. Failure of the coronary flow to augment during vasodilator stress can also occur in the absence of epicardial coronary stenosis and is typically related to microvascular dysfunction. In addition, both tachycardia (by reducing diastolic

filling time), and/or elevated preload (by reducing coronary driving pressure) can also negatively affect CFR.

8.3 Pre-clinical Experience/Validation Studies

In general, radiopharmaceuticals are considered suitable for myocardial perfusion imaging and absolute MBF quantification, if after injection, they exhibit high first-pass extraction fraction (at a wide range of flows), rapid blood pool clearance, stable myocardial retention with minimal washout, and high target-to-background ratios. Dynamic imaging is also a requirement to track the tracer activity in the myocardium and blood pool to generate time activity curves for the myocardium and the arterial input function, respectively.

Nitrogen-13 (^{13}N) ammonia is one of the most studied tracers in the pre-clinical and clinical setting. ^{13}N-ammonia enters the myocardial cells by diffusion across the sarcolemma, followed by metabolic conversion to ^{13}N-glutamine by the glutamine synthetase, becoming trapped within the cell. Schelbert et al. [4], in a landmark experiment, evaluated the kinetics of ^{13}N-ammonia in detail using an open-chest dog model. He compared the myocardial tissue concentration of ^{13}N-ammonia in vivo and ex vivo, against MBF (measured by radioactive polystyrene microspheres, which are considered the gold standard for MBF estimation) over three different flow ranges: (1) at baseline, (2) during mid-left anterior descending coronary artery (LAD) ligation; and (3) inducing hyperemia of the left circumflex coronary artery (LCx) by intracoronary Papaverine HCl administration. He found that regional myocardial $^{13}NH_3$ concentration was closely related, although in a non-linear fashion, to MBF as it decreased 62% when MBF dropped 100% from baseline, and increased 63% and 103%, when MBF augmented 100% and 200%, respectively, from baseline. Additional MBF increments resulted in disproportionately smaller ^{13}N-ammonia concentration changes. In this experiment, the first-pass extraction fraction of ^{13}N-ammonia was inversely related to MBF, as the mean first-pass extraction fraction at baseline MBF (105.7 ± 35.9 mL/min/100 g) was 72 ± 0.06%, and decreased to 55 ± 0.05% ($p < 0.001$) during MBF hyperemia (333.0 ± 69.4 mL/min/100 g). In this study myocardial ^{13}N-ammonia retention was stable, and the clearance was minimal (biological half-life of 159 min) [4].

Concomitantly, Gould et al. [5], employing a similar animal model, demonstrated that angiographycally-proven coronary artery luminal stenosis of 47% or greater diameter narrowing could be detected using a rest and vasodilator stress protocol (dypiridamole) with ^{13}N-ammonia PET. A few years later, Shah et al. [6] compared the agreement between MBF derived from serial cross-sectional PET images, and MBF determined by the standard microsphere technique in instrumented dogs at baseline, high and low blood flows. In this study, the correlation of the two techniques was excellent, showing a nearly linear relation for flows from 44 to 200 mL/min/100 g, and reaching a plateau at higher flows [6]. These and other experimental studies [7] confirmed the appropriateness of ^{13}N-ammonia as a PET perfusion tracer for: (1) qualitative assessment of the regional distribution of the

tracer in the heart and (2) quantitative measurement of MBF under a variety of physiological and pathological conditions.

Parallel to ^{13}N-ammonia, rubidium-82 (^{82}Rb) has also undergone extensive investigation. ^{82}Rb is a potassium analog with an ultra-short half-life (78 s), actively taken up by myocytes via the Na/K-ATPase. Similar to ^{13}N-ammonia, animal studies have shown that the uptake of ^{82}Rb in the myocardium is non-linearly related to blood flow due to a decrease in the first-pass extraction fraction of ^{82}Rb at high flow rates [8, 9]. Likewise, quantitative PET flow assessment of ^{82}Rb under different hemodynamic states has also been validated against microspheres using canine models of coronary artery stenosis [10, 11].

Oxygen-15 (^{15}O)-water is another important flow agent widely studied in the preclinical and clinical setting. ^{15}O-water is regarded as an ideal flow agent based on its high first-pass extraction fraction independent of flow. In an open-chest model of coronary stenosis, the first-pass extraction fraction of ^{15}O-water was in average 96 ± 5% at the baseline flows and did not change significantly between a wide range of coronary flows (0.12 and 2.3 mL/min/g) [12]. However, this tracer has a fast washout, making delayed acquisition for myocardial perfusion imaging challenging, and thus, somewhat limiting its clinical applicability, in addition to the need for an onsite cyclotron.

Lastly, the investigational radiotracer Fluorine-18 (^{18}F)-Flurpiridaz is a novel fluorinated compound undergoing extensive investigation. ^{18}F-Flurpiridaz binds to the mitochondrial complex I of the electron transport chain with high affinity, and experimental data reports a higher net myocardial uptake in relation to coronary flow compared to ^{13}N-ammonia [13], and likely comparable to ^{15}O-water, with the added advantage of having high retention in the myocardium and a longer half-life (~2 h), therefore, allowing exercise-based imaging protocols in the future.

8.4 Myocardial Blood Flow with PET: Reference Values

PET is a robust technique for MBF quantification, however, there are a number of technical, physiological, and biological considerations that may influence the MBF results, including the selection of the perfusion radiotracer (^{82}Rb vs. ^{13}N-ammonia), scanner (2D vs. 3D), method for time activity curves generation (region of interest vs. factor analysis), type of kinetic analysis performed (e.g. compartment vs. retention model), software package (e.g. 4DM vs. Cedars-Sinai), as well as subject-specific characteristics (e.g. number of risk factors) and baseline hemodynamics (e.g. blood pressure and heart rate).

Consequently, it is not surprising that the definition of PET-derived reference values for MBF remains a matter of debate. Table 8.1 depicts a summary of 30 PET studies that included over 550 healthy volunteers for the purposes of MBF quantification with various methods and radiotracers [14–43]. While the average rest MBF (0.81 mL/min/g ± 0.16), stress MBF (3.06 mL/min/g ± 0.78), and CFR (4.09 ± 1.13) were relatively similar within studies, there was, however, significant variation in stress flow and CFR ranges (large standard deviation) between studies, consequently

Table 8.1 Summary of PET literature on the mean and proposed reference values for myocardial blood flow (MBF) and coronary flow reserve (CFR) quantification in healthy volunteers

Flow	Studies (*n*)	Subjects (*n*)	Age	Tracer	Mean ± SD	Lower limits[a]	Upper limits
Rest MBF	4 [14–17]	165	30 ± 5	^{82}Rb	0.74 ± 0.18	0.29	1.19
Stress MBF	4 [14–17]	165	30 ± 5	^{82}Rb	2.75 ± 0.74	0.90	4.60
CFR	3 [14, 15, 17]	154	29 ± 5	^{82}Rb	4.08 ± 0.96	1.68	6.48
Rest MBF	15 [15, 18–32]	210	36 ± 10	^{13}N	0.74 ± 0.13	0.42	1.07
Stress MBF	15 [15, 18–32]	202	36 ± 10	^{13}N	2.72 ± 0.60	1.22	4.22
CFR	12 [15, 18, 20–23, 25, 26, 28–31]	146	39 ± 9	^{13}N	4.00 ± 0.97	1.58	6.43
Rest MBF	13 [32–43]	200	37 ± 7	^{15}O	0.92 ± 0.18	0.47	1.37
Stress MBF	10 [16, 32, 34, 35, 37–42]	183	40 ± 7	^{15}O	3.57 ± 1.08	0.87	6.27
CFR	8 [34, 35, 37–42]	157	42 ± 7	^{15}O	4.18 ± 1.43	0.61	7.76
Rest MBF	29 [14–22, 24–43]	575	36 ± 8	^{82}Rb, ^{13}N, ^{15}O	0.81 ± 0.16	0.41	1.21
Stress MBF	26 [14–23, 25–32, 34, 35, 37–42]	550	36 ± 7	^{82}Rb, ^{13}N, ^{15}O	3.06 ± 0.78	1.11	5.01
CFR	22 [14, 15, 17–21, 24, 28–31, 33–40, 42, 43]	457	37 ± 7	^{82}Rb, ^{13}N, ^{15}O	4.09 ± 1.13	1.27	6.92
Rest MBF	Largest[b]	125	29 ± 5	^{82}Rb	0.70 ± 0.15	0.33	1.08
Stress MBF	PET	125	29 ± 5	^{82}Rb	2.75 ± 0.58	1.30	4.2
CFR	Study [17]	125	29 ± 5	^{82}Rb	4.03 ± 0.84	1.93	6.13

[a]Lower reference limit and upper reference limit were defined as values 2.5 standard deviations (SD) below and above the mean, respectively
[b]Single largest PET study to date investigating MBF and CFR reference values in healthy volunteers

yielding lower than expected reference values if one were to define the lower limits of normal for stress MBF (<1.11 mL/min/g) and CFR (<1.27) using this large pool of studies. In contrast, the single largest PET study that included 125 patients found comparable rest MBF (0.70 mL/min/g ± 0.15), stress MBF (2.75 mL/min/g ± 0.58), and CFR (4.03 ± 0.84), but significantly less flow heterogeneity between patients (as shown by the narrower SD) so that the lower limits of normal for stress MBF (<1.30 mL/min/g) and CFR (1.93) would be higher based solely on this study [17].

These data (from Table 8.1) also revealed that rest (0.92 mL/min/g ± 0.18) and stress MBF (3.57 mL/min/g ± 1.08) with ^{15}O-water were significantly higher in healthy volunteers than that of ^{13}N-ammonia (0.74 mL/min/g ± 0.13 and 2.72 mL/min/g ± 0.60, respectively) or ^{82}Rb (0.74 mL/min/g ± 0.18 and 2.75 mL/min/g ± 0.74, respectively), whereas CFR was highly comparable between tracers (4.18 ± 1.43 vs. 4.00 ± 0.97 vs. 4.08 ± 0.96).

From a methodology perspective, the technique used to determine the arterial input function, and generate tissue time activity curves, and the type of kinetic analysis, and software package employed, can lead to large differences in flow estimates. For example, prior studies have found significant differences in the absolute estimates of rest and stress MBF when comparing different methods and software packages in the same population with ^{82}Rb and $^{13}NH_3$, whereas CFR tends to be less software dependent [44, 45].

Age and certain hemodynamics also appear to affect MBF. Czernin et al. [19] (using $^{13}NH_3$) observed that MBF at rest increases with age, heart rate, and systolic blood pressure in normal subjects, in contrast to dipyridamole-induced hyperemic flow, which appears to be unrelated to these baseline characteristics [19].

8.5 MBF and CFR in Ischemic Heart Disease

Similar to experimental data, PET-derived flow data has been associated with the degree of luminal stenosis severity on coronary angiography in humans [46, 47]. In general, stress MBF and CFR are inversely and non-linearly correlated to stenosis severity independent of the radiotracer investigated [46, 47]. Patients with coronary luminal stenosis <50% diameter narrowing usually have similar CFR values compared to age-matched control individuals; however, there is a stepwise decrement of CFR at increasing degrees of luminal stenosis. Importantly, PET may have the potential to differentiate coronary artery stenosis of intermediate to high-grade severity (50–70% vs. 70–90% vs. >90%) by absolute measurements of MBF [46]. Muzik et al. demonstrated similar findings using ^{13}N-ammonia (≥50% vs. ≥70% vs. ≥90%) to show the correlation between PET-derived CFR and MBF estimates with coronary angiography by means of a dynamic PET acquisition method (Table 8.2) [31]. Furthermore, this method was found to be more sensitive than coronary angiography in earlier stages of CAD, showcasing the utility of PET to evaluate blood flow at a microcirculatory level.

While the limitations of interpreting myocardial perfusion imaging based on relative analysis are known, recent studies have demonstrated that absolute blood

Table 8.2 Summary of the diagnostic accuracy of stress MBF and coronary flow reserve for detection of flow-limiting coronary artery stenosis

Author—Journal—Year	Tracer	Flow cutoff	*N*	Reference	Sensitivity	Specificity	PPV	NPV
Naya—JNM—2014 [53]	^{82}Rb	CFR ≤ 1.93	290	High-risk CAD[a]	86%	46%	15%	97%
Kajander—Circ Cardio Imaging—2011 [49]	^{15}O-water	Stress MBF < 2.50	104	FFR ≤ 0.80 or ≥50% stenosis	95%	91%	86%	97%
Muzik—JACC—1998 [31]	$^{13}NH_3$	Stress MBF < 1.52	31	≥50% stenosis	73%	80%	N/A	N/A
		Stress MBF < 1.52		≥70% stenosis	84%	78%	N/A	N/A
		Stress MBF < 1.52		≥90% stenosis	92%	75%	N/A	N/A
		CFR < 2.74		≥50% stenosis	82%	78%	N/A	N/A
		CFR < 2.74		≥70% stenosis	93%	75%	N/A	N/A
		CFR < 2.74		≥90% stenosis	97%	73%	N/A	N/A
Bravo—European Heart Journal—2017 [54]	$^{13}NH_3$	Stress MBF < 1.70	94	≥70% stenosis	92%	70%	41%	97%
Fiechter—JNM—2012 [50]	$^{13}NH_3$	CFR < 2.00	73	≥50% stenosis	96%	80%	93%	89%
Lee—Circ Cardiovasc Imaging—2016 [55]	$^{13}NH_3$	Stress MBF < 1.99	130	FFR ≤ 0.80	78%	73%	56%	88%
		CFR < 2.12		FFR ≤ 0.80	70%	66%	47%	83%
		RFR < 0.82[b]		FFR ≤ 0.80	83%	84%	69%	92%
		Stress MBF < 1.84		FFR ≤ 0.75	76%	80%	42%	94%
		CFR < 2.00		FFR ≤ 0.75	75%	72%	35%	92%
		RFR < 0.78[b]		FFR ≤ 0.75	67%	91%	61%	93%
Danad—JACC—2014 [56]	^{15}O-water	stress MBF ≤ 2.3	330	FFR ≤ 0.80 or >90% stenosis	89%	84%	79%	92%
		CFR < 2.5		FFR ≤ 0.80 or >90% stenosis	86%	72%	68%	88%

[a]High risk CAD defined as 2-vessel disease (≥70% stenosis), including the proximal left anterior descending artery; 3-vessel disease; or left main CAD (≥50% stenosis)

[b]RFR = relative flow reserve is the ratio of stress MBF in target myocardial territories to that of a reference vascular territory

flow quantification improved the accuracy of PET for identifying CAD [48]. A clinical trial studied 104 individuals with a high pretest likelihood of CAD using ^{15}O-water and found very high sensitivity (95%), and specificity (91%) in detecting flow-limiting CAD [49]. Of the 104 individuals in the trial, 38 were identified to have significant CAD, based on fractional flow reserve (FFR) ≤0.80 or angiographic coronary stenosis ≥50%, of which 24 were found to have multivessel disease. Absolute quantitative blood flow was able to accurately detect all but one of the 24 individuals with multivessel disease, but five false positives were identified where there was diminished MBF but no presence of CAD as per coronary angiography data. In comparison, relative uptake analysis accurately identified all but two of the 24 individuals with CAD but misidentified 26 other individuals in the study as having multivessel disease.

Others have also established the diagnostic value of global CFR over myocardial perfusion imaging alone to detect angiographically proven CAD [50]. In this study, coronary angiographic data identified 53 of the 73 individuals to have CAD. Initial visual PET assessment of the 73 individuals revealed ^{13}N-ammonia uptake to be abnormal in 46 and normal in 27 patients. However, when an CFR of less than 2.0 was incorporated as the model to best predict CAD, nine patients who were previously considered normal were reclassified as abnormal. These results were confirmed with coronary angiography, with improved sensitivity, specificity, negative predictive value, positive predictive value, and accuracy. This may be explained by the fact that assessing global CFR better reflects CAD beyond just the epicardial circulation and also includes endothelial dysfunction. This method may prove to be superior to regional CFR estimation due to better repeatability and reproducibility of global CFR [42, 51].

While the aforementioned studies have shown ^{13}N-ammonia and ^{15}O-water to be useful tracers for quantifying blood flow, Ziadi et al. sought to assess ^{82}Rb in quantifying CFR as an independent predictor in patients with obstructive multivessel CAD (3-vessels) [52]. Their study found that CFR was globally reduced in 22 of the 25 patients (88%), and moreover that a progressive reduction in the tracer predicted a high likelihood of triple vessel disease. Similarly, Naya and collaborators reported a high sensitivity (86%) and negative predictive value (97%) of CFR (≤1.93) ^{82}Rb PET to rule out high risk CAD defined as 2-vessel disease (≥70% stenosis), including the proximal left anterior descending artery; 3-vessel disease; or left main CAD (≥50% stenosis) [53].

Beyond the scope of CAD, quantitative MBF also provides valuable clinical information in post-transplant complications in long-term orthotopic heart transplant survivors. A study investigating the added diagnostic value of quantifying MBF to standard myocardial perfusion imaging for detecting cardiac allograft vasculopathy found that this method not only improves the ability to detect and grade the vasculopathy, but is also predictive in the outcome of major adverse cardiac events [54]. Likewise, an important correlation between stress MBF and angiographic coronary stenosis was shown (Fig. 8.1).

Table 8.2 summarizes the diagnostic performance of stress MBF and CFR for the detection of flow-limiting CAD as defined by angiographic stenosis or FFR [31, 49, 50, 53–56]. Interestingly, in many of these studies stress MBF appears to yield a

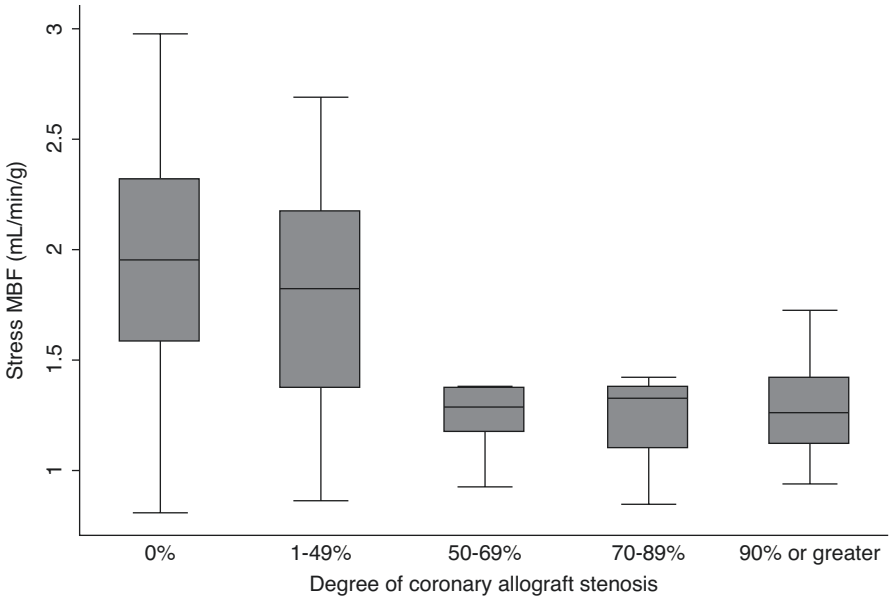

Fig. 8.1 Box plot analysis in 198 vessels of the inverse relationship between regional stress myocardial blood flow (MBF) and degree of coronary allograft stenosis ($r^2 = -0.22$, $p < 0.0001$)

higher sensitivity to detect CAD than CFR, which may reflect a cleaner assessment of the epicardial perfusion pressure than CFR which is also influenced or affected by changes in the baseline MBF. For this reason, some authors have proposed the use of coronary flow capacity, which is an integration of CFR and maximal MBF, a measure that may potentially allow for a more extensive assessment of patients with a suspected or known CAD as compared to CFR alone [57–59]. However, this remains an area of research, and further studies investigating the role of coronary flow capacity, as well as other markers such as relative flow reserve are needed [55].

8.6 Relationship of CFR with FFR in Ischemic Heart Disease

While CFR may provide information on a stenotic lesion, direct visualization of coronary microcirculation may not be possible due to the limited resolution of current imaging modalities. Fractional flow rate (FFR) is an invasive method to assess the severity of stenosis in the epicardial coronary system. It is defined as a ratio of pressure measured proximal to the stenosis and pressure distal to the stenosis, with a threshold for ischemia set at ≤0.80. Recent studies such as FAME [60], DEFER [61], and FAME 2 [62] have established evidence-based approaches to guide treatment based on FFR evaluation. Patients with FFR ≤0.80 may benefit from revascularization therapies while those with an FFR > 0.80 can be managed with medical therapy. In fact, current guidelines state that FFR may prove to be useful and is indicated in patients with moderate stenosis (e.g. 50–90%) when there is a lack of

functional information [63]. An FFR ≤0.80 with a CFR > 2.0 is indicative of flow-limiting stenosis with preserved microvascular function (or microvascular dysfunction, CFR < 2) and warrants percutaneous coronary intervention (PCI). Similarly, an FFR > 0.80 and CFR > 2 indicates non-flow-limiting stenosis with preserved microvascular function (or microvascular dysfunction, CFR < 2) and requires medical management without PCI [64]. While CFR and FFR are both used to identify ischemic areas, they are often discordances in approximately 30% of cases with intermediate stenosis [65, 66]. Moreover, the interplay between CFR and FFR, though not fully understood, is thought to be mediated by coronary microcirculation resistance which is largely responsible for the CFR-FFR discordance [67, 68]. An abnormal CFR will not be able to accurately distinguish epicardial stenotic lesions from that of non-obstructive vascular dysfunction [53]. Likewise, FFR cannot consider the presence of diffuse disease that may be present in conjunction with a focal stenosis. Garcia et al. conducted a study to better understand the relationship between the two parameters and found that both FFR and CFR (measured by ultrasound) are in fact complementary tools and moreover that both should be used simultaneously to guide percutaneous coronary intervention (PCI) [69]. This study also sought to establish the prognostic value of a CFR/FFR ratio by assessing pre- and post-PCI CFR and found that CFR in fact increased significantly post-PCI and thus, may have potential to better guide and optimize patient care.

8.7 Prognostic Value of Stress MBF and CFR for Risk Stratification

Coronary artery disease is a combination of multilevel microcirculatory obstructive alterations in the coronary circulation that can be either focal or diffuse [70]. The risk stratification of CAD and its complications requires a comprehensive assessment of the vascular disease activity. CFR's strength lies in its ability to integrate the hemodynamic effects of epicardial coronary atherosclerosis and luminal narrowing with that of microvascular dysfunction thereby being a more accurate marker of the coronary circulation, and this has translated into enhanced risk prediction of adverse cardiovascular events in addition to other indicators such as LVEF, percentage of ischemic myocardium, transient ischemic dilatation, LVEF reserve, and coronary calcium score [71].

Numerous studies have shown that impaired CFR is associated with adverse events independent of the presence of obstructive CAD [72]. A study by Tio et al. showed that after adjustment for age and sex, myocardial perfusion reserve was associated with a hazard ratio for cardiac death of 4.11 (95% CI, 2.98–5.67) per SD decrease, whereas the risk for LVEF was 2.76 (2.00–3.82) per SD which clearly underlines the advantage that coronary flow-based indices have, over left ventricular ejection fraction in predicting negative outcomes [73]. Murthy also showed in a previous study that CFR is a potent predictor of cardiovascular-related mortality independent of myocardial ischemia, scar, LV dysfunction, and traditional risk factors [74]. Table 8.3 was compiled based on several studies investigating the prognostic value of MBF and CFR [72, 73, 75–79]. Overall, all studies consistently show that CFR (typically with a cutoff ≤2.0) serves as independent risk marker for

Table 8.3 Summary of prognostic value of stress MBF and coronary flow reserve for risk prediction

Author, year	*N*	Age	PET tracer	Parameter/ cutoff	Follow-up (years)	All-cause mortality		Cardiac death		Non-fatal MI		MACE composite	
						Univariate HR	Multivariate HR	Univariate HR	Multivariate HR	Univariate HR	Multivariate HR	Univariate HR	Multivariate HR
Herzog et al. (2009) [75]	229	60 ± 12 or median [IQR]	^{13}N-ammonia	CFR < 2.0	5.5 ± 2.1 or median [IQR]	n/a	n/a	3.53 (1.56–7.97)	2.86 (1.24–6.59)	n/a	n/a	2.14 (1.35–3.37)	1.60 (1.00–2.57)
Tio et al. (2009) [73]	344	66 ± 11	^{13}N-ammonia	CFR (per SD decrease)	7.1	n/a	n/a	4.11 (2.98–5.67)	4.08 (2.50–6.65)	n/a	n/a	1.60 (1.31–1.94)	1.44 (1.14–1.84)
Fukushima et al. (2011) [76]	224	57 ± 12	^{82}Rb	CFR < 2.0	1 ± 0.76	n/a	2.93 (1.3–6.65)	n/a	n/a	n/a	n/a	n/a	n/a
Ziadi et al. (2011) [77]	677	64 ± 12	^{82}Rb	CFR < 2.0	1.1	n/a	n/a	n/a	n/a	2.33 (1.43–3.23)	3.3 (1.1–9.5)	1.74 (0.99–2.49)	2.4 (1.4–4.4)
Gupta et al. (2017) [78]	4029	66 (57–75)	^{13}N-ammonia and ^{82}Rb	CFR < 2.0	Median follow up of 5.6	n/a	n/a	3.7 (2.76–4.11)	1.83 (1.47–2.27)	n/a	n/a	n/a	n/a
Neglia et al. (2002) [72]	67	52 ± 12	^{13}N-ammonia	CFR ≤ 2.0	3.75 ± 3.08	n/a	n/a	6.92	n/a	n/a	n/a	n/a	n/a
Patel et al. (2019) [79]	12,594	68 ± 12	^{82}Rb	CFR (per 0.1 decrease)	Median 3.2		1.09 (1.08–1.10)		1.03 (1.01–1.05)				

all-cause mortality, cardiac death, and MACE. These studies also suggest that CFR may carry higher prognostic value compared to stress MBF. In fact, Gupta reported in over 4000 patients that global CFR is a stronger predictor of cardiovascular-related deaths than stress MBF after adjustment for a large number of clinical variables [78]. As previously mentioned, CFR is tightly related to oxygen consumption and the metabolic demand of the myocardium, and will be, thus, affected by any conditions that adversely rise the resting MBF and/or impair stress MBF, which may explain the stronger predictive value of CFR, by factoring in the results of rest and stress MBF.

A meta-analysis of 11 studies, including 11,867 patients, has further confirmed the power of CFR for predicting MACE (pooled HR 1.93 [95% CI 1.65–2.27]) [80]. Finally, a recent study totaling 12,594 patients who underwent ^{82}Rb for evaluation of suspected or known CAD showed a significant interaction between CFR and early coronary revascularization such that patients with CFR < 1.8 had a survival benefit with early revascularization, regardless of type of revascularization or level of myocardial ischemia, suggesting that in addition to its strong risk prediction, CFR may help identify patients with a survival benefit from early percutaneous or surgical revascularization beyond perfusion defects on MPI [79].

8.8 Summary

In summary myocardial blood flow quantification is a powerful tool that when combined with myocardial perfusion imaging may improve the diagnostic and prognostic value of cardiac PET during the evaluation of individuals with suspected or known CAD.

References

1. Duncker DJ, Bache RJ. Regulation of coronary blood flow during exercise. Physiol Rev. 2008;88:1009–86.
2. Muller JM, Davis MJ, Chilian WM. Integrated regulation of pressure and flow in the coronary microcirculation. Cardiovasc Res. 1996;32:668–78.
3. Canty JM Jr. Coronary pressure-function and steady-state pressure-flow relations during autoregulation in the unanesthetized dog. Circ Res. 1988;63:821–36.
4. Schelbert HR, Phelps ME, Hoffman EJ, Huang SC, Selin CE, Kuhl DE. Regional myocardial perfusion assessed with N-13 labeled ammonia and positron emission computerized axial tomography. Am J Cardiol. 1979;43:209–18.
5. Gould KL, Schelbert HR, Phelps ME, Hoffman EJ. Noninvasive assessment of coronary stenoses with myocardial perfusion imaging during pharmacologic coronary vasodilatation. V. Detection of 47 percent diameter coronary stenosis with intravenous nitrogen-13 ammonia and emission-computed tomography in intact dogs. Am J Cardiol. 1979;43:200–8.
6. Shah A, Schelbert HR, Schwaiger M, Henze E, Hansen H, Selin C, Huang SC. Measurement of regional myocardial blood flow with N-13 ammonia and positron-emission tomography in intact dogs. J Am Coll Cardiol. 1985;5:92–100.
7. Bergmann SR, Hack S, Tewson T, Welch MJ, Sobel BE. The dependence of accumulation of 13NH3 by myocardium on metabolic factors and its implications for quantitative assessment of perfusion. Circulation. 1980;61:34–43.

8. Selwyn AP, Allan RM, L'Abbate A, Horlock P, Camici P, Clark J, O'Brien HA, Grant PM. Relation between regional myocardial uptake of rubidium-82 and perfusion: absolute reduction of cation uptake in ischemia. Am J Cardiol. 1982;50:112–21.
9. Mullani NA, Goldstein RA, Gould KL, Marani SK, Fisher DJ, O'Brien HA Jr, Loberg MD. Myocardial perfusion with rubidium-82. I. Measurement of extraction fraction and flow with external detectors. J Nucl Med. 1983;24:898–906.
10. Herrero P, Markham J, Shelton ME, Weinheimer CJ, Bergmann SR. Noninvasive quantification of regional myocardial perfusion with rubidium-82 and positron emission tomography. Exploration of a mathematical model. Circulation. 1990;82:1377–86.
11. Lautamaki R, George RT, Kitagawa K, Higuchi T, Merrill J, Voicu C, DiPaula A, Nekolla SG, Lima JA, Lardo AC, Bengel FM. Rubidium-82 PET-CT for quantitative assessment of myocardial blood flow: validation in a canine model of coronary artery stenosis. Eur J Nucl Med Mol Imaging. 2009;36:576–86.
12. Bergmann SR, Fox KA, Rand AL, McElvany KD, Welch MJ, Markham J, Sobel BE. Quantification of regional myocardial blood flow in vivo with H215O. Circulation. 1984;70:724–33.
13. Nekolla SG, Reder S, Saraste A, Higuchi T, Dzewas G, Preissel A, Huisman M, Poethko T, Schuster T, Yu M, Robinson S, Casebier D, Henke J, Wester HJ, Schwaiger M. Evaluation of the novel myocardial perfusion positron-emission tomography tracer 18F-BMS-747158-02: comparison to 13N-ammonia and validation with microspheres in a pig model. Circulation. 2009;119:2333–42.
14. Manabe O, Yoshinaga K, Katoh C, Naya M, deKemp RA, Tamaki N. Repeatability of rest and hyperemic myocardial blood flow measurements with 82Rb dynamic PET. J Nucl Med. 2009;50:68–71.
15. Lortie M, Beanlands RS, Yoshinaga K, Klein R, Dasilva JN, deKemp RA. Quantification of myocardial blood flow with 82Rb dynamic PET imaging. Eur J Nucl Med Mol Imaging. 2007;34:1765–74.
16. Lin JW, Sciacca RR, Chou RL, Laine AF, Bergmann SR. Quantification of myocardial perfusion in human subjects using 82Rb and wavelet-based noise reduction. J Nucl Med. 2001;42:201–8.
17. Sdringola S, Johnson NP, Kirkeeide RL, Cid E, Gould KL. Impact of unexpected factors on quantitative myocardial perfusion and coronary flow reserve in young, asymptomatic volunteers. J Am Coll Cardiol Img. 2011;4:402–12.
18. Chan SY, Brunken RC, Czernin J, Porenta G, Kuhle W, Krivokapich J, Phelps ME, Schelbert HR. Comparison of maximal myocardial blood flow during adenosine infusion with that of intravenous dipyridamole in normal men. J Am Coll Cardiol. 1992;20:979–85.
19. Czernin J, Muller P, Chan S, Brunken RC, Porenta G, Krivokapich J, Chen K, Chan A, Phelps ME, Schelbert HR. Influence of age and hemodynamics on myocardial blood flow and flow reserve. Circulation. 1993;88:62–9.
20. Dayanikli F, Grambow D, Muzik O, Mosca L, Rubenfire M, Schwaiger M. Early detection of abnormal coronary flow reserve in asymptomatic men at high risk for coronary artery disease using positron emission tomography. Circulation. 1994;90:808–17.
21. Sawada S, Muzik O, Beanlands RS, Wolfe E, Hutchins GD, Schwaiger M. Interobserver and interstudy variability of myocardial blood flow and flow-reserve measurements with nitrogen 13 ammonia-labeled positron emission tomography. J Nucl Cardiol. 1995;2:413–22.
22. Beanlands RS, Muzik O, Melon P, Sutor R, Sawada S, Muller D, Bondie D, Hutchins GD, Schwaiger M. Noninvasive quantification of regional myocardial flow reserve in patients with coronary atherosclerosis using nitrogen-13 ammonia positron emission tomography. Determination of extent of altered vascular reactivity. J Am Coll Cardiol. 1995;26:1465–75.
23. Czernin J, Auerbach M, Sun KT, Phelps M, Schelbert HR. Effects of modified pharmacologic stress approaches on hyperemic myocardial blood flow. J Nucl Med. 1995;36:575–80.
24. de Jong RM, Blanksma PK, Willemsen AT, Anthonio RL, Meeder JG, Pruim J, Vaalburg W, Lie KI. Posterolateral defect of the normal human heart investigated with nitrogen-13-ammonia and dynamic PET. J Nucl Med. 1995;36:581–5.

25. Muzik O, Paridon SM, Singh TP, Morrow WR, Dayanikli F, Di Carli MF. Quantification of myocardial blood flow and flow reserve in children with a history of Kawasaki disease and normal coronary arteries using positron emission tomography. J Am Coll Cardiol. 1996;28:757–62.
26. DeGrado TR, Hanson MW, Turkington TG, Delong DM, Brezinski DA, Vallee JP, Hedlund LW, Zhang J, Cobb F, Sullivan MJ, Coleman RE. Estimation of myocardial blood flow for longitudinal studies with 13N-labeled ammonia and positron emission tomography. J Nucl Cardiol. 1996;3:494–507.
27. Nagamachi S, Czernin J, Kim AS, Sun KT, Bottcher M, Phelps ME, Schelbert HR. Reproducibility of measurements of regional resting and hyperemic myocardial blood flow assessed with PET. J Nucl Med. 1996;37:1626–31.
28. Yokoyama I, Murakami T, Ohtake T, Momomura S, Nishikawa J, Sasaki Y, Omata M. Reduced coronary flow reserve in familial hypercholesterolemia. J Nucl Med. 1996;37:1937–42.
29. Bottcher M, Czernin J, Sun K, Phelps ME, Schelbert HR. Effect of beta 1 adrenergic receptor blockade on myocardial blood flow and vasodilatory capacity. J Nucl Med. 1997;38:442–6.
30. Campisi R, Czernin J, Karpman HL, Schelbert HR. Coronary vasodilatory capacity and flow reserve in normal myocardium supplied by bypass grafts late after surgery. Am J Cardiol. 1997;80:27–31.
31. Muzik O, Duvernoy C, Beanlands RS, Sawada S, Dayanikli F, Wolfe ER Jr, Schwaiger M. Assessment of diagnostic performance of quantitative flow measurements in normal subjects and patients with angiographically documented coronary artery disease by means of nitrogen-13 ammonia and positron emission tomography. J Am Coll Cardiol. 1998;31:534–40.
32. Nitzsche EU, Choi Y, Czernin J, Hoh CK, Huang SC, Schelbert HR. Noninvasive quantification of myocardial blood flow in humans. A direct comparison of the [13N]ammonia and the [15O]water techniques. Circulation. 1996;93:2000–6.
33. Iida H, Kanno I, Takahashi A, Miura S, Murakami M, Takahashi K, Ono Y, Shishido F, Inugami A, Tomura N, et al. Measurement of absolute myocardial blood flow with H215O and dynamic positron-emission tomography. Strategy for quantification in relation to the partial-volume effect. Circulation. 1988;78:104–15.
34. Senneff MJ, Geltman EM, Bergmann SR. Noninvasive delineation of the effects of moderate aging on myocardial perfusion. J Nucl Med. 1991;32:2037–42.
35. Araujo LI, Lammertsma AA, Rhodes CG, McFalls EO, Iida H, Rechavia E, Galassi A, De Silva R, Jones T, Maseri A. Noninvasive quantification of regional myocardial blood flow in coronary artery disease with oxygen-15-labeled carbon dioxide inhalation and positron emission tomography. Circulation. 1991;83:875–85.
36. Yamamoto Y, de Silva R, Rhodes CG, Araujo LI, Iida H, Rechavia E, Nihoyannopoulos P, Hackett D, Galassi AR, Taylor CJ, et al. A new strategy for the assessment of viable myocardium and regional myocardial blood flow using 15O-water and dynamic positron emission tomography. Circulation. 1992;86:167–78.
37. Uren NG, Melin JA, De Bruyne B, Wijns W, Baudhuin T, Camici PG. Relation between myocardial blood flow and the severity of coronary-artery stenosis. N Engl J Med. 1994;330:1782–8.
38. Laine H, Raitakari OT, Niinikoski H, Pitkanen OP, Iida H, Viikari J, Nuutila P, Knuuti J. Early impairment of coronary flow reserve in young men with borderline hypertension. J Am Coll Cardiol. 1998;32:147–53.
39. Kaufmann PA, Gnecchi-Ruscone T, Schafers KP, Luscher TF, Camici PG. Low density lipoprotein cholesterol and coronary microvascular dysfunction in hypercholesterolemia. J Am Coll Cardiol. 2000;36:103–9.
40. Furuyama H, Odagawa Y, Katoh C, Iwado Y, Yoshinaga K, Ito Y, Noriyasu K, Mabuchi M, Kuge Y, Kobayashi K, Tamaki N. Assessment of coronary function in children with a history of Kawasaki disease using (15)O-water positron emission tomography. Circulation. 2002;105:2878–84.
41. Yoshinaga K, Katoh C, Noriyasu K, Iwado Y, Furuyama H, Ito Y, Kuge Y, Kohya T, Kitabatake A, Tamaki N. Reduction of coronary flow reserve in areas with and without ischemia on stress

perfusion imaging in patients with coronary artery disease: a study using oxygen 15-labeled water PET. J Nucl Cardiol. 2003;10:275–83.
42. Wyss CA, Koepfli P, Mikolajczyk K, Burger C, von Schulthess GK, Kaufmann PA. Bicycle exercise stress in PET for assessment of coronary flow reserve: repeatability and comparison with adenosine stress. J Nucl Med. 2003;44:146–54.
43. Herrero P, Markham J, Weinheimer CJ, Anderson CJ, Welch MJ, Green MA, Bergmann SR. Quantification of regional myocardial perfusion with generator-produced 62Cu-PTSM and positron emission tomography. Circulation. 1993;87:173–83.
44. Tahari AK, Lee A, Rajaram M, Fukushima K, Lodge MA, Lee BC, Ficaro EP, Nekolla S, Klein R, deKemp RA, Wahl RL, Bengel FM, Bravo PE. Absolute myocardial flow quantification with (82)Rb PET/CT: comparison of different software packages and methods. Eur J Nucl Med Mol Imaging. 2014;41:126–35.
45. Slomka PJ, Alexanderson E, Jacome R, Jimenez M, Romero E, Meave A, Le Meunier L, Dalhbom M, Berman DS, Germano G, Schelbert H. Comparison of clinical tools for measurements of regional stress and rest myocardial blood flow assessed with 13N-ammonia PET/CT. J Nucl Med. 2012;53:171–81.
46. Di Carli M, Czernin J, Hoh CK, Gerbaudo VH, Brunken RC, Huang SC, Phelps ME, Schelbert HR. Relation among stenosis severity, myocardial blood flow, and flow reserve in patients with coronary artery disease. Circulation. 1995;91:1944–51.
47. Anagnostopoulos C, Almonacid A, El Fakhri G, Curillova Z, Sitek A, Roughton M, Dorbala S, Popma JJ, Di Carli MF. Quantitative relationship between coronary vasodilator reserve assessed by 82Rb PET imaging and coronary artery stenosis severity. Eur J Nucl Med Mol Imaging. 2008;35:1593–601.
48. Hajjiri MM, Leavitt MB, Zheng H, Spooner AE, Fischman AJ, Gewirtz H. Comparison of positron emission tomography measurement of adenosine-stimulated absolute myocardial blood flow versus relative myocardial tracer content for physiological assessment of coronary artery stenosis severity and location. J Am Coll Cardiol Img. 2009;2:751–8.
49. Kajander SA, Joutsiniemi E, Saraste M, Pietila M, Ukkonen H, Saraste A, Sipila HT, Teras M, Maki M, Airaksinen J, Hartiala J, Knuuti J. Clinical value of absolute quantification of myocardial perfusion with (15)O-water in coronary artery disease. Circ Cardiovasc imaging. 2011;4:678–84.
50. Fiechter M, Ghadri JR, Gebhard C, Fuchs TA, Pazhenkottil AP, Nkoulou RN, Herzog BA, Wyss CA, Gaemperli O, Kaufmann PA. Diagnostic value of 13N-ammonia myocardial perfusion PET: added value of myocardial flow reserve. J Nucl Med. 2012;53:1230–4.
51. Kaufmann PA, Gnecchi-Ruscone T, Yap JT, Rimoldi O, Camici PG. Assessment of the reproducibility of baseline and hyperemic myocardial blood flow measurements with 15O-labeled water and PET. J Nucl Med. 1999;40:1848–56.
52. Ziadi MC, Dekemp RA, Williams K, Guo A, Renaud JM, Chow BJ, Klein R, Ruddy TD, Aung M, Garrard L, Beanlands RS. Does quantification of myocardial flow reserve using rubidium-82 positron emission tomography facilitate detection of multivessel coronary artery disease? J Nucl Cardiol. 2012;19:670.
53. Naya M, Murthy VL, Taqueti VR, Foster CR, Klein J, Garber M, Dorbala S, Hainer J, Blankstein R, Resnic F, Di Carli MF. Preserved coronary flow reserve effectively excludes high-risk coronary artery disease on angiography. J Nucl Med. 2014;55:248–55.
54. Bravo PE, Bergmark BA, Vita T, Taqueti VR, Gupta A, Seidelmann S, Christensen TE, Osborne MT, Shah NR, Ghosh N, Hainer J, Bibbo CF, Harrington M, Costantino F, Mehra MR, Dorbala S, Blankstein R, Desai A, Stevenson L, Givertz MM, Di Carli MF. Diagnostic and prognostic value of myocardial blood flow quantification as non-invasive indicator of cardiac allograft vasculopathy. Eur Heart J. 2018;39:316–23.
55. Lee JM, Kim CH, Koo BK, Hwang D, Park J, Zhang J, Tong Y, Jeon KH, Bang JI, Suh M, Paeng JC, Cheon GJ, Na SH, Ahn JM, Park SJ, Kim HS. Integrated myocardial perfusion imaging diagnostics improve detection of functionally significant coronary artery stenosis by 13N-ammonia positron emission tomography. Circ Cardiovasc imaging. 2016;9:e004768.

56. Danad I, Uusitalo V, Kero T, Saraste A, Raijmakers PG, Lammertsma AA, Heymans MW, Kajander SA, Pietila M, James S, Sorensen J, Knaapen P, Knuuti J. Quantitative assessment of myocardial perfusion in the detection of significant coronary artery disease: cutoff values and diagnostic accuracy of quantitative [(15)O]H2O PET imaging. J Am Coll Cardiol. 2014;64:1464–75.
57. van de Hoef TP, Siebes M, Spaan JA, Piek JJ. Fundamentals in clinical coronary physiology: why coronary flow is more important than coronary pressure. Eur Heart J. 2015;36:3312-9a.
58. Gould KL, Johnson NP, Bateman TM, Beanlands RS, Bengel FM, Bober R, Camici PG, Cerqueira MD, Chow BJW, Di Carli MF, Dorbala S, Gewirtz H, Gropler RJ, Kaufmann PA, Knaapen P, Knuuti J, Merhige ME, Rentrop KP, Ruddy TD, Schelbert HR, Schindler TH, Schwaiger M, Sdringola S, Vitarello J, Williams KA Sr, Gordon D, Dilsizian V, Narula J. Anatomic versus physiologic assessment of coronary artery disease. Role of coronary flow reserve, fractional flow reserve, and positron emission tomography imaging in revascularization decision-making. J Am Coll Cardiol. 2013;62:1639–53.
59. Johnson NP, Gould KL. Integrating noninvasive absolute flow, coronary flow reserve, and ischemic thresholds into a comprehensive map of physiological severity. J Am Coll Cardiol Img. 2012;5:430–40.
60. Tonino PA, De Bruyne B, Pijls NH, Siebert U, Ikeno F, Van't Veer M, Klauss V, Manoharan G, Engstrom T, Oldroyd KG, Ver Lee PN, MacCarthy PA, Fearon WF, Investigators FS. Fractional flow reserve versus angiography for guiding percutaneous coronary intervention. N Engl J Med. 2009;360:213–24.
61. Pijls NH, van Schaardenburgh P, Manoharan G, Boersma E, Bech JW, van't Veer M, Bar F, Hoorntje J, Koolen J, Wijns W, de Bruyne B. Percutaneous coronary intervention of functionally nonsignificant stenosis: 5-year follow-up of the DEFER Study. J Am Coll Cardiol. 2007;49:2105–11.
62. De Bruyne B, Pijls NH, Kalesan B, Barbato E, Tonino PA, Piroth Z, Jagic N, Mobius-Winkler S, Rioufol G, Witt N, Kala P, MacCarthy P, Engstrom T, Oldroyd KG, Mavromatis K, Manoharan G, Verlee P, Frobert O, Curzen N, Johnson JB, Juni P, Fearon WF, Investigators FT. Fractional flow reserve-guided PCI versus medical therapy in stable coronary disease. N Engl J Med. 2012;367:991–1001.
63. Yilmaz A, Sechtem U. Angina pectoris in patients with normal coronary angiograms: current pathophysiological concepts and therapeutic options. Heart. 2012;98:1020–9.
64. Corcoran D, Hennigan B, Berry C. Fractional flow reserve: a clinical perspective. Int J Cardiovasc Imaging. 2017;33:961–74.
65. Meuwissen M, Chamuleau SA, Siebes M, de Winter RJ, Koch KT, Dijksman LM, van den Berg AJ, Tijssen JG, Spaan JA, Piek JJ. The prognostic value of combined intracoronary pressure and blood flow velocity measurements after deferral of percutaneous coronary intervention. Catheter Cardiovasc Interv. 2008;71:291–7.
66. van de Hoef TP, van Lavieren MA, Damman P, Delewi R, Piek MA, Chamuleau SA, Voskuil M, Henriques JP, Koch KT, de Winter RJ, Spaan JA, Siebes M, Tijssen JG, Meuwissen M, Piek JJ. Physiological basis and long-term clinical outcome of discordance between fractional flow reserve and coronary flow velocity reserve in coronary stenoses of intermediate severity. Circ Cardiovasc Interv. 2014;7:301–11.
67. van de Hoef TP, Nolte F, Echavarria-Pinto M, van Lavieren MA, Damman P, Chamuleau SA, Voskuil M, Verberne HJ, Henriques JP, van Eck-Smit BL, Koch KT, de Winter RJ, Spaan JA, Siebes M, Tijssen JG, Meuwissen M, Piek JJ. Impact of hyperaemic microvascular resistance on fractional flow reserve measurements in patients with stable coronary artery disease: insights from combined stenosis and microvascular resistance assessment. Heart. 2014;100:951–9.
68. Meuwissen M, Chamuleau SA, Siebes M, Schotborgh CE, Koch KT, de Winter RJ, Bax M, de Jong A, Spaan JA, Piek JJ. Role of variability in microvascular resistance on fractional flow reserve and coronary blood flow velocity reserve in intermediate coronary lesions. Circulation. 2001;103:184–7.
69. Garcia D, Harbaoui B, van de Hoef TP, Meuwissen M, Nijjer SS, Echavarria-Pinto M, Davies JE, Piek JJ, Lantelme P. Relationship between FFR, CFR and coronary microvascular resis-

tance - practical implications for FFR-guided percutaneous coronary intervention. PLoS One. 2019;14:e0208612.
70. van de Hoef TP, Echavarria-Pinto M, van Lavieren MA, Meuwissen M, Serruys PW, Tijssen JG, Pocock SJ, Escaned J, Piek JJ. Diagnostic and prognostic implications of coronary flow capacity: a comprehensive cross-modality physiological concept in ischemic heart disease. JACC Cardiovasc Interv. 2015;8:1670–80.
71. Camici PG, d'Amati G, Rimoldi O. Coronary microvascular dysfunction: mechanisms and functional assessment. Nat Rev Cardiol. 2015;12:48–62.
72. Neglia D, Michelassi C, Trivieri MG, Sambuceti G, Giorgetti A, Pratali L, Gallopin M, Salvadori P, Sorace O, Carpeggiani C, Poddighe R, L'Abbate A, Parodi O. Prognostic role of myocardial blood flow impairment in idiopathic left ventricular dysfunction. Circulation. 2002;105:186–93.
73. Tio RA, Dabeshlim A, Siebelink HM, de Sutter J, Hillege HL, Zeebregts CJ, Dierckx RA, van Veldhuisen DJ, Zijlstra F, Slart RH. Comparison between the prognostic value of left ventricular function and myocardial perfusion reserve in patients with ischemic heart disease. J Nucl Med. 2009;50:214–9.
74. Murthy VL, Naya M, Foster CR, Hainer J, Gaber M, Di Carli G, Blankstein R, Dorbala S, Sitek A, Pencina MJ, Di Carli MF. Improved cardiac risk assessment with noninvasive measures of coronary flow reserve. Circulation. 2011;124:2215–24.
75. Herzog BA, Husmann L, Valenta I, Gaemperli O, Siegrist PT, Tay FM, Burkhard N, Wyss CA, Kaufmann PA. Long-term prognostic value of 13N-ammonia myocardial perfusion positron emission tomography added value of coronary flow reserve. J Am Coll Cardiol. 2009;54:150–6.
76. Fukushima K, Javadi MS, Higuchi T, Lautamaki R, Merrill J, Nekolla SG, Bengel FM. Prediction of short-term cardiovascular events using quantification of global myocardial flow reserve in patients referred for clinical 82Rb PET perfusion imaging. J Nucl Med. 2011;52:726–32.
77. Ziadi MC, Dekemp RA, Williams KA, Guo A, Chow BJ, Renaud JM, Ruddy TD, Sarveswaran N, Tee RE, Beanlands RS. Impaired myocardial flow reserve on rubidium-82 positron emission tomography imaging predicts adverse outcomes in patients assessed for myocardial ischemia. J Am Coll Cardiol. 2011;58:740–8.
78. Gupta A, Taqueti VR, van de Hoef TP, Bajaj NS, Bravo PE, Murthy VL, Osborne MT, Seidelmann SB, Vita T, Bibbo CF, Harrington M, Hainer J, Rimoldi O, Dorbala S, Bhatt DL, Blankstein R, Camici PG, Di Carli MF. Integrated noninvasive physiological assessment of coronary circulatory function and impact on cardiovascular mortality in patients with stable coronary artery disease. Circulation. 2017;136:2325–36.
79. Patel KK, Spertus JA, Chan PS, Sperry BW, Al Badarin F, Kennedy KF, Thompson RC, Case JA, McGhie AI, Bateman TM. Myocardial blood flow reserve assessed by positron emission tomography myocardial perfusion imaging identifies patients with a survival benefit from early revascularization. Eur Heart J. 2020;41:759–68.
80. Green R, Cantoni V, Acampa W, Assante R, Zampella E, Nappi C, Gaudieri V, Mannarino T, Cuocolo R, Petretta M, Cuocolo A. Prognostic value of coronary flow reserve in patients with suspected or known coronary artery disease referred to PET myocardial perfusion imaging: a meta-analysis. J Nucl Cardiol. 2021;28:904.

Hybrid PET-CT Evaluation of Myocardial Viability

9

Wail Nammas and Antti Saraste

9.1 Background

Coronary artery disease is the most prevalent etiology of heart failure. Myocardial ischemia was the underlying cause of heart failure in 62% of patients from a pooled analysis of 24 heart failure trials encompassing more than 400,000 participants [1]. Chronic repetitive myocardial ischemia may result in chronic hibernating myocardium or chronic stunning; both are potentially reversible causes of regional/global left ventricular dysfunction. Myocardial hibernation refers to chronic reversible contractile dysfunction of "viable" cardiac myocytes under conditions of long-standing myocardial ischemia; whereas the term myocardial stunning expresses prolonged suppression of contractile function after brief intense ischemic insult despite restoration of regional myocardial blood flow [2]. Ischemic myocardium presents a continuum from entirely viable, through partially viable myocardial zones, to non-viable scar tissue. The likelihood of recovery of ventricular function after coronary revascularization depends on the presence and extent of myocardial viability, and the amount of scar [3]. Patients with heart failure due to ischemic etiology have the potential to benefit from coronary revascularization in terms of recovery of contractile function, improvement of symptoms, and long-term survival provided that they have adequate myocardial viability in regions of contractile dysfunction. On the other hand, areas of scar tissue represent "non-viable" myocardium with almost no potential for improvement after revascularization. Coronary revascularization in patients with viability was associated with improvement of the annual survival rate, compared with medical treatment; in patients without viability, survival rates did not differ by the line of therapy [4]. Therefore, non-invasive

W. Nammas · A. Saraste (✉)
Heart Center, Turku University Hospital, Turku, Finland

PET Centre, Turku University Hospital, Turku, Finland
e-mail: antti.saraste@utu.fi

S. G. Nekolla, C. Rischpler (eds.), *Hybrid Cardiac Imaging*,
https://doi.org/10.1007/978-3-030-83167-7_9

detection of myocardial viability has a pivotal role in selection of patients with chronic ischemic heart failure who are likely to derive benefit from revascularization.

9.2 Patterns of Viability by PET

Positron emission tomography (PET) can serve to evaluate myocardial perfusion, glucose utilization, fatty acid oxidation, oxygen consumption, and pre- and post-synaptic neuronal activity. Assessment of myocardial viability has been one of the earliest clinical applications of PET; PET is acknowledged as the "gold standard" technique for such indication. Myocardial viability entails intact cell membrane, mitochondrial integrity, preserved glucose and fatty acid metabolism, adequate resting perfusion, and contractile reserve [5–8]. Evaluation of resting myocardial perfusion using a perfusion radiotracer [^{82}Rubidium (^{82}Rb) or ^{13}N-ammonia] can be employed to assess viability in dysfunctional myocardium analogous to single photon emission computed tomography viability protocols [9, 10]. However, the most common and accurate approach for viability assessment by PET is based on evaluation of myocardial glucose metabolism by ^{18}F-fluorodeoxyglucose (FDG). Viable myocardium shows preserved FDG uptake; whereas markedly reduced or absent uptake indicates the presence of scar [11]. Typically, hibernating myocardium is identified by comparing FDG uptake with resting perfusion. Myocardial segments with reduced perfusion but preserved or increased FDG uptake (perfusion-metabolism mismatch) are classified as viable: contractile function of such segments is most likely to improve with successful revascularization. In contrast, segments with proportional reduction of perfusion and FDG uptake (perfusion-metabolism match) are regarded as scar tissue whose contractility would probably not improve following revascularization (Figs. 9.1 and 9.2) [11]. A third category of segments is characterized by normal or near normal perfusion and preserved FDG uptake: such pattern may represent stunned myocardium after repetitive episodes of ischemia. Some studies reported functional improvement of such segments after revascularization [12, 13].

9.3 Metabolic Considerations

The normal myocardium uses a wide variety of substrates for energy production, including free fatty acids (FFA), glucose, pyruvate, lactate, and ketone bodies [14]. Under normal conditions, metabolism is primarily oxidative, and FFA represent the main source of energy; whereas glycolysis contributes nearly 30% of substrate needed for the citric acid cycle. In the fasting state, the availability of FFA in plasma is high (from lipolysis of triglycerides in peripheral tissues) and thus myocardial FFA oxidation is consistently high; this inhibits glycolysis. After ingestion of carbohydrates, plasma glucose rises with parallel increase in insulin levels. This inhibits peripheral lipolysis, thereby lowering plasma FFA levels, and increasing exogenous

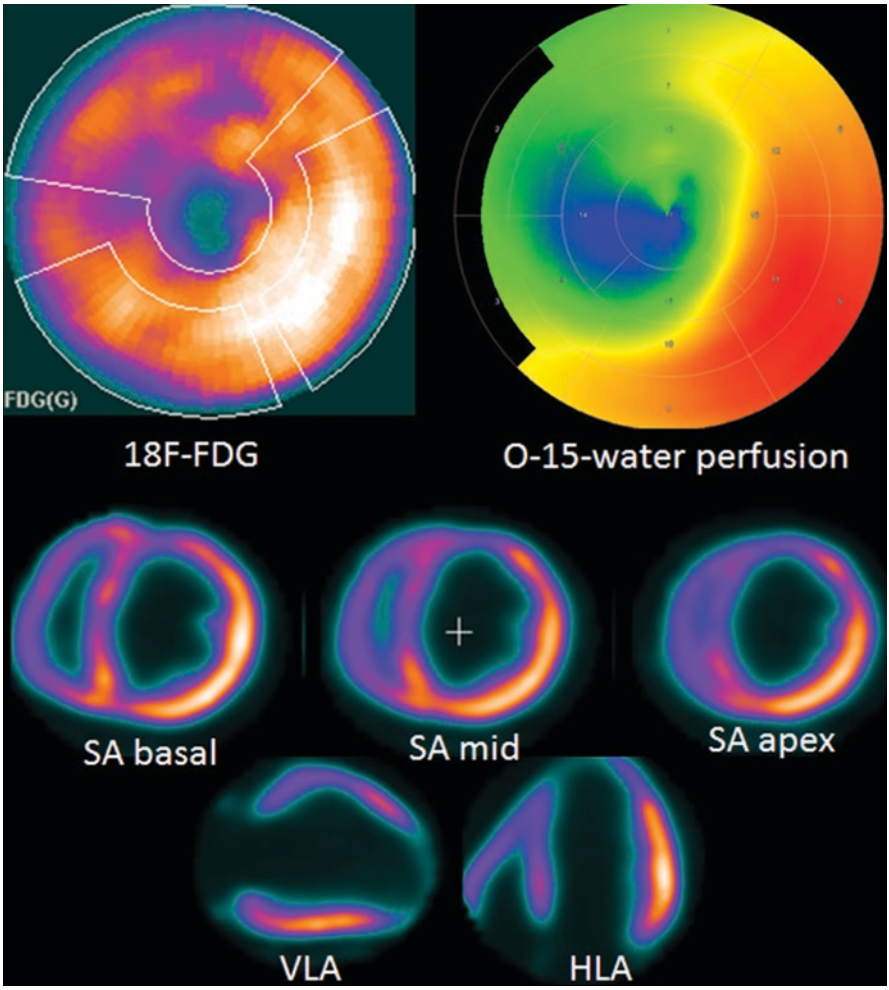

Fig. 9.1 Myocardial viability study using ^{18}F-FDG and resting myocardial perfusion study using ^{15}O-water. The patient had 3-vessel obstructive coronary artery disease, contractile dysfunction in the territory of the LAD coronary artery, reduced left ventricle ejection fraction (35%), and high surgical risk. Resting perfusion is reduced in the LAD territory. Viability study shows absence of ^{18}F-FDG uptake in the apex, but partially preserved uptake elsewhere in the LAD territory indicating partially preserved viability. *SA* short axis, *^{18}F-FDG* ^{18}F-fluorodeoxyglucose, *HLA* horizontal long axis, *LAD* left anterior descending, *VLA* vertical long axis

glucose utilization by the myocardium [15]. On the other hand, mitochondrial β oxidation of FFA is greatly dependent on oxygen supply; therefore, it markedly decreases under conditions of ischemia. Hence, during myocardial ischemia, glucose uptake and metabolism is substantially increased in the ischemic myocardium [16]. Based on this, non-invasive techniques which quantify exogenous glucose utilization can be used for assessment of residual myocardial viability in ischemic

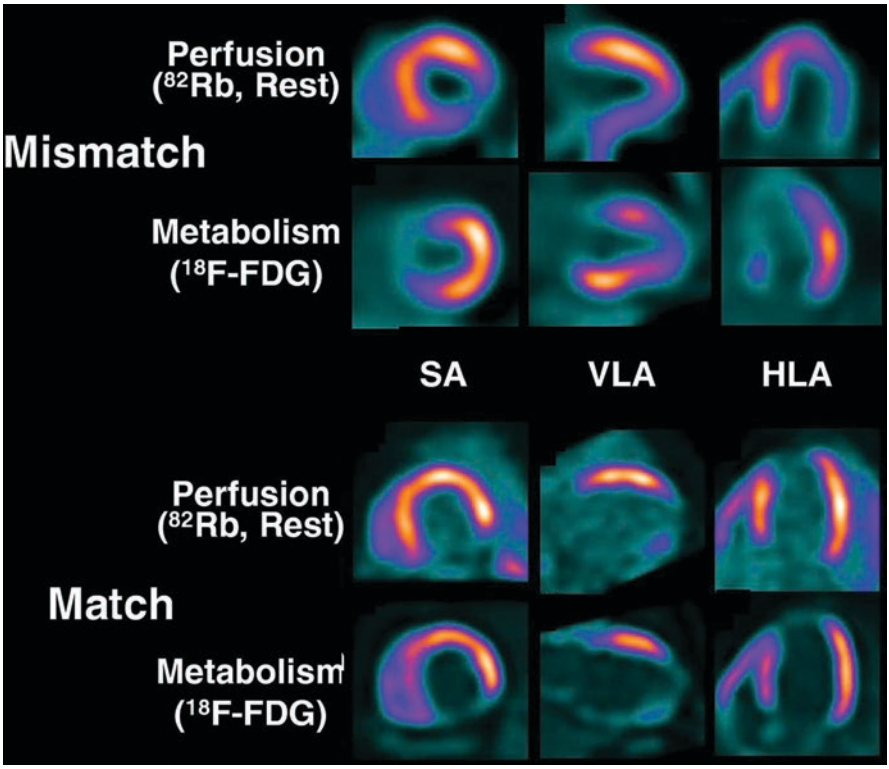

Fig. 9.2 Assessment of myocardial viability by FDG PET: Examples of perfusion–metabolism mismatch patterns. (Reprinted with permission from Bengel FM, Higuchi T, Javadi MS, Lautamäki R. J Am Coll Cardiol. 2009 Jun 30;54(1):1–15. https://doi.org/10.1016/j.jacc.2009.02.065. Review)

dysfunctional myocardium. Nevertheless, under ischemic states, glycolysis becomes uncoupled from glucose oxidation, leading to excess production of lactate and hydrogen ion. During mild ischemia, such by-products are removed from the myocardium by the residual blood flow. Prolonged severe ischemia leads to tissue accumulation of lactate and hydrogen ion, depletion of high-energy phosphate, disruption of cell membrane, and cell death [14]. Therefore, assessment of resting myocardial perfusion can still provide valued information on the presence of viability in dysfunctional myocardial zones. Following intravenous administration, FDG is taken up by cardiac myocytes, along with glucose, where it undergoes phosphorylation by hexokinase to FDG-6-phosphate. Unlike glucose-6-phosphate, FDG-6-phosphate is a poor substrate for glycolysis and glycogen synthesis, and is quite impermeable to the myocyte membrane; thus it becomes virtually trapped in the myocardium. Therein, it provides robust signal for PET imaging. Regional FDG uptake is normal or increased in viable myocardial segments with ischemic contractile dysfunction, thereby it indicates persistence of metabolic activity, and the potential for recovery of contractile function.

9.4 Protocols for Assessment of Myocardial Viability by FDG

The concentration of FDG in both the myocardium and blood determines the diagnostic quality of myocardial FDG images. Myocardial FDG—along with glucose—uptake depends essentially on plasma concentration of glucose as well as insulin level, which in turn determine the rate of glucose utilization by peripheral tissues. Additionally, myocardial glucose uptake is based on plasma levels of FFA and other substrates, oxygen supply, catecholamine levels, and myocardial work. Therefore, the FDG myocardial viability assessment protocols have sought to optimize the metabolic conditions for myocardial FDG uptake in order to maximize the quality of FDG images, and thereby improve the diagnostic accuracy. The currently implemented protocols for FDG myocardial viability assessment include:

1. Fasting: Under fasting conditions, the normally perfused myocardium utilizes predominantly FFA; whereas the uptake of glucose—and correspondingly FDG—is minimal. In contrast, glucose utilization is favored by the ischemic myocardium, and therefore FDG uptake is enhanced. In this way, a remarkable differential of FDG uptake exists between normal and ischemic myocardium, which is seen as a "hot spot." This is the simplest protocol since it does not require any substrate manipulation. However, in the fasting state FDG becomes heterogeneously distributed throughout the normal myocardium [17]. This along with lack of radiotracer uptake in the normal myocardium might overestimate the extent of residual viability in ischemic dysfunctional myocardium. Moreover, the low uptake of glucose by both cardiac and skeletal muscle results in poor image quality in nearly 50% of the cases [18]. In addition, low FDG uptake by the non-ischemic myocardium hinders the differentiation of scar tissue from normal myocardium.
2. Glucose loading: Oral or intravenous glucose load after 6-h fasting stimulates endogenous insulin release. This limits the bioavailability of FFA, and increases peripheral glucose utilization, and myocardial FDG uptake. The more homogeneous distribution of FDG uptake by the myocardium essentially promotes image quality. This is the most commonly adopted protocol for FDG myocardial viability assessment in clinical practice. However, when the plasma concentration of glucose increases, the fraction of FDG sequestered by the myocardium declines, and this might reduce the gain in image quality. Indeed, unsatisfactory images my still be obtained with this protocol in 20–25% of the patients [18, 19]. Impaired glucose tolerance or undiagnosed type 2 diabetes mellitus might underlie the suboptimal image quality in many such patients. Intravenous administration of low doses of regular insulin in diabetic patients may improve image quality, and yield a level of diagnostic accuracy similar to that in non-diabetic patients who receive oral glucose load [20, 21].
3. Hyperinsulinemic-euglycemic clamp: This protocol mimics the post-absorptive steady state by means of continuous infusion of insulin with simultaneous infusion of glucose at a variable rate, in order to maintain euglycemia [19]. Insulin clamping stimulates FDG uptake, along with glucose, in the myocardium, and

provides consistently high image quality, even in diabetic patients [19, 22]. Nevertheless, this protocol is technically demanding and time consuming; therefore most centers preserve it for complex studies, for example, in diabetics.

4. Nicotinic acid derivatives: Nicotinic acid inhibits peripheral lipolysis, and consequently, reduces the bioavailability of FFA in plasma, and switches to preferential myocardial glucose utilization. Acipimox is 20 times more potent than nicotinic acid and has more favorable kinetics [23]. It could be given combined with glucose load 60 min before FDG administration. In a small early study, image quality (expressed as the myocardium-to-blood pool FDG ratio) and myocardial FDG uptake patterns after acipimox administration were similar to those obtained during hyperinsulinemic-euglycemic clamp [24]. Another study compared three protocols in a limited sample size, and demonstrated that acipimox administration and hyperinsulinemic-euglycemic clamp achieved comparable FDG image quality and clearance rates that were superior to those obtained after oral glucose load [22]. Apart from flushing, no side effects have been reported. This protocol is simple and practical; however, acipimox is not available in all centers.

9.5 Diagnostic Accuracy of FDG Myocardial Viability Assessment

Myocardial viability assessment by FDG is the most sensitive technique for detection of viability in ischemic dysfunctional myocardial segments, and prediction of contractile recovery of such segments after revascularization. In an early pooled analysis (1980 through January 2000) of 20 studies (598 patients) which employed FDG PET to detect improvement of regional contractile function after revascularization, the weighted mean sensitivity and specificity were 93% and 58%, respectively; weighted mean positive and negative predictive values were 71% and 86%, respectively [25]. In four studies performed after 2000, the sensitivity of FDG PET to predict improvement of regional function after revascularization ranged from 86% to 100%, specificity ranged from 63% to 87%, positive and negative predictive value ranges were 75–89% and 83–100%, respectively [26–29]. In a more recent pooled analysis that included the aforementioned studies (24 studies, 756 patients), myocardial viability assessment by FDG PET predicted improvement of regional function after revascularization with a weighted mean sensitivity and specificity of 92% and 63%, respectively; weighted mean positive and negative predictive values were 74% and 87%, respectively [30]. It is worth mentioning that viability assessment by FDG PET has the highest sensitivity for prediction of functional recovery after revascularization, compared with the other imaging modalities; whereas evaluation of wall motion by dobutamine stress echocardiography and imaging modalities which evaluate myocardial scar tissue, such as contrast-enhanced magnetic resonance imaging have a higher specificity [30]. The reasons for the suboptimal specificity (absence of functional improvement after revascularization of segments classified by FDG PET as viable) seem to be multifactorial, including the presence

of subendocardial scar, advanced degenerative changes of viable myocytes, incomplete revascularization or periprocedural myocardial injury, and delayed improvement of some segments following adequate revascularization [31]. Most of the aforementioned published data were obtained from patients with normal left ventricular function or mild/moderate left ventricular dysfunction: only 3 out of 24 studies included patients with a mean left ventricular ejection fraction <30%; in four studies, there were no available data on left ventricular ejection fraction [30]. It should be noted that the diagnostic accuracy indices of viability assessment by FDG PET for prediction of ventricular function improvement after revascularization differ by severity of global ventricular function impairment before revascularization: the accuracy declines considerably with worsening global left ventricular function [32]. Therefore, data obtained from patients with a mean left ventricular ejection fraction ≥30% should not be extrapolated to those with very low ejection fraction. On the other hand, a single study (37 patients; surgical coronary revascularization; median follow-up 8 weeks) reported that the diagnostic accuracy was highest in segments with severe dysfunction and perfusion-metabolism mismatch by FDG PET [12]. Furthermore, improvement of left ventricular function after revascularization appears to be multifactorial. Many other factors might influence such improvement including the presence and extent of myocardial ischemia, the severity of degeneration of viable cardiac myocytes, success and completeness of revascularization, the state of other coronary vessels, as well as the timing of ventricular function assessment after revascularization. Integration of many of these factors along with FDG PET viability assessment in a multivariable prediction model predicted the degree of recovery [33].

9.6 Prognostic Implications of FDG Myocardial Viability Assessment

The detection of viability not only serves to predict contractile recovery of ischemic dysfunctional myocardial segments upon revascularization, but may also predict clinical outcome. In a meta-analysis of 24 viability studies (3088 patients; mean ejection fraction 32 ± 8%; viability detection by PET, single photon emission computed tomography, or dobutamine stress echocardiography) which reported long-term clinical outcome (mean follow-up 25 ± 10 months), coronary revascularization was associated with almost 80% reduction of annual mortality rate, compared with medical treatment, in patients with viability (3.2% versus 16%, respectively, $p < 0.0001$); in those without viability, annual mortality rates were not significantly different by treatment modality (7.7% versus 6.2%, respectively) [4]. In a more recent pooled analysis of ten FDG PET viability studies (1046 patients; clinical outcome assessed at variable durations of follow-up), the annualized mortality rate was 4% in patients with viability who underwent revascularization, compared with 17% in those with viability who were treated medically; in those without viability, the annualized mortality rates were 6% and 8%, respectively [30]. An observational study investigated the effect of viability (99mTc-sestamibi single photon emission

computed tomography and FDG PET) on long-term (median 6.8 years) cardiac mortality in patients with left ventricular aneurysm. Annual cardiac mortality was significantly higher in patients with viable aneurysm who were treated medically, compared with those who underwent surgical revascularization (11.6% versus 1.5%, respectively, $p < 0.0001$); the rate was also higher than in patients with a non-viable aneurysm treated medically or surgically. Viability in left ventricular aneurysm was an independent predictor of cardiac death; whereas coronary revascularization was associated with better long-term survival, symptoms, and left ventricular function in patients with a viable aneurysm [34]. In another recent observational study, both viability (mismatch score ≥2) and left ventricular remodeling (left ventricular volume index ≥60 mL/m^2) were assessed by gated PET in 126 patients with left ventricular aneurysm who were followed up for a mean of 3.9 ± 1.5 years. In such cohort, patients with viable aneurysm were at increased risk of cardiac death, compared with those who had no aneurysm viability, with or without remodeling [35]. Revascularization in patients with viable aneurysm was associated with improved long-term cardiac survival; no such improvement was observed in patients without aneurysm viability regardless the presence of remodeling [35].

9.7 FDG Myocardial Viability Assessment for Guiding Therapeutic Decision

The value of myocardial viability assessment by FDG PET for guiding therapeutic decision making in patients with severe left ventricular dysfunction and advanced coronary artery disease remains controversial [36, 37]. A relatively small randomized controlled trial (PET and Recovery Following Revascularization-2 trial, 430 patients) assessed the efficacy of FDG PET-assisted management, versus standard care, to reduce major adverse cardiac events (cardiac death, myocardial infarction, or hospitalization for a cardiac cause) in patients with severe left ventricular systolic dysfunction (ejection fraction <35%) who were considered for revascularization, transplantation, or heart failure work-up, or in whom PET was considered useful. At 1-year follow-up, there was no significant reduction of cardiac events in patients assigned to PET-assisted management, versus standard care [38]. However, at 5-year follow-up, PET-assisted management was associated with significant reduction of the composite endpoint only in the subgroup of patients who adhered to PET recommendations (hazard ratio 0.73, 95% confidence interval 0.54–0.99; $p = 0.042$) [39]. In a post-hoc analysis of the aforementioned trial, there was an interaction between the extent of viability (expressed as mismatch percent of the left ventricle) and treatment modality such that in patients with higher mismatch percent values revascularization was associated with fewer cardiac events, compared with those with lower mismatch percent values ($p = 0.042$) [40]. A cutoff value of 7% mismatch of the whole left ventricle was identified to stratify patients whose clinical outcome improves after revascularization: in patients with mismatch value ≥7%, revascularization was associated with significant reduction of the primary outcome

compared with medical treatment (p = 0.015); whereas patients with mismatch value <7% had no significant difference in the primary outcome based on treatment modality (p = 0.923) [40]. In addition, an observational study investigated the impact of hibernating versus ischemic myocardium on long-term survival after revascularization in 648 patients (age 65 ± 12 years, mean left ventricular ejection fraction 31 ± 12%) with ischemic cardiomyopathy. At a mean follow-up of 2.8 ± 1.2 years, an interaction was present between treatment modality and hibernating myocardium such that early revascularization in the presence of significant hibernating myocardium was associated with survival benefit, versus medical treatment (p = 0.0009), specifically when the extent of viability exceeds 10% of the whole myocardium; no such interaction was observed between treatment modality and ischemic myocardium [41]. In another retrospective study which explored the prognostic value of combined viability imaging (PET and single photon emission computed tomography) for prediction of survival in 224 patients with ischemic cardiomyopathy (64.0 ± 10.6 years, mean left ventricular ejection fraction ≤45%) at a median follow-up of 33 months, patients with mismatch values ≥5% who were treated medically had significantly higher mortality than those with similar mismatch values who underwent early revascularization; whereas in those with mismatch values <5%, early revascularization was associated with higher mortality compared with medical treatment [42]. The high procedural risk of revascularization complicates therapeutic decision making in patients with severe left ventricular dysfunction. Nevertheless, it is in this complex patient subset (comorbidities, prior revascularization) where both the possible risk and potential benefit of revascularization are high [36]. According to the current European Society of Cardiology guidelines for treatment of heart failure, PET may be considered for myocardial viability assessment before the decision of revascularization, in patients with heart failure and coronary artery disease whose coronary anatomy is deemed suitable for revascularization (class of recommendation IIb, level of evidence B) [43].

9.8 Hybrid PET-Computed Tomography for Myocardial Viability Assessment

Hybrid scanner systems involving both multidetector computed tomography (CT) and PET have become widespread over the past decade. Hybrid PET-CT scanners enable direct integration of PET imaging data with detailed information acquired from coronary and cardiac CT imaging. Additionally, multidetector CT can be useful for attenuation correction and coronary calcium score assessment. Radiation dose exposure from coronary CT angiography can be reduced by the modern prospective-gated CT acquisition techniques down to 1–3 mSv; this might promote more widespread use of hybrid PET-CT protocols [44]. A hybrid PET-CT scanner allows obtaining myocardial viability scan provided by FDG PET and coronary anatomy images provided by CT angiography in a single imaging session, and provides automatic fusion of the images (Fig. 9.3). Vascular mapping of the left ventricle is based on a standard template that relates each myocardial segment to the

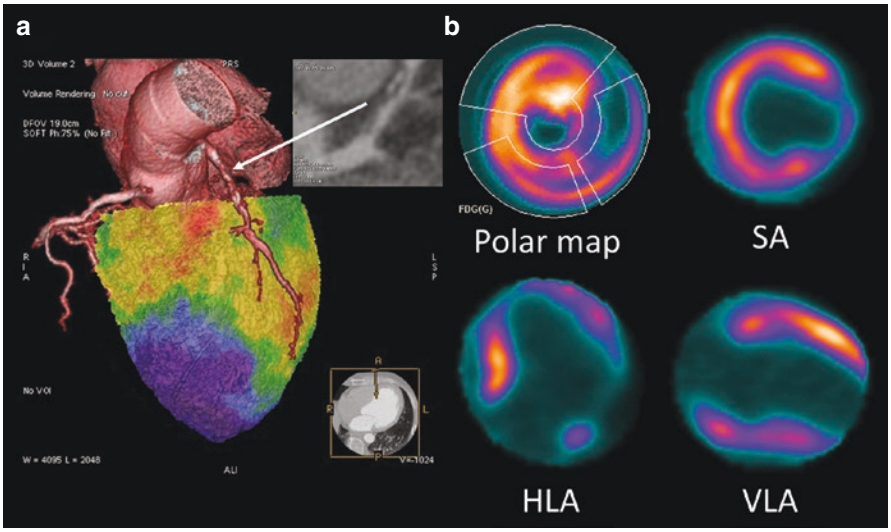

Fig. 9.3 A hybrid PET-CT study of coronary angiography and myocardial viability. The patient presented with new-onset heart failure. Echocardiography demonstrated severe left ventricular dysfunction with akinesia or hypokinesia in the apex, anterior septum, anterior free wall, as well as the posterolateral wall. Due to the presence of a left ventricular apical thrombus, coronary CT angiography was performed initially instead of invasive coronary angiography. Coronary CT angiography showed chronic total occlusion in the proximal LCx, severe stenosis in the proximal LAD (arrow), and chronic total occlusion in the mid-LAD (Panel **a**). Then, ^{18}F-FDG PET was performed to assess viability. ^{18}F-FDG PET images demonstrated local defects in ^{18}F-FDG uptake in the apex and lateral wall consistent with infarct scars. However, there was preserved ^{18}F-FDG uptake in the septum and most of the anterior wall, as well as in the inferior wall, consistent with large areas of viable myocardium (Panel **b**). Panel (**a**) demonstrates 3-D reconstruction of coronary CT angiography and ^{18}F-FDG PET. Co-registration clearly demonstrates viable myocardium (green and red colors) in the septum and anterior wall (supplied by a large diagonal branch) excluding the apical scar (blue color). The patient had successful coronary bypass surgery with venous grafts inserted on the distal LAD, diagonal branch, and LCx. Heart failure symptoms were relieved after surgery. *CT* computed tomography, *^{18}F-FDG* ^{18}F-fluorodeoxyglucose, *HLA* horizontal long axis, *LAD* left anterior descending, *LCx* left circumflex, *PET* positron emission tomography, *SA* short axis, *VLA* vertical long axis

part of coronary tree which supplies blood to that segment. Often the standard template does not mirror the real coronary anatomy; therefore, disparity between imaged myocardial perfusion defects and actual significant coronary lesions may occur [45]. In this context, hybrid PET-CT scanners which integrate FDG PET viability scans with coronary CT angiography images can mitigate such disparity, and enhance the accuracy of viability imaging. Moreover, it has been possible to evaluate myocardial perfusion in contrast-enhanced CT images. In the setting of myocardial infarction (acute, subacute, and chronic) myocardial perfusion defects become apparent during the early phase of contrast bolus (early defect). Subsequently, "delayed enhancement" of infarcts is seen 5–15 min following contrast infusion

[46]. Similar to magnetic resonance imaging, multidetector CT was employed in animal models for the assessment of myocardial viability by studying "delayed enhancement" [47, 48]. In a porcine model of myocardial infarction employing a hybrid PET-CT scanner, contrast enhancement by 64-slice CT could measure infarct size accurately and reproducibly compared with PET perfusion defect size; low-dose prospective-gated acquisition was comparable to high-dose spiral CT [49]. Early small-sized clinical studies demonstrated good agreement between delayed enhancement by multidetector CT and magnetic resonance imaging for infarct size and location [50, 51]. Whether the currently available hybrid PET-CT scanners improve the detection of viability in clinical practice remains unsettled. In a small observational study, the sensitivity, specificity, and diagnostic accuracy of multidetector CT to detect non-viable segments was 70.4%, 85.3%, and 81.4%, respectively, compared with FDG PET [52]. Yet, some segments which deemed viable by FDG PET showed delayed enhancement by multidetector CT. A preclinical study employed a hybrid PET-CT scanner to compare directly FDG PET scans with delayed enhancement by multidetector CT in a porcine model of acute and chronic myocardial infarction. Interestingly, in the acute infarct model, 68% of segments characterized by no-reflow pattern (microvascular obstruction) in multidetector CT images showed increased FDG uptake; this was explained by active inflammation as was detected in histology sections [53]. In the chronic infarct model, there was no microvascular obstruction in multidetector CT images, and areas of delayed enhancement delineated by multidetector CT corresponded well with non-viable segments depicted by FDG PET [53].

9.9 Conclusions

^{18}F-FDG PET imaging is an accurate method to detect dysfunctional, but viable myocardium that has potential to recover contractile function after revascularization. Although randomized clinical trials have not shown clinical benefit of systematic evaluation of viability in patients with ischemic left ventricle dysfunction, current guidelines indicate that it may be considered in selected heart failure patients to guide decisions on revascularization.

References

1. Gheorghiade M, Sopko G, De LL, Velazquez EJ, Parker JD, Binkley PF, et al. Navigating the crossroads of coronary artery disease and heart failure. Circulation. 2006;114:1202–13.
2. Wijns W, Vatner SF, Camici PG. Hibernating myocardium. N Engl J Med. 1998;339:173–81.
3. Shivalkar B, Maes A, Borgers M, et al. Only hibernating myocardium invariably shows early recovery after coronary revascularization. Circulation. 1996;94:308–15.
4. Allman KC, Shaw LJ, Hachamovitch R, Udelson JE. Myocardial viability testing and impact of revascularization on prognosis in patients with coronary artery disease and left ventricular dysfunction: a meta-analysis. J Am Coll Cardiol. 2002;39:1151–8.
5. Rahimtoola SH. The hibernating myocardium. Am Heart J. 1989;117:211.

6. Bax J, Wahba FF, Van der Wall EE. Myocardial viability/hibernation. In: Iskandrian AE, Verani MS, editors. Nuclear cardiac imaging. New York, NY: Oxford University Press; 2003.
7. Bolukoglu H, Liedtke JA, Nellis SH, et al. An animal model of chronic coronary stenosis resulting in hibernating myocardium. Am J Phys. 1992;263:H20.
8. Vanoverschelde JLJ, Wijns W, Depre C, et al. Mechanisms of chronic regional postischemic dysfunction in humans. New insights from the study of noninfarcted collateral-dependent myocardium. Circulation. 1993;87:1513.
9. Slart RH, Agool A, van Veldhuisen DJ, Dierckx RA, Bax JJ. Nitrate administration increases blood flow in dysfunctional but viable myocardium, leading to improved assessment of myocardial viability: a PET study. J Nucl Med. 2006;47(8):1307–11.
10. Maddahi J, Packard RR. Cardiac PET perfusion tracers: current status and future directions. Semin Nucl Med. 2014;44:333–43.
11. Knuuti J, Schelbert HR, Bax JJ. The need for standardisation of cardiac FDG PET imaging in the evaluation of myocardial viability in patients with chronic ischaemic left ventricular dysfunction. Eur J Nucl Med Mol Imaging. 2002;29:1257–66.
12. Vom Dahl J, Eitzman DT, Al-Aouar ZR, et al. Relation of regional function, perfusion and metabolism in patients with advanced coronary artery disease undergoing surgical revascularization. Circulation. 1994;90:2356–66.
13. Vom Dahl J, Altehoefer C, Sheehan FH, et al. Recovery of regional left ventricular dysfunction after coronary revascularization. Impact of myocardial viability assessed by nuclear imaging and vessel patency at follow-up angiography. J Am Coll Cardiol. 1996;28: 948–58.
14. Camici P, Ferrannini E, Opie L. Myocardial metabolism in ischemic heart disease: basic principles and application to imaging by positron emission tomography. Prog Cardiovasc Dis. 1989;32:217–38.
15. Young LH, Coven DL, Russell RR 3rd. Cellular and molecular regulation of cardiac glucose transport. J Nucl Cardiol. 2000;7(3):267–76.
16. Camici P, Araujo LI, Spinks T, Lammertsma AA, Kaski JC, Shea MJ, Selwyn AP, Jones T, Maseri A. Increased uptake of 18F-fluorodeoxyglucose in postischemic myocardium of patients with exercise-induced angina. Circulation. 1986;74(1):81–8.
17. Gropler RJ, Siegel BA, Lee KJ, Moerlein SM, Perry DJ, Bergmann SR, Geltman EM. Nonuniformity in myocardial accumulation of fluorine-18-fluorodeoxyglucose in normal fasted humans. J Nucl Med. 1990;31:1749–56.
18. Berry J, Baker J, Pieper K, Hanson M, Hoffman J, Coleman R. The effect of metabolic milieu on cardiac PET imaging using fluorine-18-deoxyglucose and nitrogen-13-ammonia in normal volunteers. J Nucl Med. 1991;32:1518–25.
19. Knuuti MJ, Nuutila P, Ruotsalainen U, et al. Euglycemic hyperinsulinemic clamp and oral glucose load in stimulating myocardial glucose utilization during positron emission tomography. J Nucl Med. 1992;33:1255–62.
20. Lewis P, Nunan T, Dynes A, Maisey M. The use of low-dose intravenous insulin in clinical myocardial F-18 FDG PET scanning. Clin Nucl Med. 1996;21:15–8.
21. Schöder H, Campisi R, Ohtake T, Hoh CK, Moon DH, Czernin J, Schelbert HR. Blood flow-metabolism imaging with positron emission tomography in patients with diabetes mellitus for the assessment of reversible left ventricular contractile dysfunction. J Am Coll Cardiol. 1999;33(5):1328–37.
22. Bax JJ, Veening MA, Visser FC, van Lingen A, Heine RJ, Cornel JH, Visser CA. Optimal metabolic conditions during fluorine-18 fluorodeoxyglucose imaging; a comparative study using different protocols. Eur J Nucl Med. 1997;24(1):35–41.
23. Schroder O, Hör G, Hertel A, Baum RP. Combined hyperinsulinemic glucose clamp and oral Acipimox for optimizing metabolic conditions during 18F-fluorodeoxyglucose gated PET cardiac imaging: comparative results. Nucl Med Commun. 1998;19:867–74.
24. Knuuti MJ, Yki-Järvinen H, Voipio-Pulkki L-M, et al. Enhancement of myocardial 18-FDG uptake by nicotinic acid derivative. J Nucl Med. 1994;35:989–98.

25. Bax JJ, Poldermans D, Elhendy A, Boersma E, Rahimtoola SH. Sensitivity, specificity, and predictive accuracies of various noninvasive techniques for detecting hibernating myocardium. Curr Probl Cardiol. 2001;26(2):147–86.
26. Slart RH, Bax JJ, van Veldhuisen DJ, van der Wall EE, Irwan R, Sluiter WJ, Dierckx RA, de Boer J, Jager PL. Prediction of functional recovery after revascularization in patients with chronic ischaemic left ventricular dysfunction: head-to-head comparison between 99mTc-sestamibi/18F-FDG DISA SPECT and 13N-ammonia/18F-FDG PET. Eur J Nucl Med Mol Imaging. 2006;33(6):716–23.
27. Nowak B, Schaefer WM, Koch KC, Kaiser HJ, Block S, Knackstedt C, Zimny M, Vom Dahl J, Buell U. Assessment of myocardial viability in dysfunctional myocardium by resting myocardial blood flow determined with oxygen 15 water PET. J Nucl Cardiol. 2003;10(1):34–45.
28. Schmidt M, Voth E, Schneider CA, Theissen P, Wagner R, Baer FM, Schicha H. F-18-FDG uptake is a reliable predictory of functional recovery of akinetic but viable infarct regions as defined by magnetic resonance imaging before and after revascularization. Magn Reson Imaging. 2004;22(2):229–36.
29. Kühl HP, Lipke CS, Krombach GA, Katoh M, Battenberg TF, Nowak B, Heussen N, Buecker A, Schaefer WM. Assessment of reversible myocardial dysfunction in chronic ischaemic heart disease: comparison of contrast-enhanced cardiovascular magnetic resonance and a combined positron emission tomography-single photon emission computed tomography imaging protocol. Eur Heart J. 2006;27(7):846–53.
30. Schinkel AF, Bax JJ, Poldermans D, Elhendy A, Ferrari R, Rahimtoola SH. Hibernating myocardium: diagnosis and patient outcomes. Curr Probl Cardiol. 2007;32:375–410.
31. Di Carli MF, Hachamovitch R, Berman DS. The art and science of predicting postrevascularization improvement in left ventricular (LV) function in patients with severely depressed LV function. J Am Coll Cardiol. 2002;40:1744–7.
32. Di Carli MF. The quest for myocardial viability: is there a role for nitrate-enhanced imaging? J Nucl Cardiol. 2003;10(6):696–9.
33. Beanlands RS, Ruddy TD, deKemp RA, Iwanochko RM, Coates G, Freeman M, Nahmias C, Hendry P, Burns RJ, Lamy A, Mickleborough L, Kostuk W, Fallen E, Nichol G, PARR Investigators. Positron emission tomography and recovery following revascularization (PARR-1): the importance of scar and the development of a prediction rule for the degree of recovery of left ventricular function. J Am Coll Cardiol. 2002;40(10):1735–43.
34. Zhang X, Liu XJ, Hu S, Schindler TH, Tian Y, He ZX, Gao R, Wu Q, Wei H, Sayre JW, Schelbert HR. Long-term survival of patients with viable and nonviable aneurysms assessed by 99mTc-MIBI SPECT and 18F-FDG PET: a comparative study of medical and surgical treatment. J Nucl Med. 2008;49(8):1288–98.
35. Wang W, Li X, Tian C, Zhao S, Hacker M, Zhang X. Cardiac death in patients with left ventricular aneurysm, remodeling and myocardial viability by gated 99mTc-MIBI SPECT and gated 18F-FDG PET. Int J Cardiovasc Imaging. 2018;34(3):485–93.
36. Bax JJ, Delgado V. Myocardial viability as integral part of the diagnostic and therapeutic approach to ischemic heart failure. J Nucl Cardiol. 2015;22:229–45.
37. Bonow RO, Maurer G, Lee KL, Holly TA, Binkley PF, Desvigne-Nickens P, et al. Myocardial viability and survival in ischemic left ventricular dysfunction. N Engl J Med. 2011;364:1617–25.
38. Beanlands RS, Nichol G, Huszti E, Humen D, Racine N, Freeman M, Gulenchyn KY, Garrard L, Dekemp R, Guo A, Ruddy TD, Benard F, Lamy A, Iwanochko RM. F-18-Fluorodeoxyglucose positron emission tomography imaging assisted management of patients with severe left ventricular dysfunction and suspected coronary disease a randomized, controlled trial (PARR-2). J Am Coll Cardiol. 2007;50:2002–12.
39. Mc Ardle B, Shukla T, Nichol G, deKemp RA, Bernick J, Guo A, et al. Long-term follow-up of outcomes with f-18-fluorodeoxyglucose positron emission tomography imaging assisted management of patients with severe left ventricular dysfunction secondary to coronary disease. Circ Cardiovasc Imaging. 2016;9:e004331.
40. D'Egidio G, Nichol G, Williams KA, Guo A, Garrard L, deKemp R, Ruddy TD, DaSilva J, Humen D, Gulenchyn KY, Freeman M, Racine N, Benard F, Hendry P, Beanlands RS,

PARR-2 Investigators. Increasing benefit from revascularization is associated with increasing amounts of myocardial hibernation: a substudy of the PARR-2 trial. JACC Cardiovasc Imaging. 2009;2(9):1060–8.
41. Ling LF, Marwick TH, Flores DR, Jaber WA, Brunken RC, Cerqueira MD, Hachamovitch R. Identification of therapeutic benefit from revascularization in patients with left ventricular systolic dysfunction: inducible ischemia versus hibernating myocardium. Circ Cardiovasc Imaging. 2013;6:363–72.
42. Uebleis C, Hellweger S, Laubender RP, Becker A, Sohn HY, Lehner S, Haug A, Bartenstein P, Cumming P, Van Kriekinge SD, Slomka PJ, Hacker M. The amount of dysfunctional but viable myocardium predicts long-term survival in patients with ischemic cardiomyopathy and left ventricular dysfunction. Int J Cardiovasc Imaging. 2013;29(7):1645–53.
43. Ponikowski P, Voors AA, Anker SD, et al. ESC guidelines for the diagnosis and treatment of acute and chronic heart failure: the task force for the diagnosis and treatment of acute and chronic heart failure of the European Society of Cardiology (ESC). Eur Heart J. 2016;37:2129–200.
44. Kajander S, Ukkonen H, Sipilä H, Teräs M, Knuuti J. Low radiation dose imaging of myocardial perfusion and coronary angiography with a hybrid PET/CT scanner. Clin Physiol Funct Imaging. 2009;29:81–8.
45. Thomassen A, Petersen H, Johansen A, Braad PE, Diederichsen AC, Mickley H, Jensen LO, Gerke O, Simonsen JA, Thayssen P, Høilund-Carlsen PF. Quantitative myocardial perfusion by O-15-water PET: individualized vs. standardized vascular territories. Eur Heart J Cardiovasc Imaging. 2015;16(9):970–6.
46. Schroeder S, Achenbach S, Bengel F, Burgstahler C, Cademartiri F, de Feyter P, George R, Kaufmann P, Kopp AF, Knuuti J, Ropers D, Schuijf J, Tops LF, Bax JJ, Working Group Nuclear Cardiology and Cardiac CT, European Society of Cardiology, European Council of Nuclear Cardiology. Cardiac computed tomography: indications, applications, limitations, and training requirements: report of a Writing Group deployed by the Working Group Nuclear Cardiology and Cardiac CT of the European Society of Cardiology and the European Council of Nuclear Cardiology. Eur Heart J. 2008;29:531–56.
47. Brodoefel H, Reimann A, Klumpp B, Fenchel M, Ohmer M, Miller S, Schroeder S, Claussen C, Scheule A, Kopp AF. Assessment of myocardial viability in a reperfused porcine model: evaluation of different MSCT contrast protocols in acute and subacute infarct stages in comparison with MRI. J Comput Assist Tomogr. 2007;31:290–8.
48. Brodoefel H, Klumpp B, Reimann A, Fenchel M, Heuschmid M, Miller S, Schroeder S, Claussen C, Scheule AM, Kopp AF. Sixty-four-MSCT in the characterization of porcine acute and subacute myocardial infarction: determination of transmurality in comparison to magnetic resonance imaging and histopathology. Eur J Radiol. 2007;62:235–46.
49. Holz A, Lautamäki R, Sasano T, Merrill J, Nekolla SG, Lardo AC, Bengel FM. Expanding the versatility of cardiac PET/CT: feasibility of delayed contrast enhancement CT for infarct detection in a porcine model. J Nucl Med. 2009;50(2):259–65.
50. Gerber BL, Belge B, Legros GJ, Lim P, Poncelet A, Pasquet A, Gisellu G, Coche E, Vanoverschelde JL. Characterization of acute and chronic myocardial infarcts by multidetector computed tomography: comparison with contrast-enhanced magnetic resonance. Circulation. 2006;113:823–33.
51. Mahnken AH, Koos R, Katoh M, Wildberger JE, Spuentrup E, Buecker A, Gunther RW, Kuhl HP. Assessment of myocardial viability in reperfused acute myocardial infarction using 16-slice computed tomography in comparison to magnetic resonance imaging. J Am Coll Cardiol. 2005;45:2042–7.
52. Lee IH, Choe YH, Lee KH, Jeon ES, Choi JH. Comparison of multidetector CT with F-18-FDG-PET and SPECT in the assessment of myocardial viability in patients with myocardial infarction: a preliminary study. Eur J Radiol. 2009;72:401–5.
53. Lautamäki R, Schuleri KH, Sasano T, Javadi MS, Youssef A, Merrill J, Nekolla SG, Abraham MR, Lardo AC, Bengel FM. Integration of infarct size, tissue perfusion, and metabolism by hybrid cardiac positron emission tomography/computed tomography: evaluation in a porcine model of myocardial infarction. Circ Cardiovasc Imaging. 2009;2:299–305.

Myocardial Inflammation: Focus on Cardiac Sarcoidosis

10

David J. Murphy and Sharmila Dorbala

10.1 Introduction

The imaging evaluation of myocardial inflammation is challenging, often requiring multimodality input for both diagnosis and monitoring. The most common causes of myocardial inflammation include myocardial infarction, myocarditis from any etiology, or sarcoidosis. While the former two pathological entities have been studied experimentally, they have not yet entered routine clinical practice and hence will not be discussed in this chapter. Cardiac sarcoidosis is the quintessential focal myocardial inflammatory condition in which hybrid imaging plays a key role in both diagnosis and management and will be the focus of this chapter.

D. J. Murphy
Department of Radiology, St Vincent's University Hospital, Dublin, Ireland

School of Medicine, University College Dublin, Dublin, Ireland
e-mail: david.murphy@svhg.ie

S. Dorbala (✉)
Cardiovascular Imaging Program, Heart and Vascular Cente, Brigham and Women's Hospital and Harvard Medical School, Boston, MA, USA

Division of Nuclear Medicine and Molecular Imaging, Department of Radiology, Brigham and Women's Hospital and Harvard Medical School, Boston, MA, USA

Division of Cardiovascular Medicine, Department of Medicine, Brigham and Women's Hospital and Harvard Medical School, Boston, MA, USA
e-mail: sdorbala@bwh.harvard.edu

S. G. Nekolla, C. Rischpler (eds.), *Hybrid Cardiac Imaging*,
https://doi.org/10.1007/978-3-030-83167-7_10

10.2 Sarcoidosis Overview

10.2.1 Epidemiology and Demographics

Sarcoidosis is a chronic systemic inflammatory disease characterized by the formation of granulomatous inflammation leading to areas of scarring. The cause is as-of yet unknown, but it is hypothesized that sarcoidosis results from abnormal immune responses from exposure to ubiquitous everyday infectious, organic, and inorganic agents [1]. The fundamental abnormality found in sarcoidosis is the development and accruement of granulomas, which are organized collections of macrophages and epithelioid cells surrounded by lymphocytes. Granulomas form as a protective mechanism to protect surrounding tissue from pathogens and inflammation, and are initiated and maintained by the presence of CD4+ T cells [1].

10.2.2 Epidemiology and Demographics

Sarcoidosis affects people of all ethnic and racial groups and can occur at all ages, but is most common before the age of 50, with a peak occurring between the ages of 20 and 39 years [2, 3]. There is varying incidence throughout the world, likely due to differing genetic predisposition and environmental agent exposure patterns, with the highest incidence observed in Northern Europeans and African Americans [2]. A recent study from Sweden using national population-based registers demonstrated an incidence of 11.5 per 100,000 persons per year, with a prevalence of 0.16% [4]. In the USA, data taken from a health claims database incorporating 15% of the US population showed an incidence rate varying from 7.6 to 8.8 per 100,000 persons per year for the population as a whole, with an incidence of 17.8 per 100,000 persons per year for African Americans, and 8.1 for Caucasians [5]. There is a slight female preponderance in sarcoidosis, with men tending to have a slightly earlier age of onset compared to women across; for example, in the Swedish registry the mean age at diagnosis was 45 years for men and 54 for women [3, 4].

10.2.3 Cardiac Sarcoidosis

Cardiac sarcoidosis (CS) is associated with increased morbidity and mortality, and affects approximately 25–60% of patients with sarcoidosis based on autopsy examinations [6], but is only clinically apparent in approximately 5–25% of patients [1]. Cardiac involvement in sarcoidosis is associated with elevated mortality and morbidity with disease manifestations include atrioventricular block, severe ventricular dysrhythmias, sudden cardiac death and heart failure due to severe left ventricular (LV) dysfunction in approximately 25% of patients with CS [1, 6]. Early diagnosis

is important, as early immunosuppressive treatment may help stop the progression of heart failure [7, 8], and implanted cardiac defibrillators (ICD) can improve overall survival in at-risk patients [9, 10].

10.3 Cardiac Sarcoidosis Diagnosis

10.3.1 Pathology

The basic pathophysiological abnormality in cardiac sarcoidosis is the accumulation of non-caseating granulomas in the heart. The interaction between antigen presenting cells and CD4+ T cells in response to an unknown antigen initiates the formation and maintenance of granulomas [1]. When these granulomas affect the heart, they can involve the myocardium, pericardium, and endocardial surface of both ventricles and both atria. Macroscopically, cardiomegaly is frequently observed in post-mortem series of patients with cardiac sarcoidosis, and CS can grossly mimic dilated, ischemic or even arrhythmogenic cardiomyopathies [11]. The most commonly affected cardiac site for granulomatous infiltration is the inter-ventricular septum, in particular the basal septum, followed by the left ventricular free wall, right ventricular free wall, atrium, pericardium, and endocardium [12, 13]. CS lesions are mainly distributed in the subepicardial layer, but they can affect anywhere in the myocardium [13].

There are two phases of CS recognized on histopathologic assessment, active and healed CS [14]. Active CS is characterized by the presence of epithelioid granulomas comprised of organized collections of epithelioid cells, macrophages, and lymphocytes, without the presence of central caseation [1]. The presence of these non-caseating granulomas is the key histological feature required to make a firm histological diagnosis of CS [1]. The absence of caseation allows differentiation from Mycobacterial infection, and the absence of eosinophils and adjacent myocyte necrosis allows differentiation from giant cell myocarditis [14]. Replacement of the granulomas with fibrosis characterizes the healed phase, which can coexist with active cardiac sarcoid granulomas-identification of the healed phase alone on histological specimens is not sufficient to make a confident diagnosis of cardiac sarcoidosis. Inflammation of intramyocardial arterioles, epicardial arteries, and the cardiac valves may also be seen infrequently [11, 13].

One of the reasons why confirmation of cardiac involvement in sarcoidosis often proves challenging is due to the unavailability of histopathological confirmation. Endomyocardial biopsies are technically challenging to perform, have an associated morbidity, and are often unsuccessful due to the patchy distribution of CS lesions, with a reported sensitivity of 19–30% [15–17]. Although active inflammation and fibrosis can coexist in the heart, biopsy may not always identify both entities in the same samples. Sarcoidosis is a systemic disease and endomyocardial biopsy cannot identify the presence or absence of systemic sarcoid granulomas. As a result, imaging plays a key role in the diagnosis of myocardial and systemic involvement in sarcoidosis.

Table 10.1 Comparison of Cardiac Imaging modalities used in the assessment of Cardiac Sarcoidosis

	Echocardiography	Cardiac CT	CMR	FDG PET/CT
Temporal resolution	15–60 ms	66–135 ms	20–50 ms	N/A
Spatial resolution	0.6–1 mm	0.4–0.6 mm	1–2 mm	4–8 mm
Acquisition time	30 min	0.5–1 min	45–60 min	20–30 min
Radiation	None	3–10 mSv [18]	None	~7 mSv[a]
Anatomical vs. functional assessment	Functional	Anatomic	Anatomic and functional	Anatomic
Myocardial tissue characterization	+	+	++	+++
Portability	++	–	–	–
Contrast agent	Bubble microspheres	Iodinated contrast	Gadolinium	N/A

[a]Using 10 mCi (370 MBq) of FDG

10.3.2 Imaging

Imaging plays a key role in the diagnosis of CS, in the assessment of disease activity and treatment response. Chest radiographs are useful in the initial detection of mediastinal and pulmonary involvement in sarcoidosis, but are not sensitive for CS detection. Echocardiography, cardiac computed tomography (CT), cardiac magnetic resonance imaging (CMR), and positron emission tomography (PET) can help characterize cardiac involvement in sarcoidosis, with CMR and PET/CT the most useful imaging modalities (see Table 10.1 for comparison between cardiac imaging modalities).

Echocardiography is widely available and is often the first imaging modality used when CS is suspected. Trans-thoracic echocardiography (TTE) is the most frequently employed technique, with trans-esophageal echocardiography (TEE) and stress echocardiography playing a limited role, if any. The majority of patients with CS will have normal LV function on TTE, with approximately 30% demonstrating LV dilatation and reduced systolic function [19]. Due to the patchy nature of myocardial sarcoid infiltration, CS can manifest on TTE as regional wall motion abnormalities and focal myocardial wall thickening in a non-coronary artery distribution [20]. The areas of mild wall thickening results from myocardial edema and infiltration, and these areas may appear mildly hyperechoic relative to normal myocardium. Ventricular aneurysms, particularly affecting the septal and anterior walls are also found in approximately 10% of CS patients [12]. These features, however, are often non-specific, rarely detected on echocardiography, and require further assessment with advanced cardiac imaging modalities.

CT is the most commonly used imaging modality in the diagnosis and assessment of mediastinal and pulmonary involvement in sarcoidosis. The typical pattern of thoracic sarcoidosis on chest CT is of bilateral, symmetric mediastinal and hilar lymphadenopathy, and micronodular, perihilar and bilateral upper lobe pulmonary opacities in a perilymphatic distribution [21]. CT currently plays a limited role in the diagnosis of CS, with the major role of cardiac CT being in the exclusion of

significant coronary artery disease as a potential alternative pathology. Occasionally active CS may manifest on chest CT as a focal area of hypoattenuating myocardial wall thickening [22]. End-stage myocardial changes may manifest on contrast enhanced CT as LV dilatation or ventricular aneurysms. Delayed phase cardiac CT acquisition after 5–8 min can also detect areas of myocardial scarring as areas of delayed iodine enhancement [23], with dual energy cardiac CT techniques with low-kV virtual monochromatic image reconstructions showing promise in the characterization of areas of myocardial scarring [24].

CMR and PET are the key advanced cardiac imaging modalities used in CS diagnosis. They play a complementary role, allowing an assessment of myocardial function, helping to determine the burden of active cardiac sarcoid inflammation and healed myocardial scar. Due to the aforementioned difficulty in diagnosing cardiac sarcoidosis based on endomyocardial biopsies, clinical scoring systems are often used to establish the diagnosis of CS, such as the Japanese Ministry of Health and Welfare (JMHW) criteria [25] and the Heart Rhythm Society (HRS) consensus document [26]. These criteria recognize that incorporating clinical and radiological features are required in order to make a diagnosis of CS, with CMR and PET playing a key role, which will be outlined in the following section.

10.4 Imaging Methods

10.4.1 Cardiac MRI

CMR is a multiparametric imaging test with excellent spatial resolution and soft tissue characterization, and is often the initial advanced cardiac imaging modality obtained in patients with suspected CS. CMR provides an assessment of ventricular function and morphology (wall thinning or aneurysms) using bright blood cine imaging (gradient echo [GRE] or steady state free precession [SSFP] sequences), and myocardial tissue characterization using T2 weighted sequences and T1 weighted late gadolinium enhancement (LGE) imaging following administration of gadolinium contrast agent. Morphological abnormalities can occur in late-stage CS [27], but detecting abnormalities in myocardial tissue characterization is the most common method of diagnosing CS on CMR. There is no pathognomonic pattern of CS abnormalities on CMR, but there are imaging features that are highly suggestive, particularly in a patient with known extra-cardiac sarcoidosis. Mesocardial and subepicardial patterns of LGE (non-infarct patterns) are the most common CMR finding in CS, primarily affecting the basal septum and basal lateral wall [28]. The presence of areas of myocardial LGE does not allow discrimination between active inflammation and fibrosis, as both processes manifest as areas of increased extracellular gadolinium accumulation secondary to expansion of the extracellular space; this slows the washout rate of gadolinium, and will manifest as areas of increased signal on T1 weighted LGE imaging [29]. T2 weighted imaging can detect areas of myocardial edema secondary to active inflammation, however, implementing and interpreting this technique in practice is often challenging due to technical difficulties and artefacts [30].

10.4.2 PET

There are several radionuclide imaging tests available to image areas of inflammation, such as ^{99m}Technetium (^{99m}Tc) or ^{111}Indium (^{111}In) labelled white blood cells, ^{99m}Tc bisphosphonates, ^{67}Gallium-citrate, ^{99m}Tc nanocolloids, and ^{99m}Tc or ^{111}In labelled proteins. ^{67}Gallium-citrate SPECT was traditional radionuclide test used for the assessment of sarcoidosis, but is now seldom used as its use is limited by poor spatial resolution and low sensitivity, particularly for extrapulmonary sarcoid when compared to PET with 2-deoxy-2-[^{18}F]fluoro-D-glucose (FDG) [12]. The areas of increased cellular FDG uptake in sarcoidosis are related to the presence of active inflammatory cells in granulomas with elevated glycolytic activity. Both FDG and glucose are taken up by cells via cellular membrane glucose transporters and are phosphorylated by the enzyme hexokinase-after this step, the phosphorylated FDG does not undergo further metabolism, and is trapped within the cells and can be imaged [31]. FDG thus accumulates in active sarcoid lesions packed with hypermetabolic inflammatory cells and will appear as focal areas of increased tracer uptake when imaged with PET. FDG PET is the only modality that can currently reliably identify myocardial inflammation. However, FDG PET cannot identify left ventricular function, and it is typically combined with echocardiography or CMR.

10.4.3 Patient Preparation for FDG Myocardial Inflammation PET

The aim of myocardial inflammation FDG PET imaging is to identify areas of active cardiac inflammation, which should manifest as focal areas of increased FDG uptake relative to normal myocardium. Normal myocardium utilizes glucose as one of its main energy sources, therefore in order to distinguish identify inflammatory from physiological myocardial uptake, normal myocyte metabolism needs to be switched from primarily glucose to free fatty acid metabolism [32]. Free fatty acids account for up to 90% of myocyte oxygen consumption in the fasting state compared to primarily glucose in the postprandial state, therefore FDG PET imaging after a prolonged fast is preferable to suppress physiological myocardial glucose uptake [32]. Prolonged fasting alone may still result in variable suppression of physiological myocardial glucose metabolism, and dietary modification with a high-fat, low-carbohydrate diet in the day before scanning has been shown to reduce FDG uptake by normal myocytes [33]. More recently, these approaches to patient preparation prior to a myocardial inflammation FDG PET have been combined, and the 2017 joint European Association of Nuclear Medicine (EANM)/European Association of Cardiovascular imaging (EACVI)/American Society of Nuclear Cardiology (ASNC) CS imaging guidelines recommend a high-fat, very low-carbohydrate diet for 12–24 h prior to the scan followed by a prolonged 12–18 h fast [20]. In addition, a bolus injection of unfractionated low molecular weight heparin approximately 15 min prior to scanning has been proposed as a potential adjunct to

Table 10.2 Sample diet options for suppressing physiological myocardial glucose utilization

Consume	• Meat fried in oil or butter without breading or broiled (chicken, turkey, bacon, meat-only sausage, hamburgers, steak, fish)
	• Eggs (prepared without milk or cheese)
	• Oil (an option for patients who are vegan or are unable to eat and have enteral access) and butter
	• Clear liquids (water, tea, coffee, diet sodas, etc.)
Acceptable	• Fasting for 18 h or longer if patient cannot eat and has no enteral access or if patient has dietary restrictions preventing consumption of advised diet
Avoid	• Vegetables, beans, nuts, fruits, and juices
	• Bread, grain, rice, pasta, and all baked goods Sweetened, grilled, or cured meats or meat with carbohydrate-containing additives (some sausages, ham, sweetened bacon)
	• Dairy products (milk, cheese, etc.) aside from butter
	• Candy, gum, lozenges, sugar, and sucralose (Splenda; Heartland Food Products Group) Alcoholic beverages, soda, and sports drinks
	• Mayonnaise, ketchup, tartar sauce, mustard, and other condiments Dextrose-containing intravenous medications

Reproduced with permission from Chareonthaitawee et al. [66]

myocardial inflammation FDG PET patient preparation, mediated by its effect on transiently increasing serum free fatty acids and causing a reduction in glucose uptake by normal myocytes [32]. Stress testing and exercise should be avoided on the day of scanning, as this may enhance physiological myocardial glucose metabolism [20] (Table 10.2).

10.4.4 Myocardial Inflammation PET Imaging Protocol

The myocardial inflammation FDG PET protocol involves cardiac image acquisition 60–90 min following intravenous injection of 2.5–5 MBq/kg of FDG [20]. The patient should continue to fast and not be physically active between tracer injection and PET image acquisition to minimize physiological myocardial FDG uptake. In addition to cardiac imaging, whole body imaging from the base of skull to mid-thighs is recommended to allow the assessment of extra-cardiac sites of disease, such as lungs, liver, spleen, lymph nodes, and bones. The cardiac and whole body FDG PET images should be reconstructed with and without attenuation correction.

It is recommended that patients undergoing FDG PET for myocardial inflammation should also have rest perfusion imaging assessment performed with either SPECT or PET myocardial perfusion imaging (MPI) using either ^{99m}Tc, ^{13}N-ammonia or ^{82}Rubidium based radiotracers, depending on local availability and expertise. Whenever possible, attenuation correction should be used with SPECT MPI. Interpretation of perfusion imaging is performed in concert with the FDG imaging, and helps differentiate of areas of scar/active inflammation from normal myocardium [34].

10.4.5 PET Image Interpretation

Interpretation of FDG PET images for myocardial inflammation is challenging, and requires an understanding of patient preparation and metabolic state required to reliably distinguish CS related myocardial inflammation from physiological myocardial glucose uptake. The FDG and rest MPI scans are usually displayed side by side with the image intensity normalized to the maximum counts per pixel of each data set. A combination of dedicated cardiac imaging plane (short-axis, horizontal and vertical long axis) and standard orthogonal plane (axial, coronal, and sagittal) nuclear medicine whole body PET images are typically reviewed.

There are four patterns of LV myocardial FDG uptake that should looked for on the cardiac FDG PET images [20, 35]:

1. "None"-no myocardial FDG uptake
2. "Diffuse"-diffuse myocardial FDG uptake
3. "Focal"-focal area(s) of increased myocardial FDG uptake
4. "Focal-on-diffuse"—focal area(s) of increased FDG uptake on a background of diffuse myocardial FDG uptake.

The "focal" or "focal-on-diffuse" patterns of myocardial FDG uptake are considered abnormal, and are likely to be consistent with CS, with the foci of increased FDG uptake felt to represent areas of myocardium infiltrated with active inflammatory sarcoid granulomas. The normal pattern of myocardial FDG uptake for an adequately prepared patient is to have no myocardial FDG uptake, with the LV blood pool demonstrating higher activity than myocardium. Diffuse, homogenous low-grade FDG uptake throughout the lateral wall is also considered to represent a physiological pattern, particularly in the absence of any superimposed focal areas of increased FDG uptake or resting perfusion defects on MPI [35]. The "diffuse" pattern of myocardial FDG uptake is the most challenging to interpret as it can be nonspecific due to poor/lack of suppression of normal myocardial glucose uptake, or it may represent extensive, diffuse sarcoid granulomatous infiltration with heterogenous FDG uptake. It is also important to evaluate PET images for any evidence of focal right ventricular FDG uptake, which appears to be an adverse prognostic feature in CS [36].

The whole body FDG PET/CT images are reviewed to assess for sites of extracardiac sarcoidosis [37]. This can be particularly useful in finding a suitable extracardiac site to biopsy to confirm sarcoid diagnosis; common sites of extra-cardiac disease include mediastinal and hilar lymph nodes, pulmonary, liver, splenic, and osseous sites of disease. For patients with implanted cardiac devices in situ, the non-attenuation corrected FDG PET images should be reviewed to avoid reporting of any false-positive lead/device FDG uptake caused by attenuation correction artefact [38].

Combined assessment of FDG and MPI images is recommended to provided additional information about the status of CS (scar versus inflammation) if present, and the extent of myocardial involvement. The rest MPI images are examined for

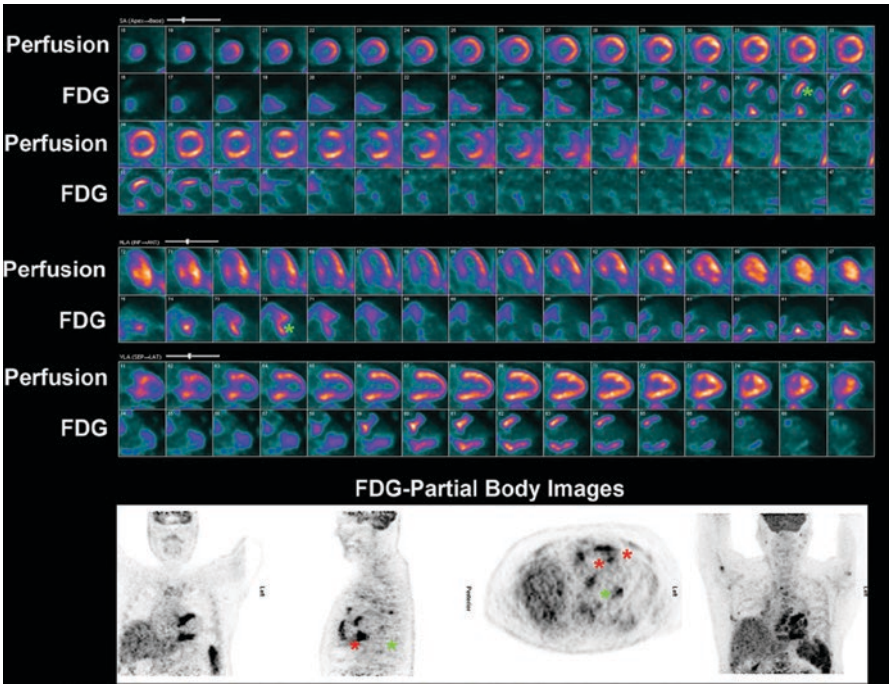

Fig. 10.1 Images from a patient with newly diagnosed cardiac sarcoidosis. Myocardial perfusion images (N-13 ammonia PET) and FDG images are shown in alternate rows. There is a small perfusion defect of moderate intensity in the basal anterolateral wall (best seen on the short-axis images). There are multiple foci of increased FDG uptake in the left ventricular (septum, and anterolateral and inferolateral segments) and right ventricular (free wall) walls. Partial body FDG images are shown below. Red asterisks indicate focus of fibrosis and inflammation in the left ventricular anterolateral wall and the septum. Green arrows indicated focus of inflammation in the right ventricular free wall. *FDG* ^{18}F-fluorodeoxyglucose

perfusion defects, and are best reviewed at the same time as the cardiac FDG PET (Fig. 10.1). CS perfusion defects on MPI may be present in active inflammatory lesions due to alteration in the coronary microcirculation, and in the chronic phase due to the presence of replacement fibrosis. The rest MPI images are very useful in individuals with a diffuse pattern of cardiac FDG uptake, as patients with diffuse cardiac sarcoid infiltration are unlikely to have a completely normal rest perfusion study. Unlike perfusion defects due to coronary artery disease, the perfusion abnormalities in CS do not match with a typical coronary artery territory.

The following CS FDG and MPI patterns, although not verified pathologically, have been described [36, 39]:

- "early"-mildly FDG positive, normal MPI;
- "progressive inflammatory"-FDG positive with small perfusion defects on MPI;
- "peak active"-high SUV FDG uptake with moderate sized perfusion defects on MPI;

- "progressive myocardial impairment"-high SUV FDG uptake with large perfusion defects on MPI;
- "fibrosis-predominant"—FDG negative with perfusion defects on MPI.

In line with Scadding system for staging pulmonary sarcoid, the following staging system for CS has also been proposed [20, 40]:

- Stage 0 = Normal FDG, normal MPI
- Stage 1 = FDG positive, normal MPI
- Stage 2 = FDG positive with perfusion defects on MPI in the same myocardial segments
- Stage 3 = FDG positive with perfusion defects in different myocardial segments on MPI
- Stage 4 = normal FDG but perfusion defects on MPI.

10.4.6 Pitfalls in FDG Image Interpretation

There are potential pitfalls in image interpretation of myocardial inflammation FDG PET that imagers should be aware of. Firstly, the use of conventional nuclear cardiology schemes to display the cardiac FDG PET images normalize the image intensity range to the most intense pixel within the sampled volume. This may falsely elevate the displayed FDG uptake, particularly when the myocardial uptake is only marginally above that of blood pool. The normalized display systems also may impair judgment of the absolute intensity of myocardial FDG uptake, which may be problematic when assessing for treatment response in follow-up studies. To overcome these difficulties, the cardiac FDG PET images should be reviewed on traditional nuclear medicine PET display systems in addition to the normalized nuclear cardiology display schemes [34].

Unfortunately, despite a better understanding of patient preparation, approximately 10–15% of myocardial inflammation FDG PET scans remain non-diagnostic due to incomplete suppression of physiological myocardial glucose uptake, even with strict adherence to the aforementioned patient preparation protocols (Fig. 10.2) [41]. This appears to especially be the case in the failing heart which can cause glucose upregulation as an adaptive mechanism, hindering conversion to free fatty acid metabolism [42]. It is also important to exclude underlying significant epicardial coronary artery disease, as the pattern of mismatched perfusion defect with increased FDG uptake may be seen hibernating ischemic myocardium as well as in myocardial inflammation. FDG is a non-specific tracer, and there are other conditions that may mimic the focal pattern of increased myocardial FDG uptake seen with CS, including other causes of myocardial inflammation such as giant cell myocarditis, other cardiomyopathies (particularly arrhythmogenic and dilated cardiomyopathies), and benign (myxomas and hemangiomas) and malignant (particularly lymphoma and metastases) cardiac tumors [42, 43]. The risk of solid and hematopoietic malignancies is increased in patients with systemic sarcoidosis [43]; hence,

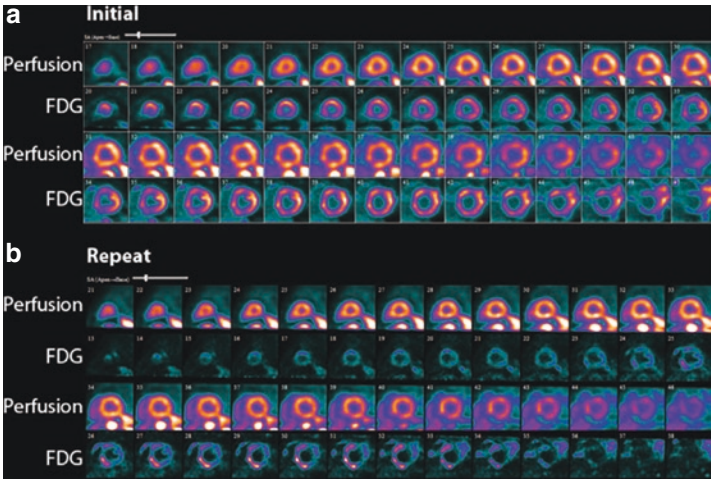

Fig. 10.2 Limited dietary preparation for FDG PET (**a**) which improved on repeat imaging (**b**). An example of perfusion and FDG images showing diffuse FDG uptake in normally perfused segments suggesting incomplete suppression of physiological uptake (**a**) Repeat images after 3 months (**b**) using a more stringent carbohydrate restriction and increase intake of high fat diet followed by 12 h fast prior to FDG imaging demonstrated better suppression of physiological myocardial glucose uptake. *FDG* ^{18}F-fluorodeoxyglucose

a careful review of the particle body images for dentification of malignancy is particularly important. If there is concern for cardiac malignancy, examination of the partial body PET images for evidence of extra-cardiac malignancy is useful, along with obtaining other cardiac imaging modalities. CMR is particularly useful in the assessment of potential cardiac masses owing to its excellent soft tissue resolution and tissue characterization capabilities [44].

10.4.7 Hybrid Imaging

The benefits of hybrid imaging in myocardial FDG PET, paired with either CT or MRI are manifest. Hybrid FDG PET/CT is currently the standard of care for myocardial inflammation assessment using molecular imaging. Aside from providing attenuation correction for the myocardial FDG PET dataset, the low dose CT component also helps with anatomical localization when viewed alongside the PET images on a hybrid nuclear medicine display system. Accurately localizing cardiac FDG uptake using the PET images alone can be challenging, particularly when there is suppression of physiological cardiac FDG uptake. Interpretation alongside the CT images allows for more accurate localization of myocardial FDG activity, for example, distinguishing papillary muscle from adjacent LV myocardium. The CT component of the PET/CT examination is also crucial in the evaluation, providing more accurate anatomical localization of any abnormal site of FDG uptake, including atrial and right ventricular uptake and in distinguishing myocardial uptake from mediastinal lymph node uptake.

The CT images may also demonstrate changes typical of sarcoidosis, such as mediastinal lymphadenopathy with amorphous central calcification, pulmonary micronodules in a perilymphatic distribution, and upper lobe predominant perihilar fibronodular pulmonary opacification with traction bronchiectasis in more advanced cases [21].

Novel integrated hybrid PET/MRI systems have the potential to marry the superior soft tissue resolution and multiparametric capabilities of MRI with the metabolic information provided by FDG PET in a single examination. Hybrid cardiac FDG PET/MRI combines the comprehensive evaluation of cardiac function, morphology and tissue characterization provided by CMR with the metabolic information provided by FDG PET. Initial series suggest that integrated FDG PET/MRI appears feasible in the evaluation of suspected cardiac sarcoidosis [45–47]. Whole body PET/MRI images should also be acquired akin to the FDG PET/CT protocol, with the caveat that MRI is inferior to CT in evaluation of the pulmonary parenchyma due to its inferior spatial resolution [48]. Recent advances in PET/MRI technology, particularly the development of new, free breathing ultrashort echo time MRI sequences greatly improves the quality of pulmonary imaging by MRI over traditional dual echo gradient echo imaging [49], and would be helpful in the evaluation of suspected pulmonary sarcoid. Integrated PET/MRI is an exciting new imaging modality with the potential to provide a comprehensive "one-stop shop" imaging test for cardiac inflammation evaluation, but its roll out will be limited by the large cost relative lack of availability of this new imaging modality, and unclear benefit when compared to sequential PET and MR imaging.

10.5 Role of Imaging

10.5.1 Cardiac Sarcoid Diagnosis

Early diagnosis of cardiac sarcoid infiltration is important, as studies suggest that steroid immunosuppressive therapy should be initiated before the inset of significant left ventricular dysfunction [8, 50]. As previously described, FDG PET and CMR playing a key role in CS diagnosis. Evaluating their diagnostic performance in CS can be difficult to the lack of definite gold standard; histopathological assessment is generally the ideal reference standard for any imaging study examining diagnostic performance, but as aforementioned endomyocardial biopsy is poorly sensitive in CS due to its focal nature [15], and is thus seldom used as the gold standard in the literature. As a result, clinical scoring systems that incorporating clinical and radiological features are often used to establish the diagnosis of CS, such as the Japanese Ministry of Health and Welfare (JMHW) criteria [25] and the Heart Rhythm Society (HRS) consensus document [26].

FDG PET/CT has a reported sensitivity and specificity of 0.89 and 0.78 respectively for the diagnosis of CS according to an initial meta-analysis published in 2012 of seven studies with incorporating 164 patients, with an overall disease prevalence of 50% in the cohort [51]. A more recent meta-analysis including 17 studies with 891 patients reports a pooled sensitivity of 0.84 and specificity of 0.83 for CS

diagnosis by FDG PET [52]. One of the problems in these FDG PET meta-analyses is the heterogeneity in the dietary and patient preparation used in the included studies, which is a potential significant confounder. Tang et al. [53] attempted to adjust for patient preparation in their 2016 systematic review and meta-analysis of 16 studies encompassing 559 patients; the authors found that FDG PET had an overall sensitivity and specificity of 0.75 and 0.81 respectively for CS diagnosis amongst the entire cohort, improving to a sensitivity and specificity of 0.88 and 0.84 on a subgroup analysis of studies that employed a prolonged >12 h fast as patient preparation.

CMR usually relies on the presence of a non-infarct pattern of LGE (typically subepicardial/mesocardial), with or without the presence of myocardial edema on T2 weighted imaging to suggest a diagnosis of CS. These changes typically affect the basal septum and lateral wall. A recent meta-analysis incorporating eight studies with 649 participants reported a sensitivity and specificity of 0.93 and 0.85 respectively for CS diagnosis using CMR [54]. The studies included in this meta-analysis have sensitivities ranging from 0.75 to 1 and specificities ranging from 0.68 to 1; this significant heterogeneity is likely due to the variation in reference standards used.

Isolated cardiac sarcoid is a well-described clinical entity, estimated to account for approximately 25% of CS cases [55]. Patients with isolated CS have worse LV systolic function at presentation compared with patients with systemic sarcoidosis [36]. Making a definite diagnosis of isolated CS is particularly challenging due to the poor sensitivity of endomyocardial biopsy, and the requirement for tissue confirmation of extra-cardiac sarcoid in the clinical criteria [41]. This difficulty in "confirming" a diagnosis of CS without recourse to reliable histological sampling is underlined by a recent series examining the hearts of 18 patients who underwent cardiac transplantation and had a pre-transplant FDG PET/CT; using a "probable" cutoff for FDG PET resulted in a sensitivity of 1.0, but a specificity of only 0.33, with 3 out of the 9 probable CS cases by FDG PET found to be cases of arrhythmogenic cardiomyopathy on histological examination of the explant [56].

There is a growing body of evidence that FDG PET and CMR play a complementary role in the diagnosis of CS, increasing diagnostic certainty in this difficult to diagnose condition. CMR and FDG PET will often show different patterns of disease in patients with CS due to differences in their technique. The added benefit of performing an FDG PET after a "positive" CMR for CS is to increase diagnostic certainty and also to provide an assessment of the burden of metabolically active disease that can be helpful to follow response to therapy (Fig. 10.3). A CMR after a "positive" FDG PET can help quantify left ventricular ejection fraction and identify patients who may benefit from an ICD (Class I indications: sustained ventricular tachycardia or cardiac arrest, left ventricular ejection fraction ≤35%; Class IIa indications: LVEF > 35% with syncope, or scar by CMR or PET, or inducible ventricular tachyarrhythmia, or any indication for pacing) [10]. Vita et al. [57] categorized the likelihood of active CS in 107 patients based on CMR and FDG PET/CT scans as (a) no (<10%); (b) possible (10–50%); (c) probable (50–90%); and (d) highly probable (>90%). Among the 85% of patients with evidence of non-infarct pattern

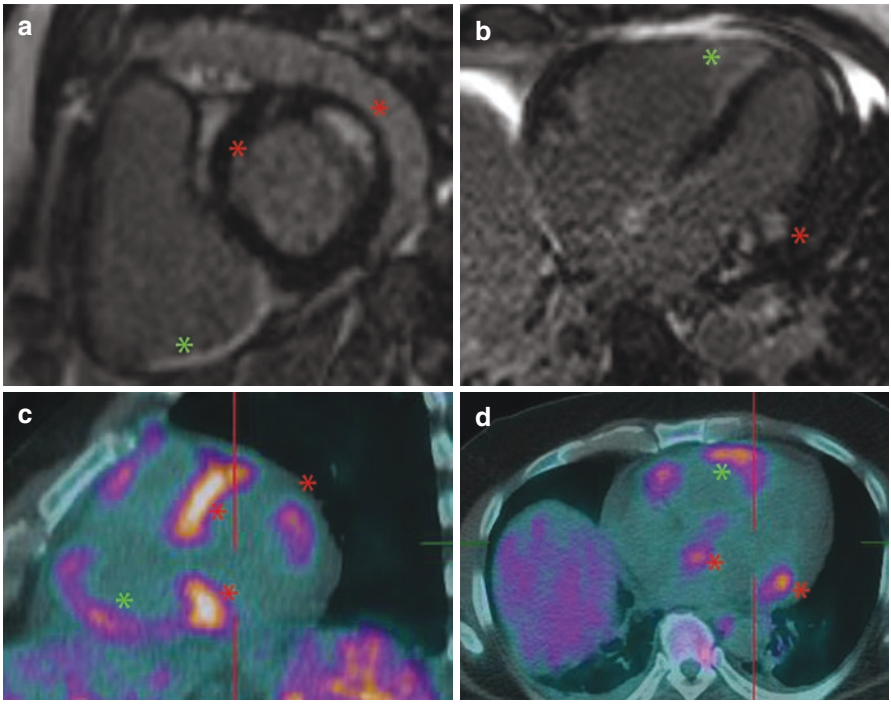

Fig. 10.3 Correlation of FDG PET and CMR-LGE. The foci of increased FDG uptake on the cardiac PET images co-localized accurately with regions of late gadolinium enhancement (LGE) on CMR images (from patient from Fig. 10.1). (**a**) short axis CMR; (**b**) 4 chamber view on CMR; (**c**) short axis FDG images; and (**d**) transaxial FDG images. Red asterisks indicate focus of fibrosis and inflammation in the left ventricular anterolateral wall and the septum. Green arrows indicated focus of inflammation in the right ventricular free wall. *FDG* ^{18}F-fluorodeoxyglucose

LGE on CMR, 66% had increased myocardial FDG uptake on FDG PET, re-enforcing the assertion that the presence of LGE alone cannot be reliably used to diagnose active inflammatory type CS. When the PET findings were added to the CMR results, the authors found that the likelihood of active CS was re-classified in 45% of cases. As expected, the advent of hybrid PET/MRI is of significant interest as a potential single test for CS [45, 46]. Wicks et al. [47] evaluated 51 patients with suspected CS with a simultaneous hybrid FDG PET/MRI protocol, and found it superior for CS diagnosis compared to either PET or CMR alone. These hybrid systems do however remain limited in availability due to cost, and the majority of combined CMR/FDG PET assessments will be performed on stand-alone PET/CT and MRI scanners for the foreseeable future.

The proposed algorithm for the combined CMR and FDG PET/CT assessment of suspected CS is to begin with CMR to determine the likelihood of CS and to evaluate for potential alternative diagnoses [57]. Patients with a CMR that is negative for CS do not need undergo FDG PET/CT scanning unless there is a persistent high clinical suspicion for CS. Individuals with a CMR that is either inconclusive or

positive for CS should proceed to FDG PET/CT to determine the likelihood of CS when uncertainty exists, to evaluate for the presence of active inflammatory disease, and to identify potential extra-cardiac sites for biopsy, if required [41].

10.5.2 Prognosis

Cardiac involvement in sarcoidosis is associated with poorer prognosis, which can be related to worsening heart failure and potentially fatal cardiac arrhythmias [1]. Blankstein et al. [36] assessed outcomes in 118 patients who underwent both MPI and FDG PET/CT for suspected CS, finding that the presence of both a perfusion defect and a pathological pattern of myocardial FDG uptake was associated with an increased risk of death or ventricular tachycardia, after adjusting for ejection fraction (Fig. 10.4). In particular, patients with evidence of right ventricular inflammation had a fivefold increased event rate compared to normal controls. In their hybrid FDG PET/MRI study on 51 patients with suspected CS, Wicks et al. [47] demonstrated that right ventricular uptake on PET was an independent predictor of adverse cardiac events, along with the presence of LGE on CMR. The presence of LGE has

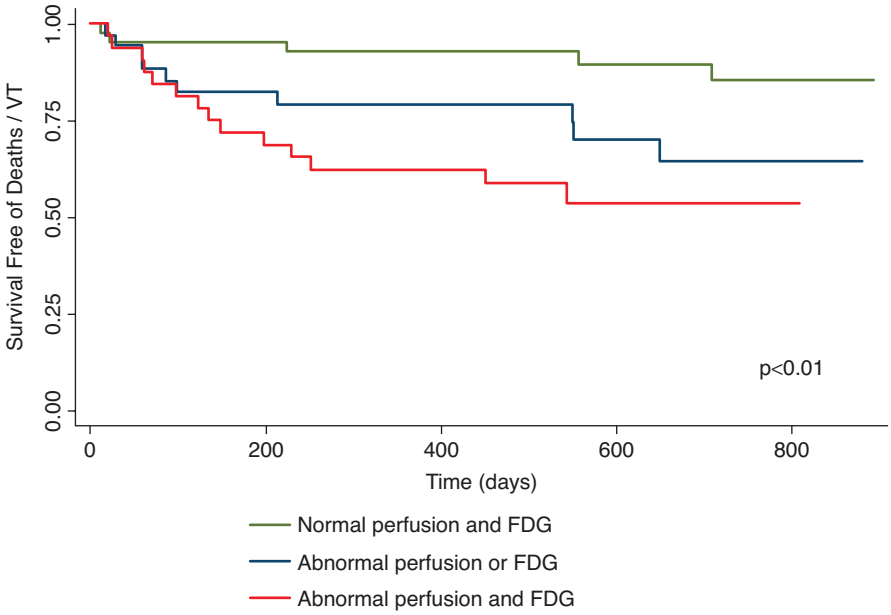

Fig. 10.4 Prognostic value of FDG and myocardial perfusion imaging. In a study of 14 subjects, Blankstein et al. [36] showed that patients with both normal perfusion and no myocardial ^{18}F-FDG uptake (green line) showed the best event free survival (survival free of ventricular arrhythmias), while those with both abnormal perfusion and abnormal ^{18}F-FDG uptake (red line) showed the worst event free survival. *FDG* ^{18}F-fluorodeoxyglucose. (Figure reproduced with permission from Blankstein et al. [36])

been demonstrated as the most prognostic CMR feature of CS-one meta-analysis of ten studies including 760 patients with known or suspected CS undergoing CMR found that individuals with LGE had higher all-cause mortality and major arrhythmogenic events [58]. This confirmed the findings on an earlier meta-analysis of seven studies of 694 patients by Hulten et al. [59].

10.5.3 Response Assessment

FDG PET has unique ability to assess the metabolic response to anti-inflammatory therapy in CS, which can improve outcomes (Figs. 10.5 and 10.6)[[60]. CMR is often limited in these circumstances due the inability to detect changes in LGE and due to the frequent implantation of cardiac pacemakers or defibrillators for heart block, ventricular tachyarrhythmias or for secondary prevention of cardiac arrest. In a small cohort of 23 patients with CS who underwent serial FDG PET/CT imaging post steroid therapy, a reduction in myocardial SUV_{max} on the post treatment PET demonstrated a significant relationship with improvement in LV ejection fraction [61]. Measuring serial myocardial SUV_{max} is straightforward to perform, but comes with the caveat that assigning strict SUV_{max} cutoff values to determine response or progression be problematic due to the myriad of factors that can affect its readings other than lesional metabolic activity, including blood glucose levels, radiotracer uptake time, scanner type, and PET reconstruction algorithm [31]. Other PET metrics such as SUV_{mean} and measurement of the volume of metabolically active myocardium have also shown efficacy in CS treatment response studies [62, 63]. Persistent and increased myocardial FDG PET positivity after steroid treatment is associated with poor clinical outcomes, may help to predict steroid-resistant CS, and indicate which patients require escalation of immunosuppressive therapy [64]. It is not clear whether performing a qualitative visual assessment of FDG uptake suffices for treatment response assessment or whether semi-quantitative measurements, such as myocardial SUV_{max}, should also be used [65], and further studies will be required to determine the optimum approach to treatment response assessment.

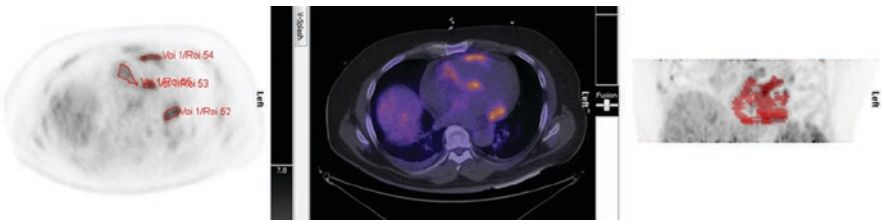

Fig. 10.5 Quantitation of volume of inflamed myocardium. Relative FDG imaging is not adequate for evaluation of response to therapy. For this reason, quantitation of FDG uptake using standardized uptake values (SUV) or volume of inflamed myocardium is important. The volume of inflamed myocardium on the cardiac FDG images of the patient from Fig. 10.1, using an SUVmax threshold of 2.7 as 138 cm^3. *FDG* ^{18}F-fluorodeoxyglucose

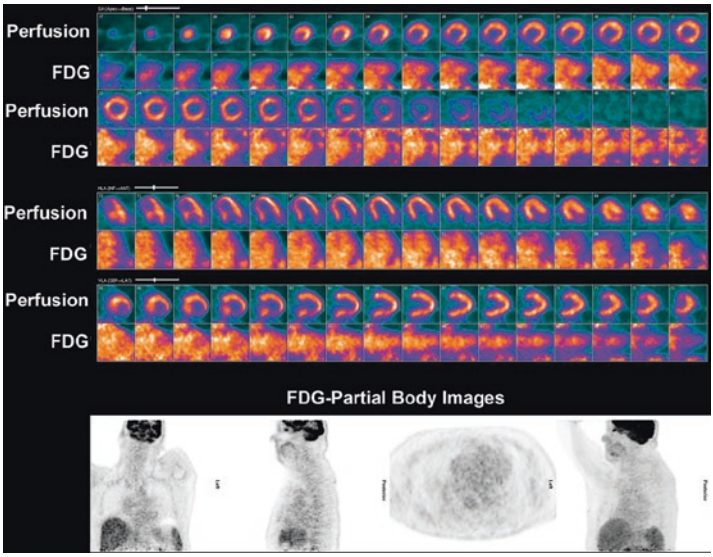

Fig. 10.6 Evaluation of response to therapy. Repeat imaging of the patient from Fig. 10.1, after 6 months of high dose oral steroid showed near complete resolution of inflammation on FDG images (cardiac and partial body images show blood pool activity without focal myocardial uptake) with a small persistent region of fibrosis in the basal anterolateral wall (perfusion defect on the basal anterolateral wall). Quantitatively, there was no detectable inflamed myocardium (no pixels with SUV > 2.7). *FDG* ^{18}F-fluorodeoxyglucose

10.6 Guidelines

Due to the difficulties in obtaining tissue confirmation in cases of suspected cardiac sarcoidosis, clinical scoring systems are often used to establish the diagnosis of CS, such as from the as the Japanese Ministry of Health and Welfare (JMHW) criteria [25] and Heart Rhythm Society (HRS) consensus document [26]. In addition, there is a joint procedural statement on CS imaging issued by the European Association of Nuclear Medicine (EANM), European Association of Cardiovascular imaging (EACVI) and American Society of Nuclear Cardiology (ASNC) [20], and a joint consensus document on the role of FDG PET/CT in CS diagnosis and management issued by the Society of Nuclear Medicine and Molecular Imaging (SNMMI) and ASNC [66].

The JMHW criteria are the longest established, and are commonly used as the reference standard for CS diagnosis in imaging research studies. The most recent iteration of these criteria provides guidance on how a clinical diagnosis of CS can be made in the absence of positive myocardial histology; this requires a positive extra-cardiac biopsy for epithelioid granulomas along with a combination of electrophysiological/ECG (high grade AV block, ventricular tachycardia/fibrillation), functional (LVEF < 50%), morphological (basal septal thinning of ventricular aneurysms), and typical imaging features (increased cardiac uptake on FDG PET/^{67}Ga

Table 10.3 Summary of the JMHW and HRS diagnostic criteria for cardiac sarcoidosis [25, 26]

JMHW	HRS
Histological diagnosis	**Histological diagnosis**
CS confirmed by histology	CS confirmed by histology
Clinical diagnosis	**Clinical diagnosis**
Histological diagnosis of extra-CS and	Histological diagnosis of extra-CS and
Two or more major criteria or one major and two minor criteria	One or more of the following is present:
Major criteria	• Steroid responsive cardiomyopathy or heart block
• Advanced AV block/VT/VF	• Unexplained reduced LVEF < 40%
• Basal thinning IV septum/ventricular aneurysms	• Unexplained sustained VT
• LVEF < 50%	• Mobitz type 2 second degree heart block/third degree heart block
• Elevated cardiac tracer uptake on Ga^{67} citrate scintigraphy or FDG PET	• Patchy uptake on dedicated FDG cardiac PET in a pattern consistent with CS
• Myocardial LGE on CMR	• LGE on CMR in a pattern consistent with CS
Minor criteria	• Positive gallium uptake in a pattern consistent with CS on Ga67 citrate scintigraphy
• Abnormal ECG: non-sustained VT, multiple PVCs, bundle branch block	
• Perfusion defects on MPI	
• Endomyocardial biopsy showing monocyte infiltration or severe myocardial interstitial fibrosis	

CS cardiac sarcoidosis, *JMHW* Japanese Ministry for Health & Welfare, *HRS* Heart Rhythm Society, *AV* atrioventricular, *IV* inter-ventricular, *LVEF* left ventricular ejection fraction, *LGE* late gadolinium enhancement, *PVC* premature ventricular contraction, *MPI* myocardial perfusion imaging

citrate scintigraphy or non-infarct pattern LGE on CMR) suggestive of CS (see Table 10.3) [25]. The updated guidelines also include a provision for diagnosing isolated cardiac sarcoidosis for patients without evidence of extra-cardiac disease, provided they demonstrate increased myocardial uptake on FDG PET/^{67}Ga citrate scintigraphy along with further ECG, functional and morphological features as described above. The HRS criteria are broadly similar, providing a pathway to make a clinical diagnosis of CS once there is a histological diagnosis of extra-cardiac sarcoidosis along with one of a number of clinical, ECG or imaging features, with the latter including patchy cardiac uptake on FDG PET and non-infarct pattern LGE on CMR (see Table 10.3) [26]. The HRS criteria do not allow for a diagnosis of isolated CS, with the HRS recommending endomyocardial biopsy in cases of suspected isolated CS or negative extra-cardiac biopsy.

The joint expert consensus document issued by SNMMI and ASNC provides guidance on the role of FDG PET/CT in CS diagnosis and monitoring [66]. This document identifies the following clinical scenarios in which FDG cardiac PET may be useful for patients with known or suspected CS:

- Patients with histological evidence of extra-cardiac sarcoidosis and abnormal screening for CS (using a combination of ECG, echocardiography, and CMR features)
- Patients under 60 with unexplained new significant conduction system disease
- Patients with idiopathic sustained VT
- Patients with proven CS as a disease response assessment.

This EANM/EACVI/ASNC joint procedural statement covers the role of multimodality imaging in the diagnosis and monitoring of CS [20]. They propose that CMR should be the first advanced cardiac imaging test for individuals with suspected CS, with FDG PET/CT scanning recommended for patients with abnormal or equivocal CMRs, or as the initial test for patients in whom an MRI is contraindicated (for example patients with a non-MRI conditional implantable cardiac device, severe claustrophobia or severe renal dysfunction precluding gadolinium administration). This multi-society join statement also recommends that FDG PET with SUV_{max} quantification be used to monitor response to therapy.

10.7 Future Directions for Myocardial Inflammation PET

The future of myocardial inflammation hybrid imaging relies on the development of radioisotopes that are more specific to areas of myocardial inflammation, preferably without physiological cardiovascular avidity. Gallium[68] linked somatostatin receptor PET radiotracers such as ^{68}Ga-DOTA-NaI-octreotide (DOTANOC), ^{68}Ga-DOTA-D-Phe-Tyr-octreotide (DOTATOC), and ^{68}Ga-DOTA-D-Phe-Tyr-octreotate (DOTATATE) are potentially useful tracers for cardiac sarcoidosis. These radiotracers are primarily used for the diagnosis and staging of neuroendocrine tumors, which abundantly express somatostatin receptors (SSTR) [67]. Activated inflammatory cells found in sarcoid granulomas such as macrophages, epithelioid cells, and multinucleated giant cells have abundant SSTRs on their cell surface, in particular SSTR2A, which is not expressed on normal cardiomyocytes [68]. Exploratory studies have demonstrated that cardiac sarcoid lesions demonstrate increased uptake on PET with ^{68}Ga-SSTR targeted radiotracer [69–71]. These radiotracers have a beneficial lack of cardiac uptake under physiological conditions, which is potentially advantageous both in CS lesion detection, and in avoiding the complex dietary preparation required for successful myocardial inflammation FDG PET. An initial pilot study comparing FDG and ^{68}Ga-DOTATE PET suggest that FDG may be more sensitive for the detection of cardiac inflammation, while ^{68}Ga-SSTR targeted radiotracers may detect more active extra-cardiac disease [72]. These early studies, however, should be interpreted with caution and regarded as preliminary pending larger studies, including treatment response assessment.

3′-Deoxy-3′-^{18}F-fluorothymidine (FLT) is a promising PET tracer for the evaluation of cell proliferation, accumulating in cells with high-turnover, such as granulomatous inflammatory cells [73]. FLT has an advantageous biodistribution for cardiac imaging with a lack of physiological myocyte uptake, and requires neither

prolonged diet nor a special diet prior to scanning. Experimental data has shown that FLT can detect sites of cardiac and extra-cardiac involvement in sarcoidosis [73]. Further clinical studies will be required, however, to evaluate the novel use of these agents in myocardial inflammation imaging before they can translate to clinical practice and supplant FDG.

10.8 Conclusions

Sarcoidosis is a complex, disease that often requires a multi-disciplinary approach for optimum management. A multimodality imaging approach is optimal in the evaluation of patients with suspected cardiac involvement, and hybrid FDG PET/CT plays an important role in both diagnosis and treatment response assessment.

Conflicts We have no conflicts of interest to disclose.

References

1. Iannuzzi MC, Rybicki BA, Teirstein AS. Sarcoidosis. N Engl J Med. 2007;357:2153–65.
2. Cozier YC. Assessing the worldwide epidemiology of sarcoidosis: challenges and future directions. Eur Respir J. 2016;48:1545–8.
3. Arkema EV, Cozier YC. Epidemiology of sarcoidosis: current findings and future directions. Ther Adv Chronic Dis. 2018;9:227–40.
4. Arkema EV, Grunewald J, Kullberg S, Eklund A, Askling J. Sarcoidosis incidence and prevalence: a nationwide register-based assessment in Sweden. Eur Respir J. 2016;48:1690–9.
5. Baughman RP, Field S, Costabel U, et al. Sarcoidosis in America. Analysis based on health care use. Ann Am Thorac Soc. 2016;13:1244–52.
6. Silverman KJ, Hutchins GM, Bulkley BH. Cardiac sarcoid: a clinicopathologic study of 84 unselected patients with systemic sarcoidosis. Circulation. 1978;58:1204–11.
7. Chiu C-Z, Nakatani S, Zhang G, et al. Prevention of left ventricular remodeling by long-term corticosteroid therapy in patients with cardiac sarcoidosis. Am J Cardiol. 2005;95:143–6.
8. Grutters JC, van den Bosch JMM. Corticosteroid treatment in sarcoidosis. Eur Respir J. 2006;28:627–36.
9. Paz HL, McCormick DJ, Kutalek SP, Patchefsky A. The automated implantable cardiac defibrillator. Prophylaxis in cardiac sarcoidosis. Chest. 1994;106:1603–7.
10. Kazmirczak F, Chen K-HA, Adabag S, et al. Assessment of the 2017 AHA/ACC/HRS guideline recommendations for implantable cardioverter-defibrillator implantation in cardiac sarcoidosis. Circ Arrhythm Electrophysiol. 2019;12:e007488.
11. Bagwan IN, Hooper LVB, Sheppard MN. Cardiac sarcoidosis and sudden death. The heart may look normal or mimic other cardiomyopathies. Virchows Arch. 2011;458:671.
12. Jeudy J, Burke AP, White CS, Kramer GBG, Frazier AA. Cardiac sarcoidosis: the challenge of radiologic-pathologic correlation: from the radiologic pathology archives. Radiographics. 2015;35:657.
13. Tavora F, Cresswell N, Li L, Ripple M, Solomon C, Burke A. Comparison of necropsy findings in patients with sarcoidosis dying suddenly from cardiac sarcoidosis versus dying suddenly from other causes. Am J Cardiol. 2009;104:571–7.
14. Hashimura H, Kimura F, Ishibashi-Ueda H, et al. Radiologic-pathologic correlation of primary and secondary cardiomyopathies: mr imaging and histopathologic findings in hearts from autopsy and transplantation. Radiographics. 2017;37:719–36.

15. Cooper LT, Baughman KL, Feldman AM, et al. The role of endomyocardial biopsy in the management of cardiovascular disease: a scientific statement from the American Heart Association, the American College of Cardiology, and the European Society of Cardiology Endorsed by the Heart Failure Society of America and the Heart Failure Association of the European Society of Cardiology. Eur Heart J. 2007;28:3076–93.
16. Roberts WC, McAllister HA, Ferrans VJ. Sarcoidosis of the heart. A clinicopathologic study of 35 necropsy patients (group 1) and review of 78 previously described necropsy patients (group 11). Am J Med. 1977;63:86–108.
17. Uemura A, Morimoto S, Hiramitsu S, Kato Y, Ito T, Hishida H. Histologic diagnostic rate of cardiac sarcoidosis: evaluation of endomyocardial biopsies. Am Heart J. 1999;138: 299–302.
18. Aghayev A, Murphy DJ, Keraliya AR, Steigner ML. Recent developments in the use of computed tomography scanners in coronary artery imaging. Expert Rev Med Devices. 2016;13:545–53.
19. Mehta D, Lubitz SA, Frankel Z, et al. Cardiac involvement in patients with sarcoidosis: diagnostic and prognostic value of outpatient testing. Chest. 2008;133:1426–35.
20. Slart RHJA, Andor WJM, Glaudemans AS, Lancellotti P. A joint procedural position statement on imaging in cardiac sarcoidosis: from the Cardiovascular and Inflammation & Infection Committees of the European Association of Nuclear Medicine, the European Association of Cardiovascular Imaging, and the American Society of Nuclear Cardiology. Eur Heart J Cardiovasc Imaging. 2017;18:1073–89.
21. Guidry C, Fricke RG, Ram R, Pandey T, Jambhekar K. Imaging of sarcoidosis: a contemporary review. Radiol Clin N Am. 2016;54:519–34.
22. Murphy DJ, Subesinghe M, Rashid I, Reyes-Torres E. Active cardiac sarcoidosis on standard chest computed tomography. Eur Heart J Cardiovasc Imaging. 2018;19:1025.
23. Muth G, Daniel WG, Achenbach S. Late enhancement on cardiac computed tomography in a patient with cardiac sarcoidosis. J Cardiovasc Comput Tomogr. 2008;2:272–3.
24. Ohta Y, Kitao S, Yunaga H, et al. Myocardial delayed enhancement CT for the evaluation of heart failure: comparison to MRI. Radiology. 2018;288:682–91.
25. Terasaki F, Yoshinaga K. New guidelines for diagnosis of cardiac sarcoidosis in Japan. Anna Nucl Cardiol. 2017;3:42–5.
26. Birnie DH, Sauer WH, Bogun F, et al. HRS expert consensus statement on the diagnosis and management of arrhythmias associated with cardiac sarcoidosis. Heart Rhythm. 2014;11:1305–23.
27. Blankstein R, Waller AH. Evaluation of known or suspected cardiac sarcoidosis. Circ Cardiovasc Imaging. 2016;9:e000867.
28. Cummings KW, Bhalla S, Javidan-Nejad C, Bierhals AJ, Gutierrez FR, Woodard PK. A pattern-based approach to assessment of delayed enhancement in nonischemic cardiomyopathy at MR imaging. Radiographics. 2009;29:89–103.
29. Murphy DJ, Kwong RY. Contrast agents in cardiovascular magnetic resonance imaging. In: Cardiovascular magnetic resonance imaging. New York, NY: Springer; 2019. p. 127–43.
30. Rajiah P, Bolen MA. Cardiovascular MR imaging at 3 T: opportunities, challenges, and solutions. Radiographics. 2014;34:1612–35.
31. Adams MC, Turkington TG, Wilson JM, Wong TZ. A systematic review of the factors affecting accuracy of SUV measurements. AJR Am J Roentgenol. 2010;195:310–20.
32. Osborne MT, Hulten EA, Murthy VL, et al. Patient preparation for cardiac fluorine-18 fluorodeoxyglucose positron emission tomography imaging of inflammation. J Nucl Cardiol. 2017;24:86–99.
33. Soussan M, Brillet P-Y, Nunes H, et al. Clinical value of a high-fat and low-carbohydrate diet before FDG-PET/CT for evaluation of patients with suspected cardiac sarcoidosis. J Nucl Cardiol. 2013;20:120–7.
34. Skali H, Schulman AR, Dorbala S. 18F-FDG PET/CT for the assessment of myocardial sarcoidosis. Curr Cardiol Rep. 2013;15:1204–11.

35. Ishimaru S, Tsujino I, Takei T, et al. Focal uptake on 18F-fluoro-2-deoxyglucose positron emission tomography images indicates cardiac involvement of sarcoidosis. Eur Heart J. 2005;26:1538–43.
36. Blankstein R, Osborne M, Naya M, et al. Cardiac positron emission tomography enhances prognostic assessments of patients with suspected cardiac sarcoidosis. J Am Coll Cardiol. 2014;63:329–36.
37. Patel DC, Gunasekaran SS, Goettl C, Sweiss NJ, Lu Y. FDG PET-CT findings of extra-thoracic sarcoid are associated with cardiac sarcoid: a rationale for using FGD PET-CT for cardiac sarcoid evaluation. J Nucl Cardiol. 2017;357:2153–7.
38. Murphy DJ, Keraliya AR, Agrawal MD, Aghayev A, Steigner ML. Cross-sectional imaging of aortic infections. Insights Imaging. 2016;7:801–18.
39. Okumura W, Iwasaki T, Toyama T, et al. Usefulness of fasting 18F-FDG PET in identification of cardiac sarcoidosis. J Nucl Med. 2004;45:1989–98.
40. Berman JS, Govender P, Ruberg FL, Mazzini M, Miller EJ. Scadding revisited: a proposed staging system for cardiac sarcoidosis. Sarcoidosis Vasc Diffuse Lung Dis. 2014;31:2–5.
41. Bravo PE, Singh A, Di Carli MF, Blankstein R. Advanced cardiovascular imaging for the evaluation of cardiac sarcoidosis. J Nucl Cardiol. 2019;26:188–99.
42. Mielniczuk LM, Birnie D, Ziadi MC, et al. Relation between right ventricular function and increased right ventricular [18F]fluorodeoxyglucose accumulation in patients with heart failure. Circ Cardiovasc Imaging. 2011;4:59–66.
43. Bonifazi M, Bravi F, Gasparini S, et al. Sarcoidosis and cancer risk: systematic review and meta-analysis of observational studies. Chest. 2015;147:778–91.
44. Mousavi N, Cheezum MK, Aghayev A, et al. Assessment of cardiac masses by cardiac magnetic resonance imaging: histological correlation and clinical outcomes. J Am Heart Assoc. 2019;8:e007829.
45. Dweck MR, Abgral R, Trivieri MG, et al. Hybrid magnetic resonance imaging and positron emission tomography with fluorodeoxyglucose to diagnose active cardiac sarcoidosis. JACC Cardiovasc Imaging. 2018;11:94–107.
46. Hanneman K, Kadoch M, Guo HH, et al. Initial experience with simultaneous 18F-FDG PET/MRI in the evaluation of cardiac sarcoidosis and myocarditis. Clin Nucl Med. 2017;42:e328–34.
47. Wicks EC, Menezes LJ, Barnes A, et al. Diagnostic accuracy and prognostic value of simultaneous hybrid 18F-fluorodeoxyglucose positron emission tomography/magnetic resonance imaging in cardiac sarcoidosis. Eur Heart J Cardiovasc Imaging. 2018;7:757–67.
48. Sawicki LM, Grueneisen J, Buchbender C, et al. Comparative performance of ^{18}F-FDG PET/MRI and ^{18}F-FDG PET/CT in detection and characterization of pulmonary lesions in 121 oncologic patients. J Nucl Med. 2016;57:582–6.
49. Burris NS, Johnson KM, Larson PEZ, et al. Detection of small pulmonary nodules with ultrashort echo time sequences in oncology patients by using a PET/MR system. Radiology. 2016;278:239.
50. Kim JS, Judson MA, Donnino R, et al. Cardiac sarcoidosis. Am Heart J. 2009;157:9–21.
51. Youssef G, Leung E, Mylonas I, et al. The use of 18F-FDG PET in the diagnosis of cardiac sarcoidosis: a systematic review and meta-analysis including the Ontario experience. J Nucl Med. 2012;53:241–8.
52. Kim S-J, Pak K, Kim K. Diagnostic performance of F-18 FDG PET for detection of cardiac sarcoidosis; A systematic review and meta-analysis. J Nucl Cardiol. 2019;336:1224–13.
53. Tang R, Wang JT-Y, Wang L, et al. Impact of patient preparation on the diagnostic performance of 18F-FDG PET in Cardiac sarcoidosis: a systematic review and meta-analysis. Clin Nucl Med. 2016;41:e327–39.
54. Zhang J, Li Y, Xu Q, Xu B, Wang H. Cardiac magnetic resonance imaging for diagnosis of cardiac sarcoidosis: a meta-analysis. Can Respir J. 2018;2018:7457369–10.
55. Okada DR, Bravo PE, Vita T, et al. Isolated cardiac sarcoidosis: a focused review of an underrecognized entity. J Nucl Cardiol. 2018;25:1136–46.

56. Divakaran S, Stewart GC, Lakdawala NK, et al. Diagnostic accuracy of advanced imaging in cardiac sarcoidosis. Circ Cardiovasc Imaging. 2019;12:e008975.
57. Vita T, Okada DR, Veillet-Chowdhury M, et al. Complementary value of cardiac magnetic resonance imaging and positron emission tomography/computed tomography in the assessment of cardiac sarcoidosis. Circ Cardiovasc Imaging. 2018;11:e007030.
58. Coleman GC, Shaw PW, Balfour PC, et al. Prognostic value of myocardial scarring on CMR in patients with cardiac sarcoidosis. JACC Cardiovasc Imaging. 2017;10:411–20.
59. Hulten E, Agarwal V, Cahill M, et al. Presence of late gadolinium enhancement by cardiac magnetic resonance among patients with suspected cardiac sarcoidosis is associated with adverse cardiovascular prognosis: a systematic review and meta-analysis. Circ Cardiovasc Imaging. 2016;9:e005001.
60. Sadek MM, Yung D, Birnie DH, Beanlands RS, Nery PB. Corticosteroid therapy for cardiac sarcoidosis: a systematic review. Can J Cardiol. 2013;29:1034–41.
61. Osborne MT, Hulten EA, Singh A, et al. Reduction in ^{18}F-fluorodeoxyglucose uptake on serial cardiac positron emission tomography is associated with improved left ventricular ejection fraction in patients with cardiac sarcoidosis. J Nucl Cardiol. 2014;21:166–74.
62. Lee P-I, Cheng G, Alavi A. The role of serial FDG PET for assessing therapeutic response in patients with cardiac sarcoidosis. J Nucl Cardiol. 2017;24:19–28.
63. Ahmadian A, Pawar S, Govender P, Berman J, Ruberg FL, Miller EJ. The response of FDG uptake to immunosuppressive treatment on FDG PET/CT imaging for cardiac sarcoidosis. J Nucl Cardiol. 2017;24:413–24.
64. Shelke AB, Aurangabadkar HU, Bradfield JS, Ali Z, Kumar KS, Narasimhan C. Serial FDG-PET scans help to identify steroid resistance in cardiac sarcoidosis. Int J Cardiol. 2017;228:717–22.
65. Sgard B, Brillet PY, Bouvry D, et al. Evaluation of FDG PET combined with cardiac MRI for the diagnosis and therapeutic monitoring of cardiac sarcoidosis. Clin Radiol. 2019;74:81.e9–81.e18.
66. Chareonthaitawee P, Beanlands RS, Chen W, et al. Joint SNMMI-ASNC expert consensus document on the role of 18F-FDG PET/CT in cardiac sarcoid detection and therapy monitoring. J Nucl Med. 2017;58:1341–53.
67. Hofman MS, Lau WFE, Hicks RJ. Somatostatin receptor imaging with 68Ga DOTATATE PET/CT: clinical utility, normal patterns, pearls, and pitfalls in interpretation. Radiographics. 2015;35:500–16.
68. Bokum Ten AM, Hofland LJ, de Jong G, et al. Immunohistochemical localization of somatostatin receptor sst2A in sarcoid granulomas. Eur J Clin Investig. 1999;29:630–6.
69. Gormsen LC, Haraldsen A, Kramer S, Dias AH, Kim WY, Borghammer P. A dual tracer (68) Ga-DOTANOC PET/CT and (18)F-FDG PET/CT pilot study for detection of cardiac sarcoidosis. EJNMMI Res. 2016;6:52.
70. Lapa C, Reiter T, Kircher M, et al. Somatostatin receptor based PET/CT in patients with the suspicion of cardiac sarcoidosis: an initial comparison to cardiac MRI. Oncotarget. 2016;7:77807–14.
71. Slart RHJA, Koopmans K-P, van Geel PP, et al. Somatostatin receptor based hybrid imaging in sarcoidosis. Eur J Hybrid Imaging. 2017;1:7.
72. Bravo PE, Bajaj N, Padera RF, et al. Feasibility of somatostatin receptor-targeted imaging for detection of myocardial inflammation: a pilot study. J Nucl Cardiol. 2021;28:1089–99.
73. Norikane T, Yamamoto Y, Maeda Y, Noma T, Dobashi H, Nishiyama Y. Comparative evaluation of 18F-FLT and 18F-FDG for detecting cardiac and extra-cardiac thoracic involvement in patients with newly diagnosed sarcoidosis. EJNMMI Res. 2017;7:69.

Novel SPECT and PET Tracers and Myocardial Imaging

11

Inga Melvinsdottir, Ricardo Avendaño, and Albert J. Sinusas

11.1 Overview

Hybrid multimodality cardiovascular imaging is routinely used to assess cardiac function, structure, and physiological parameters to facilitate the diagnosis and evaluation of myocardial diseases, along with risk stratification, and directing and monitoring therapy. There is now a focus on developing multimodality imaging strategies to assess the underlying cellular and molecular processes that underlie and/or participate in modulating the structural and pathophysiological changes in the heart. While there has been a critical advancement in hybrid imaging technology, there also needed to be a parallel development of imaging probes for improved evaluation of these physiological and molecular changes. The most widely used approaches for molecular imaging include radiotracers that allow for high-sensitivity in vivo detection and quantification of molecular processes with single photon emission computed tomography (SPECT) and positron emission tomography (PET) [1]. While SPECT and PET imaging provide high sensitivity for detection and

I. Melvinsdottir · R. Avendaño
Section of Cardiovascular Medicine, Yale University School of Medicine, New Haven, CT, USA
e-mail: inga.melvinsdottir@yale.edu; ricardo.avendano@yale.edu

A. J. Sinusas (✉)
Section of Cardiovascular Medicine, Department of Medicine, Yale University School of Medicine, New Haven, CT, USA

Department of Radiology and Biomedical Imaging, Yale University School of Medicine, New Haven, CT, USA

Department of Biomedical Engineering, Yale University, New Haven, CT, USA

Yale Translational Research Imaging Center (Y-TRIC), Yale University School of Medicine, New Haven, CT, USA
e-mail: albert.sinusas@yale.edu

S. G. Nekolla, C. Rischpler (eds.), *Hybrid Cardiac Imaging*,
https://doi.org/10.1007/978-3-030-83167-7_11

quantitative assessment of molecular and physiological processes, they suffer from limited resolution. Therefore, these radiotracer-based imaging approaches have been integrated with high resolution anatomical imaging to provide anatomic co-localization and improved quantification. This chapter will review the development of novel radiolabeled probe for both SPECT and PET imaging of myocardial flow and evaluation of critical molecular processes in the myocardium; including: inflammation, cell death, autonomic regulation, angiogenesis, and myocardial remodeling. This chapter will also introduce the use of reporter probe technology and novel theranostics.

11.2 Physiological Imaging

11.2.1 Myocardial Perfusion Imaging

Myocardial perfusion imaging is an important tool to diagnose, risk stratify, and guide interventions for coronary artery disease. Over the past few decades myocardial perfusion imaging has evolved exponentially and continues to improve with better image quality, lower scan time, and reduced radiation [2]. This has in part been partly facilitated by the introduction of hybrid imaging technology that has allowed for CT based attenuation correction (Fig. 11.1).

11.2.1.1 SPECT Perfusion Imaging

The ideal myocardial perfusion agent should have linear relationship between myocardial uptake and blood flow, low extracardial uptake, minimal myocardial redistribution, and high first pass extraction. Thalium-201 (^{201}Tl) was developed in the 1970s and has been extensively used for evaluation of myocardial perfusion [3]. It is still considered to be the gold standard for evaluation for viability assessment of the myocardium among SPECT agents [4]. However, ^{201}Tl has a long half-life (72 h) so the dose must be kept low (ideally <2 mCi) to minimize radiation, and in addition, ^{201}Tl has a low photon energy which results in more scatter and soft tissue attenuation artifact [5]. Therefore, the use of high-sensitivity imaging systems are critical for ^{201}Tl imaging along with the use of CT imaging for attenuation correction.

Technetium-99m (^{99m}Tc) based radiotracers have been around since the 1990s and been widely used in the clinical setting, with ^{99m}Tc-sestamibi and ^{99m}Tc-tetrofosmin used predominantly. Despite their widespread use they do not demonstrate linear myocardial extraction at high flow rates and have high hepatic uptake, which can interfere with interpretation of defects in the inferior wall [6, 7]. ^{99m}Tc-teboroxime is another FDA approved SPECT radiotracer for myocardial perfusion imaging. However, this agent never gained popularity in clinical use, mainly because of high initial extracardiac uptake and very rapid washout. This results in a technical challenge in performing the myocardial imaging, since the image acquisition must be performed within 2 min of injection [8].

Several other ^{99m}Tc based radiotracers are currently under investigation and show promising potential. Research efforts have been focused on to improve

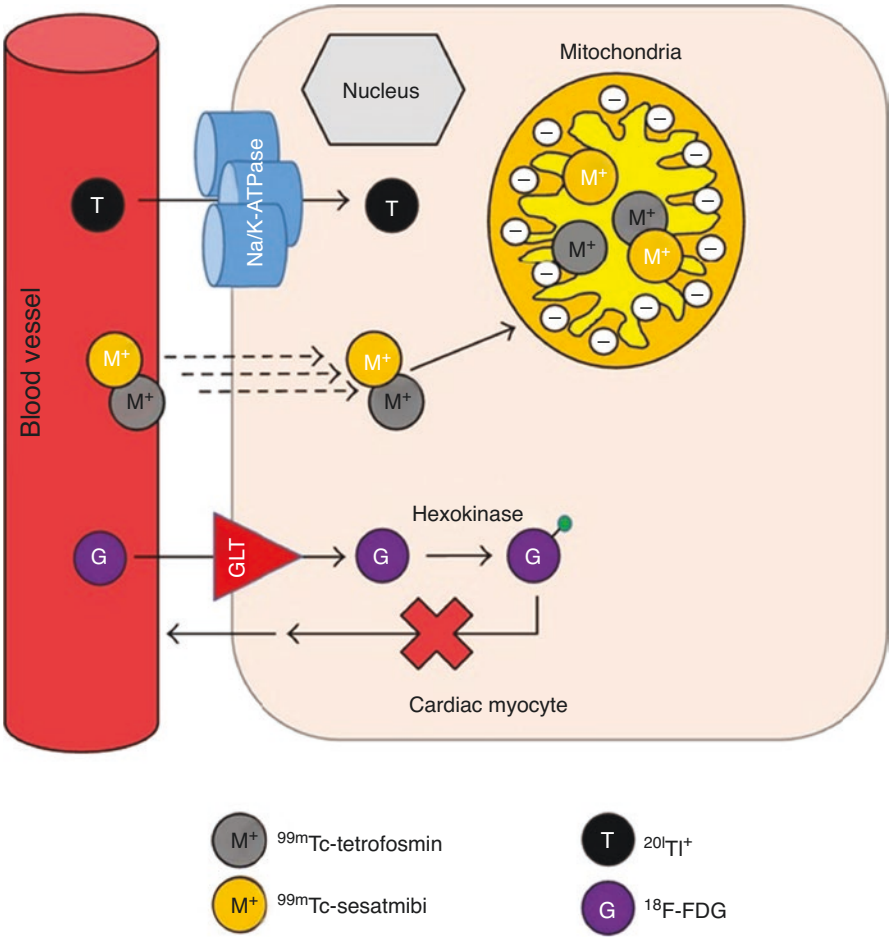

Fig. 11.1 Mechanisms of action of commercially available myocardial perfusion radiotracers in cardiac myocytes. (Reprinted from Sogbein et al. Biomed Res Int 2014)

heart-to-background ratios, specifically heart-to-liver ratio. A few of these agents are mentioned below, although the list is not exhaustive. The ^{99m}Tc-nitrido complex (DBODC5) has high cardiac uptake and shows improved heart/liver ratio compared to ^{99m}Tc-sestamibi in animal studies due to rapid hepatic clearance. In humans, the sensitivity appeared to be similar compared to ^{99m}Tc-sestamibi with possibly improved specificity when evaluating for coronary artery disease. However, this agent needs further verification [9]. ^{99m}TcN-MPO has been tested in rodents and show promising heart-liver ratio due to rapid hepatic excretion but has yet to be tested on humans [10]. ^{99m}Tc-TMEOP showed faster liver washout and similar cardiac uptake in rodents [11].

Mitochondrial complex-1 inhibitors show great promise for cardiac imaging as mitochondria are very abundant in cardiomyocytes. A novel iodine-123 labeled

derivative of rotenone, a MC-1 inhibitor, has been tested in rodents and has shown uniform myocardial distribution and very little extracardiac activity. Cardiac uptake tracked more linearly with increased blood flow with this agent compared to standard SPECT tracers in animal studies [12, 13].

11.2.1.2 PET Perfusion Imaging

PET imaging has gained more popularity for evaluation myocardial perfusion in recent years. This is partly due to increased availability of hybrid PET/CT scanners, development of new radiotracers and post-imaging hardware and software [14]. The most common radiotracers used for myocardial perfusion for PET imaging are Rubidium-82 (^{82}Rb), N-13 Ammonia ($^{13}NH_3$), and oxygen-15 water (H_2 ^{15}O) (Fig. 11.2). Theoretically, the most ideal PET radiotracer for myocardial perfusion is H_2 ^{15}O as it has a complete extraction in the myocardium independent of flow rate and metabolic rate. Therefore, uptake was proportional to flow even at high flows. However, it freely crosses the myocyte membrane and quickly reaches equilibrium between blood and tissues without accumulation in the myocardium [15]. Thus, the images are of poor quality and have limited diagnostic value, requiring dynamic imaging and kinetic modeling for estimation of flow. ^{82}Rb and $^{13}NH_3$ are well established radiotracers used clinically to assess myocardial perfusion in PET imaging and often have improved sensitivity in diagnosing clinically significant coronary artery disease compared to available SPECT imaging agents [16, 17].

^{82}Rb is actively transferred to the myocardium via the Na/K ATP transporter rapidly and remains in the myocardium. However, the half-life of ^{82}Rb is very short (76 s) allowing only a few minutes for acquisition before the tracer has decayed to background level [18]. This radiotracer requires pharmacological stress test and

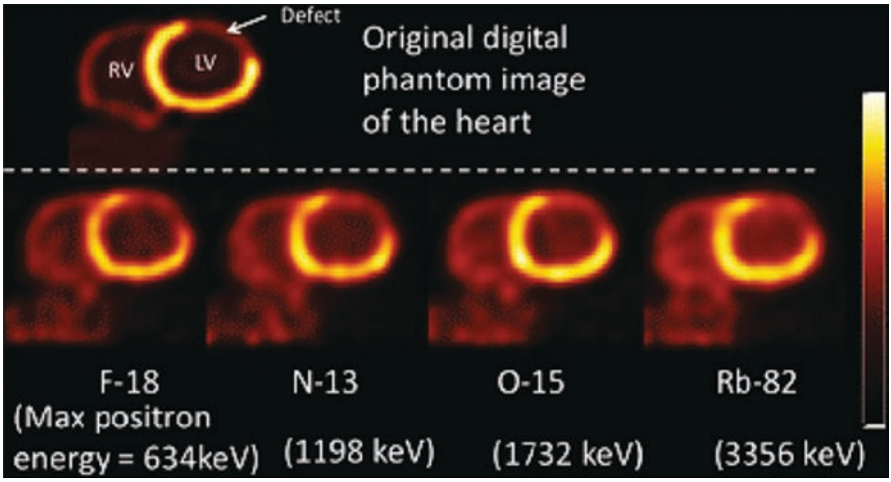

Fig. 11.2 Images of digital cardio-torso phantom in simulated short-axis view using different PET radioisotopes. Blurring effect by positron range increases with higher positron kinetic energy. (Image reprinted with permission from Rischpler et al., Ann Nucl Med 2012)

cannot be used for exercise testing. Despite this limitation, ^{82}Rb PET scan has shown superiority in diagnostic accuracy and specificity in diagnosing obstructive coronary disease compared to SPECT, specifically in extremely obese population [16, 19]. The principal benefit of this radiotracer is that no access to a cyclotron is needed, since it can be produced next to the scanner using commercially available portable elution generators.

$^{13}NH_3$ is metabolically trapped in the myocardium within the glutamine pool within the myocardial cells with both active transport and passive diffusion [20]. $^{13}NH_3$ has a longer half-life than ^{82}Rb (9.96 min) and thus exercise stress test is possible, however, an on-site cyclotron is needed for this tracer which can be costly. $^{13}NH_3$ is a good radiotracer for quantitative assessment of myocardial perfusion and provides excellent image quality. This is due to high myocardial extraction fraction (above 80%), chemical trapping of the tracer in the myocardium, and relatively long half-life of the isotope [21, 22]. $^{13}NH_3$ provides high diagnosis accuracy for obstructive coronary artery disease in men, women and obese patients [23].

Fluorine-18 (^{18}F) flurpiridaz is a PET radiotracer that is currently undergoing phase 3 clinical trials to gain FDA approval for assessment of myocardial perfusion (Fig. 11.3) [24]. ^{18}F-flurpiridaz (previously named BMS-747158-02) binds to mitochondrial complex-1 with a rapid uptake in the cardiomyocytes and slow washout [25]. This tracer has a longer half-life than ^{82}Rb and $^{13}NH_3$ (109 min) and can make use of a regional cyclotron rather than requiring an on-site cyclotron like $^{13}NH_3$.

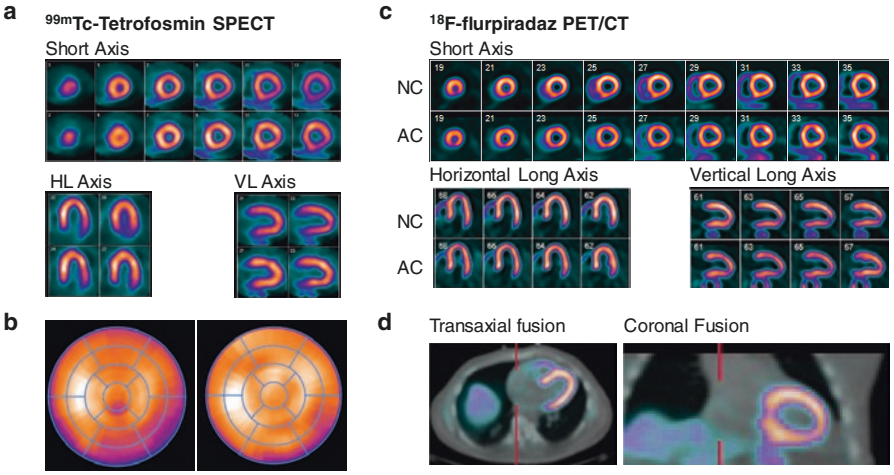

Fig. 11.3 ^{99m}Tc-tetrofosmin SPECT (**a**, **b**) and ^{18}F-flurpiradaz PET/CT (**c**, **d**) images in 65-year-old male with history of diabetes, hyperlipidemia, hypertension, and family history of coronary artery disease who presents for evaluation of dyspnea on exertion. SPECT images (**a**) and bullseye maps (**b**) were considered abnormal with a small to medium sized, mild intensity reversible perfusion defect in the inferolateral wall consistent with ischemia. The hybrid ^{18}F-flurpiradaz PET/CT images (**c**, **d**) appear normal. A cardiac catheterization revealed noncritical coronary artery disease and normal resting left ventricular end-diastolic pressure. This patient example illustrates improved specificity with ^{18}F-flurpiradaz PET/CT

Therefore, ^{18}F-flurpiridaz may be more cost effective and could allow for cardiac PET imaging at any location with access to a PET scanner, even for low volume imaging sites. The longer half-life permits exercise stress testing, although may necessitate longer imaging protocols and may be associated with higher radiation exposure. Compared to both $^{13}NH_3$ and ^{82}Rb, ^{18}F-flurpiridaz provide improved spatial resolution due to a shorter positron range [26]. ^{18}F-flurpiridaz also has a high first pass extraction, and therefore allows for very accurate assessment of quantitative flows with use of dynamic imaging and kinetic modeling.

^{18}F-labeled rhodamines have been developed for myocardial perfusion imaging as rhodamine can accumulate in the mitochondria. Several rhodamine cores have been ^{18}F labeled and assessed for cardiac imaging using hybrid PET/CT imaging. ^{18}F-6G-rhodamine showed very promising results in initial rat studies with favorable myocardial uptake and low hepatic uptake due to the lipophilic characteristic of the compound in rats [27, 28]. Recent porcine studies have demonstrated that ^{18}F-6G-rhodamine has a high first pass extraction with limited flow dependence of the extraction over a wide physiological range of flows [29]. ^{18}F-labeled fluoro-alkyl-phosphonium cations such as ^{18}F-Fluorobenzyl Triphenyl Phosphonium (^{18}F-FBnTP), (4-^{18}F-Fluorophenyl)triphenylphosphonium (^{18}F-FTTP), (6-^{18}F-fluorohexyl)triphenylphosphonium (^{18}F-FHTP), (2-(2-^{18}F-fluoroethoxy) ethyl) tris(4-methoxyphenyl) phosphonium (^{18}F-FETMP), and 1-halomethyl-^{18}F-fluoromethylbenzenes (^{18}F-FMBTP) have shown encouraging properties in preclinical studies, but no human trials are available [30]. When compared to ^{13}N-NH_3 in rat models of coronary occlusion ^{18}F-labeled fluoro-alkyl-phosphonium cations showed rapid hepatic and pulmonary clearance which lead to excellent image quality [31]. When compared to ^{99m}Tc-tetrofosmin for assessment of myocardial perfusion in dogs with varying stenosis of coronary arteries ^{18}F-FBnTP showed superior diagnostic performance, specifically in mild or severe stenosis [32].

Copper labeled PET agents have been used in the research setting in the past three decades for assessment of myocardial perfusion but have never been approved for clinical use. ^{62}Cu-PTSM is metabolically trapped in the mitochondria and thus was thought to be attractive agent for myocardial perfusion assessment. However, high liver uptake compromises inferior wall assessment and due to binding to albumin the uptake of this radiotracer in the myocardium was reduced [33].

Among the new ^{18}F-labeled PET imaging agents, ^{18}F-flurpiridaz remains the most promising myocardial perfusion agent, since the initial Phase III clinical trials with ^{18}F-flurpiridaz have shown favorable results (Table 11.1).

11.3 Targeted Molecular Imaging

There are a wide range of new molecular targeted imaging agents for both SPECT and PET imaging. Many of these agents target important molecular processes involved with cardiovascular disease including; inflammation, cell death, autonomic regulation, angiogenesis, and myocardial remodeling. These agents often result in "hot spot" images of the heart that are difficult to reconstruct or interpret without

Table 11.1 Comparison of representative ^{18}F-labeled compounds as potential MPI agents. Reproduced with permission from Mou and Zhang, Molecules 2017

Probes	^{18}F-FDG-rhodamine	^{18}F-FBnTP	^{18}F-FTTP	^{18}F-mFMTP	^{18}F-flurpiridaz	^{18}F-Fmpp2
Class	Ammonium cation	Phosphonium cation	Phosphonium cation	Phosphonium cation	MC-1 inhibitors	MC-1 inhibitors
Charge	Cationic	Cationic	Cationic	Cationic	Neutral	Neutral
Log *P*	−1.64 ± 0.03	–	1.78 ± 0.05	1.05 ± 0.01	–	1.73 ± 0.05
RCY (%)	97.0 ± 1.9 (based on ^{18}F-FDG)	62 ± 1.4 (NDC)	10–15 (EOS)	50 (DC)	25 (DC)	58 ± 7.1 (DC)
Heart uptake (%ID/g)	11.24 ± 1.97 (rat)	–	1.51 ± 0.04 (rat)	27.39 ± 1.46 (mice)	9.5 ± 0.5 (mice)	27.15 ± 3.58 (mice)
Heart/liver ratio	21.2 (rat)	1.2 (dog)	8 (rat)	4.84 (mice)	8.3 (mice)	3.96 (mice)
Heart/blood ratio	28.10 (rat)	16.6 (dog)	75.5 (rat)	23.82 (mice)	–	10.29 (mice)
Time point (min)[a]	–	60	30	30	60	30
Current status	Rats	Dogs	Rabbits	Dogs	Clinic trial (Phase III)	Pigs
References	[26]	[21, 32, 37]	[39]	[44]	[53]	[62]

[a]Time point means the time point of heart uptake and heart/liver ratios in this table

integration and registration with a reference physiological imaging agent and anatomical structure provided by hybrid imaging systems.

11.3.1 Inflammation

Myocardial inflammation is a complex process that involves multiple cells, signaling proteins, and receptor–ligand interactions that are directed at repair and removal of damaging or harmful substances. Inflammation also involves a complex cascade of events that include the myocardial cells, the extracellular matrix, cells from the vascular system and inflammatory cells such as lymphocytes, neutrophils, and macrophages. Thus, inflammation plays a crucial role in the etiology and modulation of many cardiac diseases such as myocardial infarction, reperfusion injury, angiogenesis, cardiac allograft rejection, sarcoidosis, and myocarditis [34, 35].

11.3.1.1 SPECT Radiotracers

One of the early techniques used to assess inflammation within the myocardium involved radiolabeling leukocytes with ^{99m}Tc or ^{111}In [36, 37]. This involves removal of blood, in vitro labeling and reinjecting the labeled cells intravenously in the patient. This approach provides an opportunity to track active inflammatory cell recruitment within the myocardium, however, this approach evokes non-specific activation of the labeled cells, interfering with the specificity of the image [36]. ^{111}In-Oxine is an FDA approved lipid soluble isotope cell tracker used to label leukocytes and track their in vivo distribution by SPECT imaging. This radiotracer has also been used for tracking the molecular and cellular mechanisms of inflammation or for the study the dynamic biodistribution of labeled cells used for therapeutic purposes [38–41]. SPECT imaging with ^{111}In-oxine radiolabeled autologous white blood cells has also been proven to be a useful tool for detection of infective endocarditis [42]. However, potential newer approaches for identification of endocarditis or other bacterial infections involve the actual direct imaging of bacteria with ^{111}In-labeled agents [43].

Tenascin-C is an extracellular matrix protein that is present in wound healing and inflammation and ^{111}In labeled monoclonal antibody anti-tenascin-C has been identified as a potential inflammation imaging agent. Rodents with experimental autoimmune myocarditis showed increased uptake of the tracer compared to control rats [44]. Dual isotope SPECT imaging approach with ^{125}I labeled anti-tenascin-C antibody or ^{111}In-anti-tenascin-C antibody and ^{99m}Tc-sestamibi has been used to monitor ischemia and reperfusion injury in rodents [45, 46]. These studies demonstrate that increased anti-tenascin-C antibody activity was correlated with the ^{99m}Tc-sestamibi perfusion defect indicating the potential for this imaging agent to monitor inflammation associated with myocardial infarction.

Another potential approach for imaging inflammation in the myocardium is to target a chemotactic agent, called leukotriene B4. The receptor is found on neutrophils and when activated it stimulates endothelial adhesion and superoxide production [47]. ^{99m}Tc-RP517 is a leukotriene B4 receptor antagonist and has been shown to have inverse relationship with occlusion flow in open chested dogs, suggesting

increased uptake of the tracer at the site of the ischemic inflammation [48]. However, this agent is very lipophilic which results in high hepatobiliary uptake and has not been tested in humans.

11.3.1.2 PET Radiotracers

Inflammatory cells show increased metabolism when activated and this can be targeted for imaging by using specific metabolic tracers. For example, in activated macrophages glucose utilization is significantly increased [49]. ^{18}F-labeled fluorodeoxyglucose (^{18}F-FDG) has been used to assess inflammatory cell activity in the myocardium and has showed focal uptake following a myocardial infarction [50, 51]. However, suppression of cardiomyocyte uptake of ^{18}F-FDG is required to isolate the leukocyte signal to optimize the target-to-background signal. Current evidence suggests that administering high fat, no carbohydrate diet for at least two meals with a fast of 4–12 h prior to ^{18}F-FDG PET imaging [52] is sufficient for optimization of the signal. Other methods include intravenous heparin administered just prior to imaging following at least one high fat, no carbohydrate meal, and overnight fast [52]. Clinical studies show increased ^{18}F-FDG uptake in infarcted regions compared to remote myocardium 5–7 days post first myocardial infarction [51, 53]. The magnitude of the increase in ^{18}F-FDG uptake in the infarct has been associated with late outcomes [51]. PET imaging with ^{18}F-FDG has also been proved to be valuable in the evaluation of active cardiac sarcoidosis. ^{18}F-FDG has also been applied in evaluation of microvascular disease. However, the use of ^{18}F-FDG imaging is not as well established in evaluation of the role of inflammation in this setting [54].

Another method to assess the metabolism of activated leukocytes within the myocardium is to track amino acid metabolism. The benefit of using amino acid metabolism over glucose metabolism is that amino acids are a minor metabolic substrate for healthy myocardium although are heavily used in activated leukocytes [55]. Transient increase of ^{14}C- or ^{11}C-labeled methionine uptake has been identified both in mice and in humans on Days 3–7 after a myocardial infarction [55–57]. The PET imaging method with ^{11}C-labeled methionine has the potential to provide a valuable localization of inflammation of the myocardium in the acute phase of myocardial infarction.

Mitochondrial translocator protein (TSPO) is another viable molecular target for evaluation of inflammation and is the target of ^{18}F-GE180. This protein is upregulated in activated macrophages, and therefore would be useful for imaging inflammation in mitochondria abundant organ such as the heart. Increased uptake of this radiotracer was seen 1 week post-myocardial infarction and was predictive of LV remodeling 8 weeks post-MI in a mouse model. In the same study, an increase of TPSO signaling was also found in the brain in the setting of a myocardial infarction, both in humans and in mice, suggesting a potential link between inflammation in heart and brain [58].

Targeting leukocyte recruitment rather than targeting leukocyte metabolism can be achieved with chemokine receptor type 4 (CXCR4). The pentapeptide ^{68}Ga-pentixafor is a CXCR4 targeted PET tracer and was originally designed for imaging CXCR4 upregulated tumors [59]. CXCR4 upregulation to the infarct territory has been shown 3 days post-permanent coronary artery occlusion in mice [60].

Furthermore, on Days 4 through 6 following the ischemic insult the signal was more heterogenous. Other investigators demonstrated high levels of ^{68}Ga-pentixafor binding in areas that showed evidence of hypoperfusion, late gadolinium enhancement, and T2-positive edema. Thus, ^{68}Ga-pentixafor PET imaging has the potential to identify patients at increased risk of post-myocardial infarction cardiomyopathy, however, further investigation is required.

CCR2 is an inflammatory monocyte marker that activates monocyte recruitment and ^{64}Cu- or ^{68}Ga-radiolabeled CCR2 binding peptide (^{64}Cu-DOTA-ECL1i or ^{68}Ga-DOTA-ECL1i) have been used for PET imaging to assess myocardial inflammation after ischemia and reperfusion in the heart [61] (Fig. 11.4) as well as to visualize

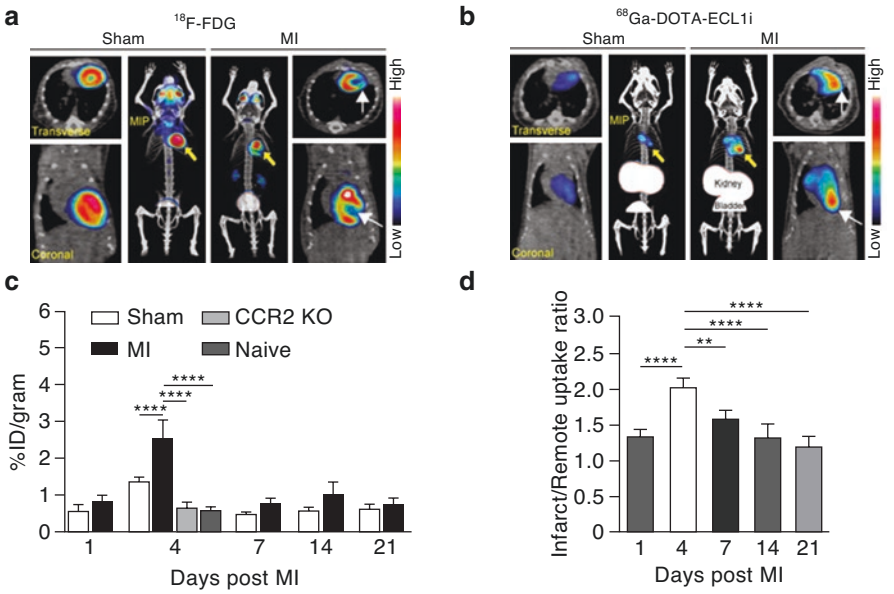

Fig. 11.4 Hybrid PET/CT images of ^{18}F-fluorodeoxyglucose (^{18}F-FDG) and ^{68}Ga-DOTA (1,4,7,10-tetraazacyclododecane-1,4,7,10-tetraacetic acid)-ECL1i (extracellular loop 1 inverso) in sham control mice and mice following ischemia reperfusion (I-R) injury. (**a**) ^{18}F-FDG PET/CT images 5 days after 90 min of I-R injury compared to sham procedure as controls. Maximal-intensity projected views (MIP), transverse and coronal views are shown. White arrows indicate a myocardial infarct (MI) area. (**b**) Transverse, coronal, and MIP ^{68}Ga-DOTA-ECL1i PET/CT images obtained 4 days after I-R injury showing regional accumulation of ^{68}Ga-DOTA-ECL1i in the MI and border zone. Yellow arrow indicates tracer uptake in hearts that underwent ischemia reperfusion injury compared to sham procedure as controls. White arrows indicate infarct area defined on ^{18}F-FDG imaging. (**c**) Quantitative analysis of ^{68}Ga-DOTA-ECL1i accumulation in hearts from naïve, sham, I-R injury, and CCR2 (C-C chemokine receptor type 2) KO (knockout) mice with the different timepoints marked after they underwent I-R injury. Each experimental group had $n = 4–5$ mice. (**d**) Regional accumulation of ^{68}Ga-DOTA-ECL1i uptake in the MI and remote areas of sham procedure and at different timepoints post I-R injury. (Modified, with permission from Heo et al., Circulation Research 2019)

monocyte recruitment in atherosclerosis plaques [62]. Autoradiography demonstrated that ^{68}Ga-DOTA-ECL1i specifically binds to human tissue specimens from patients with heart failure and that the signal intensity was associated with CCR2+ macrophage abundance. This highlights the translational potential of this agent to non-invasively visualize CCR2+ monocyte recruitment and inflammatory macrophage accumulation in patients. However, this tracer has not been tested in vivo in humans.

11.3.2 Cell Death

Two important markers of cell death are necrosis and apoptosis. Apoptosis is a natural process which involves a tightly regulated process where pathways are turned on or off to get rid of unwanted cells such as senescent cells without provoking significant inflammatory response. These pathways are sometimes activated in certain diseases such as cardiomyopathy, myocarditis, heart failure, reperfusion injury, and myocardial infarction. Necrosis is a well-established form of cell death that involves irreversible damage and disruption of the cell membrane. Necrosis is often an acute process that is associated with a significant inflammatory and immune response [63]. This is particularly troublesome in the myocardium as cardiomyocytes have limited regenerative capacities [63]. Thus, visualizing cell death with non-invasive imaging for assessment, and monitoring a therapeutic response is attractive.

11.3.2.1 Apoptosis Imaging

One of the earlier events in apoptosis is disruption of lipid bilayer of the cell membrane which leads to asymmetric distribution of phospholipids which then leads to increased phosphatidyl serine on the outer cell membrane [64]. Annexin-V is an endogenous human protein that has high affinity for phosphatidyl serine and has been used as a target for molecular imaging of apoptosis [64]. Annexin-V has been radiolabeled for both PET (^{18}F, ^{68}Ga, ^{124}I) and SPECT (^{99m}Tc, ^{123}I) imaging techniques [64, 65]. Most studies have involved ^{99m}Tc-labeling and several animal studies have shown increased annexin-V uptake in ischemic myocardium [66–69]. However, due to the size of the molecule it clears slowly and this results in significant off target radiation, specifically in the kidneys and liver [70]. Annexin-V imaging has been used in clinical studies for non-invasive detection of cardiac transplant rejection [71], and for identification of apoptosis following myocardial infarction, and more specifically associated with ischemia reperfusion injury [72].

Apoptotic cell membranes show increased concentration of phosphatidylethanolamine similar to phosphatidyl serine described above [73]. ^{99m}Tc labeled Duramycin binds to externalized phosphatidylethanolamine in a similar fashion as Annexin-V binds to phosphatidyl serine, and therefore is another useful imaging marker for apoptosis (Fig. 11.5) [74]. In preclinical studies in rabbits, ^{99m}Tc-Duramycin provided a similar efficacy for apoptosis imaging compared to Annexin-V. Duramycin is also significantly smaller compared to Annexin-V and is more rapidly cleared by the kidneys, which leads to lower off target retention and

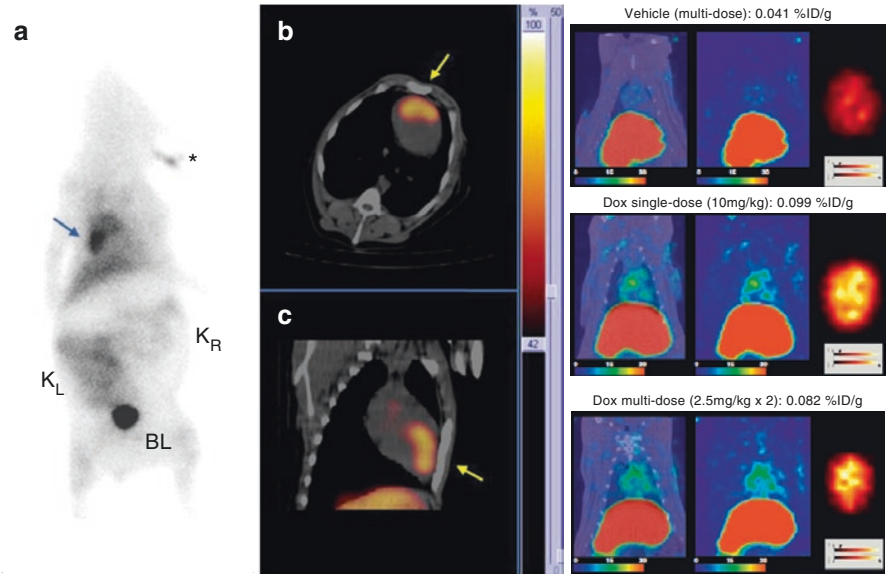

Fig. 11.5 (**left**) ^{99m}Tc-duramycin images from ischemic reperfusion injury in a pig model. (**a**) Whole body anterior planar image was obtained 30 min post-myocardial infarction demonstrating tracer uptake in the ischemic heart region (indicated with blue arrow). (**b**) Short- and (**c**) long-axis SPECT/CT fusion images obtained 1 h post-myocardial infarction and show tracer uptake in the left ventricular free wall. Modified, with permission from Wang et al., Nucl Med Biol 2014. (**right**) ^{99m}Tc-duramycin ex vivo SPECT images demonstrating myocardial apoptosis induced be chemotherapy. Multi-dose vehicle shows low uptake. Single injection of doxorubicin (10 mg/kg) show high uptake. Two injections of doxorubicin (2.5 mg/kg) shows high uptake. (Modified, with permission from Nakahara et al., JACC: Cardiovascular imaging 2018)

radiation exposure [75]. However, further validation of the safety profile and efficacy of this agent for apoptosis imaging is needed prior to clinical use.

Phosphatidyl serine can also be exposed on the outer surface of the cell membrane in necrosis [76], and accordingly there is a growing interest for developing more specific target for imaging of apoptosis. Activation of either intrinsic or extrinsic pathways ultimately leads to activation of caspase-3 or caspase-7, which are termed the executioner caspases and continue to regulate the cascade that leads to apoptosis [77]. These caspases represent alternative attractive targets, but require probes that are membrane permeable or would only target cells having increased membrane permeability. Isatin sulfonamide analogues are membrane-permeable inhibitors of caspases and have been radiolabeled with ^{18}F and are able to detect apoptotic myocardium in vivo [78–80]. Although caspase inhibitors are considered safe for human use, their true safety has not been established in clinical practice [81].

11.3.2.2 Cell Necrosis Imaging

Myosin is not normally found in the extracellular environment but after cell membrane disruption after necrosis it can be exposed. Therefore, radiolabeled antimyosin antibodies have been used for imaging of necrosis in the myocardium [82, 83]. Antimyosin imaging has been used to detect necrosis in pathologies such as myocardial infarction, myocarditis, cardiomyopathy, and transplant rejection [82, 84, 85]. When compared to endomyocardial biopsy, which is the gold standard of diagnosis of myocarditis, the antimyosin scanning showed similar specificity [82]. Antimyosin antibody conjugated to monocrystalline iron oxide nanoparticles [86] and ^{111}In-antimyosin antibody have been used to detect myocardial infarction [87, 88]. ^{111}In-antimyosin Fab antibody imaging has also been used to detect human cardiac transplant rejection but has shown high false positive rate so a biopsy is still needed for confirmation [85, 89].

Following necrosis there is a sudden influx of calcium ions which accumulate within the mitochondria in the crystalline structure, hydroxyapatite. Using ^{99m}Tc-pyrophosphate, which labels hydroxyapatite for bone scanning, myocardial infarct can be visualized (Fig. 11.6) [90]. This method has not gained widespread use due to limited sensitivity in detection of early infarction and persistence of the signal late post-myocardial infarction [91]. More recently, quantitative ^{99m}Tc-pyrophosphate imaging has been used for identification of amyloidosis. This tracer has shown 85% sensitivity and 95% specificity for the diagnosis of transthyretin-related cardiac amyloidosis (ATTR) as a cause of heart failure when computing the ratio of mean myocardial counts to mean ventricular counts [92]. Other investigators have focused on calculating the heart-to-contralateral chest ratio, and when using a cutoff value >1.5, ATTR subtype amyloidosis can be diagnosed with a 97% sensitivity and 100% specificity [93]. Furthermore, ^{99m}Tc-pyrophosphate has shown to differentiate between immunoglobulin light chain (AL) from ATTR amyloid, which shows much higher tracer retention [93]. Another trial using the ^{99m}Tc-pyrophosphate heart-to-contralateral ratio showed that a ratio greater than 1.6 was associated with worse survival among patients diagnosed with ATTR cardiac amyloidosis [94]. Interestingly, serial ^{99m}Tc-pyrophosphate imaging does not show progressive changes despite obvious clinical progression in ATTR amyloidosis [95].

Another SPECT imaging approach to detect necrosis involves the use of ^{99m}Tc-glucarate, which binds to exposed histones in the nucleus of the myocytes. Canine models have shown that the compound has high affinity for necrotic myocardial tissue but no uptake was observed in an ischemic but viable tissue [96]. ^{99m}Tc-glucarate has also been used to assess acute myocardial infarction and reperfusion injury in rabbits, showing an ability to detect myocardial infarcts in both the presence of permanent coronary occlusion and following reperfusion within minutes [97]. In humans, it was able to detect ischemia within 9 h from onset of symptoms, but the sensitivity of this method depends heavily on the onset of symptoms [98].

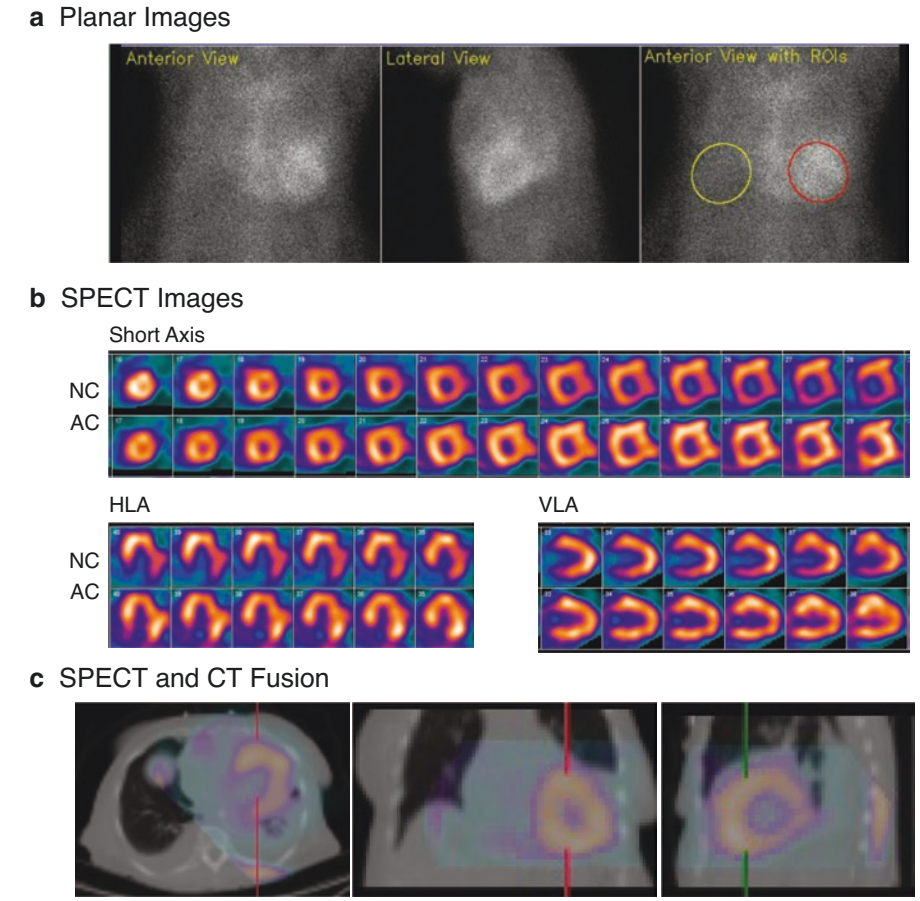

Fig. 11.6 Abnormal ^{99m}Tc-pyrophosphate (PYP) images consistent with TTR cardiac amyloidosis. 88-year-old woman with history of heart failure mildly depressed ejection fraction (40%), severe left ventricular hypertrophy, diastolic dysfunction, and moderate mitral regurgitation and severe tricuspid regurgitation, along with chronic kidney disease, hypertension, and breast cancer. (**a**) Anterior and lateral planar images with heart: contralateral chest ratio of 1.73 (normal <1.5) and a visual uptake score of 3 (0 = normal, 1 = equivocal, 2 = positive; equal to ribs, 3 = positive, greater than ribs). (**b**) Short axis, horizontal long axis (HLA), and vertical long axis (VLA) SPECT images with no attenuation correction (NC) and with attenuation correction (AC) showing diffuse PYP myocardial uptake. (**c**) Fusion of SPECT image with attenuation CT

11.4 Sympathetic and Parasympathetic Imaging

The autonomic nervous system (ANS) is composed of the sympathetic nervous system (SNS) and the parasympathetic nervous system (PNS) both play a key role in regulating blood flow, heart rate, and contractility which translates into cardiac

function. The SNS promotes positive chronotropy, excitability, contractility and increases conduction on heart myocytes; the PNS in turn promotes the opposite. These regulations are possible via the release of neurotransmitters that act directly or indirectly on myocardium and the peripheral vasculature [99–103]. The use of radiotracers to non-invasively image the ANS has become of great interest in the cardiovascular field as it can provide diagnostic and prognostic information in patients with heart failure, arrhythmias, and ischemic heart disease (Fig. 11.7) [100, 104, 105].

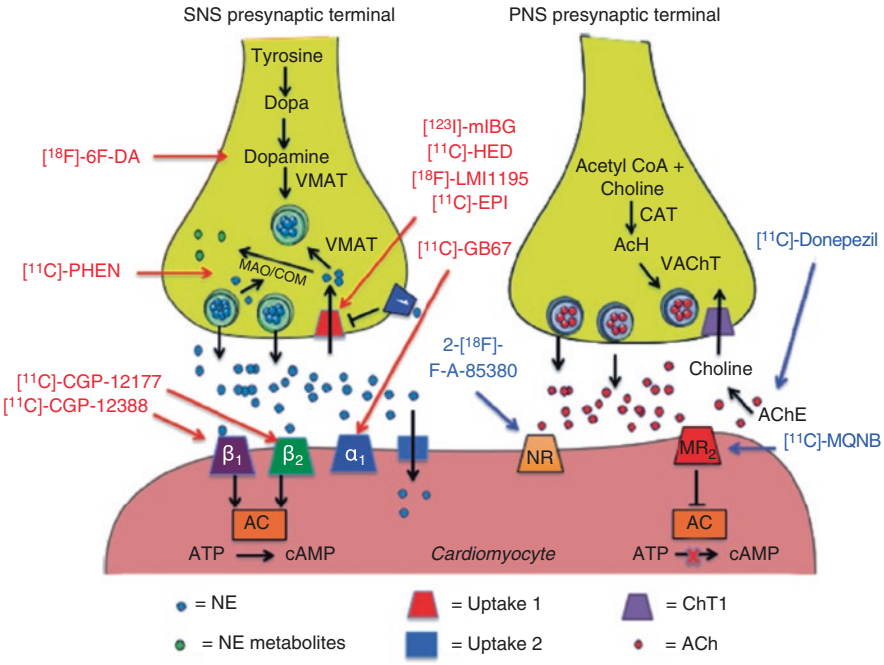

Fig. 11.7 Depiction of postganglionic sympathetic nervous system (SNS) and parasympathetic nervous system (PNS) nerve endings (**Left panel**) The synthesis and release of norepinephrine in postganglionic SNS nerve endings and subsequent binding to postsynaptic receptors on cardiomyocytes. The tracers in red depict SNS pre- and post-synaptic radioanalogs. (**Right panel**) The synthesis and release of acetylcholine in the terminal nerve ending and varicosities of postganglionic PNS nerve endings and subsequent binding to postsynaptic receptors on cardiomyocytes. Tracers in blue depict PNS pre- and post-synaptic radioanalogs. *AC* adenylyl cyclase, *ACh* acetylcholine, *AChE* acetylcholinesterase, *ATP* adenosine triphosphate, *CAT* choline-acetyl-transferase, *COM* catechol-*O*-methyltransferase, *cAMP* cyclic adenosine monophosphate, *MAO* monoamine oxidase, *mIBG* metaiodobenzyl guanidine, *MR2* muscarinic receptor 2, *NE* norepinephrine, *NR* nicotinic receptor, *VMAT* vesicular monoamine ^{18}F-^{18}F-transporter, *6F-DA* 6fluorodopamine, *PHEN* phenylephrine, *EPI* epinephrine, *HED* hydroxyephedrine, *[^{11}C] MQNB* (R,S)-*N*-[^{11}C]-methyl-quinuclidin-3-yl benzilate. (Modified, with permission, from Boutagy NE, Curr Cardiol Rep. 2017)

11.5 Sympathetic Imaging

The basis by which molecular imaging is used to image ANS relies on the normal physiology of how the ANS exerts peripheral effects. These are mediated by the release of norepinephrine (NE) from secretory vesicles in the postganglionic region, NE subsequently binds to G coupled receptor on effector cells (α,β), which in turn will promote a specific function on the cell [106]. After NE has been released by the efferent receptor, about 80% is reabsorbed in an energy dependent manner by reuptake at the presynaptic nerve terminal via the NE reuptake transporter (NET or uptake 1) [106], while the remaining 20% of the NE is reabsorbed by the postsynaptic terminal in an energy-independent fashion [106]. Therefore, the majority of the tracers developed to evaluate the SNS assess cardiac sympathetic nerve density and neuronal integrity.

11.5.1 SPECT Radiotracers

The most common tracer used to assess the integrity of the presynaptic nerve activity is ^{123}I-metaiodobenzylguanidine (^{123}I-mIBG) with planar or SPECT imaging [107, 108]. Most of the literature related to the use of ^{123}I-mIBG has employed planar scintigraphy for risk stratification of patients with heart failure [109, 110]. Quantification of planar ^{123}I-mIBG images involves the calculation of the heart to mediastinal (H/M) ratio as a surrogate for cardiac SNS innervation, whereas the washout ratio from early and late ^{123}I-mIBG images has been used as a surrogate for presynaptic nerve activity [111, 112]. However, 2D planar imaging is not fully quantitative, because of the superposition of background structures with the 2D heart region of interest and lack of corrections for attenuation and scatter. Three-dimensional (3D) SPECT ^{123}I-mIBG imaging has been proposed to overcome this limitation and enable evaluation of regional myocardial tracer uptake [113–115]. Absolute quantification of ^{123}I-mIBG requires hybrid SPECT/CT imaging and kinetic modeling, and the use of CT for both attenuation and partial volume correction [116].

11.5.2 PET Radiotracers

Many agents have been developed for presynaptic SNS PET imaging, but to date the most clinically relevant has been ^{11}C-meta-hydroxyephedrine (^{11}C-HED), which is the most well studied in animal and human models [117–120]. ^{11}C-HED PET imaging offers advantages over ^{123}I-MIBG due to the higher spatial resolution with PET, providing more precise volumetric and regional information (Fig. 11.8). However, the use of ^{11}C-HED is limited by the short half-life and the requirement for a cyclotron. Another presynaptic SNS tracer with a longer half-life and similar kinetics to

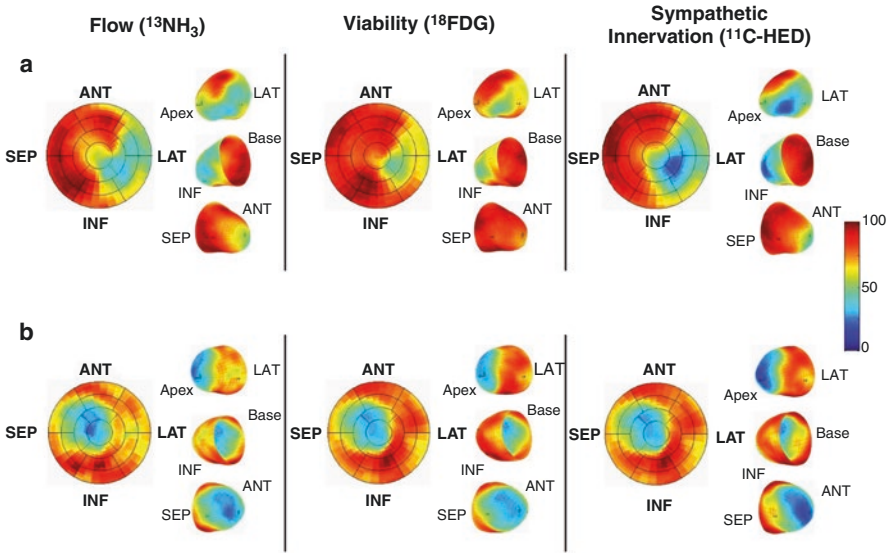

Fig. 11.8 Images from PARAPET trial. PET quantification of flow, viable myocardium, and sympathetic innervation from two representative subjects. (**a**) Subject with sudden cardiac arrest (SCA) where there is a mismatch in infarct size (reduced ^{18}F-FDG) and volume of sympathetic denervation (reduced ^{11}C-HED), which was smaller. There was also reduced perfusion (^{13}N-ammonia [13NH3]) with preserved ^{18}FDG indicating hibernating myocardium. (**b**) Subject with matched reductions in flow, infarct volume, and sympathetic denervation. Anterior (ANT), Inferior (INF), lateral (LAT), and septum (SEP). (Reproduced with permission from Fallavollita et al., J Am Coll Cardiol. 2014 Jan, 63 (2) 141–149)

^{123}I-MIBG is ^{18}F-LMI1195 [121]. Sinusas et al. showed promising properties of this radiotracer in the first-in-human study, demonstrating patient safety, and favorable dosimetry and biodistribution along with excellent kinetics for myocardial imaging [122]. Less clinically used radiotracers that provide vesicular storage and metabolic information, are the neurotransmitter ^{11}C-Epinephrine (EPI) and the synthetic catecholamine ^{11}C-Phenylephrine (^{11}C-PHEN). ^{11}C-EPI provides favorable images due to the rapid blood clearance and slow myocardial clearance [119, 120]. In contrast, ^{11}C-PHEN is susceptible to intraneuronal monoamine oxidase (MAO), and therefore myocardial washout tends to be rapid with lower myocardial retention in comparison to the other presynaptic agents [123]. The targeting of postsynaptic β_1 and β_2 receptors with the ^{11}C-labeled non-selective receptor antagonists such as ^{11}C-CGP-12177 and ^{11}C-CGP-12388 provide acceptable quality images with the possibility of quantitative analyses. However, there has not been any widespread clinical use of these agents due to difficulties in synthesis and the short half-life of ^{11}C [124, 125]. A radiotracer targeting α_1 receptors (^{11}C-GB67) was developed and validated in preclinical studies, although the potential for clinical application has yet to be determined in human studies [126].

11.6 Clinical Applications of SNS Imaging

Most of the clinical evaluations of sympathetic function with radiolabeled probes have been with the use of ^{123}I-MIBG and ^{11}C-HED. These agents have provided mechanist insights in the setting of cardiac transplantation [127, 128], a guide for placement of implantable cardioverter defibrillators for primary prevention in sudden cardiac death (SCD) [109, 129], and to establish prognosis in patients with cardiomyopathies [130, 131]. The imaging of the ganglionated plexi (GPs) has more recently been of interest in the electrophysiology community, since it has been demonstrated that catheter ablation of the GPs as an add-on to pulmonary vein isolation in patients with atrial fibrillation (AF) may improve clinical outcomes [132, 133]. Furthermore, it has been also reported that the presence of residual GP activity after pulmonary vein isolation (PVI) might predict likelihood of AF recurrence [134]. However, a major limitation for the use of SPECT imaging technology has been the limited resolution of most SPECT cameras, especially because of the small size of these structures (5–10 mm) [135]. More recently, a pilot study showed that the use of CZT SPECT cameras and ^{123}I-MIBG imaging allowed for detection of the GPs in 20 patients with the diagnosis of paroxysmal AF who underwent PVI. These patients had ^{123}I-MIBG imaging performed prior to ablation and SPECT images were registered with pre-PVI cardiac contrast CT imaging. Again, highlighting the importance of hybrid imaging technology or image fusion for clinical application of autonomic imaging. In these studies, uptake of ^{123}I-MIBG correlated with areas of high frequency stimulation demonstrating that SPECT/CT imaging can accurately identify GPs prior to PVI ablation (Fig. 11.9) [136]. However, due to the lack of larger prospective and randomized control trials, the widespread use of this approach in clinical practice is still lacking.

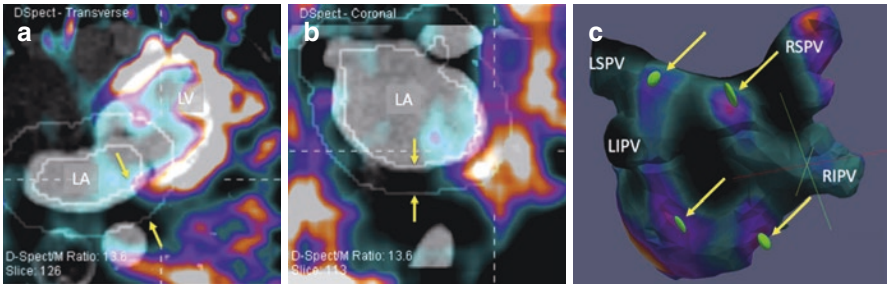

Fig. 11.9 (**a**, **b**) Co-registered SPECT ^{123}I-mIBG and cardiac CT images in transverse (**a**) and coronal (**b**) planes. The LA region of search is defined (solid lines, arrows) by the CT-derived LA compartment. (**c**) Color-coded 3D maps of ^{123}I-mIBG uptake and distribution on CT-derived LA compartments, as well as 3D ellipsoidal DUA representations (ellipsoids, arrows). *LSPV* left superior pulmonary vein, *LIPV* left inferior pulmonary vein, *RSPV* right superior pulmonary vein, *RIPV* right inferior pulmonary vein, *DUA* discrete uptake area, *LA* left atrium, *LV* left ventricle. (Modified with permission, from Stirrup, J., Gregg, S., Baavour, R. et al. J. Nucl. Cardiol. 2019 [136])

11.7 Parasympathetic Imaging

Nerve conduction in the PNS is mediated by the release of acetylcholine (ACh) from postganglionic terminals. The release of ACh after a depolarization of the cell follows coupling of ACh to the muscarinic and nicotinic receptors to exert effect. The predominant effect following activation of these receptors in the heart is reduction of heart rate and myocardial contraction. The remaining choline after cleavage by acetylcholinesterase (AChE) is taken up by terminal nerve endings which results in a continuous resynthesized of ACh [106]. The particularly dense distribution of the terminal efferent nerves and receptors in the thinner-wall atria compared to the ventricle in conjunction with the rapid degradation of Ach by AChE make the imaging of the PNS in the heart more challenging than SNS imaging. Therefore, there are not many clinically SPECT radiotracer available for this purpose and only PET radiotracers have been developed. Despite these limitations, the use of ^{11}C-Donezepil in preclinical studies has showed promising results as a presynaptic PNS imaging agent, which might provide prognostic information in certain patients [137]. Similar to imaging of the SNS, imaging of the postsynaptic parasympathetic receptors is also of great interest. The use of ^{11}C-MQNB to measure the density of the muscarinic receptors has been validated in preclinical and human studies [138, 139]. More recently, the use of a novel fluorinated agent (^{18}F-85380), which targets $\alpha_4\beta_2$ has showed favorable results in terms of quality of imaging in healthy patients and in those with neurodegenerative disease [140]. In contrast to SNS imaging, the clinical use of PNS radiotracers is far more limited and requires further evaluation to determine potential clinical applications.

11.7.1 Angiogenesis

Angiogenesis is defined as new capillary formation from preexisting microvessels, and is stimulated by tissue hypoxia via activation of hypoxia-inducible factor (HIF) 1-α, which triggers the transcription of numerous angiogenic genes, such as vascular endothelial growth factor (VEGF), VEGF receptors (VEGFR), neuropilin-1, and angiopoietin-2 [141]. Besides the transcription of growth factors and their receptors, hypoxia also triggers inflammatory cells to secrete soluble pro-angiogenic and anti-angiogenic molecules that regulate this process [142]. The secretion of pro-angiogenic molecules induces the migration of endothelial or progenitor cells that proliferate and form new vessels. Activated and proliferating endothelial cells express integrins, which are crucial to the angiogenic process [143]. Targeted imaging of any of these molecular signals allows in vivo evaluation of myocardial angiogenesis in the setting of acute or chronic ischemia with nuclear imaging techniques [141, 144].

11.7.1.1 αvβ3 Integrin Targeted Imaging

The most widely applied strategy for molecular imaging of angiogenesis has been with the use of SPECT and PET tracers that target the αvβ3 integrin, which is a cell

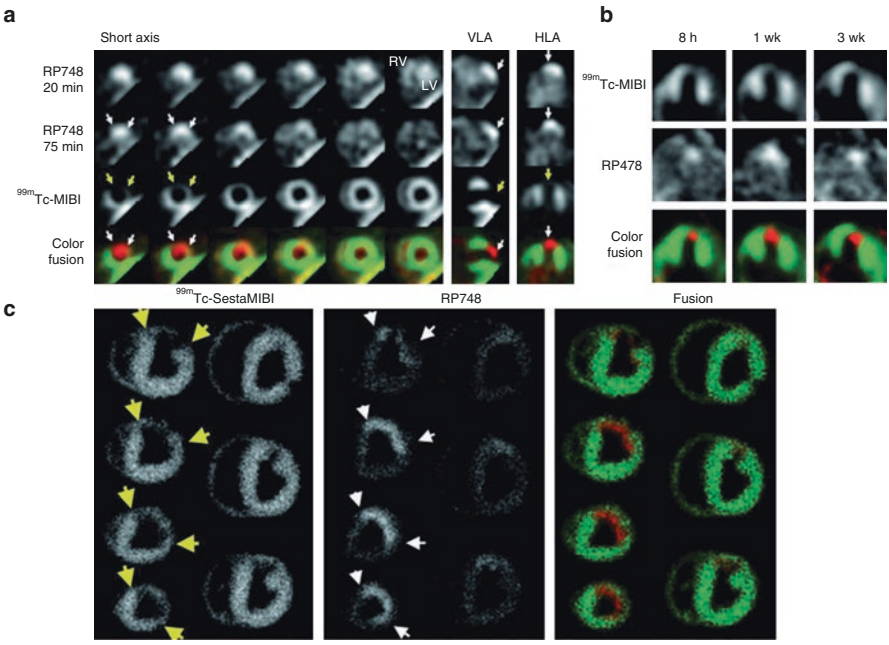

Fig. 11.10 In vivo and ex vivo ^{111}In-RP748 and ^{99m}Tc-sestamibi (^{99m}Tc-MIBI) images from dogs with chronic infarction. (**a**) In vivo short axis, vertical long axis (VLA) and horizontal long axis (HLA) serial images in a dog 3 weeks after left anterior descending (LAD) coronary artery infarction. Images were at 20 min and 75 min after injection. ^{99m}Tc-MIBI images (third row) demonstrate the anteroapical perfusion defect (yellow arrows). The 75 min ^{111}In-RP748 SPECT images were colored red and the ^{99m}Tc-MIBI images were colored green and the images fused together (bottom row). This demonstrates the localization of the ^{111}In-RP748 activity within the heart (white arrows). Right ventricular and left ventricular blood pool activity is seen at 20 min. (**b**) In vivo ^{99m}Tc-MIBI and ^{111}In-RP748 SPECT images from a canine model at 8 h, 1 week and 3 weeks after LAD infarction. At all three timepoints increased myocardial ^{111}In-RP748 uptake is seen in the anteroapical wall. When the ^{99m}Tc-MIBI (green) and ^{111}In-RP748 (red) images are fused the perfusion defect can be appreciated with increased uptake of ^{111}In-RP748. (**c**) Ex vivo ^{99m}Tc-MIBI (left) and ^{111}In-RP748 (center) images of myocardial slices from a canine model 3 weeks post-LAD occlusion. Short-axis slices are in standard orientation. Yellow arrows indicate perfusion defect of the ^{99m}Tc-MIBI images and the white arrows indicate increased uptake of ^{111}In-RP748. Color fused images are seen on the right and demonstrate increased uptake of ^{111}In-RP748 in the nontransmural perfusion defect. (Modified from Meoli DF, J Clin Invest. 2004)

membrane glycoprotein that is highly expressed on endothelial cells during angiogenesis, but not on normal quiescent endothelial cells [145]. Meoli et al. were the first to report that the αvβ3 integrin antagonist, ^{111}In-RP748, could bind with high affinity and selectivity to the αvβ3 integrin, providing an in vivo index of angiogenesis in the setting of ischemic myocardial injury with SPECT imaging (Fig. 11.10) [146]. Later generation SPECT and PET tracers have employed the arginine-glycine-aspartic acid (RGD) peptide or derivatives for angiogenesis imaging, since this sequence is highly selective for the αvβ3 integrin [147–150]. Commonly used

tracers that target αvβ3 integrin activation in the heart include the SPECT tracer, ^{99m}Tc-NC100692 (^{99m}Tc-maraciclatide) [149], and the PET tracers, ^{18}F-galacto-RGD [151], ^{68}Ga-PRGD2 [152], and ^{18}F-Fluciclatide [153]. Clinical imaging of myocardial angiogenesis has already been performed with ^{99m}Tc-maraciclatide SPECT imaging [154], and PET imaging of ^{18}F-galacto-RGD [155], ^{68}Ga-PRGD2 [152], and ^{18}F-Fluciclatide (Fig. 11.11) [153].

11.7.1.2 Vascular Endothelial Growth Factor (VEGF) and Endothelial Cell Imaging

VEGF is a growth factor that is expressed in response to tissue hypoxia that stimulates angiogenesis via binding and activation of cognate receptors (VEGFR-1, VEGFR-2) [156, 157]. Significant efforts have been made to radiolabel VEGF isoforms or antibodies against specific VEGF receptors for PET and SPECT imaging of angiogenesis [158, 159]. Multiple VEGF isoforms have been radiolabeled for SPECT imaging of angiogenesis. Investigators have also developed radiotracers that target membrane proteins of activated endothelial cells (CD13) or endothelial cells of newly formed vessels (CD105) [160, 161].

11.8 Imaging Fibrosis and Extracellular Matrix (ECM)

Many pathological conditions lead to the deposition of components of the ECM in the heart, this process also known as fibrosis usually occurs as a response to different types of insults such as ischemia, pressure, volume overload, and certain cardiomyopathies [162–164]. Briefly, fibrosis is characterized by a complex process of cytokine release, inflammatory cells migration, angiogenesis trough endothelial cell proliferation, and ultimately the presence of myofibroblasts which promote the deposition of collagen to support scar formation [165]. Given the presence of fibrosis in many cardiovascular diseases targeted ECM imaging has been proposed as a tool to assess disease progression, evaluate treatment response, and provide prognosis.

11.8.1 Clinical Applications

Currently, the vast majority of ECM targeted imaging research has been performed in the setting of acute myocardial infarction or for the evaluation of post-infarct remodeling. Here, we will present the most common targets for imaging fibrosis and the ECM.

11.8.1.1 Imaging Somatostatin Receptor

Fibroblasts become activated, proliferate, and differentiate into myofibroblasts during the process of fibrosis. Somatostatin receptors expressed on fibroblasts become upregulated during fibrosis [166]. Therefore, imaging of somatostatin receptors represents a potential target for evaluation of myocardial fibrosis. ^{111}In-Octreotride is

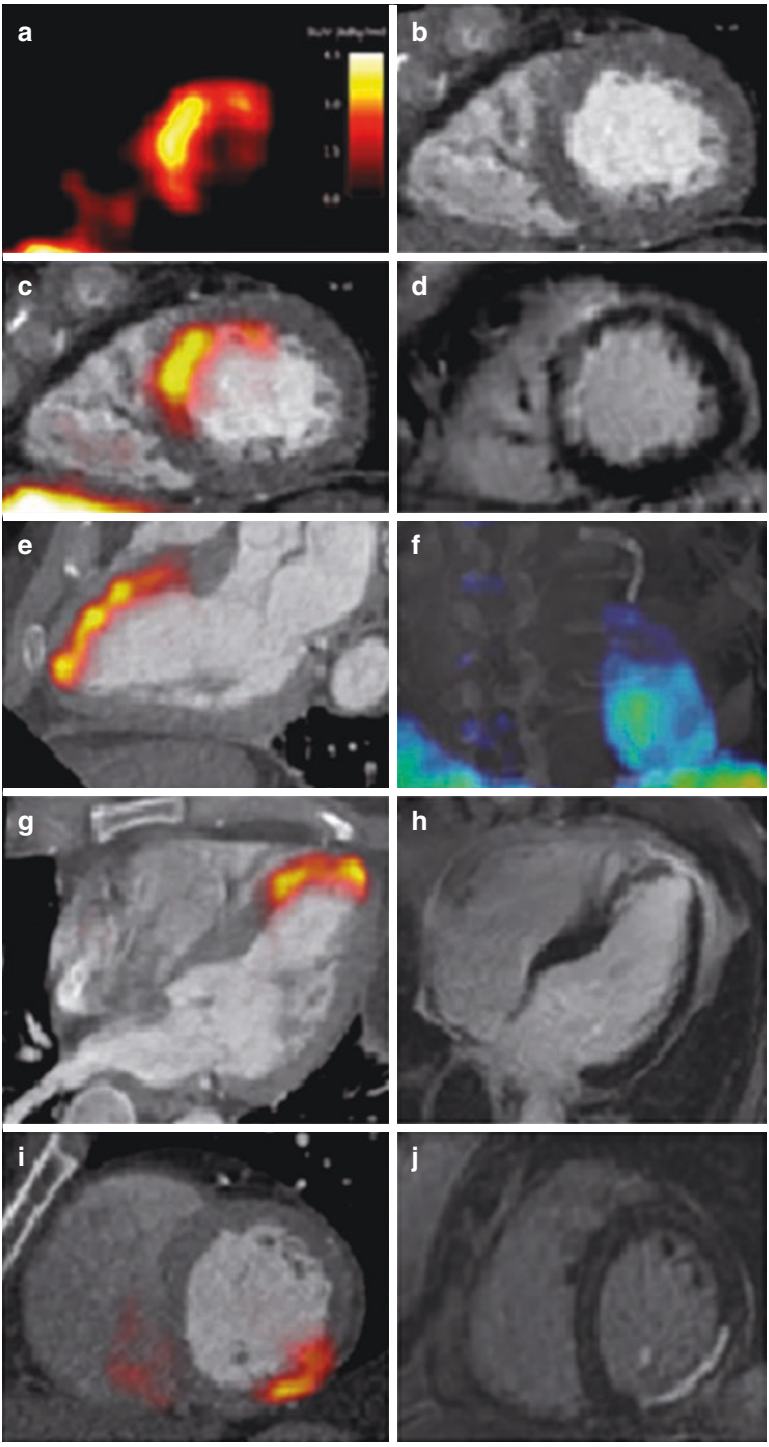
a
b
c
d
e
f
g
h
i
j

an FDA approved SPECT radiotracer that has been used to image fibrosis in pulmonary sarcoidosis, and may also play a role in imaging cardiac sarcoidosis. ^{68}Ga-DOTA-NaI-octreotide (^{68}Ga-DOTANOC) is a PET radiotracer that also binds to somatostatin receptors on inflammatory cells in sarcoid granulomas. PET imaging with ^{68}Ga-DOTANOC has provided better diagnostic accuracy and inter-observer agreement than FDG-PET, which is used more routinely in the evaluation of cardiac sarcoidosis (Fig. 11.12) [167].

11.8.1.2 Imaging Integrins

Integrins are also expressed on myofibroblasts, and therefore integrin targeted imaging has also been used to image myocardial fibrosis. The binding of the αvβ3 integrin to the ECM is dependent on an amino acid complex consisting of arginine-glycine-aspartic acid (RGD). SPECT imaging of a ^{99m}Tc-labeled Cy5.5-RGD imaging peptide (^{99m}Tc-CRIP) has been shown to co-localize with myofibroblasts and track fibrosis following myocardial infarction [168]. A similar ^{99m}Tc-labeled RGD peptide has been shown to identify scar in patients following myocardial infarction [169]. The αvβ6 integrin is another important activator of the profibrotic cytokine TGF-β that is upregulated following tissue injury. SPECT/CT imaging of ^{111}In-labeled A20FMDV2 has enabled detection of increased αvβ6 integrin in fibrotic tissues [170]. Other PET probes targeted at the αvβ6 integrin are now in clinical trials in patients with pulmonary fibrosis.

11.8.1.3 Imaging Collagen

Molecular imaging of the ECM can involve targeting collagen, which reaches high concentration with fibrosis. There are both indirect and direct approaches for imaging collagen in fibrosis. The MRI extracellular contrast agent, Gd-DOTA is commonly used for the indirect evaluation of fibrosis and viability after MI [171, 172]. DOTA has also been labeled with ^{64}Cu for PET imaging, and has similar properties to the MRI tracers providing good localization and visualization of the MI region

Fig. 11.11 ^{18}F-Fluciclatide uptake in acute myocardial infarction (MI) in three patients with recent subendocardial MI. Patient 1 (**a**–**f**), 13 days after anterior MI, displaying a short-axis PET image of the left ventricle with crescentic ^{18}F-fluciclatide uptake (**a**) that correlates with the interventricular septum and anterior wall on CT angiography (**b**). The fused PET/CT angiography image (**c**) shows this uptake to correspond exactly with the region of late gadolinium enhancement (LGE) on cardiac magnetic resonance (CMR) (**d**). Delineation of myocardial uptake on PET/CT is clearer in the two-chamber view (**e**) and on a fused CT/three-dimensional-Patlak image, which shows this uptake to follow a watershed-pattern emerging from the coronary stents present in the left anterior descending coronary artery (**f**). Patient 2 (**g**, **h**), 8 days following anterior MI, displaying focal uptake of ^{18}F-fluciclatide in the anterior wall and apex in the 3-chamber view on PET/CT (**g**) which corresponds to the region of MI on LGE CMR imaging (**h**). Patient 3 (**i**, **j**), showing focal uptake of ^{18}F-fluciclatide in the inferior wall 19 days following MI on PET/CT (**i**) that again corresponds to the infarction on CMR LGE imaging (**j**). (Reproduced with permission from Jenkins WSA, et al. Heart 2017;103:607–615)

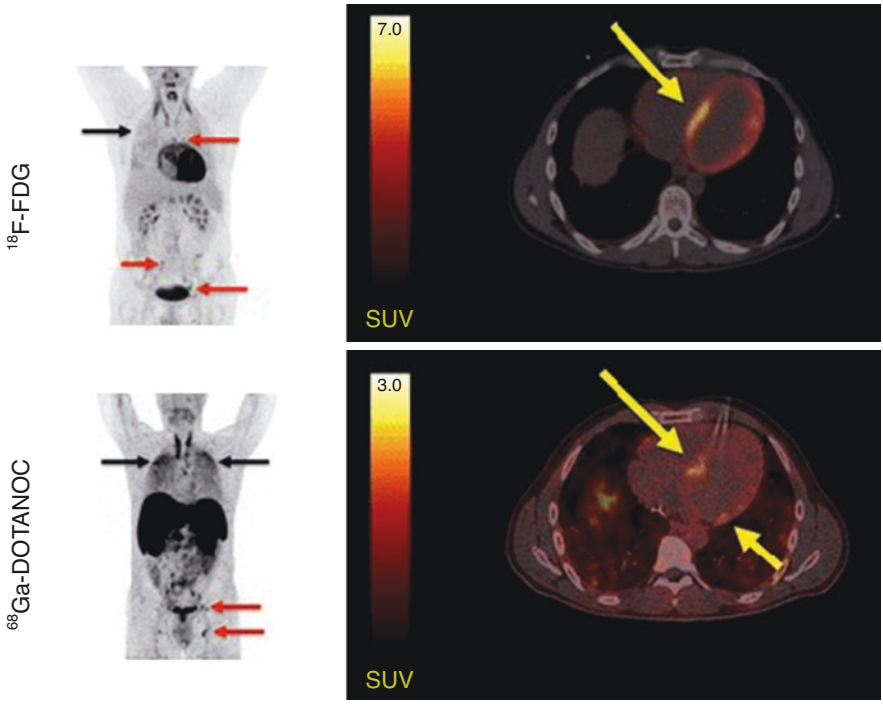

Fig. 11.12 Patient with cardiac sarcoidosis in which the ^{18}F-FDG PET/CT was inconclusive due to insufficiently suppressed physiological ^{18}F-FDG uptake by the myocardium. (**Left panel**) MIPs showing a patient with dilated cardiomyopathy and multiple ^{18}F-FDG and ^{68}Ga-DOTANOC avid lymph nodes (red arrows) both above and below the diaphragm. Furthermore, there is massive and diffusely increased activity in the lung parenchyma (black arrows) reflecting active pulmonary sarcoidosis. (**Right panel**) The top image raises suspicious for cardiac involvement with a region of focal on diffuse pattern of ^{18}F-FDG uptake in the PET/CT transaxial slices (SUVmax 21 at the septum). This scan was considered non-conclusive by a reviewer panel. In contrast, all reviewers rated the ^{68}Ga-DOTANOC uptake (SUVmax 2.8, target-to-background 3.04) in the septum pathological (**bottom**). The patient was treated with corticosteroids and recovered. *MIP* maximum intensity projections. (Reproduced with permission from Gormsen LC, et al. *EJNMMI Res*. 2016;6:52)

[173, 174]. Although, these agents provide indirect localization of fibrosis, their lack of sensitivity made them unable to detect diffuse fibrosis which can sometimes be observed in cardiomyopathies or secondary to conditions of volume and/or pressure overload. Therefore, collagen specific tracers have been developed to overcome this problem, although these approaches detect an end result of collagen deposition. The first molecule developed was ^{99m}Tc-collagelin for SPECT imaging. Although ^{99m}Tc-collagelin demonstrated a high binding capability to Collagen I and

II, the image quality was compromised by a high liver uptake [175]. Analogous PET probes were synthetized to overcome this limitation, including ^{68}Ga- and ^{64}Cu-labeled probes that demonstrated improved target-to-noise and good quality images in vitro, however, the in vivo kinetics did not differ from the non-specific collagen probes during in vivo imaging [174, 176]. For example, ^{68}Ga-CBP8 demonstrated excellent binding to type 1 collagen in human tissue ex vivo, although in vivo binding has not been demonstrated.

11.8.1.4 Imaging of Extracellular Matrix Proteases

Another target of particular interest for imaging the ECM are the matrix metalloproteases (MMPs), which are zinc-dependent proteases that play an important role in the turnover of ECM during normal physiologic conditions [177], and are upregulated during the inflammatory phase of many cardiovascular conditions such as acute MI. The activation of MMPs are kept in balance by tissue inhibitors of MMPs (TIMPs). If this MMP/TIMP balance becomes disrupted, adverse consequences can ensue such as left ventricular remodeling [178]. To date, the most important imaging agent for MMPs in the setting of acute MI is the ^{99m}Tc-labeled peptidomimetic probe, RP-805, which is a broad spectrum inhibitor of MMPs that binds to the catalytic site of activated MMPs [179, 180]. The effectiveness of ^{99m}Tc-RP805 for imaging of cardiac remodeling has been demonstrated in both small and large animal models of post-MI remodeling (Fig. 11.13). ^{99m}Tc-RP805 uptake was found to be the highest at 1 week after MI within the central infarct region, and importantly remained elevated for the following 3–4 weeks after injury [179, 180]. Interestingly, although the majority of the uptake was in the MI region, a modest increase in uptake was also observed in the border and remote regions of the left ventricle as well as the atria of the heart [176]. Therefore, this radiotracer provides and index of global remodeling of the myocardium following MI. Non-invasive dual isotope hybrid SPECT/CT imaging of ^{99m}Tc-RP805 and ^{201}Tl was also shown to provide a quantitative regional map of MMP activation in the myocardium in relation to regional myocardial blood flow. This hybrid imaging methodology was specifically used to assess the efficacy of the intracoronary delivery of an MMP inhibitor, rTIMP-3, to the MI region, and demonstrated a reduction in MMP activity in association with an increase in myocardial blood flow as assessed with dynamic ^{201}Tl imaging [181]. The myocardial uptake of ^{99m}Tc-RP805 has also been shown to be increased in models of chemotherapy induced cardiotoxicity and uptake of this compound was found to be directly related to a decline in global left ventricular function [182].

Although, still in a preclinical mouse model, the more selective targeting of MMP-2 with an activatable fluorescent probe (MMP-P12) was developed to non-invasively image the development and treatment response in models of hindlimb ischemia [183]. The value of this probe for cardiac imaging remains uncertain.

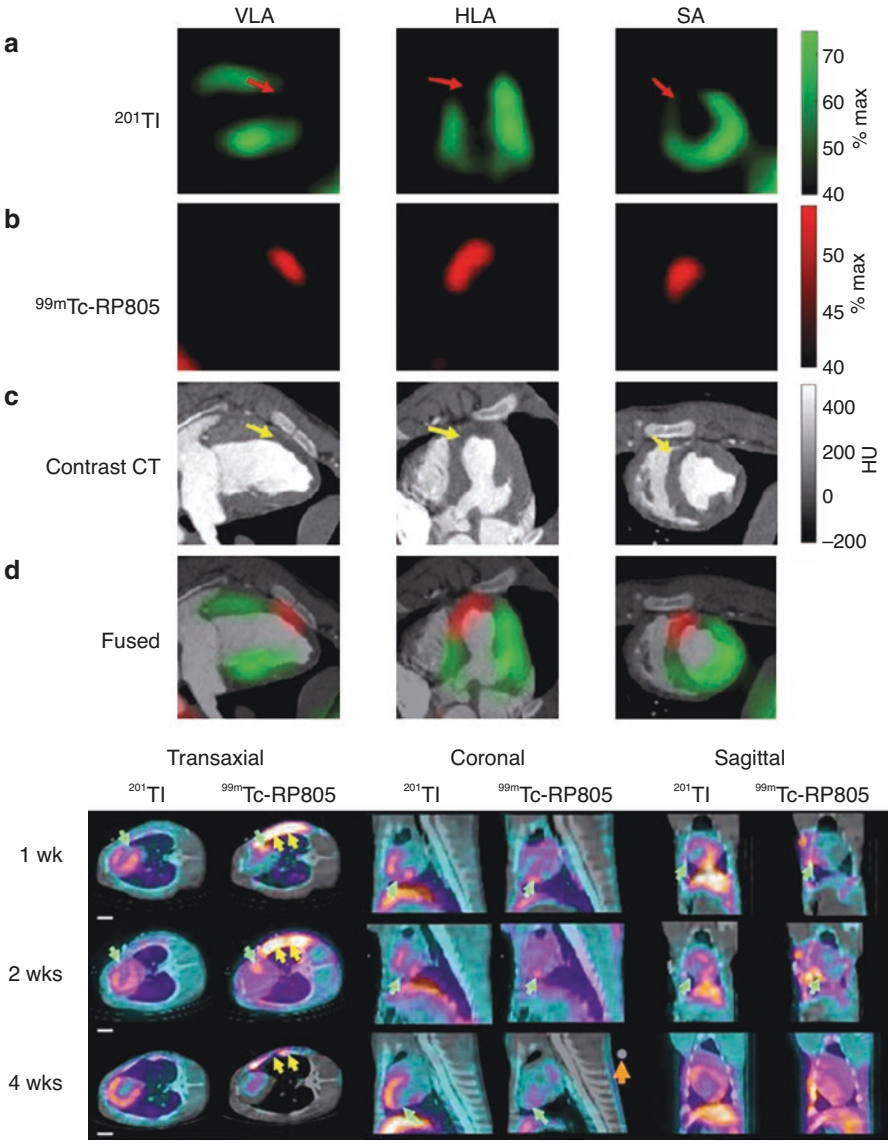
VLA
HLA
SA
a
201TI
70
60
50
40
% max
b
99mTc-RP805
50
45
40
% max
c
Contrast CT
400
200
0
–200
HU
d
Fused
Transaxial
Coronal
Sagittal
201TI
99mTc-RP805
201TI
99mTc-RP805
201TI
99mTc-RP805
1 wk
2 wks
4 wks

11.9 Monitoring Cell and Gene-Based Therapies with Novel Reporter Probe Imaging

Cell and gene-based therapies provide potential new approaches to treat cardiovascular diseases. While many clinical trials have been conducted using cell and gene-based therapy to treat ischemic heart disease the overall benefit has been mixed [184–187]. One limitation of these trials is the inability to non-invasively track the initial delivery and in vivo quantitative effects of these therapies. The high sensitivity of nuclear imaging to detect cellular and molecular events offers a unique opportunity to address these limitations. The ability to visualize cellular and gene-based therapies with nuclear relies on two distinct strategies that include, (1) direct labeling and (2) the use of reporter genes.

11.9.1 Direct Labeling

Stem cells have been directly radiolabeled with techniques that allow for cellular incorporation or uptake of radiotracers for SPECT and PET imaging [188]. A gene or components of a gene delivery system have been directly radiolabeled with both gamma (^{111}In) and positron emitting (^{124}I) isotopes for SPECT and PET imaging, respectively [189]. Although useful for monitoring initial cell/gene delivery to a target tissue, major issues exist with these techniques. The direct labeling approach does not facilitate long-term follow-up due to the loss of imaging signal strength because of radioactive isotope decay. More importantly, direct labeling does not allow for the ability to differentiate viable cells from dead cells or even retained isotope by infiltrating inflammatory cells or within cellular debris [188].

Fig. 11.13 In vivo ^{99m}Tc-RP805 SPECT/CT images. (**Top**) Representative in vivo hybrid dual isotope SPECT/CT images are shown in vertical long axis (VLA), horizontal long axis (HLA), and short axis (SA) from a pig post-MI. ^{201}Tl SPECT images are shown in green (**a**), ^{99m}Tc-RP805 uptake in red (**b**), and contrast CT in black and white (**c**). A dense ^{201}Tl perfusion defect (red arrow) is seen in the anteroseptal wall with corresponding hypoperfusion zone on the contrast CT image (yellow arrow). The fusion of the SPECT and CT images (**d**) demonstrates focal ^{99m}Tc-RP805 uptake within the perfusion defect. Reproduced with permission from Thorn et al., Circ Cardiovasc Imaging 2019. (**Bottom**) Dual isotope in vivo SPECT/CT imaging reflecting ^{201}Tl myocardial perfusion and ^{99m}Tc-RP805 uptake reflecting matrix metalloproteinase activity. In vivo ^{201}Tl and ^{99m}Tc-RP805 SPECT/CT images of pigs at 1, 2, and 4 weeks post-myocardial infarction are shown in transaxial, coronal, and sagittal views. Note the perfusion defect in the lateral wall and the time-dependent changes in the intensity of ^{99m}Tc-RP805 retention in the same regions (green arrows). The yellow double arrows point to ^{99m}Tc-RP805 activity in the surgical sternal wound. A point source of known activity (orange arrow) can be used to quantify radiotracer uptake. Scale bars: 2 cm. (Modified, with permission, from Sahul ZH, Circ Cardiovasc Imaging. 2011 [180])

11.9.2 Reporter Genes

Reporter gene technology overcomes many of the limitations of direct labeling. Reporter genes are genes for specific proteins that elicit an imaging signal by biochemically interacting with an imageable probe. In gene therapy applications, the reporter gene is attached to the regulatory sequence of the protein of interest, and therefore the intensity of signal is related to gene expression of both the report gene and the associated therapeutic gene of interest. Similarly, in stem cell applications, reporter genes are introduced into stem cells prior to delivery. Therefore, probe uptake directly relates to viable stem cell numbers.

Two common reporter genes for nuclear imaging are the herpes simplex virus type 1 thymidine kinase (HSV1-tk) and the human sodium iodide symporter (hNIS). Each of these proteins interact with reporter probes differently. Expression of the HSV1-tk in the target cell leads to the production of thymidine kinase, which in the presence of the radioisotope substrates, 9-(4-^{18}F-fluoro-3-[hydroxymethyl]butyl)guanine (^{18}F-FHBG) and 2'-[^{18}F]fluoro-5-ethyl-1-beta-D-arabinofuranosyluracil (^{18}F-FEAU), causes phosphorylation and trapping of these probes in the cell. The hNIS is a membrane protein capable of transporting several radioisotopes (e.g., ^{99m}TcO4-, ^{123}I, ^{18}F-tetrofluroborate) when expressed in a target cell. Uptake is facilitated by active transport of Na^+, thus uptake can occur against a concentration gradient and lead to higher radiotracer accumulation and image sensitivity than with the use of enzymes or receptors [190]. Nuclear imaging of reporter genes, especially when combined with anatomical CT imaging, offers adequate image sensitivity for detecting in vivo processes, and are widely used for evaluating these novel therapies.

11.10 Theranostics

Theranostics represents the combination of a molecular diagnostic probe with a targeted therapeutic. The use of theranostics offers many potential advantages, including: (1) improving drug efficacy by directing a therapy to those most likely to benefit, (2) improving the safety profile of a therapeutic by minimizing off target effects, and (3) ultimately improving cost effectiveness and therapeutic drug development or improving selection of clinical trial participants. The initial use of theranostics involved radionuclide therapies with imageable radioisotopes that yield therapeutic radiation. Some prototypical isotopes include ^{177}Lu or ^{186}Re for SPECT imaging or ^{90}Y for PET imaging. More recent efforts in the development of theranostics involve the use of nanoparticles of multiple configurations that can be engineered to locally delivery therapeutics over a prescribed time frame. This might include the use of micelles, liposomes, dendrimers, or lipoprotein nanoparticles. The application of theranostics for the evaluation and treatment of cardiovascular diseases has been recently reviewed [191, 192].

References

1. Boutagy NE, Feher A, Alkhalil I, Umoh N, Sinusas AJ. Molecular imaging of the heart. Compr Physiol. 2019;9:477–533.
2. Sogbein OO, Pelletier-Galarneau M, Schindler TH, Wei L, Wells RG, Ruddy TD. New SPECT and PET radiopharmaceuticals for imaging cardiovascular disease. Biomed Res Int. 2014;2014:942960.
3. Strauss HW, Harrison K, Langan JK, Lebowitz E, Pitt B. Thallium-201 for myocardial imaging. Relation of thallium-201 to regional myocardial perfusion. Circulation. 1975;51:641–5.
4. Dilsizian V, Rocco TP, Freedman NM, Leon MB, Bonow RO. Enhanced detection of ischemic but viable myocardium by the reinjection of thallium after stress-redistribution imaging. N Engl J Med. 1990;323:141–6.
5. Baggish AL, Boucher CA. Radiopharmaceutical agents for myocardial perfusion imaging. Circulation. 2008;118:1668–74.
6. Zaret BL, Rigo P, Wackers FJ, Hendel RC, Braat SH, Iskandrian AS, Sridhara BS, Jain D, Itti R, Serafini AN, et al. Myocardial perfusion imaging with 99mTc tetrofosmin. Comparison to 201Tl imaging and coronary angiography in a phase III multicenter trial. Tetrofosmin International Trial Study Group. Circulation. 1995;91:313–9.
7. Hurwitz GA, Clark EM, Slomka PJ, Siddiq SK. Investigation of measures to reduce interfering abdominal activity on rest myocardial images with Tc-99m sestamibi. Clin Nucl Med. 1993;18:735–41.
8. Johnson LL, Seldin DW. Clinical experience with technetium-99m teboroxime, a neutral, lipophilic myocardial perfusion imaging agent. Am J Cardiol. 1990;66:63E–7E.
9. Bruschi G, Colombo T, Oliva F, Botta L, Morici N, Cannata A, Vittori C, Turazza F, Garascia A, Pedrazzini G, Frigerio M, Martinelli L. Heart transplantation: 25 years' single-centre experience. J Cardiovasc Med. 2013;14:637–47.
10. Kim YS, Shi J, Zhai S, Hou G, Liu S. Mechanism for myocardial localization and rapid liver clearance of Tc-99m-N-MPO: a new perfusion radiotracer for heart imaging. J Nucl Cardiol. 2009;16:571–9.
11. Goethals LR, Santos I, Caveliers V, Paulo A, De Geeter F, Lurdes PG, Fernandes C, Lahoutte T. Rapid hepatic clearance of 99mTc-TMEOP: a new candidate for myocardial perfusion imaging. Contrast Media Mol Imaging. 2011;6:178–88.
12. Wells RG, Wei L, Petryk J, Duan Y, Marvin B, Timmins R, Soueidan K, Fernando P, Bensimon C, Ruddy TD. Flow-dependent uptake of (1)(2)(3)I-CMICE-013, a Novel SPECT perfusion agent, compared with standard tracers. J Nucl Med. 2015;56:764–70.
13. Duan Y, Yan X, Wei L, Bensimon C, Fernando P, Ruddy TD. Acute and subacute toxicity studies of CMICE-013, a novel iodinated rotenone-based myocardial perfusion tracer, in Sprague Dawley rats and Gottingen minipigs. Regul Toxicol Pharmacol. 2016;80:195–209.
14. Driessen RS, Raijmakers PG, Stuijfzand WJ, Knaapen P. Myocardial perfusion imaging with PET. Int J Cardiovasc Imaging. 2017;33:1021–31.
15. Di Carli MF, Hachamovitch R. New technology for noninvasive evaluation of coronary artery disease. Circulation. 2007;115:1464–80.
16. Mc Ardle BA, Dowsley TF, deKemp RA, Wells GA, Beanlands RS. Does rubidium-82 PET have superior accuracy to SPECT perfusion imaging for the diagnosis of obstructive coronary disease?: a systematic review and meta-analysis. J Am Coll Cardiol. 2012;60:1828–37.
17. Fiechter M, Ghadri JR, Gebhard C, Fuchs TA, Pazhenkottil AP, Nkoulou RN, Herzog BA, Wyss CA, Gaemperli O, Kaufmann PA. Diagnostic value of 13N-ammonia myocardial perfusion PET: added value of myocardial flow reserve. J Nucl Med. 2012;53:1230–4.
18. Huang SC, Williams BA, Krivokapich J, Araujo L, Phelps ME, Schelbert HR. Rabbit myocardial 82Rb kinetics and a compartmental model for blood flow estimation. Am J Phys. 1989;256:H1156–64.
19. Harnett DT, Hazra S, Maze R, Mc Ardle BA, Alenazy A, Simard T, Henry E, Dwivedi G, Glover C, deKemp RA, Davies RA, Ruddy TD, Chow BJW, Beanlands RS, Hibbert

B. Clinical performance of Rb-82 myocardial perfusion PET and Tc-99m-based SPECT in patients with extreme obesity. J Nucl Cardiol. 2019;26:275–83.
20. Schelbert HR, Phelps ME, Huang SC, MacDonald NS, Hansen H, Selin C, Kuhl DE. N-13 ammonia as an indicator of myocardial blood flow. Circulation. 1981;63:1259–72.
21. El Fakhri G, Kardan A, Sitek A, Dorbala S, Abi-Hatem N, Lahoud Y, Fischman A, Coughlan M, Yasuda T, Di Carli MF. Reproducibility and accuracy of quantitative myocardial blood flow assessment with (82)Rb PET: comparison with (13)N-ammonia PET. J Nucl Med. 2009;50:1062–71.
22. Anagnostopoulos C, Georgakopoulos A, Pianou N, Nekolla SG. Assessment of myocardial perfusion and viability by positron emission tomography. Int J Cardiol. 2013;167:1737–49.
23. Fathala A, Aboulkheir M, Shoukri MM, Alsergani H. Diagnostic accuracy of (13)N-ammonia myocardial perfusion imaging with PET-CT in the detection of coronary artery disease. Cardiovasc Diagn Ther. 2019;9:35–42.
24. Maddahi J, Bengel F, Czernin J, Crane P, Dahlbom M, Schelbert H, Sparks R, Phelps M, Lazewatsky J. Dosimetry, biodistribution, and safety of flurpiridaz F 18 in healthy subjects undergoing rest and exercise or pharmacological stress PET myocardial perfusion imaging. J Nucl Cardiol. 2019;26:2018.
25. Yalamanchili P, Wexler E, Hayes M, Yu M, Bozek J, Kagan M, Radeke HS, Azure M, Purohit A, Casebier DS, Robinson SP. Mechanism of uptake and retention of F-18 BMS-747158-02 in cardiomyocytes: a novel PET myocardial imaging agent. J Nucl Cardiol. 2007;14: 782–8.
26. Iskandrian AE, Dilsizian V, Garcia EV, Beanlands RS, Cerqueira M, Soman P, Berman DS, Cuocolo A, Einstein AJ, Morgan CJ, Hage FG, Schelbert HR, Bax JJ, Wu JC, Shaw LJ, Sadeghi MM, Tamaki N, Kaufmann PA, Gropler R, Dorbala S, Van Decker W. Myocardial perfusion imaging: lessons learned and work to be done-update. J Nucl Cardiol. 2018;25:39–52.
27. Al Jammaz I, Al-Otaibi B, Al Hindas H, Okarvi SM. Novel synthesis and initial preclinical evaluation of (18)F-[FDG] labeled rhodamine: a potential PET myocardial perfusion imaging agent. Nucl Med Biol. 2015;42:804–8.
28. Bartholoma MD, Zhang S, Akurathi V, Pacak CA, Dunning P, Fahey FH, Cowan DB, Treves ST, Packard AB. (18)F-labeled rhodamines as potential myocardial perfusion agents: comparison of pharmacokinetic properties of several rhodamines. Nucl Med Biol. 2015;42:796–803.
29. Thorn S, Huang Y, Labaree D, Nabulsi N, Emery P, Felchner Z, Lee S, Avendano R, Hawley C, Mamarian M, Treves T, Inkster J, Packard A, Sinusas AJ. Evaluation of myocardial extraction fraction with variable pharmacological vasodilation for a novel pet myocardial perfusion tracer, 18F-Rho6G. In: Paper presented at ASNC2019, Chicago, IL, USA; 2019.
30. Mou T, Zhang X. Research progress on (18)F-labeled agents for imaging of myocardial perfusion with positron emission tomography. Molecules. 2017;22:562.
31. Kim DY, Kim HS, Reder S, Zheng JH, Herz M, Higuchi T, Pyo AY, Bom HS, Schwaiger M, Min JJ. Comparison of 18F-labeled fluoroalkylphosphonium cations with 13N-NH3 for PET myocardial perfusion imaging. J Nucl Med. 2015;56:1581–6.
32. Madar I, Ravert H, Dipaula A, Du Y, Dannals RF, Becker L. Assessment of severity of coronary artery stenosis in a canine model using the PET agent 18F-fluorobenzyl triphenyl phosphonium: comparison with 99mTc-tetrofosmin. J Nucl Med. 2007;48:1021–30.
33. Herrero P, Hartman JJ, Green MA, Anderson CJ, Welch MJ, Markham J, Bergmann SR. Regional myocardial perfusion assessed with generator-produced copper-62-PTSM and PET. J Nucl Med. 1996;37:1294–300.
34. Hansson GK. Inflammation, atherosclerosis, and coronary artery disease. N Engl J Med. 2005;352:1685–95.
35. Thackeray JT, Bengel FM. Molecular imaging of myocardial inflammation with positron emission tomography post-ischemia: a determinant of subsequent remodeling or recovery. JACC Cardiovasc Imaging. 2018;11:1340–55.
36. Peters AM, Danpure HJ, Osman S, Hawker RJ, Henderson BL, Hodgson HJ, Kelly JD, Neirinckx RD, Lavender JP. Clinical experience with 99mTc-hexamethylpropyleneamineoxime for labelling leucocytes and imaging inflammation. Lancet. 1986;2: 946–9.

37. Peters AM, Saverymuttu SH. The value of indium-labelled leucocytes in clinical practice. Blood Rev. 1987;1:65–76.
38. Nahrendorf M, Swirski FK, Aikawa E, Stangenberg L, Wurdinger T, Figueiredo JL, Libby P, Weissleder R, Pittet MJ. The healing myocardium sequentially mobilizes two monocyte subsets with divergent and complementary functions. J Exp Med. 2007;204:3037–47.
39. Kraitchman DL, Tatsumi M, Gilson WD, Ishimori T, Kedziorek D, Walczak P, Segars WP, Chen HH, Fritzges D, Izbudak I, Young RG, Marcelino M, Pittenger MF, Solaiyappan M, Boston RC, Tsui BM, Wahl RL, Bulte JW. Dynamic imaging of allogeneic mesenchymal stem cells trafficking to myocardial infarction. Circulation. 2005;112:1451–61.
40. Elmadbouh I, Ashraf M. Tadalafil, a long acting phosphodiesterase inhibitor, promotes bone marrow stem cell survival and their homing into ischemic myocardium for cardiac repair. Physiol Rep. 2017;5:e13480.
41. Swirski FK, Libby P, Aikawa E, Alcaide P, Luscinskas FW, Weissleder R, Pittet MJ. Ly-6Chi monocytes dominate hypercholesterolemia-associated monocytosis and give rise to macrophages in atheromata. J Clin Invest. 2007;117:195–205.
42. Caobelli F, Wollenweber T, Bavendiek U, Kuhn C, Schutze C, Geworski L, Thackeray JT, Bauersachs J, Haverich A, Bengel FM. Simultaneous dual-isotope solid-state detector SPECT for improved tracking of white blood cells in suspected endocarditis. Eur Heart J. 2017;38:436–43.
43. Welling MM, Bunschoten A, Kuil J, Nelissen RG, Beekman FJ, Buckle T, van Leeuwen FW. Development of a hybrid tracer for SPECT and optical imaging of bacterial infections. Bioconjug Chem. 2015;26:839–49.
44. Sato M, Toyozaki T, Odaka K, Uehara T, Arano Y, Hasegawa H, Yoshida K, Imanaka-Yoshida K, Yoshida T, Hiroe M, Tadokoro H, Irie T, Tanada S, Komuro I. Detection of experimental autoimmune myocarditis in rats by 111In monoclonal antibody specific for tenascin-C. Circulation. 2002;106:1397–402.
45. Taki J, Inaki A, Wakabayashi H, Imanaka-Yoshida K, Ogawa K, Hiroe M, Shiba K, Yoshida T, Kinuya S. Dynamic expression of tenascin-C after myocardial ischemia and reperfusion: assessment by 125I-anti-tenascin-C antibody imaging. J Nucl Med. 2010;51:1116–22.
46. Odaka K, Uehara T, Arano Y, Adachi S, Tadokoro H, Yoshida K, Hasegawa H, Imanaka-Yoshida K, Yoshida T, Hiroe M, Irie T, Tanada S, Komuro I. Noninvasive detection of cardiac repair after acute myocardial infarction in rats by 111 In Fab fragment of monoclonal antibody specific for tenascin-C. Int Heart J. 2008;49:481–92.
47. Yokomizo T, Izumi T, Shimizu T. Leukotriene B4: metabolism and signal transduction. Arch Biochem Biophys. 2001;385:231–41.
48. Riou LM, Ruiz M, Sullivan GW, Linden J, Leong-Poi H, Lindner JR, Harris TD, Beller GA, Glover DK. Assessment of myocardial inflammation produced by experimental coronary occlusion and reperfusion with 99mTc-RP517, a new leukotriene B4 receptor antagonist that preferentially labels neutrophils in vivo. Circulation. 2002;106:592–8.
49. Satomi T, Ogawa M, Mori I, Ishino S, Kubo K, Magata Y, Nishimoto T. Comparison of contrast agents for atherosclerosis imaging using cultured macrophages: FDG versus ultrasmall superparamagnetic iron oxide. J Nucl Med. 2013;54:999–1004.
50. Lee WW, Marinelli B, van der Laan AM, Sena BF, Gorbatov R, Leuschner F, Dutta P, Iwamoto Y, Ueno T, Begieneman MP, Niessen HW, Piek JJ, Vinegoni C, Pittet MJ, Swirski FK, Tawakol A, Di Carli M, Weissleder R, Nahrendorf M. PET/MRI of inflammation in myocardial infarction. J Am Coll Cardiol. 2012;59:153–63.
51. Rischpler C, Dirschinger RJ, Nekolla SG, Kossmann H, Nicolosi S, Hanus F, van Marwick S, Kunze KP, Meinicke A, Gotze K, Kastrati A, Langwieser N, Ibrahim T, Nahrendorf M, Schwaiger M, Laugwitz KL. Prospective evaluation of 18F-fluorodeoxyglucose uptake in postischemic myocardium by simultaneous positron emission tomography/magnetic resonance imaging as a prognostic marker of functional outcome. Circ Cardiovasc Imaging. 2016;9:e004316.
52. Osborne MT, Hulten EA, Murthy VL, Skali H, Taqueti VR, Dorbala S, DiCarli MF, Blankstein R. Patient preparation for cardiac fluorine-18 fluorodeoxyglucose positron emission tomography imaging of inflammation. J Nucl Cardiol. 2017;24:86–99.

53. Wollenweber T, Roentgen P, Schafer A, Schatka I, Zwadlo C, Brunkhorst T, Berding G, Bauersachs J, Bengel FM. Characterizing the inflammatory tissue response to acute myocardial infarction by clinical multimodality noninvasive imaging. Circ Cardiovasc Imaging. 2014;7:811–8.
54. Prato FS, Butler J, Sykes J, Keenliside L, Blackwood KJ, Thompson RT, White JA, Mikami Y, Thiessen JD, Wisenberg G. Can the inflammatory response be evaluated using 18F-FDG within zones of microvascular obstruction after myocardial infarction? J Nucl Med. 2015;56:299–304.
55. Thackeray JT, Bankstahl JP, Wang Y, Wollert KC, Bengel FM. Targeting amino acid metabolism for molecular imaging of inflammation early after myocardial infarction. Theranostics. 2016;6:1768–79.
56. Morooka M, Kubota K, Kadowaki H, Ito K, Okazaki O, Kashida M, Mitsumoto T, Iwata R, Ohtomo K, Hiroe M. 11C-methionine PET of acute myocardial infarction. J Nucl Med. 2009;50:1283–7.
57. Taki J, Wakabayashi H, Inaki A, Imanaka-Yoshida K, Hiroe M, Ogawa K, Morooka M, Kubota K, Shiba K, Yoshida T, Kinuya S. 14C-Methionine uptake as a potential marker of inflammatory processes after myocardial ischemia and reperfusion. J Nucl Med. 2013;54:431–6.
58. Thackeray JT, Hupe HC, Wang Y, Bankstahl JP, Berding G, Ross TL, Bauersachs J, Wollert KC, Bengel FM. Myocardial inflammation predicts remodeling and neuroinflammation after myocardial infarction. J Am Coll Cardiol. 2018;71:263–75.
59. Herrmann K, Lapa C, Wester HJ, Schottelius M, Schiepers C, Eberlein U, Bluemel C, Keller U, Knop S, Kropf S, Schirbel A, Buck AK, Lassmann M. Biodistribution and radiation dosimetry for the chemokine receptor CXCR4-targeting probe 68Ga-pentixafor. J Nucl Med. 2015;56:410–6.
60. Thackeray JT, Derlin T, Haghikia A, Napp LC, Wang Y, Ross TL, Schafer A, Tillmanns J, Wester HJ, Wollert KC, Bauersachs J, Bengel FM. Molecular imaging of the chemokine receptor CXCR4 after acute myocardial infarction. JACC Cardiovasc Imaging. 2015;8:1417–26.
61. Heo GS, Kopecky B, Sultan D, Ou M, Feng G, Bajpai G, Zhang X, Luehmann H, Detering L, Su Y, Leuschner F, Combadiere C, Kreisel D, Gropler RJ, Brody SL, Liu Y, Lavine KJ. Molecular imaging visualizes recruitment of inflammatory monocytes and macrophages to the injured heart. Circ Res. 2019;124:881–90.
62. Li W, Luehmann HP, Hsiao HM, Tanaka S, Higashikubo R, Gauthier JM, Sultan D, Lavine KJ, Brody SL, Gelman AE, Gropler RJ, Liu Y, Kreisel D. Visualization of monocytic cells in regressing atherosclerotic plaques by intravital 2-photon and positron emission tomography-based imaging-brief report. Arterioscler Thromb Vasc Biol. 2018;38:1030–6.
63. Hotchkiss RS, Strasser A, McDunn JE, Swanson PE. Cell death. N Engl J Med. 2009;361:1570–83.
64. Blankenberg FG, Katsikis PD, Tait JF, Davis RE, Naumovski L, Ohtsuki K, Kopiwoda S, Abrams MJ, Darkes M, Robbins RC, Maecker HT, Strauss HW. In vivo detection and imaging of phosphatidylserine expression during programmed cell death. Proc Natl Acad Sci U S A. 1998;95:6349–54.
65. Shekhar A, Heeger P, Reutelingsperger C, Arbustini E, Narula N, Hofstra L, Bax JJ, Narula J. Targeted imaging for cell death in cardiovascular disorders. JACC Cardiovasc Imaging. 2018;11:476–93.
66. Kenis H, Zandbergen HR, Hofstra L, Petrov AD, Dumont EA, Blankenberg FD, Haider N, Bitsch N, Gijbels M, Verjans JW, Narula N, Narula J, Reutelingsperger CP. Annexin A5 uptake in ischemic myocardium: demonstration of reversible phosphatidylserine externalization and feasibility of radionuclide imaging. J Nucl Med. 2010;51:259–67.
67. Sarda-Mantel L, Michel JB, Rouzet F, Martet G, Louedec L, Vanderheyden JL, Hervatin F, Raguin O, Vrigneaud JM, Khaw BA, Le Guludec D. (99m)Tc-annexin V and (111) In-antimyosin antibody uptake in experimental myocardial infarction in rats. Eur J Nucl Med Mol Imaging. 2006;33:239–45.

68. Davidson BP, Chadderdon SM, Belcik JT, Gupta S, Lindner JR. Ischemic memory imaging in nonhuman primates with echocardiographic molecular imaging of selectin expression. J Am Soc Echocardiogr. 2014;27:786–793.e2.
69. Tanimoto T, Parseghian MH, Nakahara T, Kawai H, Narula N, Kim D, Nishimura R, Weisbart RH, Chan G, Richieri RA, Haider N, Chaudhry F, Reynolds GT, Billimek J, Blankenberg FG, Sengupta PP, Petrov AD, Akasaka T, Strauss HW, Narula J. Cardioprotective effects of HSP72 administration on ischemia-reperfusion injury. J Am Coll Cardiol. 2017;70:1479–92.
70. Dumont EA, Hofstra L, van Heerde WL, van den Eijnde S, Doevendans PA, DeMuinck E, Daemen MA, Smits JF, Frederik P, Wellens HJ, Daemen MJ, Reutelingsperger CP. Cardiomyocyte death induced by myocardial ischemia and reperfusion: measurement with recombinant human annexin-V in a mouse model. Circulation. 2000;102:1564–8.
71. Narula J, Acio ER, Narula N, Samuels LE, Fyfe B, Wood D, Fitzpatrick JM, Raghunath PN, Tomaszewski JE, Kelly C, Steinmetz N, Green A, Tait JF, Leppo J, Blankenberg FG, Jain D, Strauss HW. Annexin-V imaging for noninvasive detection of cardiac allograft rejection. Nat Med. 2001;7:1347–52.
72. Hofstra L, Liem IH, Dumont EA, Boersma HH, van Heerde WL, Doevendans PA, De Muinck E, Wellens HJ, Kemerink GJ, Reutelingsperger CP, Heidendal GA. Visualisation of cell death in vivo in patients with acute myocardial infarction. Lancet. 2000;356:209–12.
73. Maulik N, Kagan VE, Tyurin VA, Das DK. Redistribution of phosphatidylethanolamine and phosphatidylserine precedes reperfusion-induced apoptosis. Am J Phys. 1998;274:H242–8.
74. Wang L, Wang F, Fang W, Johnson SE, Audi S, Zimmer M, Holly TA, Lee DC, Zhu B, Zhu H, Zhao M. The feasibility of imaging myocardial ischemic/reperfusion injury using (99m) Tc-labeled duramycin in a porcine model. Nucl Med Biol. 2015;42:198–204.
75. Kawai H, Chaudhry F, Shekhar A, Petrov A, Nakahara T, Tanimoto T, Kim D, Chen J, Lebeche D, Blankenberg FG, Pak KY, Kolodgie FD, Virmani R, Sengupta P, Narula N, Hajjar RJ, Strauss HW, Narula J. Molecular imaging of apoptosis in ischemia reperfusion injury with radiolabeled duramycin targeting phosphatidylethanolamine: effective target uptake and reduced nontarget organ radiation burden. JACC Cardiovasc Imaging. 2018;11:1823–33.
76. Krysko O, De Ridder L, Cornelissen M. Phosphatidylserine exposure during early primary necrosis (oncosis) in JB6 cells as evidenced by immunogold labeling technique. Apoptosis. 2004;9:495–500.
77. Slee EA, Adrain C, Martin SJ. Executioner caspase-3, -6, and -7 perform distinct, non-redundant roles during the demolition phase of apoptosis. J Biol Chem. 2001;276:7320–6.
78. Lee D, Long SA, Adams JL, Chan G, Vaidya KS, Francis TA, Kikly K, Winkler JD, Sung CM, Debouck C, Richardson S, Levy MA, DeWolf WE Jr, Keller PM, Tomaszek T, Head MS, Ryan MD, Haltiwanger RC, Liang PH, Janson CA, McDevitt PJ, Johanson K, Concha NO, Chan W, Abdel-Meguid SS, Badger AM, Lark MW, Nadeau DP, Suva LJ, Gowen M, Nuttall ME. Potent and selective nonpeptide inhibitors of caspases 3 and 7 inhibit apoptosis and maintain cell functionality. J Biol Chem. 2000;275:16007–14.
79. Thukkani AK, Shoghi KI, Zhou D, Xu J, Chu W, Novak E, Chen DL, Gropler RJ, Mach RH. PET imaging of in vivo caspase-3/7 activity following myocardial ischemia-reperfusion injury with the radiolabeled isatin sulfonamide analogue [(18)F]WC-4-116. Am J Nucl Med Mol Imaging. 2016;6:110–9.
80. Zhou D, Chu W, Rothfuss J, Zeng C, Xu J, Jones L, Welch MJ, Mach RH. Synthesis, radiolabeling, and in vivo evaluation of an 18F-labeled isatin analog for imaging caspase-3 activation in apoptosis. Bioorg Med Chem Lett. 2006;16:5041–6.
81. Challapalli A, Kenny LM, Hallett WA, Kozlowski K, Tomasi G, Gudi M, Al-Nahhas A, Coombes RC, Aboagye EO. 18F-ICMT-11, a caspase-3-specific PET tracer for apoptosis: biodistribution and radiation dosimetry. J Nucl Med. 2013;54:1551–6.
82. Khaw BA, Narula J. Non-invasive detection of myocyte necrosis in myocarditis and dilated cardiomyopathy with radiolabelled antimyosin. Eur Heart J. 1995;16(Suppl O):119–23.
83. Matsumori A, Yamada T, Tamaki N, Kawai C, Watanabe Y, Yonekura Y, Endo K, Konishi J, Yoshida A, Tamaki S. Persistent uptake of indium-111-antimyosin monoclonal antibody in patients with myocardial infarction. Am Heart J. 1990;120:1026–30.

84. Narula J, Southern JF, Dec GW, Palacios IF, Newell JB, Fallon JT, Strauss HW, Khaw BA, Yasuda T. Antimyosin uptake and myofibrillarlysis in dilated cardiomyopathy. J Nucl Cardiol. 1995;2:470–7.
85. Frist W, Yasuda T, Segall G, Khaw BA, Strauss HW, Gold H, Stinson E, Oyer P, Baldwin J, Billingham M, et al. Noninvasive detection of human cardiac transplant rejection with indium-111 antimyosin (Fab) imaging. Circulation. 1987;76:V81–5.
86. Weissleder R, Lee AS, Khaw BA, Shen T, Brady TJ. Antimyosin-labeled monocrystalline iron oxide allows detection of myocardial infarct: MR antibody imaging. Radiology. 1992;182:381–5.
87. Tamaki N, Yamada T, Matsumori A, Yoshida A, Fujita T, Ohtani H, Watanabe Y, Yonekura Y, Endo K, Konishi J, et al. Indium-111-antimyosin antibody imaging for detecting different stages of myocardial infarction: comparison with technetium-99m-pyrophosphate imaging. J Nucl Med. 1990;31:136–42.
88. Flotats A, Carrio I. Non-invasive in vivo imaging of myocardial apoptosis and necrosis. Eur J Nucl Med Mol Imaging. 2003;30:615–30.
89. Hesse B, Mortensen SA, Folke M, Brodersen AK, Aldershvile J, Pettersson G. Ability of antimyosin scintigraphy monitoring to exclude acute rejection during the first year after heart transplantation. J Heart Lung Transplant. 1995;14:23–31.
90. Bonte FJ, Parkey RW, Graham KD, Moore J, Stokely EM. A new method for radionuclide imaging of myocardial infarcts. Radiology. 1974;110:473–4.
91. Corbett JR, Lewis M, Willerson JT, Nicod PH, Huxley RL, Simon T, Rude RE, Henderson E, Parkey R, Rellas JS, et al. 99mTc-pyrophosphate imaging in patients with acute myocardial infarction: comparison of planar imaging with single-photon tomography with and without blood pool overlay. Circulation. 1984;69:1120–8.
92. Yamamoto Y, Onoguchi M, Haramoto M, Kodani N, Komatsu A, Kitagaki H, Tanabe K. Novel method for quantitative evaluation of cardiac amyloidosis using (201)TlCl and (99m)Tc-PYP SPECT. Ann Nucl Med. 2012;26:634–43.
93. Bokhari S, Castano A, Pozniakoff T, Deslisle S, Latif F, Maurer MS. Tc-99m-pyrophosphate scintigraphy for differentiating light-chain cardiac amyloidosis from the transthyretin-related familial and senile cardiac amyloidoses. Circ Cardiovasc Imaging. 2013;6:195–201.
94. Castano A, Haq M, Narotsky DL, Goldsmith J, Weinberg RL, Morgenstern R, Pozniakoff T, Ruberg FL, Miller EJ, Berk JL, Dispenzieri A, Grogan M, Johnson G, Bokhari S, Maurer MS. Multicenter study of planar technetium 99m pyrophosphate cardiac imaging: predicting survival for patients with ATTR cardiac amyloidosis. JAMA Cardiol. 2016;1:880–9.
95. Castano A, DeLuca A, Weinberg R, Pozniakoff T, Blaner WS, Pirmohamed A, Bettencourt B, Gollob J, Karsten V, Vest JA, Chiuzan C, Maurer MS, Bokhari S. Serial scanning with technetium pyrophosphate ((99m)Tc-PYP) in advanced ATTR cardiac amyloidosis. J Nucl Cardiol. 2016;23:1355–63.
96. Orlandi C, Crane PD, Edwards DS, Platts SH, Bernard L, Lazewatsky J, Thoolen MJ. Early scintigraphic detection of experimental myocardial infarction in dogs with technetium-99m-glucaric acid. J Nucl Med. 1991;32:263–8.
97. Narula J, Petrov A, Pak KY, Lister BC, Khaw BA. Very early noninvasive detection of acute experimental nonreperfused myocardial infarction with 99mTc-labeled glucarate. Circulation. 1997;95:1577–84.
98. Mariani G, Villa G, Rossettin PF, Spallarossa P, Bezante GP, Brunelli C, Pak KY, Khaw BA, Strauss HW. Detection of acute myocardial infarction by 99mTc-labeled D-glucaric acid imaging in patients with acute chest pain. J Nucl Med. 1999;40:1832–9.
99. Floras JS. Sympathetic activation in human heart failure: diverse mechanisms, therapeutic opportunities. Acta Physiol Scand. 2003;177:391–8.
100. Barron HV, Lesh MD. Autonomic nervous system and sudden cardiac death. J Am Coll Cardiol. 1996;27:1053–60.
101. La Rovere MT, Bigger JT Jr, Marcus FI, Mortara A, Schwartz PJ. Baroreflex sensitivity and heart-rate variability in prediction of total cardiac mortality after myocardial infarction. ATRAMI (Autonomic Tone and Reflexes After Myocardial Infarction) Investigators. Lancet. 1998;351:478–84.

102. Nolan J, Batin PD, Andrews R, Lindsay SJ, Brooksby P, Mullen M, Baig W, Flapan AD, Cowley A, Prescott RJ, Neilson JM, Fox KA. Prospective study of heart rate variability and mortality in chronic heart failure: results of the United Kingdom heart failure evaluation and assessment of risk trial (UK-heart). Circulation. 1998;98:1510–6.
103. Shen MJ, Zipes DP. Role of the autonomic nervous system in modulating cardiac arrhythmias. Circ Res. 2014;114:1004–21.
104. Malpas SC. Sympathetic nervous system overactivity and its role in the development of cardiovascular disease. Physiol Rev. 2010;90:513–57.
105. Olshansky B, Sabbah HN, Hauptman PJ, Colucci WS. Parasympathetic nervous system and heart failure: pathophysiology and potential implications for therapy. Circulation. 2008;118:863–71.
106. Hall JE, Guyton AC. Guyton and Hall textbook of medical physiology. Philadelphia, PA: Saunders Elsevier; 2015. p. 748–60.
107. Henneman MM, Bengel FM, van der Wall EE, Knuuti J, Bax JJ. Cardiac neuronal imaging: application in the evaluation of cardiac disease. J Nucl Cardiol. 2008;15:442–55.
108. Travin MI, Feng D, Taub CC. Novel imaging approaches for predicting arrhythmic risk. Circ Cardiovasc Imaging. 2015;8:e003019.
109. Jacobson AF, Senior R, Cerqueira MD, Wong ND, Thomas GS, Lopez VA, Agostini D, Weiland F, Chandna H, Narula J, Investigators A-H. Myocardial iodine-123 meta-iodobenzylguanidine imaging and cardiac events in heart failure. Results of the prospective ADMIRE-HF (AdreView Myocardial Imaging for Risk Evaluation in Heart Failure) study. J Am Coll Cardiol. 2010;55:2212–21.
110. Dae MW, O'Connell JW, Botvinick EH, Ahearn T, Yee E, Huberty JP, Mori H, Chin MC, Hattner RS, Herre JM, et al. Scintigraphic assessment of regional cardiac adrenergic innervation. Circulation. 1989;79:634–44.
111. Henderson EB, Kahn JK, Corbett JR, Jansen DE, Pippin JJ, Kulkarni P, Ugolini V, Akers MS, Hansen C, Buja LM, et al. Abnormal I-123 metaiodobenzylguanidine myocardial washout and distribution may reflect myocardial adrenergic derangement in patients with congestive cardiomyopathy. Circulation. 1988;78:1192–9.
112. Alvi R, Miller EJ, Zonouz TH, Sandoval V, Tariq N, Lampert R, Sinusas AJ, Liu YH. Quantification and determination of normal (123)I-meta iodobenzylguanidine heart-to-mediastinum ratio (HMR) from cardiac SPECT/CT and correlation with planar HMR. J Nucl Med. 2018;59:652–8.
113. Wu J, Lin SF, Gallezot JD, Chan C, Prasad R, Thorn SL, Stacy MR, Huang Y, Zonouz TH, Liu YH, Lampert RJ, Carson RE, Sinusas AJ, Liu C. Quantitative analysis of dynamic 123I-mIBG SPECT imaging data in healthy humans with a population-based metabolite correction method. J Nucl Med. 2016;57:1226–32.
114. Arimoto T, Takeishi Y, Fukui A, Tachibana H, Nozaki N, Hirono O, Yamaguchi H, Itoh M, Miyamoto T, Takahashi H, Okada A, Takahashi K, Kubota I. Dynamic 123I-MIBG SPECT reflects sympathetic nervous integrity and predicts clinical outcome in patients with chronic heart failure. Ann Nucl Med. 2004;18:145–50.
115. van der Veen BJ, Al Younis I, de Roos A, Stokkel MP. Assessment of global cardiac I-123 MIBG uptake and washout using volumetric quantification of SPECT acquisitions. J Nucl Cardiol. 2012;19:752–62.
116. Wu J, Liu H, Hashemi Zonouz T, Sandoval VM, Mohy-Ud-Din H, Lampert RJ, Sinusas AJ, Liu C, Liu YH. A blind deconvolution method incorporated with anatomical-based filtering for partial volume correction: validations with (123) I-mIBG cardiac SPECT/CT. Med Phys. 2017;44:6435–46.
117. Travin MI. Clinical applications of myocardial innervation imaging. Cardiol Clin. 2016;34:133–47.
118. Raffel DM, Chen W, Jung YW, Jang KS, Gu G, Cozzi NV. Radiotracers for cardiac sympathetic innervation: transport kinetics and binding affinities for the human norepinephrine transporter. Nucl Med Biol. 2013;40:331–7.

119. Munch G, Nguyen NT, Nekolla S, Ziegler S, Muzik O, Chakraborty P, Wieland DM, Schwaiger M. Evaluation of sympathetic nerve terminals with [(11)C]epinephrine and [(11)C]hydroxyephedrine and positron emission tomography. Circulation. 2000;101: 516–23.
120. Tipre DN, Fox JJ, Holt DP, Green G, Yu J, Pomper M, Dannals RF, Bengel FM. In vivo PET imaging of cardiac presynaptic sympathoneuronal mechanisms in the rat. J Nucl Med. 2008;49:1189–95.
121. Yu M, Bozek J, Lamoy M, Guaraldi M, Silva P, Kagan M, Yalamanchili P, Onthank D, Mistry M, Lazewatsky J, Broekema M, Radeke H, Purohit A, Cdebaca M, Azure M, Cesati R, Casebier D, Robinson SP. Evaluation of LMI1195, a novel 18F-labeled cardiac neuronal PET imaging agent, in cells and animal models. Circ Cardiovasc Imaging. 2011;4: 435–43.
122. Sinusas AJ, Lazewatsky J, Brunetti J, Heller G, Srivastava A, Liu YH, Sparks R, Puretskiy A, Lin SF, Crane P, Carson RE, Lee LV. Biodistribution and radiation dosimetry of LMI1195: first-in-human study of a novel 18F-labeled tracer for imaging myocardial innervation. J Nucl Med. 2014;55:1445–51.
123. Del Rosario RB, Jung YW, Caraher J, Chakraborty PK, Wieland DM. Synthesis and preliminary evaluation of [11C]-(-)-phenylephrine as a functional heart neuronal PET agent. Nucl Med Biol. 1996;23:611–6.
124. Nishijima K, Kuge Y, Seki K, Ohkura K, Morita K, Nakada K, Tamaki N. Preparation and pharmaceutical evaluation for clinical application of high specific activity S-(-)[11C]CGP-12177, a radioligand for beta-adrenoreceptors. Nucl Med Commun. 2004;25:845–9.
125. Delforge J, Syrota A, Lancon JP, Nakajima K, Loc'h C, Janier M, Vallois JM, Cayla J, Crouzel C. Cardiac beta-adrenergic receptor density measured in vivo using PET, CGP 12177, and a new graphical method. J Nucl Med. 1991;32:739–48.
126. Law MP, Osman S, Pike VW, Davenport RJ, Cunningham VJ, Rimoldi O, Rhodes CG, Giardina D, Camici PG. Evaluation of [11C]GB67, a novel radioligand for imaging myocardial alpha 1-adrenoceptors with positron emission tomography. Eur J Nucl Med. 2000;27:7–17.
127. Awad M, Czer LS, Hou M, Golshani SS, Goltche M, De Robertis M, Kittleson M, Patel J, Azarbal B, Kransdorf E, Esmailian F, Trento A, Kobashigawa JA. Early denervation and later reinnervation of the heart following cardiac transplantation: a review. J Am Heart Assoc. 2016;5:e004070.
128. Bengel FM, Ueberfuhr P, Hesse T, Schiepel N, Ziegler SI, Scholz S, Nekolla SG, Reichart B, Schwaiger M. Clinical determinants of ventricular sympathetic reinnervation after orthotopic heart transplantation. Circulation. 2002;106:831–5.
129. Fallavollita JA, Heavey BM, Luisi AJ Jr, Michalek SM, Baldwa S, Mashtare TL Jr, Hutson AD, Dekemp RA, Haka MS, Sajjad M, Cimato TR, Curtis AB, Cain ME, Canty JM Jr. Regional myocardial sympathetic denervation predicts the risk of sudden cardiac arrest in ischemic cardiomyopathy. J Am Coll Cardiol. 2014;63:141–9.
130. Nagamachi S, Fujita S, Nishii R, Futami S, Tamura S, Mizuta M, Nakazato M, Kurose T, Wakamatsu H. Prognostic value of cardiac I-123 metaiodobenzylguanidine imaging in patients with non-insulin-dependent diabetes mellitus. J Nucl Cardiol. 2006;13:34–42.
131. Stevens MJ, Raffel DM, Allman KC, Schwaiger M, Wieland DM. Regression and progression of cardiac sympathetic dysinnervation complicating diabetes: an assessment by C-11 hydroxyephedrine and positron emission tomography. Metabolism. 1999;48:92–101.
132. Po SS, Nakagawa H, Jackman WM. Localization of left atrial ganglionated plexi in patients with atrial fibrillation. J Cardiovasc Electrophysiol. 2009;20:1186–9.
133. Pokushalov E, Romanov A, Artyomenko S, Turov A, Shirokova N, Katritsis DG. Left atrial ablation at the anatomic areas of ganglionated plexi for paroxysmal atrial fibrillation. Pacing Clin Electrophysiol. 2010;33:1231–8.
134. Kurotobi T, Shimada Y, Kino N, Ito K, Tonomura D, Yano K, Tanaka C, Yoshida M, Tsuchida T, Fukumoto H. Features of intrinsic ganglionated plexi in both atria after extensive pulmonary isolation and their clinical significance after catheter ablation in patients with atrial fibrillation. Heart Rhythm. 2015;12:470–6.

135. Pauza DH, Skripka V, Pauziene N, Stropus R. Morphology, distribution, and variability of the epicardiac neural ganglionated subplexuses in the human heart. Anat Rec. 2000;259:353–82.
136. Stirrup J, Gregg S, Baavour R, Roth N, Breault C, Agostini D, Ernst S, Underwood SR. Hybrid solid-state SPECT/CT left atrial innervation imaging for identification of left atrial ganglionated plexi: technique and validation in patients with atrial fibrillation. J Nucl Cardiol. 2020;27:1939.
137. Gjerloff T, Fedorova T, Knudsen K, Munk OL, Nahimi A, Jacobsen S, Danielsen EH, Terkelsen AJ, Hansen J, Pavese N, Brooks DJ, Borghammer P. Imaging acetylcholinesterase density in peripheral organs in Parkinson's disease with 11C-donepezil PET. Brain. 2015;138:653–63.
138. Delforge J, Janier M, Syrota A, Crouzel C, Vallois JM, Cayla J, Lancon JP, Mazoyer BM. Noninvasive quantification of muscarinic receptors in vivo with positron emission tomography in the dog heart. Circulation. 1990;82:1494–504.
139. Le Guludec D, Delforge J, Syrota A, Desruennes M, Valette H, Gandjbakhch I, Merlet P. In vivo quantification of myocardial muscarinic receptors in heart transplant patients. Circulation. 1994;90:172–8.
140. Bucerius J, Manka C, Schmaljohann J, Mani V, Gundisch D, Rudd JH, Bippus R, Mottaghy FM, Wullner U, Fayad ZA, Biersack HJ. Feasibility of [18F]-2-Fluoro-A85380-PET imaging of human vascular nicotinic acetylcholine receptors in vivo. JACC Cardiovasc Imaging. 2012;5:528–36.
141. Simons M, Alitalo K, Annex BH, Augustin HG, Beam C, Berk BC, Byzova T, Carmeliet P, Chilian W, Cooke JP, Davis GE, Eichmann A, Iruela-Arispe ML, Keshet E, Sinusas AJ, Ruhrberg C, Woo YJ, Dimmeler S, American Heart Association Council on Basic Cardiovascular S, Council on Cardiovascular S and Anesthesia. State-of-the-art methods for evaluation of angiogenesis and tissue vascularization: a scientific statement from the American Heart Association. Circ Res. 2015;116:e99–132.
142. Nahrendorf M, Sosnovik DE, French BA, Swirski FK, Bengel F, Sadeghi MM, Lindner JR, Wu JC, Kraitchman DL, Fayad ZA, Sinusas AJ. Multimodality cardiovascular molecular imaging, Part II. Circ Cardiovasc Imaging. 2009;2:56–70.
143. Hendrikx G, Voo S, Bauwens M, Post MJ, Mottaghy FM. SPECT and PET imaging of angiogenesis and arteriogenesis in pre-clinical models of myocardial ischemia and peripheral vascular disease. Eur J Nucl Med Mol Imaging. 2016;43:2433–47.
144. Dobrucki LW, de Muinck ED, Lindner JR, Sinusas AJ. Approaches to multimodality imaging of angiogenesis. J Nucl Med. 2010;51(Suppl 1):66S–79S.
145. Dijkgraaf I, Boerman OC. Radionuclide imaging of tumor angiogenesis. Cancer Biother Radiopharm. 2009;24:637–47.
146. Meoli DF, Sadeghi MM, Krassilnikova S, Bourke BN, Giordano FJ, Dione DP, Su H, Edwards DS, Liu S, Harris TD, Madri JA, Zaret BL, Sinusas AJ. Noninvasive imaging of myocardial angiogenesis following experimental myocardial infarction. J Clin Invest. 2004;113:1684–91.
147. Johnson LL, Schofield L, Donahay T, Bouchard M, Poppas A, Haubner R. Radiolabeled arginine-glycine-aspartic acid peptides to image angiogenesis in swine model of hibernating myocardium. JACC Cardiovasc Imaging. 2008;1:500–10.
148. Dimastromatteo J, Riou LM, Ahmadi M, Pons G, Pellegrini E, Broisat A, Sancey L, Gavrilina T, Boturyn D, Dumy P, Fagret D, Ghezzi C. In vivo molecular imaging of myocardial angiogenesis using the alpha(v)beta3 integrin-targeted tracer 99mTc-RAFT-RGD. J Nucl Cardiol. 2010;17:435–43.
149. Dobrucki LW, Tsutsumi Y, Kalinowski L, Dean J, Gavin M, Sen S, Mendizabal M, Sinusas AJ, Aikawa R. Analysis of angiogenesis induced by local IGF-1 expression after myocardial infarction using microSPECT-CT imaging. J Mol Cell Cardiol. 2010;48:1071–9.
150. Laitinen I, Notni J, Pohle K, Rudelius M, Farrell E, Nekolla SG. Comparison of cyclic RGD peptides for alpha(v)beta(3) integrin detection in a rat model of myocardial infarction. EJNMMI Res. 2013;3:38.
151. Higuchi T, Bengel FM, Seidl S, Watzlowik P, Kessler H, Hegenloh R, Reder S, Nekolla SG, Wester HJ, Schwaiger M. Assessment of alphavbeta3 integrin expression after myocardial infarction by positron emission tomography. Cardiovasc Res. 2008;78:395–403.

152. Sun Y, Zeng Y, Zhu Y, Feng F, Xu W, Wu C, Xing B, Zhang W, Wu P, Cui L, Wang R, Li F, Chen X, Zhu Z. Application of (68)Ga-PRGD2 PET/CT for alphavbeta3-integrin imaging of myocardial infarction and stroke. Theranostics. 2014;4:778–86.
153. Jenkins WS, Vesey AT, Stirrat C, Connell M, Lucatelli C, Neale A, Moles C, Vickers A, Fletcher A, Pawade T, Wilson I, Rudd JH, van Beek EJ, Mirsadraee S, Dweck MR, Newby DE. Cardiac alphaVbeta3 integrin expression following acute myocardial infarction in humans. Heart. 2017;103:607–15.
154. Mozid AM, Holstensson M, Choudhury T, Ben-Haim S, Allie R, Martin J, Sinusas AJ, Hutton BF, Mathur A. Clinical feasibility study to detect angiogenesis following bone marrow stem cell transplantation in chronic ischaemic heart failure. Nucl Med Commun. 2014;35:839–48.
155. Makowski MR, Ebersberger U, Nekolla S, Schwaiger M. In vivo molecular imaging of angiogenesis, targeting alphavbeta3 integrin expression, in a patient after acute myocardial infarction. Eur Heart J. 2008;29:2201.
156. Carmeliet P, Jain RK. Molecular mechanisms and clinical applications of angiogenesis. Nature. 2011;473:298–307.
157. Moens S, Goveia J, Stapor PC, Cantelmo AR, Carmeliet P. The multifaceted activity of VEGF in angiogenesis - implications for therapy responses. Cytokine Growth Factor Rev. 2014;25:473–82.
158. Lu E, Wagner WR, Schellenberger U, Abraham JA, Klibanov AL, Woulfe SR, Csikari MM, Fischer D, Schreiner GF, Brandenburger GH, Villanueva FS. Targeted in vivo labeling of receptors for vascular endothelial growth factor: approach to identification of ischemic tissue. Circulation. 2003;108:97–103.
159. Backer MV, Levashova Z, Patel V, Jehning BT, Claffey K, Blankenberg FG, Backer JM. Molecular imaging of VEGF receptors in angiogenic vasculature with single-chain VEGF-based probes. Nat Med. 2007;13:504–9.
160. Hendrikx G, De Saint-Hubert M, Dijkgraaf I, Bauwens M, Douma K, Wierts R, Pooters I, Van den Akker NM, Hackeng TM, Post MJ, Mottaghy FM. Molecular imaging of angiogenesis after myocardial infarction by (111)In-DTPA-cNGR and (99m)Tc-sestamibi dual-isotope myocardial SPECT. EJNMMI Res. 2015;5:2.
161. Orbay H, Zhang Y, Valdovinos HF, Song G, Hernandez R, Theuer CP. Positron emission tomography imaging of CD105 expression in a rat myocardial infarction model with (64) Cu-NOTA-TRC105. Am J Nucl Med Mol Imaging. 2013;4:1–9.
162. Tandri H, Saranathan M, Rodriguez ER, Martinez C, Bomma C, Nasir K, Rosen B, Lima JA, Calkins H, Bluemke DA. Noninvasive detection of myocardial fibrosis in arrhythmogenic right ventricular cardiomyopathy using delayed-enhancement magnetic resonance imaging. J Am Coll Cardiol. 2005;45:98–103.
163. French BA, Kramer CM. Mechanisms of post-infarct left ventricular remodeling. Drug Discov Today Dis Mech. 2007;4:185–96.
164. Borer JS, Truter S, Herrold EM, Falcone DJ, Pena M, Carter JN, Dumlao TF, Lee JA, Supino PG. Myocardial fibrosis in chronic aortic regurgitation: molecular and cellular responses to volume overload. Circulation. 2002;105:1837–42.
165. Frangogiannis NG. Targeting the inflammatory response in healing myocardial infarcts. Curr Med Chem. 2006;13:1877–93.
166. Montesi SB, Desogere P, Fuchs BC, Caravan P. Molecular imaging of fibrosis: recent advances and future directions. J Clin Invest. 2019;129:24–33.
167. Gormsen LC, Haraldsen A, Kramer S, Dias AH, Kim WY, Borghammer P. A dual tracer (68) Ga-DOTANOC PET/CT and (18)F-FDG PET/CT pilot study for detection of cardiac sarcoidosis. EJNMMI Res. 2016;6:52.
168. van den Borne SW, Isobe S, Zandbergen HR, Li P, Petrov A, Wong ND, Fujimoto S, Fujimoto A, Lovhaug D, Smits JF, Daemen MJ, Blankesteijn WM, Reutelingsperger C, Zannad F, Narula N, Vannan MA, Pitt B, Hofstra L, Narula J. Molecular imaging for efficacy of pharmacologic intervention in myocardial remodeling. JACC Cardiovasc Imaging. 2009;2:187–98.
169. Verjans J, Wolters S, Laufer W, Schellings M, Lax M, Lovhaug D, Boersma H, Kemerink G, Schalla S, Gordon P, Teule J, Narula J, Hofstra L. Early molecular imaging of interstitial

changes in patients after myocardial infarction: comparison with delayed contrast-enhanced magnetic resonance imaging. J Nucl Cardiol. 2010;17:1065–72.
170. John AE, Luckett JC, Tatler AL, Awais RO, Desai A, Habgood A, Ludbrook S, Blanchard AD, Perkins AC, Jenkins RG, Marshall JF. Preclinical SPECT/CT imaging of alphav-beta6 integrins for molecular stratification of idiopathic pulmonary fibrosis. J Nucl Med. 2013;54:2146–52.
171. Pereira RS, Prato FS, Wisenberg G, Sykes J, Yvorchuk KJ. The use of Gd-DTPA as a marker of myocardial viability in reperfused acute myocardial infarction. Int J Cardiovasc Imaging. 2001;17:395–404.
172. Perea RJ, Ortiz-Perez JT, Sole M, Cibeira MT, de Caralt TM, Prat-Gonzalez S, Bosch X, Berruezo A, Sanchez M, Blade J. T1 mapping: characterisation of myocardial interstitial space. Insights Imaging. 2015;6:189–202.
173. Kim H, Lee SJ, Davies-Venn C, Kim JS, Yang BY, Yao Z, Kim I, Paik CH, Bluemke DA. 64Cu-DOTA as a surrogate positron analog of Gd-DOTA for cardiac fibrosis detection with PET: pharmacokinetic study in a rat model of chronic MI. Nucl Med Commun. 2016;37:188–96.
174. Kim H, Lee SJ, Kim JS, Davies-Venn C, Cho HJ, Won SJ, Dejene E, Yao Z, Kim I, Paik CH, Bluemke DA. Pharmacokinetics and microbiodistribution of 64Cu-labeled collagen-binding peptides in chronic myocardial infarction. Nucl Med Commun. 2016;37:1306–17.
175. Muzard J, Sarda-Mantel L, Loyau S, Meulemans A, Louedec L, Bantsimba-Malanda C, Hervatin F, Marchal-Somme J, Michel JB, Le Guludec D, Billiald P, Jandrot-Perrus M. Non-invasive molecular imaging of fibrosis using a collagen-targeted peptidomimetic of the platelet collagen receptor glycoprotein VI. PLoS One. 2009;4:e5585.
176. Velikyan I, Rosenstrom U, Estrada S, Ljungvall I, Haggstrom J, Eriksson O, Antoni G. Synthesis and preclinical evaluation of 68Ga-labeled collagelin analogs for imaging and quantification of fibrosis. Nucl Med Biol. 2014;41:728–36.
177. Spinale FG. Myocardial matrix remodeling and the matrix metalloproteinases: influence on cardiac form and function. Physiol Rev. 2007;87:1285–342.
178. Spinale FG. Matrix metalloproteinases: regulation and dysregulation in the failing heart. Circ Res. 2002;90:520–30.
179. Su H, Spinale FG, Dobrucki LW, Song J, Hua J, Sweterlitsch S, Dione DP, Cavaliere P, Chow C, Bourke BN, Hu XY, Azure M, Yalamanchili P, Liu R, Cheesman EH, Robinson S, Edwards DS, Sinusas AJ. Noninvasive targeted imaging of matrix metalloproteinase activation in a murine model of postinfarction remodeling. Circulation. 2005;112:3157–67.
180. Sahul ZH, Mukherjee R, Song J, McAteer J, Stroud RE, Dione DP, Staib L, Papademetris X, Dobrucki LW, Duncan JS, Spinale FG, Sinusas AJ. Targeted imaging of the spatial and temporal variation of matrix metalloproteinase activity in a porcine model of postinfarct remodeling: relationship to myocardial dysfunction. Circ Cardiovasc Imaging. 2011;4:381–91.
181. Thorn SL, Barlow SC, Feher A, Stacy MR, Doviak H, Jacobs J, Zellars K, Renaud JM, Klein R, deKemp RA, Khakoo AY, Lee T, Spinale FG, Sinusas AJ. Application of hybrid matrix metalloproteinase-targeted and dynamic (201)Tl single-photon emission computed tomography/computed tomography imaging for evaluation of early post-myocardial infarction remodeling. Circ Cardiovasc Imaging. 2019;12:e009055.
182. Boutagy NE, Wu J, Cai Z, Zhang W, Booth CJ, Kyriakides TC, Pfau D, Mulnix T, Liu Z, Miller EJ, Young LH, Carson RE, Huang Y, Liu C, Sinusas AJ. In vivo reactive oxygen species detection with a novel positron emission tomography tracer, (18)F-DHMT, allows for early detection of anthracycline-induced cardiotoxicity in rodents. JACC Basic Transl Sci. 2018;3:378–90.
183. Sun Z, Ma N, Fan W, Guo L, Chen J, Zhu L, Tong G. Noninvasive monitoring of the development and treatment response of ischemic hindlimb by targeting matrix metalloproteinase-2 (MMP-2). Biomater Sci. 2019;7:4036–45.
184. Nguyen PK, Rhee JW, Wu JC. Adult stem cell therapy and heart failure, 2000 to 2016: a systematic review. JAMA Cardiol. 2016;1:831–41.

185. Mathur A, Fernandez-Aviles F, Dimmeler S, Hauskeller C, Janssens S, Menasche P, Wojakowski W, Martin JF, Zeiher A, Investigators B. The consensus of the Task Force of the European Society of Cardiology concerning the clinical investigation of the use of autologous adult stem cells for the treatment of acute myocardial infarction and heart failure: update 2016. Eur Heart J. 2017;38:2930–5.
186. Gabisonia K, Recchia FA. Gene therapy for heart failure: new perspectives. Curr Heart Fail Rep. 2018;15:340–9.
187. Yla-Herttuala S, Martin JF. Cardiovascular gene therapy. Lancet. 2000;355:213–22.
188. Ruggiero A, Thorek DL, Guenoun J, Krestin GP, Bernsen MR. Cell tracking in cardiac repair: what to image and how to image. Eur Radiol. 2012;22:189–204.
189. Kothari P, De BP, He B, Chen A, Chiuchiolo MJ, Kim D, Nikolopoulou A, Amor-Coarasa A, Dyke JP, Voss HU, Kaminsky SM, Foley CP, Vallabhajosula S, Hu B, DiMagno SG, Sondhi D, Crystal RG, Babich JW, Ballon D. Radioiodinated capsids facilitate in vivo non-invasive tracking of adeno-associated gene transfer vectors. Sci Rep. 2017;7:39594.
190. Boutagy NE, Ravera S, Papademetris X, Onofrey JA, Zhuang ZW, Wu J, Feher A, Stacy MR, French BA, Annex BH, Carrasco N, Sinusas AJ. Noninvasive in vivo quantification of adeno-associated virus serotype 9-mediated expression of the sodium/iodide symporter under hindlimb ischemia and neuraminidase desialylation in skeletal muscle using single-photon emission computed tomography/computed tomography. Circ Cardiovasc Imaging. 2019;12:e009063.
191. Stendahl J, Sinusas AJ. Nanoparticles for cardiovascular imaging and therapeutic delivery, Part 2: Radiolabeled probes. J Nucl Med. 2015;56(11):1637–41. https://doi.org/10.2967/jnumed.115.164145. PMID: 26294304.
192. Stendahl JC, Sinusas AJ. Nanoparticles for cardiovascular imaging and therapeutic delivery. Part 1: Compositions and features. J Nucl Med. 2015;56(10):1469–75. https://doi.org/10.2967/jnumed.115.160994. PMID: 26272808.

Part IV

PET/MR

PET/MR: Perfusion and Viability

12

Lukas Kessler and Christoph Rischpler

12.1 Introduction

In the last years PET/MR hybrid imaging entered the market and revealed a variety of possible clinical applications. The first integrated PET/MRI scanner was installed in 2010 and initially the clinical applications focused on oncological examination [1]. It took a few years for this new technology to be implemented in the workup of cardiovascular diseases and until 2013 no original research article was published about PET/MRI applications for cardiovascular diseases. This was because of multiple reasons: One reason was that healthcare professionals (e.g. physicians, physicists, technicians and researchers) needed to get used to this complex technology, which was obviously easier in organs without movement and motion artifacts due to respiration and the heartbeat. Further there are fewer patients who receive PET imaging with cardiovascular diseases than, for example, in Oncology. Nonetheless there are rising applications for PET/MRI in cardiology with promising data and a joint position statement by the ESCR and EANM has been published as a guideline [2]. But PET/MRIs full potential has not been exploited yet. This chapter will focus on PET/MRI in myocardial perfusion, viability imaging, and technical peculiarities of current PET/MRI systems which have to be considered.

12.2 Technical Specialities of PET/MRI Systems

The development and construction of integrated PET/MRI systems was a technically and financially challenging task due to certain technical and physical restraints. On one hand, high magnetic fields, quickly switching gradient fields,

L. Kessler · C. Rischpler (✉)
Department of Nuclear Medicine, University Hospital Essen, University of Duisburg-Essen, Essen, Germany
e-mail: Christoph.rischpler@uk-essen.de

S. G. Nekolla, C. Rischpler (eds.), *Hybrid Cardiac Imaging*,
https://doi.org/10.1007/978-3-030-83167-7_12

and radiofrequency signals from MRI technology may interfere with the electronics and imaging components (e.g. photomultiplier tubes) of regular PET scanners. On the other hand, MR image quality may suffer from PET components in the scan field of view. Today there are two different kinds of PET/MRI commercially available, the first being a PET connected with a stand-alone MR scanner via table (Philips Ingenuity TF PET/MR) [3]. The second has a PET detector ring installed inside the MR tube and can therefore be referred to as a true integrated PET/MRI (Siemens Biograph mMR, GE SIGNA PET/MR) [1, 4]. For the latter constructional approach new detector technologies had to be engineered. Siemens focused on avalanche photodiodes (ADPs), for example, made of lutetium oxyorthosilicate crystals. These crystals can resist strong magnetic fields without major interference. Compared to that GE-scanners use silicon photomultiplier technology (SiPM)-based PET detectors, which allow time-of-flight PET imaging [5].

A major problem with the integrated scanners has been the attenuation correction (AC) which is most crucial for PET imaging in general. With non-AC PET data only, quantification of absolute activity values is not possible and therefore PET data interpretation would gravely suffer.

Because of the missing CT data and the old time-consuming methods from stand-alone PET were not a real alternative, new methods had to be engineered for AC of PET/MR images. There is a variety of approaches for example tissue classification, maximum likelihood estimation of activity and attenuation (MLAA), homogenization using gradient enhancement (HUGE) or the novel CAIPIRINHA attenuation correction [6–11]. Most approaches for generating AC-maps from MR data are based on templates, segmentation or atlases and of course PET emission data. In concise sentences, segmentation-based algorithms generate AC-maps taking into account different tissue types with varying attenuation coefficients for 511 keV photons [12]. This method, for instance, is applied in the Siemens Biograph mMR. From a Dixon VIBE MR sequence water and fat images are generated and air, lung, fat, and soft tissue are segmented and represented afterwards in the AC-map [6, 13]. A requirement for this method is a breath-hold time of approx. 18 s per bed position, which can be problematic in older, very sick or respiratory impaired patients. An alternative approach is using a T1-weighted (T1w) turbo spin echo sequence to reduce image acquisition time for AC-map generation, however, this method ignores the minor density difference between fat and soft tissue [14]. Lately, a new technique was introduced which also models bone by using an atlas [15]. This approach has already been implemented into the Siemens mMR. In the GE SIGNA PET/MRI a multi-station, whole-body, three-dimensional, dual-echo, RF-spoiled gradient recalled echo (SPGR) sequence (LAVA-Flex) is used and images are also segmented into air, lung, fat, and soft tissue. The Siemens Biograph mMR and the GE Signa approaches are quite similar, the difference lies in slightly different and variable attenuation coefficients of the tissues in the GE scanner [16]. As a result a limited number of tissue types may cause a higher variance in radiotracer uptake estimation for thoracic tumors, which has been reported as 5–23% [6, 14, 17]. Despite that, studies indicate a close agreement between PET/MRI and PET/CT for

cardiac viability imaging with fludeoxyglucose (FDG) [7]. Another approach is the emission-based maximum likelihood estimation of activity and attenuation (MLAA), where non-AC PET data is utilized to calculate the μ-map, but a limitation of this method is photon scatter [8]. Due to the discrepancy of a larger-field of view in PET versus MR imaging, this approach is used to recover parts of the body which cannot be "seen" by MRI but contribute to attenuation (e.g. arms and shoulders) [18]. A constraint of this procedure is variability of tracer uptake in truncated parts of the body depending on the used radiotracer and therefore these parts of the body might be "overlooked" by this method. A novel approach to overcome this constraint has been introduced lately—the so-called B0 homogenization using gradient enhancement (HUGE) technique [10]. Briefly, a reduction of the truncations outside the field of view of the MR scanner can be achieved by optimization of the readout gradient, more specifically by local compensation of B0 inhomogeneities via gradient enhancement. Recent studies suggest that the HUGE method might be more accurate than commonly used MLAA method, especially in radiotracers other than FDG [9].

A novel sequence for AC is the 'controlled aliasing in parallel imaging results in higher acceleration', the so-called CAIPIRINHA. It offers higher resolution but identical scan-time [11]. With this sequence other diagnostic sequences with longer acquisition times could potentially be omitted and therefore overall scan time could be drastically reduced (which often poses a downside of PET/MRI compared to PET/CT).

Another peculiarity of PET/MRI is that devices in or around the heart may result in a MRI signal which is larger than the actual size of the device. This may result in an underestimation of the attenuation (in contrast to CT, where metallic objects cause an overestimation of the caused attenuation) and radiotracer uptake. A large number of cardiac devices are implanted every year and numbers are even rising. Not only the compatibility for MRI of the device has to be checked before performing MRI for safety reasons, also it is often not clear if the device is going to cause artifacts which may result in erroneous readings. In a recent study of 20 patients who underwent combined viability and perfusion PET/MR imaging, 20–30% of subjects demonstrated artifacts caused by sternal wires or other metallic implants and maximum relative differences in tracer uptake were observed between 11% and 196% when correcting for artifacts [22]. Figure 12.1 demonstrates a possible artifact on MRI and PET images by a coronary stent.

12.3 Myocardial Perfusion Imaging

In nuclear cardiology myocardial perfusion imaging (MPI) with SPECT and PET is the most common study [19]. It has great impact in the diagnostic workup of coronary artery disease and clinically emerging questions such as hemodynamic significance and extent of ischemia may be answered [20–23]. For quantitative assessment of myocardial blood flow and coronary reserve PET MPI may be seen as the gold standard because of higher image quality and the possibility to quantify the myocardial blood flow (MBF) compared to SPECT MPI [24].

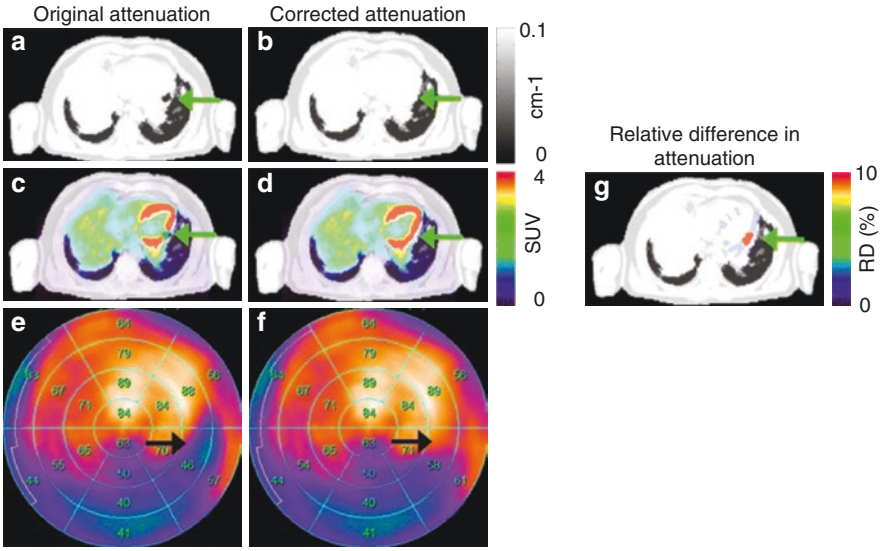

Fig. 12.1 (**a**–**g**) Attenuation artifacts in PET/MRI. Cardiac devices may cause artifacts on MR images which translate into PET images. In the depicted case a susceptibility artifact in the left circumflex caused by stent (**a**, green arrow) resulted in an apparent defect in the lateral wall (**c**, green arrow; **e**, black arrow). When correcting for this artifact, the tracer uptake normalized in this region (**d**, green arrow; **f**, black arrow). This artifact caused a relative difference of more than 10% in the respective region (**g**). (Reprinted with permission from Lassen, M.L., Rasul, S., Beitzke, D. et al. J. Nucl. Cardiol. (2017). https://doi.org/10.1007/s12350-017-1118-2)

There are various radiotracers for PET MPI with different limitations and pitfalls. N-13 ammonia and Rubidium-82 are the only FDA-approved radiotracers for this indication. Other radiotracers are O-15 water and the recently introduced F-18-Flurpiridaz. O-15 water (T1/2 = 122 s), Rubidium-82 (T1/2 = 76 s) and N-13 ammonia (T1/2: 10 min) are radiotracers with a short half-life and consequently, as a prerequisite an on-site cyclotron is needed or a cost-intensive generator has to be purchased every month. Therefore absolute blood flow quantification is often only available at specialized centers. O-15 water has been extensively studied as perfusion tracer and is thought to be superior due to its free diffusion and thus almost perfect first pass extraction. However, O-15 water is not FDA-approved and there is no reimbursement from healthcare insurance companies.

Because of the accessibility and beneficial properties of F-18 for PET imaging, novel F-18-labeled perfusion radiotracers are being developed. One of the most prominent PET perfusion tracers is F-18-Flupiridaz, which is still evaluated in clinical phase 3 trials [25–27].

F-18 flurpiridaz has a high first pass extraction of 94% [25] and F-18 has the advantage of a low positron energy (Emax = 634 keV). Furthermore, neither a cost-intensive and MRI-noncompatible Rb-82 generator nor an onsite cyclotron is needed because of its longer half-life (T1/2 = 110 min). These novel F-18-labeled radiotracers might lead to a wide availability of PET MPI.

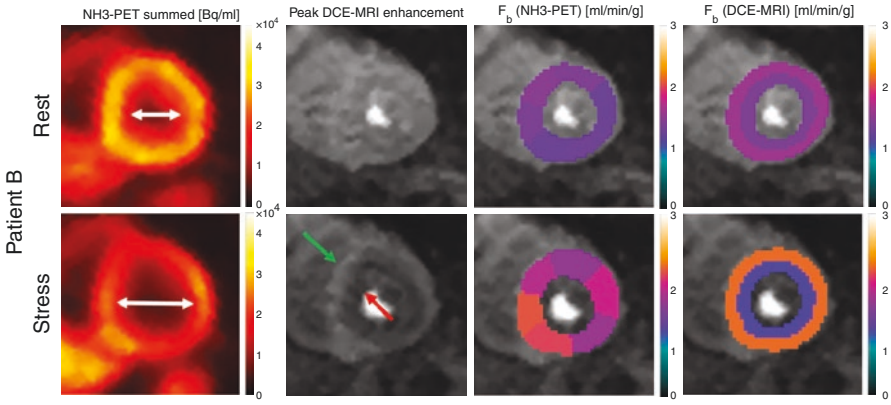

Fig. 12.2 Simultaneous myocardial perfusion imaging using PET/MRI. This figure depicts a combined PET/MRI perfusion study of a patient with hypertrophic cardiomyopathy. On N-13 ammonia images a dilation of the left ventricle from rest to stress and a inhomogeneous myocardial perfusion during pharmacological stress can be observed. MR images demonstrate that this apparent dilation of the left ventricle is actually caused by a hypoperfusion of the endocardium during hyperemia. (Reprinted with permission from Kunze KP, Nekolla SG, Rischpler C, et al. Myocardial perfusion quantification using simultaneously acquired 13NH3-ammonia PET and dynamic contrast-enhanced MRI in patients at rest and stress. Magn Reson Med. 2018;00:1–14. https://doi.org/10.1002/mrm.27213)

In contrast to that MRI has different advantages and disadvantages in myocardial perfusion imaging and MRI MPI has been widely established. It provides high spatial resolution and is potentially capable to detect small subendocardial areas of ischemia without exposing the patient to ionizing radiation. In the early 1990s the feasibility of MRI with gadolinium-based contrast agents for detecting flow-limiting coronary artery disease (CAD) was first demonstrated [28] and since then many studies reaffirmed its value [29, 30]. Nonetheless one limitation of these studies is that they are mostly based on visual analysis which makes detection of balanced ischemia in advanced CAD difficult (similar to SPECT MPI) [31, 32]. To exceed these limitations many approaches focus on quantifying myocardial blood flow using MRI. One of the simplest methods is the upslope ratio to determine the coronary flow reserve [33]. The central volume principle of quantifying myocardial blood flow is a more complex method that has been used to compare PET and MRI MPI in a group of 41 patients [34, 35]. In that study a good agreement with coronary flow reserve was observed whereas the absolute myocardial blood flow values showed a high variance. Kunze et al. showed recently a good agreement between the two methods in absolute flow values but with underestimated coronary flow reserve by MRI because of an overestimation of resting perfusion in MRI irrespective of the applied MRI deconvolution method [36]. Additionally, in that study it was demonstrated in one patient with hypertrophic cardiomyopathy that MRI is capable of the differentiation between subepicardial and subendocardial blood flow due to higher spatial resolution (see Fig. 12.2). The problems of flow quantification in MRI are mainly but not solely because of the Gd-based contrasted agents. These contrast agents are not taken up by the

cardiomyocytes and suffer from a low "extraction fraction," which is also not only perfusion dependent. Therefore, this makes quantitative myocardial perfusion assessment using MRI challenging. Another disadvantage is that MRI MPI usually images only a certain number of slices of the left ventricle but does not cover the whole left ventricle like in PET or SPECT MPI. For therapy guidance the extent of whole left ventricular ischemia is a key factor [22], the estimation of this parameter in MRI may be inaccurate when using only three slices of the left ventricle. While approaches have been undertaken to enable 3D first pass perfusion MRI for the estimation of myocardial blood flow in the whole left ventricle, this technique is far from being used in clinical routine.

Hybrid PET/MRI may be a great tool for cross-validation of the two modalities with respect to complicated quantification methods in MRI. It allows the detection of subendocardial ischemia in MRI while PET MPI provides a reliable way to measure absolute myocardial perfusion of the whole left ventricle.

12.4 Myocardial Viability Imaging

Myocardial viability imaging is used to identify chronically hypoperfused myocardium. This myocardium has a changed metabolism from fatty acids to glucose and often shows contractile dysfunction, which is called "hibernation" [37]. Hibernating myocardium has prognostic relevance because its presence is associated with poor cardiovascular outcome and its extent is important in therapeutic guidance, because hibernating myocardium is prone to recover after revascularization [38–42].

Non-invasive methods for the assessment of myocardial viability are, for example, dobutamine stress echocardiography and MRI, Thallium-201 SPECT or F-18 FDG-PET, and late gadolinium enhancement (LGE) MRI, the latter two being two most commonly used methods [43].

For F-18-FDG-PET viability imaging a special metabolic preparation is needed to increase myocardial glucose uptake. A variety of methods are known to increase the glucose transporter expression on cardiomyocytes. A common one is oral glucose loading and the hyperinsulinemic-euglycemic clamp technique. Based on a meta-analysis, FDG-PET has a 92% sensitivity and 63% specificity among viability imaging approaches [44].

As an alternative cardiac MR late gadolinium enhanced (LGE) imaging has emerged lately. LGE utilizes the fact that Gadolinum-chelate-based contrast agents have a slower wash-out in areas with increased extravascular space, e.g. fibrotic/scarred myocardial tissue, compared to a normal wash-out from viable, non-scarred myocardium [45, 46]. Therefore, LGE MR images scarred, non-viable, myocardium compared to F-18-FDG-PET whose objective is to identify viable, hibernating myocardium. But despite these fundamentally different approaches a good agreement between both modalities has been shown [47]. In comparison to FDG-PET LGE MRI has a higher spatial resolution which opens up the opportunity to differentiate between transmural and non-transmural scarring; furthermore, small myocardial scars can be unmasked which proposes prognostic value and clinical relevance [48, 49].

A recent study showed different diagnostic accuracies of PET and cardiac MR depending on the left ventricular function [50]. In that study cardiac MR revealed more scars in patients with ejection fraction (EF) of <30% and 30–50% compared to FDG-PET, but FDG-PET found more scars in patients with EF > 50%. In terms of functional recovery prediction (e.g. after revascularization) PET was found more optimistic than cardiac MR.

Up to date F-18-FDG-PET/MRI in viability imaging is not thoroughly researched and there are only few representative studies. The three currently published studies reported variable agreement between FDG-PET and MRI ranging from moderate to significant (Fig. 12.3) [51–53]. One of those studies recruited a small patient cohort prior to elective revascularization for coronary artery disease and observed a reclassification in 19% of segments in hybrid FDG-PET/MRI compared to SPECT and CMR alone [51]. However, the investigators did not show follow-up data to validate the clinical impact of the reclassification. The other two mentioned studies focused on FDG-PET/MRI after myocardial infarction rather than prior to revascularization and a high intermethod-agreement for transmurality of LGE and reduced FDG uptake in myocardial segments was found. Furthermore, in one study a better recovery of wall motion of both PET and MRI viable dysfunctional segments could be shown. Additionally, segments with a contradicting pattern of FDG uptake and LGE transmurality were demonstrated, namely a decreased FDG uptake with a non-transmural or minor LGE. Only 40% of these contradicting patterns had an improved wall motion after 6 months. [52]. Nensa et al. investigated the alteration of glucose metabolism in the area of infarction in relation to the infarct size measured by LGE MRI and to the myocardium at risk, which was assessed by the endocardial surface area method (ESA) [54]. By definition of this method all myocardial segments which demonstrate any LGE (regardless of degree and transmurality) define the area at risk. As anticipated, the area at risk was larger than the actual infarct area

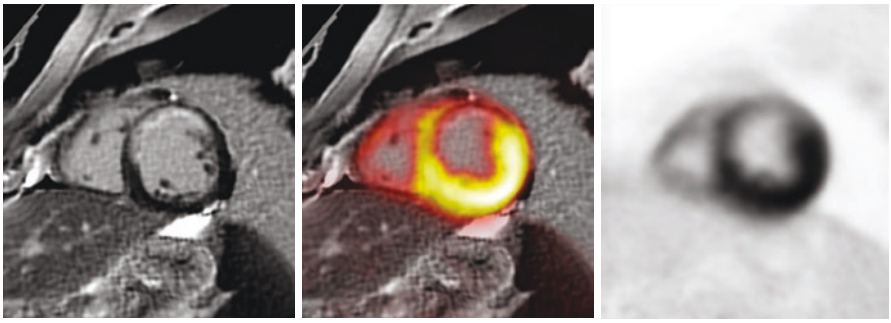

Fig. 12.3 FDG PET/MRI for viability imaging. A 63-year old man was referred to our institution for FDG PET/MRI viability imaging for a known chronic total occlusion of the left anterior descending artery (LAD). Late gadolinium enhancement (LGE) MRI depicts a transmural scar of the anterior wall (left panel). FDG PET shows a well-matched reduction of FDG uptake in the identical region (right and middle panel). Also, a severe wall motion abnormality was observed in this area. Taken together these images demonstrate that myocardium is non-viable in the LAD territory

(31 ± 11% vs. 10 ± 10%). Interestingly, the area at risk correlated with the extent of reduced glucose metabolism suggesting that myocardium has a decreased FDG uptake early after an ischemic event. But there is no conclusive pathophysiological rationale for this so far and further studies are needed to clarify those findings. To this date no prospective study has been published which evaluated the diagnostic value of myocardial viability FDG-PET/MRI prior to revascularization with follow-up examinations after treatment to estimate the predictive value of hybrid imaging in this setting.

12.5 Conclusion

In cardiac imaging PET/MRI offers unique possibilities not just as a research tool but as well in specific clinical questions. Combined analysis of PET and MR in perfusion and viability imaging successfully provides synergistic functional and morphological information. New radiotracers might further uplift cardiac PET/MRI in the future. Nonetheless the current technologies still have constraints which need to be overcome. Long acquisition times, narrow scanners, and a strong magnetic field need thorough patient screening and preparation and on top of that PET/MRI is very cost-intensive and will therefore not be broadly available.

References

1. Delso G, Furst S, Jakoby B, et al. Performance measurements of the siemens mMR integrated whole-body PET/MR scanner. J Nucl Med. 2011;52:1914–22.
2. Nensa F, Bamberg F, Rischpler C, et al. Hybrid cardiac imaging using PET/MRI: a joint position statement by the European Society of Cardiovascular Radiology (ESCR) and the European Association of Nuclear Medicine (EANM). Eur Radiol. 2018;28:4086–101.
3. Zaidi H, Ojha N, Morich M, et al. Design and performance evaluation of a whole-body ingenuity TF PET-MRI system. Phys Med Biol. 2011;56:3091–106.
4. Levin CS, Maramraju SH, Khalighi MM, Deller TW, Delso G, Jansen F. Design features and mutual compatibility studies of the time-of-flight PET capable GE SIGNA PET/MR system. IEEE Trans Med Imaging. 2016;35:1907–14.
5. Levin C, Deller T, Peterson W, Maramraju SH, Kim C, Prost R. Initial results of simultaneous whole-body ToF PET/MR. J Nucl Med. 2014;55:660.
6. Martinez-Moller A, Souvatzoglou M, Delso G, et al. Tissue classification as a potential approach for attenuation correction in whole-body PET/MRI: evaluation with PET/CT Data. J Nucl Med. 2009;50:520–6.
7. Lau JMC, Laforest R, Sotoudeh H, et al. Evaluation of attenuation correction in cardiac PET using PET/MR. J Nucl Cardiol. 2017;24:839–46.
8. Nuyts J, Dupont P, Stroobants S, Benninck R, Mortelmans L, Suetens P. Simultaneous maximum a posteriori reconstruction of attenuation and activity distributions from emission sinograms. IEEE Trans Med Imaging. 1999;18:393–403.
9. Lindemann ME, Oehmigen M, Blumhagen JO, Gratz M, Quick HH. MR-based truncation and attenuation correction in integrated PET/MR hybrid imaging using HUGE with continuous table motion. Med Phys. 2017;44:4559–72.

10. Blumhagen JO, Braun H, Ladebeck R, et al. Field of view extension and truncation correction for MR-based human attenuation correction in simultaneous MR/PET imaging. Med Phys. 2014;41:22303.
11. Freitag MT, Fenchel M, Bäumer P, et al. Improved clinical workflow for simultaneous whole-body PET/MRI using high-resolution CAIPIRINHA-accelerated MR-based attenuation correction. Eur J Radiol. 2017;96:12–20.
12. Huang SH, Carson RE, Phelps ME, Hoffman EJ, Schelbert HR, Kuhl DE. A Boundary method for attenuation correction in positron computed tomography. J Comput Assist Tomogr. 1981;5:950.
13. Coombs BD, Szumowski J, Coshow W. Two-point Dixon technique for water-fat signal decomposition with B0 inhomogeneity correction. Magn Reson Med. 1997;38:884–9.
14. Schulz V, Torres-Espallardo I, Renisch S, et al. Automatic, three-segment, MR-based attenuation correction for whole-body PET/MR data. Eur J Nucl Med Mol Imaging. 2011;38:138–52.
15. Paulus DH, Quick HH, Geppert C, et al. Whole-body PET/MR imaging: quantitative evaluation of a novel model-based MR attenuation correction method including bone. J Nucl Med. 2015;56:1061–6.
16. Beyer T, Lassen ML, Boellaard R, et al. Investigating the state-of-the-art in whole-body MR-based attenuation correction: an intra-individual, inter-system, inventory study on three clinical PET/MR systems. MAGMA. 2016;29:75–87.
17. Samarin A, Burger C, Wollenweber SD, et al. PET/MR imaging of bone lesions - implications for PET quantification from imperfect attenuation correction. Eur J Nucl Med Mol Imaging. 2012;39:1154–60.
18. Nuyts J, Bal G, Kehren F, Fenchel M, Michel C, Watson C. Completion of a truncated attenuation image from the attenuated PET emission data. IEEE Trans Med Imaging. 2013;32:237–46.
19. Klocke FJ, Baird MG, Lorell BH, et al. ACC/AHA/ASNC Guidelines for the clinical use of cardiac radionuclide imaging—executive summary. J Am Coll Cardiol. 2003;42:1318–33.
20. Yoshinaga K, et al. What is the prognostic value of myocardial perfusion imaging using rubidium-82 positron emission tomography? J Am Coll Cardiol. 2006;48:1029–39.
21. Schwaiger M, Melin J. Cardiological applications of nuclear medicine. Lancet. 1999;354:661–6.
22. Hachamovitch R, Hayes SW, Friedman JD, Cohen I, Berman DS. Comparison of the short-term survival benefit associated with revascularization compared with medical therapy in patients with no prior coronary artery disease undergoing stress myocardial perfusion single photon emission computed tomography. Circulation. 2003;107:2900–7.
23. Merhige ME, Breen WJ, Shelton V, Houston T, D'Arcy BJ, Perna AF. Impact of myocardial perfusion imaging with PET and 82Rb on downstream invasive procedure utilization, costs, and outcomes in coronary disease management. J Nucl Med. 2007;48:1069–76.
24. Flotats A, Bravo PE, Fukushima K, Chaudhry MA, Merrill J, Bengel FM. 82Rb PET myocardial perfusion imaging is superior to 99mTc-labelled agent SPECT in patients with known or suspected coronary artery disease. Eur J Nucl Med Mol Imaging. 2012;39:1233–9.
25. Huisman MC, Higuchi T, Reder S, et al. Initial characterization of an 18F-labeled myocardial perfusion tracer. J Nucl Med. 2008;49:630–6.
26. Berman DS, Maddahi J, Tamarappoo BK, et al. Phase II safety and clinical comparison with single-photon emission computed tomography myocardial perfusion imaging for detection of coronary artery disease. J Am Coll Cardiol. 2013;61:469–77.
27. Sherif HM, Nekolla SG, Schwaiger M. Reply: simplified quantification of myocardial flow reserve with 18F-flurpiridaz: validation with microspheres in a pig model. J Nucl Med. 2011;52:1835–6.
28. Manning WJ, Atkinson DJ, Grossman W, Paulin S, Edelman RR. First-pass nuclear magnetic resonance imaging studies using gadolinium-DTPA in patients with coronary artery disease. J Am Coll Cardiol. 1991;18:959–65.
29. Nandalur KR, Dwamena BA, Choudhri AF, Nandalur MR, Carlos RC. Diagnostic performance of stress cardiac magnetic resonance imaging in the detection of coronary artery disease. J Am Coll Cardiol. 2007;50:1343–53.

30. de Jong MC, Genders TSS, van Geuns R-J, Moelker A, Hunink MGM. Diagnostic performance of stress myocardial perfusion imaging for coronary artery disease: a systematic review and meta-analysis. Eur Radiol. 2012;22:1881–95.
31. Parkash R, DeKemp RA, Ruddy TD, et al. Potential utility of rubidium 82 PET quantification in patients with 3-vessel coronary artery disease. J Nucl Cardiol. 2004;11:440–9.
32. Kajander SA, Joutsiniemi E, Saraste M, et al. Clinical value of absolute quantification of myocardial perfusion with 15 O-water in coronary artery disease. Circ Cardiovasc Imaging. 2011;4:678–84.
33. Schwitter J, Nanz D, Kneifel S, et al. Assessment of myocardial perfusion in coronary artery disease by magnetic resonance. Circulation. 2012;103:2230–5.
34. Jerosch-Herold M. Quantification of myocardial perfusion by cardiovascular magnetic resonance. J Cardiovasc Magn Reson. 2010;12:57.
35. Morton G, Chiribiri A, Ishida M, et al. Quantification of absolute myocardial perfusion in patients with coronary artery disease. J Am Coll Cardiol. 2012;60:1546–55.
36. Kunze KP, Nekolla SG, Rischpler C, et al. Myocardial perfusion quantification using simultaneously acquired 13NH3-ammonia PET and dynamic contrast-enhanced MRI in patients at rest and stress. Magn Reson Med. 2018;80:2641–54.
37. Ghosh N, Rimoldi OE, Beanlands RSB, Camici PG. Assessment of myocardial ischaemia and viability: role of positron emission tomography. Eur Heart J. 2010;31:2984–95.
38. Di Carli MF. Predicting improved function after myocardial revascularization. Curr Opin Cardiol. 1998;13:415–24.
39. Beanlands RS, Hendry PJ, Masters RG, deKemp RA, Woodend K, Ruddy TD. Delay in revascularization is associated with increased mortality rate in patients with severe left ventricular dysfunction and viable myocardium on fluorine 18-fluorodeoxyglucose positron emission tomography imaging. Circulation. 1998;98:II51–6.
40. Di Carli MF, Davidson M, Little R, et al. Value of metabolic imaging with positron emission tomography for evaluating prognosis in patients with coronary artery disease and left ventricular dysfunction. Am J Cardiol. 1994;73:527–33.
41. D'Egidio G, Nichol G, Williams KA, et al. Increasing benefit from revascularization is associated with increasing amounts of myocardial hibernation: a substudy of the PARR-2 trial. JACC Cardiovasc Imaging. 2009;2:1060–8.
42. Allman KC, Shaw LJ, Hachamovitch R, Udelson JE. Myocardial viability testing and impact of revascularization on prognosis in patients with coronary artery disease and left ventricular dysfunction: a meta-analysis. J Am Coll Cardiol. 2002;39:1151–8.
43. Tillisch J, Brunken R, Marshall R, et al. Reversibility of cardiac wall-motion abnormalities predicted by positron tomography. N Engl J Med. 1986;314:884–8.
44. Schinkel AFL, Poldermans D, Elhendy A, Bax JJ. Assessment of myocardial viability in patients with heart failure. J Nucl Med. 2007;48:1135–46.
45. Klein C, Schmal TR, Nekolla SG, Schnackenburg B, Fleck E, Nagel E. Mechanism of late gadolinium enhancement in patients with acute myocardial infarction. J Cardiovasc Magn Reson. 2007;9:653–8.
46. Klein C, Nekolla SG, Balbach T, et al. The influence of myocardial blood flow and volume of distribution on late Gd-DTPA kinetics in ischemic heart failure. J Magn Reson Imaging. 2004;20:588–94.
47. Klein C, Nekolla SG, Bengel FM, et al. Assessment of myocardial viability with contrast-enhanced magnetic resonance imaging. Circulation. 2002;105:162–7.
48. Kim RJ, Wu E, Rafael A, et al. The use of contrast-enhanced magnetic resonance imaging to identify reversible myocardial dysfunction. N Engl J Med. 2000;343:1445–53.
49. Kwong RY, Chan AK, Brown KA, et al. Impact of unrecognized myocardial scar detected by cardiac magnetic resonance imaging on event-free survival in patients presenting with signs or symptoms of coronary artery disease. Circulation. 2006;113:2733–43.
50. Hunold P, Jakob H, Erbel R, Barkhausen J, Heilmaier C. Accuracy of myocardial viability imaging by cardiac MRI and PET depending on left ventricular function. World J Cardiol. 2018;10:110–8.

51. Priamo J, Adamopoulos D, Rager O, et al. Downstream indication to revascularization following hybrid cardiac PET/MRI. Nucl Med Commun. 2017;38:515–22.
52. Rischpler C, Langwieser N, Souvatzoglou M, et al. PET/MRI early after myocardial infarction: evaluation of viability with late gadolinium enhancement transmurality vs. 18F-FDG uptake. Eur Heart J Cardiovasc Imaging. 2015;16:661–9.
53. Nensa F, Poeppel TD, Beiderwellen K, et al. Hybrid PET/MR imaging of the heart: feasibility and initial results. Radiology. 2013;268:366–73.
54. Nensa F, Poeppel T, Tezgah E, et al. Integrated FDG PET/MR imaging for the assessment of myocardial salvage in reperfused acute myocardial infarction. Radiology. 2015;276:400–7.

PET/MRI: "Inflammation"

13

Mohamed Y. Elwazir, John P. Bois, Pamela K. Woodard, and Panithaya Chareonthaitawee

Abbreviations

ESCR	European Society of Cardiovascular Radiology
FDA	Food and Drugs Act
FDG	Fluorodeoxyglucose
FLASH	Fast Low Angle Shot
FOV	Field of View
GE	General Electric
GLUT	Glucose Transporter
HED	Hydroxyephedrine
HFLC	High-Fat Low Carbohydrate
HRS	Heart Rhythm Society
HUGE	B_0 Homogenization Using Gradient Enhancement
ICD	Implantable Cardioverter-Defibrillator
ICM	Ischemic Cardiomyopathy
LGE	Late Gadolinium Enhancement
LV	Left Ventricle
MBF	Myocardial Blood Flow
MLAA	Maximum Likelihood Reconstruction of Attenuation and Activity
MR	Magnetic Resonance
MRA	Magnetic Resonance Angiography
MRCA	Magnetic Resonance Coronary Angiography

M. Y. Elwazir · J. P. Bois · P. Chareonthaitawee (✉)
Department of Cardiovascular Medicine, Mayo Clinic, Rochester, MN, USA
e-mail: chareonthaitawee.panithaya@mayo.edu

P. K. Woodard
Mallinckrodt Institute of Radiology, Washington University School of Medicine, St. Louis, MO, USA

S. G. Nekolla, C. Rischpler (eds.), *Hybrid Cardiac Imaging*,
https://doi.org/10.1007/978-3-030-83167-7_13

MRI	Magnetic Resonance Imaging
PET	Positron Emission Tomography
PMT	Photomultiplier Tube
RF	Radiofrequency
RV	Right Ventricle
SCD	Sudden Cardiac Death
SNR	Signal to Noise Ratio
SPAIR	Spectral Attenuated Inversion Recovery
SPECT	Single Photon Emission Computed Tomography
SUV	Standardized Uptake Value
TEE	Transesophageal Echocardiography
TSE	Turbo Spin Echo
UTE	Ultrashort Echo Time

13.1 Introduction: A Brief History of Hybridization

Positron emission tomography (PET) and magnetic resonance imaging (MRI) are among the most advanced cardiovascular imaging modalities currently available. PET, first introduced in its modern form in 1990 [1], uses scintillation mapping to detect positrons released from administered radiotracer-labeled chemicals [2]. Based on the chemical-radiotracer combination used, various physiologic processes can be assessed including myocardial blood flow, metabolism, and inflammation. However, the lack of precise anatomical localization of functional abnormalities as well as the need for a more rapid and consistent source for attenuation correction have prompted the development of hybrid PET imaging. Following the successful example of SPECT/CT [3], PET/CT was introduced in 2001, and found widespread usage due to its more rapid image acquisition than the traditional germanium-68 rod sources [4] as well as its ability to accurately detect coronary artery calcifications [5] and to identify clinically relevant extra-cardiac findings [6]. These advantages of hybrid PET/CT were sufficient to overcome initial reluctance to its use due to its increased relative cost over germanium-68 rods.

MRI was the natural next target for hybrid PET imaging. Since the first commercial system was made available in 1980 [7], MRI has revolutionized medical imaging with its unsurpassed tissue characterization [8]. By detecting energy emitted from radiofrequency (RF) pulse-aligned protons as they process in a magnetic field, MRI can generate images without the hazards of exposure to ionizing radiation [9]. Furthermore, cardiac magnetic resonance (CMR) excels at delineating anatomy, quantifying left and right ventricular function, and assessing global and regional myocardial contractility. Diffusion MRI offers the ability to measure myocardial blood flow, and late gadolinium enhancement (LGE) on contrast studies can accurately identify regions of myocardial scar [10]. The further development of parametric mapping techniques including T1 and T2 mapping has allowed for quantification of myocardial inflammation and fibrosis [11]. Therefore, cardiac PET and MRI

provide both complementary and potentially corroborative information rendering them potentially ideal partners for hybridization.

13.2 Challenges to PET/MRI

There are several challenges to the successful application of PET/MRI, many of which have not been completely solved. These can broadly be classified into technical issues, patient/workflow issues, and personnel issues.

13.2.1 Technical Issues

13.2.1.1 Hardware Incompatibilities

While Garlick and colleagues pioneered hybrid cardiac PET/MRI imaging using isolated mammalian hearts [12], true clinical hybrid cardiac PET/MRI was not available until 2011 [13]. The major barrier to an integrated PET/MRI scanner at the time had been the incompatibility between the hardware components of the two systems. For instance, the presence of unshielded PET detectors within the MRI magnet coils could disrupt the uniformity of the generated magnetic field, a stringent prerequisite to obtaining MRI images, necessitating the use of PET crystals that have inherently favorable magnetic properties such as lutetium-based crystals [14]. Furthermore, shielding the PET detectors in copper and in essence creating a small Faraday cage around each detector has been demonstrated to inhibit electromagnetic interference emanating from the detector which would otherwise distort the MRI image [13].

Conversely, PET image quality can be negatively impacted by the MRI hardware. For example, the photomultiplier tubes (PMT) used in conventional PET detectors to convert scintillation events into electronic signals fail to function properly in a strong magnetic field due to the Lorentz force [14]. Fortunately, the advent of semiconductor-based avalanche photodiodes, which are not affected by magnetic fields, has alleviated this concern [13].

13.2.1.2 Attenuation Correction

Another pertinent challenge with PET/MRI is the difficulty in performing PET attenuation correction (AC). Attenuation is the phenomenon where positrons are lost from the detector's field of view (FOV) due to dispersion or absorption in dense tissues, leading to weaker signal in denser/deeper regions with the consequent possibility of missing existing areas of abnormal radiotracer uptake. Conventionally, initial transmission scans with germanium-68 radionuclide rods were performed to create an electron density map of the tissues which was subsequently applied to PET data to correct for attenuation artifacts [4]. With the advent of PET/CT, attenuation correction is now increasingly performed using co-registered CT density data. With PET/MRI, MRI measures *proton spin* density, which does not correlate with electron density and consequently cannot be used to perform attenuation correction.

Furthermore, the limited space inside the PET/MR scanner (see Sect. 13.2.2) does not allow for the installation of additional equipment for germanium-68 transmission scans. Several approaches have been considered to address this issue [15–17], with the Dixon 2-point method as one potential solution [18, 19]. This system employs Dixon sequencing to segment tissues into four classes, each with a predetermined attenuation coefficient: lung, fat, soft tissue, and background (Fig. 13.1). While shown to provide results comparable to CT attenuation, this method, however, does not separately classify bone, but rather considers it in the same category with soft tissue, underestimating attenuation values near bony areas such as retrosternally [20]. Potential workarounds include semi-automated addition of atlas-based bone information [21] or using ultrashort echo time (UTE) sequences to separately segment bone [22].

A more recent approach is using MR data to generate "pseudo-CT" images for the patient which can be used for AC. These images are computed based on observed relationships between MR and CT images from population studies and can be either voxel, patch or machine-learning based [23]. This approach has been well-validated in neuroimaging [24], but has yet to be tested for cardiac or whole-body applications.

Patient tissues are not the only concern when performing attenuation correction in PET/MRI. Fixed and flexible phased-array RF coils are routinely used for MRI signal enhancement, with the fixed components being part of the patient table, and the flexible components placed anteriorly on the patient's chest. Since these components are not entirely PET transparent [25], their attenuation effects need to be accounted for as well. This is performed using pre-acquired CT density maps which

Fig. 13.1 Part of an MR segmented four-class attenuation map generated by the two-point Dixon method (Lean tissue = white, adipose tissue = pink, lung = blue, air = black). (Reproduced with permission from Muzic RF, Jr., DiFilippo FP. Positron emission tomography-magnetic resonance imaging: technical review)

are aligned to the coils using the table position as a reference in the case of stationary coils [26], and MRI-detectable position tags for the flexible components [27].

13.2.1.3 Motion Correction

Although integrated PET/MR scanners boast the benefit of "simultaneous" acquisition, this is not entirely the case; since MRI acquisition is sequential (milliseconds to a few seconds) while PET acquisition is volumetric, typically over a period of 10–30 min. These longer acquisition times render PET motion artifact-prone. While modern PET scanners can reach spatial resolutions up to 4–6 mm in still tissues [28], cardiac PET resolution is typically less due to cardiac and respiratory motion [29], the combination of which can cause myocardial tissue to move by as much as 5–10 mm between respiratory cycles. Motion can also lead to faulty attenuation correction if the patient moves after generation of the tissue density map.

To address this issue, ECG gating is commonly used to generate the image over multiple cardiac cycles. Respiratory gating is also sometimes employed. However, both come at the cost of increased noise (expressed as signal to noise ratio, SNR) which results from the rejection of too many beats in a short interval [30]. In addition, gating techniques are not suitable for imaging of rapidly-changing processes such as myocardial blood flow quantification.

The PET/MRI combination has the potential to solve this dilemma by incorporating real-time MRI generated motion data to correct for cardiac, respiratory, and patient motion, as well as to apply the necessary adjustments to the density map prior to AC [31]. Tissue deformation is measured using MRI "tagging," where a sequence of RF pulses is used to create a lattice of magnetization "tags" in the tissue which persist long enough to allow their tracking by MRI as they move. MRI motion correction of PET data has the promise of providing images with excellent spatial resolution without the reduction in SNR that occurs with "stop-motion" ECG gating [31].

13.2.1.4 Magnet Bore and FOV

A consequence of placing the 360 degree PET detector array within the MRI scanner is that the magnet bore is smaller than in a conventional MRI machine (60 cm vs. 70 cm respectively), precluding the imaging of larger patients (Fig. 13.2) [14]. Furthermore, the FOV of the magnet is even smaller, typically 50 cm, which means that in large patients who do fit inside the magnet, peripheral parts of the body may fall outside the magnet FOV (especially when acquisition is performed with the patient's arms at his sides as is frequently the case) and are hence "truncated" (and fail to appear on the Dixon attenuation maps), leading to inaccurate attenuation correction [14]. Proposed solutions to circumvent this issue include utilizing nonspecific PET tracer uptake data from the truncated regions to complete the MRI AC map using a maximum likelihood reconstruction of attenuation and activity (MLAA) algorithm [32] or extending the MRI FOV by applying B_0 homogenization using gradient enhancement (HUGE) [33]. The latter solution is preferable since some tracers are highly specific and do not show significant uptake outside target areas.

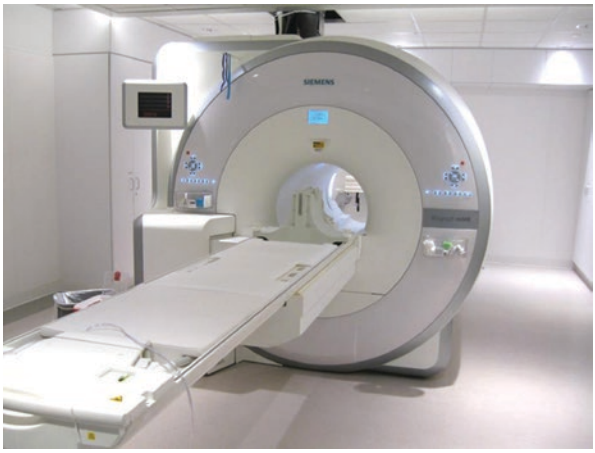

Fig. 13.2 The Siemens biograph hybrid mMR. The white (innermost) circumference represents the PET detectors within the MRI bore (grey bore). (Adjusted and reproduced with permission from Muzic RF, Jr., DiFilippo FP. Positron emission tomography-magnetic resonance imaging: technical review)

13.2.1.5 Software Considerations

While there are no available software packages to date with support for fully integrated PET/MRI data, there are several which can handle fusion and analysis of co-acquired or even separately acquired PET and MRI data, although most are geared toward oncology and are not designed for optimal performance for processing cardiology-specific tasks such as ventricular volume and function calculation, myocardial blood flow estimation, and polar map generation. A technique for integrated analysis of cardiac PET and MRI data using co-registered polar maps and mutual segmentation of myocardial boundaries has recently been developed, which may allow for accurate segmentation and inherent co-registration [34].

In addition, with the amount of information generated by both PET and MRI data as well as the post-generated co-registration and attenuation data among others, the size of the resultant datasets is unusually large, and devising efficient strategies for handling, storing, displaying, and reconstructing these large datasets poses numerous technical challenges.

13.2.2 Patient/Workflow Issues

The long acquisition times required for PET/MRI may be difficult for some patients, especially with breath-hold MRI sequences which require increased patient compliance. Longer scan times also make it more difficult to establish an efficient laboratory workflow, especially in the case of separate MRI and PET machines. Integrated PET/MRI machines offer shorter scanning times, particularly with newer acquisition protocols where redundant/overlapping information is eliminated but is currently limited by availability and technical issues described.

13.2.3 Personnel Issues

The degree of complexity involved in the acquisition, processing, and interpretation of PET/MRI data brings with it the need for highly trained personnel including technologists, physicists, and physicians of multiple disciplines interacting as a team. While there is no formal certification process as of yet for hybrid PET/MRI technologists, the skills involved—aside from operation of the MR scanner—include hotlab work, managing and monitoring the patient after radiotracer administration, as well as any necessary troubleshooting and data post-processing. This entails not only the presence of both a traditional MRI technologist and a nuclear medicine certified technologist, but also that they preferably be dual-trained to optimize seamless integration of the two modalities [35].

13.2.4 Cost

Cost remains a significant barrier to widespread clinical acceptance of PET/MRI. PET/MRI scanners are currently approximately twice as expensive as PET/CT scanners [36], a cost which could be prohibitive in many institutions. Further clinical studies are required to establish the cost-effectiveness of PET/MR before widespread application.

13.3 Advantages of PET/MRI

13.3.1 Compared to Separate PET and MRI

Aside from the potential advantage of improved sensitivity and specificity resulting from combining two already accurate modalities, co-acquisition of PET and MRI data, rather than performing each scan separately, offers several benefits. Simultaneous scanning ensures that patient position is preserved between PET and MRI acquisitions, allowing for more accurate co-registration and minimizing alignment artifacts. In addition, the ability to use real-time MRI data for motion correction of PET images offers the promise of improved spatial resolution without compromising SNR. The simultaneous response on PET and MR imaging to a single stimulus, such as adenosine or regadenoson, in myocardial perfusion imaging is also an advantage. Finally, the ability to combine two examinations into one is more comfortable and efficient for patients, and more conducive to a streamlined workflow, particularly with short acquisition protocols.

13.3.2 Compared to PET/CT

The advantages of PET/MRI over its more established counterpart PET/CT relate to the advantages of MRI over CT, namely, the improved temporal resolution, superior

myocardial tissue characterization, and the lack of iodinated contrast and additional ionizing radiation exposure. It is noteworthy that, with the time spent in MR acquisition, PET acquisition time is also increased, allowing for the use of even lower radiotracer concentrations (as low as one half the usual dose), without compromising image quality [37].

Cardiac MRI can also elicit important information similar to cardiovascular PET, such as myocardial blood flow (MBF) and late gadolinium enhancement (LGE) of the myocardium denoting scar or inflammation.

13.4 Applications of PET/MRI in Inflammatory Heart Disease

Integrated or simultaneous PET/MRI is particularly suited for imaging inflammation in the heart due to the ability to combine tissue characterization, and to visualize, measure, and follow disease activity. The prognostic strength of both modalities has made the hybrid approach an appealing tool in the diagnosis and management of complex disease entities such as cardiac sarcoidosis (CS). Other promising targets in inflammatory heart disease include myocarditis and endocarditis. We will discuss each of these in detail below.

13.4.1 Sarcoidosis

13.4.1.1 Background

Sarcoidosis is a multisystem granulomatous inflammatory disease of uncertain etiology. While involvement of the lungs and lymph nodes is most common, sarcoidosis can also affect the heart, occurring anywhere from 5% in those with clinically manifest disease to 80% in imaging series of sarcoidosis patients [38]. Importantly, CS is the most common cause of death in sarcoidosis patients [38]. Detection of CS is critical but challenging, due to the lack of clinical manifestations during the initial stages in the majority of patients. Furthermore, traditional diagnostic techniques such as right ventricular biopsy and echocardiography have poor sensitivity for the detection of CS [39]. Therefore, the need for advanced diagnostic imaging is critical for this patient population. Both cardiac PET and MRI have emerged as important tools for evaluating patients with known or suspected CS. Both tests provide useful information to help establish the diagnosis, determine prognosis, guide management, and follow response to therapy [40]. Below we first discuss each modality, including unique strengths and limitations. We then examine how the combination of PET and MRI together may provide complementary clinical information and add incremental diagnostic and prognostic value in patients with known or suspected CS than each imaging modality alone.

Cardiac PET may be performed for suspected or known CS in the following scenarios: (1) In the presence of known extra-cardiac sarcoidosis and abnormal screening for CS, including electrocardiographic, Holter, or imaging abnormalities, or unexplained palpitations or syncope; (2) the young patient with advanced

conduction system disease, (3) patients with idiopathic VT; or (4) patients with proven CS to follow response to treatment [41]. PET imaging for CS requires two sets of images, a myocardial perfusion image, preferably with PET, and a dedicated cardiac ^{18}F-Fluorodeoxyglucose (FDG) image, to differentiate the diagnostic and prognostic spectrum of CS. FDG is a glucose analogue widely used to assess inflammation. FDG has the unique ability to detect and quantify disease activity at the cardiac and extra-cardiac levels [41]. With the same injection of FDG, a limited whole-body acquisition that includes at a minimum the chest, liver, and spleen is also recommended, as the presence of extra-cardiac disease (Fig. 13.3) is important not only for the diagnosis of CS, but also for prognosis, potential biopsy sites, and for overall management of patients with known or suspected CS. Focal or multifocal myocardial FDG uptake, particularly in the presence of associated perfusion defect(s) (Fig. 13.4) and in the absence of coronary artery disease, is consistent with CS, especially when extra-cardiac activity is present, and warrants consideration of immunosuppressive therapy in the appropriate clinical context [42]. Areas of

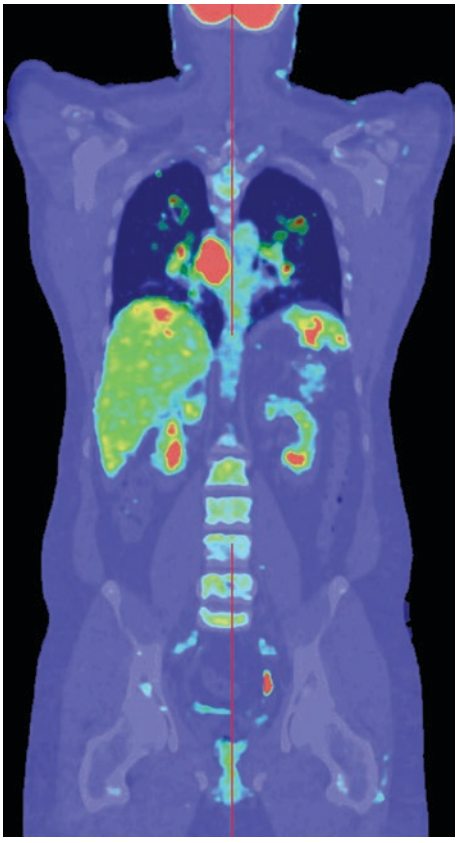

Fig. 13.3 FDG-PET/CT fusion image showing multifocal metabolic activity in the lower neck and chest and lungs, as well as spleen and possibly the right hepatic lobe, compatible with active extra-cardiac sarcoidosis

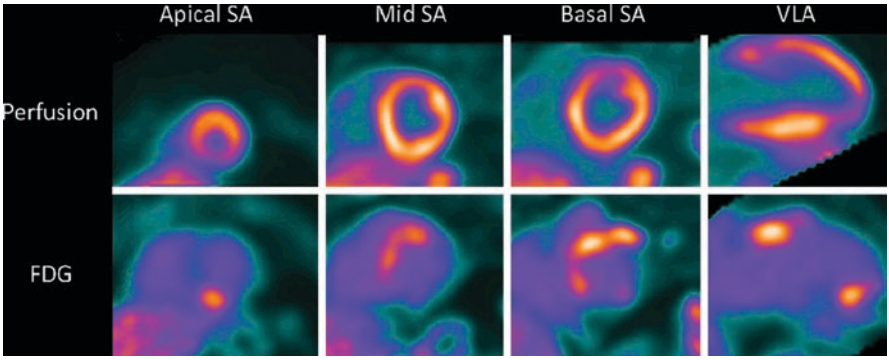

Fig. 13.4 PET perfusion with N13-ammonia (top row) and FDG (bottom row). Left 3 columns: short-axis view showing moderate to severe perfusion abnormalities in the apical inferior, basal anterior and septal segments with corresponding focal myocardial FDG uptake in the same segments. Right column: Vertical long-axis view showing perfusion defect in basal anterior segment and apex, with corresponding FDG uptake. Results compatible with active cardiac sarcoidosis

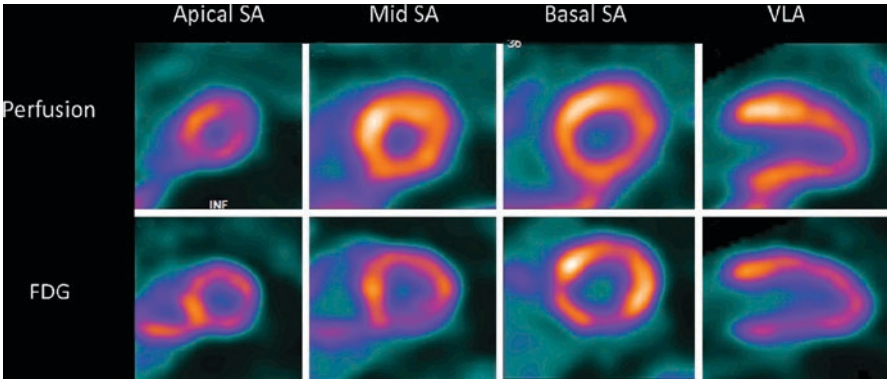

Fig. 13.5 PET perfusion with N13-ammonia (top row) and FDG (bottom row). Left 3 columns: short-axis view, right column: vertical long-axis view. Diffuse (physiologic) FDG uptake is observed, secondary to suboptimal patient preparation

fibrosis are more difficult to identify by PET than by MRI but may include a perfusion defect without associated FDG uptake. A limitation of FDG is that glucose also serves as an energy substrate for the myocardium and nonspecific physiological myocardial FDG uptake (Fig. 13.5) can occur despite adequate patient preparation with high-fat, low carbohydrate meals and/or prolonged fasting. Another useful feature of cardiac PET is the ability to quantify FDG uptake which is particularly suitable for serial imaging to follow the effects of treatment. The prognostic value of cardiac PET in CS has also been demonstrated in several observational studies. Blankstein et al. demonstrated that patients with both a perfusion defect and abnormal FDG uptake had a fourfold risk of death or ventricular arrhythmia [43]. Sperry

et al. corroborated these findings by showing that patients with abnormal FDG-PET were more likely to meet the same composite endpoint [44]. Total cardiac metabolic activity (tCMA), LV standardized-uptake-value (SUV) max, pathological right ventricular FDG uptake were specific markers shown in a number of studies [43, 45, 46] to correlate with the rate of adverse cardiac events, and their interval improvement on serial studies was found to be associated with reduction of adverse cardiac event risk [47].

MRI is powerful in its ability to provide detailed tissue characterization and cardiac morphology, in addition to accurate assessments of cardiac function [9]. A typical MRI protocol for cardiac sarcoidosis commences with a localizer scan followed by balanced steady-state free procession imaging to assess cardiac chamber size and function. Short-axis T2-weighted, fat-suppressed imaging is then performed to assess for the presence of edema (representing inflammation). Next intravenous gadolinium is administered, and first past resting perfusion imaging is assessed. Finally, delayed enhancement imaging is performed to assess for inflammation and/or scar. Late gadolinium enhancement (LGE) permits visualization of myocardial injury or fibrosis due to CS [40] and is often subepicardial, midmyocardial, and transseptal in location in CS [48]. Fibrosis or scar by MRI LGE is observed more frequently than fibrosis by PET [48]. While myocardial edema signifying inflammation can also be observed as increased T2-weighted signal on MRI, this approach is technically challenging and continues to have difficulties in differentiating between active disease (inflammation) and scar in CS. As shown in Fig. 13.6, an area of transmural LGE in the basal lateral aneurysm was initially thought to represent scar but FDG-PET demonstrated activity consistent with inflammation in a substantial portion of the area of LGE. Another drawback of MRI is its limitations in detecting extra-cardiac disease, which is necessary to diagnose CS via the clinical pathway of most diagnostic algorithms [49, 50]. Complementary to PET, however, MRI has the major advantage of assessing for alternative diagnoses to CS, which also has important diagnostic and prognostic implications [51]. In regard to prognosis, more studies are available with MRI than with PET and are consistent in showing that the presence of delayed enhancement portends a substantial increase in the risk of death or appropriate shock from an internal cardiac defibrillator [52]. In a meta-analysis of 694 patients from seven studies, a sixfold increase in the risk of a composite endpoint of mortality or ventricular arrhythmia was observed in the presence of abnormal delayed enhancement [53]. Another similar meta-analysis of 760 patients from ten studies showed an even higher (tenfold) risk of the composite endpoint [54].

Although studies have attempted to determine the diagnostic accuracy of cardiac PET and MRI for CS, these studies were severely limited by the use of the JMHW criteria as the reference standard [55]. A recent meta-analysis [56] that included 17 studies, representing 891 patients, reported a pooled sensitivity of 84% and a pooled specificity of 83% for PET. A similar meta-analysis for CMR [57] reported a pooled sensitivity of 93% and a pooled specificity of 85%. However, these estimates are biased as the lower specificity of PET in some studies may reflect the fact that this test is more sensitive than the JMHW criteria for identifying CS.

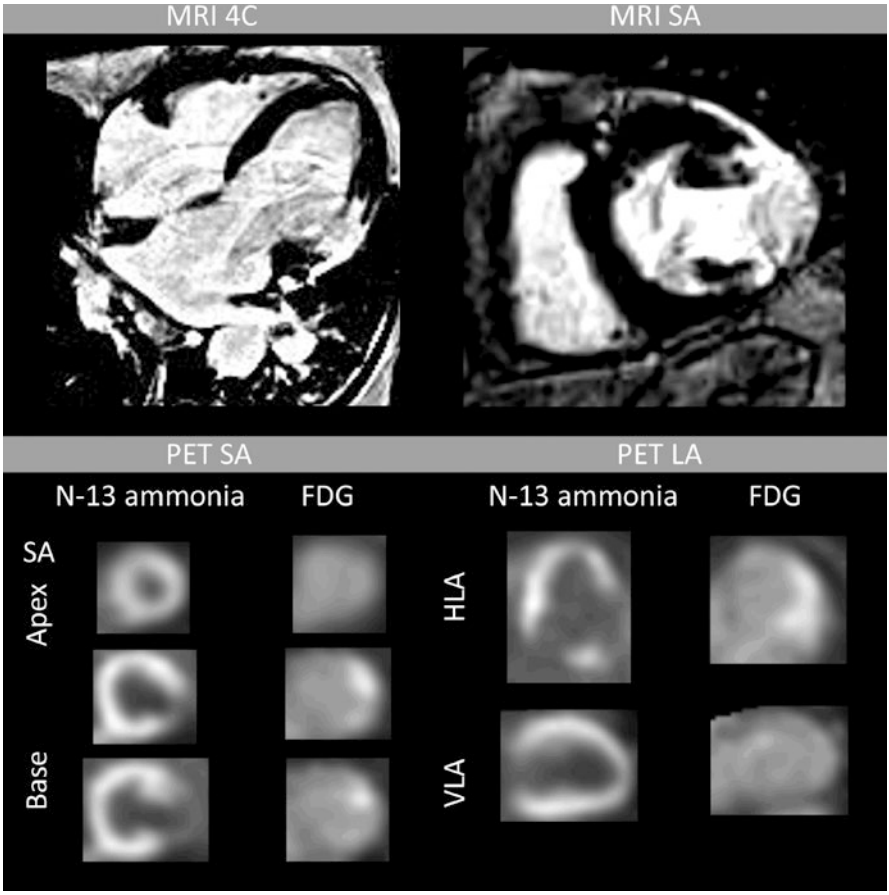

Fig. 13.6 Top: MRI 4-chamber (left) and basal short-axis views (right) showing an aneurysmal basal lateral segment with transmural delayed enhancement denoting scar. Bottom: N-13 ammonia and FDG-PET showing decreased perfusion but intense FDG uptake in the corresponding segment, indicating active inflammation as opposed to scar

The Hybrid Approach

The 2014 HRS expert consensus statement [49] and the Japanese Society of Sarcoidosis [50] recommend performing either CMR or FDG-PET in patients with biopsy-proven extra-cardiac sarcoidosis and suspected CS. The preference of one over the other has been a source of debate, and in practice both modalities are frequently ordered for the same patient owing to the lack of defining features on either and the complementary nature of the information they afford. By conveniently bundling the two, PET/MRI offers a one-stop solution to the conundrum, with emerging evidence to support the hybrid approach over separate PET and MRI [58, 59].

Studies have shown that using the hybrid approach can correctly classify patients missed by using either modality alone, thereby reducing false negatives. Vita et al. showed that including patients with either LGE on MRI or FDG on PET correctly reclassified 36% of patients to a higher or lower likelihood of CS [60].

Wicks et al. [61] supported this finding by demonstrating the superior sensitivity of the hybrid approach compared to either MRI or PET (sensitivity 94% versus 82% and 85% respectively). They went further to show that having abnormalities on both modalities (Fig. 13.7) was the strongest predictor for major adverse cardiac events (Fig. 13.8), highlighting not only the diagnostic but also the prognostic role of the hybrid approach.

Interestingly, the same study found that correlation between the two modalities in terms of the location of abnormalities was actually quite poor (Cohen's kappa: 0.02) [61], although this may simply represent disease progression/regression between scans.

Dweck et al. examined in closer detail the cases where LGE and FDG did not match [62]. In the one patient who had LGE on MRI but no FDG uptake on PET, the clinical scenario was consistent with inactive cardiac sarcoidosis and residual

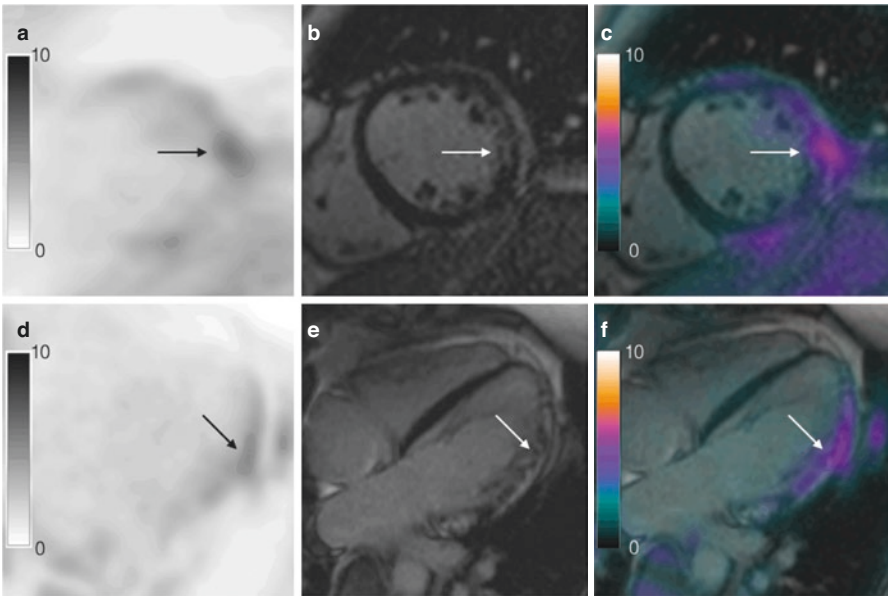

Fig. 13.7 Concordant LGE and FDG uptake on PET/MR images in a patient with biopsy-proven cardiac sarcoidosis in short axis (top row—**a**–**c**) and long axis (bottom row—**d**–**f**). *Left columns*: MIP images depicting lateral FDG uptake (arrow). Middle column: patchy epicardial and mid-myocardial LGE (arrow). Right column: fused images demonstrating corresponding LGE and FDG uptake (arrow). *FDG* fluorodeoxyglucose, *LGE* late gadolinium enhancement, *MIP* maximum intensity projection, *PET* positron emission tomography. (Reproduced with permission from Wicks EC et al. Diagnostic accuracy and prognostic value of simultaneous hybrid ^{18}F-fluorodeoxyglucose positron emission tomography/magnetic resonance imaging in cardiac sarcoidosis)

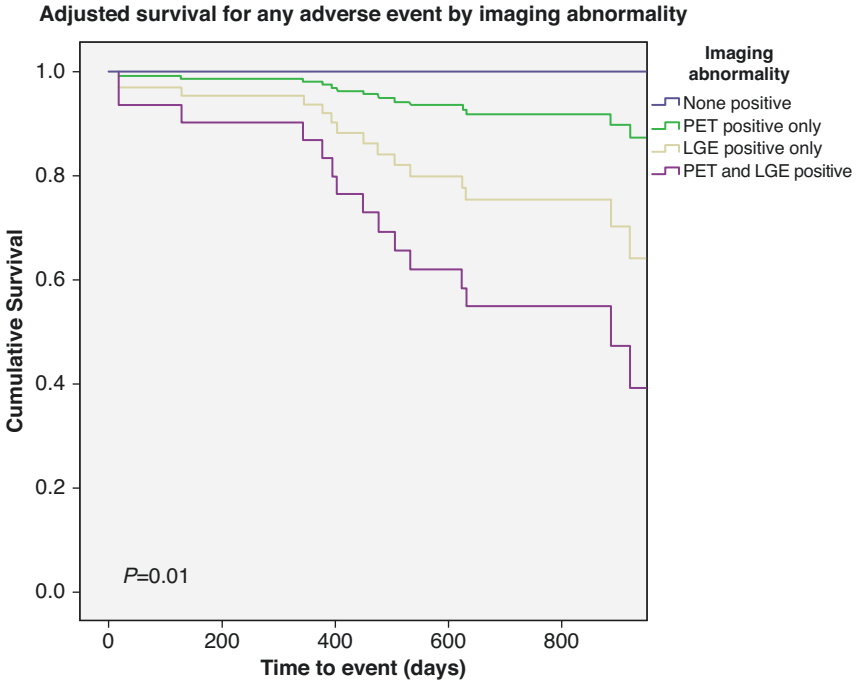

Fig. 13.8 Kaplan-Meier curve showing adjusted survival in cardiac sarcoidosis patients for any adverse event by imaging abnormality after adjustment for age, sex, and LVEF. *LVEF* left ventricle ejection fraction, *LGE* late gadolinium enhancement, *PET* positron emission tomography. (Reproduced with permission from Wicks EC et al. Diagnostic accuracy and prognostic value of simultaneous hybrid ^{18}F-fluorodeoxyglucose positron emission tomography/magnetic resonance imaging in cardiac sarcoidosis)

myocardial scar. Conversely, MRI negative, PET positive patients were compared to a cohort of normal controls, 58% of which also showed the same discrepancy. The authors therefore concluded this was due to failure of physiologic myocardial suppression, including cases with focal on diffuse FDG uptake pattern, which in both groups were localized to the inferolateral wall [62].

13.4.2 Myocarditis

PET/MRI findings in myocarditis are similar to findings in sarcoidosis (Fig. 13.9), namely LGE and increased T2 signal on MRI and increased FDG uptake on PET, with the distinction being mainly based on the clinical context. Several case reports have demonstrated the usefulness of PET/MRI in diagnosing viral myocarditis [63, 64], with a more recent study showing higher detection rates with PET/MRI than either PET or MRI alone, although the study was not sufficiently powered to reach statistical significance [65]. In addition to detection, PET/MRI is useful for

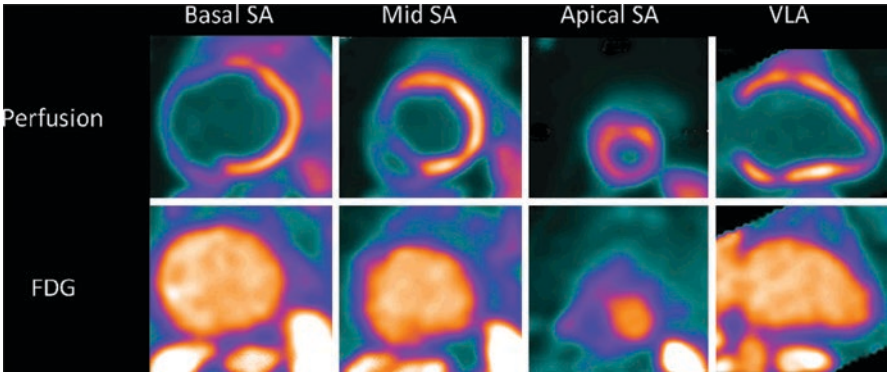

Fig. 13.9 Myocardial FDG-PET of a patient with biopsy-proven giant cell myocarditis "burnt-out" showing a large perfusion defect involving the basal and mid ventricular septal as well as mid ventricular inferior wall with no definitive abnormal FDG uptake

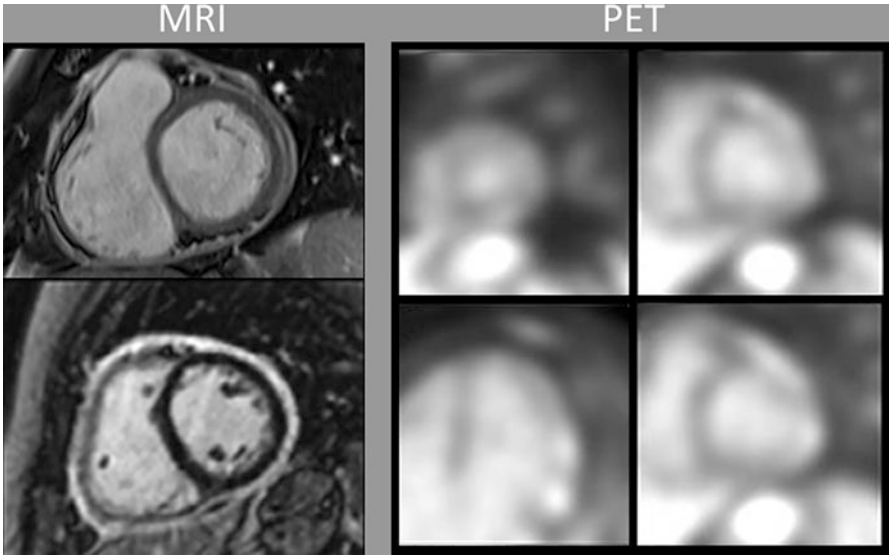

Fig. 13.10 Patient with pericarditis. Left: MRI short-axis views showing significantly increased pericardial thickness (top) with circumferential late gadolinium enhancement (bottom). Right: FDG-PET of the same patient showing intense pericardial FDG uptake. PET views clockwise from top left: apical short axis, mid-short axis, basal short axis, horizontal long axis

monitoring disease activity, response to therapy, and distinguishing between the acute and chronic/persistent variants of myocarditis.

Pericarditis (Fig. 13.10) is often associated with myocarditis (perimyocarditis), and while there is a paucity of literature on the role of PET/MRI in the diagnosis, a recent study has demonstrated feasibility and potential usefulness [66].

13.4.3 Endocarditis

Endocarditis is a dreaded complication affecting prosthetic and native heart valves alike. While transesophageal echocardiography (TEE) shows excellent sensitivity for the detection of the disease in native valves (as high as 92% in some studies) [67], it may not be able to detect the sequelae of the disease in prosthetic heart valves. In these patients, FDG-PET can detect valvular and perivalvular inflammation at an early stage and, when combined with CT, has a higher sensitivity than TEE or multidetector CT angiography (83% vs 75% for both) [68].

MRI can visualize prosthetic valve morphology and identify flow abnormalities as well as annular dehiscence [69], although metal extinction artifacts can significantly interfere with image quality and, in the case of PET/MRI, be incorporated into attenuation correction maps leading to PET tracer uptake underestimation. Data on integrated PET/MR imaging of infective endocarditis patients is lacking, but an ongoing study might hopefully shed some light once completed [70].

13.4.4 Atherosclerotic Plaque Risk Stratification

PET has recently been used to image and risk-stratify inflammation in the aortic valve [71, 72] and arterial atherosclerotic plaques [73], and MRI's tissue characterization makes it an ideal adjunct to PET in that regard since the combination can provide both accurate morphological information on plaque composition as well as visualization of relevant biological processes such as inflammation or neovascularization.

In a more recent study, coronary artery imaging was successfully performed using hybrid PET/MRI with either FDG or the novel radiotracer ^{18}F-NaF, and was able to demonstrate elevated radiotracer uptake localized to individual coronary lesions [74].

This is an attractive prospect since acute complications of atherosclerosis frequently occur in the absence of significant luminal occlusive disease, with no single marker for what constitutes an "unstable" plaque but rather an incompletely understood interplay between a multitude of factors. With MRI's safety profile and the potential for whole-body imaging, atherosclerosis imaging of the entire vascular tree could soon become a reality.

13.4.5 Preclinical Applications

PET/MRI has tremendous potential to help further our understanding of various biological and pathological processes. With the availability of integrated PET/MR scanners for animal models and novel radiotracers being continually developed which can map new molecular and cellular markers and/or even deliver treatment, PET/MRI has become an attractive target for preclinical research. A number of trials are already ongoing which hold exciting prospects (see Sect. 13.7).

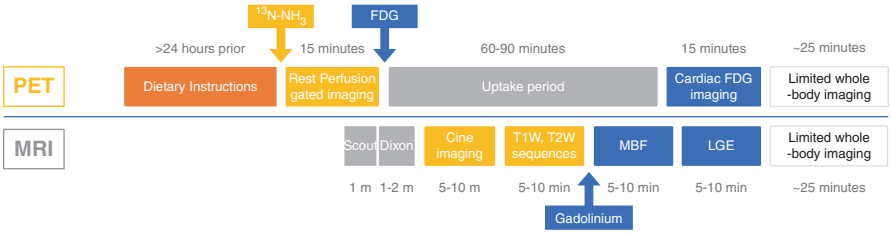

Fig. 13.11 Hybrid PET/MRI inflammation imaging protocol. For PET, ^{13}N-NH$_3$ is administered followed by rest perfusion imaging and MBF. FDG is then administered and inflammation imaging is performed, followed by limited whole-body imaging for extra-cardiac disease. For MRI, after the initial scouting images and Dixon attenuation sequencing, Cine MRI images are obtained followed by T1 + T2 mapping. Gadolinium is then administered, followed by perfusion imaging/MBF (this step can potentially be skipped in favor of PET perfusion alone) and LGE mapping, then limited whole-body imaging for extra-cardiac co-localization. T2 weighted sequences and T1 and T2 mapping could potentially be dropped for hybrid acquisition, and similarly gating information can be acquired from MRI only. *MBF* myocardial blood flow, *LGE* late gadolinium enhancement

13.5 Acquisition Protocol and Patient Preparation

13.5.1 Inflammation Protocol

Normal myocardium exhibits some degree of physiological glucose avidity through GLUT4 transporters activated by insulin in response to dietary glucose intake. Inflammation imaging with FDG-PET requires that myocardial metabolism be shifted from glucose utilization to almost exclusive fatty acid consumption, ensuring that any subsequent FDG uptake will be by abnormal, inflamed tissues in which glucose (or FDG) can enter through the constitutively expressed GLUT1 and GLUT3 transporters. FDG is then phosphorylated intracellularly and hence trapped, enabling metabolic imaging by PET [75].

Myocardial glucose suppression can be achieved by prolonged (12–18 h) fasting or high-fat low-carbohydrate (HFLC) diet, with a combination of the two shown to be superior at suppressing physiological myocardial FDG uptake [76]. Based on expert consensus [41] and clinical experience, we recommend at least a 1-day high-fat, low-carbohydrate diet followed by a 12–15 h fast for optimal myocardial suppression, with up to a 91% success rate [41].

A proposed protocol for inflammation imaging by hybrid PET/MRI is outlined in Fig. 13.11 [77].

13.6 Study Interpretation and Reporting

These suggestions are based in part on the ESCR and EANM guidelines with modifications by the authors [77]. The guidelines recommend a unified report for hybrid PET/MR findings, but in practice reimbursement policies require two separate CPT codes for PET and MRI (there is yet to be a CPT code for hybrid

PET/MRI), often each with separate pre-authorizations, which may entail the writing of two separate reports which can reference each other's findings. Patient name, age, weight, and height should be reported, along with a brief medical history. Any relevant patient preparation should be described (see Sect. 13.5). The type and dose of any drug used (e.g. vasodilators) should be specified. For radiotracers, the name, route, and time of administration and amount of activity in MBq should be listed. Time interval between radiotracer administration and acquisition should be noted, and details on the PET/MR equipment should be included along with a short description of the protocol used. The dose of gadolinium administered—if any—should be indicated.

The location, extent, and degree of perfusion defects both on PET and MRI as well as abnormal myocardial FDG uptake on PET and LGE on MRI should be reported in accordance with standardized references [78]. The degree of abnormal FDG uptake should be classified as mild, moderate, or intense, and supported with quantitative measures when applicable (e.g. SUV, perfusion in mL/min/g). The span of LGE should be noted as subendocardial, mid-myocardial, subepicardial, or transmural. For the cardiac MRI examination, the standard components, EDV, ESV, SV, EF, CO, and CI should be reported, along with any abnormal increased wall thickness, focal wall thinning, or wall motion abnormality at rest. If there are other imaging studies or previous PET/MRI exams, then they should be used for comparison and the discrepancies/similarities reported.

Finally, caveats should be noted when present which might adversely affect exam accuracy such as significant patient motion or extra-cardiac radiotracer uptake interference.

The report summary should include overall normality/abnormality of the study, along with a final diagnosis if possible. The referring physician's specific questions should be clearly answered. Approval of the interpreting physicians should be documented together with communication of urgent findings to the referring physician.

13.7 Future Directions

The long scan times in PET/MRI are a source of significant discomfort for some patients. As our understanding of the information provided by PET/MRI evolves, overlapping and redundant information can be identified and shed from acquisition protocols to save time and cost. Achieving this objective will pave the way for yet another future target: PET/MR whole-body imaging, which can revolutionize our conception of "cardiac" diseases once thought to be localized to the heart.

On a different note, the concept of multifunctional molecular imaging agents which can be used to perform PET acquisition, deliver targeted therapy, and at the same time act as an MR probe to detect treatment response is arguably one of the most compelling future directions of PET/MR research [79], and has the potential to transform PET/MR from a mere imaging modality to a therapeutic intervention.

To conclude, PET/MRI is an exciting new modality which has demonstrated a great deal of potential, but the ultimate judge of whether a technology will persist is its ability to influence patient outcomes. Such data is still lacking for PET/MRI, and future studies will be required to determine whether the added benefit of hybrid PET/MRI is worth the associated economic cost.

References

1. Jones T, Townsend D. History and future technical innovation in positron emission tomography. J Med Imaging (Bellingham). 2017;4:011013.
2. Shukla AK, Kumar U. Positron emission tomography: an overview. J Med Phys. 2006; 31:13–21.
3. Levin DN, Pelizzari CA, Chen GT, Chen CT, Cooper MD. Retrospective geometric correlation of MR, CT, and PET images. Radiology. 1988;169:817–23.
4. Dilsizian V, Bacharach SL, Beanlands RS, et al. ASNC imaging guidelines/SNMMI procedure standard for positron emission tomography (PET) nuclear cardiology procedures. J Nucl Cardiol. 2016;23:1187–226.
5. Chow BJ, Wells GA, Chen L, et al. Prognostic value of 64-slice cardiac computed tomography severity of coronary artery disease, coronary atherosclerosis, and left ventricular ejection fraction. J Am Coll Cardiol. 2010;55:1017–28.
6. Shawgi M, Arumugam P. Looking outside the "cardiac" box: incidental detection of a metastatic lung tumor on cardiac position emission tomography/computed tomography. World J Nucl Med. 2014;13:197–200.
7. Edelman RR. The history of MR imaging as seen through the pages of radiology. Radiology. 2014;273:S181–200.
8. Hendrick RE. Spatial resolution in magnetic resonance imaging. In: Hendrick RE, editor. Breast MRI: fundamentals and technical aspects. New York, NY: Springer; 2008. p. 31–45.
9. McMahon KL, Cowin G, Galloway G. Magnetic resonance imaging: the underlying principles. J Orthop Sports Phys Ther. 2011;41:806–19.
10. Boxt L, Abbara S, Miller S. Cardiac imaging: the requisites. 3rd ed. Amsterdam: Elsevier; 2018.
11. Hamilton-Craig CR, Strudwick MW, Galloway GJ. T1 mapping for myocardial fibrosis by cardiac magnetic resonance relaxometry-a comprehensive technical review. Front Cardiovasc Med. 2016;3:49.
12. Garlick PB, Marsden PK, Cave AC, et al. PET and NMR dual acquisition (PANDA): applications to isolated, perfused rat hearts. NMR Biomed. 1997;10:138–42.
13. Delso G, Furst S, Jakoby B, et al. Performance measurements of the Siemens mMR integrated whole-body PET/MR scanner. J Nucl Med. 2011;52:1914–22.
14. Muzic RF Jr, DiFilippo FP. Positron emission tomography-magnetic resonance imaging: technical review. Semin Roentgenol. 2014;49:242–54.
15. Hofmann M, Steinke F, Scheel V, et al. MRI-based attenuation correction for PET/MRI: a novel approach combining pattern recognition and atlas registration. J Nucl Med. 2008; 49:1875–83.
16. Kops ER, Herzog H. Alternative methods for attenuation correction for PET images in MR-PET scanners. In: IEEE Conference 26 Oct.-3 Nov. 2007, Honolulu, HI, USA. Washington, DC: IEEE; 2007. https://doi.org/10.1109/NSSMIC.2007.4437073.
17. Kops ER, Qin P, Müller-Veggian M, Herzog H. MRI based attenuation correction for brain PET images. In: Advances in medical engineering. Springer proceedings in physics, vol. 114. Berlin: Springer; 2007. p. 93–7.
18. Eiber M, Martinez-Moller A, Souvatzoglou M, et al. Value of a Dixon-based MR/PET attenuation correction sequence for the localization and evaluation of PET-positive lesions. Eur J Nucl Med Mol Imaging. 2011;38:1691–701.

19. Lau JMC, Laforest R, Sotoudeh H, et al. Evaluation of attenuation correction in cardiac PET using PET/MR. J Nucl Cardiol. 2017;24:839–46.
20. Samarin A, Burger C, Wollenweber SD, et al. PET/MR imaging of bone lesions--implications for PET quantification from imperfect attenuation correction. Eur J Nucl Med Mol Imaging. 2012;39:1154–60.
21. Paulus DH, Quick HH, Geppert C, et al. Whole-body PET/MR imaging: quantitative evaluation of a novel model-based MR attenuation correction method including bone. J Nucl Med. 2015;56:1061–6.
22. Keereman V, Fierens Y, Broux T, De Deene Y, Lonneux M, Vandenberghe S. MRI-based attenuation correction for PET/MRI using ultrashort echo time sequences. J Nucl Med. 2010;51:812–8.
23. Chen Y, An H. Attenuation Correction of PET/MR Imaging. Magn Reson Imaging Clin N Am. 2017;25:245–55.
24. Juttukonda MR, Mersereau BG, Chen Y, et al. MR-based attenuation correction for PET/MRI neurological studies with continuous-valued attenuation coefficients for bone through a conversion from R2* to CT-Hounsfield units. NeuroImage. 2015;112:160–8.
25. MacDonald LR, Kohlmyer S, Liu C, Lewellen TK, Kinahan PE. Effects of MR surface coils on PET quantification. Med Phys. 2011;38:2948–56.
26. Delso G, Martinez-Moller A, Bundschuh RA, et al. Evaluation of the attenuation properties of MR equipment for its use in a whole-body PET/MR scanner. Phys Med Biol. 2010;55:4361–74.
27. Kartmann R, Paulus DH, Braun H, et al. Integrated PET/MR imaging: automatic attenuation correction of flexible RF coils. Med Phys. 2013;40:082301.
28. Sureau FC, Reader AJ, Comtat C, et al. Impact of image-space resolution modeling for studies with the high-resolution research tomograph. J Nucl Med. 2008;49:1000–8.
29. Blume M, Navab N, Rafecas M. Joint image and motion reconstruction for PET using a B-spline motion model. Phys Med Biol. 2012;57:8249–70.
30. Petibon Y, Ouyang J, Zhu X, et al. Cardiac motion compensation and resolution modeling in simultaneous PET-MR: a cardiac lesion detection study. Phys Med Biol. 2013;58:2085–102.
31. Ouyang J, Li Q, El Fakhri G. Magnetic resonance-based motion correction for positron emission tomography imaging. Semin Nucl Med. 2013;43:60–7.
32. Nuyts J, Bal G, Kehren F, Fenchel M, Michel C, Watson C. Completion of a truncated attenuation image from the attenuated PET emission data. IEEE Trans Med Imaging. 2013;32:237–46.
33. Blumhagen JO, Ladebeck R, Fenchel M, Scheffler K. MR-based field-of-view extension in MR/PET: B0 homogenization using gradient enhancement (HUGE). Magn Reson Med. 2013;70:1047–57.
34. Nensa F, Poeppel TD, Tezgah E, et al. Integrated assessment of cardiac PET/MRI: co-registered PET and MRI polar plots by mutual MR-based segmentation of the left ventricular myocardium. World J Cardiovasc Dis. 2017;07:91–104.
35. Parikh N, Friedman KP, Shah SN, Chandarana H. Practical guide for implementing hybrid PET/MR clinical service: lessons learned from our experience. Abdom Imaging. 2015;40:1366–73.
36. Nappi C, El Fakhri G. State of the art in cardiac hybrid technology: PET/MR. Curr Cardiovasc Imaging Rep. 2013;6:338–45.
37. Oehmigen M, Ziegler S, Jakoby BW, Georgi JC, Paulus DH, Quick HH. Radiotracer dose reduction in integrated PET/MR: implications from national electrical manufacturers association phantom studies. J Nucl Med. 2014;55:1361–7.
38. Silverman KJ, Hutchins GM, Bulkley BH. Cardiac sarcoid: a clinicopathologic study of 84 unselected patients with systemic sarcoidosis. Circulation. 1978;58:1204–11.
39. From AM, Maleszewski JJ, Rihal CS. Current status of endomyocardial biopsy. Mayo Clin Proc. 2011;86:1095–102.
40. Ishimaru S, Tsujino I, Sakaue S, et al. Combination of 18F-fluoro-2-deoxyglucose positron emission tomography and magnetic resonance imaging in assessing cardiac sarcoidosis. Sarcoidosis Vasc Diffuse Lung Dis. 2005;22:234–5.

41. Chareonthaitawee P, Beanlands RS, Chen W, et al. Joint SNMMI-ASNC expert consensus document on the role of (18)F-FDG PET/CT in cardiac sarcoid detection and therapy monitoring. J Nucl Med. 2017;58:1341–53.
42. Bravo PE, Singh A, Di Carli MF, Blankstein R. Advanced cardiovascular imaging for the evaluation of cardiac sarcoidosis. J Nucl Cardiol. 2019;26:188–99.
43. Blankstein R, Osborne M, Naya M, et al. Cardiac positron emission tomography enhances prognostic assessments of patients with suspected cardiac sarcoidosis. J Am Coll Cardiol. 2014;63:329–36.
44. Sperry BW, Tamarappoo BK, Oldan JD, et al. Prognostic impact of extent, severity, and heterogeneity of abnormalities on (18)F-FDG PET scans for suspected cardiac sarcoidosis. JACC Cardiovasc Imaging. 2018;11:336–45.
45. Ahmadian A, Brogan A, Berman J, et al. Quantitative interpretation of FDG PET/CT with myocardial perfusion imaging increases diagnostic information in the evaluation of cardiac sarcoidosis. J Nucl Cardiol. 2014;21:925–39.
46. Tuominen H, Haarala A, Tikkakoski A, Kahonen M, Nikus K, Sipila K. FDG-PET in possible cardiac sarcoidosis: right ventricular uptake and high total cardiac metabolic activity predict cardiovascular events. J Nucl Cardiol. 2021;28:199.
47. Muser D, Santangeli P, Castro SA, et al. Prognostic role of serial quantitative evaluation of (18) F-fluorodeoxyglucose uptake by PET/CT in patients with cardiac sarcoidosis presenting with ventricular tachycardia. Eur J Nucl Med Mol Imaging. 2018;45:1394–404.
48. Sharma S. Cardiac imaging in myocardial sarcoidosis and other cardiomyopathies. Curr Opin Pulm Med. 2009;15:507–12.
49. Birnie DH, Sauer WH, Bogun F, et al. HRS expert consensus statement on the diagnosis and management of arrhythmias associated with cardiac sarcoidosis. Heart Rhythm. 2014;11:1305–23.
50. Terasaki F, Yoshinaga K. New guidelines for diagnosis of cardiac sarcoidosis in Japan. Ann Nucl Cardiol. 2017;3:42–5.
51. Cain MA, Metzl MD, Patel AR, et al. Cardiac sarcoidosis detected by late gadolinium enhancement and prevalence of atrial arrhythmias. Am J Cardiol. 2014;113:1556–60.
52. Greulich S, Deluigi CC, Gloekler S, et al. CMR imaging predicts death and other adverse events in suspected cardiac sarcoidosis. JACC Cardiovasc Imaging. 2013;6:501–11.
53. Hulten E, Agarwal V, Cahill M, et al. Presence of late gadolinium enhancement by cardiac magnetic resonance among patients with suspected cardiac sarcoidosis is associated with adverse cardiovascular prognosis: a systematic review and meta-analysis. Circ Cardiovasc Imaging. 2016;9:e005001.
54. Coleman GC, Shaw PW, Balfour PC Jr, et al. Prognostic value of myocardial scarring on CMR in patients with cardiac sarcoidosis. JACC Cardiovasc Imaging. 2017;10:411–20.
55. Youssef G, Leung E, Mylonas I, et al. The use of 18F-FDG PET in the diagnosis of cardiac sarcoidosis: a systematic review and metaanalysis including the Ontario experience. J Nucl Med. 2012;53:241.
56. Kim SJ, Pak K, Kim K. Diagnostic performance of F-18 FDG PET for detection of cardiac sarcoidosis; a systematic review and meta-analysis. J Nucl Cardiol. 2020;27:2103.
57. Zhang J, Li Y, Xu Q, Xu B, Wang H. Cardiac magnetic resonance imaging for diagnosis of cardiac sarcoidosis: a meta-analysis. Can Respir J. 2018;2018:7457369.
58. Schneider S, Batrice A, Rischpler C, Eiber M, Ibrahim T, Nekolla SG. Utility of multimodal cardiac imaging with PET/MRI in cardiac sarcoidosis: implications for diagnosis, monitoring and treatment. Eur Heart J. 2014;35:312.
59. Nensa F, Tezgah E, Poeppel T, Nassenstein K, Schlosser T. Diagnosis and treatment response evaluation of cardiac sarcoidosis using positron emission tomography/magnetic resonance imaging. Eur Heart J. 2015;36:550.
60. Vita T, Okada DR, Veillet-Chowdhury M, et al. Complementary value of cardiac magnetic resonance imaging and positron emission tomography/computed tomography in the assessment of cardiac sarcoidosis. Circ Cardiovasc imaging. 2018;11:e007030.

61. Wicks EC, Menezes LJ, Barnes A, et al. Diagnostic accuracy and prognostic value of simultaneous hybrid 18F-fluorodeoxyglucose positron emission tomography/magnetic resonance imaging in cardiac sarcoidosis. Eur Heart J Cardiovasc Imaging. 2018;19:757–67.
62. Dweck MR, Abgral R, Trivieri MG, et al. Hybrid magnetic resonance imaging and positron emission tomography with fluorodeoxyglucose to diagnose active cardiac sarcoidosis. JACC Cardiovasc Imaging. 2018;11:94–107.
63. von Olshausen G, Hyafil F, Langwieser N, Laugwitz KL, Schwaiger M, Ibrahim T. Detection of acute inflammatory myocarditis in Epstein Barr virus infection using hybrid 18F-fluorodeoxyglucose-positron emission tomography/magnetic resonance imaging. Circulation. 2014;130:925–6.
64. Nensa F, Poeppel TD, Krings P, Schlosser T. Multiparametric assessment of myocarditis using simultaneous positron emission tomography/magnetic resonance imaging. Eur Heart J. 2014;35:2173.
65. Hanneman K, Kadoch M, Guo HH, et al. Initial experience with simultaneous 18F-FDG PET/MRI in the evaluation of cardiac sarcoidosis and myocarditis. Clin Nucl Med. 2017;42:e328–34.
66. Xu B, Huang SS, Jellis C, Flamm SD. Diagnosis of active pericarditis by positron emission tomography (PET)/cardiac magnetic resonance (CMR) imaging. Eur Heart J. 2018;39:179.
67. Shively BK, Gurule FT, Roldan CA, Leggett JH, Schiller NB. Diagnostic value of transesophageal compared with transthoracic echocardiography in infective endocarditis. J Am Coll Cardiol. 1991;18:391–7.
68. Gomes A, van Geel PP, Santing M, et al. Imaging infective endocarditis: adherence to a diagnostic flowchart and direct comparison of imaging techniques. J Nucl Cardiol. 2020; 27:592–608.
69. Pham N, Zaitoun H, Mohammed TL, et al. Complications of aortic valve surgery: manifestations at CT and MR imaging. Radiographics. 2012;32:1873–92.
70. ClinicalTrials.gov. PET/MR imaging in patients with infective endocarditis; 2018.
71. Chin CW, Pawade TA, Newby DE, Dweck MR. Risk stratification in patients with aortic stenosis using novel imaging approaches. Circ Cardiovasc Imaging. 2015;8:e003421.
72. Dweck MR, Boon NA, Newby DE. Calcific aortic stenosis: a disease of the valve and the myocardium. J Am Coll Cardiol. 2012;60:1854–63.
73. Rudd JH, Warburton EA, Fryer TD, et al. Imaging atherosclerotic plaque inflammation with [18F]-fluorodeoxyglucose positron emission tomography. Circulation. 2002;105:2708–11.
74. Robson PM, Dweck MR, Trivieri MG, et al. Coronary artery PET/MR imaging: feasibility, limitations, and solutions. JACC Cardiovasc Imaging. 2017;10:1103–12.
75. Mochizuki T, Tsukamoto E, Kuge Y, et al. FDG uptake and glucose transporter subtype expressions in experimental tumor and inflammation models. J Nucl Med. 2001;42:1551–5.
76. Christopoulos G, Jouni H, Acharya GA, et al. Suppressing physiologic 18-fluorodeoxyglucose uptake in patients undergoing positron emission tomography for cardiac sarcoidosis: the effect of a structured patient preparation protocol. J Nucl Cardiol. 2021;28:661.
77. Nensa F, Bamberg F, Rischpler C, et al. Hybrid cardiac imaging using PET/MRI: a joint position statement by the European Society of Cardiovascular Radiology (ESCR) and the European Association of Nuclear Medicine (EANM). Eur Radiol. 2018;28:4086–101.
78. Cerqueira MD, Weissman NJ, Dilsizian V, et al. Standardized myocardial segmentation and nomenclature for tomographic imaging of the heart. A statement for healthcare professionals from the Cardiac Imaging Committee of the Council on Clinical Cardiology of the American Heart Association. Circulation. 2002;105:539–42.
79. Majmudar MD, Keliher EJ, Heidt T, et al. Monocyte-directed RNAi targeting CCR2 improves infarct healing in atherosclerosis-prone mice. Circulation. 2013;127:2038–46.

Innovations in Cardiovascular MR and PET-MR Imaging

14

Camila Munoz, Gastao Cruz, Claudia Prieto, and René M. Botnar

14.1 Introduction

Cardiac magnetic resonance (MR) and positron emission tomography (PET) imaging have been areas of active research for over three decades. Throughout this time, technical advances in scanner hardware, data acquisition, and image reconstruction techniques have resulted in the clinical adoption of cardiac MR and PET examinations for the assessment of a wide range of cardiovascular diseases.

Conventional cardiac MR and PET imaging have focused on the depiction of the cardiac anatomy and characterization of myocardial function. In clinical practice, both PET and MR images are typically analysed qualitatively, by looking at areas of higher or lower signal intensity in the images as compared to surrounding healthy tissue. However, recently proposed techniques for MR-based tissue characterization and novel target specific PET radiotracers have encouraged a change in the way images are acquired and analysed, moving towards more objective, reproducible, and quantitative cardiovascular imaging. These advanced techniques have great potential to enable early detection of cardiovascular diseases, and accurate quantification of disease progression and therapy response.

Moreover, the introduction of hybrid PET-MR systems in the early 2010s has opened new possibilities for the simultaneous acquisition of complementary information with both imaging modalities, showing promising results for a comprehensive assessment of the cardiovascular system, and potentially improving patient care. This chapter describes state-of-the-art and emerging methods for cardiac MR and PET-MR imaging, highlighting the trends of current research and discussing some their potential for clinical translation.

C. Munoz (✉) · G. Cruz · C. Prieto · R. M. Botnar
School of Biomedical Engineering and Imaging Sciences, King's College London, London, UK
e-mail: camila.munoz@kcl.ac.uk; rene.botnar@kcl.ac.uk

S. G. Nekolla, C. Rischpler (eds.), *Hybrid Cardiac Imaging*,
https://doi.org/10.1007/978-3-030-83167-7_14

14.2 Innovations in Cardiac MR: Quantitative Cardiac MRI

Conventionally, image contrast in cardiac MR is determined by optimal sequence parameters, such that disease appears as a hyper-intense or hypo-intense area in the image compared to surrounding healthy tissue. While this approach can been successfully applied when disease is focal and there is enough healthy tissue for comparison purposes, it does not allow to relate the changes in image contrast to the severity of the disease, and it results in a decreased sensitivity to diffuse disease or global changes in tissue characteristics.

More recently, approaches that allow the measurement of intrinsic tissue properties, such as longitudinal relaxation (T_1) or transverse relaxation (T_2), have been proposed for truly quantitative cardiac imaging [1]. These techniques, usually known as tissue parameter mapping or relaxometry techniques, have opened new possibilities for objective tissue characterization, early detection of disease, and improved monitoring of disease progression. This section summarizes established quantitative cardiac MR techniques, including conventional cardiac T_1 and T_2 mapping, and describes some novel techniques for multi-parametric mapping.

14.2.1 Cardiac T_1 and T_2 mapping

T_1 and T_2 relaxation times are key physical properties that play a central role in differentiating healthy from diseased tissue in cardiac MR. As such, these relaxation times are viable biomarkers for disease and have recently emerged as a solution for objective and quantitative tissue characterization. T_1 mapping has been shown to be sensitive to most cardiomyopathies, including myocardial infarction, amyloidosis, and diffuse fibrosis [2], while T_2 mapping has shown value in diagnosing myocarditis, iron overload, and heart transplant rejection, among others. One of the major challenges in cardiac parametric mapping is dealing with physiological (respiratory and cardiac) motion, which must be accounted for in order to avoid errors in the parameter maps.

Conventional myocardial T_1 mapping is generally achieved with 2D breath-held, cardiac triggered sequences. The two most popular approaches are the modified Look-Locker inversion recovery (MOLLI) [3] and the saturation recovery single-shot acquisition (SASHA) [4].

MOLLI encodes T_1 information using a 180° inversion recovery (IR) pulse, acquiring images with different T_1 weightings that are then fitted to an exponential model in order to estimate T_1 values for each pixel in the image. The conventional MOLLI sequence uses a first IR pulse and acquires data over multiple heartbeats. After this, a period of typically three heartbeats without data acquisition follows, allowing the magnetization to return nearly to equilibrium. Another IR pulse is then used, but the data acquisition takes place at a different inversion delay times (TI), effectively sampling new data points along the longitudinal relaxation (Fig. 14.1a). The set of inversion-weighted images are re-sorted by TI and fitted to the equation $M_z(\mathrm{TI}) = A - B\exp\left(-\mathrm{TI}/T_1^*\right)$, where T_1^* is an underestimated apparent T_1, related to the actual T_1 by the expression $T_1 = T_1^*\left(B/A - 1\right)$. MOLLI produces precise T_1

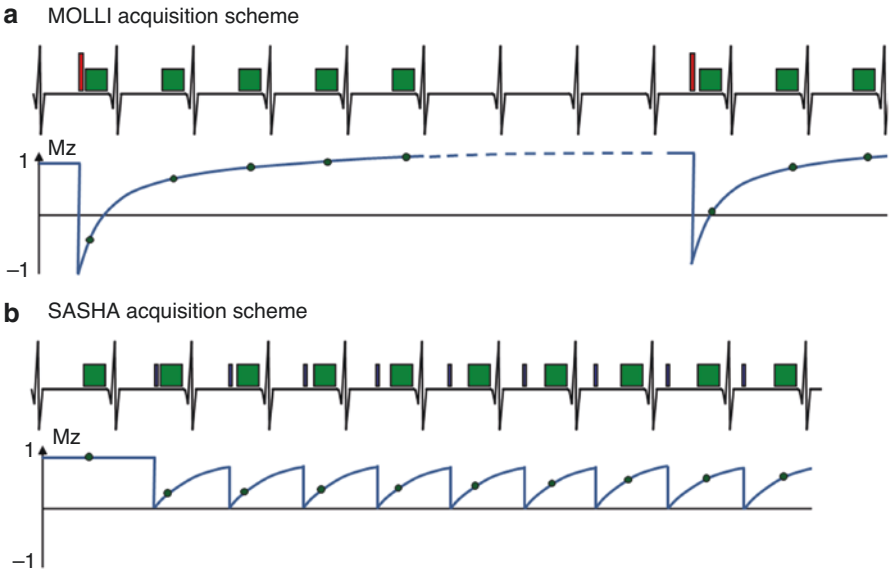

Fig. 14.1 (**a**) MOLLI sequence diagram, red blocks represent inversion recovery (IR) pulses, green blocks represent data acquisition. An IR pulse is used to produce the required T_1 encoding, which is sampled over several heartbeats. A few recovery heartbeats are interleaved to ensure that the second IR pulse produces the same exponential recovery, however, different time-points are sampled. Here the 5(3)3 MOLLI variant is depicted. (**b**) SASHA sequence diagram, blue blocks represent saturation recovery (SR) pulses. An initial 'infinity' image is acquired; following images are acquired at varying time delays after a SR pulse, sampling different points along the T_1 recovery curve

maps, albeit with a negative bias [5, 6]. This is due to several factors: the RF excitation pulses used for imaging disturb T_1 relaxation, there is a T_2 dependency caused by the commonly used b-SSFP readouts [7] and the sequence is intrinsically sensitive to magnetization transfer effects [8]. Furthermore, MOLLI is sensitive to changes in the heart rate, as the length of the cardiac cycle determines which points along longitudinal relaxation are sampled.

SASHA uses a similar acquisition strategy, but relies on saturation recovery (SR) pulses instead of IR pulses to achieve T_1 encoding. An initial image without SR preparation is first acquired; and in the following heartbeats a SR pulse is used with varying saturation time delays (TS), such that different points along the T_1 recovery curve are sampled (Fig. 14.1b). Saturation-weighted images are sorted by TS and fitted to the equation $M_z(\mathrm{TS}) = A[1 - B\exp(-\mathrm{TS}/T_1)]$. The SR pulse halves the T_1 encoding range, reducing the precision of this technique compared to MOLLI. However, the use of SR pulses reduces heart rate dependency, disturbance due to RF excitation pulses and sensitivity to magnetization transfer, increasing the accuracy of the technique. Both MOLLI and SASHA approaches deliver diagnostic T_1 parametric maps (Fig. 14.2), with MOLLI being currently the preferred choice in clinical practice.

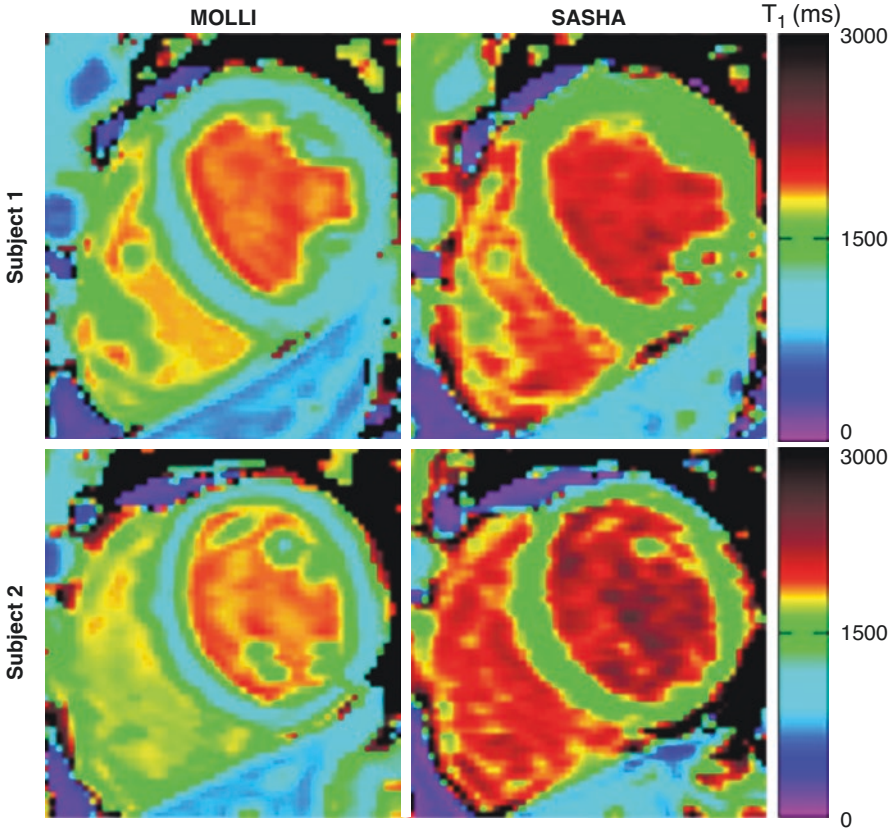

Fig. 14.2 Representative cases for MOLLI and SASHA T_1 mapping at 3 T. MOLLI generally achieves better precision, albeit with a negative bias. SASHA is more accurate, but suffers in precision. (Adapted with permission from Weingärtner S, Meßner NM, Budjan J, et al. *Myocardial T1-mapping at 3T using saturation-recovery: reference values, precision and comparison with MOLLI*. J Cardiovasc Magn Reson. 2016;18:1–9)

T_2 mapping encounters similar challenges as T_1 mapping in terms of requiring mechanisms to deal with physiological motion during data acquisition, therefore images are conventionally acquired in 2D, with cardiac triggering and under breathhold to minimize cardiac and respiratory motion, respectively. Common methods for cardiac T_2 mapping use either T_2 preparation (T2prep) pulses together with b-SSFP sequences [9] or gradient and spin echo (GraSE) sequences [10] in order to achieve the necessary T_2 encoding.

The T2prep b-SSFP approach achieves T_2 mapping with as few as three images, acquired with T_2 preparation modules of different echo times (TE_{T2p}), producing images with different T_2 weightings that are then fitted to a model, in a similar fashion to T_1 mapping techniques. A common choice for TE_{T2p} values is TE = [0, 24, 55] ms, which has been shown to provide good T_2 encoding and signal-to-noise ratio

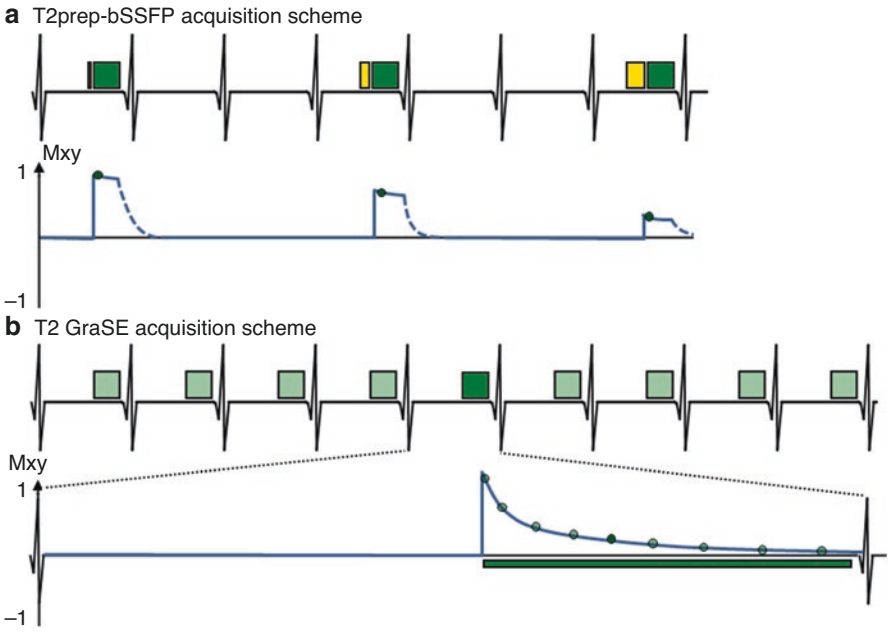

Fig. 14.3 (**a**) T2prep bSSFP diagram, yellow blocks represent T_2 preparation pulses (T2prep), green blocks represent data acquisition. T_2 encoding is achieved with T2prep pulses, spaced over several recovery heartbeats to allow (near) complete longitudinal recovery of the magnetization. (**b**) T2 GraSE diagram, a single heartbeat is highlighted to depict the evolution of the transverse magnetization. In each heartbeat, a GraSE readout is employed. The echo time at which the *k*-space centre is sampled is changed every heartbeat, such that a different T_2 contrast is sampled

(SNR) for the myocardium [11]. The acquisition of images for each TE_{T2p} is typically interleaved with a number of heartbeats where no imaging is performed, to allow for magnetization recovery and reduce potential bias arising from T_1 effects (Fig. 14.3a). Finally, the T_2 value for each pixel is obtained with the following exponential fit: $M_{xy}(TE_{T2p}) = A \exp(-TE_{T2p}/T_2)$. This approach can suffer from bias arising from several sources: the T_1 recovery occurring in the interval between the application of the T2prep pulse and the acquisition of the centre of *k*-space readout is typically not modelled in the fitting equation, and the T2prep pulse itself is sensitive to both B0 and B1 inhomogeneities, although these errors may be reduced by using adiabatic T2prep pulses [12]. Finally, relying on T2prep pulses for encoding limits the number of data points along the T_2 decay curve that are used for fitting, which can impact accuracy and precision of the resulting T_2 maps.

T2 GraSE is an alternative approach that encodes T_2 information via spin echoes. T_2-weighted images are acquired in a segmented fashion using EPI readouts in the T2 GraSE approach. In each GraSE block, the central *k*-space line determines the effective TE (Fig. 14.3b). In this approach, the following fitting model is used: $M_{xy}(TE) = A \exp(-TE/T_2) + B$. Partial volume effect arising from

blood signal can introduce bias in the resulting T_2 maps; so double inversion recovery preparation pulses are commonly employed to enforce a dark-blood contrast. T2 GraSE also has some limitations: long GraSE readouts and the use of spin echoes increase sensitivity to motion. Furthermore, while the EPI component of this approach enables considerable acceleration, it is also known to cause errors due to T_2* decay, image distortions and artefacts due to fat chemical shift. Both T2prep b-SSFP and T2 GraSE have been shown to produce diagnostic T_2 parameter maps (Fig. 14.4).

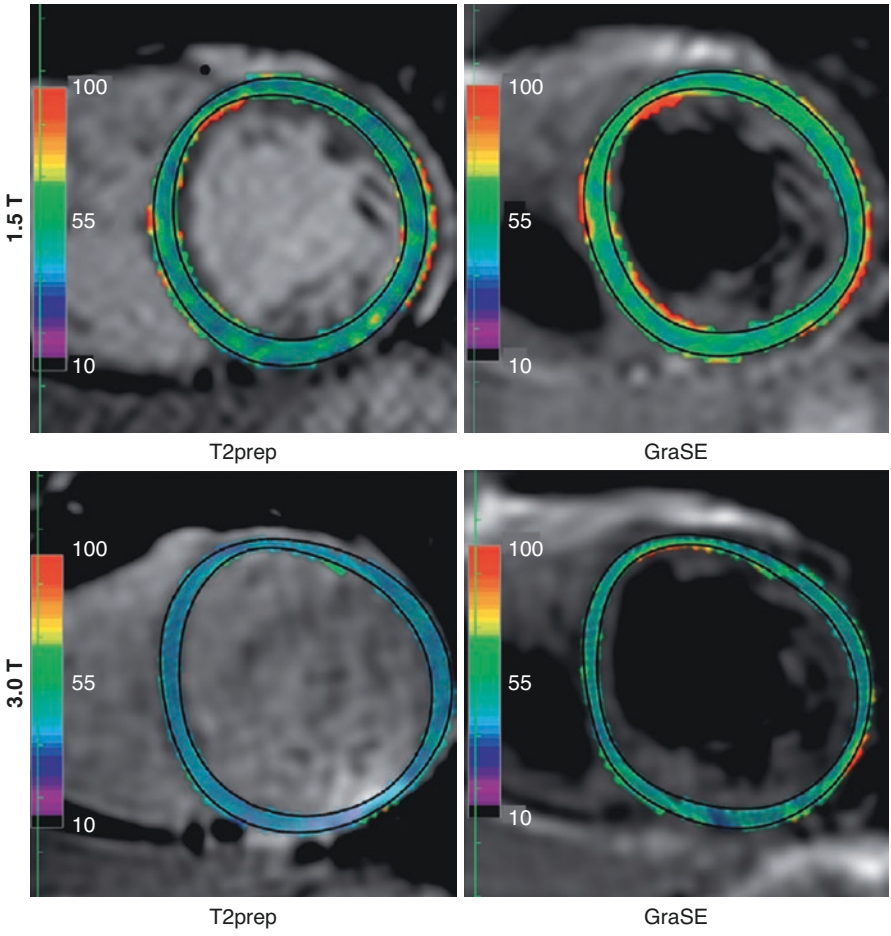

Fig. 14.4 Representative cases for T2prep bSSFP and T2 GraSE mapping techniques at 1.5 and 3 T. Lower T_2 values are obtained T2prep bSSFP, particularly at 3 T. (Adapted with permission from Baeßler B, Schaarschmidt F, Stehning C, et al. *A systematic evaluation of three different cardiac T2-mapping sequences at 1.5 and 3T in healthy volunteers*. Eur J Radiol. Elsevier; 2015;84:2161–70)

14.2.2 Cardiac MR Fingerprinting

Conventional parametric mapping approaches, such as MOLLI or T2prep b-SSFP described above, sample T_1 and T_2 relaxation curves at a few discrete points, relying on steady state conditions and simplified fitting models of the MR physics. Magnetic Resonance Fingerprinting (MRF) proposes an alternative approach where the transient state of the magnetization is continuously sampled and then compared to the signal evolution predicted by the Bloch equation [13]. In the MRF framework, some imaging sequence parameters (for instance, flip angle and repetition time) are continuously varied to sensitize the sequence to tissue parameters of interest such as T_1 and T_2. Prior to the MRF acquisition, Bloch equations are used to simulate the magnetization evolution, so-called fingerprint, for a set of tissues creating a dictionary of expected fingerprints. MRF data acquisition is performed at high acceleration rates leading to considerable noise amplification. However, voxel-by-voxel template matching can be used to identify the correct fingerprint in the pre-computed dictionary, revealing the underlying T_1 and T_2 values.

The MRF framework has been extended to cardiac applications where respiratory and cardiac motion compensation strategies must be considered. Cardiac MRF (cMRF) [14] uses inversion and T2prep pulses in a cardiac triggered acquisition acquired under breath-hold, to simultaneously estimate 2D T_1 and T_2 maps. In each heartbeat a different magnetization preparation pulse (or none) is used; in particular, in the original cMRF implementation, a block of four heartbeats was used with an IR pulse, no preparation pulses, T2prep with a TE_{T2p} = 40 ms, and T2prep with TE_{T2p} = 80 ms. This block can be repeated with increasing TIs to improve parametric encoding and SNR (Fig. 14.5). While the original MRF idea of varying the flip angles and repetition times throughout data acquisition is still employed by cMRF, most the signal encoding comes from the magnetization preparation pulses. Furthermore, since the cardiac triggering depends on the subject's heart rate, a patient-specific dictionary must be computed every time an acquisition is performed. An initial validation study showed that cMRF produces T_1 and T_2 maps comparable to conventional MOLLI and T2prep bSSFP, but with the advantage of producing co-registered parametric maps in reduced scan times (Fig. 14.6).

In a similar manner to conventional T_1 and T_2 mapping techniques, confounding factors arising from field errors (B0 or B1), magnetization transfer effects or motion will also affect cMRF accuracy and precision. However, the flexibility of the MRF approach provides mechanisms to reduce bias and imprecision in the parametric maps. For instance, while errors coming from B1 and slice profile are present in cMRF, they can be minimized with appropriate corrections or sequences designed to be less sensitive to such errors [15]. Residual cardiac or respiratory motion can also be present in cMRF and affect the accuracy and precision of the maps. Indeed, more recent works expanded on the cMRF framework to include water/fat separation or to resolve cardiac motion using a free-running acquisition [16, 17]. Additional parameters of interest for cardiac imaging, such as T_2*, $T_{1\rho}$ or MT could also be incorporated into the cMRF framework by using appropriate preparatory pulses and could be investigated in the future studies. Initial studies in patient populations to

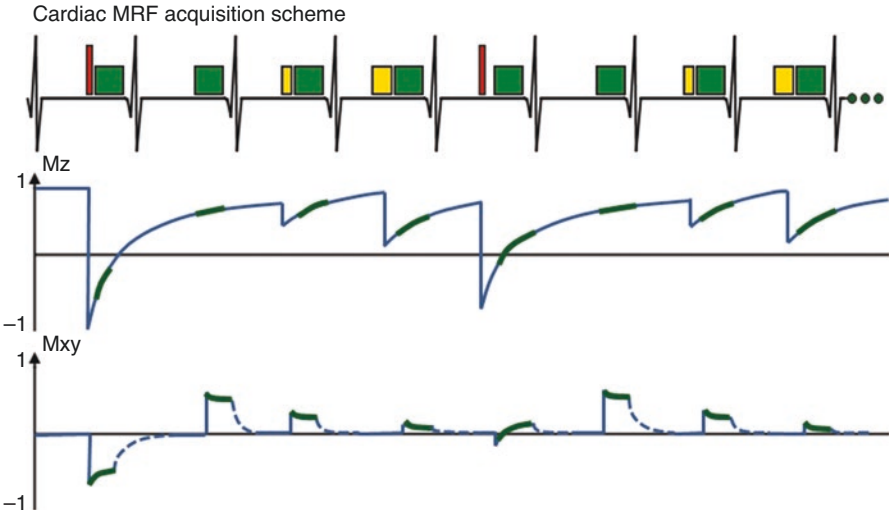

Fig. 14.5 cMRF diagram, red blocks represent IR pulses, yellow represent T2prep pulses and green represent acquisition. A combination of both IR and T2prep pulses are used to sensitize the magnetization to both T_1 and T_2 recovery in different heartbeats. Additional heartbeats can be acquired (with different TI) to further improve the precision of the parameter maps

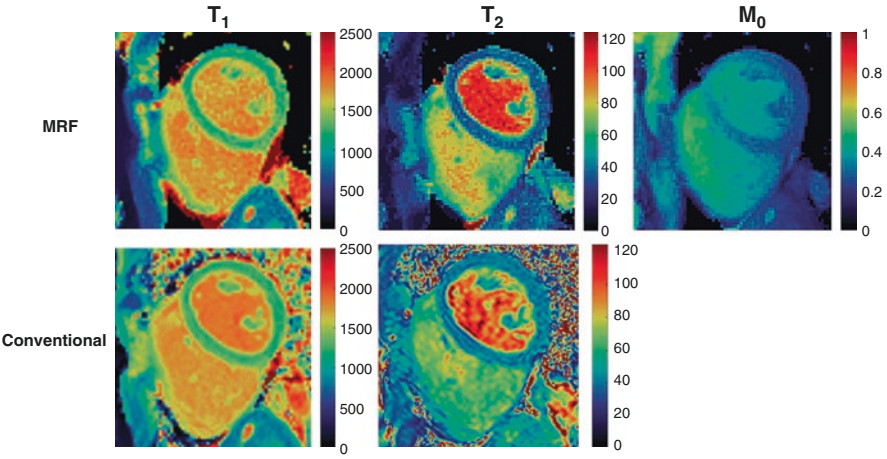

Fig. 14.6 Representative case with conventional cMRF compared to conventional T_1 MOLLI and T2prep bSSFP. Comparable parametric maps are obtained; however in cMRF these co-registered maps are obtained in reduced scan time. (Reproduced with permission from Hamilton JI, Jiang Y, Chen Y, et al. *MR fingerprinting for rapid quantification of myocardial T1, T2, and proton spin density*. Magn Reson Med. 2017;77:1446–58)

thoroughly evaluate the potential of cMRF have recently started, aiming to demonstrate the value of cMRF in clinical setting.

14.2.3 Cardiovascular MRI Multitasking

As mentioned before, most parametric mapping techniques rely on breath-holds and ECG triggering to avoid artefacts arising from respiratory and cardiac motion, respectively. An alternative approach is to attempt to capture and resolve motion as additional dimensions of the imaging object. This is what Multitasking (MTT) [18] proposes, by casting the problem as a low-rank tensor. Within this framework, the imaged object is framed as a tensor with spatial, parametric (T_1 and T_2) and temporal (respiratory and cardiac) dimensions. Whereas in conventional approaches scan time would increase exponentially with the number of dimensions, in MTT the scan time increases approximately linearly with the number of dimensions, as correlated information is naturally shared in the low-rank tensor formulation.

In the MTT approach, data is acquired continuously with a low flip angle FLASH readout, and parametric encoding is obtained by the application of magnetization preparation pulses that periodically interrupt the data acquisition. For native T_1 mapping an inversion pulse is used, whereas for perfusion T_1 mapping a saturation pulse is used instead. For native T_1/T_2 mapping T2prep-IR preparation pulses are employed, generating T_2 weighted inverted magnetization. These preparation pulses are repeated every 2.5 s, with the aim of placing them out of synchronization with physiological motion in order to provide partial parametric encoding along different motion dimensions.

The low-rank tensor framework used in MTT requires prior knowledge about the basis functions that describe each dimension. MTT assumes the parametric and temporal basis functions are known (or can be estimated from the data itself) and recover the spatial basis functions during image reconstruction. MTT acquires data following a golden radial trajectory where every other readout is used as training data for estimation of basis functions. For example, in simultaneous T_1/T_2 mapping, this training data can be used to span the subspace of the respiratory and cardiac dimensions, whereas a training dictionary is used to span the basis of the relaxation (parametric) dimension. Since in this case the reconstructed object is a four-dimensional tensor, it is possible to characterize T_1 and T_2 in every combination of respiratory and cardiac motion states. MTT has been shown to produce parametric maps comparable to conventional methods with the addition of respiratory and cardiac resolved information without the need for patient cooperation (breath-holds) or external sensors (ECG devices) (Fig. 14.7). The first MTT studies focused on the acquisition of multi-parametric 2D images, however, the framework is applicable to volumetric imaging, which could enable whole-heart coverage. In the near future, this technique could be used to obtain fully quantitative information, including, for instance, native and post-contrast parametric maps, perfusion and late gadolinium enhancement (LGE), from a single scan with minimum setup required.

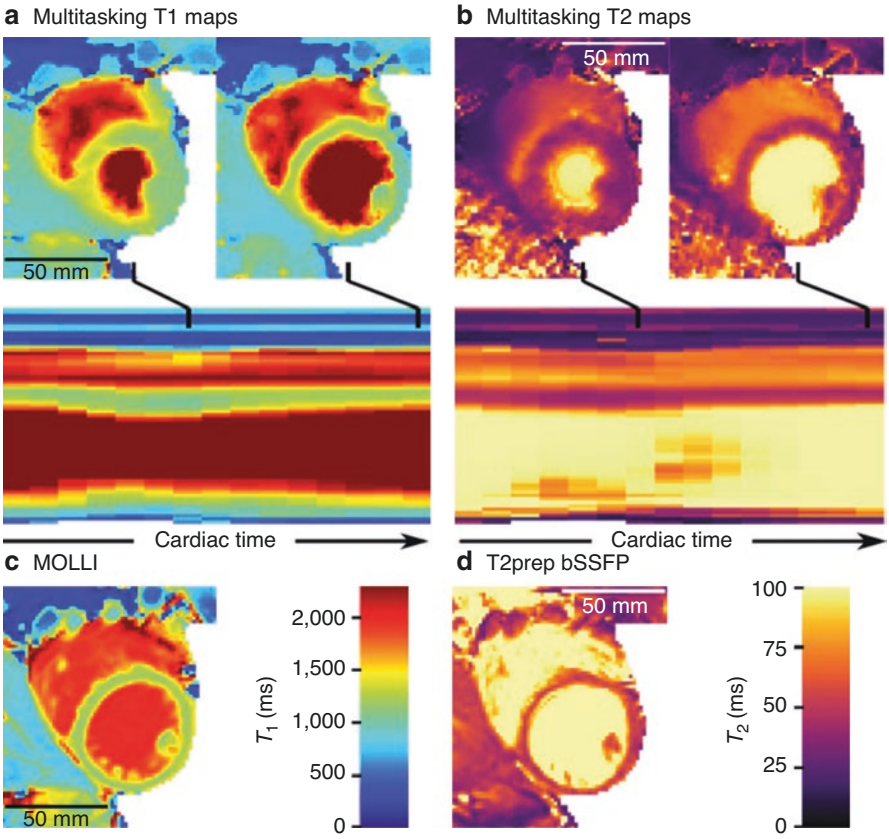

Fig. 14.7 Representative case for Multitasking, compared with standard T_1 MOLLI and T2prep bSSFP. Multitasking T_1 and T_2 maps not only are co-registered, but are also cardiac resolved, generating T_1 and T_2 maps at every cardiac phase. (Adapted by permission from Christodoulou AG, Shaw JL, Nguyen C, et al. *Magnetic resonance multitasking for motion-resolved quantitative cardiovascular imaging*. Nat Biomed Eng 2018;2:215–26)

14.3 Innovations in Cardiac MR: Towards Efficient 3D Whole-Heart Imaging

The ability of MR to produce high-resolution images with excellent soft-tissue contrast has encouraged the adoption of cardiac MR in the clinical routine. However, some challenges remain for improving efficiency and patient throughput. MR data acquisition is slower than the physiological motion of the heart; so compensation for respiratory- and cardiac-induced motion of the heart is fundamental to avoid ghosting and/or blurring artefacts in the images, especially for 3D whole-heart MR imaging.

Conventional approaches for motion compensation in cardiac MR rely on acquiring data under breath-holds to minimize respiratory motion, and/or only during

periods of minimal cardiac motion (for instance, during mid-diastole). While these approaches are routinely used in clinical MR examinations, they reduce the time available for data acquisition, so that only a limited spatial coverage can be achieved. Indeed, most clinical cardiac MR protocols consist of the acquisition of several 2D images with different geometries and orientations, including 4-chamber, 3-chamber, 2-chamber and a set of short-axis views of the heart. In order to obtain a sufficient SNR, these images are typically acquired with a large slice thickness (8–10 mm), which can result in partial volume effects that degrade the depiction of small features. Furthermore, as they are acquired under a series of breath-holds, they can be misaligned, which may result in inaccuracies when assessing, for instance, the size of a lesion.

Three-dimensional whole-heart MR imaging offers increased SNR, improved volumetric coverage, and higher spatial resolution, and has progressively been proposed for different cardiac MR applications. However, such approaches require longer acquisition times and therefore advanced motion compensation techniques and/or the use of accelerated MR data acquisition are required in order to acquire whole-heart datasets within a clinically feasible scan time. This section describes some approaches for 3D whole-heart MR imaging, focusing in novel developments for coronary artery imaging, myocardial viability imaging, and quantitative mapping.

14.3.1 Dealing with Physiological Motion

The heart is continuously moving due to the cardiac and respiratory cycles. The cardiac cycle induces periodic motion of the heart due to the contraction and relaxation of the atria and ventricles, with a frequency that ranges from 50 to 80 beats/min in healthy adults but that can vary significantly more in patients with cardiovascular disease. The breathing cycle also induces motion of the heart, due to movement of both the diaphragm and the chest wall, resulting in a complex non-rigid deformation of the heart, with a dominant component that can be represented by superior-inferior (SI) translation. A healthy adult in rest state breathes at a rate of 12–20 times/min, with an inspiration length ranging 1–2 s, and a slightly longer expiration period of 2–3 s. Both the cardiac-induced and the respiratory-induced motion of the heart have significant inter-subject variability, so subject-specific motion compensation schemes are required to minimize blurring and artefacts in the resulting MR images and consequently avoid compromising their diagnostic quality.

The effect of cardiac motion is conventionally minimized by synchronizing data acquisition with the cardiac cycle using an external ECG device. Assuming that cardiac motion is periodic, data is grouped according to their position within the cardiac cycle to produce images with minimal cardiac motion. There are two main approaches for performing this task: ECG-triggered and ‘free-running’ acquisitions, as depicted in Fig. 14.8.

In ECG-triggered approaches, data are acquired only during a short time window within each heartbeat over multiple cardiac cycles, and then combined into a single *k*-space to produce a ‘motion-free’ image [19]. The *R*-wave is used as reference for

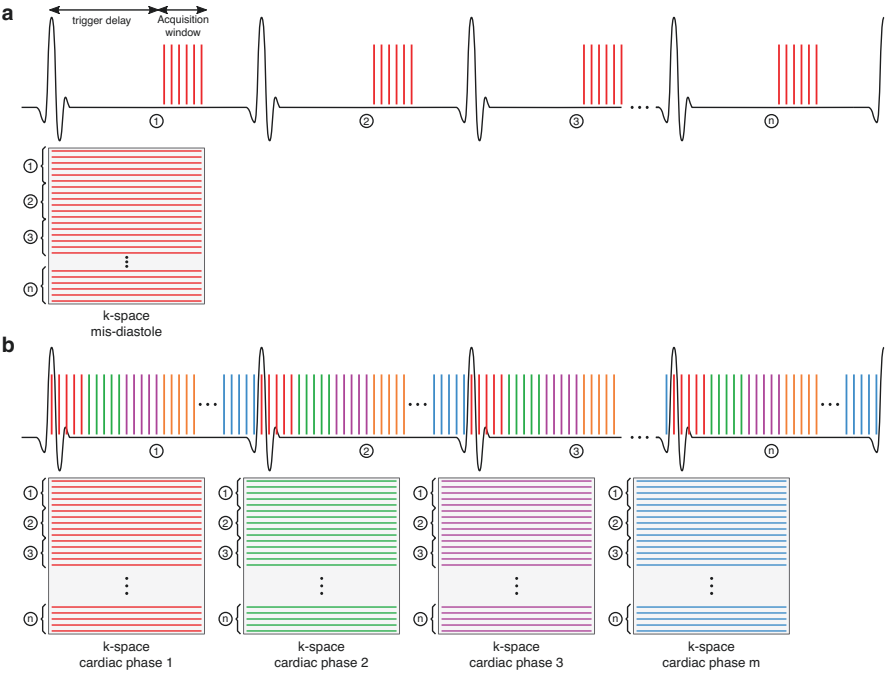

Fig. 14.8 Conventional approaches for minimizing cardiac motion in cardiac MR imaging. (**a**) ECG-triggered segmented acquisition. In each heartbeat, a segment of *k*-space is acquired during a period of minimal motion, typically mid-diastole, so that *k*-space is filled in a series of *n* subsequent cardiac cycles. (**b**) Free-running acquisition. Data are continuously acquired and retrospectively sorted into *m* cardiac phases, each of them with minimal cardiac motion

triggering the start of the data acquisition, so that the acquisition window coincides with a period of minimal cardiac motion. There is not an exact correspondence between the motions of different cardiac structures, and therefore, the period of minimal cardiac motion is different for different structures of interest such as the left ventricle or the coronary arteries. For instance, for the coronary arteries the period of minimal motion for adults often corresponds to mid-diastole, with a duration of ~100 ms, while in paediatric patients or patients with variable heart rate the end-systolic period may be more stable [20–22], with the disadvantage of being a shorter quiescent period (~50 ms). In order to acquire ECG-triggered images, the MR operator is required to set two subject-specific parameters: the trigger delay and the duration of the acquisition window. This approach is routinely used in the clinical practice for both 2D and 3D cardiac MR imaging, when visualization of the heart anatomy at a single cardiac phase is required.

In the so-called free-running approaches, data are continuously acquired during the cardiac cycle. Using the ECG signal as a reference, the data are retrospectively sorted into a number of cardiac phases, assuming that within each of them there is minimal cardiac motion, so that ‘motion-free’ images can be reconstructed at each

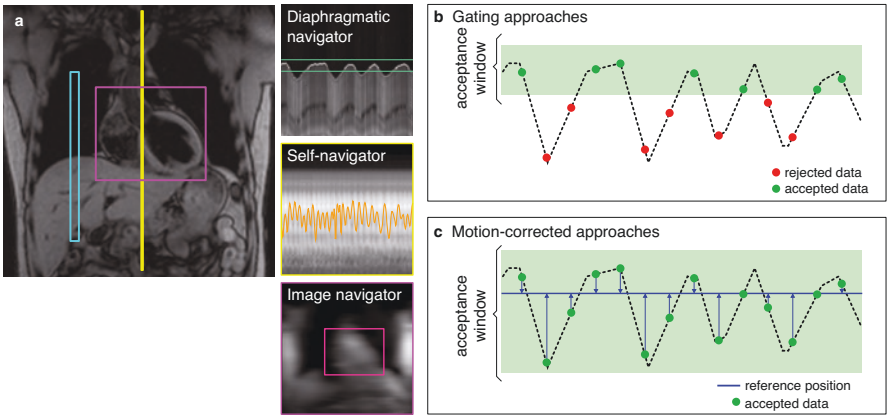

Fig. 14.9 (**a**) Options for respiratory motion tracking in cardiac MR, including diaphragmatic 1D navigator (in blue), self-navigation (in yellow), and image-based navigation (in magenta). (**b**) In gating approaches, acquired data is accepted (green dots) for image reconstruction only when the respiratory signal is within a predefined acceptance window (in green); otherwise, data is rejected (red dots). (**c**) In motion-corrected approaches, the acceptance window can be enlarged or entirely removed, so that all acquired data is accepted for image reconstruction. The data is corrected to a reference position (blue line) in a beat-to-beat fashion

phase. The free-running approach is widely used for 2D cine imaging, and more recently it has been demonstrated for whole-heart 3D coronary MR angiography (CMRA) and for 3D cine imaging in combination with undersampled and motion-compensated image reconstruction techniques [23, 24]. Thanks to its ability to produce images at different cardiac phases, the free-running approach is conventionally used to assess cardiac function, through the calculation of clinically relevant parameters such as ventricular volumes and ejection fraction.

Free-running approaches have the advantage of not requiring the operator to prospectively define the length of the acquisition window and trigger delay, reducing operator dependency during data acquisition. Furthermore, the cardiac phase with minimal motion can be found retrospectively, which could be advantageous in patients with irregular heart rate. However, since data are acquired continuously, the longitudinal magnetization does not recover between consecutive excitations, resulting in a loss of contrast and SNR in the images. Moreover, since free-running approaches acquire data in multiple cardiac phases, larger amounts of data and correspondingly longer scan times are needed compared to ECG-triggered scans.

An approach analogous to ECG-triggering can be used for minimizing the effect of respiratory motion, by using a signal related to the breathing cycle to combine data acquired at a similar respiratory position during multiple breathing cycles. External devices such as respiratory bellows can be used for respiratory gating, assuming a high correlation between the motion of the heart and the motion of the abdomen. Alternatively, the respiratory cycle can be directly monitored from the MR images (Fig. 14.9a).

In clinical routine, the most common approach uses interleaved one-dimensional (1D) navigator echoes in the MR acquisition sequence. A navigator echo consists of an image representing a thin column of tissue that can be used to monitor the position of a high-contrast moving structure, such as the liver-lung interface. When this interface is within a predefined window, usually placed at end-expiration with a width of 3–5 mm [25], the acquired data is accepted for image reconstruction. Otherwise, the data is rejected and reacquired in a later breathing cycle (Fig. 14.9b). The information provided by the navigator echoes can also be used to further reduce motion artefacts by correcting for motion within the acceptance window. This approach, known as gating and tracking, corrects for the SI translation of the heart assuming that it is directly proportional to the displacement of the diaphragm [26].

Although 1D navigator approaches are widely used in the clinical setting for 3D whole-heart imaging due to its robustness, they have several limitations. Firstly, the motion of the heart is not measured directly, but it is inferred from the motion of the diaphragm. A population-based tracking factor of 0.6 to relate the motion of the diaphragm to the motion of the heart is commonly used for this purpose. However, this factor is not appropriate for all subjects [27]. Furthermore, even if subject-specific tracking factors were used [28, 29], the 1D navigator approach only accounts for translational motion in the SI direction, does not consider hysteretic effects, and is incapable of including corrections for the complex non-rigid deformations of the heart during the breathing cycle. Finally, the efficiency of the acquisition (i.e. the percentage of acquired data that is accepted for image reconstruction) varies significantly between subjects, typically ranging from 20% to 60%, leading to prolonged and unpredictable scan times.

Self-navigation methods that estimate the respiratory motion of the heart from the acquired data itself have been proposed in the literature to address some of the limitations of diaphragmatic navigators. These methods derive a respiratory signal from a repeated acquisition of either the centre of *k*-space [30] or a central line in *k*-space [31], usually acquired in the SI direction. Compared to diaphragmatic navigation, self-navigation methods have the advantage of directly measuring the motion of the heart and thus not relying on a motion model. However, they also perform motion correction in the SI direction only and motion estimation is only relative as the motion signal is unit less. Furthermore, their ability to estimate a respiratory signal is impaired by the presence of static tissue, as both the centre of *k*-space and the central line of *k*-space are projections of the whole field of view.

In order to address these limitations, respiratory motion compensation techniques that use image-based navigators (iNAVs) have been proposed more recently. By acquiring low-resolution 2D [32–34] or 3D images [35–40] before or after the high-resolution 3D data acquisition, respiratory motion can be directly measured in the heart by tracking a region of interest.

Both self-navigation and iNAV-based methods can be used for gating the acquisition and correcting for respiratory motion within a small gating window in a similar manner to 1D navigator echoes. However, since these methods directly measure the motion of the heart and correct for it, a much larger gating window can be used (Fig. 14.9c). These approaches usually incorporate most of the acquired data for

image reconstruction (i.e. achieving near 100% scan efficiency), leading to predictable and significantly reduced acquisition times. Several self-navigated and iNAV-based techniques correct for respiratory motion in a beat-to-beat fashion, by applying a linear phase shift in *k*-space corresponding to the estimated 1D, 2D, or 3D translation of the heart [32, 33, 36, 41, 42]. While enabling 100% scan efficiency, these techniques do not account for the complex non-linear motion of the heart, thus remaining motion artefacts can affect the quality of the images.

Respiratory binning techniques have been more recently introduced to handle higher-order motion models (Fig. 14.10a). In this approach, the SI displacement obtained from the iNAVs or from self-navigation signals is used to sort the acquired data into a number of respiratory bins representing different respiratory positions

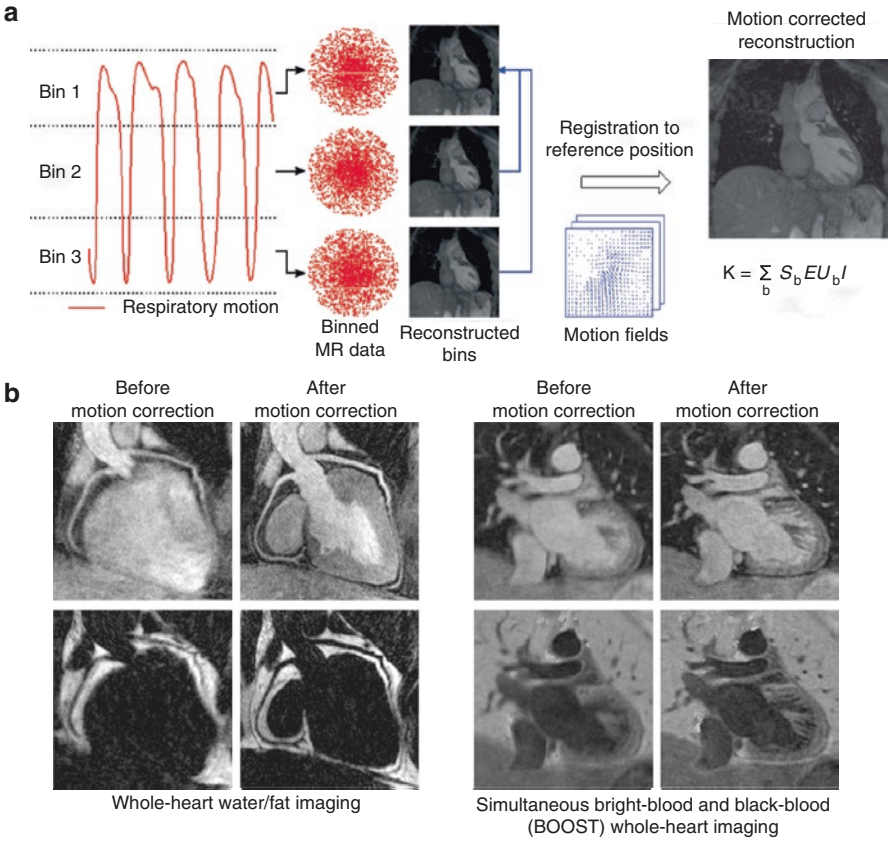

Fig. 14.10 Advanced respiratory motion compensation approach using binning. (**a**) The respiratory signal is used to group the acquired the MR data into several states of the breathing cycle or 'bins' with high spatial resolution. The bin images are registered to a reference position, in order to estimate motion fields. This motion information can be then incorporated directly in the image reconstruction process. (**b**) Examples showing the impact of respiratory motion correction in whole-heart water/fat imaging and in simultaneous bright- and black-blood imaging

throughout the breathing cycle. Then, images reconstructed at each respiratory position can be used to estimate, for instance, 3D affine motion parameters. The acquired *k*-space can be then corrected in a bin-to-bin fashion, as shown in [43–46] for various cardiac MR applications.

Although the 3D affine motion model is a better approximation of the respiratory-induced motion of the heart, it assumes that the whole field of view is affected by a unique transformation. In practice, some tissues remain mostly static during the acquisition, such as the spine and subcutaneous fat; and different organs in the thorax are affected differently by the expansion and contraction of the lungs. Thus, applying a global *k*-space correction using motion parameters estimated by tracking the heart will induce ghosting and artefacts arising from an erroneous correction of the surrounding organs and tissues. Instead, a more general non-rigid motion model can be used.

Approaches that include the non-rigid deformation fields as part of an iterative image reconstruction algorithm have been proposed for coronary MR imaging [47] and more recently for multi-contrast cardiac MR imaging [48, 49], and techniques that use local auto-focus to model the non-rigid motion of the heart have also been proposed [40, 50]. Example images before and after non-rigid motion correction for different clinical applications can be seen in Fig. 14.10b. It is worth noting that these approaches seek to produce one respiratory motion-corrected image that includes all the acquired data. Alternatively, the respiratory-binned data can be simultaneously reconstructed by exploiting sparsity along the respiratory dimension, so that high-quality respiratory-resolved images can be obtained [51, 52]. Indeed, this technique can be extended to obtain cardiac and respiratory-resolved images, as demonstrated in [53].

14.3.2 Accelerating Data Acquisition

As discussed in the previous section, the use of motion compensation techniques can reduce average cardiac MR scan time by providing higher scan efficiency. However, even when motion correction techniques are used, the acquisition of 3D cardiac MR images with sufficient spatial resolution and coverage takes several minutes. Indeed, a 100% efficient fully sampled whole-heart 3D CMRA scan with a spatial resolution of 0.9 mm^3 isotropic resolution may take as long as 30 min at an average heart rate of 70 beats/min.

Beyond motion compensation, more advanced methods that combine faster acquisition trajectories and undersampled reconstruction techniques can be used to increase acquisition speed and thereby achieve clinically feasible scan times. Although several of these techniques have focused on accelerating CMRA imaging, due to the high resolution and volumetric coverage required to accurately depict the coronary arteries, they have also been used for other cardiac applications.

Fast non-Cartesian acquisition trajectories, such as radial and spiral trajectories, enable to fill the *k*-space in a more efficient manner, and produce incoherent motion artefacts and noise-like undersampling aliasing, making them suitable for advanced

undersampled reconstruction techniques, such as compressed sensing [54]. One of the most prevalent of these is the spiral phyllotaxis 3D radial trajectory. Originally proposed for CMRA imaging [42, 55], this trajectory has now been applied to late gadolinium enhancement (LGE) imaging [56], T_2 mapping [57], and 'free-running' CMRA imaging for the simultaneous assessment of cardiac anatomy and function [23]. A closely related trajectory is the 'spiral on the sphere' radial trajectory, which has been extensively used for conventional and free-running CMRA [41, 44, 45, 58]. Other trajectories include 3D cones [59], stack of stars [46], and stack of spirals [60]. The main disadvantages of these non-Cartesian trajectories are a reduced SNR, higher sensitivity to off-resonance effects and gradient delays, and the complexity they pose for image reconstruction. On the other hand, novel Cartesian trajectories that follow spiral-like sampling patterns on the Cartesian grid [43, 61] or variable density Poisson discs [62] can alleviate these issues while maintaining many of the benefits of non-Cartesian trajectories.

A clinically established method for accelerating data acquisition is the use of parallel imaging undersampled MR reconstruction. Techniques such as SMASH [63], SENSE [64], and GRAPPA [65] pioneered this field, by using spatial information obtained from the sensitivity of multiple receiver coils to partially recover samples not acquired in *k*-space. These approaches are widely used in cardiac MR protocols, to reduce acquisition time by a factor of 2–3 without affect the diagnostic quality of the resulting images.

In order to achieve higher acceleration, compressed sensing and other sparsity-based image reconstruction techniques have been applied to cardiac MR imaging. These techniques use assumptions about the compressibility of the image in some domain to reduce the amount of data required to produce a good quality image. For instance, the compressibility of the wavelet coefficients was used in [62] to accelerate CMRA imaging up to 6 times, while a similar technique was used in [66] to enable single breath-hold whole-heart cine imaging. The difference between respiratory states has also been used as a sparsifying transformation to reconstruct respiratory-resolved CMRA images from undersampled data [51, 52] (Fig. 14.11a). Instead of reducing scan time, these methods can be used to increase spatial resolution, as recently demonstrated in [67], where a patch-based undersampled reconstruction technique was used to achieve sub-millimetre resolution in CMRA with a scan time of approximately 5 min (Fig. 14.11b).

14.3.3 Coronary MR Imaging

An accurate visualization of the coronary artery anatomy is fundamental for the detection of coronary artery disease. Although invasive X-ray angiography remains the reference modality for imaging of the coronary lumen and detection of coronary stenosis, non-invasive imaging, including computed tomography (CT) and MRI, are increasingly being used as alternative diagnostic tools. Indeed, CT coronary angiography (CTCA) has been recently incorporated into healthcare guidelines as a cost-effective first test for patients with suspected coronary disease [68] due to its high

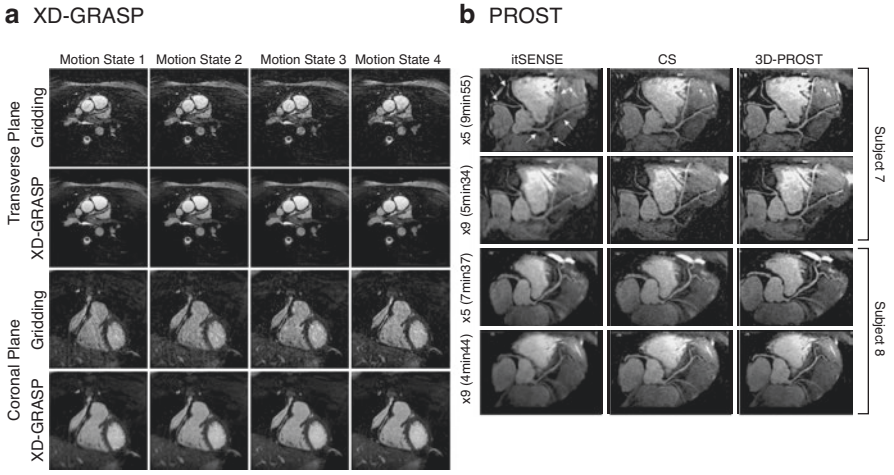

Fig. 14.11 Advanced image reconstruction methods for accelerated CMRA. (**a**) The XD-GRASP method enables respiratory-resolved image reconstruction, by exploiting sparsity in the respiratory dimension, resulting in improved image quality compared to conventional Gridding reconstructions (reproduced with permission from Piccini D, Feng L, Bonanno G, et al. *Four-dimensional respiratory motion-resolved whole heart coronary MR angiography*. Magn Reson Med. 2017;77:1473–84). (**b**) The 3D-PROST method exploits the similarity between 3D patches in the CMRA image, achieving improved image quality compared to conventional iterative SENSE (itSENSE) and conventional compressed sensing (CS) reconstructions for acquisitions with up to ninefold acceleration. (Reproduced with permission from Bustin A, Ginami G, Cruz G, et al. *Five-minute whole-heart coronary MRA with sub-millimeter isotropic resolution, 100% respiratory scan efficiency, and 3D-PROST reconstruction*. Magn Reson Med. 2019;81:102–15)

spatial resolution and short acquisition time. Although CTCA has the advantage of being a non-invasive procedure, it results in an average radiation dose of 16 mSv to the patient [69]. On the contrary, MR is a radiation-free imaging modality, which enables the visualization of the coronary artery lumen while also providing a depiction of vessel wall and characterization of atherosclerotic plaque, including imaging of intraplaque haemorrhage and thrombi.

The depiction of the coronary artery lumen via CMRA requires the use of contrast mechanisms to suppress the signal arising from surrounding tissues such as epicardial fat and myocardium. Some of the current CMRA imaging protocols rely on the use of exogenous gadolinium-based contrast agents to increase the contrast between blood and myocardium, resulting in bright-blood images [70]. Alternatively, the difference in the T_2 relaxation time between the arterial blood pool and the surrounding tissues can be used as an endogenous contrast mechanism by including a T_2 preparatory pulse (T2prep) before the acquisition of imaging data [71]. Adipose tissue has a short T_1 and long T_2 relaxation times, leading to a strong signal arising from the epicardial fat in most CMRA acquisition sequences. Such signal can obscure the visualization of the coronary arteries if not adequately suppressed. While conventional fat suppression techniques based on SPIR [72] have been shown

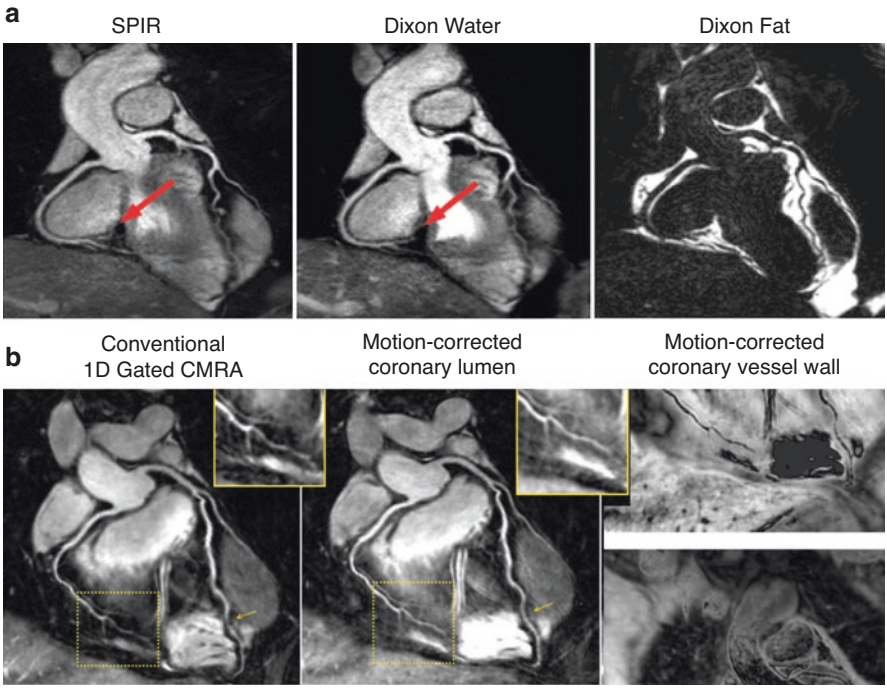

Fig. 14.12 Innovations in coronary MR imaging. (**a**) Water/fat coronary MR angiography improves fat suppression and contrast-to-noise ratio at 3 T compared to conventional fat suppression (SPIR) (adapted from Nezafat, M., Henningsson, M., Ripley, D.P. et al. *Coronary MR angiography at 3T: fat suppression versus water-fat separation*. Magn Reson Mater Phy (2016) 29: 733). (**b**) Interleaved T_2-preparation can be used for simultaneous imaging of the coronary vessel wall and coronary lumen. (Adapted from Cruz G, Atkinson D, Henningsson M, et al. *Highly efficient non-rigid motion-corrected 3D whole-heart coronary vessel wall imaging*. Magn Reson Med. 2017;77:1894–908)

to be robust at 1.5 T, they can result in incomplete fat suppression at higher magnetic fields due to their sensitivity to field inhomogeneities. Alternatively, the difference in resonance frequency (i.e. the chemical shift) between water and fat can be used to separate the two species into images that reflect the water and fat content of each voxel in the image, using the so-called water/fat or Dixon separation methods. The water/fat separation approach has been applied to 1D navigator gated CMRA imaging, where it has been shown to improve image quality both at 1.5 T [73] and 3 T [74] compared to conventional fat saturation, increasing SNR of the arterial blood and improving blood-to-fat contrast-to-noise (CNR) ratio in the water images (Fig. 14.12a). A motion-corrected water/fat CMRA approach with ~100% scan efficiency has been recently demonstrated at 3 T [75]. An alternative approach for improving fat suppression is the use of efficient water-selective excitation pulses in order to obtain 'fat-free' images, as recently proposed in [76], however, their impact in cardiac imaging remains to be studied. Finally, advances that combine T_2

preparation and water-selective RF excitation pulses have been proposed in the literature [77].

While high-resolution bright-blood CMRA can be used to detect proximal luminal stenosis, it is known that early stages of the disease involve changes in the arterial wall without luminal narrowing. In order to visualize the coronary artery wall with sufficient contrast, several black-blood imaging techniques have been proposed in the literature. The first approaches for black-blood coronary imaging used double inversion recovery (DIR) preparation pulses to null the signal arising from the blood [78, 79]. The DIR technique enables the selective depiction of static tissue within the field of view, relying on the blood flow perpendicular to the imaging plane to achieve blood nulling, and thereby limiting this approach to the acquisition of 2D slices or carefully planned targeted 3D acquisitions. Therefore, flow-insensitive techniques have been more recently introduced to enable 3D whole-heart volumetric coverage. Techniques based on a T2prep-IR preparation pulse have been shown to produce good quality images of the aortic and peripheral vessel wall [80, 81], while an interleaved acquisition of data with and without T2prep has shown promising results for the simultaneous visualization of the coronary lumen and vessel wall [47, 82] (Fig. 14.12b). The interleaved T2prep approach acquires two bright-blood volumes, and uses a patient-specific weighted subtraction to produce an additional black-blood image where the vessel wall can be visualized. A novel interleaved T2prep-IR acquisition has been recently proposed [49], which produces the black-blood image by direct subtraction of the two bright-blood images, removing the need for a weighting factor and increasing the robustness of the technique.

14.3.4 Myocardial Viability MR Imaging

Late Gadolinium enhancement (LGE) is an established technique for the assessment of myocardial scar and fibrosis. Most LGE imaging sequences are based on the use of an IR preparation pulse, which enables the exploitation of the differences in the T_1 relaxation time between healthy and diseased myocardium. This difference in T_1 arises from the different wash-in and wash-out rates of the contrast agent in different tissues, resulting in an optimal time window for image acquisition, typically between 10 and 30 min after injection of contrast. Conventional LGE imaging protocols null the signal arising from the normal myocardium by selecting an appropriate inversion time (TI) from visual inspection of a so-called TI-scout acquisition. Although routinely used in the clinical practice, this approach is highly sensitive to the selection of TI. Phase-sensitive IR (PSIR) [83] is a more robust technique that interleaves the acquisition of the IR-prepared data with a low flip angle reference scan, so that this additional information can be used to preserve the polarity of the magnetization, enabling a better separation between signal arising from scar and myocardium.

As in most conventional cardiac MR sequences, LGE images are conventionally acquired under breath-hold as a series of 2D slices, with reasonably good in-plane

spatial resolution but large slice thickness and limited volumetric coverage. Motion correction techniques have been introduced to enable free-breathing 2D LGE imaging [84, 85], achieving similar resolution and contrast-to-noise ratio compared to conventional breath holding. In order to achieve higher spatial resolution and whole-heart coverage, several approaches have been proposed for 3D LGE imaging, either using diaphragmatic navigators to enable free-breathing acquisitions [86, 87] or using fast trajectories and undersampled acquisitions to enable single breath-hold imaging [60, 88]. The single breath-hold techniques acquire images in ~20 s, compared to the several minutes required by free-breathing techniques. While efficient, these long breath-holds might be difficult to achieve for the patients. Furthermore, the single-breath-hold approach can only achieve a limited spatial resolution, with a typical slice thickness of 5–7 mm, and normally acquires data at each heartbeat, preventing the use of the PSIR technique. On the other hand, free-breathing techniques have enabled the acquisition of high-resolution LGE PSIR images with whole-heart coverage and isotropic image resolution of 1.4–2 mm^3 [86, 87].

While both conventional IR and PSIR LGE imaging achieve an excellent contrast between non-viable and normal myocardium, the contrast between the blood pool and the non-viable myocardium is significantly reduced, as the blood pool also appears bright. Therefore, the delineation of the scar may be impaired, particularly in cases of sub-endocardial infarct. Combined IR-T2prep [89, 90] and T2prep-IR [91] pulses have been recently introduced for dark-blood PSIR LGE imaging, showing promising results for enhanced depiction of gadolinium enhancement. A different approach for dark-blood IR-prepared PSIR LGE imaging is proposed in [92], where the TI is selected to null the blood signal instead of nulling the viable myocardium. In this approach, the PSIR reconstruction produces images with grey blood, while the nulled viable myocardium and bright scar signal are preserved.

Most conventional LGE imaging sequences do not include any mechanism for fat suppression. Both myocardial fibrosis and intramyocardial fat can appear bright in LGE images since they both have a low T_1, hindering the distinction between both types of tissue. Multi-echo Dixon approaches have been incorporated to breath-held 2D PSIR LGE imaging for the assessment of fibro-fatty infiltration in the myocardium [93], and more recently extended to single breath-hold 3D LGE imaging [94] (Fig. 14.13).

14.3.5 Multi-Contrast Whole-Heart MR Imaging

Cardiac MR offers a multitude of possible image contrasts that reflect different tissue characteristics and provide complementary information about different disease mechanisms. The conventional methodology for cardiac MR in the clinical routine consists of acquiring each of these image contrasts in a sequential fashion. However, an alternative and more efficient approach is the acquisition of two or more of such contrasts interleaved in a single scan, so that the resulting images are better aligned and can be more easily fused and interpreted together.

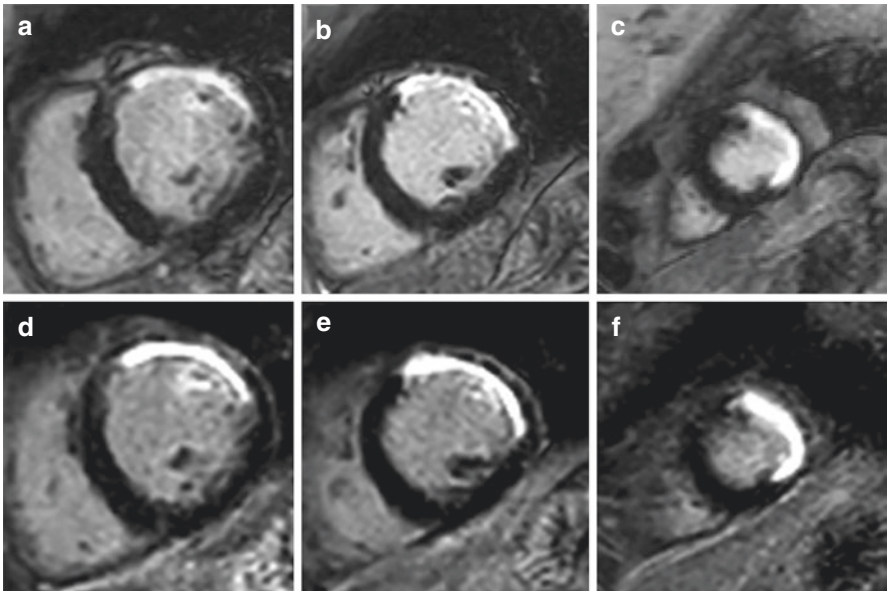

Fig. 14.13 A visual comparison shows good correspondence between short-axis LGE images acquired with (**a**–**c**) conventional 2D multi breath-hold PSIR and (**d**–**f**) single breath-hold 3D mDIXON acquisition, with a clear depiction of anterolateral scar in both sets of images. However, the 3D image acquisition (~15 s) required approximately 5% of the time required for acquiring the 2D images (~320 s). (Reproduced from Foley JRJ, Fent GJ, Garg P, et al. *Feasibility study of a single breath-hold, 3D mDIXON pulse sequence for late gadolinium enhancement imaging of ischemic scar*. J Magn Reson Imaging 2019;49:1437–45)

An interleaved scheme was proposed by Xie et al. in [95], where an IR pulse is applied every other heartbeat in order to obtain a T_1-weighted black-blood volume and a bright-blood image reference. This sequence, known as CATCH, enables the depiction of high-risk atherosclerotic plaque by the T_1-weighted black-blood image, where intraplaque haemorrhage and coronary thrombus appear as hyper-intense features, while simultaneously providing a bright-blood image that can be used as anatomical reference (Fig. 14.14a). The CATCH sequence integrates respiratory self-navigation and affine bin-to-bin motion correction, resulting in a highly efficient examination. However, it has some limitations. First, due to the lack of signal in the T_1-weighted black-blood images, the CATCH sequence relies only on the bright-blood data for motion tracking and correction, assuming that the respiratory motion between consecutive heartbeats is negligible. Furthermore, the lack of preparatory pulses in the bright-blood image results in contrast degradation, limiting the diagnostic use of this image. An extension of this approach has been recently proposed [96], where an acquisition scheme that interleaves a T2prep-IR pulse in even heartbeats with a T2prep pulse in odd heartbeats is used. This sequence, called BOOST, results in two bright-blood volumes with different T_1 weighting, which can be combined in a PSIR reconstruction to produce a complementary black-blood volume where signal from thrombus is enhanced. Compared to the CATCH

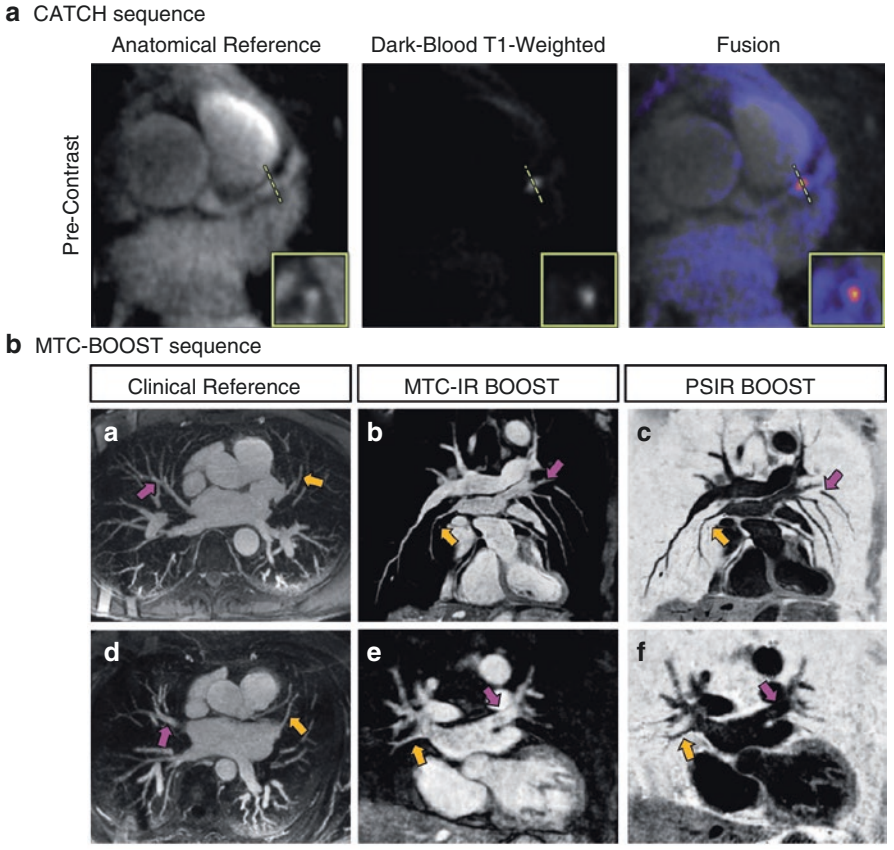

Fig. 14.14 Examples of novel multi-contrast whole-heart imaging sequences. (**a**) CATCH sequence for visualization of vulnerable plaque and coronary anatomy (adapted from Xie Y, Kim YJ, Pang J, et al. *Coronary Atherosclerosis T1-Weighed Characterization With Integrated Anatomical Reference: Comparison With High-Risk Plaque Features Detected by Invasive Coronary Imaging.* JACC Cardiovasc Imaging. 2017;10:637–48). (**b**) MTC-BOOST sequence for simultaneous visualization of the pulmonary veins and assessment of atrial wall thickness. (Adapted from Ginami G, Lopez K, Mukherjee RK, et al. *Non-contrast enhanced simultaneous 3D whole-heart bright-blood pulmonary veins visualization and black-blood quantification of atrial wall thickness*. Magn Reson Med. 2019;81:1066–79)

sequence, BOOST has the advantage of producing two bright-blood volumes, enabling respiratory motion estimation at each heartbeat. Indeed, the BOOST sequence integrates an iNAV-based motion compensation scheme. Furthermore, the anatomical reference (given by the T2prep-IR image) has a higher blood-to-myocardium contrast, making it suitable for assessment of the coronary lumen.

The BOOST sequence provides a flexible framework for the acquisition of bright-blood images that provide complementary information. The framework has also been used after injection of a Gadolinium-based contrast agent for

simultaneous bright-blood CMRA and black-blood LGE [91], improving the contrast between blood pool and scar. Furthermore, BOOST approach has been extended to the pulmonary circulation, for the visualization of bright-blood pulmonary veins and black-blood quantification of atrial wall thickness, using an interleaved Magnetization Transfer Contrast (MTC)-IR and MTC preparation [97] (Fig. 14.14b).

14.3.6 Whole-Heart Quantitative T_1 and T_2 Mapping

As described in Sect. 14.2, quantitative mapping techniques for cardiac MR have commonly relied on breath-holds to avoid respiratory motion artefacts. However this strategy typically limits the available scan time, resulting in limited volumetric coverage, spatial resolution, and SNR. Furthermore, repeated breath holding is challenging to achieve for some patient populations, which may result in suboptimal image quality. In this section, some of the advances made to move from breath-held 2D toward free-breathing 3D cardiac quantitative mapping are discussed.

Free-breathing solutions for both inversion-based and saturation-based 3D T_1 mapping have been proposed in the literature, using respiratory triggering [98] and diaphragmatic navigators [99]. These methods monitor respiratory motion and accept data only in end-expiration, effectively reducing respiratory-induced motion artefacts. However, as the remainder of the respiratory cycle is excluded from data acquisition, this approach significantly lengthens the scan time. Instead of using this inefficient (cardiac or respiratory) triggering approach, it is possible to estimate and correct for motion, minimizing residual artefacts. Approaches for 3D T_2 mapping using diaphragmatic navigator [100] and self-navigation techniques [57] have been demonstrated in the literature, and the combination of free-breathing motion-corrected 3D T_2 mapping has also been developed using navigators to guide the motion model [46]. These techniques have the potential of providing a high-resolution T_2 parametric map for improved quantification (Fig. 14.15).

14.4 Innovations in Cardiac PET-MR Imaging

Since the development of simultaneous PET-MR scanners, cardiovascular imaging has been proposed as one of the clinical applications that could benefit the most from this new technology. The complementary anatomical and functional information offered by both imaging modalities, and the ability to simultaneously produce MR images with high spatial and temporal resolution and superior tissue contrast and quantitative PET images that can target a variety of molecular processes has a great potential for improving the diagnosis and monitoring of different cardiac conditions from a single scan session.

In the early days of cardiac PET-MR, most research studies focused on either cross-validating both imaging modalities, particularly for the assessment of myocardial viability and perfusion [101–105], or on studying the potential added value

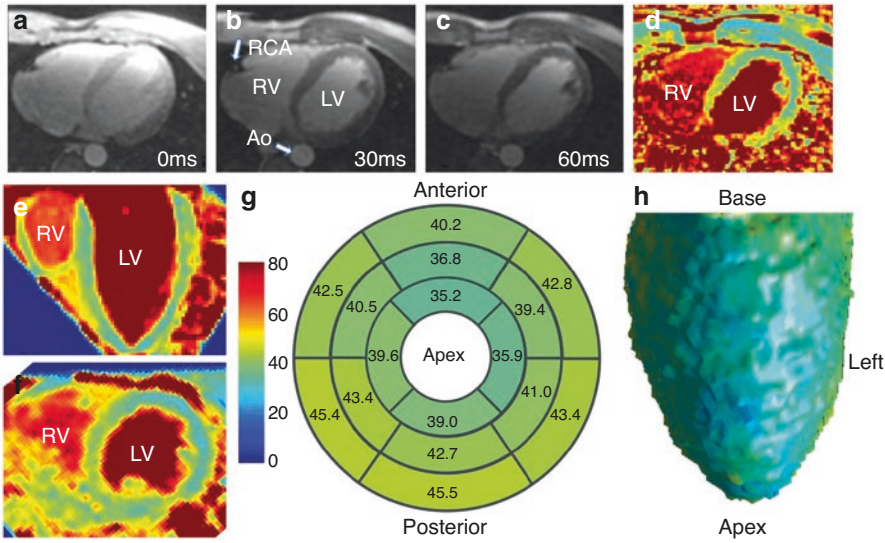

Fig. 14.15 Self-navigated 3D T_2 mapping technique. (**a**–**c**) Three images with different T2Prep times are used to produce the (**d**) T_2 map. The isotropic resolution enables reformatting in any cardiac plane including (**e**) long-axis and (**f**) short-axis. A homogeneous distribution of the resulting T_2 values can be observed in the myocardium, both in (**g**) 17-segment plot and (**h**) a volumetric rendering of the left ventricle. (Reproduced from Van Heeswijk RB, Piccini D, Feliciano H, et al. *Self-navigated isotropic three-dimensional cardiac T2 mapping*. Magn Reson Med. 2015;73:1549–54)

of the complementary information offered by ^{18}F-FDG PET images and MR images for the diagnosis and management of several cardiac conditions, including myocarditis [106–108], congestive heart failure [109], and cardiac sarcoidosis [107, 110–113].

In most of such studies, the imaging workflow consisted of the acquisition of a conventional cardiac MR imaging protocol, simultaneously acquired with list-mode PET data throughout the whole or most of the scanning session, resulting in a cardiac PET-MR exam duration ranging from 30 to 90 min [112, 114, 115]. This approach led to some challenges in terms of analysis and interpretability of the simultaneously acquired PET and MR data. Whereas cardiac MR images are typically acquired with different geometries and orientations, including, for instance, two-chamber, four-chamber, and short-axis 2D cine and LGE images and occasionally whole-heart 3D CMRA, the simultaneously acquired cardiac PET images are intrinsically 3D. Moreover, while several of these MR images are acquired using ECG-triggering techniques to minimize cardiac motion and are usually performed under breath-hold to minimize respiratory motion, cardiac PET imaging protocols rarely incorporate motion compensation techniques, producing images blurred by physiological motion, leading to misaligned PET and MR images that are difficult to interpret together.

More recently, technical developments in motion compensation for cardiac PET-MR have focused on improving PET image quality by acquiring MR images with enough resolution and soft-tissue contrast simultaneously with PET, so that motion information obtained from such MR images can be used to correct the PET data. Some of these approaches have been also used to correct the MR data, enabling the acquisition of truly simultaneous diagnostic co-registered MR and PET images. Furthermore, the flexibility of PET to target specific molecular processes has stimulated the development of novel radiotracers for targeting different mechanisms of cardiovascular disease, for both conventional PET imaging and simultaneous PET-MR imaging. This section describes technical innovations for cardiac PET-MR, focusing on novel motion compensation techniques, and describes recently introduced PET radiotracers that could be of particular interest for cardiac PET-MR imaging.

14.4.1 Motion-Compensated Cardiac PET-MR Imaging

Simultaneous PET-MR systems have made possible the use of MR-measured motion information to correct the motion-degraded PET data. While the first approaches for MR-based PET respiratory motion compensation focused mainly on enhancing image quality for ^{18}F-FDG PET-MR in thoracic and abdominal oncology imaging, the growing interest in cardiovascular PET-MR applications has encouraged the extension of such techniques to cardiac imaging. Most of the current approaches for motion compensation in cardiac PET-MR estimate the motion-induced deformation of the heart by using one of the following techniques: (1) pre-calibrated motion modelling, where MR images are acquired before or during the first few minutes of the PET acquisition to create a motion model that is then used to correct for motion during the whole PET acquisition or (2) simultaneous motion modelling techniques, where motion information is obtained by applying image-based registration algorithms to MR images acquired throughout the whole PET data acquisition (Fig. 14.16).

In order to measure cardiac or respiratory motion from MR images, two components are required: first, a signal related to the cardiac and/or breathing cycle is

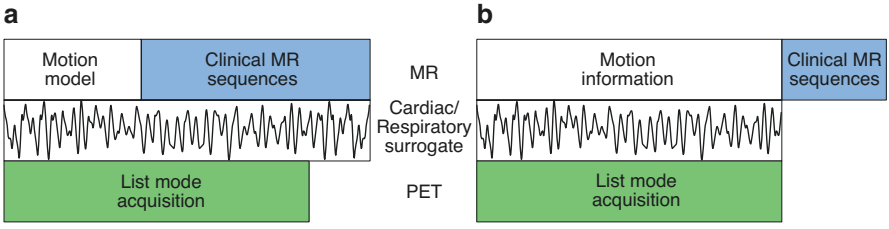

Fig. 14.16 Conventional approaches for MR-based motion correction of PET data in cardiac PET-MR imaging. (**a**) Pre-calibrated motion models estimate a motion model before or during the first part of the PET-MR examination. (**b**) Simultaneous motion models estimate motion information by using MR images acquired throughout the whole PET data acquisition

needed for assigning the acquired data to one of a number of bins or gates, so that each of these bins contains data acquired at similar position over multiple cardiac and breathing cycles. Second, a suitable MR data acquisition protocol that allows the creation of a patient-specific motion model is required. In general, the surrogate signal is acquired simultaneously with the imaging data or derived from the data itself, so that the created model approximates the relationship between the surrogate and the motion.

Once the motion information is available, two different approaches can be used to compensate for motion in the PET images: reconstruct transform average (RTA) or motion-compensated image reconstruction (MCIR). In RTA approaches [116], the acquired data is first binned into a number of near motion-free datasets which are reconstructed independently. Once all datasets have been reconstructed, motion information is used to transform the frames back to a reference position, and subsequently transformed frames are aggregated so that one motion-compensated image is obtained using all measured data. Alternatively, in MCIR approaches [117] the motion information is incorporated as an additional term in the update equation of an iterative PET image reconstruction algorithm, so that a motion-corrected image is directly obtained by modelling the motion during the image reconstruction process. Since the introduction of simultaneous PET-MR scanners, a variety of MR imaging sequences have been proposed to estimate respiratory-, cardiac-, or respiratory and cardiac-induced motion of the heart. Such sequences have been used in combination with either method of motion compensation of the cardiac PET data, as described hereafter.

14.4.1.1 Respiratory Motion Compensation

Although variety approaches have been proposed to measure and correct for respiratory motion in oncologic PET-MR imaging [118–120], just a couple of studies have been performed to assess the impact of respiratory motion correction of cardiac PET data in the context of cardiac PET-MR imaging. In the study by Fieseler et al. [121], a pre-calibrated motion model is created by acquiring 35 near real-time 3D T_1-weighted MR images. Using an image-based navigator as MR surrogate respiratory signal, each acquired volume is classified according to their position within the respiratory cycle, and six of them covering the whole respiratory cycle are chosen to form the motion model. In parallel, a PET data-driven respiratory surrogate is obtained, which allows the binned PET data to be related to the MR-based motion model. This approach was used in an RTA framework to correct PET data acquired throughout 20 min from a cardiac phantom that modelled both respiratory and cardiac motion, and an improved correspondence to the anatomy depicted in the MR images was observed after motion correction.

A pre-calibrated motion model approach was also proposed by Kolbitsch et al. [122] where a short 75 s MR acquisition was used to simultaneously provide respiratory motion information and respiratory-resolved attenuation maps for accurate attenuation correction of the PET data. In this study, the proposed MR sequence consisted of a triple-echo Dixon scan acquired following a 3D golden radial phase encoding (GRPE) trajectory [123], which can be used to extract a respiratory signal from the

data itself (i.e. a self-navigator signal), sampled every 750 ms. Interestingly, the proposed MR sequence not only provided a motion model but also motion-resolved attenuation maps, that were incorporated in a MCIR framework for improved accuracy of attenuation correction of the PET data. This framework was tested in a cohort of six patients without known cardiac disease, and findings show improvements in PET image quantification compared to uncorrected reconstructions. While this approach was also used to correct the triple-echo Dixon images for respiratory motion, these MR images showed reduced contrast between blood and myocardium due to the absence of preparation pulses, and limited spatial resolution for visualization of the relevant cardiac structures, impairing the diagnostic use of such MR images.

A different approach for simultaneous respiratory motion-corrected cardiac MR angiography and cardiac PET imaging was proposed by Munoz et al. [124]. In this work, 3D CMRA data is acquired using a T_1-weighted gradient echo sequence, following a golden-step Cartesian spiral (CASPR) sampling trajectory [43]. The acquisition scheme also includes the acquisition of 2D iNAVs at each heartbeat enabling the estimation of foot-head and right-left motion of the heart during the respiratory cycle in a heartbeat-to-heartbeat fashion. Using the foot-head motion as a respiratory signal surrogate, both the PET and CMRA data are binned into a number of respiratory windows. Then, MR images reconstructed at each respiratory position are used to estimate 3D non-rigid motion fields, which are used for correcting both the CMRA and PET data to the same respiratory position, using an RTA approach to correct the PET data (Fig. 14.17). While this is a simultaneous motion model approach, which measures motion throughout the whole PET-CMRA acquisition, it produces co-registered diagnostic images in both imaging modalities, potentially improving the interpretability of both PET and MR images together. This approach

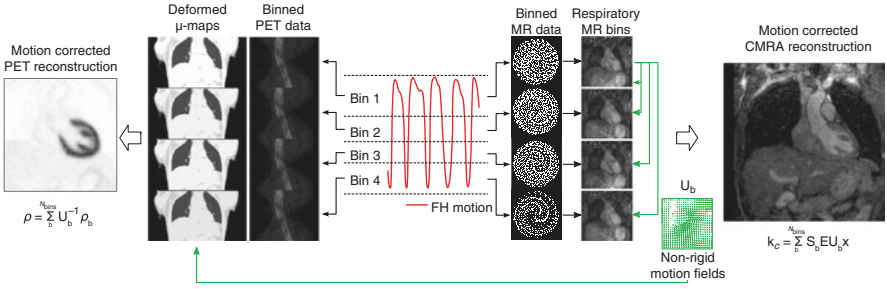

Fig. 14.17 Motion-corrected PET-CMRA reconstruction scheme proposed in [124]. Foot-head (FH) respiratory motion, estimated from image navigators integrated in the CMRA acquisition sequence, is used to bin the acquired 3D CMRA and PET data into respiratory windows or 'bins'. MR images reconstructed at each of these respiratory positions are used to estimate 3D non-rigid motion fields (in green). These motion fields are then used to correct both PET (emission and attenuation) and CMRA data to the same respiratory position, resulting in co-registered diagnostic images, facilitating the fusion and joint interpretation of findings from both imaging modalities. (Modified from Munoz C, Neji R, Cruz G, et al. *Motion-corrected simultaneous cardiac positron emission tomography and coronary MR angiography with high acquisition efficiency*. Magn Reson Med. 2017;79:339–50)

was first tested in oncology patients [124], and then in a small cohort of patients with cardiovascular disease [125], showing promising results for a comprehensive assessment of coronary disease.

14.4.1.2 Cardiac Motion Compensation

Cine MR imaging is one of the most widely used approaches for tracking cardiac-induced motion of the heart. For instance, a stack of 2D cine MR images is proposed in [121] to estimate cardiac motion in a phantom PET-MR study, using non-rigid registration of 25 cardiac phases with respect to an arbitrary reference phase and an RTA approach to correct the PET images for cardiac motion. A drawback of this approach is that as the motion is estimated from 2D images, no information about 3D motion is available. Furthermore, if such an approach were applied to patient studies, the acquisition of the stack of 2D cine images would be performed in a series of breath-holds, leading to potential inaccuracies in the motion estimation due to misalignment between slices.

An alternative sequence commonly used for measuring cardiac motion is tagged MRI. In this approach, a sinusoidal pattern of alternating bright and dark stripes is superimposed over the MR image being acquired, and the deformation of the pattern over time enables the visualization and estimation of cardiac motion. In the context of cardiac PET-MR, tagged MR images have been successfully used in cardiac beating phantom studies [126], proof-of-concept clinical studies [127] and more recently in myocardial perfusion pre-clinical studies [128], using MCIR for cardiac motion correction of the PET data in all cases.

One of the main advantages of the tagged MR approach is that thanks to the superimposed pattern, accurate motion measurements can be performed even in regions with uniform contrast such as the left ventricle myocardium. Furthermore, by acquiring a set of tagged MR images in multiple orthogonal planes (i.e. coronal, sagittal, transverse) a complete description of 3D cardiac motion can be obtained, though at the expense of prolonged acquisition times. As reported in [127], the acquisition time of fully sampled tagged MR images for nine cardiac phases was longer than 8 min, so that this technique would likely be used as a simultaneous motion model. In order to move towards a pre-calibrated motion model approach, half *k*-space acquisition [126] and compressed sensing and parallel imaging techniques [127] have been proposed to accelerate the acquisition of tagged MR images. Indeed, Huang et al. [127] demonstrated that measuring cardiac motion from tagged MR images acquired with up to 3×-accelerated GRAPPA parallel imaging [65] or up to 8×-accelerated kt-FOCUSS compressed sensing [129] yields cardiac motion-corrected PET images with similar image quality as those corrected with cardiac motion measured from fully sampled tagged MR images. This significant reduction of time dedicated to cardiac motion estimation could enable the acquisition of clinically relevant MR sequences during the simultaneous PET-MR examination.

14.4.1.3 Respiratory and Cardiac Motion Compensation

Although cardiac-only and respiratory-only motion correction studies have showed promising results in terms of PET image quality and quantification, a more general

approach to motion compensation in cardiac PET-MR requires addressing both cardiac and respiratory motion simultaneously. Several approaches have been recently proposed in the literature, focusing on the impact of accurate motion correction in simulations, oncologic patients, and preliminary studies in cardiovascular patients.

A popular choice for MR-based cardiac and respiratory motion estimation is the 3D golden radial stack-of-stars T_1-weighted MR sequences. This sequence has the advantage of enabling the estimation of cardiac and respiratory surrogates from the MR data itself, removing the need of using additional motion surrogates. For instance, in [130] a 3D golden radial stack-of-stars sequence is continuously acquired during 5 min. Using cardiac and respiratory motion surrogates estimated from the *k*-space centre, the acquired MR data was sorted into 20 respiratory and 12 cardiac overlapping phases. In order to produce images with sufficient quality for motion estimation, a two-step approach was used in this study. In the first step, MR data was binned into 20 respiratory phases neglecting any cardiac motion, and images were used to estimate respiratory motion only. In the second step, respiratory motion was used to correct the MR raw data to a reference respiratory position, and then the corrected MR data is binned into 12 cardiac phases to produce cardiac motion estimates. The respiratory and cardiac motion fields can then be combined to warp the data at any cardiac and respiratory phase to the reference mid-diastolic, end-expiratory position.

The same stack-of-stars trajectory was used in [131] to correct PET data for cardiac and respiratory motion. However, in this study authors stated that cardiac-induced motion of the heart is more complex than the respiratory-induced motion, so images of higher resolution are required to estimate it accurately. Therefore, they propose the use of two separate acquisitions to create the cardiac and respiratory motion model: a first low-resolution acquisition covering the whole thorax for respiratory motion estimation only, and a second high-resolution whole-heart acquisition for cardiac motion estimation only (Fig. 14.18). In this study, PET data was binned into four respiratory and three cardiac phases, and each bin was independently reconstructed following an RTA approach for motion correction. The PET images were first transformed to end-expiration using the corresponding respiratory motion transformation, and then transformed to late-diastole using the cardiac motion fields.

Due to the length of the MR data acquisition, both of these studies used a simultaneous motion model approach. However, similar acquisition approaches have been used to create pre-calibrated motion models. For instance, the GRPE trajectory described before was used in [132] to produce cardiac and respiratory motion estimates in less than 5 min. Using a self-navigator for respiratory gating and an external ECG device for cardiac gating, the acquired MR data was sorted in to eight respiratory and 8–12 cardiac phases. Following an approach similar to [130], in a first step the cardiac binning is ignored to produce good quality images for respiratory motion estimation, while in the second step respiratory motion-corrected data is used for cardiac binning, and subsequently for cardiac motion estimation. Finally, motion fields are combined and used in a MCIR framework (Fig. 14.19).

An even shorter MR acquisition is proposed in [133], where a 90 s 3D Cartesian acquisition was used to create a cardiac and respiratory motion model. In this study,

the MR data was acquired following a variable density Cartesian pattern called ESPReSSo [134], which provides a self-navigator signal for respiratory binning in a similar fashion to previously described approaches. Using a sensor-fusion

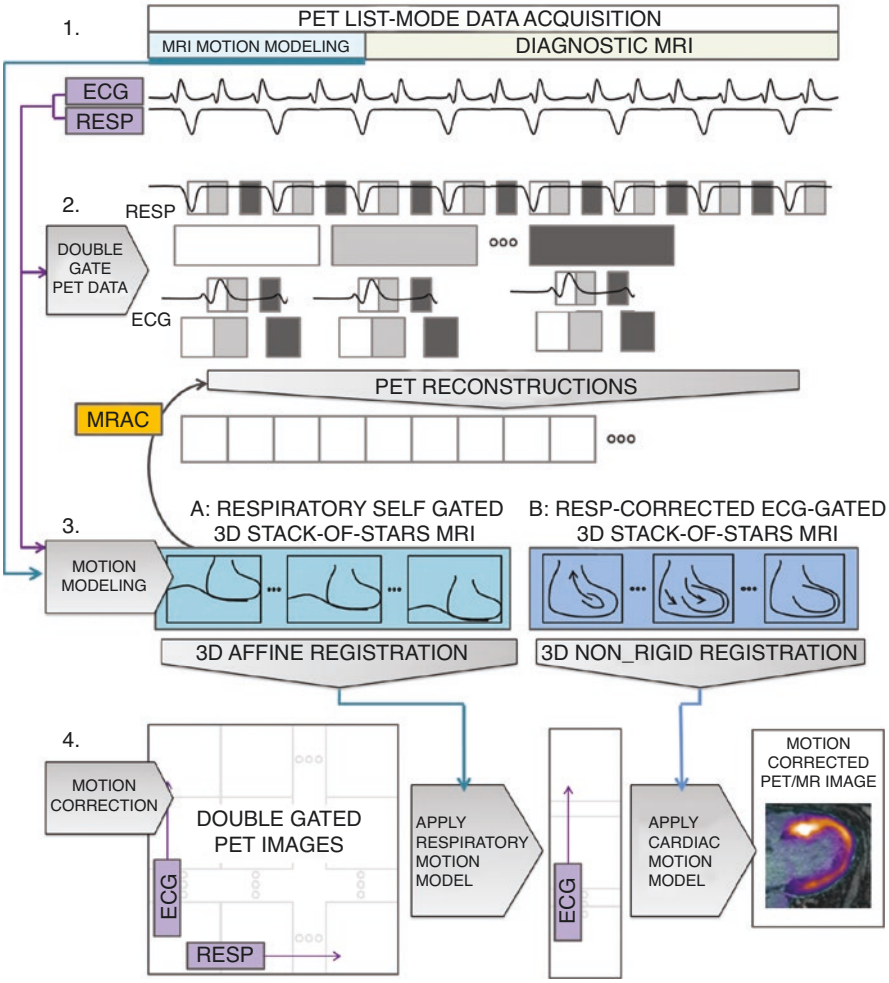

Fig. 14.18 MR-based cardiac and respiratory motion-corrected PET reconstruction proposed in [131]. List-mode PET data is dual-gated into N respiratory and M cardiac bins. PET images for each bin are then reconstructed independently. Using two dedicated MR acquisition sequences performed at the beginning of the simultaneous PET-MR acquisition, respiratory and cardiac motion fields are estimated using image registration. For respiratory motion, a 3D affine motion model is used, while for cardiac motion 3D non-rigid registration is applied. Finally, the $N \times M$ dual-gated PET images are transformed by applying the corresponding respiratory and cardiac motion fields into a reference frame and aggregated to produce the final motion-compensated PET image. (Reproduced from Robson PM, Trivieri M, Karakatsanis NA, et al. *Correction of respiratory and cardiac motion in cardiac PET/MR using MR-based motion modeling*. Phys Med Biol; 2018;63:225011)

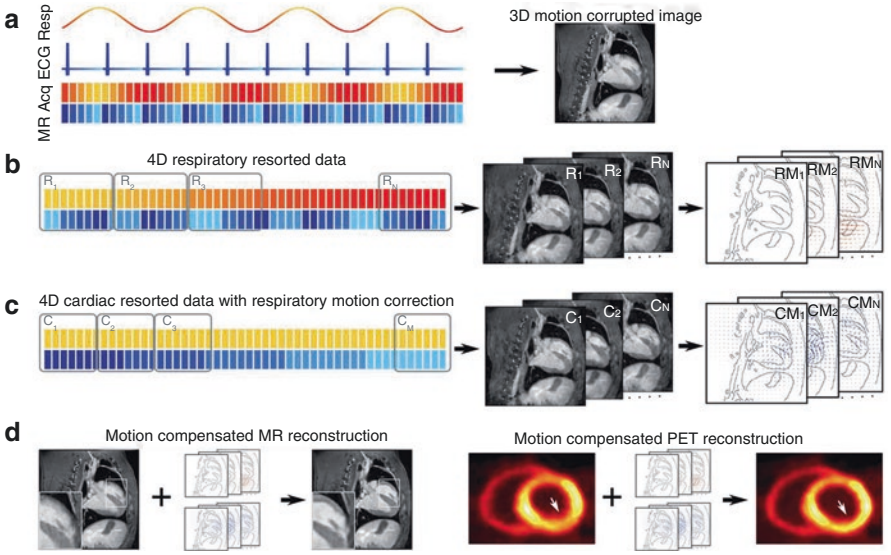

Fig. 14.19 (**a**–**d**) Cardiac and respiratory motion correction for cardiac PET/MR proposed in [132]. 3D MR data are continuously acquired during free-breathing without ECG-triggering gating over several respiratory and cardiac cycles. First, MR data are grouped in *N* different respiratory bins, and images are reconstructed for each respiratory state. Affine registration is used to estimate respiratory motion fields ($RM_1 \ldots RM_N$), which is used to correct the acquired MR data to the same respiratory position. Then, the MR data is sorted into *M* cardiac phases, and non-rigid registration is used to estimate cardiac motion fields ($CM_1 \ldots CM_M$). Finally, respiratory and cardiac motion information is used to correct both MR and PET datasets, by including the motion fields in the image reconstruction process, resulting in co-registered motion-compensated PET and MR images. (Reproduced from Kolbitsch C, Ahlman MA, Davies-Venn C, et al. *Cardiac and respiratory motion correction for simultaneous cardiac PET-MR*. J Nucl Med. 2017;58:846–52)

approach, data were binned into eight respiratory and eight cardiac phases, and a joint MR reconstruction and motion estimation scheme was used to produce the motion estimates, which were incorporated into a MCIR framework to produce motion-corrected PET images.

While the approaches described above rely on non-rigid registration of T_1-weighted images to produce motion estimates, the contrast of such images might not be optimal to track the motion of smaller cardiac structures. In [135], fat-only MR images were used to track respiratory and cardiac motion of the coronary arteries. This proof-of-concept study used simulated fat-only images for eight cardiac and six respiratory phases, showing improvements in the detectability of coronary plaques in ^{18}F-NaF PET motion-corrected images.

Other research groups have focused on the use of both MR and PET datasets to improve the reliability of cardiac and respiratory motion estimation. For instance, in the myocardial perfusion simulation study presented by Wang et al. [136], respiratory motion was estimated from cardiac-uncorrected PET images, while cardiac motion was estimated from 3D T_1-weighted MR images simulated at end-expiration.

Interestingly, in this study a combination of MCIR and RTA motion correction was used, so that respiratory motion was included in a MCIR approach at each cardiac phase and RTA was used to warp all the cardiac phases into one final motion-corrected image.

A joint image registration functional that enables the estimation of motion from PET and MR images was used in [137] to exploit the complementary information from both imaging modalities. In this study, whereas MR images provided excellent respiratory motion information, the lack of contrast between blood and myocardium impaired the MR-based cardiac motion estimation. On the contrary, ^{18}F-FDG PET images provided excellent myocardial depiction, enabling an accurate cardiac motion tracking. Results from a cohort of oncologic patients showed improved image quality when using motion fields estimated from both PET and MR compared to using either only MR or only PET to estimate motion.

14.4.2 Novel PET Radiotracers for Clinical Cardiac PET-MR Applications

A recently published joint statement by the European Society of Cardiovascular Radiology (ESCR) and the European Association of Nuclear Medicine (EANM) suggests that including hybrid PET-MR examinations in the routine clinical practice could enhance the diagnosis and aid decisions in the management of a variety of cardiac conditions, including stable coronary artery disease, acute coronary syndrome, ischaemic cardiomyopathies, and cardiac inflammation [138]. While some of these clinical applications are based on exploiting the complementary information offered by MR and conventional PET radiotracers (i.e. ^{13}N-NH_3, ^{15}O-H_2O and ^{18}F-FDG), an increasing number of them could benefit from novel PET radiotracers that target specific disease mechanisms. Table 14.1 summarizes some of these recently introduced radiotracers, indicating their mechanism and potential clinical uses.

While some of these tracers have been used for cardiac PET/CT or cardiac PET-MR in small proof-of-concept human studies, many of them have only been used in pre-clinical studies or for studying other tissues/organs. In particular, most of the radiotracers proposed for atherosclerotic plaque imaging have been demonstrated in the carotid arteries as opposed to the coronary arteries. A notable exception is ^{18}F-NaF, which has been recently demonstrated in the context of cardiac PET-MR in a cohort of 12 patients with either documented coronary artery disease or documented risk factors for developing this disease [115]. Thanks to its ability to target micro-calcification, ^{18}F-NaF has shown promise for identifying high-risk and ruptured atherosclerotic plaque. In combination with simultaneously acquired MR anatomical images that provide information about the plaque location and integrity of the artery lumen (Fig. 14.20), and in addition to novel MR sequences that allow for characterization of intraplaque haemorrhage [95, 96], the ^{18}F-NaF PET-CMR approach could potentially allow for a comprehensive non-invasive assessment of vulnerable plaque. Furthermore, simultaneous PET-MR imaging could aid the

Table 14.1 Novel radiotracers with clinical potential for cardiac PET and PET-MR imaging

Radiotracer	Mechanism	Clinical application	Selected references
^{18}F-fluciclatide	$\alpha_v\beta_3$ integrin receptors	Imaging of angiogenesis post myocardial infarction for predicting functional recovery	[139]
^{18}F-flutemetamol	β amyloid deposition	Diagnosis of cardiac amyloidosis	[140–142]
^{18}F-florbetaben			
^{18}F-florbetapir			
^{11}C-PiB	β amyloid deposition	Diagnosis of cardiac amyloidosis	[143–145]
^{18}F-NaF	Micro-calcification	Differentiation between light-chain (AL) and transthyretin (ATTR) cardiac amyloidosis	[146–148]
		Atherosclerotic plaque imaging (plaque calcification)	[149–151]
^{18}F-FMISO	Tissue hypoxia	Atherosclerotic plaque imaging (plaque hypoxia)	[152, 153]
^{18}F-choline	Inflammatory macrophages	Atherosclerotic plaque imaging (intraplaque inflammation)	[154]
^{11}C-choline			
^{18}F-flurpiridaz	Myocardial mitochondria	Myocardial perfusion/coronary artery disease	[155, 156]
^{11}C-hydroxyephedrine	Myocardial innervation	Monitoring of ischaemic cardiomyopathy, heart failure	[157, 158]
^{11}C-PK11195	Macrophages	Atherosclerotic plaque imaging (intraplaque inflammation)	[159]
^{64}Cu-DOTATATE	Macrophages	Atherosclerosis plaque imaging (inflammation)	[160, 161]
^{68}Ga-DOTATATE			
^{64}Cu-ATSM	Tissue hypoxia	Myocardial ischemia	[162, 163]

translation of the intraplaque inflammation radiotracers to coronary artery imaging, as the focal nature of the tracer uptake would require accurate cardiac and respiratory motion compensation techniques.

Another particularly promising radiotracer for cardiac PET-MR imaging is ^{18}F-flurpiridaz. PET has been long established as the reference modality for myocardial perfusion imaging, allowing for an accurate diagnosis of obstructive coronary artery disease through the assessment of stress-induced myocardial perfusion defects. However, most of the conventionally used perfusion radiotracers (i.e. ^{13}N-NH_3, ^{15}O-H_2O) require an on-site cyclotron because of their short half-life, which has prevented the wide clinical adoption of perfusion PET imaging. The introduction of ^{18}F-labelled perfusion radiotracers, such as ^{18}F-flurpiridaz (in clinical phase 3 trials at the time of writing) could advance the adoption of this technique in the clinical practice. Furthermore, in the context of cardiac PET-MR, encouraging results have been shown in a pre-clinical study for MR-based cardiac motion correction of simultaneously acquired ^{18}F-flurpiridaz data, with significant improvements in depiction of the left ventricular myocardium after motion correction [128].

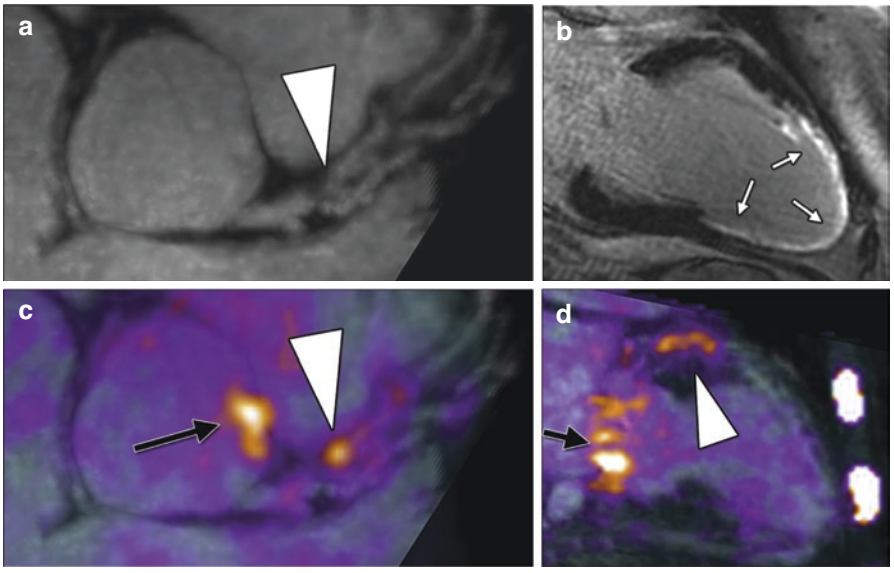

Fig. 14.20 Example images from a cardiac ^{18}F-NaF PET-MR examination. Patient exhibited an increased uptake of the radiotracer in a culprit atherosclerotic plaque in the left anterior descending coronary artery. (**a**) Luminal stenosis is observed on the MRA image, which corresponds to an area of focal ^{18}F-NaF uptake (**b**). (**c**) LGE images from the same patient show a near-transmural myocardial infarction in the corresponding territory of this lesion. (**d**) The increased ^{18}F-NaF uptake in the culprit lesion can also be observed on a 2-chamber view of the left ventricle. Please note that all images were acquired during a single PET-MR scan session. (Reproduced from Robson PM, Dweck MR, Trivieri MG, et al. *Coronary Artery PET/MR Imaging: Feasibility, Limitations, and Solutions*. JACC Cardiovasc Imaging 2017;10:1103–12)

Finally, by using an appropriate suppression of normal physiological glucose metabolism, the widely available ^{18}F-FDG can be used for imaging inflammatory response in the myocardium, reflecting only the increased glucose uptake by macrophages and other inflammatory cells. This suppression can be achieved in numerous ways [164], namely by prolonged fasting (more than 12 h), by prescribing a high-fat low-carbohydrate and protein-permitted diet for approximately 24 h before examination, by intravenous administration of unfractionated heparin or a combination of the latter two. In combination with LGE MRI, the glucose-suppressed ^{18}F-FDG PET approach has been used in several cardiac PET-MR studies, showing promise for improving the differential diagnosis in myocardial inflammation. Recent clinical experience has been reported in [109], including cases of myocarditis, congestive heart failure, and cardiac sarcoidosis. In particular, the latter has received considerable attention in the cardiac PET-MR community, as early reports suggest that the complementary information obtained by PET and MR improves the diagnostic accuracy of cardiac sarcoidosis compared to each modality alone [110–112]. Therefore, cardiac PET-MR could potentially become in the future the reference modality for a non-invasive tool for the detection and monitoring of cardiac involvement in patients with known or suspected sarcoidosis.

14.5 Concluding Remarks

MR and PET imaging are established non-invasive techniques for the diagnosis, therapy planning, and monitoring of cardiovascular disease. While conventional MR protocols have focused on the depiction of the heart anatomy and ventricular function, the introduction of advanced quantitative MR T_1, T_2 and joint T_1/T_2 mapping sequences has enabled tissue characterization, and demonstrated the potential use of these tissue properties as biomarkers for specific disease mechanisms. Moreover, novel technical developments in efficient motion compensation and accelerated data acquisition techniques have shown a variety of possible solutions for cardiac MR to achieve higher spatial resolution and whole-heart volumetric coverage within clinically feasible acquisition times.

On the other hand, cardiac PET has traditionally concentrated on imaging myocardial integrity, including perfusion and viability for the assessment of coronary disease. Emerging radiotracers could expand the range of conditions for which PET imaging can make a difference in patient care. In particular, tracers that target vascular inflammation, micro-calcification, and hypoxia in atherosclerosis have shown promising results for the identification of vulnerable plaque, and novel tracers and imaging protocols for myocardial inflammation could improve diagnosis of diseases such as myocarditis and cardiac sarcoidosis.

Despite the introduction of several technical advances that have improved image quality over the last decades, some challenges remain in both PET and MR imaging. Particularly, most of clinically available solutions to prevent image degradation due to physiological motion are based on rejecting data acquired outside quiescent periods in the cardiac and breathing cycles. These techniques require long acquisition times in order to acquire enough data, i.e. with enough signal-to-noise ratio for PET and enough samples for a desired spatial resolution and coverage for MR, increasing overall scan time and negatively impacting patient comfort and throughput.

The introduction of hybrid PET-MR scanners has enabled the development of novel techniques to alleviate the problem of motion simultaneously for both modalities. Recently proposed approaches for motion-corrected cardiac PET-MR could enable increased efficiency and improved resolution and quality in both imaging modalities, with promising results that remain to be translated to the clinical practice. This, in addition to the complementary information about different disease processes that each modality offers, could open the door for PET-MR to become the preferred modality for the assessment of the cardiovascular system from a single, efficient and comprehensive examination.

References

1. Salerno M, Kramer CM. Advances in parametric mapping with CMR imaging. JACC Cardiovasc Imaging. 2013;6:806–22.
2. Moon JC, Messroghli DR, Kellman P, Piechnik SK, Robson MD, Ugander M, et al. Myocardial T1 mapping and extracellular volume quantification: a Society for Cardiovascular Magnetic

Resonance (SCMR) and CMR Working Group of the European Society of Cardiology consensus statement. J Cardiovasc Magn Reson. 2013;15:92.
3. Messroghli DR, Radjenovic A, Kozerke S, Higgins DM, Sivananthan MU, Ridgway JP. Modified look-locker inversion recovery (MOLLI) for high-resolution T1 mapping of the heart. Magn Reson Med. 2004;52:141–6.
4. Chow K, Flewitt JA, Green JD, Pagano JJ, Friedrich MG, Thompson RB. Saturation recovery single-shot acquisition (SASHA) for myocardial T1 mapping. Magn Reson Med. 2014;71:2082–95.
5. Roujol S, Weingärtner S, Foppa M, Chow K, Kawaji K, Ngo LH, et al. Accuracy, precision, and reproducibility of four T1 mapping sequences: a head-to-head comparison of MOLLI, ShMOLLI, SASHA, and SAPPHIRE. Radiology. 2014;272:683–9.
6. Kellman P, Hansen MS. T1-mapping in the heart: accuracy and precision. J Cardiovasc Magn Reson. 2014;16:1–20.
7. Gai ND, Stehning C, Nacif M, Bluemke DA. Modified Look-Locker T1 evaluation using Bloch simulations: human and phantom validation. Magn Reson Med. 2013;69:329–36.
8. Robson MD, Piechnik SK, Tunnicliffe EM, Neubauer S. T1 measurements in the human myocardium: the effects of magnetization transfer on the SASHA and MOLLI sequences. Magn Reson Med. 2013;70:664–70.
9. Giri S, Chung YC, Merchant A, Mihai G, Rajagopalan S, Raman SV, et al. T2 quantification for improved detection of myocardial edema. J Cardiovasc Magn Reson. 2009;11:1–13.
10. Sprinkart AM, Luetkens JA, Träber F, Doerner J, Gieseke J, Schnackenburg B, et al. Gradient Spin Echo (GraSE) imaging for fast myocardial T2 mapping. J Cardiovasc Magn Reson. 2015;17:1–9.
11. Bano W, Feliciano H, Coristine AJ, Stuber M, van Heeswijk RB. On the accuracy and precision of cardiac magnetic resonance T2 mapping: a high-resolution radial study using adiabatic T2 preparation at 3 T. Magn Reson Med. 2017;77:159–69.
12. Jenista ER, Rehwald WG, Chen EL, Kim HW, Klem I, Parker MA, et al. Motion and flow insensitive adiabatic T2-preparation module for cardiac MR imaging at 3 tesla. Magn Reson Med. 2013;70:1360–8.
13. Ma D, Gulani V, Seiberlich N, Liu K, Sunshine JL, Duerk JL, et al. Magnetic resonance fingerprinting. Nature. 2013;495:187–92.
14. Hamilton JI, Jiang Y, Chen Y, Ma D, Lo W-C, Griswold M, et al. MR fingerprinting for rapid quantification of myocardial T 1, T 2, and proton spin density. Magn Reson Med. 2017;77:1446–58.
15. Hamilton JI, Jiang Y, Ma D, Lo WC, Gulani V, Griswold M, et al. Investigating and reducing the effects of confounding factors for robust T1 and T2 mapping with cardiac MR fingerprinting. Magn Reson Imaging. 2018;53:40–51.
16. Jaubert O, Cruz G, Bustin A, Schneider T, Botnar RM, Prieto C. Dixon-cMRF: cardiac tissue characterization using three-point Dixon MR fingerprinting. In: Proc ISMRM 27th Annu Meet Exhib. ISMRM; 2019. p. 1100.
17. Jaubert O, Cruz G, Bustin A, Schneider T, Koken P, Doneva M, et al. Cardiac motion resolved Magnetic Resonance Fingerprinting with joint reconstruction: jMORE-MRF. In: Proc ISMRM 27th Annu Meet Exhib. ISMRM; 2019. p. 808.
18. Christodoulou AG, Shaw JL, Nguyen C, Yang Q, Xie Y, Wang N, et al. Magnetic resonance multitasking for motion-resolved quantitative cardiovascular imaging. Nat Biomed Eng. 2018;2:215–26.
19. Stuber M, Weiss RG. Coronary magnetic resonance angiography. J Magn Reson Imaging. 2007;26:219–34.
20. Jahnke C, Paetsch I, Achenbach S, Schnackenburg B, Gebker R, Fleck E, et al. Coronary MR imaging: breath-hold capability and patterns, coronary artery rest periods, and β-blocker use. Radiology. 2006;239:71–8.
21. Gharib AM, Herzka DA, Ustun AO, Desai MY, Locklin J, Pettigrew RI, et al. Coronary MR angiography at 3T during diastole and systole. J Magn Reson Imaging. 2007;26:921–6.

22. Greil GF, Seeger A, Miller S, Claussen CD, Hofbeck M, Botnar RM, et al. Coronary magnetic resonance angiography and vessel wall imaging in children with Kawasaki disease. Pediatr Radiol. 2007;37:666–73.
23. Coppo S, Piccini D, Bonanno G, Chaptinel J, Vincenti G, Feliciano H, et al. Free-running 4D whole-heart self-navigated golden angle MRI: initial results. Magn Reson Med. 2015;74:1306–16.
24. Pang J, Chen Y, Fan Z, Nguyen C, Yang Q, Xie Y, et al. High efficiency coronary MR angiography with nonrigid cardiac motion correction. Magn Reson Med. 2016;76:1345–53.
25. Firmin D, Keegan J. Navigator echoes in cardiac magnetic resonance. J Cardiovasc Magn Reson. 2001;3:183–93.
26. Wang Y, Riederer SJ, Ehman RL. Respiratory motion of the heart: kinematics and the implications for the spatial resolution in coronary imaging. Magn Reson Med. 1995;33:713–9.
27. Danias PG, Stuber M, Botnar RM, Kissinger KV, Edelman RR, Manning WJ. Relationship between motion of coronary arteries and diaphragm during free breathing: lessons from real-time MR imaging. Am J Roentgenol. 1999;172:1061–5.
28. Taylor AM, Keegan J, Jhooti P, Firmin DN, Pennell DJ. Calculation of a subject-specific adaptive motion-correction factor for improved real-time navigator echo-gated magnetic resonance coronary angiography. J Cardiovasc Magn Reson. 1999;1:131–8.
29. Moghari MH, Hu P, Kissinger KV, Goddu B, Goepfert L, Ngo L, et al. Subject-specific estimation of respiratory navigator tracking factor for free-breathing cardiovascular MR. Magn Reson Med. 2012;67:1665–72.
30. Buehrer M, Curcic J, Boesiger P, Kozerke S. Prospective self-gating for simultaneous compensation of cardiac and respiratory motion. Magn Reson Med. 2008;60:683–90.
31. Lai P, Bi X, Jerecic R, Li D. A respiratory self-gating technique with 3D-translation compensation for free-breathing whole-heart coronary MRA. Magn Reson Med. 2009;62:731–8.
32. Henningsson M, Koken P, Stehning C, Razavi R, Prieto C, Botnar RM. Whole-heart coronary MR angiography with 2D self-navigated image reconstruction. Magn Reson Med. 2012;67:437–45.
33. Wu HH, Gurney PT, Hu BS, Nishimura DG, McConnell MV. Free-breathing multiphase whole-heart coronary MR angiography using image-based navigators and three-dimensional cones imaging. Magn Reson Med. 2013;69:1083–93.
34. Kawaji K, Spincemaille P, Nguyen TD, Thimmappa N, Cooper MA, Prince MR, et al. Direct coronary motion extraction from a 2D fat image navigator for prospectively gated coronary MR angiography. Magn Reson Med. 2014;71:599–607.
35. Keegan J, Gatehouse PD, Yang GZ, Firmin DN. Non-model-based correction of respiratory motion using beat-to-beat 3D spiral fat-selective imaging. J Magn Reson Imaging. 2007;26:624–9.
36. Scott AD, Keegan J, Firmin DN. Beat-to-beat respiratory motion correction with near 100% efficiency: a quantitative assessment using high-resolution coronary artery imaging. Magn Reson Imaging. 2011;29:568–78.
37. Moghari MH, Roujol S, Henningsson M, Kissinger KV, Annese D, Nezafat R, et al. Three-dimensional heart locator for whole-heart coronary magnetic resonance angiography. Magn Reson Med. 2014;71:2118–26.
38. Moghari MH, Annese D, Geva T, Powell AJ. Three-dimensional heart locator and compressed sensing for whole-heart MR angiography. Magn Reson Med. 2016;75:2086–93.
39. Addy NO, Ingle RR, Luo J, Baron CA, Yang PC, Hu BS, et al. 3D image-based navigators for coronary MR angiography. Magn Reson Med. 2017;77:1874–83.
40. Luo J, Addy NO, Ingle RR, Baron CA, Cheng JY, Hu BS, et al. Nonrigid motion correction with 3D image-based navigators for coronary MR angiography. Magn Reson Med. 2017;77:1884–93.
41. Stehning C, Börnert P, Nehrke K, Eggers H, Stuber M. Free-breathing whole-heart coronary MRA with 3D radial SSFP and self-navigated image reconstruction. Magn Reson Med. 2005;54:476–80.

42. Piccini D, Littmann A, Nielles-Vallespin S, Zenge MO. Respiratory self-navigation for whole-heart bright-blood coronary MRI: methods for robust isolation and automatic segmentation of the blood pool. Magn Reson Med. 2012;68:571–9.
43. Prieto C, Doneva M, Usman M, Henningsson M, Greil G, Schaeffter T, et al. Highly efficient respiratory motion compensated free-breathing coronary MRA using golden-step Cartesian acquisition. J Magn Reson Imaging. 2015;41:738–46.
44. Pang J, Bhat H, Sharif B, Fan Z, Thomson LEJ, Labounty T, et al. Whole-heart coronary MRA with 100% respiratory gating efficiency: self-navigated three-dimensional retrospective image-based motion correction (TRIM). Magn Reson Med. 2014;71:67–74.
45. Bhat H, Ge L, Nielles-Vallespin S, Zuehlsdorff S, Li D. 3D radial sampling and 3D affine transform-based respiratory motion correction technique for free-breathing whole-heart coronary MRA with 100% imaging efficiency. Magn Reson Med. 2011;65:1269–77.
46. Yang HJ, Sharif B, Pang J, Kali A, Bi X, Cokic I, et al. Free-breathing, motion-corrected, highly efficient whole heart T2 mapping at 3T with hybrid radial-cartesian trajectory. Magn Reson Med. 2016;75:126–36.
47. Cruz G, Atkinson D, Henningsson M, Botnar RM, Prieto C. Highly efficient nonrigid motion-corrected 3D whole-heart coronary vessel wall imaging. Magn Reson Med. 2017;77:1894–908.
48. Ginami G, Lòpez K, Mukherjee RK, Neji R, Munoz C, Roujol S, et al. Non-contrast enhanced simultaneous 3D whole-heart bright-blood pulmonary veins visualization and black-blood quantification of atrial wall thickness. Magn Reson Med. 2019;81:1066–79.
49. Milotta G, Ginami G, Neji R, Prieto C, Botnar R. Simultaneous 3D whole-heart bright-blood and black blood imaging for cardiovascular anatomy and wall assessment with interleaved T2prep-IR. Magn Reson Med. 2019;82:312–25.
50. Ingle RR, Wu HH, Addy NO, Cheng JY, Yang PC, Hu BS, et al. Nonrigid autofocus motion correction for coronary MR angiography with a 3D cones trajectory. Magn Reson Med. 2014;72:347–61.
51. Piccini D, Feng L, Bonanno G, Coppo S, Yerly J, Lim RP, et al. Four-dimensional respiratory motion-resolved whole heart coronary MR angiography. Magn Reson Med. 2017;77:1473–84.
52. Correia T, Ginami G, Cruz G, Neji R, Rashid I, Botnar RM, et al. Optimized respiratory-resolved motion-compensated 3D Cartesian coronary MR angiography. Magn Reson Med. 2018;80:2618–29.
53. Feng L, Coppo S, Piccini D, Yerly J, Lim RP, Masci PG, et al. 5D whole-heart sparse MRI. Magn Reson Med. 2018;79:826–38.
54. Lustig M, Donoho D, Pauly JM. Sparse MRI: the application of compressed sensing for rapid MR imaging. Magn Reson Med. 2007;58:1182–95.
55. Piccini D, Littmann A, Nielles-Vallespin S, Zenge MO. Spiral phyllotaxis: the natural way to construct a 3D radial trajectory in MRI. Magn Reson Med. 2011;66:1049–56.
56. Rutz T, Piccini D, Coppo S, Chaptinel J, Ginami G, Vincenti G, et al. Improved border sharpness of post-infarct scar by a novel self-navigated free-breathing high-resolution 3D whole-heart inversion recovery magnetic resonance approach. Int J Cardiovasc Imaging. 2016;32:1735–44.
57. Van Heeswijk RB, Piccini D, Feliciano H, Hullin R, Schwitter J, Stuber M. Self-navigated isotropic three-dimensional cardiac T2 mapping. Magn Reson Med. 2015;73:1549–54.
58. Pang J, Sharif B, Arsanjani R, Bi X, Fan Z, Yang Q, et al. Accelerated whole-heart coronary MRA using motion-corrected sensitivity encoding with three-dimensional projection reconstruction. Magn Reson Med. 2015;73:284–91.
59. Addy NO, Ingle RR, Wu HH, Hu BS, Nishimura DG. High-resolution variable-density 3D cones coronary MRA. Magn Reson Med. 2015;74:614–21.
60. Shin T, Lustig M, Nishimura DG, Hu BS. Rapid single-breath-hold 3D late gadolinium enhancement cardiac MRI using a stack-of-spirals acquisition. J Magn Reson Imaging. 2014;40:1496–502.

61. Cheng JY, Zhang T, Ruangwattanapaisarn N, Alley MT, Uecker M, Pauly JM, et al. Free-breathing pediatric MRI with nonrigid motion correction and acceleration. J Magn Reson Imaging. 2015;42:407–20.
62. Moghari MH, Uecker M, Roujol S, Sabbagh M, Geva T, Powell AJ. Accelerated whole-heart MR angiography using a variable-density poisson-disc undersampling pattern and compressed sensing reconstruction. Magn Reson Med. 2018;79:761–9.
63. Sodickson DK, Manning WJ. Simultaneous acquisition of spatial harmonics (SMASH): fast imaging with radiofrequency coil arrays. Magn Reson Med. 1997;38:591–603.
64. Pruessmann KP, Weiger M, Scheidegger MB, Boesiger P. SENSE: sensitivity encoding for fast MRI. Magn Reson Med. 1999;42:952–62.
65. Griswold MA, Jakob PM, Heidemann RM, Nittka M, Jellus V, Wang J, et al. Generalized autocalibrating partially parallel acquisitions (GRAPPA). Magn Reson Med. 2002;47:1202–10.
66. Vincenti G, Monney P, Chaptinel J, Rutz T, Coppo S, Zenge MO, et al. Compressed sensing single-breath-hold CMR for fast quantification of LV function, volumes, and mass. JACC Cardiovasc Imaging. 2014;7:882–92.
67. Bustin A, Ginami G, Cruz G, Correia T, Ismail TF, Rashid I, et al. Five-minute whole-heart coronary MRA with sub-millimeter isotropic resolution, 100% respiratory scan efficiency, and 3D-PROST reconstruction. Magn Reson Med. 2019;81:102–15.
68. Moss AJ, Williams MC, Newby DE, Nicol ED. The updated NICE guidelines: cardiac CT as the first-line test for coronary artery disease. Curr Cardiovasc Imaging Rep. 2017;10:15.
69. Mettler FA, Huda W, Yoshizumi TT, Mahesh M. Effective doses in radiology and diagnostic nuclear medicine: a catalog. Radiology. 2008;248:254–63.
70. Stuber M, Botnar RM, Danias PG, McConnell MV, Kissinger KV, Yucel EK, et al. Contrast agent-enhanced, free-breathing, three-dimensional coronary magnetic resonance angiography. J Magn Reson Imaging. 1999;10:790–9.
71. Botnar RM, Stuber M, Danias PG, Kissinger KV, Manning WJ. Improved coronary artery definition with T2-weighted, free-breathing, three-dimensional coronary MRA. Circulation. 1999;99:3139–48.
72. Börnert P, Stuber M, Botnar RM, Kissinger KV, Manning WJ. Comparison of fat suppression strategies in 3D spiral coronary magnetic resonance angiography. J Magn Reson Imaging. 2002;15:462–6.
73. Börnert P, Koken P, Nehrke K, Eggers H, Ostendorf P. Water/fat-resolved whole-heart Dixon coronary MRA: an initial comparison. Magn Reson Med. 2014;71:156–63.
74. Nezafat M, Henningsson M, Ripley DP, Dedieu N, Greil G, Greenwood JP, et al. Coronary MR angiography at 3T: fat suppression versus water-fat separation. Magn Reson Mater Phys Biol Med. 2016;29:733–8.
75. Munoz C, Cruz G, Neji R, Botnar RM, Prieto C. Motion corrected water/fat whole-heart coronary MR angiography with 100% respiratory efficiency. Magn Reson Med. 2019;82:732–42.
76. Bastiaansen JAM, Stuber M. Flexible water excitation for fat-free MRI at 3T using lipid insensitive binomial off-resonant RF excitation (LIBRE) pulses. Magn Reson Med. 2018;79:3007–17.
77. Coristine AJ, van Heeswijk RB, Stuber M. Fat signal suppression for coronary MRA at 3T using a water-selective adiabatic T2 -preparation technique. Magn Reson Med. 2014;72:763–9.
78. Botnar RM, Stuber M, Kissinger KV, Kim WY, Spuentrup E, Manning WJ. Noninvasive coronary vessel wall and plaque imaging with magnetic resonance imaging. Circulation. 2000;102:2582–7.
79. Fayad ZA, Fuster V, Fallon JT, Jayasundera T, Worthley SG, Helft G, et al. Noninvasive in vivo human coronary artery lumen and wall imaging using black-blood magnetic resonance imaging. Circulation. 2000;102:506–10.
80. Xie J, Bi X, Fan Z, Bhat H, Shah S, Zuehlsdorff S, et al. 3D flow-independent peripheral vessel wall imaging using T 2-prepared phase-sensitive inversion-recovery steady-state free precession. J Magn Reson Imaging. 2010;32:399–408.

81. Liu CY, Bley TA, Wieben O, Brittain JH, Reeder SB. Flow-independent T2-prepared inversion recovery black-blood MR imaging. J Magn Reson Imaging. 2010;31:248–54.
82. Andia ME, Henningsson M, Hussain T, Phinikaridou A, Protti A, Greil G, et al. Flow-independent 3D whole-heart vessel wall imaging using an interleaved T2-preparation acquisition. Magn Reson Med. 2013;69:150–7.
83. Kellman P, Arai AE, McVeigh ER, Aletras AH. Phase-sensitive inversion recovery for detecting myocardial infarction using gadolinium-delayed hyperenhancement. Magn Reson Med. 2002;47:372–83.
84. Kellman P, Larson AC, Hsu L-Y, Chung Y-C, Simonetti OP, McVeigh ER, et al. Motion-corrected free-breathing delayed enhancement imaging of myocardial infarction. Magn Reson Med. 2005;53:194–200.
85. Ledesma-Carbayo MJ, Kellman P, Arai AE, McVeigh ER. Motion corrected free-breathing delayed-enhancement imaging of myocardial infarction using nonrigid registration. J Magn Reson Imaging. 2007;26:184–90.
86. Kino A, Zuehlsdorff S, Sheehan JJ, Weale PJ, Carroll TJ, Jerecic R, et al. Three-dimensional phase-sensitive inversion-recovery turbo FLASH sequence for the evaluation of left ventricular myocardial scar. Am J Roentgenol. 2009;193:W381–8.
87. Basha TA, Akçakaya M, Liew C, Tsao CW, Delling FN, Addae G, et al. Clinical performance of high-resolution late gadolinium enhancement imaging with compressed sensing. J Magn Reson Imaging. 2017;46:1829–38.
88. Roujol S, Basha TA, Akçakaya M, Foppa M, Chan RH, Kissinger KV, et al. 3D late gadolinium enhancement in a single prolonged breath-hold using supplemental oxygenation and hyperventilation. Magn Reson Med. 2013;72:850–7.
89. Kellman P, Xue H, Olivieri LJ, Cross RR, Grant EK, Fontana M, et al. Dark blood late enhancement imaging. J Cardiovasc Magn Reson. 2016;18:1–11.
90. Basha TA, Tang MC, Tsao C, Tschabrunn CM, Anter E, Manning WJ, et al. Improved dark blood late gadolinium enhancement (DB-LGE) imaging using an optimized joint inversion preparation and T 2 magnetization preparation. Magn Reson Med. 2018;79:351–60.
91. Ginami G, Neji R, Rashid I, Chiribiri A, Ismail TF, Botnar RM, et al. 3D whole-heart phase sensitive inversion recovery CMR for simultaneous black-blood late gadolinium enhancement and bright-blood coronary CMR angiography. J Cardiovasc Magn Reson. 2017;19:94.
92. Holtackers RJ, Chiribiri A, Schneider T, Higgins DM, Botnar RM. Dark-blood late gadolinium enhancement without additional magnetization preparation. J Cardiovasc Magn Reson. 2017;19:64.
93. Kellman P, Hernando D, Shah S, Zuehlsdorff S, Jerecic R, Mancini C, et al. Multiecho dixon fat and water separation method for detecting fibrofatty infiltration in the myocardium. Magn Reson Med. 2009;61:215–21.
94. Foley JRJ, Fent GJ, Garg P, Broadbent DA, Dobson LE, Chew PG, et al. Feasibility study of a single breath-hold, 3D mDIXON pulse sequence for late gadolinium enhancement imaging of ischemic scar. J Magn Reson Imaging. 2019;49:1437–45.
95. Xie Y, Kim YJ, Pang J, Kim JS, Yang Q, Wei J, et al. Coronary atherosclerosis T1-weighed characterization with integrated anatomical reference: comparison with high-risk plaque features detected by invasive coronary imaging. JACC Cardiovasc Imaging. 2017;10:637–48.
96. Ginami G, Neji R, Phinikaridou A, Whitaker J, Botnar RM, Prieto C. Simultaneous bright- and black-blood whole-heart MRI for noncontrast enhanced coronary lumen and thrombus visualization. Magn Reson Med. 2018;79:1460–72.
97. Ginami G, Lopez K, Mukherjee RK, Neji R, Munoz C, Roujol S, et al. Non-contrast enhanced simultaneous 3D whole-heart bright-blood pulmonary veins visualization and black-blood quantification of atrial wall thickness. Magn Reson Med. 2019;81:1066–79.
98. Coniglio A, Di Renzi P, Vilches Freixas G, Della Longa G, Santarelli A, Capparella R, et al. Multiple 3D inversion recovery imaging for volume T1 mapping of the heart. Magn Reson Med. 2013;69:163–70.
99. Nordio G, Henningsson M, Chiribiri A, Villa ADM, Schneider T, Botnar RM. 3D myocardial T1 mapping using saturation recovery. J Magn Reson Imaging. 2017;46:218–27.

100. Ding H, Fernandez-De-Manuel L, Schär M, Schuleri KH, Halperin H, He L, et al. Three-dimensional whole-heart T2 mapping at 3T. Magn Reson Med. 2015;74:803–16.
101. Nensa F, Poeppel TD, Beiderwellen K, Schelhorn J, Mahabadi AA, Erbel R, et al. Hybrid PET/MR imaging of the heart: feasibility and initial results. Radiology. 2013;268: 366–73.
102. Nensa F, Poeppel T, Tezgah E, Heusch P, Nassenstein K, Mahabadi AA, et al. Integrated FDG PET/MR imaging for the assessment of myocardial salvage in reperfused acute myocardial infarction. Radiology. 2015;276:400–7.
103. Bulluck H, White SK, Fröhlich GM, Casson SG, O'Meara C, Newton A, et al. Quantifying the area at risk in reperfused st-segment-elevation myocardial infarction patients using hybrid cardiac positron emission tomography-magnetic resonance imaging. Circ Cardiovasc Imaging. 2016;9:e003900.
104. Rischpler C, Langwieser N, Souvatzoglou M, Batrice A, van Marwick S, Snajberk J, et al. PET/MRI early after myocardial infarction: evaluation of viability with late gadolinium enhancement transmurality vs. 18F-FDG uptake. Eur Heart J Cardiovasc Imaging. 2015;16:661–9.
105. Kunze KP, Nekolla SG, Rischpler C, Zhang SH, Hayes C, Langwieser N, et al. Myocardial perfusion quantification using simultaneously acquired 13NH3-ammonia PET and dynamic contrast-enhanced MRI in patients at rest and stress. Magn Reson Med. 2018;80:2641.
106. Von Olshausen G, Hyafil F, Langwieser N, Laugwitz KL, Schwaiger M, Ibrahim T. Detection of acute inflammatory myocarditis in Epstein barr virus infection using hybrid 18F-fluorodeoxyglucose-positron emission tomography/magnetic resonance imaging. Circulation. 2014;130:925–6.
107. Hanneman K, Kadoch M, Guo HH, Jamali M, Quon A, Iagaru A, et al. Initial experience with simultaneous 18F-FDG PET/MRI in the evaluation of cardiac sarcoidosis and myocarditis. Clin Nucl Med. 2017;42:e328–34.
108. Nensa F, Kloth J, Tezgah E, Poeppel TD, Heusch P, Goebel J, et al. Feasibility of FDG-PET in myocarditis: comparison to CMR using integrated PET/MRI. J Nucl Cardiol. 2018;25:785–94.
109. Abgral R, Dweck MR, Trivieri MG, Robson PM, Karakatsanis N, Mani V, et al. Clinical utility of combined FDG-PET/MR to assess myocardial disease. JACC Cardiovasc Imaging. 2017;10:594–7.
110. Schneider S, Batrice A, Rischpler C, Eiber M, Ibrahim T, Nekolla SG. Utility of multimodal cardiac imaging with PET/MRI in cardiac sarcoidosis: implications for diagnosis, monitoring and treatment. Eur Heart J. 2014;35:312.
111. Wada K, Niitsuma T, Yamaki T, Masuda A, Ito H, Kubo H, et al. Simultaneous cardiac imaging to detect inflammation and scar tissue with 18F-fluorodeoxyglucose PET/MRI in cardiac sarcoidosis. J Nucl Cardiol. 2016;23:1180–2.
112. Dweck MR, Abgral R, Trivieri MG, Robson PM, Karakatsanis N, Mani V, et al. Hybrid magnetic resonance imaging and positron emission tomography with fluorodeoxyglucose to diagnose active cardiac sarcoidosis. JACC Cardiovasc Imaging. 2017;11:94–107.
113. Wicks EC, Menezes LJ, Barnes A, Mohiddin SA, Sekhri N, Porter JC, et al. Diagnostic accuracy and prognostic value of simultaneous hybrid 18F-fluorodeoxyglucose positron emission tomography/magnetic resonance imaging in cardiac sarcoidosis. Eur Heart J Cardiovasc Imaging. 2018;19:757–67.
114. Rischpler C, Nekolla SG, Kunze KP, Schwaiger M. PET/MRI of the heart. Semin Nucl Med. 2015;45:234–47.
115. Robson PM, Dweck MR, Trivieri MG, Abgral R, Karakatsanis NA, Contreras J, et al. Coronary Artery PET/MR imaging: feasibility, limitations, and solutions. JACC Cardiovasc Imaging. 2017;10:1103–12.
116. Picard Y, Thompson CJ. Motion correction of PET images using multiple acquisition frames. IEEE Trans Med Imaging. 1997;16:137–44.
117. Qiao F, Pan T, Clark JW, Mawlawi OR. A motion-incorporated reconstruction method for gated PET studies. Phys Med Biol. 2006;51:3769–83.

118. Fürst S, Grimm R, Hong I, Souvatzoglou M, Casey ME, Schwaiger M, et al. Motion correction strategies for integrated PET/MR. J Nucl Med. 2015;56:261–9.
119. Catana C. Motion correction options in PET/MRI. Semin Nucl Med. 2015;45:212–23.
120. Munoz C, Kolbitsch C, Reader AJ, Marsden P, Schaeffter T, Prieto C. MR-based cardiac and respiratory motion-compensation techniques for PET-MR imaging. PET Clin. 2016;11:179–91.
121. Fieseler M, Kugel H, Gigengack F, Kosters T, Buther F, Quick HH, et al. A dynamic thorax phantom for the assessment of cardiac and respiratory motion correction in PET/MRI: a preliminary evaluation. Nucl Inst Methods Phys Res A. 2012;702:59–63.
122. Kolbitsch C, Neji R, Fenchel M, Mallia A, Marsden P, Schaeffter T. Respiratory-resolved MR-based attenuation correction for motion-compensated cardiac PET-MR. Phys Med Biol. 2018;63:135008.
123. Prieto C, Uribe S, Razavi R, Atkinson D, Schaeffter T. 3D undersampled golden-radial phase encoding for DCE-MRA using inherently regularized iterative SENSE. Magn Reson Med. 2010;64:514–26.
124. Munoz C, Neji R, Cruz G, Mallia A, Jeljeli S, Reader AJ, et al. Motion-corrected simultaneous cardiac positron emission tomography and coronary MR angiography with high acquisition efficiency. Magn Reson Med. 2017;79:339–50.
125. Munoz C, Kunze KP, Neji R, Vitadello T, Rischpler C, Botnar RM, et al. Motion-corrected whole-heart PET-MR for the simultaneous visualisation of coronary artery integrity and myocardial viability: an initial clinical validation. Eur J Nucl Med Mol Imaging. 2018;45:1975–86.
126. Petibon Y, Ouyang J, Zhu X, Huang C, Reese TG, Chun SY, et al. Cardiac motion compensation and resolution modeling in simultaneous PET-MR: a cardiac lesion detection study. Phys Med Biol. 2013;58:2085–102.
127. Huang C, Petibon Y, Ouyang J, Reese TG, Ahlman MA, Bluemke DA, et al. Accelerated acquisition of tagged MRI for cardiac motion correction in simultaneous PET-MR: phantom and patient studies. Med Phys. 2015;42:1087–97.
128. Petibon Y, Guehl NJ, Reese TG, Ebrahimi B, Normandin MD, Shoup TM, et al. Impact of motion and partial volume effects correction on PET myocardial perfusion imaging using simultaneous PET-MR. Phys Med Biol. 2017;62:326–43.
129. Jung H, Sung K, Nayak KS, Kim EY, Ye JC. K-t FOCUSS: a general compressed sensing framework for high resolution dynamic MRI. Magn Reson Med. 2009;61:103–16.
130. Rank CM, Heußer T, Wetscherek A, Freitag MT, Schlemmer HP, Kachelrieß M. Five-dimensional respiratory and cardiac motion compensation for simultaneous PET/MR. In: 2016 IEEE Nucl Sci Symp Med Imaging Conf Room-Temperature Semicond Detect Work NSS/MIC/RTSD 2016. Washington, DC: IEEE; 2017. p. 1–4.
131. Robson PM, Trivieri M, Karakatsanis NA, Padilla M, Abgral R, Dweck MR, et al. Correction of respiratory and cardiac motion in cardiac PET/MR using MR-based motion modeling. Phys Med Biol. 2018;63:225011.
132. Kolbitsch C, Ahlman MA, Davies-Venn C, Evers R, Hansen M, Peressutti D, et al. Cardiac and respiratory motion correction for simultaneous cardiac PET-MR. J Nucl Med. 2017;58:846–52.
133. Küstner T, Schwartz M, Martirosian P, Gatidis S, Seith F, Gilliam C, et al. MR-based respiratory and cardiac motion correction for PET imaging. Med Image Anal. 2017;42:129–44.
134. Kustner T, Wurslin C, Gatidis S, Martirosian P, Nikolaou K, Schwenzer NF, et al. MR image reconstruction using a combination of compressed sensing and partial Fourier Acquisition: ESPReSSo. IEEE Trans Med Imaging. 2016;35:2447–58.
135. Petibon Y, El Fakhri G, Nezafat R, Johnson N, Brady TJ, Ouyang J. Towards coronary plaque imaging using simultaneous PET-MR: a simulation study. Phys Med Biol. 2014;59:1203–22.
136. Wang X, Rahmim A, Tang J. MRI-assisted dual motion correction for myocardial perfusion defect detection in PET imaging. Med Phys. 2017;44:4536–47.
137. Kolbitsch C, Neji R, Fenchel M, Schuh A, Mallia A, Marsden P, et al. Joint cardiac and respiratory motion estimation for motion-corrected cardiac PET-MR. Phys Med Biol. 2019;64:015007.

138. Nensa F, Bamberg F, Rischpler C, Menezes L, Poeppel TD, la Fougère C, et al. Hybrid cardiac imaging using PET/MRI: a joint position statement by the European Society of Cardiovascular Radiology (ESCR) and the European Association of Nuclear Medicine (EANM). Eur Radiol. 2018;2:14.
139. Jenkins WSA, Vesey AT, Stirrat C, Connell M, Lucatelli C, Neale A, et al. Cardiac α V β 3 integrin expression following acute myocardial infarction in humans. Heart. 2017;103:607–15.
140. Lhommel R, Sempoux C, Ivanoiu A, Michaux L, Gerber B. Is 18F-flutemetamol PET/CT able to reveal cardiac amyloidosis? Clin Nucl Med. 2014;39:747–9.
141. Law WP, Wang WYS, Moore PT, Mollee PN, Ng ACT. Cardiac amyloid imaging with 18F-florbetaben PET: a pilot study. J Nucl Med. 2016;57:1733–9.
142. Dorbala S, Vangala D, Semer J, Strader C, Bruyere JR, Di Carli MF, et al. Imaging cardiac amyloidosis: a pilot study using 18 F-florbetapir positron emission tomography. Eur J Nucl Med Mol Imaging. 2014;41:1652–62.
143. Antoni G, Lubberink M, Estrada S, Axelsson J, Carlson K, Lindsjo L, et al. In vivo visualization of amyloid deposits in the heart with 11C-PIB and PET. J Nucl Med. 2013;54:213–20.
144. Lee S-P, Lee ES, Choi H, Im H-J, Koh Y, Lee M-H, et al. 11C-Pittsburgh B PET imaging in cardiac amyloidosis. JACC Cardiovasc Imaging. 2015;8:50–9.
145. Pilebro B, Arvidsson S, Lindqvist P, Sundström T, Westermark P, Antoni G, et al. Positron emission tomography (PET) utilizing Pittsburgh compound B (PIB) for detection of amyloid heart deposits in hereditary transthyretin amyloidosis (ATTR). J Nucl Cardiol. 2018;25:240–8.
146. Trivieri MG, Dweck MR, Abgral R, Robson PM, Karakatsanis NA, Lala A, et al. 18 F-sodium fluoride PET/MR for the assessment of cardiac amyloidosis. J Am Coll Cardiol. 2016;68:2712–4.
147. Martineau P, Finnerty V, Giraldeau G, Authier S, Harel F, Pelletier-Galarneau M. Examining the sensitivity of 18F-NaF PET for the imaging of cardiac amyloidosis. J Nucl Cardiol. 2021;28:209–18.
148. Morgenstern R, Yeh R, Castano A, Maurer MS, Bokhari S. 18Fluorine sodium fluoride positron emission tomography, a potential biomarker of transthyretin cardiac amyloidosis. J Nucl Cardiol. 2018;25:1559–67.
149. Dweck MR, Chow MWL, Joshi NV, Williams MC, Jones C, Fletcher AM, et al. Coronary arterial 18F-sodium fluoride uptake: a novel marker of plaque biology. J Am Coll Cardiol. 2012;59:1539–48.
150. Joshi NV, Vesey AT, Williams MC, Shah ASV, Calvert PA, Craighead FHM, et al. 18F-fluoride positron emission tomography for identification of ruptured and high-risk coronary atherosclerotic plaques: a prospective clinical trial. Lancet. 2014;383:705–13.
151. Irkle A, Vesey AT, Lewis DY, Skepper JN, Bird JLE, Dweck MR, et al. Identifying active vascular microcalcification by 18F-sodium fluoride positron emission tomography. Nat Commun. 2015;6:7495.
152. Mateo J, Izquierdo-Garcia D, Badimon JJ, Fayad ZA, Fuster V. Noninvasive assessment of hypoxia in rabbit advanced atherosclerosis using 18f-fluoromisonidazole positron emission tomographic imaging. Circ Cardiovasc Imaging. 2014;7:312–20.
153. Joshi FR, Manavaki R, Fryer TD, Figg NL, Sluimer JC, Aigbirhio FI, et al. Vascular imaging with 18 F-fluorodeoxyglucose positron emission tomography is influenced by hypoxia. J Am Coll Cardiol. 2017;69:1873–4.
154. Voo S, Kwee RM, Sluimer JC, Schreuder FH, Wierts R, Bauwens M, et al. Imaging intraplaque inflammation in carotid atherosclerosis with 18F-fluorocholine positron emission tomography-computed tomography: prospective study on vulnerable atheroma with immunohistochemical validation. Circ Cardiovasc Imaging. 2016;9:e004467.
155. Huisman MC, Higuchi T, Reder S, Nekolla SG, Poethko T, Wester H-J, et al. Initial characterization of an 18F-labeled myocardial perfusion tracer. J Nucl Med. 2008;49:630–6.
156. Berman DS, Maddahi J, Tamarappoo BK, Czernin J, Taillefer R, Udelson JE, et al. Phase II safety and clinical comparison with single-photon emission computed tomography myocardial perfusion imaging for detection of coronary artery disease: flurpiridaz F 18 positron emission tomography. J Am Coll Cardiol. 2013;61:469–77.

157. Harms HJ, Lubberink M, de Haan S, Knaapen P, Huisman MC, Schuit RC, et al. Use of a single 11C-meta-hydroxyephedrine scan for assessing flow-innervation mismatches in patients with ischemic cardiomyopathy. J Nucl Med. 2015;56:1706–11.
158. Aikawa T, Naya M, Obara M, Manabe O, Tomiyama Y, Magota K, et al. Impaired myocardial sympathetic innervation is associated with diastolic dysfunction in heart failure with preserved ejection fraction: 11 C-hydroxyephedrine PET study. J Nucl Med. 2016;58:784–90.
159. Gaemperli O, Shalhoub J, Owen DRJ, Lamare F, Johansson S, Fouladi N, et al. Imaging intraplaque inflammation in carotid atherosclerosis with 11 C-PK11195 positron emission tomography/computed tomography. Eur Heart J. 2012;33:1902–10.
160. Pedersen SF, Sandholt BV, Keller SH, Hansen AE, Clemmensen AE, Sillesen H, et al. ^{64}Cu-DOTATATE PET/MRI for detection of activated macrophages in carotid atherosclerotic plaques. Arterioscler Thromb Vasc Biol. 2015;35:1696–703.
161. Tarkin JM, Joshi FR, Evans NR, Chowdhury MM, Figg NL, Shah AV, et al. Detection of atherosclerotic inflammation by 68Ga-DOTATATE PET compared to [18F]FDG PET imaging. J Am Coll Cardiol. 2017;69:1774–91.
162. Fujibayashi Y, Cutler CS, Anderson CJ, McCarthy DW, Jones LA, Sharp T, et al. Comparative studies of Cu-64-ATSM and C-11-acetate in an acute myocardial infarction model: ex vivo imaging of hypoxia in rats. Nucl Med Biol. 1999;26:117–21.
163. Lewis JS, Herrero P, Sharp TL, Engelbach JA, Fujibayashi Y, Laforest R, et al. Delineation of hypoxia in canine myocardium using PET and copper(II)-diacetyl-bis(N4-Methylthiosemicarbazone). J Nucl Med. 2002;43:1557–69.
164. Dilsizian V, Bacharach SL, Beanlands RS, Bergmann SR, Delbeke D, Dorbala S, et al. ASNC imaging guidelines/SNMMI procedure standard for positron emission tomography (PET) nuclear cardiology procedures. J Nucl Cardiol. 2016;23:1187–226.